

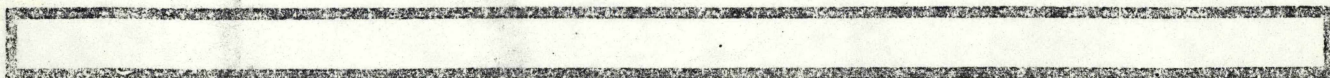
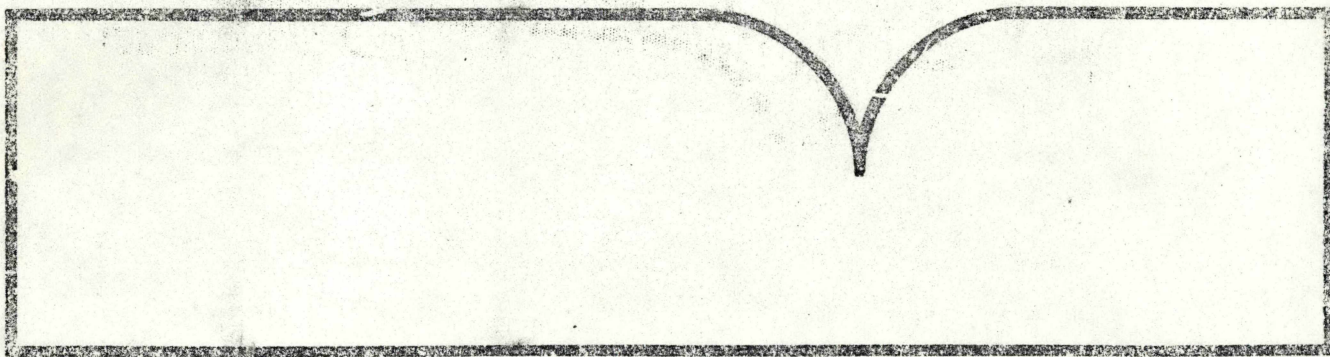
PB82-129610

Engineering Analysis of
Stresses in Railroad Rails

Battelle Columbus Labs., OH

Prepared for
Federal Railroad Administration
Washington, DC

Oct 81



U.S. Department of Commerce
National Technical Information Service

NTIS

PB82-129610



U.S. Department
of Transportation
Federal Railroad
Administration

Engineering Analysis of Stresses in Railroad Rails

T. G. Johns
S. G. Sampath
J. C. Bell
K. B. Davies

Battelle Columbus Laboratories
505 King Avenue
Columbus, OH 43201

Office of Research
and Development
Washington, D.C. 20590

FRA/ORD-81/51
Final Report
October 1981

This document is available to
the U.S. public through the
National Technical Information
Service, Springfield, Virginia
22161

REPRODUCED BY
NATIONAL TECHNICAL
INFORMATION SERVICE
U.S. DEPARTMENT OF COMMERCE
SPRINGFIELD, VA 22161

Technical Report Documentation Page

1. Report No. FRA/ORD-81/51		2. Government Accession No.		3. Recipient's Catalog No. PB82 1 2961 0	
4. Title and Subtitle ENGINEERING ANALYSIS OF STRESSES IN RAILROAD RAILS				5. Report Date October 1981.	
				6. Performing Organization Code 314012	
7. Author(s) T.G. Johns, S.G. Sampath, J.C. Bell, K.B. Davies				8. Performing Organization Report No. G-6266-0100 DOT-TSC-FRA-81-8	
9. Performing Organization Name and Address Battelle Columbus Laboratories* 505 King Avenue Columbus OH 43201				10. Work Unit No. (TRAIS) RR119/R1327	
				11. Contract or Grant No. DOT/TSC-1038	
12. Sponsoring Agency Name and Address U.S. Department of Transportation Federal Railroad Administration Office of Research and Development Washington DC 20590				13. Type of Report and Period Covered Final Report Jan 1977-June 1981	
				14. Sponsoring Agency Code	
15. Supplementary Notes *Under contract to:		U.S. Department of Transportation Research and Special Programs Administration Transportation Systems Center Cambridge MA 02142			
16. Abstract One portion of the Federal Railroad Administration's (FRA) Track Performance Improvement Program is the development of engineering and analytic techniques required for the design and maintenance of railroad track of increased integrity and safety. Under the program management of Transportation Systems Center (TSC), a part of this program is to predict the reliability of rail in track. A necessary requirement for development of these techniques is the ability to determine the stress and strain history of the rails in service. This is necessary to form a more comprehensive basis for a quantitative understanding of flaw initiation and growth. This report is to provide a comprehensive description of stresses in rail required for predicting reliability of rail in track structures. Contained is a description of stresses encountered in cracked and uncracked railroad rails at midrail stations and bolted joints as computed using analytical techniques developed in this program.					
17. Key Words rail joints, head/web separations, rail, rail stress, stress, flexural stresses, contact stresses, plastic flow, railroad track, transverse fis- sure, vertical and horizontal split head, bolt hole cracks				18. Distribution Statement DOCUMENT IS AVAILABLE TO THE PUBLIC THROUGH THE NATIONAL TECHNICAL INFORMATION SERVICE, SPRINGFIELD, VIRGINIA 22161	
19. Security Classif. (of this report) Unclassified		20. Security Classif. (of this page) Unclassified		21. No. of Pages 396	22. Price

NOTICE

This document is disseminated under the sponsorship of the U.S. Departments of Defense and Transportation in the interest of information exchange. The U.S. Government assumes no liability for its contents or use thereof.

NOTICE

The U.S. Government does not endorse products or manufacturers. Trade or manufacturers' names appear herein solely because they are considered essential to the objectives of this report.

PREFACE

This report presents the results of a two-phase program on an Engineering Analysis of Stresses in Railroad Rails. It has been prepared by Battelle's Columbus Laboratories (BCL) under Contract DOT-TSC-1038 for the Transportation Systems Center (TSC) and the Department of Transportation. The program was conducted under the technical direction of Donald McConnell, Code 744, at the Transportation Systems Center.

This report is one of a series prepared to provide a comprehensive description of stresses in rail required for predicting reliability of rail in track structures. It deals with mid rail sections, away from rail joints and with bolted joint. The work performed in this study was directed at providing comprehensive descriptions of the stresses in rail in sufficient detail that they may be used for predicting reliability of rail in these structures. This work extends the preliminary description of stresses in railroad rail as reported in FRA-ORD-76-294.* The previous report, which documents the literature, contains much data which are not reported herein.

In addition, numerous analysis tools were developed which will prove to be useful in the design of track structures. These tools are briefly described herein, but described in greater detail in separate report documents.

The cooperation and assistance of Donald McConnell of TSC, P. McGuire, R. Mesloh, and J. Kennedy of BCL, and R. Steele of the Transportation Test Center, Pueblo, Colorado, are gratefully acknowledged.

*Johns, T.G., and Davies, K.B., "A Preliminary Description of Stresses in Railroad Rail", Battelle Columbus Laboratories DOT-TSC-FRA-76-23/FRA-ORD-76-294 (November 1976). The NTIS Accession Number for this report is: PB272 054.

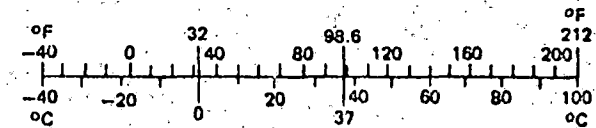
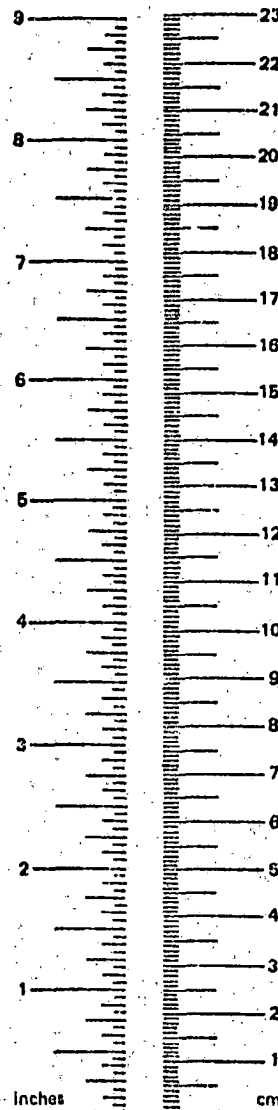
METRIC CONVERSION FACTORS

Approximate Conversions to Metric Measures

Symbol	When You Know	Multiply by	To Find	Symbol
LENGTH				
in	inches	2.5	centimeters	cm
ft	feet	30	centimeters	cm
yd	yards	0.9	meters	m
mi	miles	1.6	kilometers	km
AREA				
in ²	square inches	6.5	square centimeters	cm ²
ft ²	square feet	0.09	square meters	m ²
yd ²	square yards	0.8	square meters	m ²
mi ²	square miles	2.6	square kilometers	km ²
	acres	0.4	hectares	ha
MASS (weight)				
oz	ounces	28	grams	g
lb	pounds	0.45	kilograms	kg
	short tons (2000 lb)	0.9	tonnes	t
VOLUME				
tsp	teaspoons	5	milliliters	ml
Tbsp	tablespoons	15	milliliters	ml
fl oz	fluid ounces	30	milliliters	ml
c	cups	0.24	liters	l
pt	pints	0.47	liters	l
qt	quarts	0.95	liters	l
gal	gallons	3.8	liters	l
ft ³	cubic feet	0.03	cubic meters	m ³
yd ³	cubic yards	0.76	cubic meters	m ³
TEMPERATURE (exact)				
°F	Fahrenheit temperature	5/9 (after subtracting 32)	Celsius temperature	°C

Approximate Conversions from Metric Measures

Syn.ool	When You Know	Multiply by	To Find	Symbol
LENGTH				
mm	millimeters	0.04	inches	in
cm	centimeters	0.4	inches	in
m	meters	3.3	feet	ft
m	meters	1.1	yards	yd
km	kilometers	0.6	miles	mi
AREA				
cm ²	square centimeters	0.16	square inches	in ²
m ²	square meters	1.2	square yards	yd ²
km ²	square kilometers	0.4	square miles	mi ²
ha	hectares (10,000 m ²)	2.5	acres	
MASS (weight)				
g	grams	0.035	ounces	oz
kg	kilograms	2.2	pounds	lb
t	tonnes (1000 kg)	1.1	short tons	
VOLUME				
ml	milliliters	0.03	fluid ounces	fl oz
l	liters	2.1	pints	pt
l	liters	1.06	quarts	qt
l	liters	0.26	gallons	gal
m ³	cubic meters	36	cubic feet	ft ³
m ³	cubic meters	1.3	cubic yards	yd ³
TEMPERATURE (exact)				
°C	Celsius temperature	9/5 (then add 32)	Fahrenheit temperature	°F



*1 in. = 2.54 cm (exactly). For other exact conversions and more detail tables see NBS Misc. Publ. 286, Units of Weight and Measures, Price \$2.25 SO Catalog No. C13 10 286.

TABLE OF CONTENTS

<u>Section</u>	<u>Page</u>
1. EXECUTIVE DIGEST.	1-1
1.1 THE PROBLEM OF RAIL FRACTURES	1-1
1.2 STRESSES CONTRIBUTING TO RAIL FRACTURES	1-5
1.3 OBSERVATIONS CONCERNING CRACK INITIATION AND GROWTH	1-24
1.4 REPORT ORGANIZATION	1-27
2. STRESSES DUE TO FLEXURE	2-1
2.1 ANALYTICAL MODELS FOR THE CALCULATION OF FLEXURAL STRESSES.	2-1
2.2 FLEXURAL STRESSES IN RAILS UNDER VARIOUS CONDITIONS	2-9
2.3 CONCLUSIONS REGARDING BENDING STRESS.	2-24
3. STRESSES LOCAL TO THE WHEEL/RAIL CONTACT REGION	3-1
3.1 LOADS AND STRESSES FROM CONTACT BETWEEN REGULAR SURFACES.	3-1
3.2 CONTACT PRESSURES BETWEEN WORN WHEELS AND RAILS . . .	3-12
3.3 SUBSURFACE RAIL STRESS DISTRIBUTION FROM WHEEL/RAIL CONTACT	3-37
4. SUBSURFACE STRESS DISTRIBUTION IN RAIL HEADS DUE TO PLASTIC DEFORMATION.	4-1
4.1 PREVIOUS INVESTIGATIONS OF SUBSURFACE STRESSES DUE TO PLASTIC DEFORMATION.	4-1
4.2 RECENT INVESTIGATIONS OF RESIDUAL STRESSES IN RAIL HEADS.	4-8
5. STRESSES AROUND RAIL-HEAD CRACKS	5-1
5.1 SOME FUNDAMENALS OF FRACTURE MECHANICS.	5-1

TABLE OF CONTENTS
(Continued)

<u>Section</u>	<u>Page</u>
5.2 ANALYSES OF STRESSES AROUND CRACKS IN RAIL HEADS. . .	5-6
6. LABORATORY STUDY OF BOLTED-JOINT BEHAVIOR	6-1
6.1 DESCRIPTION OF THE TEST SETUP AND PROCEDURES.	6-1
6.2 RESULTS OF LABORATORY EVALUATIONS	6-8
7. LOAD TRANSFER IN BOLTED JOINTS.	7-1
7.1 A SIMPLIFIED APPROACH TO LOAD TRANSFER: BEAM ON ELASTIC-FOUNDATION MODEL OF JOINTED-RAIL TRACK. . .	7-1
7.2 NUMERICAL LOAD TRANSFER MODELING.	7-17
7.3 *COMPARISON OF APPROACHES TO CALCULATING JOINT REACTIONS	7-26
8. STRESSES IN THE RAIL END.	8-1
8.1 METHODS OF CALCULATING RAIL-END STRESSES.	8-1
8.2 FINITE-ELEMENT RESULTS.	8-4
9. STRESS-INTENSITY FACTORS FOR RAIL-END CRACKS.	9-1
9.1 METHODS OF CALCULATING STRESS-INTENSITY FACTORS FOR CRACKED-RAIL ENDS	9-1
9.2 STRESS-INTENSITY-FACTOR RESULTS FOR BOLT-HOLE CRACKS.	9-5
9.3 STRESS-INTENSITY-FACTOR VALUES FOR HEAD-WEB SEPARATION SITUATION.	9-14
10. CONCLUSIONS AND SUGGESTIONS FOR FUTURE WORK	10-1
REFERENCES	R-1

TABLE OF CONTENTS
(Continued)

<u>Appendix</u>	<u>Page</u>
A. VALIDATION OF FINITE ELEMENT FULL-RAIL MODELS	A-1
B. FLEXURAL STRESSES (NEAR WHEEL/RAIL CONTACT COMPUTED FROM FINITE MODELS)	B-1
C. SHAKEDOWN OF STRESSES FROM ROLLING CONTACT	C-1
D. DESCRIPTION OF A MODEL FOR DETERMINING RESIDUAL STRESSES IN RAILS.	D-1
E. MEASUREMENTS OF REPRESENTATIVE RESIDUAL STRESSES DUE TO ROLLING CONTACT ON RAILS	E-1
F. STRESS INTENSITY FACTORS FOR LOADED ELLIPTICAL CRACKS	F-1
G. REPORT OF NEW TECHNOLOGY	G-1

LIST OF ILLUSTRATIONS

<u>Figure</u>		<u>Page</u>
1-1.	Typical Railhead Defects	1-4
1-2.	Typical Contributions of Bending to Longitudinal Stress on Top of Rail.	1-8
1-3.	Stresses Developed in 132-Lb RE Rail head at Depth of 0.10-Inch Due to 35-Inch Diameter Wheel and Wheel Load of 19,000 Lb.	1-11
1-4.	Measured Values of Residual Stresses in a Used Rail	1-14
1-5.	Geometry of Joint Assembly	1-17
1-6.	Most Common Hole Crack Geometry.	1-19
1-7.	Combined Head Web Separation and Bolt-Hole Crack	1-20
1-8.	Axial Stress Distribution Around a Circular Crack Loaded in Bending.	1-23
1-9.	Fatigue Test on 109-Lb/7/8 FB Rail Drilled with Standard Bolt Holes	1-26
1-10.	Modeling Approach to Rail End Failure.	1-29
2-1.	Infinite Rail with Central Point Load.	2-4
2-2.	Maximum Tie Spacing Allowable While Using Winkler Model	2-5
2-3.	Normalized Rail Deflection and Bending Moment Curves	2-5
2-4.	Finite Element Model for 132-Lb RE Rail Near Position of Wheel Contact.	2-10
2-5.	Contours of Longitudinal Stress on Plane Through Load Point of 132-Lb RE Rail Under 19,000-Lb Vertical Wheel Load (Case 1).	2-13
2-6.	Longitudinal Stress σ_x in a 132-Lb RE Rail at Five Sections Along Rail Under 19,000-Lb Wheel Load (Case 1)	2-14

LIST OF ILLUSTRATIONS
(Continued)

<u>Figure</u>	<u>Page</u>
2-7. Contours of Vertical Shear Stress on Plane 1.0 Inch From Load Point of 132-Lb RE Rail Under 19,000-Lb Wheel Load (Case 1)	2-16
2-8. Vertical Shear Stress Through 132-Lb RE Rail at Five Sections Along Rail Under 19,000-Lb Wheel Load (Case 1)	2-17
2-9. Contours of Octahedral Shear Stress on Plane Through Load Point of 132-Lb RE Rail Under 19,000-Lb Vertical Wheel Load (Case 1)	2-18
2-10. Effect of Foundation Stiffness on Longitudinal Stress on Plane 1 Inch from Load Point on 132-Lb Rail Under 19,000-Lb Wheel Load	2-21
2-11. Illustrative Patterns of Stresses in a 132-Lb RE Rail Under a 19,000-Lb Wheel Load Applied 3/4 Inch Aside from Top of Rail Crown (Case 4)	2-22
2-12. Illustrative Patterns of Stresses in a 132-Lb RE Rail Under a 19,000-Lb Wheel Load Together with a 10,000-Lb Lateral Load (Case 5)	2-23
3-1. Wheel/Rail Contact as Quadratic Surfaces in Contact	3-3
3-2. Proportionality Factors for Quantities Associated with Hertz Contact	3-5
3-3. Elastic Stress Distribution in Rail Head Below Center of Contact with Wheel	3-6
3-4. Maximum Compressive, Octahedral Shear, and Alternating Longitudinal Shear Stress for New 33-Inch Diameter Wheel and Rail Having 10-Inch Crown Radius	3-9
3-5. Form of Shear Stress Distribution Found by Carter for Rolling Contact with Partial Slip	3-11
3-6. Influence of Component of Friction on Tangential Force Between Partly Slipping Cylinders	3-11
3-7. Proposed Zone of Contact Showing Rectangular Array of Nodes Representing Potential Contact Spots	3-13

LIST OF ILLUSTRATIONS
(Continued)

<u>Figure</u>	<u>Page</u>
3-8. Comparison Between "CONTACT" and Hertzian Results for Crossed Cylinders ($P_o = 19,000$ Lb, $R_r = 12.0$ Inches, and $R_w = 14.0$ Inches)	3-15
3-9. Eight Rail Specimens for Which Surface Contours Were Measured.	3-17
3-10. Surface Contour Measurement Procedure.	3-17
3-11. Surface Contours of Measured Rail Sections	3-18
3-12. Relationship Between Profiles of a 33-Inch Wheel and a 133-Lb Rail, Both New and Worn	3-20
3-13. Worn Wheel Profiles.	3-22
3-14. Heumann Wheel Profile.	3-23
3-15. Wheel Rail Contact Geometry.	3-24
3-16. Analytical and Experimental Results for Wheel/Rail Contact Positions	3-26
3-17. Typical Contact Regions in Rail Profile.	3-27
3-18. Contact Stress Distributions	3-30
3-19. Contours of Constant Second Stress Invariant Beneath the Contact Area Between Cylinders	3-39
3-20. Contours of Constant Second Stress Invariant Beneath the Contact Area Between Spheres	3-41
3-21. Comparison Contours of Second Stress Invariant for Cylindrical Contact with Slip Form FRAC3D.	3-43
3-22. Stress Calculation Locations Within Elastic Brick Model.	3-45
3-23. Stress Contours for (Baseline) Load Case 1 (19,000-Lb Load, 33-Inch Wheel, 10-Inch Crown Radius).	3-47
3-24. Stress Contours for Non-Hertzian and Hertzian Pressure Distributions	3-49

LIST OF ILLUSTRATIONS
(Continued)

<u>Figure</u>	<u>Page</u>
3-25. Effect of Wheel Radius on Octahedral Shear Stress in Rail with 10-Inch Crown Radius and 19,000-Lb Load . . .	3-51
3-26. Effects of Rail Crown Radius and of Vertical Load on Octahedral Shear Stress in Rail Under 33-Inch Wheel. . .	3-53
3-27. Stress Contours for Combined Vertical and Lateral Loading (33-Inch Wheel, 10-Inch Rail Crown, 19,000-Lb Vertical Load)	3-54
3-28. Stress Contours for Combined Vertical and Longitudinal Loading (33-Inch Wheel, 10-Inch Rail Crown, 19,000-Lb Vertical Load)	3-58
3-29. Possible Relationship Between Edge Cracks in Rails and Transverse Stresses from Lateral Friction Load . . .	3-61
3-30. Effects of Wheel Load and Wear on Shear Stress in Rail Head.	3-62
4-1. Stress Field Beneath a Cylinder Contacting a Plane, Including Residual Stresses Promoting Shakedown.	4-5
4-2. Buildup of Residual Stress (σ_x) and (σ_y) with Repeated Passages of the Load Due to Cylindrical Contact.	4-6
4-3. Strain and Stress Cycles at a Subsurface as Used in Computing Residual Stresses	4-9
4-4. Calculated Vertical Residual Stress After One and After Six Load Cycles	4-10
4-5. Tensile Stress-Strain Curve for Longitudinal Rail-Head Specimen.	4-12
4-6. Longitudinal Strains Due to Cylindrical Contact in Elastic and Elastic/Plastic Bodies	4-14
4-7. Vertical Strains Due to Cylindrical Contact, in Elastic and Elastic/Plastic Bodies	4-15
4-8. Longitudinal Residual Stresses Measured After One and Three Load Cycles Respectively	4-17

LIST OF ILLUSTRATIONS
(Continued)

<u>Figure</u>		<u>Page</u>
4-9.	Transverse Residual Stresses Measured After One and Three Load Cycles Respectively	4-18
4-10.	Vertical Residual Stresses Measured After One and Three Load Cycles Respectively	4-19
4-11.	Residual Stresses Measured in Rail From Service.	4-21
5-1.	Three Modes of Crack Propagation	5-3
5-2.	Notation for Elliptical Crack.	5-9
5-3.	Relation Between Rail Coordinate and Local Coordinates for a Transverse Fissure	5-9
5-4.	Stress Intensity Factor K_I Around Circular Transverse Cracks Below the Center of Wheel/Rail Contact.	5-16
5-5.	Stress Intensity Factor K_I Around Elliptical Transverse Cracks Below the Center of Wheel/Rail Contact.	5-17
5-6.	Stress Intensity Factors K_I , K_{II} , K_{III} Around Elliptical Transverse Crack in Plane 1 Inch from Center of Contact.	5-21
6-1.	Joint Geometry and Strain Gage Locations	6-2
6-2.	Test Setup for Laboratory Validation Studies	6-4
6-3.	Aluminum Tie Calibration Curves--Bending (Strain Gage Bridge Output Versus Vertical Load).	6-6
6-4.	Aluminum Tie Calibration Curves--Tension (Strain Gage Bridge Output Versus Lateral Load)	6-7
6-5.	Contribution to Bolt Hole Stresses (in ksi) by Various Bolt Tensions.	6-11
6-6.	Effect of Bolt Tension Only on Web Stresses.	6-12
6-7.	Bolt Hole Stresses Due to Bolt Tension Approximately Equal to 30 kips and Two Vertical Loads Centered on the Joint	6-13

LIST OF ILLUSTRATIONS
(Continued)

<u>Figure</u>	<u>Page</u>
6-8. Variation of Tangential Stress on Front Side of First Bolt Hole Due to Bolt Tension and Two Vertical Loads . .	6-14
6-9. Influence of Longitudinal Position of Load on Incremental Bolt-Hole Stresses (in ksi) Due to 20,000-Lb Vertical Load.	6-16
6-10. Longitudinal Variations of Bolt-Hole-Stress Increments Due to 20,000-Lb Vertical Load (Bolt Tension 20 kips). .	6-17
6-11. Effect of Eccentricity on Bolt-Hole Stresses Due to 20,000-Lb Vertical Load (with Bolt Tension Approximately Equal to 30 kips).	6-18
6-12. Increments of Tangential Stress on Front Side of First Bolt Hole Due to Eccentricity of 20,000-Lb Vertical Load at Joint.	6-19
6-13. Effect of Lateral and Vertical Loads on Bolt-Hole Stresses (with Bolt Tension 30 kips)	6-21
6-14. Influence of Foundation Modulus on Incremental Bolt-Hole Stresses Due to 20,000-Lb Vertical Load	6-22
6-15. Influence of Foundation Modulus on Incremental Tangential Stress on Front Side of First Bolt Hole Due to 20,000-Lb Vertical Load at Joint.	6-23
7-1. Rail Joint Dimensions and Joint Bar Free-Body Diagram, Inches.	7-2
7-2. Division of Moment Between Rail and Joint Bars.	7-4
7-3. Moment in Rail and Joint Bars - Wheel Away from Rail End.	7-4
7-4. Depression of Rail and Upward Reaction Forces at and from the Ties for a Single Wheel Load When No Moment is Resisted at the Rail Ends.	7-7
7-5. Depression of Rail and Upward Reaction Forces at End From the Ties for a Single-Wheel Load	7-7
7-6. Free-Body and Shear Diagram for a Rail End for Various Wheel Load Positions	7-9

LIST OF ILLUSTRATIONS
(Continued)

<u>Figure</u>	<u>Page</u>
7-7. Joint Resultant Q as a Function Wheel Load for Foundation Stiffness $k = 200$ psi	7-12
7-8. Joint Resultant Q as a Function Wheel Load for Foundation Stiffness $k = 500$ psi	7-13
7-9. Joint Resultant Q as a Function Wheel Load for Foundation Stiffness $k = 1,000$ psi	7-14
7-10. Joint Resultant Q as a Function Wheel Load for Foundation Stiffness $k = 2,000$ psi	7-15
7-11. Joint Resultant Q as a Function Wheel Load for $k = 5,000$ psi.	7-16
7-12. Two-Dimensional Load-Transfer Symmetrical Model.	7-18
7-13. Full Rail-Joint Two-Dimensional Load-Transfer Model.	7-19
7-14. Simplified 132-Lb RE Joint Bar Cross Section	7-21
7-15. Simplified 132-Lb RE Rail Simulated by 2-D Elements of Varying Thickness	7-22
7-16. Cantilever Bending Stress Comparison for a Plan 8.2 Inches From Loaded End for the Finite Element Rail End and Strength-of-Materials Solutions.	7-25
7-17. Joint Bar Bending Moments for 20 kip Wheel Load.	7-29
7-18. Joint Bar Bending Moments for 35 kip Wheel Load.	7-29
7-19. Comparison of Finite Element, Beam-on-Elastic Foundation and Experimental Results for Q	7-31
8-1. Three Views of the Finite-Element/Rail-End Model	8-2
8-2. Maximum Tangential Stress as a Function of Wheel Load for 132-Lb RE Joint at Various Foundation Moduli	8-5
8-3. Polar Plot Comparison of Experimental, Finite Element and Approximate Analytical Results for Bolt-Hole Stresses (Vertical Wheel Load of 10 kips at Rail End).	8-7

LIST OF ILLUSTRATIONS
(Continued)

<u>Figure</u>	<u>Page</u>
A-1. 132-Lb Rail Core with RTV and Aluminum Flanges Installed.	A-3
A-2. Completed Mold with 132-Lb Rail Core Still in Place	A-4
A-3. Photograph of the Instrumented Model Installed in the Loading Fixture	A-7
A-4. Strain Gage Locations.	A-9
A-5. Photograph of the Loading Fixture and Model in the Oven	A-11
A-6. Photograph of the Stress Frozen Rail	A-13
A-7. Isochromatic Fringe Pattern in the Central Portion of the Rail Prior to Slicing	A-15
A-8. Diagram of Slicing Strategy.	A-16
A-9. Isochromatic Fringe Patterns in Slice 2.	A-18
A-10. Isochromatic Fringe Patterns in Slice 3.	A-19
A-11. Comparison of Tangential Surface Stress on Plane 2	A-20
A-12. Comparison of Tangential Surface Stress on Plane 3	A-21
A-13. Full Rail Model (Using 20-Noded Elements).	A-22
A-14. Comparison of Tangential Stress Found by Strain Gages and From Finite Element Model.	A-24
A-15. Comparison of Rail Deflections From the Finite Element Model and From Simple Beam Theory.	A-25
B-1. Longitudinal Stress in 132-Lb RE Rail Under 19,000-Lb Centered Vertical Load.	B-1
B-2. Lateral Stress in 132-Lb RE Rail Under 19,000-Lb Centered Vertical Load	B-2

LIST OF ILLUSTRATIONS
(Continued)

<u>Figure</u>	<u>Page</u>
B-3. Vertical Stress in 132-Lb RE Rail Under 19,000-Lb Centered Vertical Load.....	B-3
B-4. Shear Stress τ_{yz} in 132-Lb RE Rail Under 19,000-Lb Centered Vertical Load.....	B-4
B-5. Shear Stress τ_{zx} in 132-Lb RE Rail Under 19,000-Lb Centered Vertical Load.....	B-5
B-6. Shear Stress τ_{xy} in 132-Lb RE Rail Under 19,000-Lb Centered Vertical Load.....	B-6
B-7. Octahedral Shear Stress in 132-Lb RE Rail Under 19,000-Lb Centered Vertical Load.....	B-7
B-8. Effect of Foundation Stiffness on Longitudinal Stress in 132-Lb RE Rail Under 19,000-Lb Centered Vertical Load.....	B-8
B-9. Effect of Foundation Stiffness on Octahedral Shear Stress in 132-Lb RE Rail Under 19,000-Lb Centered Vertical Load.....	B-10
B-10. Longitudinal Stress in 132-Lb RE Rail Under 19,000-Lb Eccentric Vertical Load.....	B-12
B-11. Shear Stress Components in 132-Lb RE Rail Under 19,000-Lb Eccentric Vertical Load.....	B-13
B-12. Octahedral Shear Stress in 132-Lb RE Rail Under 19,000-Lb Eccentric Vertical Load.....	B-14
B-13. Longitudinal Stress in 132-Lb RE Rail Under 19,000-Lb Vertical and 10,000-Lb Lateral Load.....	B-15
B-14. Shear Stress Components in 132-Lb RE Rail Under 19,000-Lb Vertical and 10,000-Lb Lateral Load.....	B-16

LIST OF ILLUSTRATIONS
(Continued)

<u>Figure</u>	<u>Page</u>
8-4. Central Vertical Load Results--Bolt-Hole Stresses are Tangential, All Others are Vertical Stresses (Wheel Load 8 Inches from Rail End for All Cases)	8-8
8-5. Eccentric Vertical Load Results.	8-9
8-6. Lateral Load Results	8-10
9-1. Semi-Elliptical Surface Flaw Geometry.	9-3
9-2. Through-Crack from Hole.	9-3
9-3. Bolt-Hole Crack Finite Element Model	9-6
9-4. Head/Web Separation Finite Element Model	9-6
9-5. K_I for Bolt-Hole Crack Computed on the Basis that the Flaw is a Surface Flaw; Joint Bar Reaction $Q = 39$ kips.	9-8
9-6. K_I for Bolt-Hole Crack which is Assumed to be a Through Thickness Flaw; Joint Bar Reaction $Q = 39$ kips	9-9
9-7. Stress-Intensity Factors for a Lower Bolt-Hole Crack	9-10
9-8. Stress-Intensity Factor for Cracks Emanating from Diametrically Opposite Points of a Bolt Hole; Joint Bar Reaction $Q = 39$ kips	9-11
9-9. Stress-Intensity Factor for a Bolt-Hole Crack Emanating from Diametrically Opposite Points of the Hole (Lower Emanation has Turned and Broken Through to Rail End); Joint Bar Reaction $Q = 39$ kips	9-12
9-10. K_I for Head/Web Separation Modeled as Circular Embedded Crack for $\sigma = 25,000$ psi.	9-15
9-11. Stress-Intensity Factor for Head/Web Separation Growing Both Directions; Crack Configuration (A), with $\sigma = 25,000$ psi	9-16
9-12. Stress-Intensity Factor for an Open Head/Web Separation with $\sigma = 25,000$ psi.	9-17

LIST OF ILLUSTRATIONS
(Continued)

<u>Figure</u>		<u>Page</u>
B-15.	Octahedral Shear Stress in 132-Lb RE Rail Under 19,000-Lb Vertical and 10,000-Lb Lateral Load,	B-17
D-1.	Flowchart of Residual Stress Calculation Procedure . . .	D-2
D-2.	Elastic Strains Along Rail Axis on Longitudinal Plane of Symmetry and Depth = 0.075 Inch, Due to 19,000-Lb Load	D-6
D-3.	Elastic-Plastic Strains Along Rail Axis on Longitudinal Plane of Symmetry and Depth = 0.075 Inch, Due to 19,000-Lb Load	D-7
E-1.	Cross Section Through Test Specimen.	E-2
E-2.	Stress-Strain Characteristics for Rail Test Specimen . .	E-4
E-3.	Rail Coordinate System.	E-6
E-4.	Sectioning of Rail Specimens	E-9
F-1.	Notation Used for Elliptical Flaw in Rail.	F-2
F-2.	Stress Intensity Factors From Normal Loads of Basic Types Acting on an Elliptical Crack.	F-9
F-3.	Stress Intensity Factors Along Representative Elliptical Cracks From a Normal Load Including a Bending Load . . .	F-10

LIST OF TABLES

<u>Table</u>		<u>Page</u>
1-1.	TYPES OF MOST COMMONLY ENCOUNTERED RAIL DEFECTS.	1-2
1-2.	TYPICAL MAXIMUM AND MINIMUM STRESSES IN A 132-LB RAIL HEAD AWAY FROM BOLTED JOINTS UNDER A VERTICAL LOAD OF 19,000 LB	1-15
2-1.	TYPICAL DATA FOR THE CHARACTERISTIC LENGTHS X_1 AND X_2	2-6
2-2.	SPECIFICATIONS FOR FINITE ELEMENT CALCULATIONS OF STRESSES IN RAIL	2-11
3-1.	WHEEL AND RAIL VARIABLES FOR ELASTIC CALCULATIONS.	3-8
3-2.	DESCRIPTION OF WORN-RAIL CONTOURS.	3-19
3-3.	DESCRIPTION OF CONTACT REGIONS ON RAIL RUNNING SURFACE OF COOPERRIDER AND LAW WORN RAIL DATA, WORN WHEEL NO. 3.	3-28
3-4.	SUMMARY OF WORN WHEEL/RAIL CONTACTS ANALYZED	3-29
3-5.	CASES ANALYZED FOR SUBSURFACE STRESS DISTRIBUTIONS	3-44
4-1.	EFFECT OF FULL-SLIP SURFACE TRACTIONS ON SHAKEDOWN LOAD	4-7
6-1.	MEASURED BOLT HOLES STRESSES UNDER LOADS OF VARIOUS KINDS.	6-9
7-1.	SPRING STIFFNESS FOR SIMULATING CONTINUOUS RAIL RESISTANCE TO BENDING.	7-23
7-2.	MATRIX OF EVALUATIONS PERFORMED AND NUMERICAL RESULTS FOR FINITE-ELEMENT LOAD-TRANSFER MODELS.	7-27
7-3.	EXPERIMENTALLY DETERMINED VALUES FOR JOINT BAR RESULTANT.	7-30
A-1.	REDUCED STRAIN DATA.	A-10
D-1.	TENSILE TEST DATA ON RAIL STEEL.	D-4
E-1.	SPECTROGRAPHIC ANALYSIS OF CRANE RAIL STEEL.	E-1
E-2.	SUMMARY OF THE STRESS RELIEVING PROCEDURE.	E-3

LIST OF TABLES
(Continued)

<u>Table</u>		<u>Page</u>
E-3.	SURFACE RESIDUAL STRESSES WITH STATISTICAL EVALUATIONS .	E-12
E-4.	SUBSURFACE STRAIN AND DISPLACEMENT MEASUREMENTS.	E-13
E-5.	SUBSURFACE RESIDUAL STRAINS AND STRESSES	E-14
F-1.	COEFFICIENTS FOR REVISED FUNCTIONS $\kappa_{i,j}$ (Before Correction)	F-18
F-2.	COEFFICIENTS FOR REVISED FUNCTIONS $\kappa_{i,j}$ (After Correction)	F-34

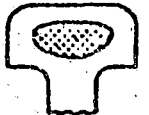
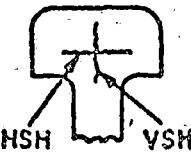
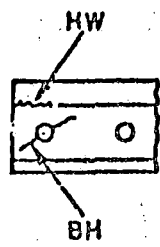
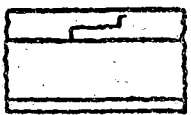
1. EXECUTIVE DIGEST

1.1 THE PROBLEM OF RAIL FRACTURES

In recent years, railroads in the United States have experienced over 800 derailments annually due to broken rails resulting in over 60 million dollars in direct costs [1-1]. These derailments occur despite a substantial inspection program by the railroads and contract inspection services which collectively locate and identify nearly 200,000 defective rails every year [1-2]. The replacement of these flawed rails involves removal of over 100,000 tons of rail. In addition, rails that have reached superannuation are also being replaced at the rate of nearly 700,000 tons per year [1-3]. Despite these actions, the rate of occurrence of cracks in rails has increased in recent years. Furthermore, rail fractures rank as the single most severe cause of accidents [1-4]. These failures have been attributed to the high stresses resulting from the increasingly severe operating conditions. Thus, there has been renewed interest in developing a better understanding of the states of stress in rail. Until very recently, the analytical problems associated with the task of accurately determining stresses in rails have been intractable. This is because the rail, a seemingly simple structural member, is, in fact, the site of an extremely complex, fully three-dimensional stress state. Thus, past studies have generally approached the problem of rail stress either from an experimental or a simplified strength-of-materials standpoint.

The types of defects most commonly encountered are summarized in Table 1-1 with a ranking of the percentage cause of derailments and frequency of type details [1-5]. The actions required by Federal regulation [1-6] for train operation until a defective rail is replaced are also listed. As may be seen in Table 1-1, rail-end failures represent the most troublesome category though not necessarily the most dangerous in terms of derailments. FRA statistics [1-1] suggest that approximately 22 percent of all derailments result from failure of one or more components at the joint region as opposed to the 17 percent shown in the table for rail failure alone at the joint region. However, of all defects that are detected, 56 percent were in the rail end and these were principally associated with the action of bolted-rail joints.

TABLE 1-1. TYPES OF MOST COMMONLY ENCOUNTERED RAIL DEFECTS

DEFECT	LOCATION/ SHAPE	% FREQUENCY DERAIL/DETECT	SIZE	ACTION REQUIRED UNTIL DEFECTIVE RAIL IS REPLACED
TRANSVERSE FISSURE		24%/12%	HEAD AREA (a) <100%	10 mph MAX.
			(b) 100% (+)	VISUAL SUPERVISION
VERTICAL/ HORIZONTAL SPLIT HEAD		26%/18%	LENGTH (a) <2"	50 mph OR LESS [#] ; INSPECT IN 90 DAYS
			(b) 2" TO 4"	30 mph OR LESS [#] ; INSPECT IN 30 DAYS
			(c) >4"	10 mph MAX.
			(d) CHUNK MISSING	VISUAL SUPERVISION
BOLT HOLE/ HEAD WEB SEPARATION		17%/56%	LENGTH (a) <1/2"	50 mph OR LESS [#] ; INSPECT IN 90 DAYS
			(b) 1/2" TO $\begin{cases} 3" \text{ (HW)} \\ 1-1/2" \text{ (BH)} \end{cases}$	30 mph OR LESS [#] ; INSPECT IN 30 DAYS
			(c) $> \begin{cases} 3" \text{ (HW)} \\ 1-1/2" \text{ (BH)} \end{cases}$	10 mph MAX.
			(d) CHUNK MISSING	VISUAL SUPERVISION
DETAIL FRACTURE/ COMPOUND FISSURE		8%/5%	HEAD AREA (a) <20% (DF)	30 mph OR LESS [#] UNTIL JOINT BARS ARE APPLIED AND THEN 50 mph OR LESS [#]
			20% TO 100% (DF)	
			<100% (DF)	10 mph MAX.
			(b) 100% (+)	VISUAL SUPERVISION

Δ SPERRY DATA, 1967-1973 AVG.

SET BY CLASS OF TRACK

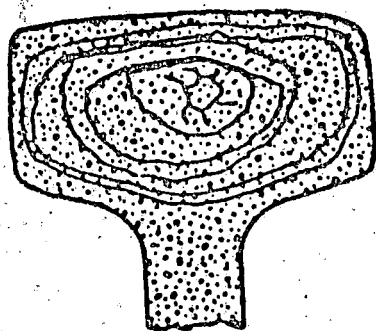
The recent trend in railroad construction, particularly in Europe and more lately in the United States, has been to eliminate most bolted joints through the use of continuous welded rail (CWR). There are at present approximately 80,000,000 bolted joints in the United States. At the current rate of installation, only small amounts of CWR will be installed in anything other than primary lines before the year 2000 [1-7]. Hence joint caused maintenance/failure costs will continue to constitute a significant proportion of the total maintenance of way expenditure.

Transverse fissures are detected less frequently, but appear to account for a disproportionately large number of derailments. Vertical/horizontal split heads and detail/compound fractures, which are characterized by a crack which travels some distance along the rail before it turns and runs transversely, constitute the other major categories. Some rail defects can be considered as surface failures resulting from large wheel-rail contact stresses, but this report deals primarily with those initiating more deeply in the rail head. In particular, the types of defects that this report addresses specifically include the transverse fissure, and cracks emanating from bolt holes at rail joints. However, the reader may use the procedures used in the context of transverse fissures, and the applicable stress distributions given in this report to study hypothetical vertical and horizontal split heads.

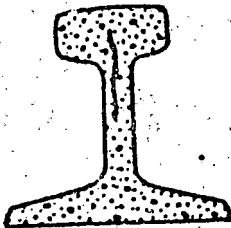
The growth of cracks in rails in service is not well documented, but available information [1-7] suggests that a transverse fissure, for example, may grow slowly to somewhat more than 20 percent of the rail head cross section before growth becomes rapid and rupture of the entire rail occurs suddenly. Growth of this kind beginning from an internal nucleus is illustrated in Figure 1-1. Sometimes more than one transverse fissure develops within a single rail. The transverse fissure is regarded as particularly dangerous, both because it is so apt to result in a complete break of the rail head and because it seldom becomes visible before final failure occurs. Transverse fissures may also initiate at the surface, but since analysis of surface cracks involves rather special considerations [1-8, 1-9, 1-10], the treatment of surface initiated transverse fissures has been deferred.

The vertical split illustrated in Figure 1-1 is a progressive longitudinal fracture which grows through the head vertically and longitudinally near

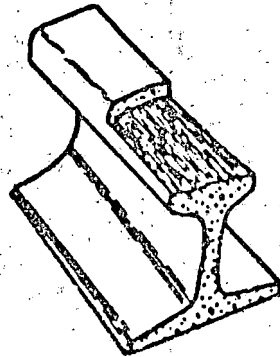
7-1



(a) Typical Transverse Fissure



(b) Vertical Split Head Defect



(c) Horizontal Split Head

FIGURE 1-1. TYPICAL RAILHEAD DEFECTS

the center of the rail. It may begin at a seam, segregation or inhomogeneous inclusion of material. The vertical split head may grow to be several feet long before it can be observed on the surface of the rail head [1-7]. The flaw usually terminates by turning and growing out to the side of the rail head. This results in breaking out approximately half of the head.

The horizontal split, illustrated at an advanced stage in Figure 1-1, is a progressive longitudinal fracture growing parallel to the running surface at a depth of at least one third of the rail head. It begins at an internal longitudinal seam, segregation or inclusion. Prior to reaching the free surfaces of the sides of the rail, the horizontal split results in the appearance of a flat spot on the rail surface together with a slight depression of the entire rail head. It is reported that breakout first occurs in uncanted rail on the gage side and in canted rail on the field side. According to Reference 1-7, such flaws usually develop into a compound fissure leaving vertically oriented crack surfaces which resulted in a complete transverse break.

The two most important types of rail-end defects have been shown in Table 1-1. One type is that of bolt-hole cracks initiating from bolt-hole defects (burrs or fretting) and propagating along directions inclined 45 degrees to the running surface of the rail. These cracks may change direction at the rail head fillet and run horizontally, leading to head-web separations. Head-web separations may also initiate independently in the upper fillet of the rail end and travel away from the joint center. This type of flaw may attain considerable length before turning upwards into the rail head and causing a chunk of the rail head to break out.

Wise, et al [1-11], reported data on the frequency of occurrence of various bolt-hole cracks for the British Railway in 1955. The most common mode of failure they found consisted of bolt-hole cracks proceeding simultaneously to the upper fillet and the rail end as shown in Figure 1-1.

1.2 STRESSES CONTRIBUTING TO RAIL FRACTURES

A rail section originates from a large steel ingot. Inherent in the manufacturing process are the consequences due to solidification of a large molten metal mass, such as normal segregation of metallic phases and slight

porosity. Potential defect sites are created at this stage, metallic and non-metallic inclusions being common forms. These exacerbate the intensity of stresses around them when the rail is placed in service. The mechanics of the rolling load from rail cars causes every point in the rail to experience both tensile and compressive stresses which depend on the weights and the positions of the rail car wheels. As is well known, alternating stresses can lead to failure through a process of fatigue damage, which typically consists of nucleation of microcracks, subsequent growth of such cracks to reach macro-dimensions, and finally fracture. At present, experimental data suggest that damage rates which are applicable to crack initiation and propagation are strong functions of the stress range experienced by the point in the rail and of the alternating component of stress intensity factors K which describe the stress concentration near the crack front. Thus, for interpretation of crack growth in a rail, it is important to know how stresses vary in the rail, and in particular, to know the mean level and range of the stress intensity factors K along the crack front.

The stresses in a rail arise from the loads applied to the rail. The direct loads include the vertical, lateral, and longitudinal wheel forces from passing vehicles and the compensating support offered by the ties and ballast and joint bars. During consideration of the effects of these direct loads, it is convenient to separate remote effects--to which the rail responds as a beam under flexure--from the highly local effects in the wheel-rail contact area and at bolt holes. Further, stresses which may be significant include those due to cumulative permanent deformation by which residual stresses are locked in the rail head, and the more slowly changing thermal loads associated with daily and seasonal changes. The inability of rail to transmit stresses in a normal fashion where a crack intervenes gives rise to additional, highly concentrated, crack-front stresses. These crack-front stresses, characterized by parameters called stress intensity factors, are the stresses most responsible for crack growth. In view of the multiplicity of kinds of loads affecting crack growth, it is appropriate to discuss briefly the various kinds of stresses which arise.

1.2.1 Flexural Stresses at Mid-Rail Sections

When a wheel comes to within 6 to 12 feet of a particular point in a rail head, the vertical load causes longitudinal bending stresses, tensile at the top of the rail head, through bending of the full rail resting on the elastic foundation of the ties, ballast and subgrade. As the wheel comes closer, the flexural stress in the rail head becomes compressive, having a magnitude greater than that of the previous tensile stress. A typical example of this stress variation is shown in Figure 1-2, with longitudinal stress due to two 19,000 lb wheel loads varying from about 4,000 psi tension to -10,000 psi compression.* At points within a few inches of the point of load application, vertical bending of the rail head on the elastic foundation provided by the web may add as much as -8000 psi to the stress due to overall rail bending. This effect is usually termed as head-on-web bending. Significant changes in these stresses can arise from variations in the wheel loads, including dynamic effects from wheel irregularities. Wear of 3/8-inches of the head can cause some of these stresses to increase over 100 percent. Of course, the longitudinal stress varies with depth, such that at the base of the rail head the contribution due to rail flexure would be significantly reduced while the head-on-web bending contribution would be nearly the negative of that on top of the rail head. The related shearing stresses also vary. Thus simple vertical loads produce very complex bending stresses in the rail head.

Significant stresses are produced also by lateral wheel loads (as from flanging forces arising at curves and from self-excited hunting motions) and from eccentric application of vertical wheel loads (when the contact area is off the center plane of the rail) [1-12]. These loads produce distortion of the bending stresses in the rail. Thus, for a 132-lb rail supported by a foundation with lateral stiffness of 600 (lb/in.)/inch the longitudinal stresses due to a 10,000-lb lateral load reach \pm 11,000 psi in the rail head and \pm 21,000 psi in the base. Warping stresses under comparable conditions can reach 7,000 psi in the rail head and 11,000 psi in the base.

*Curves in Figure 1-2 were computed by methods described in Chapter 2. For further discussion of these methods, see Reference 1-12.

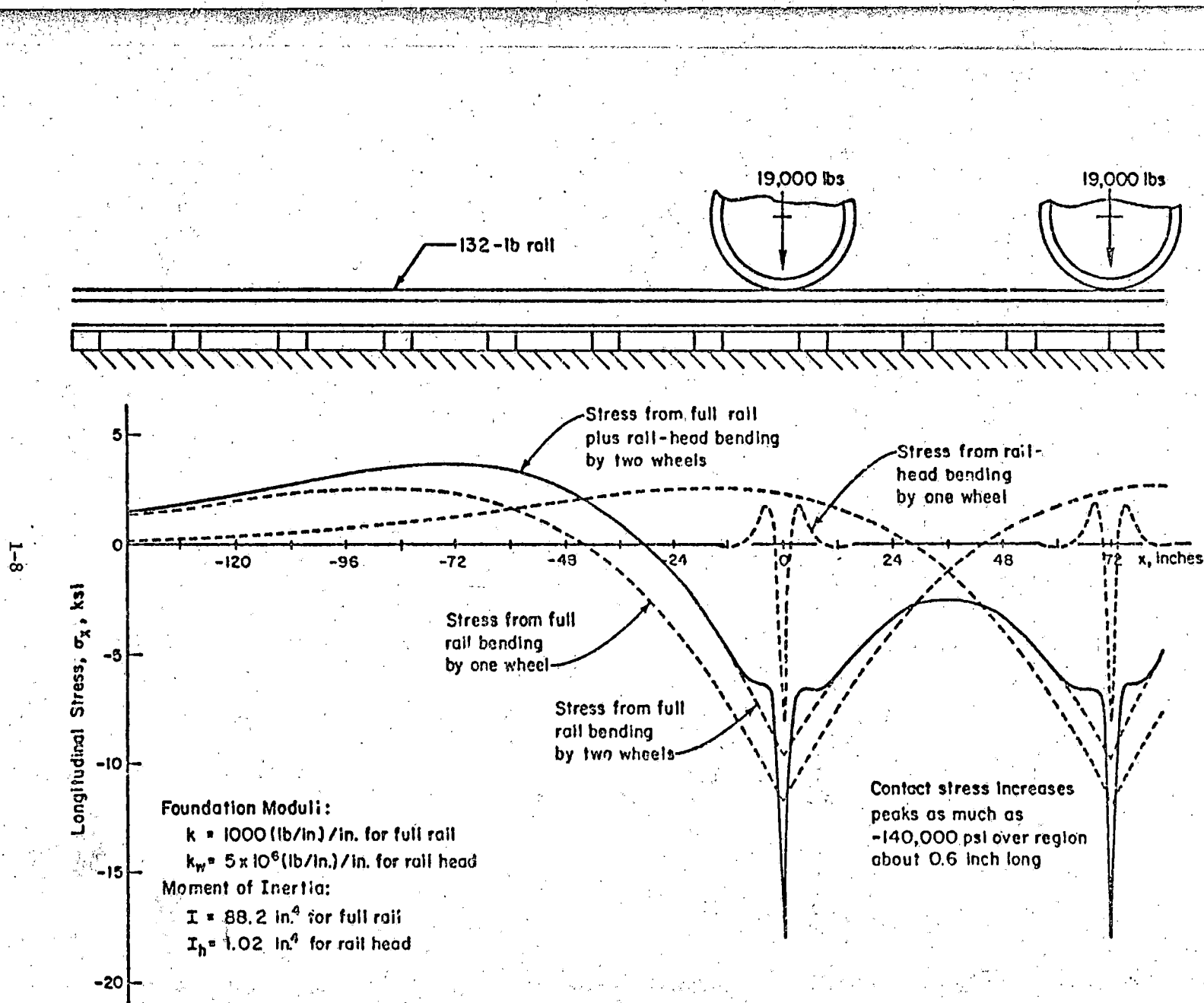


FIGURE 1-2. TYPICAL CONTRIBUTIONS OF BENDING TO LONGITUDINAL STRESS ON TOP OF RAIL.

The torsion produced by eccentrically applied vertical loads causes additional stress in the head-web fillet region up to 10,000 psi for a 19,000-lb applied wheel load. When accompanied by high lateral flanging forces, its maximum can exceed 30,000 psi in compression. The vertical stress produced in the web by lateral loads also can be significant when superimposed on stresses from eccentric vertical loads. Because of the above, the 132-lb RE rail underwent considerable design change in the fillet region to correct a fatigue crack problem in the 131-lb RE rail [1-13].

Additional forces which may induce longitudinal stresses in the rail arise from traction and braking. Longitudinal shear forces are particularly important to curved track. Stresses in rails, viewed as beams, also vary because support by the ties is localized, and the wheel loads are concentrated at positions which vary according to track and operating conditions. Thus, viewed simply as beams, rails must support complex and variable stress patterns.

The many variations of loading, plus the relevance of details of stress distributions, commend the use of new, more detailed forms of beam analysis. Such analysis is the subject of Chapter 2.

1.2.2 Contact Stresses

When a wheel load is within an inch of a point in the rail head, large contact stresses are imposed (as noted for example in Figure 1-2) which are not treated by beam analysis. These stresses generally reach much larger magnitude than do the flexural stresses. Contact stresses are generally compressive, but they also include large shearing stresses, including a particularly large transverse shearing stress component which reverses as the wheel passes. Contact stresses frequently exceed the yield stress of the virgin material and they have long been suspected as an important cause of rail head failure.

To illustrate contact stresses, continue the example in Figure 1-2 by assuming the use of new, 33-inch wheels and rail with a 10-inch crown radius. Hertz contact stress theory [1-14] shows that the contact pressure is distributed ellipsoidally over an area about 0.53 inch long (in the rolling direction) and 0.38 inch wide, reaching a peak of -182,000 psi, while implying a

peak longitudinal stress of -140,000 psi. A measure from the standpoint of yielding, however, is the octahedral shear stress (τ_{oct}) which can be shown [1-15] to reach 52,000 psi at a point about 0.10 inch below the center of contact. From fatigue considerations, the worst stress is probably the alternating transverse shear stress [1-15] (τ_{xz}) which can be shown [1-16] to reach 34,000 psi at points also about 0.10 inch below the leading and trailing points of the contact area. The variations of several stress components for this example are shown in Figure 1-3.

The size and shape of the contact area are influenced by the topographic contours of the mating surfaces prior to contact as well as by the load. If the mating surfaces are non-ellipsoidal, then the Hertz contact stress theory does not apply. Wearing of the wheel tread and the running surface of the rail head thus produces departures from Hertz patterns. Again, contact stresses are affected by tangential loads such as arise from acceleration and deceleration of the locomotive and from "stick-slip" of wheels due to axle windup on curves. The pattern of tangential forces on the interface is complicated by the tendency of the contacting surfaces to slip over part of their interface while adhering over the rest of it, so that tangential forces are not simply proportional to the contact pressure. These complications produce a need for a more comprehensive method to determine the patterns of contact forces between a wheel and rail, and to predict the resulting stress patterns in the rail. The variation in contact stresses with the variation in contact condition is considered in Chapter 3, where a substantial variety of contact stress patterns are considered.

Contact stresses, in conjunction with other stresses such as those due to bending, are often large enough to cause plastic flow and fatigue failure. These latter issues are treated within the Chapter 4 pertaining to residual stresses and crack stresses.

1.2.3 Thermal Stress

It has been generally accepted that stresses due to thermal expansion or contraction of rails are small in comparison with those of wheel loads. A temperature variation of 100°F produces a change of about 11,000 psi in longitudinal stress if the rail is fully constrained against expansion or

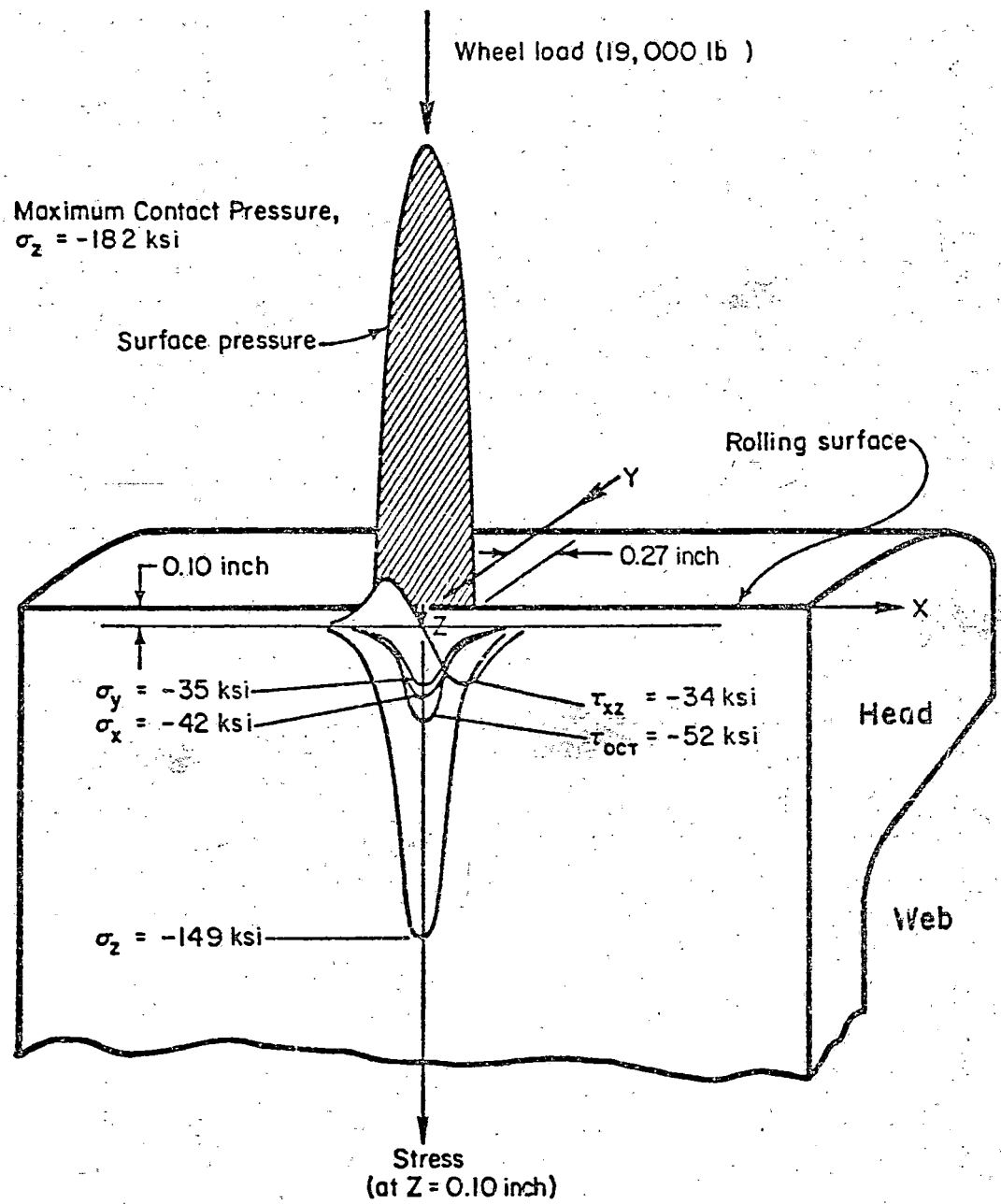


FIGURE 1-3. STRESSES DEVELOPED IN 132-LB RE RAIL HEAD AT DEPTH OF 0.10-INCH DUE TO 33-INCH DIAMETER WHEEL AND WHEEL LOAD OF 19,000 LB

contraction. Because such a stress change would occur quite slowly, it may be considered as a constant prestress when analyzing stresses in the presence of plastic deformation, or when evaluating fatigue damage.

1.2.4 Residual Stresses

When wheel loads exceed approximately 19,000 lb, new rails deform plastically upon passage of the first trains and residual stresses are locked into the rail head in a region under the tread surface. Under normal traffic, these stresses are known to increase as traffic continues, and to extend more deeply into the rail head. Depending on circumstances of the traffic, the belief was that the growth of these stresses may eventually reach a state of "shakedown", a condition at which further plastic deformation ceases and the residual stress pattern in the rail stabilizes. However, recent evidence indicates that a shakedown condition is never reached, primarily because of cyclic strain softening of the rail steel [1-17].

When the rail yields, a residual compressive zone is established directly beneath the rail surface. Beneath the compressive zone a tensile zone is developed through a substantial part of the thickness of the rail head. Horizontal cracks and split heads are known to originate in this area. The tensile residual stresses could contribute to the propagation of these flaws. Cracks occurring near the rail head surface would tend to stop or turn as they encounter compressive residual stresses. Near the running surface, reversal of shear stress occurs, but cracks propagated by this stress may be slowed or even diverted into pitting by the compressive longitudinal residual stress, so that gross vertical or horizontal splits may be averted.

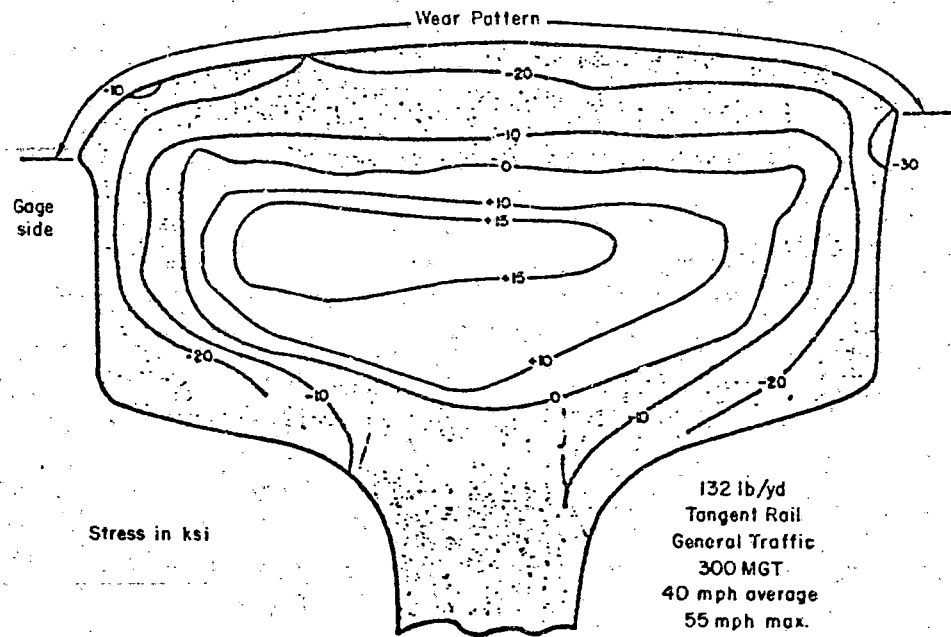
Residual stresses in a rail head are exacerbated by complex transient stress patterns caused by the wide range of wheel loads. There is the possibility that some patterns of residual stresses can greatly inhibit or even prevent further change of residual stresses. Therefore, it is well to have experimental evidence for the levels of residual stresses in used rails, though measurements from a single or even a few rails will not show the great variety of stress patterns that may exist among used rails. Dependable measurements of residual stresses in rails are few, but those reported by Groom

recently to the Department of Transportation [1-18] provide some useful data for mid rail sections. Those measurements were made on rails of each of two weights after each of two levels of service. Those for 132-lb rail after passage of 300 million gross tons (MGT), the longer service, are sketched in Figure 1-4. These stresses were generally higher than those after 100 MGT, so that they do not necessarily show a state of shakedown.

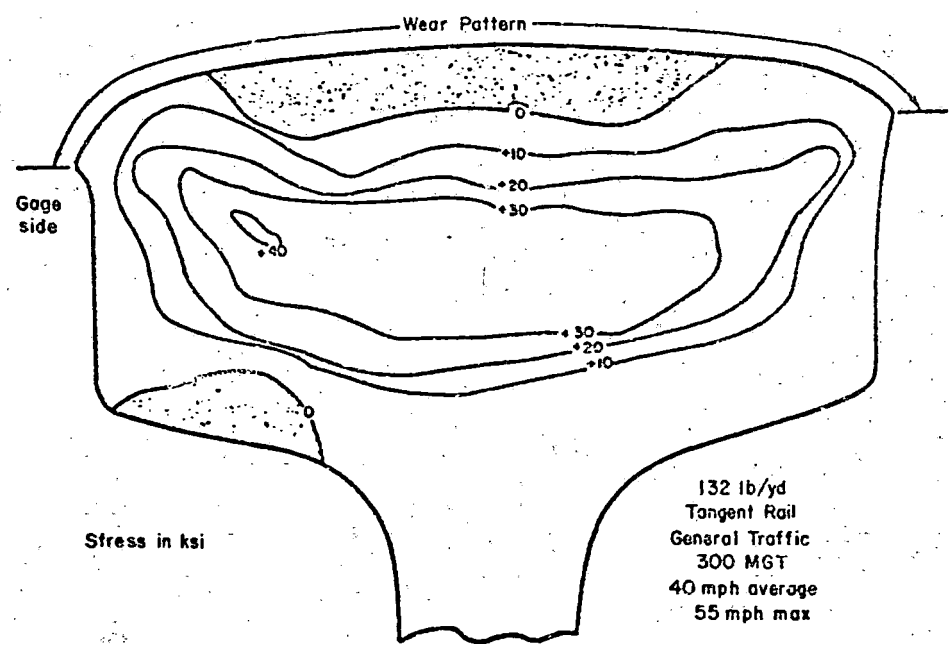
Figure 1-4 shows a tensile residual axial stress over a large region around the center of the rail head. This stress exceeded +15,000 psi over a fairly wide area and reached a maximum of +18,400 psi. The in-plane stresses shown in the second drawing are the more tensile of the two local principal stresses. The orientation of these latter stresses is not shown, but it was nearly horizontal over most of the region where the stress exceeded +30,000 psi, so that these stresses would promote fracture in vertical planes. The maximum among these stresses was +41,300 psi. To put these stresses in perspective, they are listed in Table 1-2 together with high values already cited previously for stresses from other sources. Values in this table are not upper limits among possible stresses, they are merely typically high values.

The level of residual stresses to be expected in a given rail after specified service is a complex issue which is treated in Chapter 4 for sections away from bolted joints. Unfortunately, significant effort, experimental or otherwise, for determining typical residual stresses at bolted joints is yet to be undertaken.

An evaluation of the stresses identified in Table 1-2 indicates that, although stresses of each kind may be severe, the combined action of these stresses may be more damaging than simple addition of the stresses would imply. That is especially true when the frequent plastic yielding and resultant residual stress conditions are considered. Furthermore, the complex factors associated with build-up of residual rail stresses appear to be closely linked to conditions controlling rail wear. At a minimum, rail wear leads to increased flexural stresses because of the reduced area of the rail head. Wear is also a strong mechanism in determining the wheel/rail contact pressure. Frequently, the concave and false flange regions on severely worn wheels cause greater contact pressures between the wheel and rail and, therefore, excessive plastic flow of the rail. An understanding of the combined actions of rail stresses is crucial to the understanding of rail reliability.



(a) Axial stress contours



(b) In-plane tensile stress magnitude contours

FIGURE 1-4. MEASURED VALUES OF RESIDUAL STRESSES IN A USED RAIL [1-18]

TABLE 1-2. TYPICAL MAXIMUM AND MINIMUM STRESSES IN A 132-LB RAIL HEAD AWAY FROM BOLTED JOINTS UNDER A VERTICAL LOAD OF 19,000 LB

Stress Component	Flexural Stress (1) (ksi)	Contact Stress (2) (ksi)	Thermal Stress (3) (ksi)	Residual Stress (4) (ksi)
Longitudinal σ_x	4 -18	0 -140	7 -7	+18 -32
Lateral σ_y	0 0	0 -152	0 0	+40 -50
Vertical σ_z	0 0	0 -182	0 0	+20 -30
Transverse Shear τ_{zx}	0(5)	34 -34	0 0	0 0
Octahedral Shear τ_{oct}	- -	52 0	0 -	- -

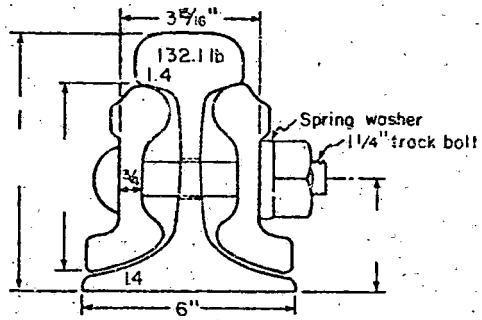
- (1) These are tread surface values from vertical loads as shown in Figure 1-2. Longitudinal stresses up to +11,000 psi may arise in the head from lateral loads, and additional stresses can arise from eccentric loading. See text.
- (2) The values for σ_x , σ_y and σ_z are surface values. Those for the shear stresses are values at depth 0.10 inch, as shown in Figure 1-3.
- (3) This thermal stress presumes a temperature change of 65 F.
- (4) These are experimental values for the case shown in Figure 1-4.
- (5) Warping stresses in the fillet can reach 10,000 psi due to eccentric vertical loads.

1.2.5 Consideration Governing Stresses at Bolted Joints

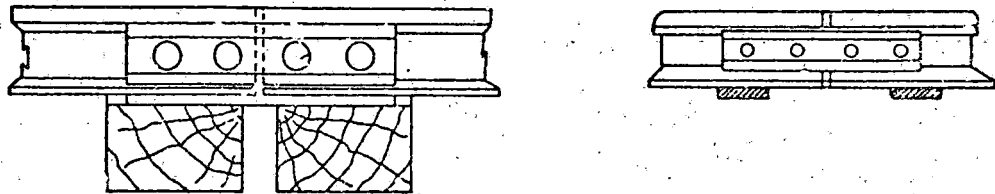
The bolted rail joint constitutes the oldest and most commonly used connection between rail sections. Much progress in the design of bolted joints has occurred since the earliest days of railroading when joint bars consisted of flat straps bolted across the rail ends. In this situation, moments were transmitted largely by frictional forces developed between the straps and webs by the action of bolt tension. Since those times, joint bars have been devised to transmit moments by forces acting on bearing areas on the underside of the rail head and on the rail base. Many bar configurations have been developed including a large variety of "patent" joint bars which have long since disappeared from trackwork catalogs. Bolted joints now consist of the two rail ends clamped by bolts and/or adhesive action between two joint bars. Spring washers are generally used to provide reserve tension and retain track nuts under vibration due to train passage. A cross section of a typical bolted joint connection is shown in Figure 1-5.

Rail joints may be supported in the track in two different ways: 1) they may be supported (with ties placed at the rail end), or 2) they may be suspended (without immediate tie support). In addition, the joints may be placed in the track either in a staggered pattern joints placed one half rail length in the track, or they may be placed opposite each other in the track. Figure 1-5 shows typical supported and suspended joint geometries.

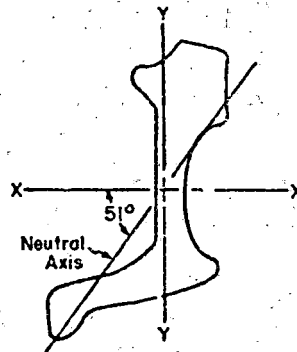
A variety of joint bar types have been used. Except in the case of the "compromise joint bar", such bars are symmetric about a transverse plane. Compromise joints are inserted for joining rails of different size (section). Otherwise, joint bars are symmetrical about their mid section. Symmetric and near-symmetric joint bars (Figure 1-5) have a horizontal neutral plane. Nonsymmetric joint bars have a neutral plane which is inclined at some angle to the horizontal and hence undergo rotation as well as deflection when subjected to bending in the vertical plane. The nonsymmetric joint bars may be further divided into categories of angle bars (Figure 1-5) and continuous bars. Angle bars represent an attempt at increasing the section modulus of



(a) Typical joint assembly



(b) Typical supported and suspended joint geometrics



(c) Angle type of joint bar

FIGURE 1-5. GEOMETRY OF JOINT ASSEMBLY

the joint bar by the addition of a projecting "toe" of metal. Continuous bars envelope the base of the rail increasing not only the section modulus, but also provide additional contact area and support.

The bolted joint would make the action in the track there approximate that in continuous rail except for adding opportunity for longitudinal motion between rail ends to accommodate temperature changes. It would also not promote failures. Despite the progress made in joint design, the bolted joint remains a truly "weak link" in the track structure, as the many rail-end failures attest. Photographic examples of the two main kinds of rail-end failure, that is bolt-hole cracks and head-web separation, have been provided by R. Steele of DOT-TSC, here shown as Figures 1-6 and 1-7. From these examples it can be seen that rail-end stresses of particular interest are circumferential stresses around the bolt holes and stresses in the upper fillet region.

The stresses that arise in the rail-end region depend, of course, on how the bars transmit bending moments to the rail. They do it at the lower head surface and upper flange surface in a manner that depends on geometric factors, such as bar length and cross section, and on bolt tension. Even wear on joint contacting surfaces is important. Thus it has been observed that in a new joint, tightened initially to 20,000 to 30,000 pounds per bolt, there can be as much as a 10,000 pound per bolt decrease during the first month of service, followed then by a 500 to 1,000 pound per month decrease. The recommended 5,000 pounds per bolt tension probably does not exist in most tracks.

The pattern of stresses developed in the rail end depends of course on the detailed shape of the structure. The bolt holes act to concentrate stresses in their neighborhoods, and, as Figures 1-6 and 1-7 suggest, the circumferential stress around each hole varies around the periphery of the hole. Because of the oversize holes used in joints, the bolts ordinarily do not participate directly in load transfer by transmission of vertical shear force when vertical bending occurs. However, bolts do play a direct role in lateral bending.

In general, joint bars are designed to fit closely to the rail and should be well finished so that potential sites for fatigue crack initiation can be avoided. Laboratory fatigue tests [1-19] have shown that bolt hole imperfections such as gouges and burrs have a highly detrimental effect on fatigue life, and this applies to rail ends.

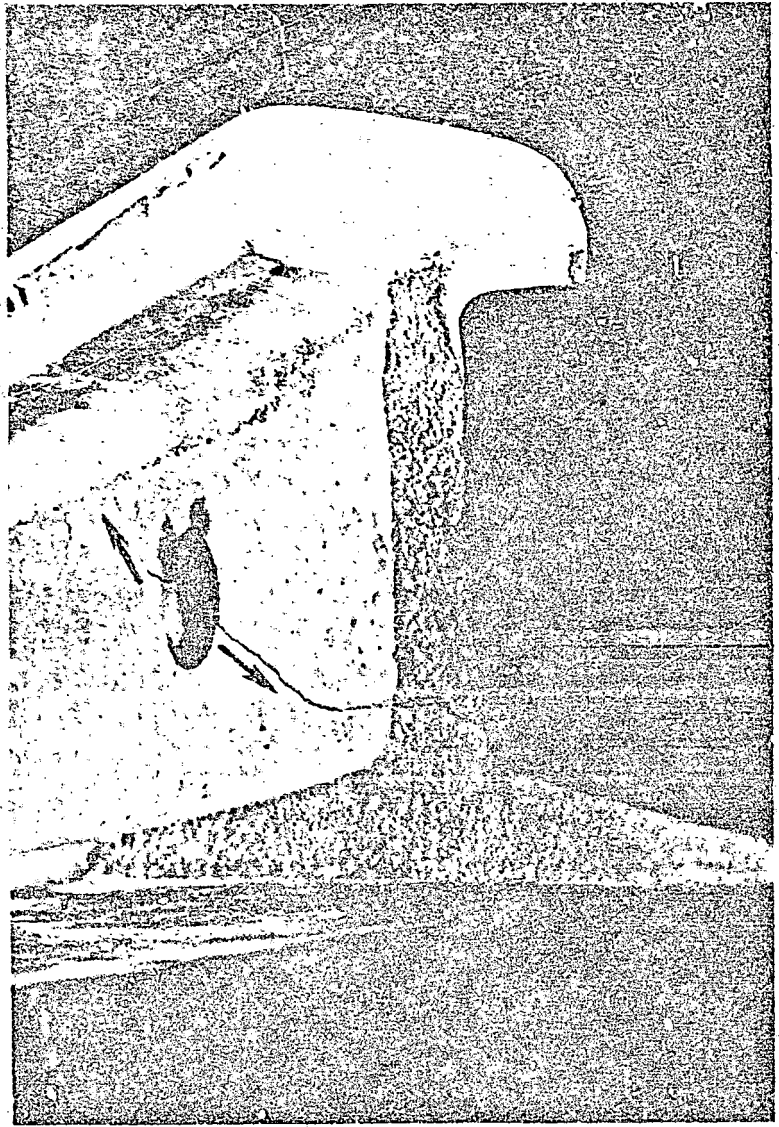


FIGURE 1-6. MOST COMMON HOLE CRACK GEOMETRY

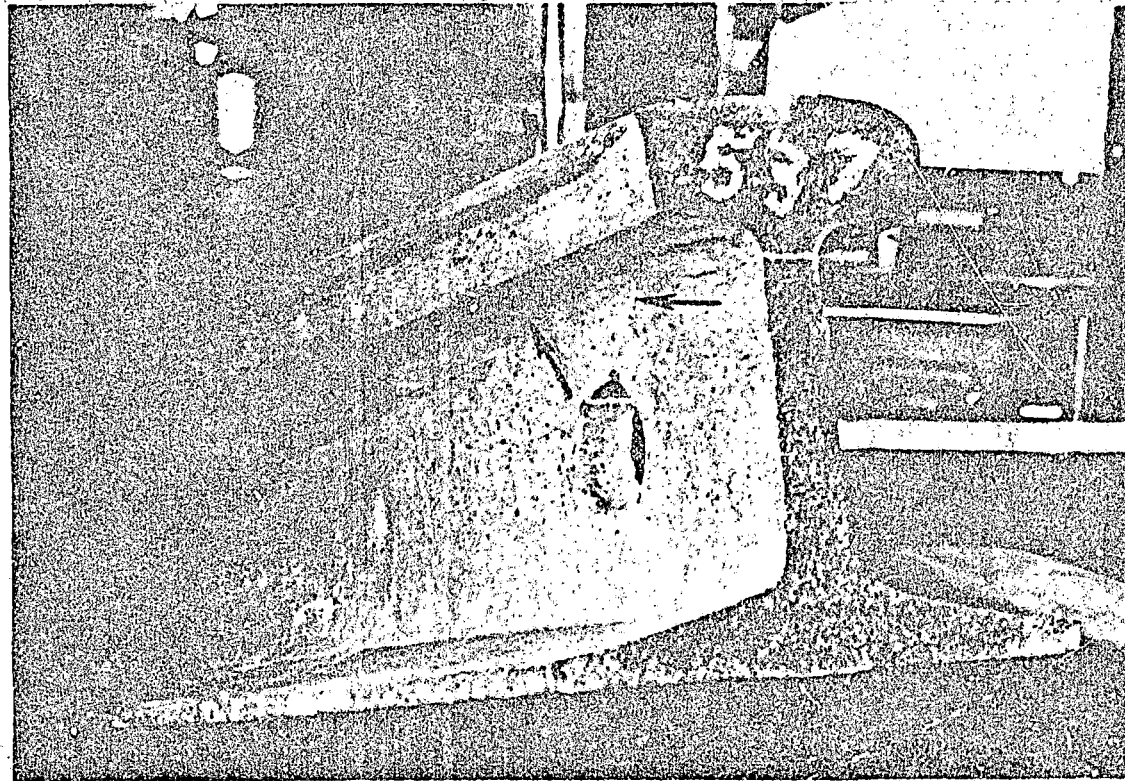


FIGURE 1-7. COMBINED HEAD WEB SEPARATION AND BOLT-HOLE CRACK

Considerable interest has been shown recently in measuring and predicting dynamic wheel/rail loads at joints, particularly where the foundation is degraded and permanent dipping occurs. There are two characteristic impulses, often identified as P_1 and P_2 , which contribute significant dynamic stresses in the joint and rail end. These stresses are superposed on the static stresses that would arise from wheel resting on the rail. Static stresses will be emphasized in this report, assuming that a dynamic load amplification factor could be used to scale the static results.

The most comprehensive study of the many aspects of bolted joint action is that of the Talbot Committee [1-20], which published the first of its series of memoirs in 1930. Their results, particularly with respect to joint bar stresses, are of great interest, despite the lack of modern strain gages at that time. Babb [1-21] later presented strain gage results for several British rail sections, and the AREA [1-22] gave laboratory results for U.S. rail joints having various bolt spacings. A similar study for Japanese rail sections was presented by Koyama and Sasaki [1-23]. The effects of longitudinal tension on bolt-hole stress was examined in another AREA study in 1953 [1-24]. Measurements of rail stresses in service conditions were studied by Wise, et al [1-11], who also considered fatigue; and two AREA Proceedings, [1-25] and [1-26] describe joint stresses under revenue traffic. The deleterious effects of bolt-hole imperfections were studied by the AREA [1-19] and by Code [1-27]. References [1-28] and [1-29] report effects of hole broaching.

The effects of dynamic loads at joints have been studied with a one-dimensional model by Nield and Goodman [1-30], and with a sophisticated model by Jenkins, et al [1-31]. The effect of resilient wheels on dynamic forces was described by Bjork [1-32]. Experimental results for such effects were reported by AREA [1-33] and more recently by Ahlbeck, et al [1-34].

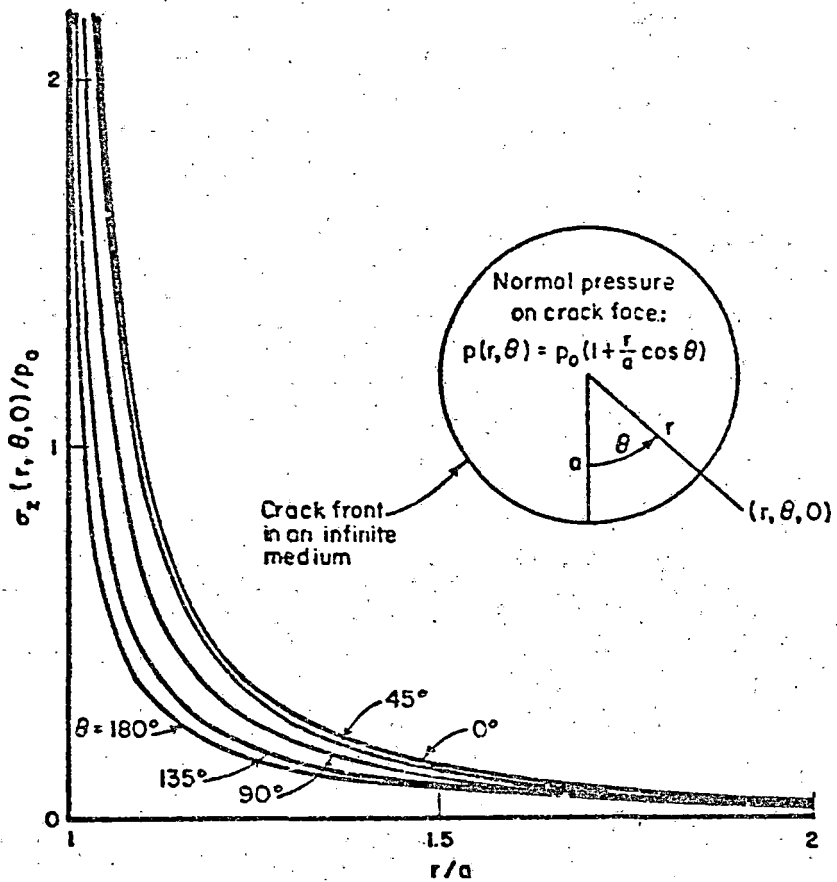
1.2.6 Stresses in the Presence of Cracks

This report deals primarily with defects including the transverse fissure, vertical split and horizontal split in rail heads and with bolt-hole cracks. Understanding the effect due these kinds of flaws involves postulating some small crack and determining what stresses would make it grow.

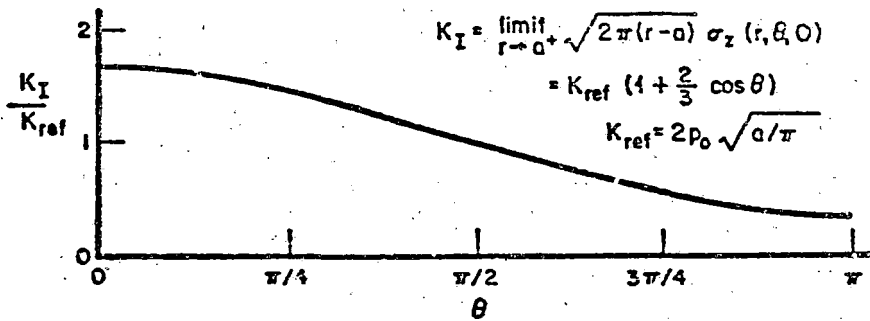
Of course, the presence of a crack would alter the nominal stress fields because stresses cannot be transmitted in the usual fashion where there is a crack. The changes in the stress patterns due to the presence of the crack may be described as crack stresses, and near the edge (or front) of the crack these stresses may be large and indeed dominant in crack growth. It is necessary to provide some description of these crack stresses.

Near a crack front, stresses actually become large enough to induce local plastic flow, but in analyzing crack stresses, it is convenient to regard the cracked body as being fully elastic even where the stress exceeds the yield point. The stresses predicted by elastic stress theory approach infinity near the front, but it has been found that rate of change of stress in that region can be used to estimate crack growth. Since the governing stress components become large in proportion to $1/\sqrt{r'}$, where r' is the local distance measured from the crack front towards the uncracked region, their limiting factors of proportionality to $(2\pi r')^{1/2}$ as $r' \rightarrow 0$ are taken as indicators of the severity of the local crack stresses. These "stress intensity factors" are commonly denoted as K_I , K_{II} , K_{III} depending on whether the stress component being considered would pull the crack surfaces apart or shear them radially or tangentially with respect to the crack front. The levels these factors reach depend on the stresses which fail to be transmitted because of the presence of the crack. Thus, the crack stresses crucial to crack growth are crack-induced stresses which arise because other stresses are present in the body. The estimation of these crack-induced stresses for a large variety of relevant conditions is the subject of Chapter 5 through its treatment of stress intensity factors.

To illustrate the nature of crack stresses, one may consider stresses in the vicinity of a circular (penny-shaped) crack which is deeply embedded in a body subject to tension in the direction perpendicular to the crack. These stresses were first treated by Sneddon [1-35] for a uniform remote tension. More recently Bell [1-36] analyzed them for an arbitrarily distributed normal (or tangential) load. Figure 1-8 shows results from these analyses for stress normal to the crack plane for a particular load pattern similar to the state that would tend to bend longitudinal fibers in the rail [1-37]. (Such a load would arise for a crack suitably placed on the rail section shown in



(a) Normal stress in axial direction around a circular crack loaded in bending (as shown above)



(b) Stress intensity factor around a circular crack front loaded in bending (as shown above)

FIGURE 1-5. AXIAL STRESS DISTRIBUTION AROUND A CIRCULAR CRACK LOADED IN BENDING

Figure 1-1a.) The great increase in this normal stress near the crack is shown for various angular positions in Figure 1-8. The rate at which the stress increases toward infinity varies with the angular position, and that variation is shown by the stress intensity factor in Figure 1-8. The reference stress intensity factor used there is that which would arise if the load were that of uniform remote tension.

Of course, cracks in rails are not always loaded with linearly varying tension, nor are they always circular, nor are they always deeply embedded. Since cracks are frequently more-or-less elliptical in shape [1-38], it is often convenient to use a related theory for stresses around elliptical cracks under tension, as treated by Shah and Kobayashi [1-39], or under shearing loads, as treated by Smith and Sorenson [1-40]. These theories are somewhat limited by requiring that the load distribution on the crack be describable by a polynomial of third order, but if the untransmittable load on the crack can be described in that way, then stress intensity factors can be found along the entire crack front. Chapter 5 shows the variation of stress intensity factors around a variety of elliptical cracks embedded in rail heads subjected to load distributions of kinds that may be expected in rail heads in service. It may be noted that the assumption of deep embedding implies that the effects of proximity to the rail surface are neglected. A scheme exists for taking into account neighboring surfaces, including surfaces which the crack crosses [1-10, 1-40, 1-41], but the theory is sufficiently cumbersome so that its use has been deferred here.

1.3 OBSERVATIONS CONCERNING CRACK INITIATION AND GROWTH

A rail newly placed in service but free of cracks would not experience the extreme stresses associated with crack fronts, but would be expected to yield somewhat under the high octahedral shearing stress due to contact loads. The yielding process would not necessarily produce any cracks, yet it is known that under cyclic stress conditions the rail does develop small cracks which can grow until the rail eventually breaks. Both the nucleation and growth processes for the crack are tied to stresses. However, knowledge about this connection is somewhat limited, especially as regards the crack nucleation

process. A review of this knowledge is to be provided elsewhere [1-42]; only a summary of it will be presented here.

Cracks are most apt to arise from inhomogeneities in the material being subjected to stress. Given the presence of an inhomogeneity, it is possible to hypothesize a process whereby a crack may nucleate, using a model such as the one proposed by Lankford and Kusenberger [1-43]. In their model, the process begins when the steel and the inclusion debond over parts of their interface under tension. Such separation might arise from local stress concentration due to inequalities in elastic properties in the two materials and /or from weakness of the interfacial bond. Following this first separation, minute cracks begin to radiate from the inclusion in directions normal to the tensile force, presumably because of local redistribution of loads resulting from the initial interface separation. Eventually the new surfaces created by these two processes merge, and thus a crack is nucleated. Lankford and Kusenberger made observations of this process using electron microscopy and 4340 steel. Several other authors [1-44, 1-45] have reported somewhat similar studies using other materials, also showing a strong relationship between inclusions and crack nucleation under stress. Thus, some of the elements for understanding crack nucleation are available, though the intricacies of the process continue to make prediction of crack nucleation largely empirical. In particular, much remains to be understood about crack nucleation in rail steels.

Some experimental information is available about crack initiation and growth in rail steels. Thus, Wise, et al [1-11], performed fatigue tests on drilled rail ends subjected to repetitive loading. Although this type of loading may produce effects different from those produced by a rolling load on a resiliently supported rail subjected to spectrum-type loads, the results are of great interest. The data reported in [1-11] were obtained by using wire crack gauges to signal the onset of cracking, thus establishing the number of cycles to crack initiation, as well as the number of cycles to complete failure. Figure 1-9 shows the specimen configuration used, and presents curves for crack initiation and final failure. It is interesting to observe that the ratio of cycles for crack initiation to final failure remains about the same regardless of the stress level. Thus, for a load of 20,000 pounds, 0.9×10^6 cycles elapsed in crack initiation while an additional 1.4×10^6

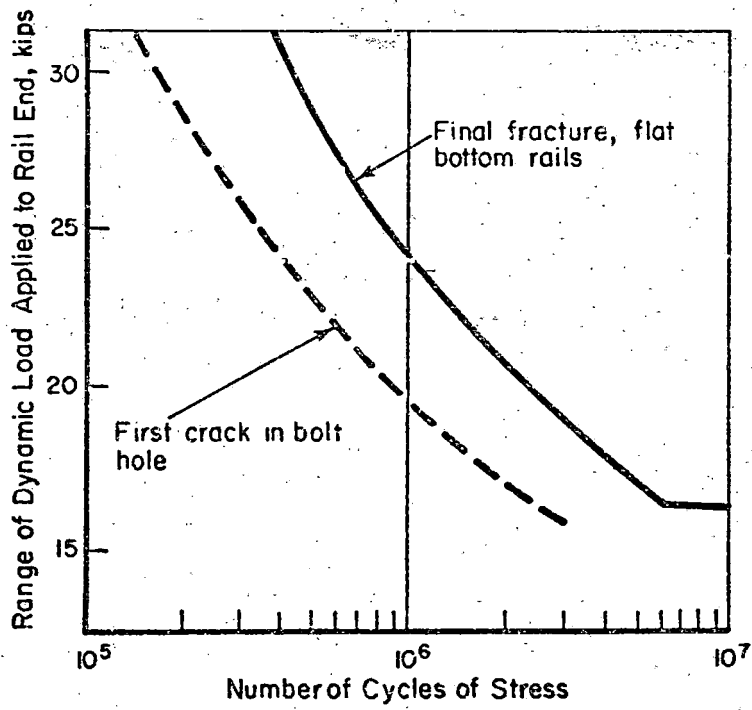
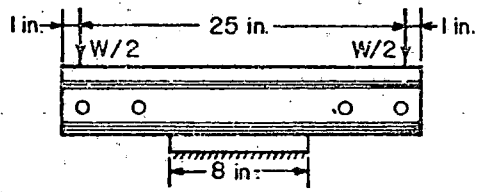


FIGURE 1-9. FATIGUE TEST ON 109-LB/YD FB RAIL DRILLED WITH STANDARD BOLT HOLES[1-11]

cycles were required for final failure to occur. At 30,000 pounds, 0.17×10^6 cycles are indicated as the time for initiation and an additional 0.28×10^6 cycles for final failure. Thus, these tests suggest that the residual life (about 1.5 the time required to induce cracking) of the cracked rail end is significant enough to warrant efforts to predict its magnitude.

After a crack has begun, repeated stressing at sufficiently high levels makes it grow, slowly at first, then more rapidly, and finally catastrophically. The rate of crack growth has been expressed by empirical formulas of several forms. An early formulation was that of Paris [1-46, 1-47], which showed the growth rate per load cycle as a power function of the range of the stress intensity factor experienced during the cycle. Parameters for the formula were to be found empirically for the relevant material and test conditions. Other authors have elaborated this relationship so that Forman [1-48] included also the absolute levels of the stress intensity factor and a critical stress intensity factor K_{IC} at which catastrophic failure would occur. Collipriest [1-49], using a still more intricate equation, also included a lower threshold stress intensity factor K_{Ith} , below which no crack growth would occur. These formulas characterize the crack size by a single dimension, and the constants fitted to them are usually found using quite simple stress fields. Yet they do offer some basis for predicting how cracks will grow under repeated loading.

This report is not intended to give broad coverage of either the processes of crack nucleation or crack growth. It is intended instead to provide information about stress distributions and stress intensity factors associated with service conditions because of their connection with the rail damage process.

1.4 REPORT ORGANIZATION

The chapters within this report that pertain specifically to midrail section have been organized as follows. Chapter 2 pertains to a study of flexural stresses in rails showing how bending stress distributions are affected by the type of load (vertical concentric, vertical eccentric, or

lateral), and by the foundation of the ties. Chapter 3 treats contact load distribution as influenced by realistic wheel and rail profiles, and from those finds subsurface stress distributions, sometimes including tangential as well as vertical loads. Chapter 4 examines information available about residual stresses in rails and theories about how these stresses grow. Chapter 5 considers how various representative stress patterns in rail heads would influence stress intensity factors along the fronts of cracks if they are there, thus providing input for possible crack growth studies. The calculation of these stress intensity factors is based on a new formulation of the theory for stresses around elliptical cracks.

Organization of the present investigation relating to the failure of rail ends is to be found in Figure 1-10. The approach shown in this figure can be summarized as follows:

Load Transfer Analysis--This phase is concerned with achieving a basic understanding of how load is transferred through a bolted joint. The internal joint forces which arise due to wheel loading were calculated using the two different approaches shown in the figure, and detailed in Chapters 7 and 8. These methods are capable of displaying the parametric effect of rail and joint bar size, load intensity and position, foundation modulus, and joint efficiency (representing the totality of load effects, including bolt tension joint-bar/rail-end fit). The understanding of the system of forces occurring at the rail end makes possible the explanation of why cracks initiate where they do. A three-dimensional finite-element model of the rail end which was used to compute magnitude and location of maximum stress for a variety of loading conditions is also described in Chapter 8. This model utilizes joint bar reactions developed in Chapters 7 and 8.

Experimental Validation--A rail joint was assembled in the laboratory and was subjected to simulated loading and support conditions to produce data for validating both the load transfer and three-dimensional stress-analysis models. Chapter 6 contains a description of the tests that were performed.

Stress-Intensity-Factor Calculation--Two-dimensional models of the rail end were used to calculate stress-intensity factors (K_I) as a function

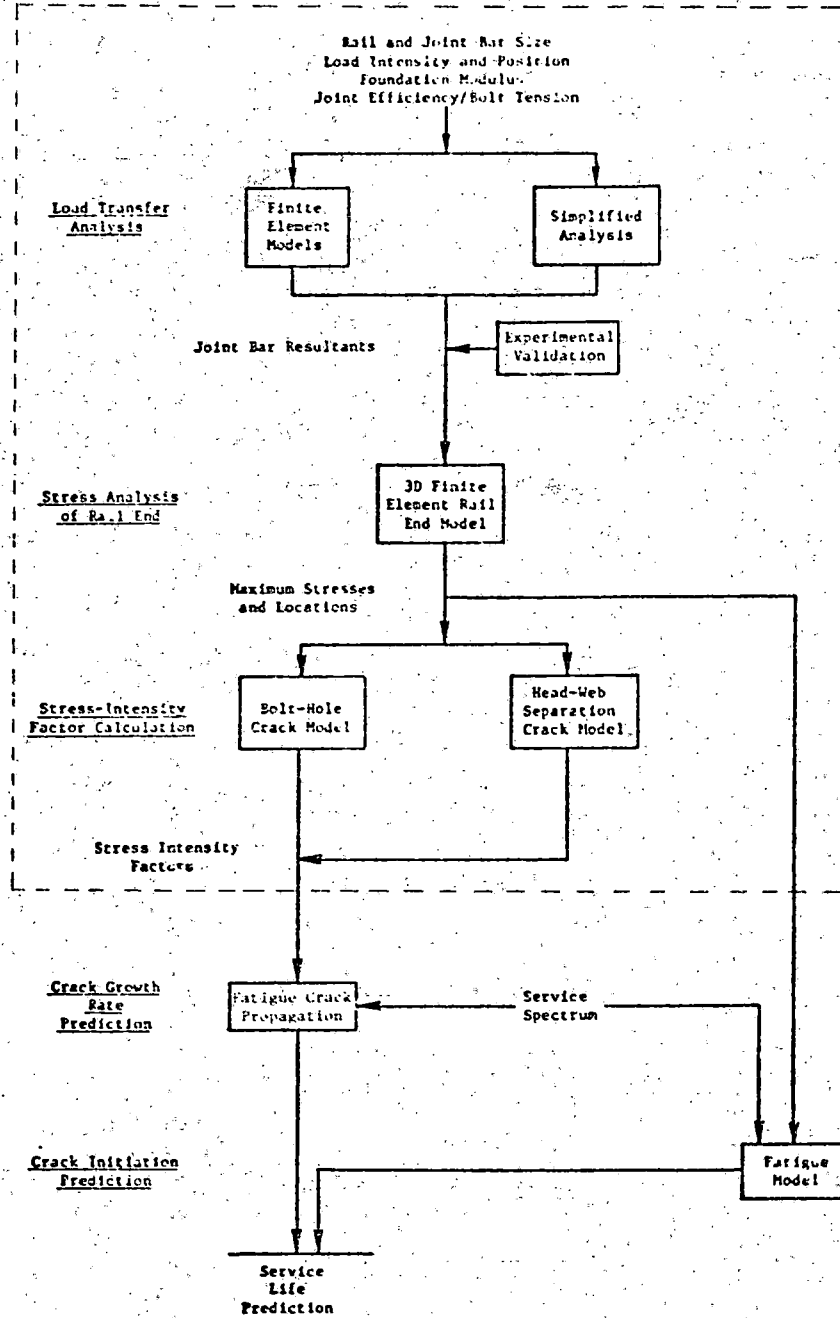


FIGURE 1-10. MODELING APPROACH TO RAIL END FAILURE

of crack lengths for two flaw geometries in Chapter 9. Closed-form solutions were used to check the results for small flaws emanating from the bolt-hole and for a head web separation initiating as a penny-shaped crack. These models also utilized the joint bar reactions developed in item (1).

In developing this analysis, approaches based on particular assumptions about the nature of the rail failure problem were consistently used. Because of inaccuracies which are both the result of rail steel material variability and of statistical nature of wheel/rail loading particularly at joints, it was concluded that a quasi-static analysis would be adequate even though the rail joint is the site of complex localized dynamic events. The wheel/rail loads which were applied in a quasi-static manner were, however, derived from a dynamic model of joint interaction.

Rather than developing a compendium of data covering many possible track conditions, the work was oriented towards producing practical analytical methods which were illustrated by a few typical joint situations. For this reason, a single joint bar and rail size were used throughout. The methods to be presented here are, however, perfectly adaptable to other commonly used joint geometries.

Further information on stresses at bolted joints is in a survey by Davies and Johns [1-50].

2. STRESSES DUE TO FLEXURE

The flexural component of stress is the one most commonly associated with rail and its function as a beam supporting rail car wheels. Consequently, the rail bending mode has been the most intensively studied in the past. From an analytical standpoint, flexural stresses are perhaps the easiest to evaluate, yet the complexities of combined vertical and lateral loading and the bending behavior of elements within the rail cross section result in complex stress cycles.

Flexural stresses in rails are produced by wheel loads applied vertically, laterally or longitudinally. The vertical loading may be centered on the head, or it may be eccentric so that the rail is twisted. Twisting and bending of the rail can also be induced by lateral loads. Non-uniformity of the tie support conditions complicate bending behavior of rails. In addition, the cross section commonly employed for rail causes analytic complexity in that the rail head acts as a beam supported by the elastic foundation provided by the web to produce secondary stresses. Varying demands for accuracy therefore lead to varying treatments of flexural stresses at different levels of complexity. This suggests the use of different levels of analysis, as is to be illustrated by the following discussion.

2.1 ANALYTICAL MODELS FOR THE CALCULATION OF FLEXURAL STRESSES

2.1.1 Beam-on-Elastic Foundation Model

The bending mode of deformation of rails under vertical wheel loads has been traditionally analyzed by applying strength of materials approaches to beam-on-elastic foundation models. As early as 1867, Winkler [2-1] proposed an analysis for calculating bending stresses in rail due to vertical loading by considering the rails as being continuously supported by an elastic foundation. The differential equation governing the bending of a beam supported in this way is

$$EI \frac{d^4 W}{dx^4} + kW = q(x) , \quad (2-1)$$

where $W(x)$ is the vertical deflection at x , EI is the flexural rigidity of the rail, $q(x)$ is the distributed vertical load and k is the uniform foundation constant associated with the linear Winkler foundation model known as the track modulus. In 1882 Schwedler [2-2] presented the following solution of Equation (2-1) for bending of a tie track for the case where an infinite beam is subjected to a single concentrated force P , as in Figure 2-1:

$$W(x) = \frac{P\beta}{2k} A(x) , \quad (2-2)$$

and the corresponding expression for the bending moment

$$M(x) = EI \frac{d^2 W}{dx^2} = \frac{P}{4\beta} B(x) , \quad (2-3)$$

where

$$\beta = \sqrt[4]{\frac{k}{4EI}} ,$$

$$A(x) = e^{-\beta x} (\cos \beta x + \sin \beta x) \quad (2-4)$$

$$B(x) = e^{-\beta x} (\cos \beta x - \sin \beta x) .$$

The track stiffness K_r is commonly written

$$K_r = \frac{2k}{\beta} , \quad (2-5)$$

where K_r has the dimensions of force/unit deflection. This stiffness represents the rail's local deflection behavior under a load in terms of the effective stiffness of the track under load. In 1885, a book containing many examples of solutions of interest for the analysis of railroad track was published by Zimmerman [2-3]. These examples were for longitudinal tie track which was in keeping with the assumptions of Winkler's original analysis. Timoshenko [2-4] pointed out, however, that the analysis can be suitable for cross tie

track if the foundation modulus k is properly chosen. Hetenyi [2-5] showed that such an assumption is appropriate for cross tie track if the tie spacing l_t (see Figure 2-1) obeys the relation

$$l_t \cong \left(\frac{\pi}{4}\right) \left(\frac{4EI}{k}\right)^{1/4} = \left(\frac{\pi}{4}\right)/B ,$$

or

$$\beta l_t \cong \left(\frac{\pi}{4}\right) . \quad (2-6)$$

Figure 2-2 shows Equation (2-6) plotted for various foundation moduli and its relation to various rail sections. For most rail (115-lb RE or larger) with well supported cross ties at a 22-inch tie spacing the beam-on-elastic foundation model is adequate for evaluating typical stress levels due to vertical bending despite the discontinuity of the supports.

Normalized curves for the rail deflection and rail bending moment due to a unit concentrated force P are shown in Figure 2-3. The distance from the loading point to the nearest point of zero bending moment is used as a convenient reference distance. This distance can be calculated from Equation (2-3) as

$$X_1 = \frac{\pi}{4\beta} , \quad (2-7)$$

and the distance from the load to the point of zero rail deflection, X_2 , is

$$X_2 = 3X_1 . \quad (2-8)$$

For reference purposes, Table 2-1 lists typical data for the characteristic lengths X_1 and X_2 for rails of the size range normally used by the railroad industry. Using these numbers, one can readily interpret Figure 2-3 in terms of distances along particular kinds of track.

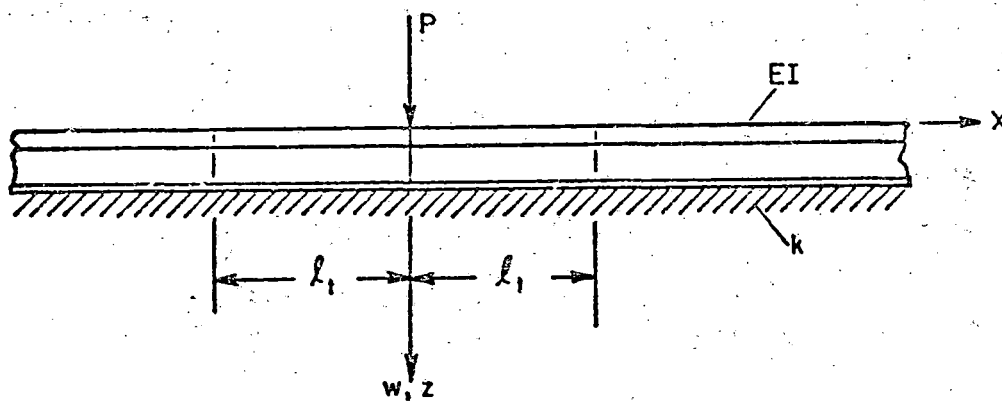


FIGURE 2-1. INFINITE RAIL WITH CENTRAL POINT LOAD

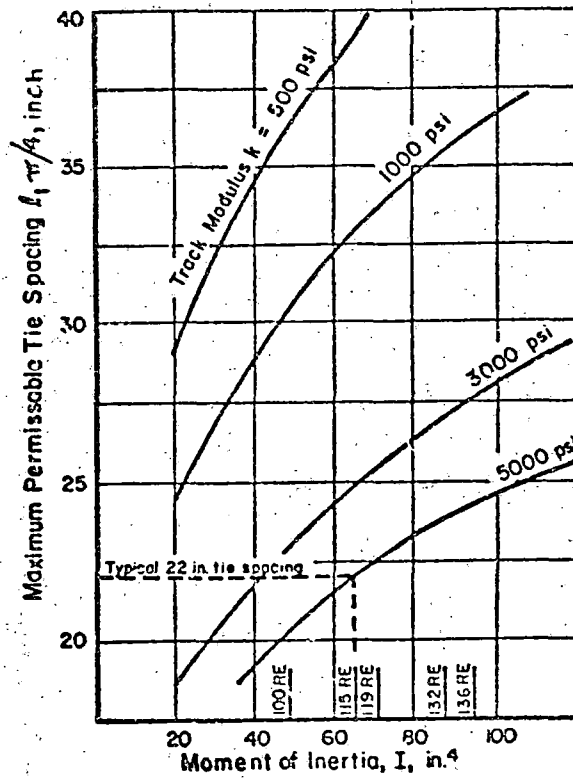


FIGURE 2-2. MAXIMUM TIE SPACING ALLOWABLE WHILE USING WINKLER MODEL [2-6]

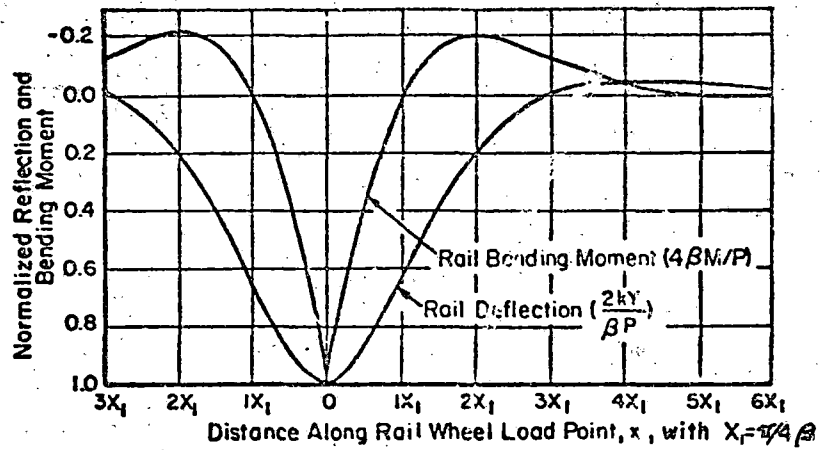


FIGURE 2-3. NORMALIZED RAIL DEFLECTION AND BENDING MOMENT CURVES [2-7]

TABLE 2-1. TYPICAL DATA FOR THE CHARACTERISTIC LENGTHS X_1 AND X_2 *

Track modulus, k (psi)	100# Rail		115# Rail		132# Rail	
	X_1 (in.)	X_2 (ft)	X_1 (in.)	X_2 (ft)	X_1 (in.)	X_2 (ft)
500	45.9	11.5	49.4	12.3	53.1	13.3
1000	38.6	9.7	41.5	10.4	44.7	11.2
1500	34.9	8.7	37.5	9.4	40.4	10.1
2000	32.4	8.1	34.9	8.7	37.6	9.4
3000	29.3	7.3	31.5	7.9	34.0	8.5
4000	27.2	6.8	29.3	7.3	31.6	7.9

*See Equations (2-7) and (2-8).

The deflections or bending moments resulting from multiple wheel loads can be calculated by superposing contributions due to individual wheels. Normal axle spacings of 6 to 8 feet are typically equivalent to $2X_1$ to $3X_1$, and examination of Figure 2-3 shows that two deflection distributions translated by distance in the range $2X_1$ to $3X_1$ reinforce each other at their peaks, but moment distributions thus combined tend to counteract each other at their peaks. Mutual reduction of peak moments can be seen implicitly in Figure 1-2 by comparing the one-wheel and two-wheel values for the top-surface longitudinal stresses, which are proportional to the bending moments, though the soft foundation assumed there puts the axle separation in the range X_1 to $2X_1$.*

The analytical results based on Equation (2-1) have been generally accepted and proven by test results to provide acceptable values for overall rail deflections and remote fiber bending stresses in regions adjacent to the point of application of load when the assumptions of the Winkler model are not

*The stresses shown in Figure 1-2 are proportional to bending moments derived from Equations (2-3) and (2-4). Those equations were used for both overall-rail and head-on-web bending. For overall-rail bending, $X_1 = 44.7$ inches.

violated. Representative applications of simple beam-on-elastic foundation analysis were presented by Talbot [2-8], Timoshenko and Langer [2-9], and more recently by Eisenmann [2-10]. Innumerable other applications exist in the literature. As pointed out by Kerr [2-11], these methods are used by many railroads for design purposes. The 'practical' application of the analyses to track design is presented by Clarke [2-12] in the series on "Track Design Fundamentals", and by Prause, et al [2-7]. A new study, including many ramifications, is one by McConnell and Perlman [2-13].

It is generally accepted that rail deflections and bending stresses can be predicted with acceptable accuracy for uniform track conditions if the foundation modulus k has been determined by prior measurement. Even here, large variations of k produce only small deviations in bending stress. Thus, from Equation (2-3) and the definition of β it can be seen that a doubling of k produces only a 16 percent decrease in the bending moment and hence in the maximum bending stress. As Figure 1-2 illustrates, a significant addition to the longitudinal stress occurs in the vicinity of the application of the load since the rail head itself behaves as a beam on an elastic foundation provided by the web. Applying the Winkler model to the rail head supported by the web, the foundation modulus for the rail head under vertical loading is [2-6]

$$k = \frac{tE}{d} , \quad (2-9)$$

where

d = web height,
 t = average web thickness.

When the load is lateral, the support of the rail head provided by the web comes from bending of the web, and in that case the foundation modulus produced by the web is

$$k = Et^3/d^3 . \quad (2-10)$$

Solutions for rail head bending presuming the Winkler model can again be obtained from Equations (2-2) and (2-3) using the moment of inertia of the rail

head and k that is appropriate for the web. (This is the basis for the rail head bending stresses included in Figure 1-2.)

Beam theory of Winkler's type, can be applied to analysis of stress arising not only from vertical loads but also from lateral loads and longitudinal surface loads. The further prospect of eccentric loading and of having the loads present in varying proportions makes the range of such possible beam analyses for rails very great. The recent report by McConnell and Perlman [2-13] illustrates a wide range of these possibilities. This kind of beam theory, however, has its limitations, such as inability to provide detailed information on local stresses near detailed cross-section geometry such as at the head-web fillet. Various investigations have been undertaken to address problems such as finding fillet stresses by empirical or semi-empirical methods. Thus, two-dimensional photoelastic stress analyses have been conducted by Timoshenko and Langer [2-9] and by Leaf [2-14]. Also a semi-empirical method for analyzing fillet stresses was presented by Code [2-15]. These analyses are summarized in Reference [2-6].

The utilization of beam theory to compute nominal longitudinal bending stresses in the rail cross-section assumes simple linear variation of the stress components across the rail section passing from peak tensile stress to peak compressive stress. This analysis provides an adequate description of general bending stress behavior, but fails to reflect accurately the distortions in stress fields caused by changes in the section at the head-web and web base regions.

2.1.2 Finite Element Models for Computing Flexural Stresses

For analysis of detailed rail stresses which vary over the rail cross section in a manner more complex than simple beam theory would indicate, finite element methods can be used. Three dimensional models of this type were developed in this program both for the purposes of analyzing flexural stresses more fully and for providing detailed stress field information for analysis of stresses in rails containing flaws.

As a major thrust of the research reported herein, computer programs for analyses of flexural stresses were developed employing two kinds of finite

element models for rails. One of these models, intended for use over a moderately long span, treats the rail as a beam supported by discrete ties. The other model, intended for use over a short span, provides more detailed stresses near the wheel/rail contact. The programs were arranged so that the latter could be applied for a short section of rail and the ends be merged with the program covering the longer span. Thus both wheel/rail contact and tie support could be treated in a unified analysis.

The model for use near the wheel/rail contact point treats cases symmetric around a plane $x = 0$, as shown in Figure 2-4. It has 189 isoparametric, three dimensional, 20-node brick elements, which include 63 elements in each of three longitudinal sections. It has 857 nodal points. In practice, the longitudinal sections were taken to be 1.0, 1.5, and 1.0 inches long, so by applying symmetry about $x = 0$ this model covered a span of 7.0 inches.

The longer range model provided for support by 40 ties resting on a linear elastic half-space. The rail was divided into sections and these, as well as the ties, were represented by beam elements.

In order to appraise the validity of finite elements stress calculations for rails, several photoelastic and strain-gage measurements of stresses in rails were conducted. Further strain gage measurements were obtained also from laboratory experiments at AAR and from field tests on the Florida East Coast Railroad which were part of the overall DOT-TSC program. As described in Appendix A, these measurements were compared with finite element stress calculations using a mesh somewhat coarser than that in Figure 2-4. Agreement was reasonably good, being poorest near the top of the rail. For this reason, the finer mesh shown in Figure 2-4 was chosen for later calculations.

2.2 FLEXURAL STRESSES IN RAILS UNDER VARIOUS CONDITIONS

The finite element models described above were used to compute stress distributions in rails for various load and support conditions, to find particularly how the stresses near the wheel/rail contact differ from those implied by simple beam theory. Beam theory primarily considers simple variations in longitudinal normal and shear stress due to σ_x and τ_{zx} , neglecting the other stress components, yet the concentrated load and the shape of

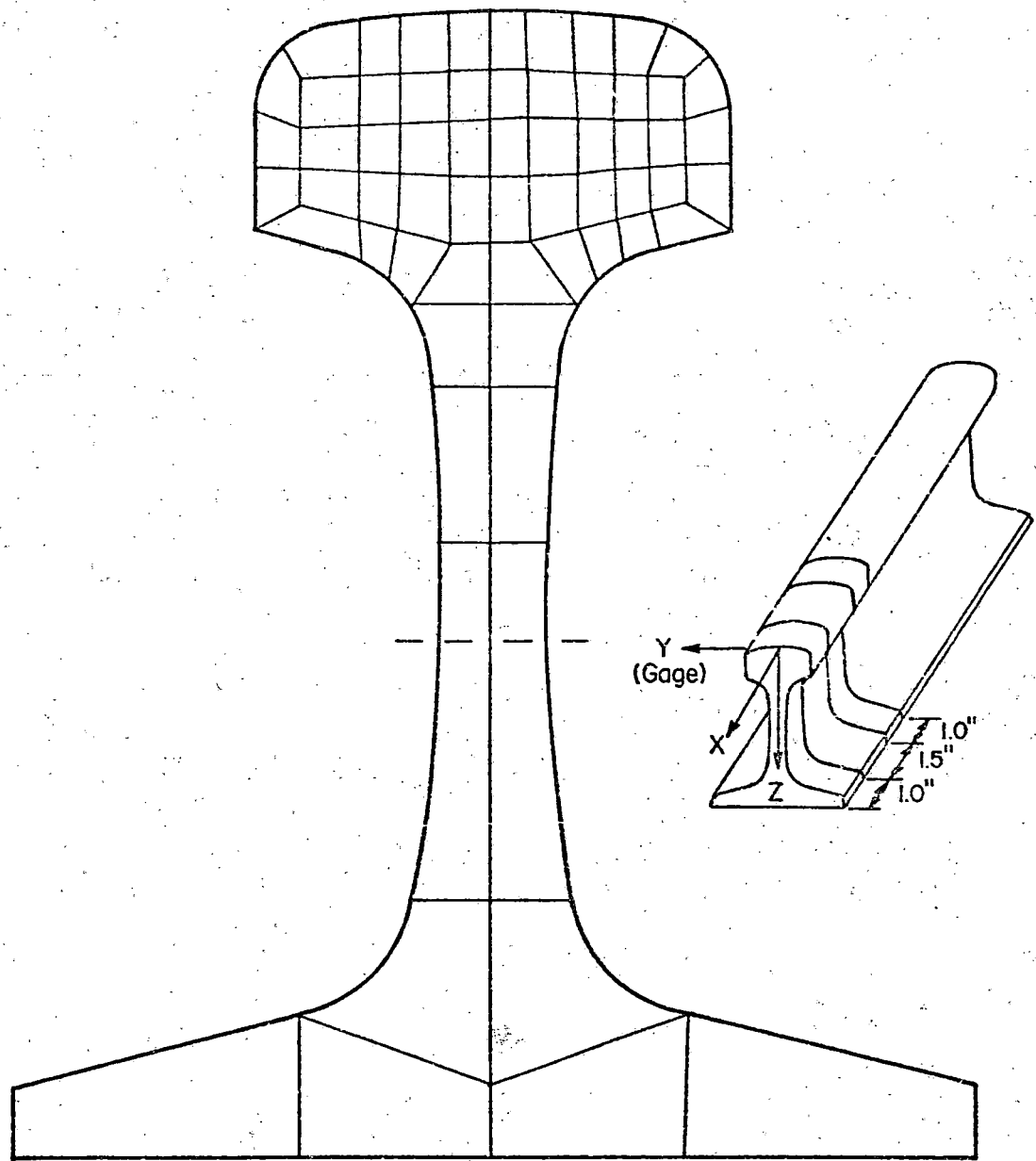


FIGURE 2-4. FINITE ELEMENT MODEL FOR 132-LB RE RAIL NEAR POSITION OF WHEEL CONTACT

the rail cross section make all the stress components vary locally within the section. The finite element stress calculations were intended to investigate these variations.

The rail chosen for the calculations was 132-lb RE rail, without substantial wear so that its cross section has its original rolled shape. As a baseline test case, the rail was considered to have a 19,000-lb vertical load*, but the load could be applied centrally or eccentrically. A 10,000-lb horizontal load could be added to represent flange contact. To maximize rail bending, the load was centered between two ties. The tie spacing was 20 inches, and various levels of support stiffness were treated by varying the foundation modulus. The moduli employed were 2000 psi for a soft foundation, 5000 psi for a fairly normal foundation, and 7000 psi for a stiff one. The foundation modulus for resistance to lateral motion was taken to be 85 percent of that for vertical motion as indicated by McConnell and Perlman [2-13]. Five cases were analyzed, using combinations of load and support conditions as shown in Table 2-2. The Young's modulus was assumed to be 28.9×10^6 psi and Poisson's ratio equal to 0.30.

TABLE 2-2. SPECIFICATIONS FOR FINITE ELEMENT CALCULATIONS OF STRESSES IN RAIL^(a)

Case	Load Description ^(b)			Support Conditions ^(c)			
	Vertical, 19,000-lb Eccentricity, inch		Lateral, 10,000-lb	Foundation Moduli, psi			
	0	+0.75		Vertical		Lateral	
				2000	5000	7000	4250
1	X				X		
2	X			X			
3	X					X	
4		X			X		
5	X		X		X		X

- (a) The rail was chosen to be new 132-lb RE rail.
 (b) All loads were applied midway between two ties.
 (c) The tie spacing was 20 inches.

* The 19,000-lb load level was selected as a basis for comparison with earlier rail stress investigations by Martin [2-16] which suggested that this load was the limit for stability of the rail residual stress field.

For these calculations, loads were applied at nodal points of the four elements adjoining the center of contact, varying their magnitudes to simulate a contact load. Since the elements were an inch long, that is about three times the half length of a typical contact patch, the load representation was somewhat coarse. Nevertheless, at points more than an element away from the center of contact the calculated stresses were expected to be realistic since the overall load was distributed to give net force vector identical to the contact load.

Stresses calculated for these cases are compiled in detail in Appendix B. In particular, for the more or less standard conditions of Case 1 all six stress components plus the octahedral shear stress are shown in terms of their contours on cross sections at several longitudinal positions. The results also illustrate the influences of foundation stiffness, eccentric loading, and lateral loading.

As an example of the stress patterns that were found, consider the variation of longitudinal stress σ_x , starting at the plane $x = 0$ which passes through the center of contact. Contours for this stress are shown in Figure 2-5. The contour where $\sigma_x = 0$ is near the neutral plane for the rail bending as a beam. Above that contour the stress is everywhere compressive, but the shapes of the contact area and the rail cross section distort the contours. Below that contour the stress is everywhere tensile, but the spacing of the contours narrows where the cross section widens. Pursuing σ_x further, one may plot the variations of σ_x as z varies from top to bottom of the rail along the vertical axis of the rail. By using graphs such as those in Appendix B this may be done for several positions along the rail (that is several values of x) to obtain the results shown in Figure 2-6. Here the non-linearity of σ_x as z varies shows departure from the expectations of simple beam theory. The distortion near the tread surface where $x = 0$ or 0.5 inches results for contact effects and head-on-web bending. Those effects are thought to be underestimated by the results shown here since the contact load was spread artificially, resulting in the distortion of σ_x . It can be seen, however, that this distortion decreases rapidly away from the contact region, so that the curves for $x = 1.75$ inch and 2.5 inch are close to each other and do not depart greatly from straight lines.

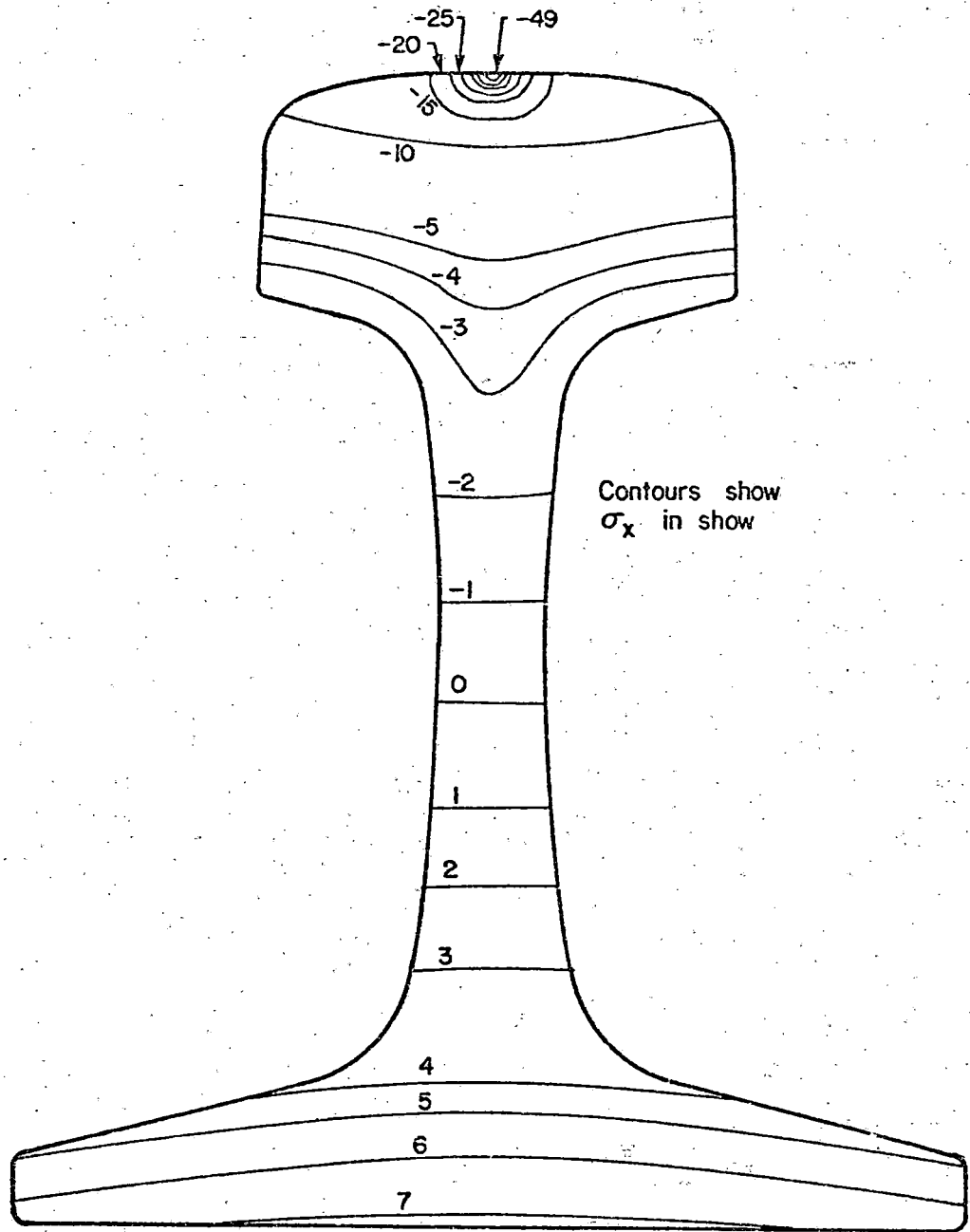


FIGURE 2-5. CONTOURS OF LONGITUDINAL STRESS ON PLANE THROUGH LOAD POINT OF 132-LB RE RAIL UNDER 19,000-LB VERTICAL WHEEL LOAD (CASE 1)

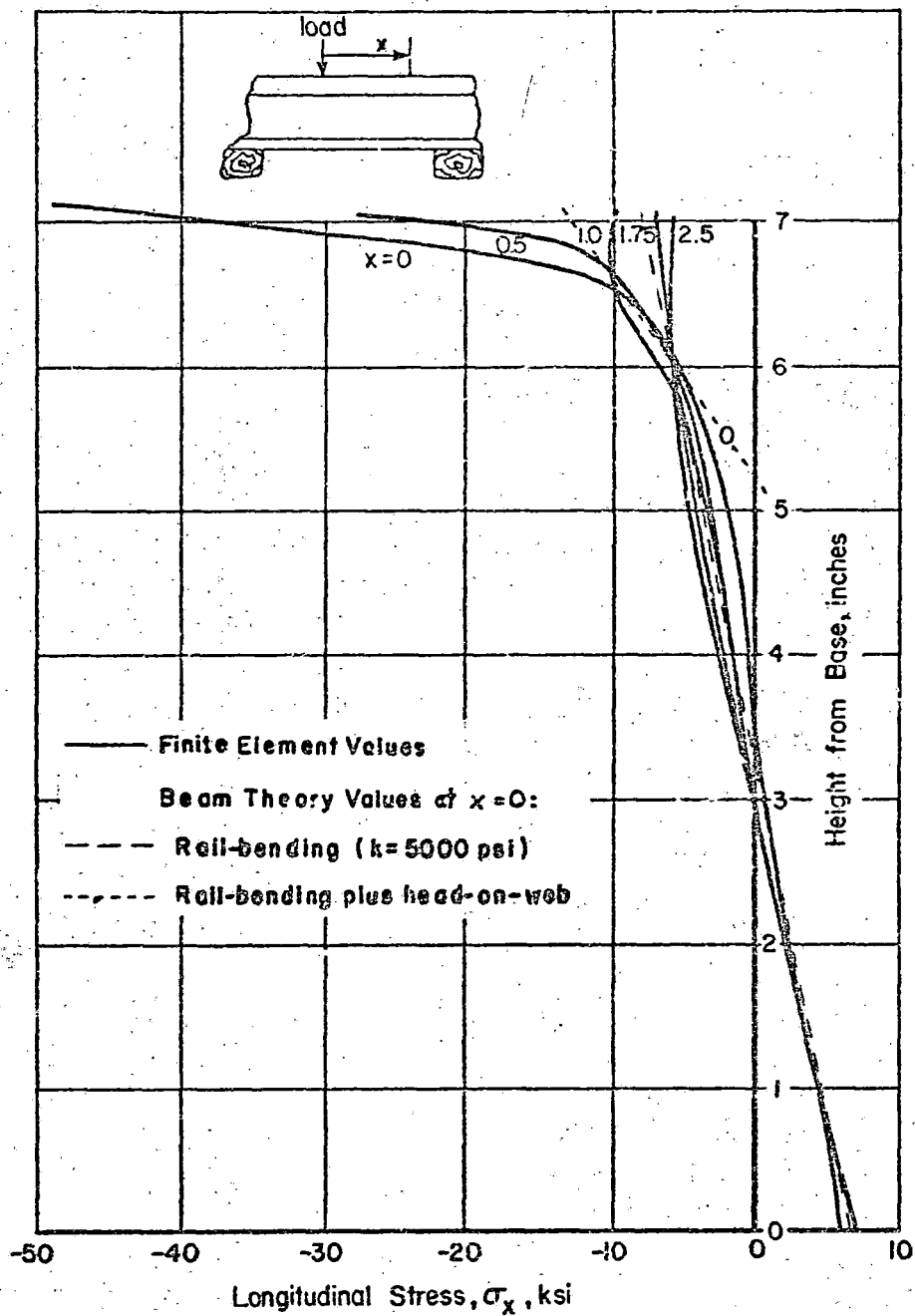


FIGURE 2-6. LONGITUDINAL STRESS σ_x IN A 132-LB RE RAIL AT FIVE SECTIONS ALONG RAIL UNDER 19,000-LB WHEEL LOAD (CASE 1)

As Appendix B shows, the components σ_y and σ_z also reach quite large values near the contact region, but these damp out very rapidly away from the contact area. Since these components do not offer primary resistance to rail bending, they damp out to zero rather than to the linear vertical variations characteristic of σ_x .

Away from the ties, the shearing stress τ_{zx} provides the vertical reaction for the load, so its integral over the cross section must equal half the contact load. Since τ_{zx} must also vanish on free horizontal surfaces, it follows that for simple beam theory its z-variation should reach a maximum near the neutral plane for bending. This behavior is substantially different from the expectations of contact stress theory. The shear τ_{zx} due to wheel/rail contact would make τ_{zx} greatest just below the edge of the contact patch. The way these competing influences are resolved for Case 1 at $x = -1.0$ in. is shown in Figure 2-7. The largest value of τ_{zx} on that plane was computed to be -4216 psi at a depth of 0.45 in. The variations of τ_{zx} with depth z along lines on the plane $y = 0$ are shown for several values of x in Figure 2-8. This figure shows how contact stresses dominate near the contact patch, but for $x = -1.75$ inches and $x = -2.5$ inches, the behavior becomes more nearly like that expected from beam theory. Variations over the section $x = -1.0$ inches represent a composite of the two forms of influence.

Caution should be observed in evaluating the τ_{zx} results for the plane $x = 0$. The values computed for τ_{zx} at $x = 0$ show spurious results close to the running surface. This conclusion stems from the simple observation that τ_{zx} should be antisymmetric around the plane $x = 0$ if the loading and supports are symmetric around it, as they are for Cases 1 to 5. Thus τ_{zx} should vanish at $x = 0$. Figure B-5 in Appendix B shows that τ_{zx} was indeed computed to be near zero over most of that plane, but to a depth of about a half inch below the contact patch it varied significantly. This variation comes from inaccuracy inherent in the coarse finite element mesh. It provides a warning not to overemphasize values computed for stresses in that small region with a coarse mesh model.

It is also proper here to reexamine the concept of the rail head bending as a beam on the elastic foundation provided by the web. Figures 2-8 and B-5 provide some support for this idea, since they show that the fraction of the

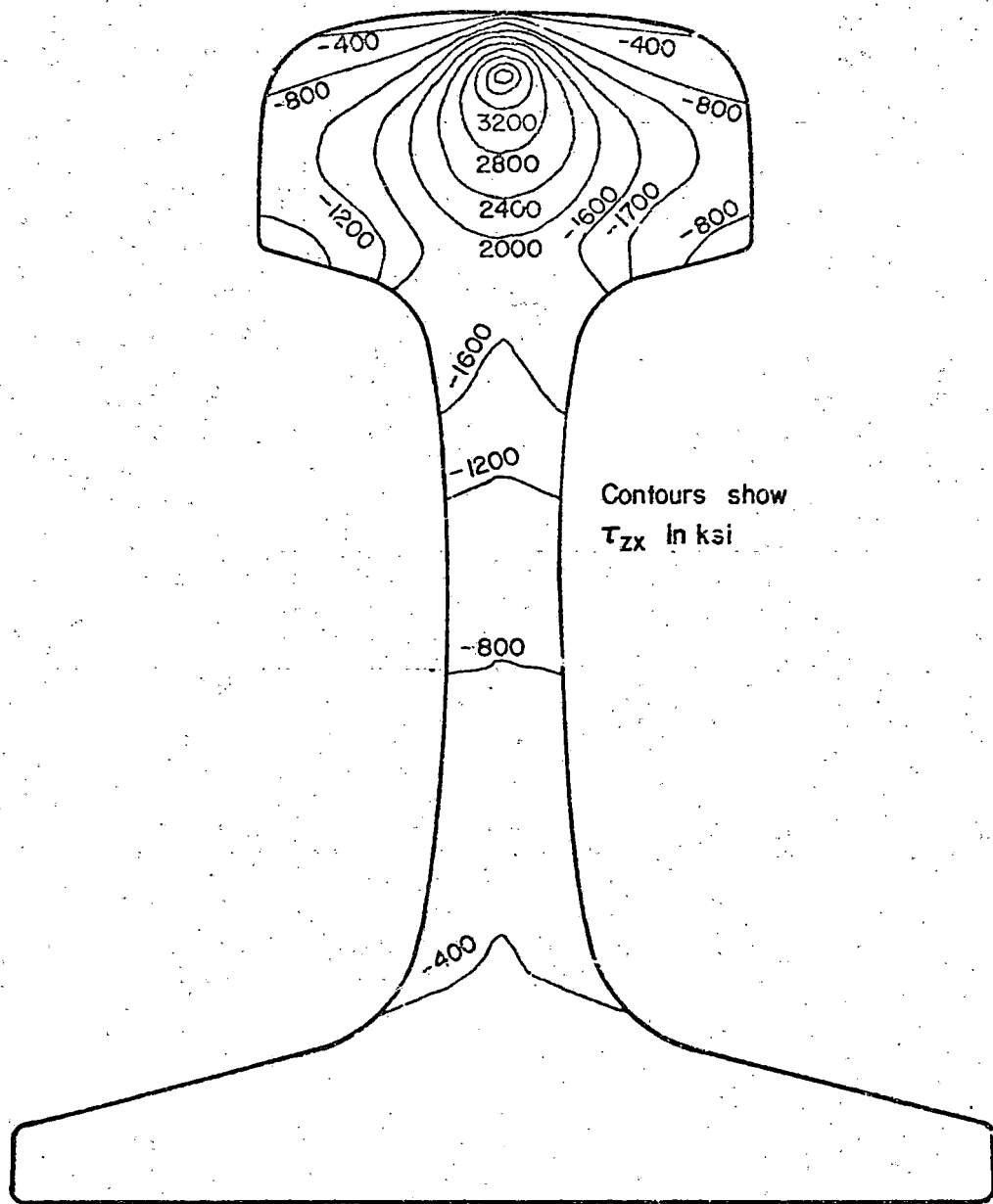


FIGURE 2-7. CONTOURS OF VERTICAL SHEAR STRESS ON PLANE 1.0 INCH FROM LOAD POINT OF 132-LB RE RAIL UNDER 19,000-LB WHEEL LOAD (CASE 1)

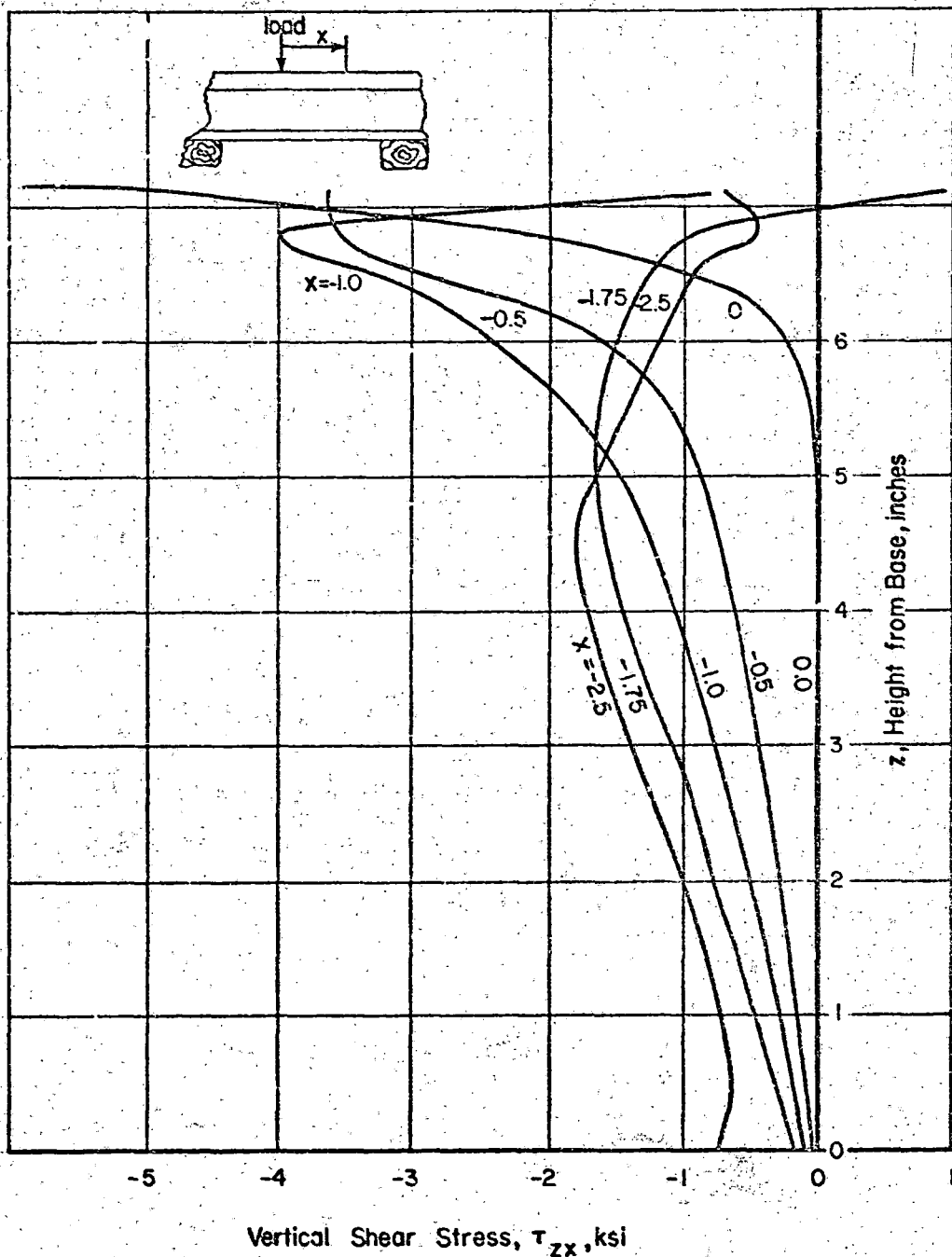


FIGURE 2-8. VERTICAL SHEAR STRESS THROUGH 132-LB RE RAIL AT FIVE SECTIONS ALONG RAIL UNDER 19,000-LB WHEEL LOAD (CASE 1)

load support by the head is greater at $x = -1.0$ inches than it is at $x = -1.75$ inches, which in turn is somewhat greater than the fractional support by the head at $x = -2.5$ inches. For greater values of x this effect apparently diminishes. The sideward bulges of the contours for the rail head in Figure 2-7 (so that the vertical variation of τ_{zx} there is roughly parabolic) also suggest that the sideward extensions of the rail tend to act as independent beams. However, the overall variations of σ_x and τ_{zx} are sufficiently complex so that the concept of rail head bending is somewhat obscure. In particular the prospect of tensile values of σ_x near the base of the rail head (on account of rail head bending), once regarded as a real possibility, does not materialize in the calculations shown here. Recomposition of stresses calculated for Figure 1-2 to estimate the stress at the base of the rail head, shows that the prospect for tensile stress at that position, is not strong even by the theory used there. For track with a very stiff foundation, the stress σ_x there may become tensile [2-6], since the compressive contribution from overall rail bending is then lessened.

The octahedral shear stress, defined as

$$\tau_{\text{oct}} = \left[\frac{2}{3} \left(\frac{1}{6} [(\sigma_x - \sigma_y)^2 + (\sigma_y - \sigma_z)^2 + (\sigma_z - \sigma_x)^2] + \tau_{yz}^2 + \tau_{zx}^2 + \tau_{xy}^2 \right) \right]^{1/2}, \quad (2-11)$$

is frequently used as an indicator of whether plastic flow will occur, so it was included in the calculations performed here. Under normal contact loads, this stress reaches its greatest value beneath the center of contact, so contours for it at $x = 0$ are shown in Figure 2-9 for the conditions of Case 1. Its highest value computed on that plane section was 14606 psi at depth 0.202 inches below the center of contact. The accuracy of such a value is somewhat disturbed by its proximity to the contact patch, so it would be desirable to evaluate it again by other means. Nevertheless, the contours in Figure 2-9 provide useful information regarding possible plastic flow, since only a small region is probably affected by the proximity to the contact patch.

Cases 2 and 3 of Table 2-2 were chosen to illustrate the effect of variations in foundation stiffness, and together their stiffnesses (2000 psi for Case 2 and 7000 psi for Case 3) bracket the more normal stiffness (5000 psi) presumed for Case 1. The principal effect of varying stiffness should be on

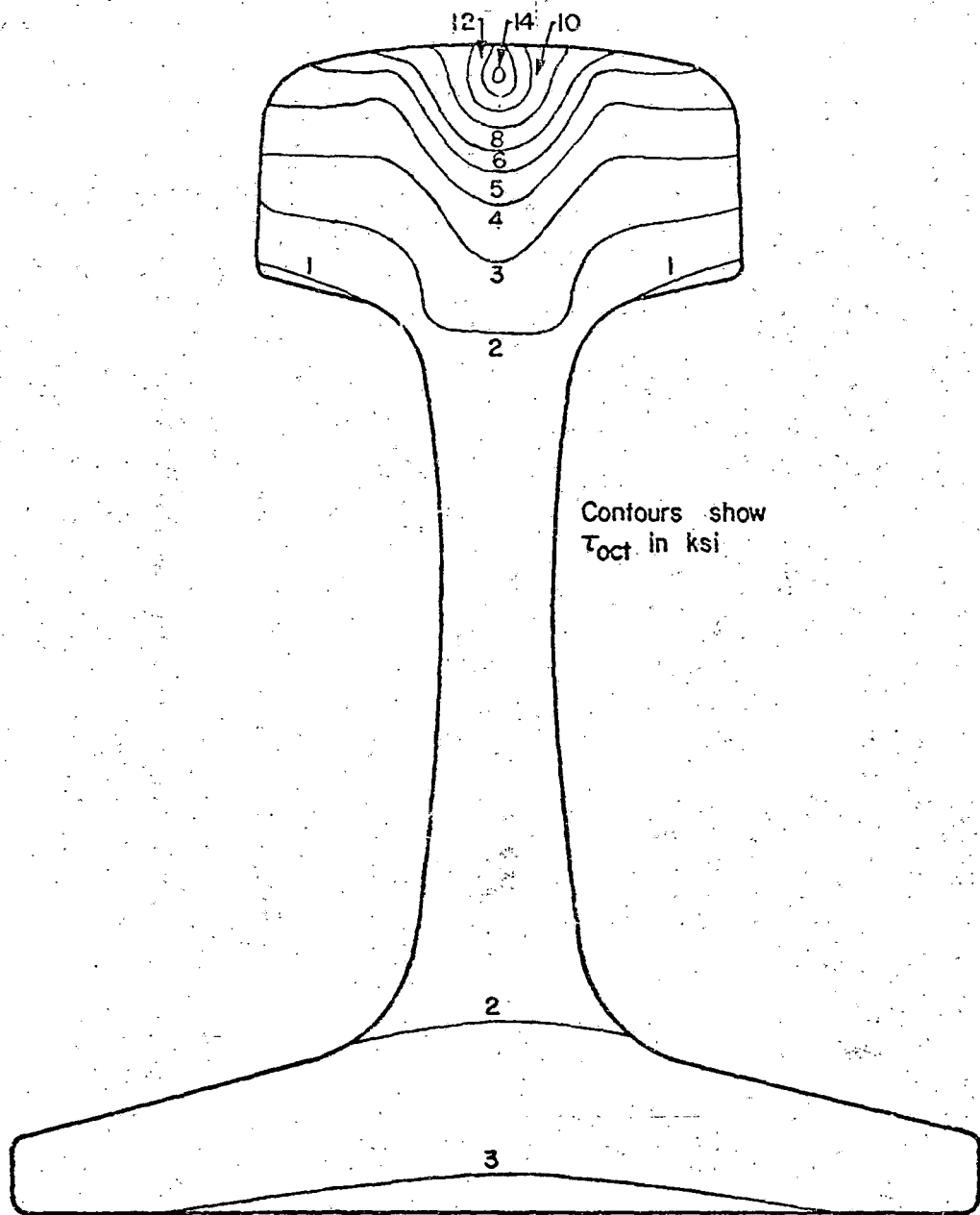


FIGURE 2-9. CONTOURS OF OCTAHEDRAL SHEAR STRESS ON PLANE THROUGH LOAD POINT OF 132-LB RE RAIL UNDER 19,000-LB VERTICAL WHEEL LOAD (CASE 1)

the longitudinal stress, σ_x , and the calculations agree with this. Indeed the values computed for the shearing component τ_{zx} were so similar for all three of these stiffnesses that graphical results for Cases 2 and 3 were indistinguishable from those for Case 1 and were therefore omitted from Appendix B. (The computed extrema of τ_{zx} were -4233, -4216 and -4213 respectively for Cases 2, 1 and 3 at $x = -1.0$ inch.)

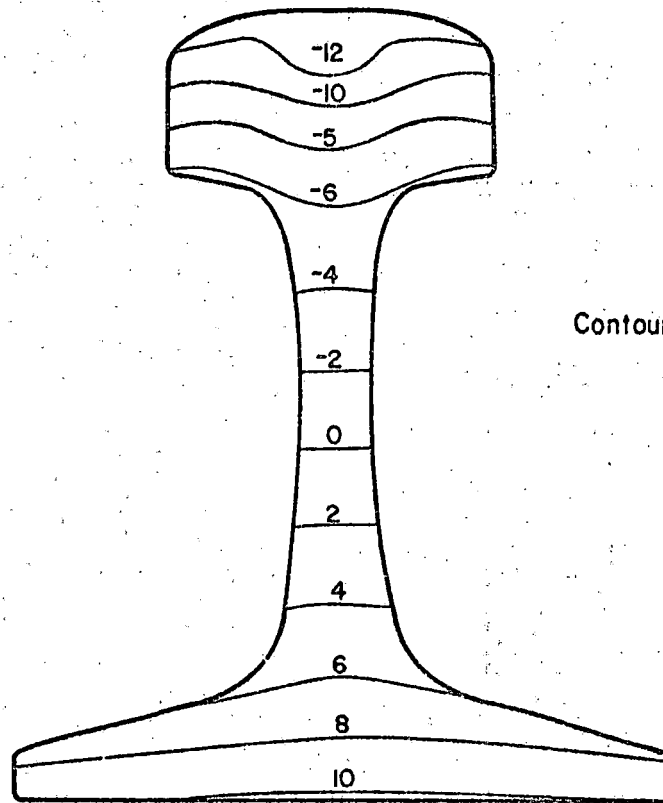
The longitudinal stress σ_x , however, did change with the foundation stiffness, as Figure 2-10 shows if one compares the results at $x = -1.0$ inch for Cases 2 and 3. (The comparison is made there rather than at $x = 0$ to avoid overemphasis of contact stress.) Nevertheless, at $x = -1.0$ inch the ratio between the largest σ_x 's for Cases 2 and 3 was computed to be $13953/10402 = 1.34$, whereas by simple bending theory, the ratio at $x = 0$ would have been nearly the same, namely $\sqrt[4]{7000/2000} = 1.37$. The stress contours in Figure 2-10 broadly follow this same proportionality. Of course the changes in σ_x for varying foundation stiffness contribute to changes in τ_{oct} . Results for τ_{oct} for Cases 2 and 3 are included in Appendix B. At considerably greater distances from the contact the alteration of σ_x and τ_{oct} due to varying foundation stiffness would differ from that shown here, but the behavior there should be estimable from beam theory.

Comparison of these cases also provides a measure for the effect of a slight mismatch of merging conditions between the two computer programs. An estimate of that mismatch indicated that the bending moment applied to the short interior span of the track was perhaps 3 percent too high.

Rails are not always loaded centrally as in the somewhat idealized Cases 1, 2 and 3. To illustrate how the stress patterns change when the load is applied differently, Case 4 was included to illustrate shifts caused by eccentric loading (when the wheel moves toward the gage side of the rail) and Case 5 was included to illustrate added effects from flange contact. Stresses calculated for these cases are included in Appendix B. Representative results for σ_x at $x = 0$ and τ_{zx} at $x = -1.0$ inch are shown in Figures 2-11 and 2-12.

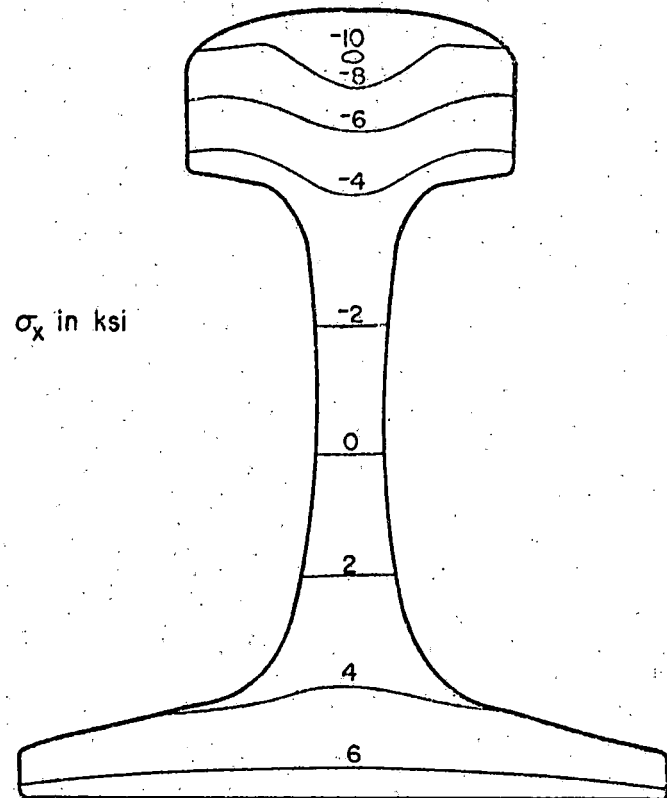
The changes in the load in Cases 4 and 5 as compared to Case 1 did not greatly alter the maximum values attained by the stress components. The principal change in stresses produced by eccentricity of the load was simply to

2-21



(a) $k = 2000$ psi (Case 2)

Contours show σ_x in ksi



(b) $k = 7000$ psi (Case 3)

FIGURE 2-10. EFFECT OF FOUNDATION STIFFNESS ON LONGITUDINAL STRESS ON PLANE 1 INCH FROM LOAD POINT ON 132-LB RAIL UNDER 19,000-LB WHEEL LOAD

2-22

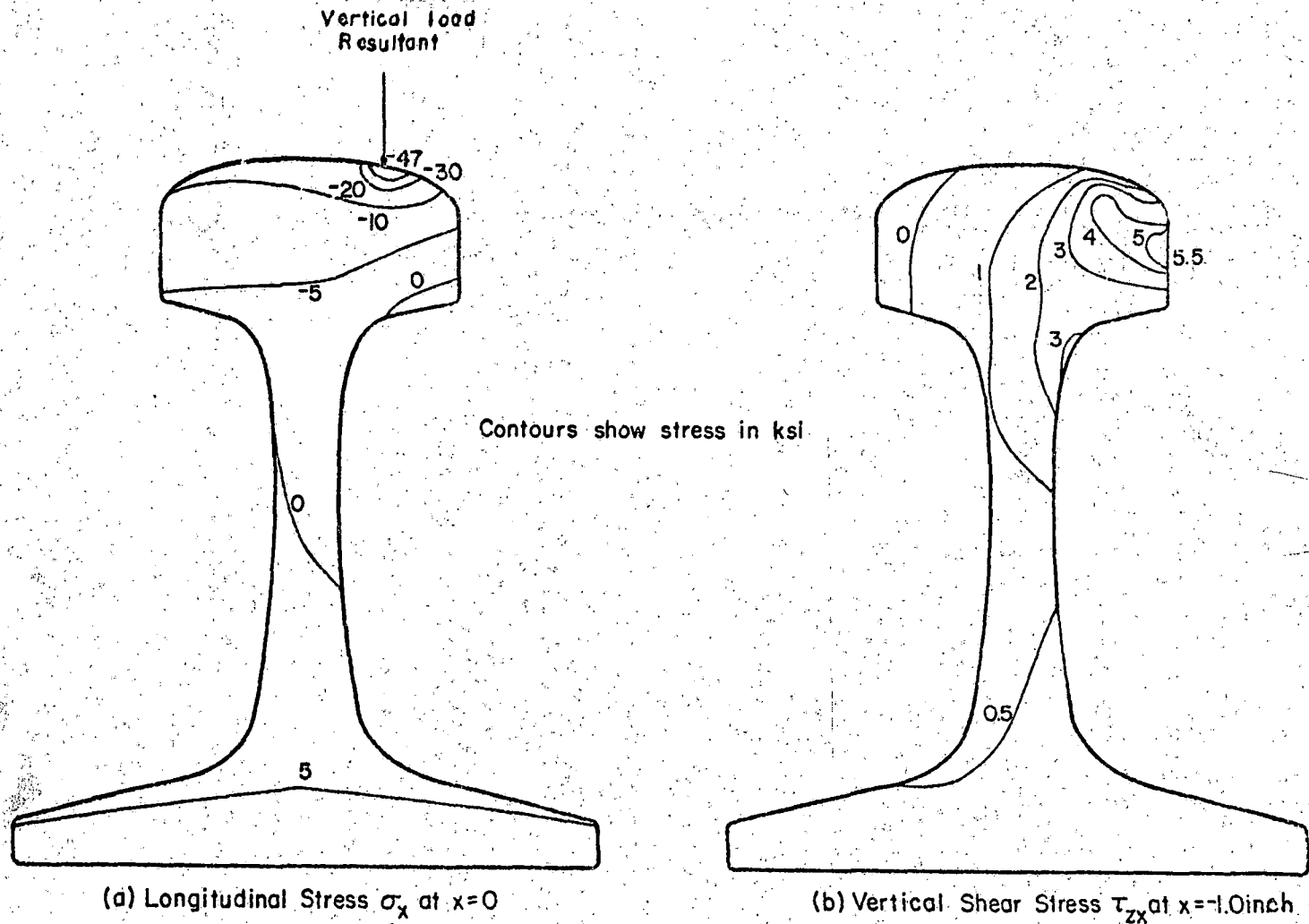


FIGURE 2-11. ILLUSTRATIVE PATTERNS OF STRESSES IN A 132-LB RE RAIL UNDER A 19,000-LB WHEEL LOAD APPLIED 3/4-INCH ASIDE FROM TOP OF RAIL CROWN (CASE 4)

2-23

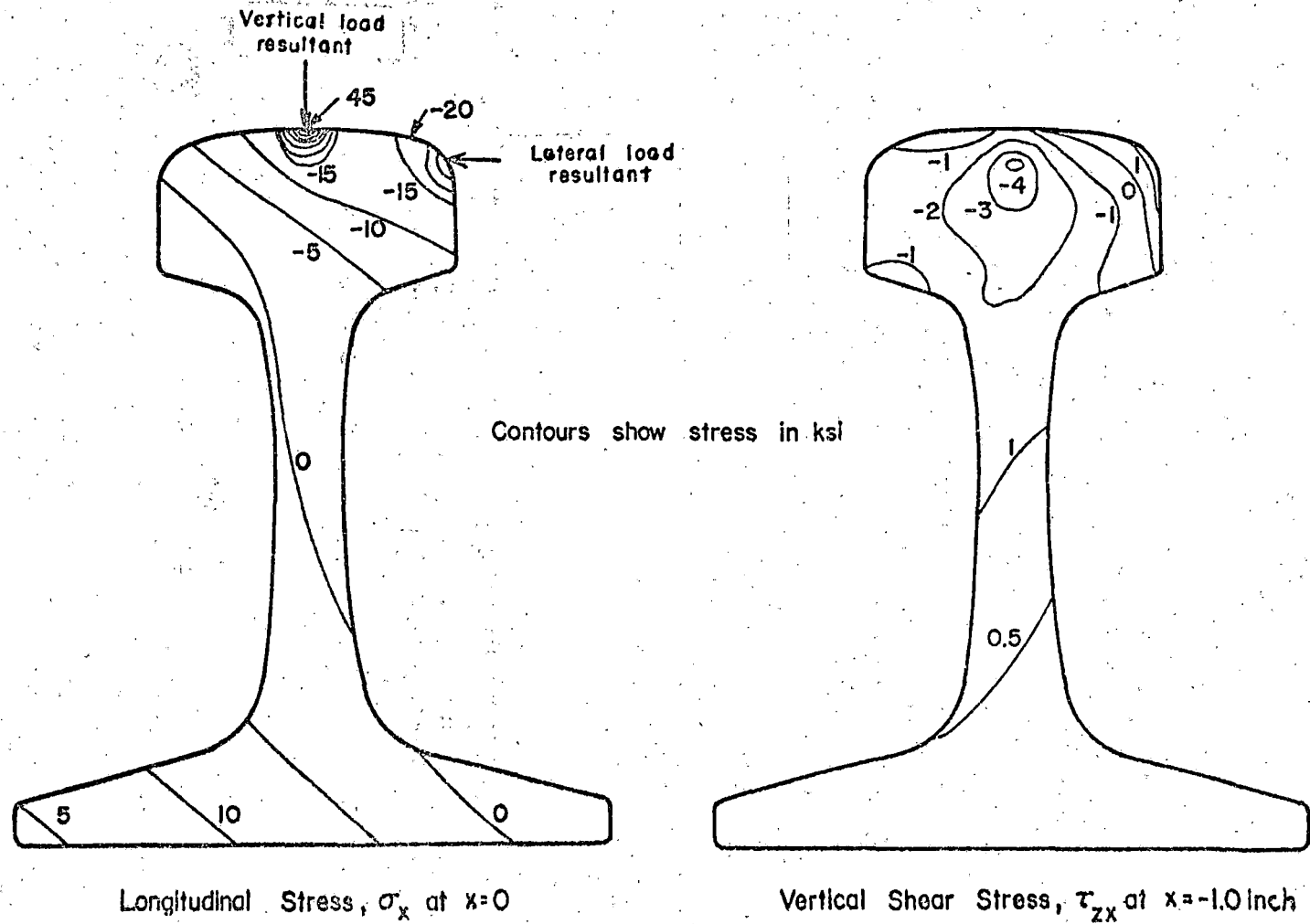


FIGURE 2-12. ILLUSTRATIVE PATTERNS OF STRESSES IN A 132-LB RE RAIL UNDER A 19,000-LB. WHEEL LOAD TOGETHER WITH A 10,000-LB LATERAL LOAD (CASE 5)

change where the high stresses arise. This shifting of course means that if there is plastic flow it can be distributed more widely than a particular load case calculation would suggest, and regions where crack growth might be promoted also are more widely spread. With the added flange load it can be seen that while the peak stresses were not changed there is, however, significant broadening of the regions where high stress levels occur so that the average level of stress is increased. Thus flange contact conceivably can contribute to rail damage in curves even though it may not increase the maximum stresses significantly because of the redistribution of stresses which occur around the crack front.

2.3 CONCLUSIONS REGARDING BENDING STRESS

- 1) The beam-on-elastic foundation model provides reasonable approximations of bending stresses in the base of the rail and in the head at distances more than about 1.5 inches from the wheel/rail contact point.
- 2) The beam-on-elastic foundation theory provides an improved picture of stresses in the rail head if a correction is made for the local bending behavior in the head of rail near the load.
- 3) Finite element results show substantial departure from simple beam theory across the head depth and in the head-to-web and web-to-base fillets.
- 4) The coarse grid found practical for the finite-element model for rail flexure does not accurately portray stresses local to the contact area, as the non-vanishing τ_{zx} there shows. Further analysis is required to compute the total stress state there.
- 5) The influence of increasing track modulus, more fully developed in Reference [2-6] for beam bending, does show in redistribution of stress and diminution of peak values of stress with increasing foundation support. The beam-on-elastic-foundation theory gives accurate assessment of the influence of changes in support on peak stress values, but not necessarily on the entire distribution of that influence.

- 6) The action of lateral loads is to raise the total stress levels moderately and to broaden the regions of the railhead exposed to the highest stress levels.
- 7) The action of combined stresses due to vertical and lateral loads results in increasing the region where high octahedral shear occurs. This spreading may broaden plastic deformations and redistribute stresses in interior regions where transverse and longitudinal railhead cracks occur (that is, transverse fissures, detail fractures, horizontal and vertical split heads).

3. STRESSES LOCAL TO THE WHEEL/RAIL CONTACT REGION

The contact pressure between the rail and the wheel is important in the study of plastic flow and fatigue life of the rail head. The elastic and plastic deformation of the head produced by contact pressure may also hasten the development of certain types of rail flaws. While a wheel is passing a fixed point of the rail head, the contact stresses are negligible until the wheel is about an inch away; then they rise to high maxima before falling again to nearly zero. Typically, when little or no plastic deformation is involved, the loaded contact area is elliptical, having a long axis of 0.5 to 0.75 inches in the direction of rolling. A typical load and some of its accompanying stresses are illustrated in Figure 1-3. The stress with the greatest absolute value is the compressive stress directly beneath the load, but the most deleterious, in the context of plastic yielding, is the subsurface octahedral shearing stress (τ_{oct}) that occurs under the load center. Also, an alternating subsurface shear stress below the edge of the loaded area plays an important role in causing fatigue damage. The maxima of these latter shear stresses typically occur 0.1 to 0.2 inches below the surface and they can be high ($\tau_{oct} = 52$ ksi and the vertical shear = $+34$ ksi in the example of Figure 1-3).

Even for contact between regular surfaces, the load and subsurface stress patterns may be complicated by the addition of tangential surface loads, as from friction or creep forces. Actual wheels and rails, of course, may have irregular shapes which distort the contact load patterns and hence the subsurface stress patterns. Thus several characterizations are to be provided here for contact loads between both regular and some typically irregular surfaces (and for subsurface stresses which the contact loads induce) to identify the range of stresses induced by typical wheel/rail contact conditions.

3.1 LOADS AND STRESSES FROM CONTACT BETWEEN REGULAR SURFACES

3.1.1 Elastic Contact Pressures for New Wheel and Rail Geometries

While the initial contact between a wheel and rail is determined by the geometric features of the bodies, the final contact area is determined also by

the amount they deform under the applied forces. The stresses developed during elastic contact of wheels and rails have long been of great concern to the railroad industry. The general theory of localized contact between elastic bodies with simple local curvatures was formulated by Heinrich Hertz [3-1] in 1881. Hertz assumed that each surface, prior to contact, can be described by two local principal curvatures so that the analytical methods of potential theory could be applied to the contacting bodies viewed as semi-infinite spaces. His solutions, found by the semi-inverse method, have long served as the basis for evaluating contact stresses.

The first extensive evaluation of the stress field arising in general Hertzian contact is due to Belyayev [3-2]. Many other papers which came later expanded upon these results. Those include the works of Dinnik [3-3], Way [3-4], Karas [3-5], Radzimovsky [3-6], Palmgren [3-7], Thomas and Hoersch [3-8], Weibull [3-9], Lundberg and Odqvist [3-10], and Fessler and Ollerton [3-11]. A concise summary of Hertzian contact theory was provided by Seely and Smith [3-12], and as it pertains to stresses in rails has been sketched by Johns and Davies [3-13].

The Hertz theory approximates contacting bodies, such as the wheel and rail, as semi-infinite bodies with separation f in the undeformed state having the form

$$f = Ax^2 + By^2, \quad (3-1)$$

where x and y correspond to longitudinal and lateral distances from the center of contact, as shown in Figure 3-1. The constants A and B are surface-defining parameters which for wheel/rail contact depend on the rail crown radius R_1 and the wheel radius R_2 and are given by

$$A = \frac{1}{2R_2}, \quad B = \frac{1}{2R_1}. \quad (3-2)$$

If w_1 and w_2 represent the vertical deformations within the rail and wheel, respectively, the sum of these deformations at any point in the contact area under the load is given by

$$w_1 + w_2 = \alpha - Ax^2 - By^2, \quad (3-3)$$

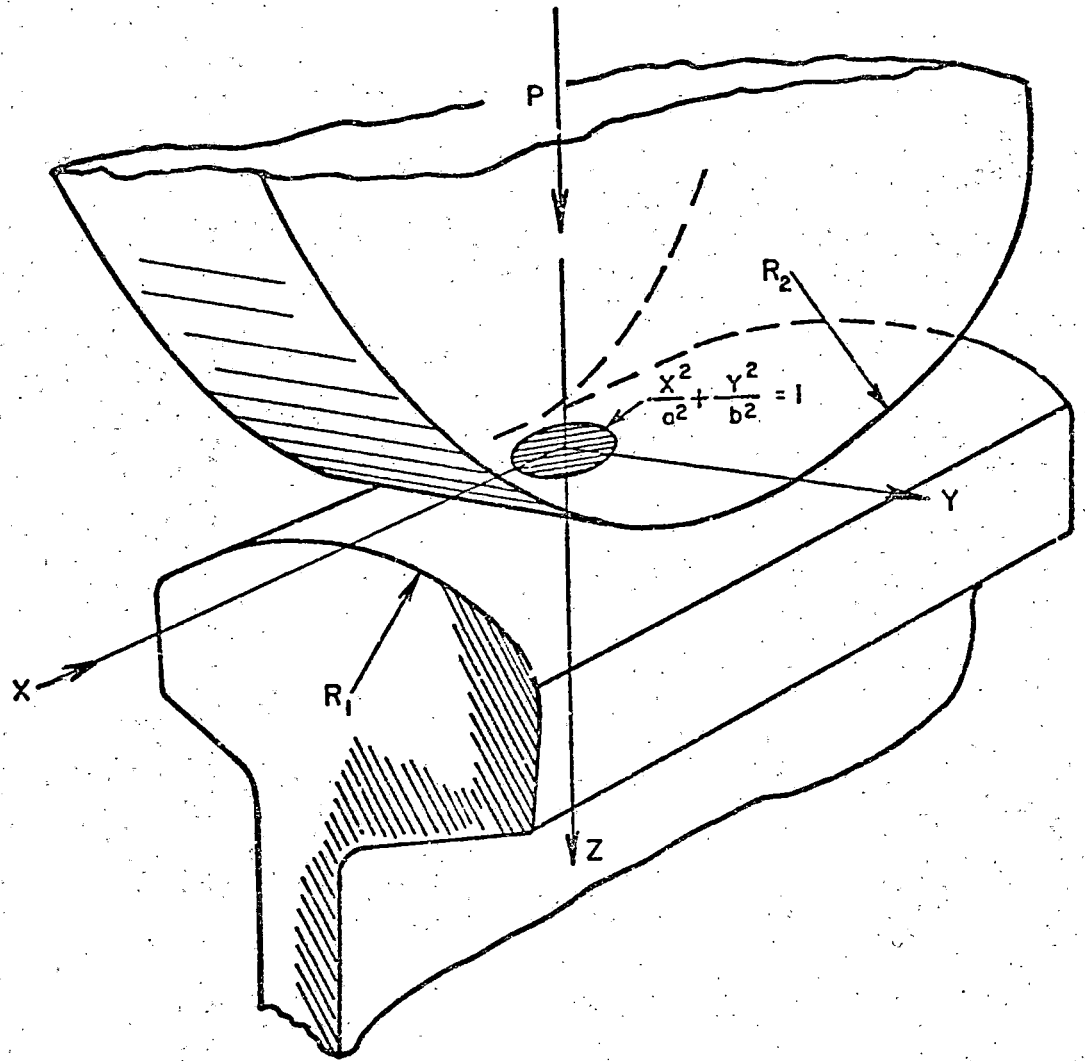


FIGURE 3-1. WHEEL/RAIL CONTACT AS QUADRATIC SURFACES IN CONTACT

where α is the approach of the two bodies or the distance they move toward each other due to load. The relation between this function and the Newtonian potential for attraction by a homogeneous ellipsoidal mass provided Hertz with a method for finding the contact pressure and hence the stresses. The theory makes use of elliptic integrals which have been well studied and tabulated. From the Hertz theory, the contact region is elliptical, so that if a and b are its major and minor axes the boundary of the area is

$$\frac{x^2}{a^2} + \frac{y^2}{b^2} = 1 \quad (3-4)$$

The pressure distribution over this area is ellipsoidal and of the form

$$\sigma_z = \sigma_{\max} \left(1 - \frac{x^2}{a^2} - \frac{y^2}{b^2} \right) \quad (3-5)$$

It can be shown that

$$a = C_b \sqrt[3]{P\Delta/k}, \quad b = C_b \sqrt[3]{P\Delta}, \quad \sigma_{\max} = -C_\sigma(b/\Delta) \quad (3-6)$$

where P is applied load, and

$$\Delta = \frac{1}{A+B} \left(\frac{1-\nu_1^2}{E_1} + \frac{1-\nu_2^2}{E_2} \right) \quad (3-7)$$

Here E_1 and E_2 are Young's moduli for the rail and wheel, respectively, while ν_1 and ν_2 are their Poissons' ratios, and the quantities k , C_b and C_σ are functions of B/A plotted in Figure 3-2 (Cf. Figure 183 of Reference 3-1).

Figure 3-3 shows curves for various stress components directly beneath the center of a contact with $B/A=1.68$ (so that $k=0.7071$), which is nearly the same as $B/A=1.65$ that corresponds to a 33-inch diameter wheel pressing against a rail with a 10-inch crown radius. This case was treated in Reference 3-8 for $\nu_1 = \nu_2 = 0.25$, so that is presumed here, along with $E_1 = E_2 = 30 \times 10^6$ psi and $P = 19,000$ -lb. The curves show that the magnitudes of σ_x and σ_y decrease more rapidly than that of σ_z . The interrelation of these

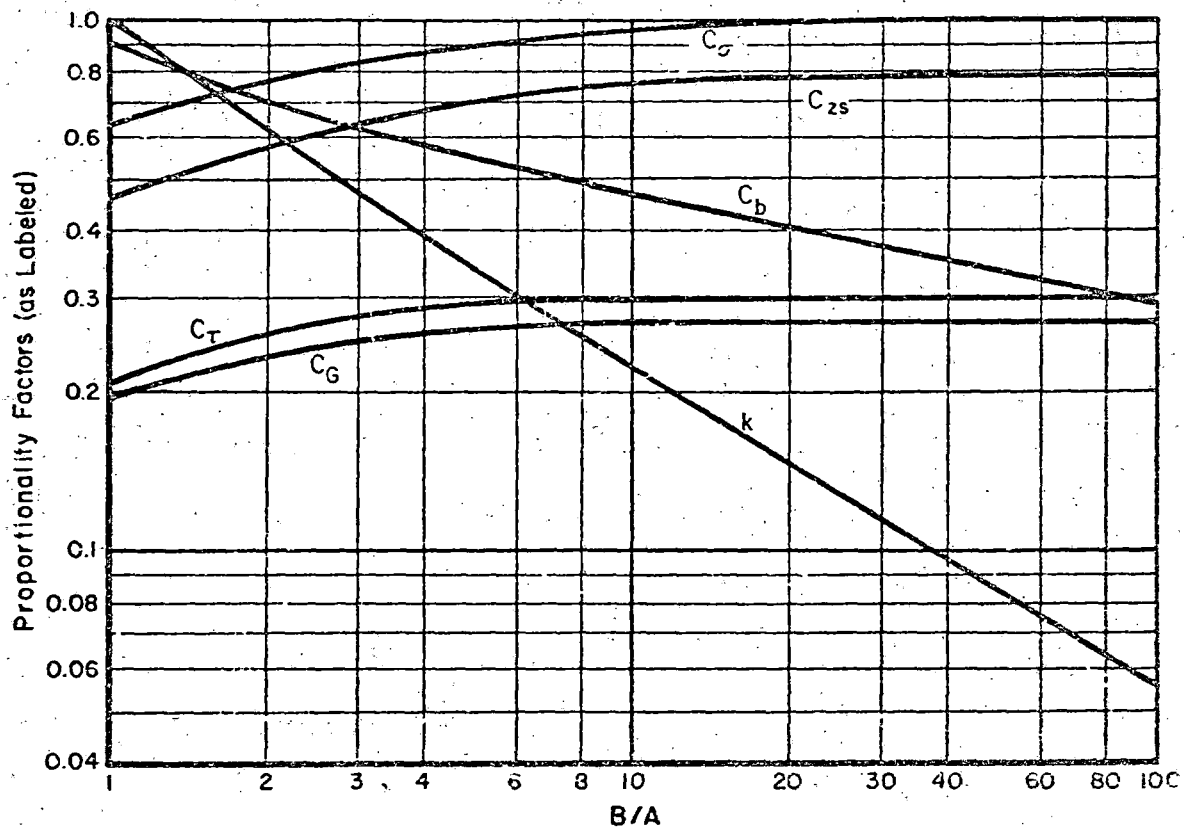


FIGURE 3-2. PROPORTIONALITY FACTORS FOR QUANTITIES ASSOCIATED WITH HERTZ CONTACT (cf. [3-12])

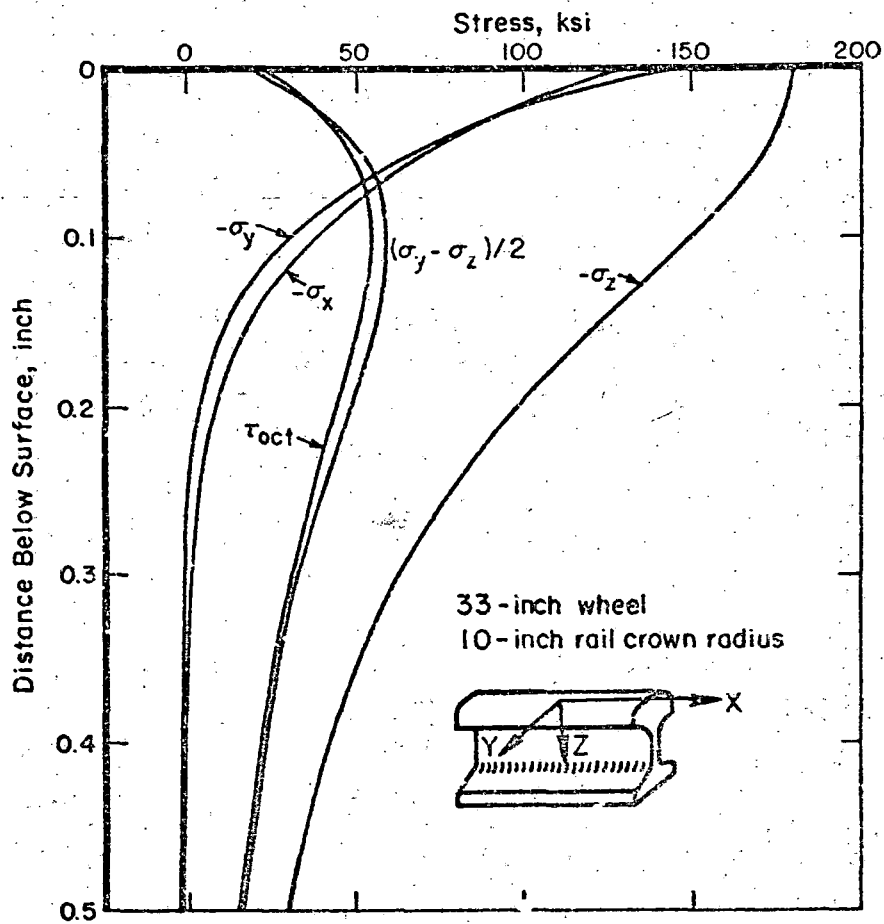


FIGURE 3-3. ELASTIC STRESS DISTRIBUTION IN RAIL-HEAD BELOW CENTER OF CONTACT WITH WHEEL

stresses makes the maximum shearing stress below the center of contact to take on the value of $(\sigma_z - \sigma_y)/2$ at a depth of about 0.10 inch. In general, the maximum value of shearing stress below the center of contact can be represented as

$$\tau_{\max} = c_T b/\Delta \quad (3-8)$$

occurring at depth

$$z_s = C_{zs} b \quad (3-9)$$

where C_T and C_{zs} are shown in Figure 3-2 as functions of B/A . (The factors of Figure 3-2 were computed assuming the Poisson's ratio to be 0.25, but fortunately these factors are not sensitive to the value of that ratio.) The von Mises' criterion, which has been shown to predict the yielding of steel adequately, is expressed in terms of the second invariant of the stress tensor or the related octahedral shearing stress. Beneath the center of Hertzian contact the octahedral shearing stress is

$$\tau_{\text{oct}} = \frac{1}{3} [(\sigma_x - \sigma_y)^2 + (\sigma_y - \sigma_z)^2 + (\sigma_z - \sigma_x)^2]^{1/2} \quad (3-10)$$

The maximum value of this stress can be expressed as

$$\tau_G = C_G b/\Delta \quad (3-11)$$

where again C_G is shown in Figure 3-2. As Figure 3-3 illustrates, the depths for the maximum values τ_{\max} and τ_G are nearly equal. For the case of Figure 3-3, those maximum values are 59000 psi and 54000 psi, respectively, which are at about the level for the onset of yielding for work hardened rail steel.

For new wheels and rails, variation in parameters such as wheel diameter and crown radius, within practical limits, does not have major effects upon the stresses developed during rolling contact. Table 3-1 shows the stresses developed for a number of such cases. The parameter having the most significant effect upon these stresses is the wheel load. Figure 3-4 gives the maximum compressive stress, the maximum octahedral shear stress, and the alternating longitudinal shear stress (which occurs beneath the edges of the contact area) for new 33-inch diameter wheels on rail with a 10-inch crown for a broad

TABLE 3-1. WHEEL AND RAIL VARIABLES FOR ELASTIC CALCULATIONS

Case	Wheel Diameter (inch)	Crown Radius (inch)	Wheel Load (10^3 lb)	Semi-Major Axis (inch)	Semi-Minor Axis (inch)	Maximum Compressive Contact Stress (10^3 psi)
1	33	10	19	0.264	0.189	-182
2	33	10	25	0.289	0.207	-200
3	33	10	30	0.307	0.220	-212
4	33	10	40	0.338	0.242	-233
5	33	10	50	0.364	0.261	-252
6	36	10	19	0.282	0.181	-173
7	40	10	19	0.297	0.181	-169
8	33	14	19	0.250	0.225	-162

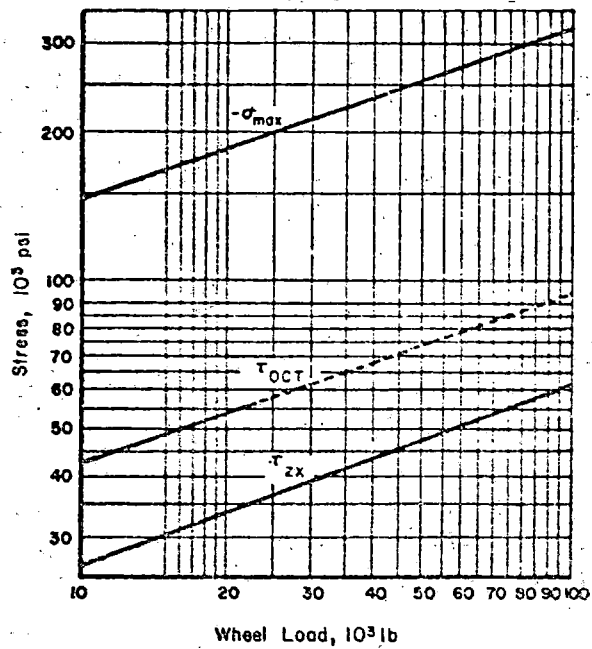


FIGURE 3-4. MAXIMUM COMPRESSIVE, OCTAHEDRAL SHEAR, AND ALTERNATING LONGITUDINAL SHEAR STRESS FOR NEW 33-INCH DIAMETER WHEEL AND RAIL HAVING 10-INCH CROWN RADIUS

range of wheel loads. More detail on subsurface stress distributions is given in a later section.

3.1.2 Calculation of Surface Traction

When a wheel rolls along a rail, even without overall sliding, microslip may be taking place between the surfaces over part of the contact region, while over the rest of the contact the surfaces do not slip. Thus the contact area may be viewed as divided between a slip region and a "locked" region. The distribution of tangential surface tractions within the contact region was first formulated by Carter [3-14], treating the contact as being effectively like that of a roller on a plane.

Carter found that the maximum surface shearing stress occurs at the edge of the locked region (at a distance c from the center of contact) and is given by

$$\tau_M = \frac{2fN}{\pi a f} \left(1 - \frac{c^2}{a^2} \right)^{1/2}, \quad (3-12)$$

where

- $2a$ = length of the contact region in the rolling direction,
- f = effective transverse width of the contact zone,
- f = coefficient of friction,
- N = total normal load on the contact area.

Carter found

$$c = a \left[1 - 2 \left(1 - \frac{T}{fN} \right)^{1/2} \right], \quad (3-13)$$

where T is the traction (or braking) force. The general pattern of the shearing stress according to Carter is shown in Figure 3-5.

Tractive stresses in rolling contact have been studied further by Mindlin [3-15], Poritsky [3-16], and Johnson [3-17, 3-18, 3-19], with the work of Poritsky being directly applicable to wheel-rail contact. Johnson [3-20, 3-21] shows the effect of the coefficient of friction on partial slip and the distribution of the surface shear stress presuming the tangential force T to

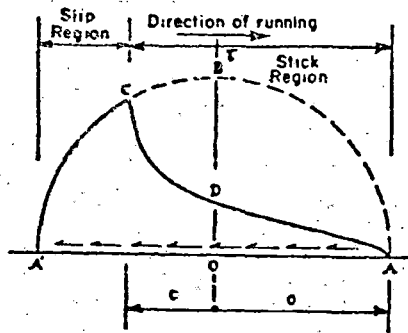


FIGURE 3-5. FORM OF SHEAR STRESS DISTRIBUTION FOUND BY CARTER FOR ROLLING CONTACT WITH PARTIAL SLIP (Cf. [3-14])

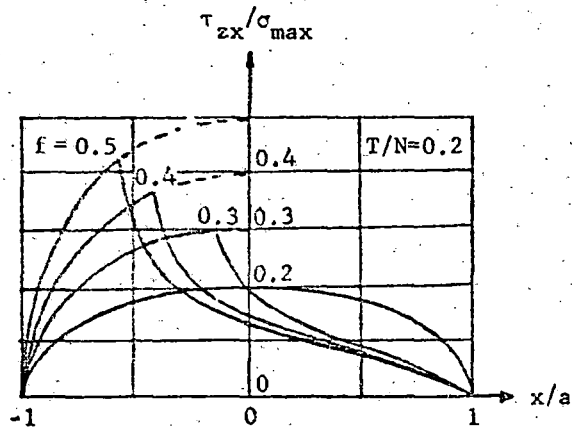


FIGURE 3-6. INFLUENCE OF COMPONENT OF FRICTION ON TANGENTIAL FORCE BETWEEN PARTLY SLIPPING CYLINDERS (Cf. [3-21])

be 0.2 times the normal load N . Figure 3-6 shows a rearrangement of Johnson's results for the surface shear stress as a function of f [3-21], x being a longitudinal coordinate, τ_{zx} being the longitudinal surface shear stress, and σ_{max} being the maximum normal pressure. (For information on validation of these formulations see Johns and Davies [3-13].)

3.2 CONTACT PRESSURES BETWEEN WORN WHEELS AND RAILS

3.2.1 Method for Calculating Elastic Contact Pressure Between Worn Wheels and Rails

In the past, all investigations of contact pressures developed during the contact of wheels and rails have used the approach described in Section 3.1.1 and therefore the results have been restricted to cases where the wheel and rail geometries are representable by quadratic functions. Although this assumption is valid for new wheels and rails it fails to be generally valid for worn rail and wheel geometries where plasticity and wear have changed the original geometries to something other than those describable by quadratic functions. Often for worn wheels, the contact condition departs strongly from its original form as the profiles become more broadly conformal. Nevertheless, in the past the Hertzian method was the only method available to investigators and therefore in some cases attempts have been made to approximate the worn surface geometries by quadratic surfaces and use it. As was found in this study, this procedure is valid in many cases, but it frequently needs modification.

Recently a method for analyzing the contact of elastic bodies whose surfaces were of arbitrary geometries, as in rails, was developed by Conry and Seirig [3-22] and extended by Johns and Leissa [3-23].

In this method, the contacting surfaces are divided into predetermined rectangular arrays of possible contact points or nodes, Figure 3-7. At any node within the proposed zone of contact, the sum of the elastic deformation and the initial separation will be equal to the rigid body approach. For points outside the proposed zone of contact this sum will be greater than the rigid body approach. The distribution of pressure over the finite, proposed

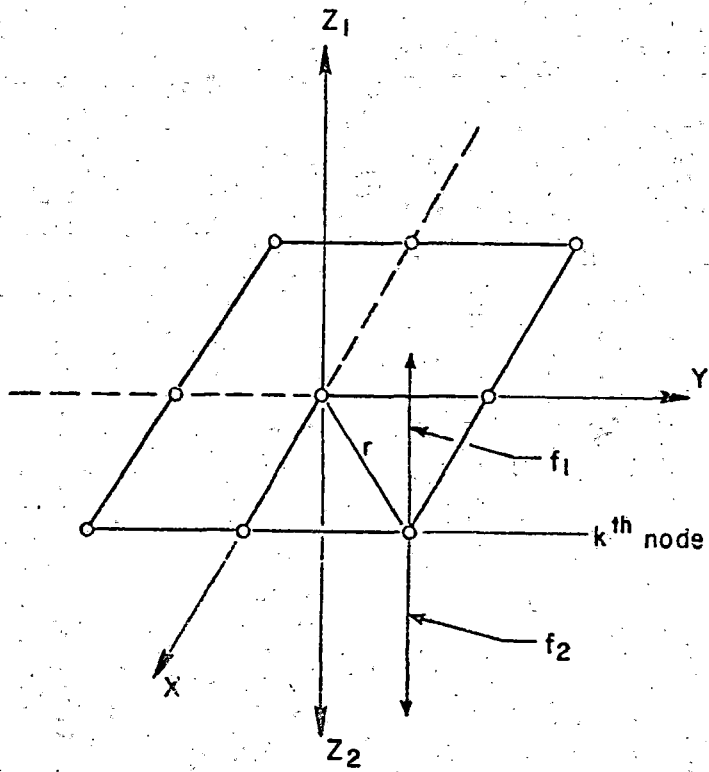


FIGURE 3-7. PROPOSED ZONE OF CONTACT SHOWING RECTANGULAR ARRAY OF NODES REPRESENTING POTENTIAL CONTACT SPOTS

contact zone is represented by a system of discrete forces at the nodes. The sum of all the forces acting at the nodes must balance the force pressing the bodies together. A simplex-type algorithm is then used to solve the system of equations that formulate the general problem. For a fuller description of this basic formulation see References 3-22 and 3-23.

This approach has been incorporated directly into a computer program called CONTACT. As input to this program, it is necessary to supply the material properties of the wheel and rail, the applied load, and an estimate of an area containing the potential contact region. As output, Program CONTACT furnishes, at each of the mesh points, the values of the contact forces, pressures and displacements.

In order to make the input to CONTACT as simple as possible an additional preprocessing computer program SEPARAT was written. This program is applicable to the normal contact of any two bodies that can be described by sets of points relative to coordinate systems embedded within each body. Input to the program consists of two arrays containing the coordinates of the points defining the profile, an estimate of the contact patch size, and the location of the center of contact of the two bodies in their respective coordinate systems. The relation of the rail to its local coordinate system is shown in Figure 3-1. From the data described, program SEPARAT calculates the initial separation of the contacting unloaded surfaces at the mesh points which is needed by CONTACT. This is accomplished by first smoothing the profile data with cubic splines. The smoothed profiles are then again fitted with new cubic splines. This smoothing minimizes experimental measurement errors. Large asperities in the wheel or rail geometries remain.

Comparisons between results for quadratic surfaces obtained using this numerical procedure and the Hertzian theory show extremely good agreement, Figure 3-8. The CONTACT program can therefore be applied to the contact of worn wheel and rails.

3.2.2 Description of Worn Wheel and Rail Contours

In practice, an extremely large number of wheel and rail contours are generated by wear. The surface contours of a large number of rail specimens were determined in the laboratory. Most of these rail specimens were borrowed

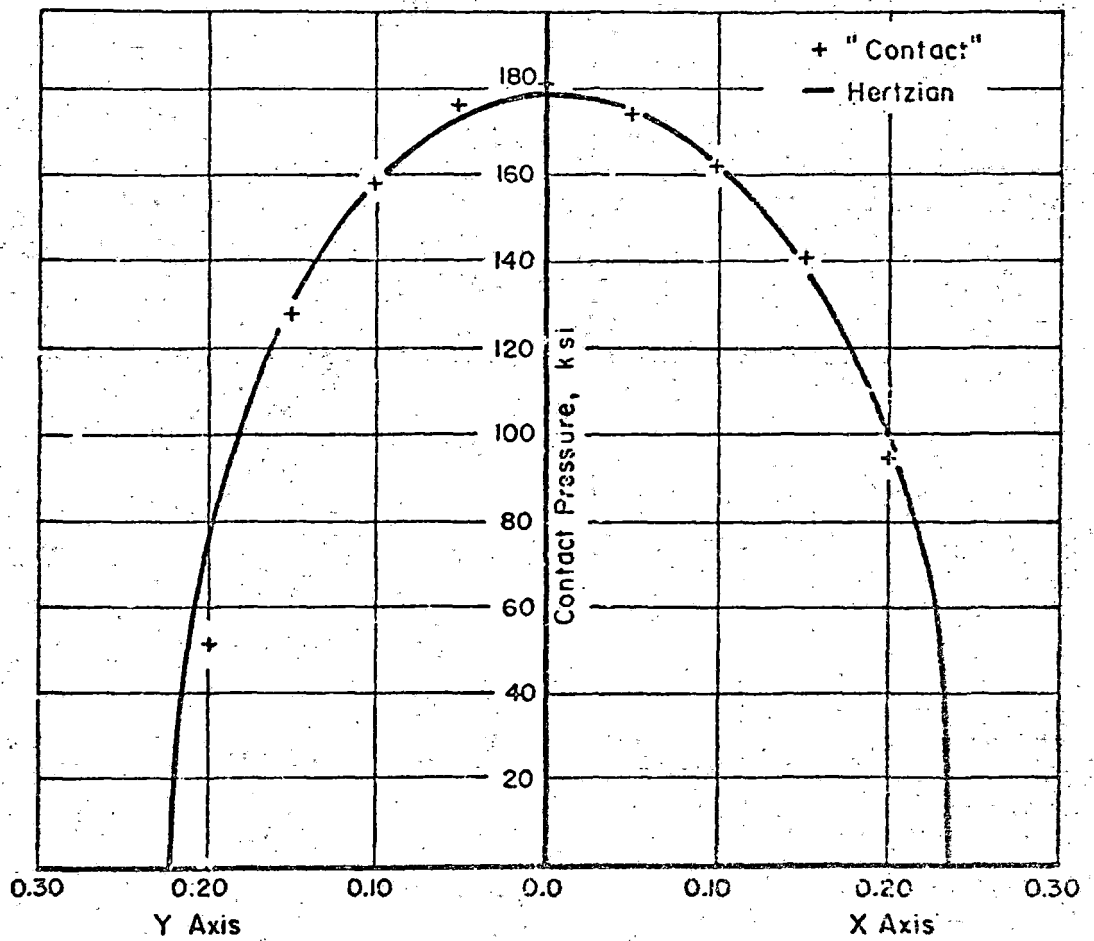


FIGURE 3-8. COMPARISON BETWEEN "CONTACT" AND HERTZIAN RESULTS FOR CROSSED CYLINDERS ($P = 15,000$ LB, $R_Y = 12.0$ INCHES AND $R_W = 14.0$ INCHES)

from the research program on materials characterization, DOT-TSC-1076. Figure 3-9 shows eight of these specimens.

The measurement procedure was to drag a stylus, on which a dial indicator was attached, across the surface, as shown in Figure 3-10. In this way measurement accuracies of ± 0.0003 inch were obtained.

A total of 12 worn rail profiles were measured, with results shown in Figure 3-11. (The vertical scale is marked in half inches without reference to a starting position.) The physical characteristics and histories of these rail samples is given in Table 3-2. It was found while examining rail sections of 85, 115, 119, and 131 RE rail that the worn contours were nearly identical in all cases except for the fact that the rails were obviously installed at different cants. This suggests that one surface profile would fit a wide variety of worn rail except for the physical description of the track parameters, if small geometric details were unimportant.

Wheels can contact rails in many lateral offsets (tape line to rail centerline), and the stresses arising from contact are sensitive to small irregularities of the surfaces. Thus it is necessary that the profile used for calculating contact stresses (and even wheel-rail contact positions) be free of unrealistic roughness. It is customary to minimize the effect of errors in the profile measurements by fitting them with polynomials over selected portions of the profile width. Cooperrider et al [3-24] in their study of contact positions employed quartic polynomials fitted piecewise to lateral profile measurements. The coefficients for a profile they measured from a section of 133-lb CP&E rail thus became a basis for a profile here listed as Number 12 in Figure 3-11 and Table 3-2, and shown again as the worn rail depicted together with a wheel in Figure 3-12. (The grid lines in that figure again represent half-inch spacings.) However, for reduction of profile data for the present work, a computer routine was used to fit the data by cubic splines, fitted so as to insure continuity through the second derivative. Since rail profile Number 12 was of particular interest, the rail itself was obtained and its profile was measured at many points to within ± 0.00015 -inch. The data were then fitted by the cubic spline routine to provide an alternative mathematical description of that profile.

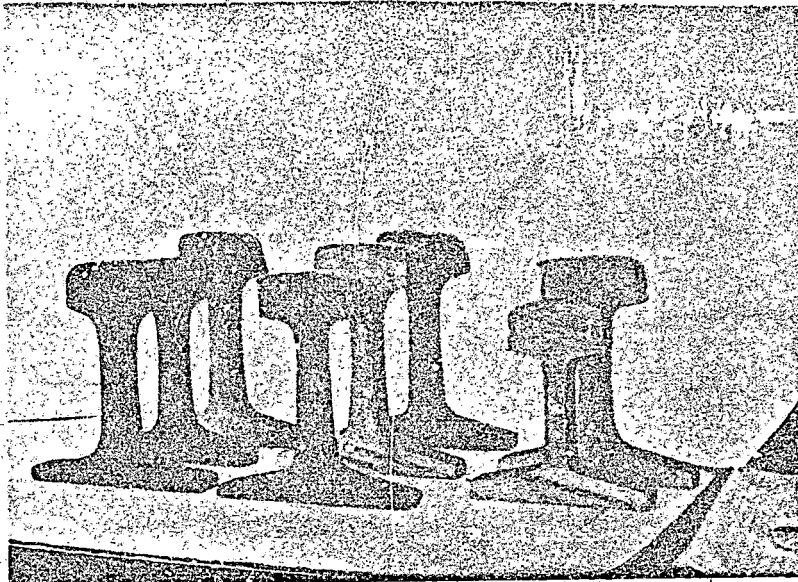


FIGURE 3-9. EIGHT RAIL SPECIMENS FOR WHICH SURFACE CONTOURS WERE MEASURED

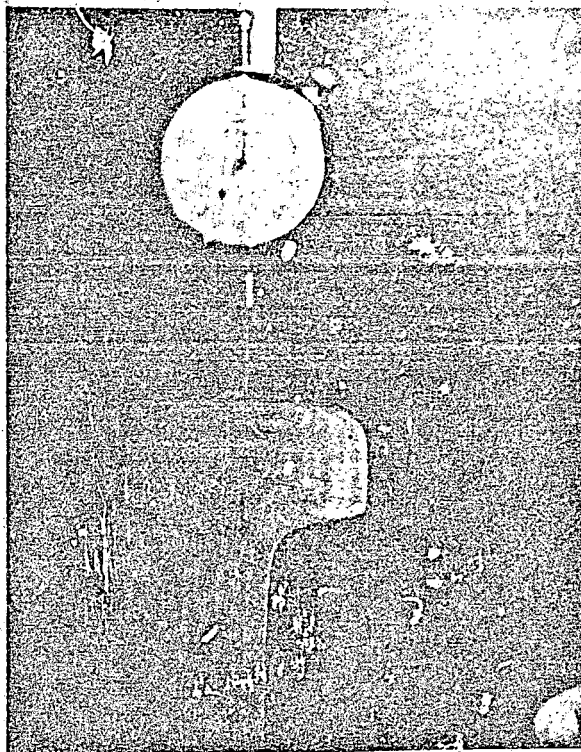
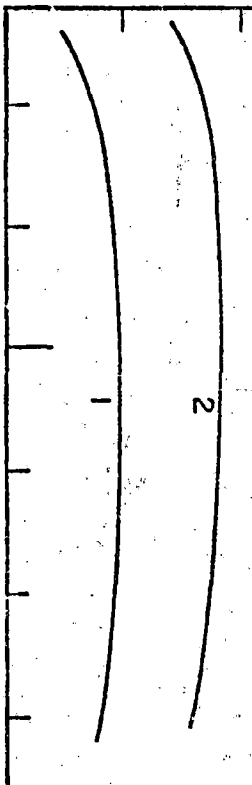


FIGURE 3-10. SURFACE CONTOUR MEASUREMENT PROCEDURE



Lateral Scale (in half inches)

FIGURE 3-11. SURFACE CONTOURS OF MEASURED RAIL SECTIONS

Profile Scale (in half inches)

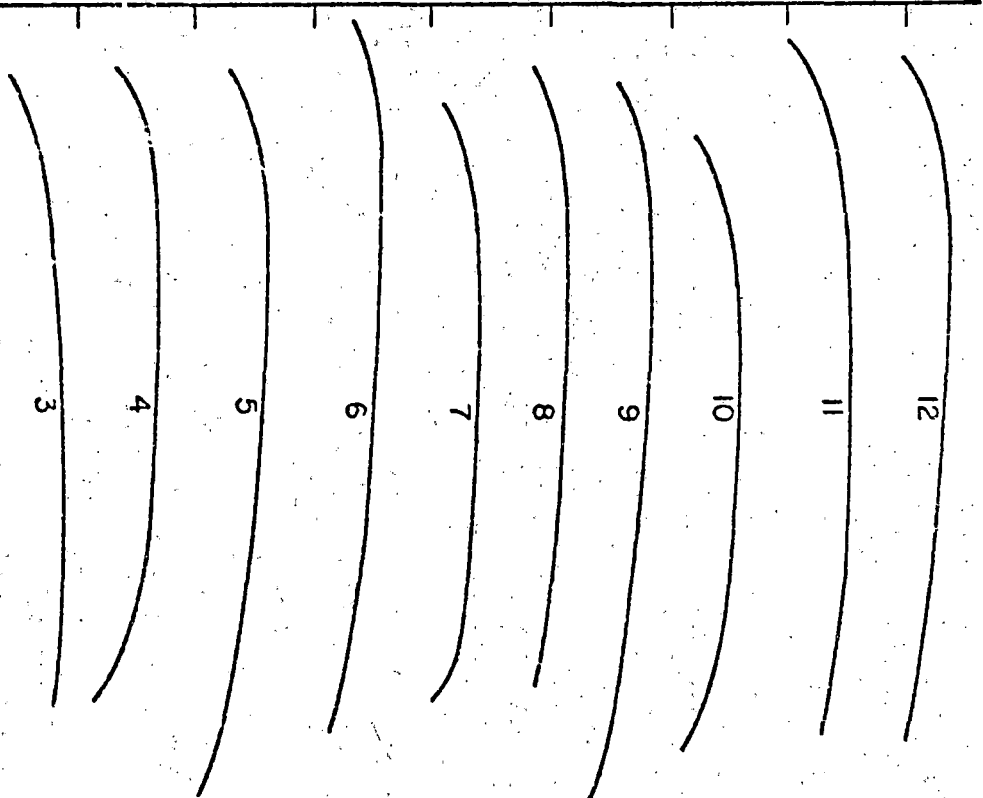


TABLE 3-2. DESCRIPTION OF WORN-RAIL CONTOURS

DOT/TSC 1076 Specimen No.	Contour Number	Condition	Rail Size	Vintage	Manufacturer	Curve or Tangent
055	1	some gage wear	131 RE	9/1947	Lack.-Beth.	High rail, light curve
054	2	worn	131 RE	1935	U.S. Steel	tangent
054	3	heavy gage wear, no lip	140 RE	1956	U.S. Steel	high rail, heavy curve
052	4	light wear	100 AREA	1916	U.S. Steel	tangent
051	5	large field side lip	130 RE	1931	Inland	tangent
050	6	small field side lip	132 RE	—	—	tangent
049	7	some gage wear	115 RE	1950	U.S. Steel	high rail, light curve
048	8	field side notch	122 CB	1965	Lack.-Beth.	tangent or low rail
047	9	large field lip	130 RE	—	Lack.-Beth.	tangent
046	10	small field side lip-gage wear	140 RE	1966	CF&I	high rail curve
057	11	worn	140 RE	1953	Steelton- Beth.	tangent
—	12	Cooperrider-Law (70-90 mph passen- ger and freight)	133 RE	—	CF&I	tangent

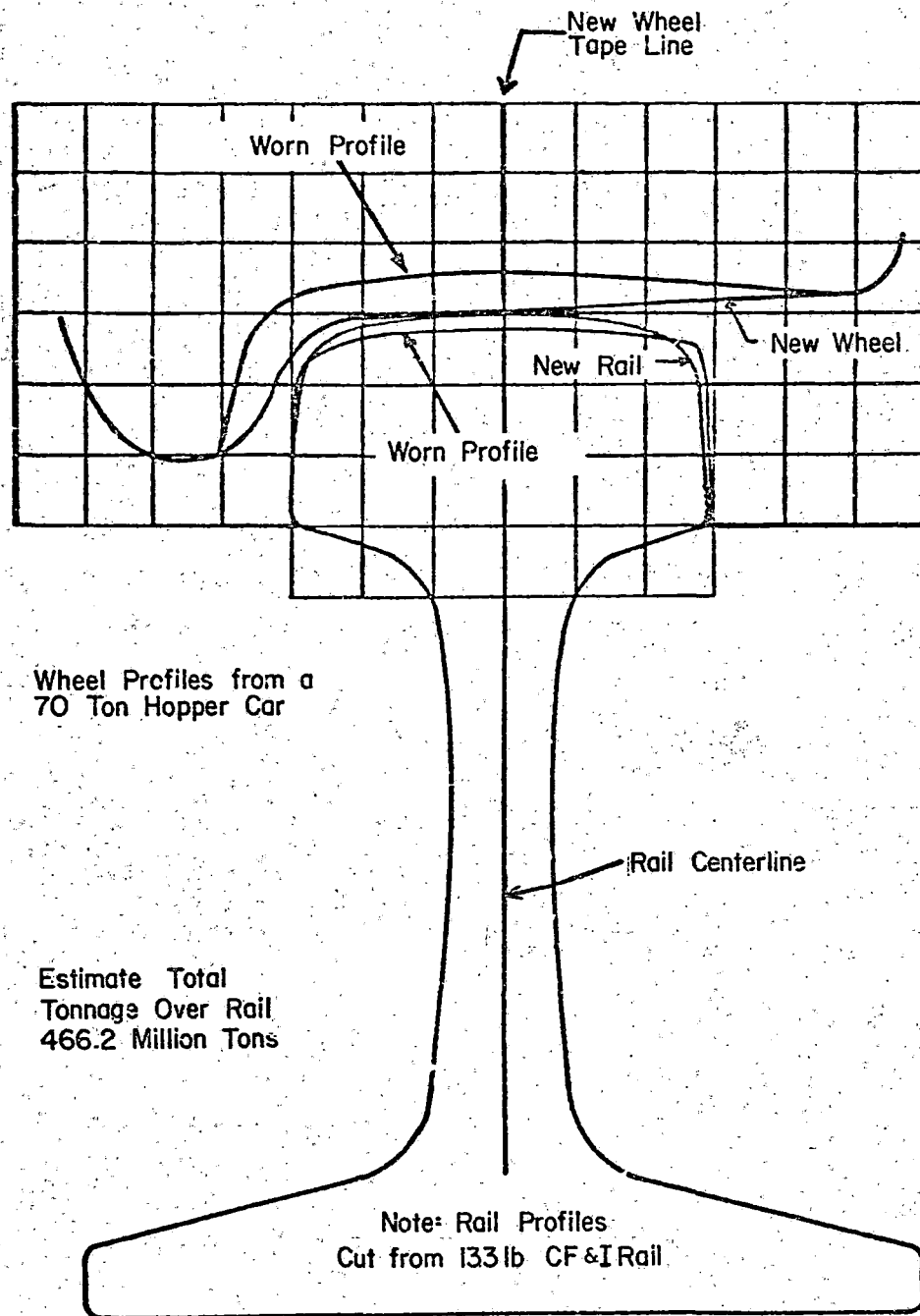


FIGURE 3-12. RELATIONSHIP BETWEEN PROFILES OF A 33-INCH WHEEL AND A 133-LB RAIL, BOTH NEW AND WORN

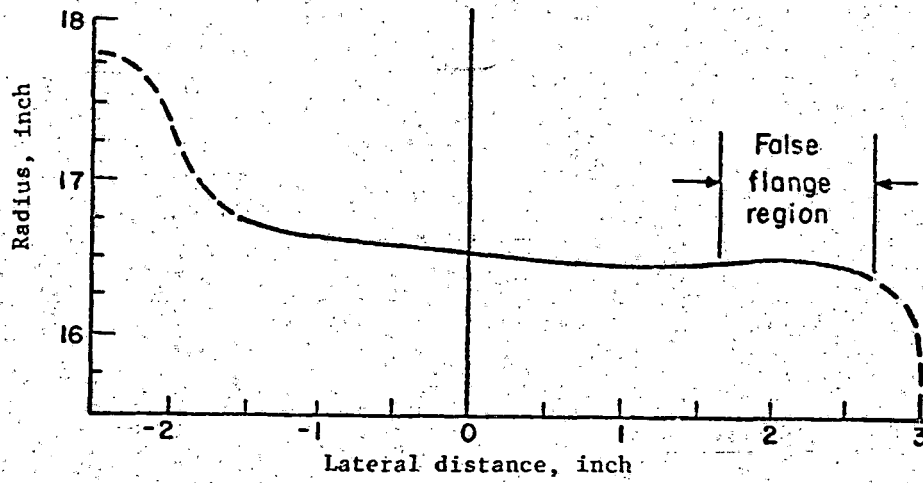
Rail profile Number 12 was taken from a heavily worn tangent track. Other profiles of note were Number 2 also from a tangent track and Number 3 from a heavily worn curve.

The wheel profile shown in Figure 3-12 was one of eight that Cooperrider et al [3-24] obtained from a 70 ton hopper car. Wheels from the same car indicated differences in wear characteristics, thus showing that simple length of service does not alone determine the extent of wheel wear. The profile shown here is the one they described as severely worn (their worn wheel Number 3). Of course, use of either the worn rail or the worn wheel would bring the wheel lower than shown, and the wheel also may be displaced laterally insofar as the flange on this wheel or its coaxial wheel would allow. Figure 3-12 provides a means for visualizing the many possibilities of wheel to rail orientation.

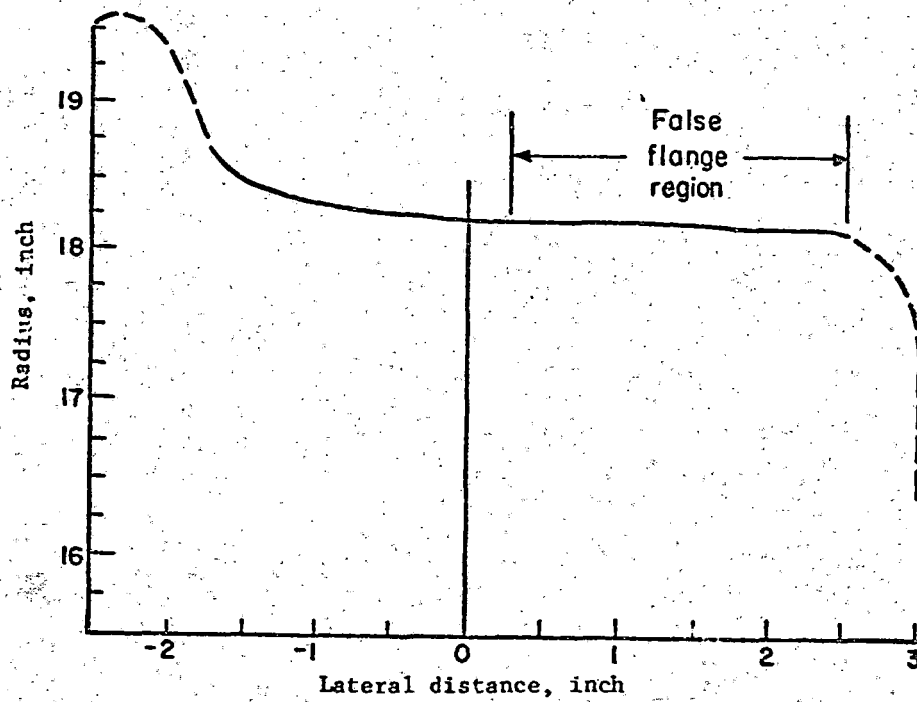
Two other worn-wheel profiles obtained from other sources for comparison are shown in Figure 3-13. They, like the first worn-wheel profile, show a hollow in the tread center which tend to develop on the part of the tread surface away from the flange. For comparison, the usual profile of a new 33-inch wheel is also shown in Figure 3-12, and the specially refined Heumann "worn" profile for new wheels is shown in Figure 3-14.

3.2.3 Examples of Contact Pressure Distributions Between Worn Wheels and Rails

Careful examination of configurations such as that shown in Figure 3-12 shows that as the profile of a worn wheel is shifted laterally with respect to a typical rail the position of the possible contact point does not move smoothly, but instead frequently jumps. Thus, for example, a band where the wheel surface is concave may not be able to touch a more gently crowned band on the rail. For this reason, the bands along which wheels and rails may contact each depend not only on the lateral wheelset displacement and wheelset rotation, but also on the profiles of the wheel and rail. In order to describe the possible contacts it is helpful to introduce notation as shown in Figure 3-15. Thus y_w is the outward distance from the tape line of the wheel (when new), and y_r is distance from the center plane of the rail measured toward the field side. (It may be noted that here the cant between the wheel and rail was taken to be that implicit in the rail profile.)



(a) Worn Wheel Profile from Service A



(b) Worn Wheel Profile from Service B

FIGURE 3-13. WORN WHEEL PROFILES

3-23

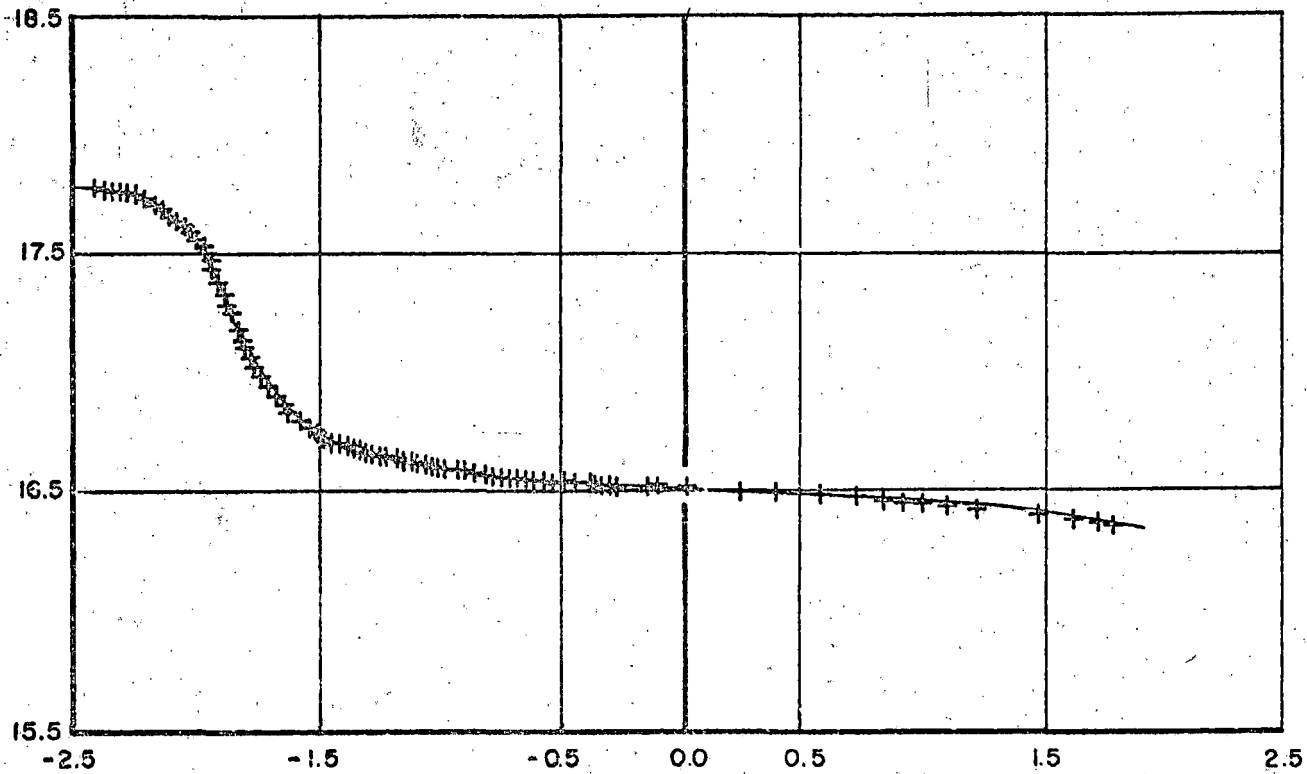


FIGURE 3-14. HEUMANN WHEEL PROFILE.

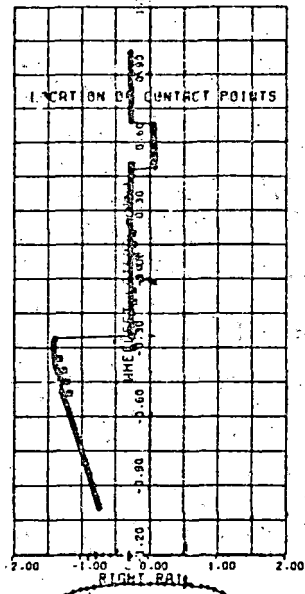
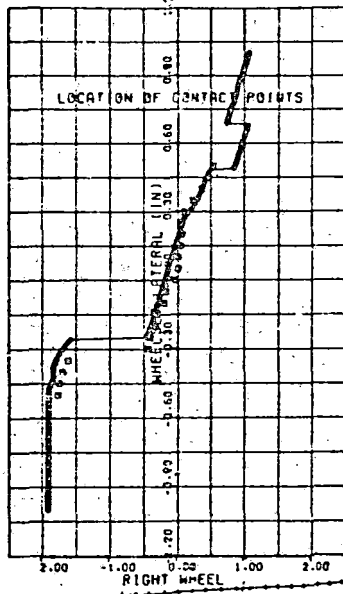
Cooperrider et al [3-24] performed analytical and experimental studies to determine the kinematically admissible axle positions and the wheel and rail contacts for selected profiles. Examples of their results for the wheel and rail contact positions y_{wc} and y_{rc} are shown in Figure 3-16, both for a new 33-inch wheel on a 133-lb CF&I rail and for the worn wheel and rail illustrated in Figure 3-12. The jumping of the contact positions (abscissae) as the wheelset position (ordinate) changes can be clearly seen, and comparison of parts (a) and (b) of the figure shows that the contact positions depend strongly on the wear patterns.

To get representative contact stress patterns, contact positions were chosen from those arising for four possible wheelset positions according to Cooperrider et al. Their polynomials describing the profiles in those areas were treated, first by computer program SEPARAT to determine the three-dimensional separation between the surfaces before loading, and then by the program CONTACT to determine the distribution of contact pressures under a typical wheel load, taken to be 19,000 pounds. The lateral variations of stresses around each center of contact is shown in Figure 3-17. The severity of the contact pressures in each case is shown by grid lines spaced at intervals of 100 ksi. The highest contact pressure among those calculated is that from load Number III, located well toward the gage side of the rail. A description of several features of these contact regions and stresses is given by Table 3-3.

In order to further illustrate possible contact stress patterns between worn rails and wheels, more cases were considered using the worn wheel profile shown in Figure 3-12 and the rail profiles Numbers 2, 3, and 12 shown in Figure 3-11, this time using the cubic spline representations for the rail profiles. Thus, the rail profile Number 12 here was obtained by a different fitting process than that underlying Figure 3-17 (which used Cooperrider's quartic polynomials). Several possible wheelset positions and loads were considered. A summary of the cases covered is shown in Table 3-4. The surface contact stress profiles deduced for these cases are shown in Figure 3-18, for Cases 1 through 15, which shows variations of normal stress σ_z in both the longitudinal (x) and transverse (y) directions around each of the contact positions. The left-hand side of each graph is toward the gage side of the rail when it refers to transverse variations. Since the longitudinal stress

Wheel Contact Position

Rail Contact Position



NEW WHEEL DATA 026

NEW RAIL SECTION D DATA 025

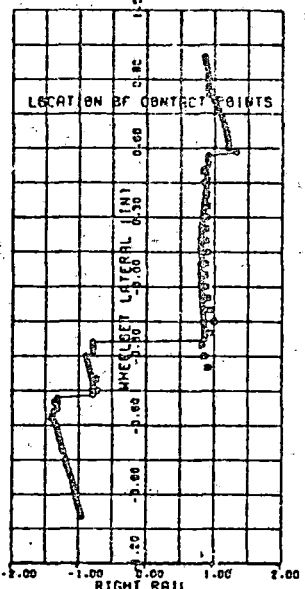
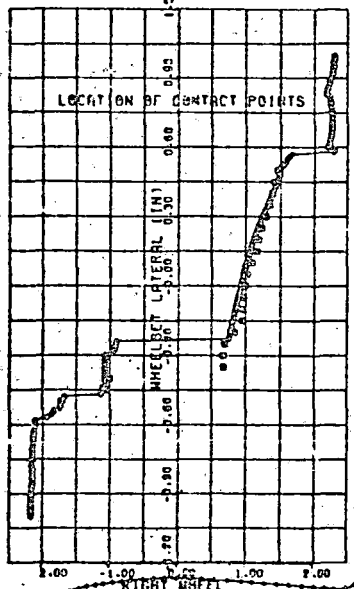
□ = EXPERIMENTAL RESULTS

WHEEL GAGE 53.000 INCH RAIL GAGE 56.500 INCH
RAIL CANT .0250

(a) New Wheels on New Rails at Nominal Gage

Wheel Contact Position

Rail Contact Position



WORN WHEEL NO 3 DATA 005

WORN RAIL DATA 013

□ = EXPERIMENTAL RESULTS

WHEEL GAGE 53.000 INCH RAIL GAGE 56.500 INCH
RAIL CANT .0250

(b) Worn Wheels on Worn Rails at Nominal Gage

FIGURE 3-16. ANALYTICAL AND EXPERIMENTAL RESULTS FOR WHEEL/RAIL CONTACT POSITIONS [3-24]

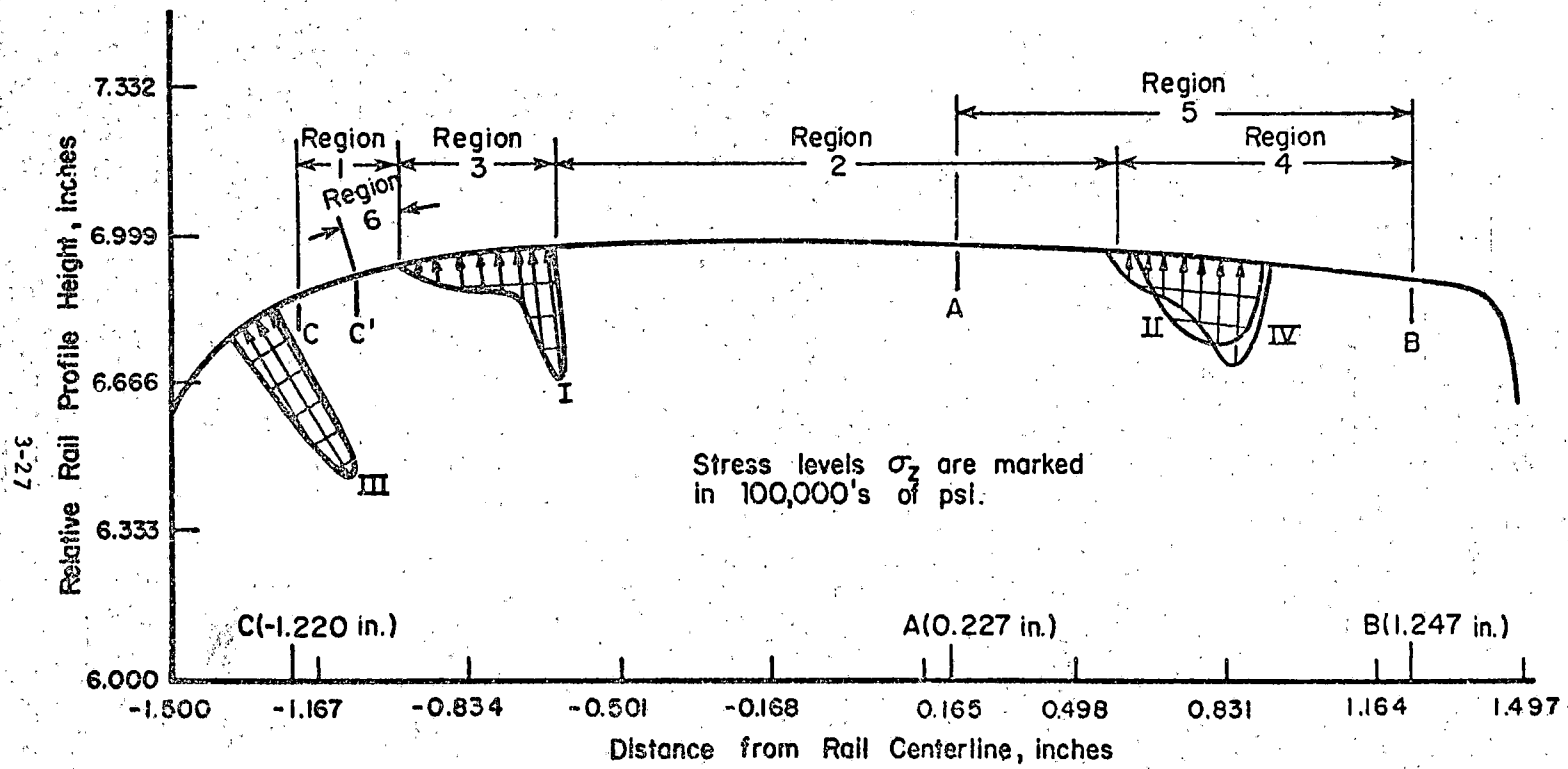


FIGURE 3-17. TYPICAL CONTACT REGIONS IN RAIL PROFILE

TABLE 3-3. DESCRIPTION OF CONTACT REGIONS ON RAIL RUNNING SURFACE OF COOPERRIDER AND LAW WORN RAIL DATA, WORN WHEEL NO. 3

Description	Number	Comments
Region	1	Kinematics of undeformed wheel-rail contact does not permit contact in this region
	2	Kinematics of undeformed wheel-rail contact does not permit contact with this region except for wide gage rail with wheel in extreme position (see Region 5)
	3	Kinematically admissible contact region
	4	Kinematically admissible contact region, nearly Hertzian contact region
	5	Kinematically admissible contact
	6	Region of theoretically high wear
Point	A	Extreme point of wheel travel; admissible position of field side of wheel, plastic indentation running surface
	B	Admissible position of field side of wheel, plastic indentation of running surface
	C-C'	Extreme point of wheel travel; admissible position of wheel flange; plastic indentation of running surface caused by wheel flange
Load	I	Non-Hertzian compressive contact stress in Region 3; distribution extends into Region 1 (see Region 6); 400,000 psi elastic maximum compressive stress
	II	Approximately Hertzian contact stress distribution in most of Region 4; distribution extends into Region 2; 260,000 elastic maximum compressive stress; wheel offset = +0.45 inch
	III	Approximately Hertzian contact stress distribution caused by flange contact; typically 550,000 psi elastic maximum compressive stress
	IV	Non-Hertzian contact stress distribution in Region 4; 290,000 psi maximum compressive contact stress: wheel offset = +1.70 inches.

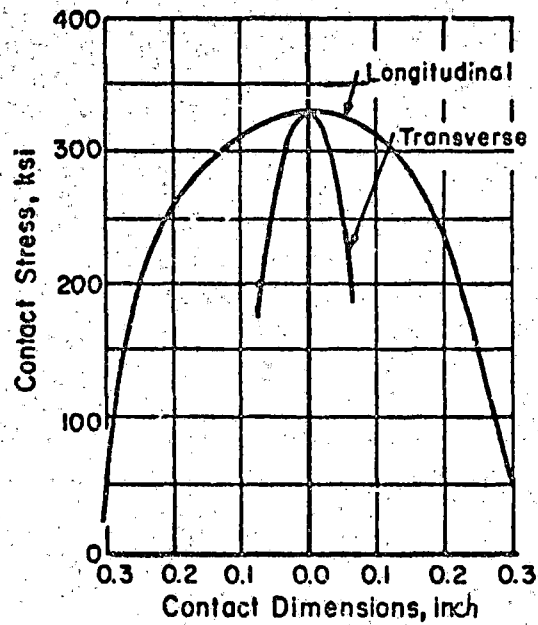
TABLE 3-4. SUMMARY OF WORN WHEEL/RAIL CONTACTS ANALYZED

Case No.	Rail No.*	Wheel Offset (inch)	Contact Positions		Loads (kips)	Max. Stress (ksi)
			y_{rc} (inch)	y_{wc} (inch)		
1**	12	-0.15	-0.80	-0.95	19	335
2	12	-0.05	0.80	0.75	19	237
3**	12	+0.45	0.80	1.25	19	192
4	12	+0.65	0.60	1.25	19	160
5	12	+0.65	0.60	1.25	30	183
6	12	+0.65	0.60	1.25	40	201
7**	12	+0.90	0.80	1.70	19	190
8	12	+1.00	0.70	1.70	19	168
9	12	+1.10	0.80	1.90	19	221
10	2	-0.20	-0.75	-0.95	19	290
11	2	+0.45	0.80	1.25	19	187
12	2	+0.65	0.60	1.25	19	160
13	2	+0.90	0.80	1.70	19	190
14	3	-0.20	-0.75	-0.95	19	350
15	3	+0.45	0.80	1.25	19	172

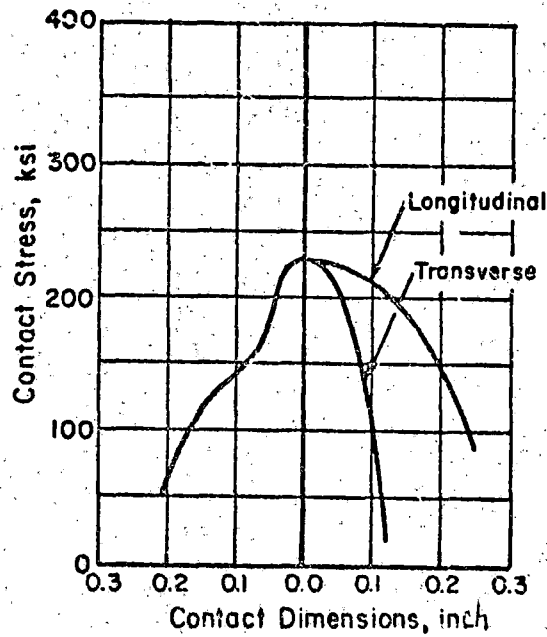
* The rail profiles here were fitted with cubic splines. The wheel profile was that of the worn wheel in Figure 3-12.

** Cases 1, 3, and 7 correspond respectively to those leading to the load pattern Numbers I, II, and IV in Figure 3-17, which were based on Cooperrider's quartic polynomial rail profile.

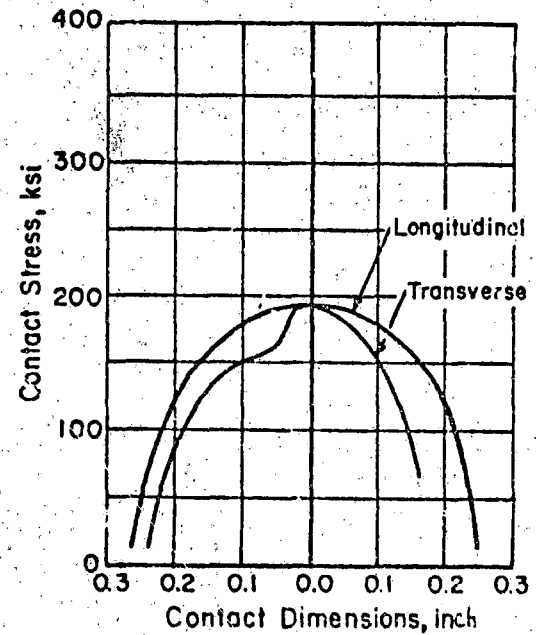
03-E



Case 1
Rail 12, Wheel Offset -0.15 inch



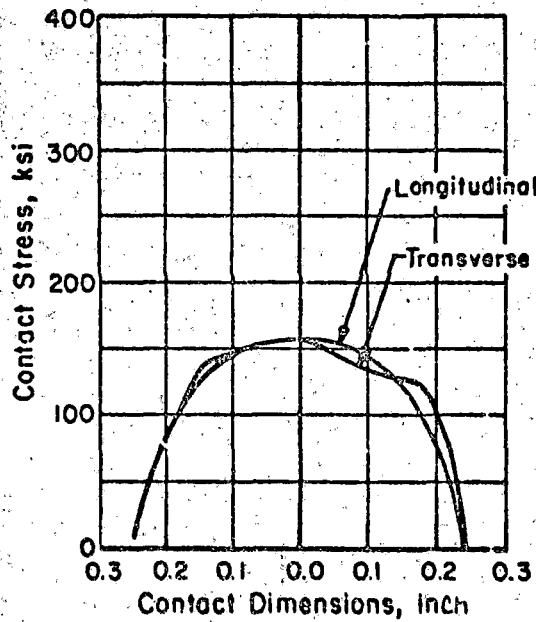
Case 2
Rail 12, Wheel Offset -0.05 inch



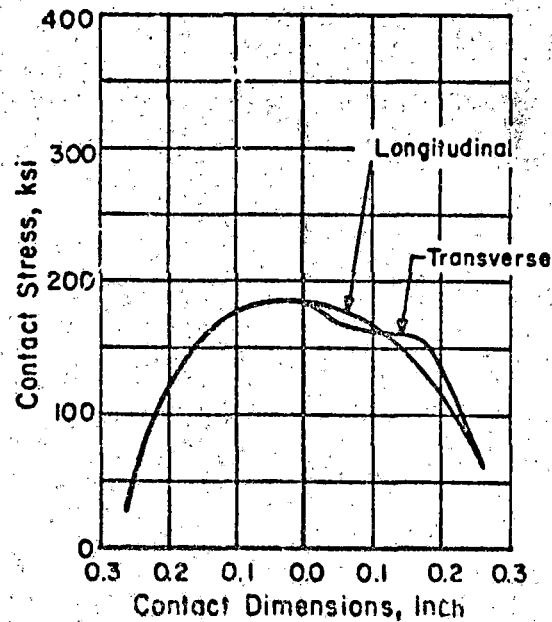
Case 3
Rail 12, Wheel Offset +0.45 inch

FIGURE 3-18. CONTACT STRESS DISTRIBUTIONS

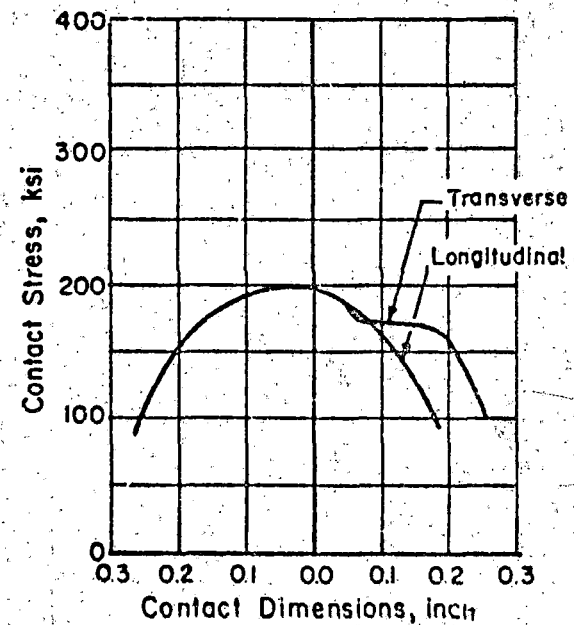
1E-3



Case 4
Rail 12, Wheel Offset +0.65 inch
Load 19,000-lb



Case 5
Rail 12, Wheel Offset +0.65 inch
Load 30,000-lb



Case 6
Rail 12, Wheel Offset +0.65 inch
Load 40,000-lb

FIGURE 3-18. (CONTINUED)

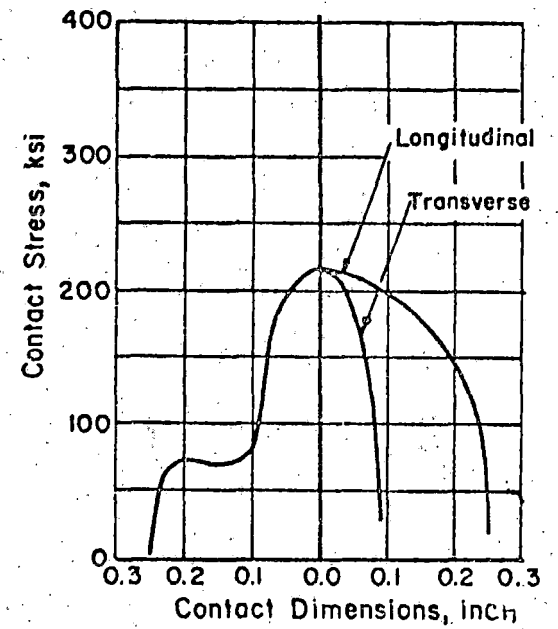
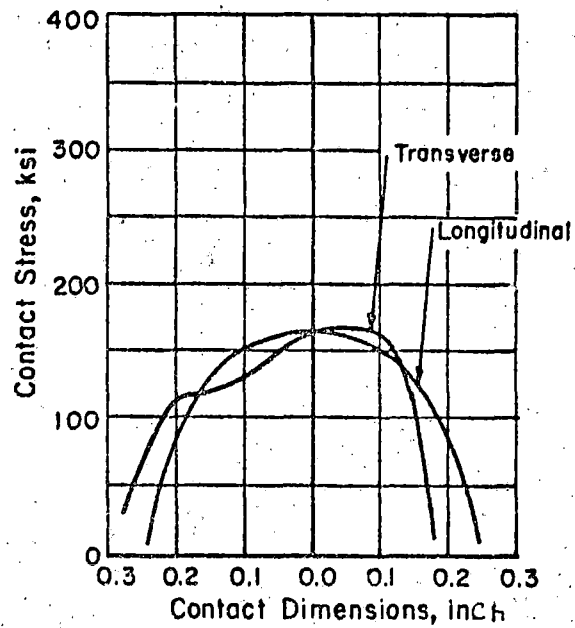
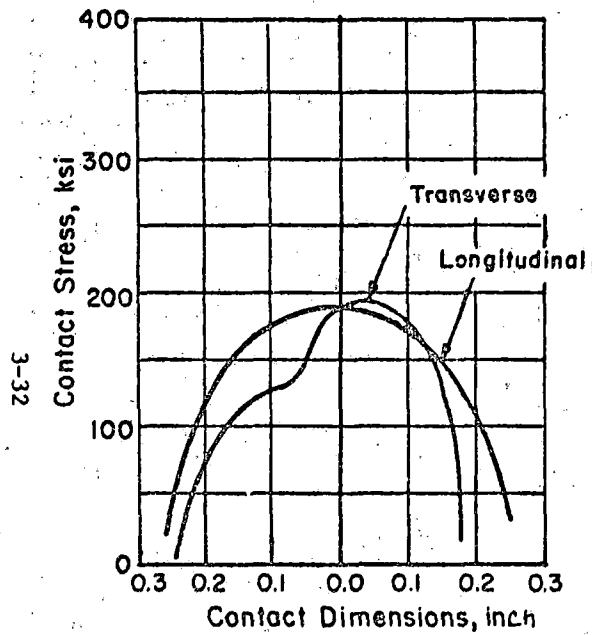
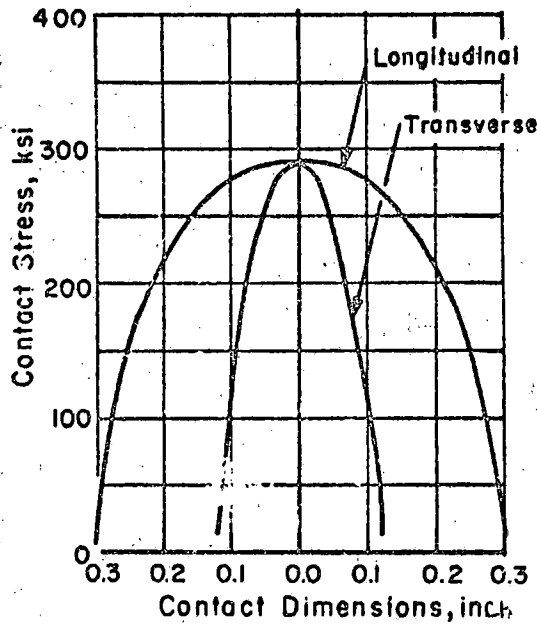
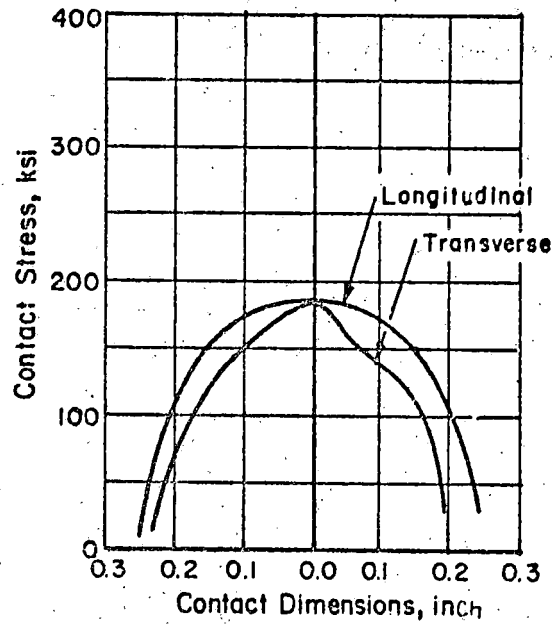


FIGURE 3-18. (CONTINUED)

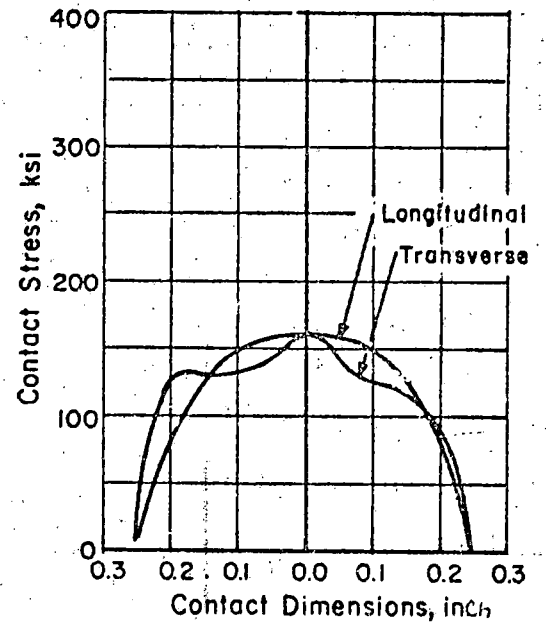
3-3-E



Case 10
Rail 2, Wheel Offset -0.20 inch



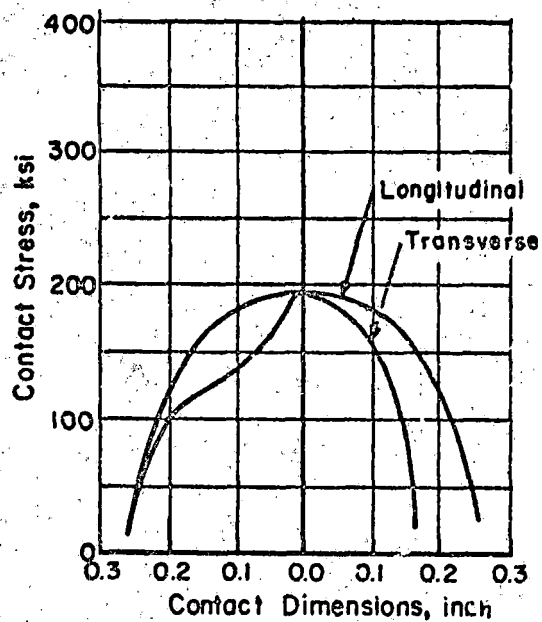
Case 11
Rail 2, Wheel Offset +0.45 inch



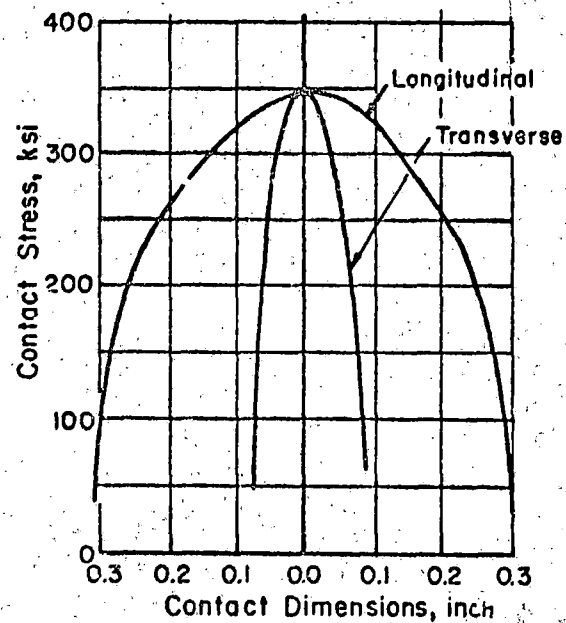
Case 12
Rail 2, Wheel Offset +0.65 inch

FIGURE 3-18. (CONTINUED)

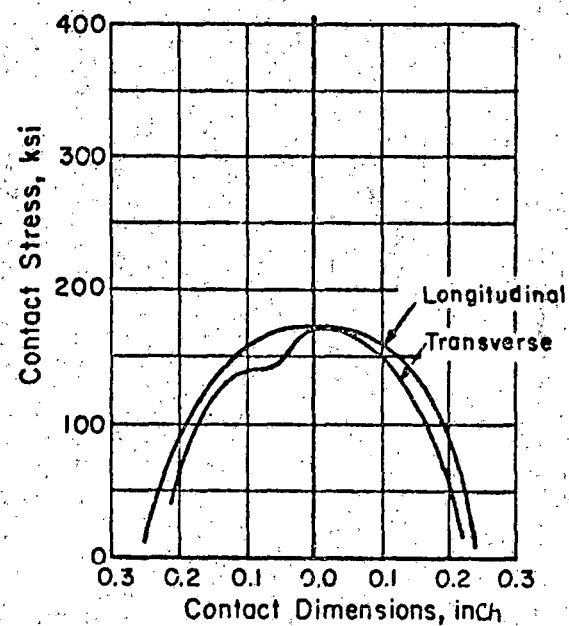
3-34



Case 13
Rail 2, Wheel Offset +0.90 inch



Case 14
Rail 3, Wheel Offset -0.20 inch



Case 15
Rail 3, Wheel Offset +0.45 inch

FIGURE 3-18. (CONTINUED)

distribution is always symmetrical about the transverse axis (because surface irregularities in the longitudinal direction were not considered), the longitudinal distribution is often plotted for only one side of the contact area.

Three of the cases in the Figure 3-18, namely Numbers 1, 3, and 7, correspond respectively to the stresses from the Loads I, II, and IV in Figures 3-17. The peak contact stresses in the Figure 3-18 are lower than those in Figure 3-17 by 170 ksi, 70 ksi and 100 ksi for these three respective cases. Since these differences arose only from the difference in the methods of fitting the rail profile, it can be seen that the calculated contact pressures are indeed sensitive to details of the profiles. Since so many small irregularities may exist in actual wheel and rail profiles, it follows that indeed many variations of contact stress distributions may exist in real wheel/rail contacts. Thus the function of the cases analyzed here is to illustrate possibilities and trends, but not to cover all possible variations of stress patterns that may arise.

With the sensitivity of the contact pressures to profile details in mind, it is plausible that waviness of the contact pressure distribution should arise, as illustrated by most of the cases in the Figure 3-18. It is not certain how much of this waviness is attributable to actual surface irregularities and how much to artificial irregularities in the fitted profiles. It is appropriate to note that a local rise on an actual rail surface would increase the contact pressure there and thus promote plastic flow to lower that rise. This kind of action repeated many times, tends to give smooth transverse profiles such as were observed in the specimens of Figures 3-9 and 3-11.

It may be recalled that Table 3-1 showed little increase of the peak contact stresses on account of design variations in the wheel or rail-crown radii, but in the Figures 3-18 there are many variations in the peak stresses which must be attributed to variations in the shapes of the surface, either from surface irregularities or from sideward shifting to other contact bands. A consequence of this is that wearing of the rails and wheels does not generally reduce the rail stresses (as comparison of Tables 3-1 and 3-4 shows), but instead frequently increases the contact stresses. The increases in peak stresses are particularly noticeable for negative wheel offsets (which tend toward flange contact) or for large positive offsets (which tend toward

"false-flange" contact). Stresses for offsets approaching flange contact are provided by Cases 1, 10, and 14 of Table 3-4, while stresses for an offset involving "false-flange" contact are provided by Case 9. The false flange is the outer region of a worn wheel that has acquired convex curvature because of higher wear near the wheel tape line. The convex curvature of the wheel profile there increases the rail stresses when the wheel offset places that part of the profile against the rail.

The highest contact stress among those computed here is due to that shown as Load Number III in Figure 3-17; it reaches 550 ksi. Other cases with contact near the gage side are also among the highest found here. The reason for this stress increase lies in the relatively strong convex curvature of the rail on the gage side. The high stresses there are concordant with the high wheel wear which occurs in that vicinity.

Concentration or wavy contact stress patterns do not of course necessarily produce highly concentrated or wavy stress patterns very far below the rail surface. The degree to which these modification of the stress patterns extend to subsurface stresses remains to be determined. Subsurface stresses from contact are discussed in Section 3.3.

3.2.4 Observations Regarding Realistic Surface Contact Stresses

The numerical analysis procedure for finding surface stress distributions from realistic wheel and rail shapes was found to be a useful tool, but care must be exercised in determining the surface shapes if the stresses are also to be realistic.

It is important to recognize that, when wheels and rails contact, small random variations in profile height can lead to large stresses when those variations occur within the contact region. The Hertzian analysis assumes the bodies are microscopically smooth and, therefore, does not ordinarily predict stress due to small surface variations. The numerical method used here is, however, sensitive enough to calculate stress variations from surface irregularities if they are properly defined as input. Thus, after careful fitting of profiles, contact stress contours have been found which appear irregular in many cases. Since local contact stresses are high enough to cause plastic

flow at shallow depths, the irregularities in contact stresses can also influence the flow of material near the running surface. However, at depths greater than about 0.2 inch below the surface it is unlikely that such irregularities are important. (This evaluation of implications of surface irregularities will be illustrated later.)

It appears from examining the stresses calculated here that wear is a strong mechanism in the determination of contact stresses between wheels and rails. The concave and false flange regions of the wheel result from this mechanism. The false flange, in turn, can produce excessive contact stress and plastic flow of both wheel and rail. It appears, however, that this flow does not compensate for the wear mechanism (since the false flange persists), and wear continues to exaggerate this condition. It should be noted that this trend may prove worst in cases where tread braking is not performed

An additional observation was that in worn regions the contact stress distribution tends to be more uniform than in Hertz contact, and that the contact area tends toward rectangularity rather than the pure ellipticity it has with new rails and wheels.

In the course of this analysis, a simplified procedure was formulated for calculating contact pressure. This method consisted of fitting (in the least square sense) a quadratic polynomial to points representing each undeformed surface prior to contact in an assumed area. The first and second derivatives calculated at the center of contact for each of these polynomials yielded a radius of curvature by the formula $R = (1+y''^2)^{3/2}/|y''|$ (primes denoting derivatives). Use of these curvatures in the Hertz theory produced a contact stress distribution which gave a plausible first approximation for the contact stresses found by the more elaborate calculations. Since (as will be illustrated later) these simply found contact pressures lead to nearly the same subsurface stresses at depths greater than 0.2 inch, it was decided to use them in later work when the only stresses of interest were at those greater depths.

3.3 SUBSURFACE RAIL STRESS DISTRIBUTION FROM WHEEL/RAIL CONTACT

Apart from possible contribution to the formation of cracks, the most damaging stresses in rails, due to rolling contact in the absence of slip,

usually occur below the surface. In a new rail under normal contact the onset of yielding occurs at the location of maximum octahedral shear which, if caused by contact stresses alone, is approximately 0.1 to 0.2 inches beneath the running surface. The longitudinal shearing stress component (τ_{zx}) also has a maximum beneath the surface. Since it reverses fully during passage of the wheel, it is believed to be very degrading from the viewpoint of fatigue damage.

Although considerable plastic flow occurs during the early service of the rail, this flow diminishes quickly with time until the stress state remains nearly, if not completely, elastic in the vicinity of the loaded area of the rail head. Against this, strain softening of the rail material under cyclic loading can cause continual plastic deformations.

3.3.1 Closed Form Solutions for Subsurface Contact Stresses in Rails

Several closed-form solutions for subsurface stress distributions due to contact presuming specific geometries have been presented in the literature. Of particular interest for approximating the nature of stresses in rails are solutions formulated by Poritsky [3-16], Smith and Liu [3-25], and Hamilton and Goodman [3-26].

Proceeding from equations derived by Poritsky for contact between parallel cylinders, and assuming a state of plane strain and rolling-direction friction ($\sim\tau_{zx}$) due to full slip with friction coefficients $f = 0, 0.25,$ and $0.50,$ Hamilton and Goodman [3-26] plotted subsurface contours of $J_2^{1/2}/\sigma_{max}$, where σ_{max} is the maximum contact pressure, and

$$J_2 = 1/6 [(\sigma_x - \sigma_y)^2 + (\sigma_y - \sigma_z)^2 + (\sigma_z - \sigma_x)^2] + \tau_{yz}^2 + \tau_{zx}^2 + \tau_{xy}^2 \quad (3-14)$$

Thus J_2 is the second invariant of the stress deviator tensor. These plots are shown in Figure 3-19. It may be noted that the friction forces presumed here differ from those deduced by Carter, being simply f times the Hertz contact pressure distribution. Since

$$\tau_{oct} = \sqrt{2/3} J_2^{1/2} \quad (3-15)$$

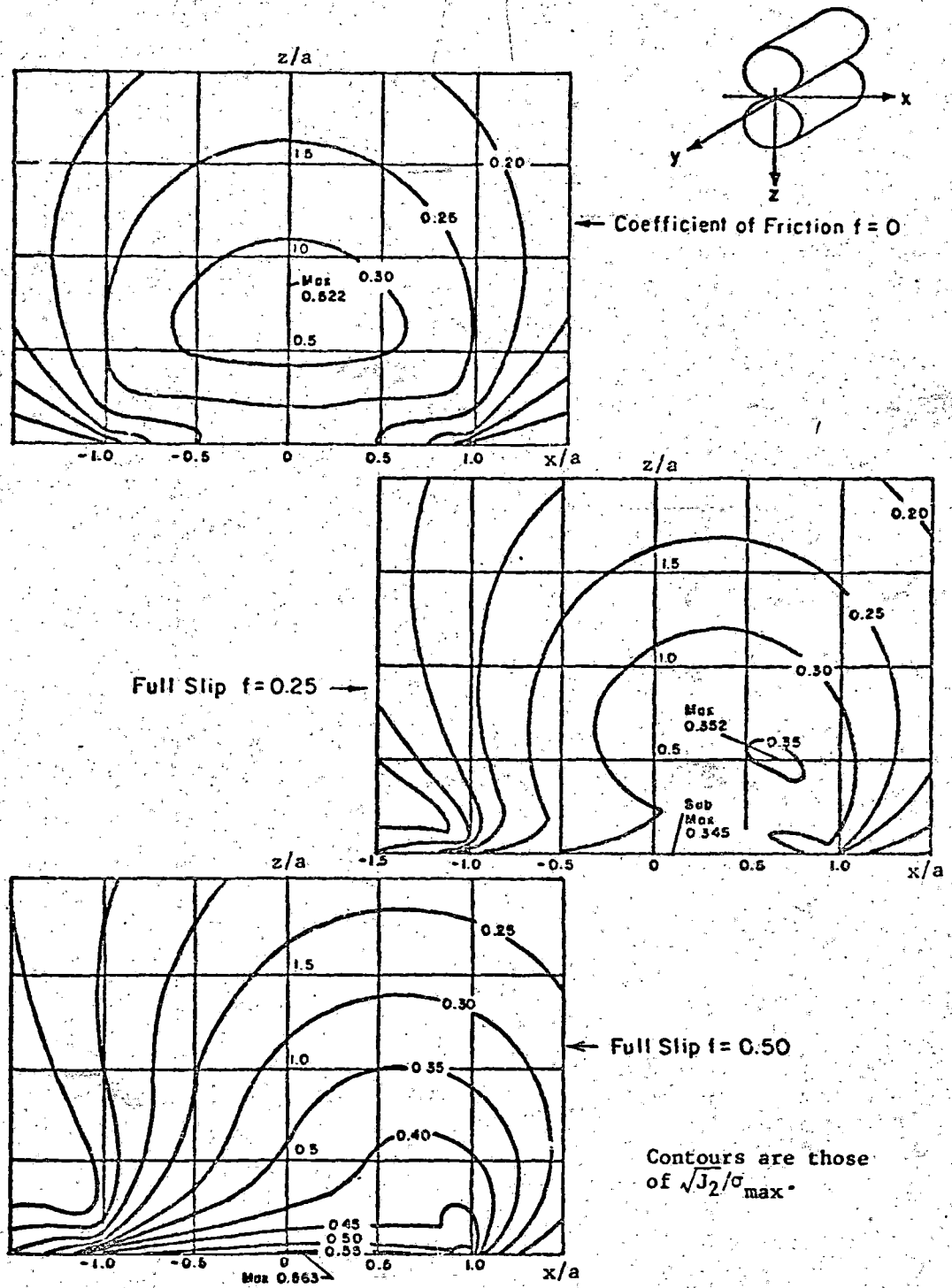


FIGURE 3-19. CONTOURS OF CONSTANT SECOND STRESS INVARIANT BENEATH THE CONTACT AREA BETWEEN CYLINDERS [3-26]

(which reduces to the form of Equation 3-10 when $\tau_{yz} = \tau_{zx} = \tau_{xy} = 0$), Figure 3-19 in effect shows the subsurface pattern of τ_{oct} . The coordinates in this figure are x/a and z/a , where x is tangential distance from the centerline of contact, z is depth, and a is the half width of contact. Since typical values of a for wheel/rail contact may be taken to be 0.15 to 0.30 inch, it can be seen that the maximum τ_{oct} in the absence of tangential load occurs at a depth around 0.10 to 0.20 inch, and that an added frictional load tends to shorten that distance.

Somewhat similar to wheel/rail contact is the case of circular contact (as between spheres) also treated by Hamilton and Goodman [3-26] using formulas of their own. Their plots for circular contact corresponding to those in Figure 3-19 are shown in Figure 3-20. Here in the absence of friction the subsurface depth of the maximum octahedral shear is about half of the half width of contact, and its maximum value is about $\sqrt{2/3}$ (0.36) σ_{max} or 0.294 σ_{max} . Applying this to the case depicted by Figure 1-3, using a half width of $1/2(0.264 + 0.189)$ inch, a maximum τ_{oct} of 53,500 psi is predicted at a depth 0.11 inch, very much as stated before for that case. Thus to a first approximation Figure 3-20 provides a means for finding subsurface values of τ_{oct} for wheel/rail contact, but further means are needed if elliptical contact is to be considered or especially if non-Hertzian contact is to be treated.

3.3.2 A Procedure for Computing Subsurface Stress from Arbitrary Surface Loads

A method devised by Bell [3-27] for analysis of stresses due to arbitrarily distributed loads on the surface of a half space, has been used as the basis for a program to compute stresses in a rectangular body with as many as six surfaces. This analytical tool, designated FRAC3D, since it also has a capability for including a circular or part circular crack, is well suited to the determination of elastic stresses within a rail head subjected to arbitrary contact pressure distributions, tractions, and support conditions. The broad plan of this program is to use analytical expressions for stresses that elemental surface loads induce throughout a half space, choosing elemental loads such that the overall stresses at the boundaries match the desired

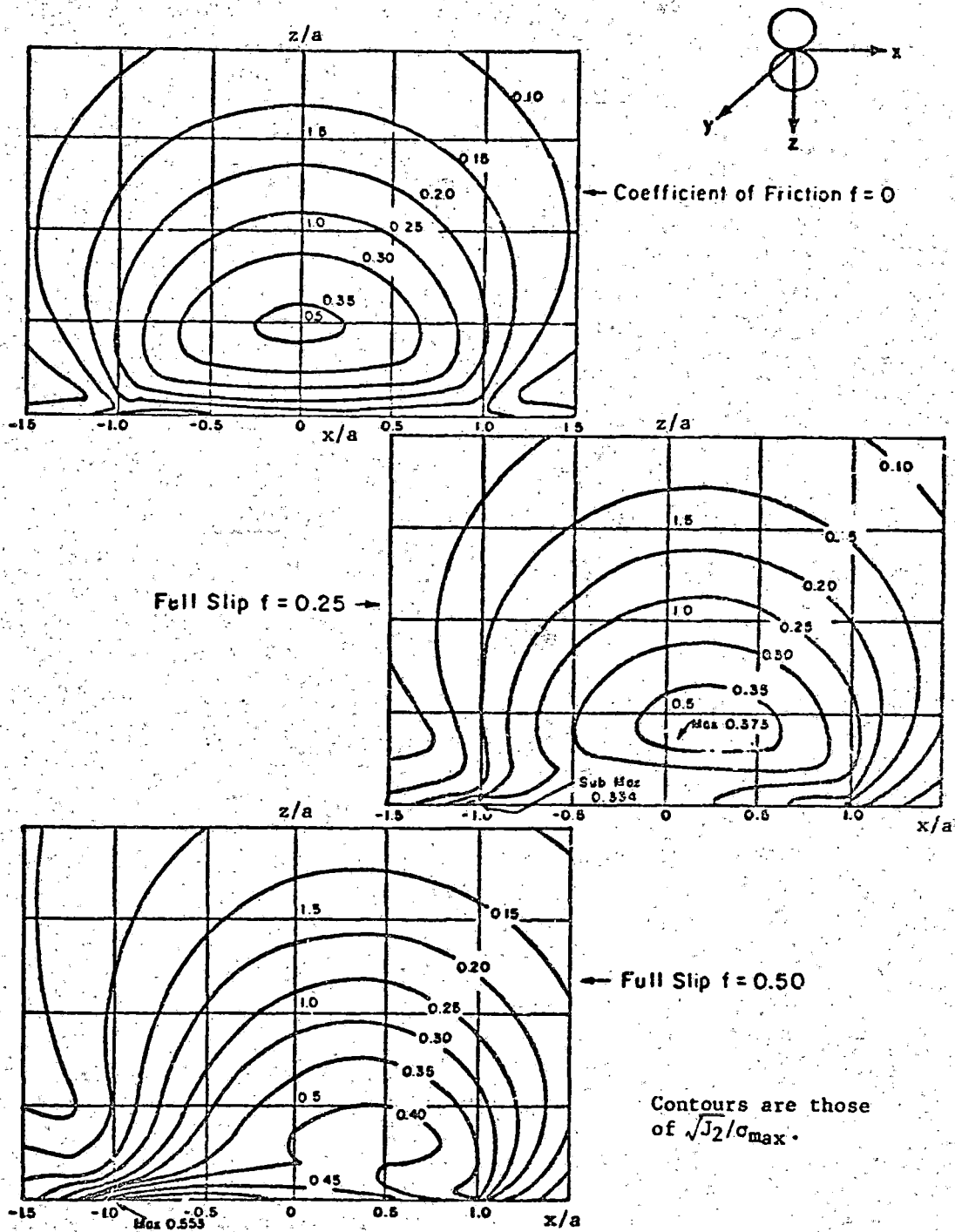


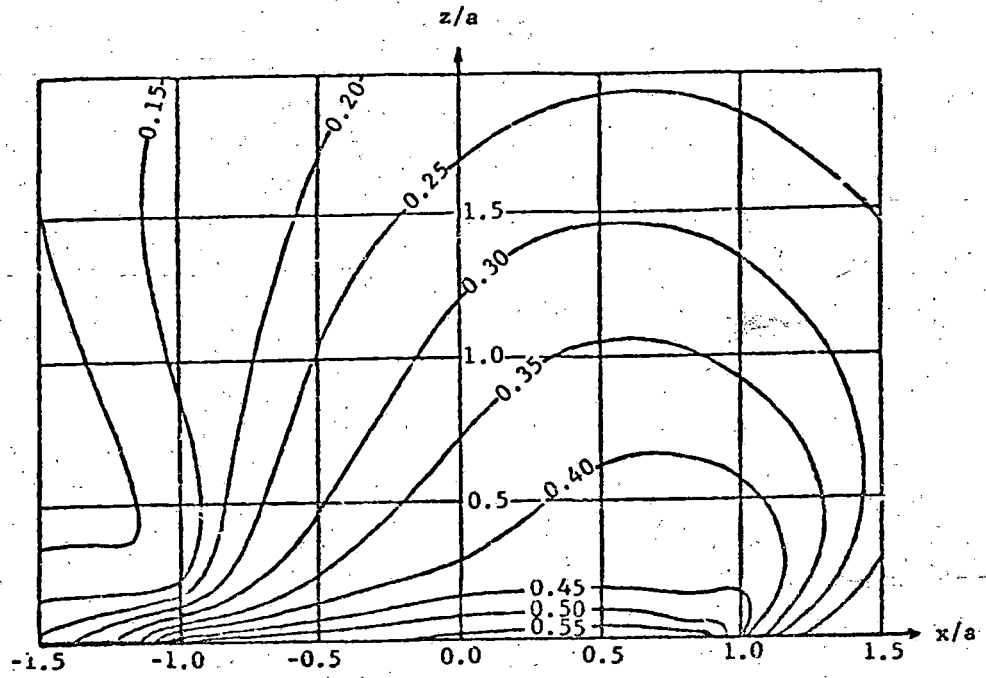
FIGURE 3-20. CONTOURS OF CONSTANT SECOND STRESS INVARIANT BENEATH THE CONTACT AREA BETWEEN SPHERES [3-26]

boundary conditions. Enforcement of continuity of the overall surface loads makes it possible to compute stress components even up to the surfaces without appreciable distortion. The success of this program can be illustrated by showing results obtained from it for the conditions treated by Hamilton and Goodman for cylindrical contact presuming friction with coefficient $f = 0.5$, as in Figure 3-19. The corresponding results found with FRAC3D are shown in Figure 3-21. As can be seen, excellent agreement was obtained between the two types of analysis.

For the purpose of illustrating subsurface contact stresses in rails a rectangular solid (or "elastic brick") with cross section like that of the head of a 132-lb RE rail was chosen to be used for stress analysis by FRAC3D. Forms of elemental surface loads were chosen in sufficient detail so that, by assigning them proper magnitudes, given normal or tangential contact loads could be approximated on the running surface, and appropriate balancing loads could be assigned elsewhere.

3.3.3 Patterns of Elastic Subsurface Stresses Below Wheel/Rail Contacts

Using the program FRAC3D, extensive calculations were made of stresses under the pressure distributions and tractions arising from a wide variety of wheel/rail contacts. The cases treated include both normal pressure and tangential tractions for various wheel sizes and rail crowns, and also some cases involving wear, as listed in Table 3-5. It may be noted that Case 1 in the table is a baseline case against which results for the other cases can be compared to see the effect of varying some particular specification. The baseline case employs Hertzian contact between a 33-inch wheel and a rail with 10-inch crown radius under a load of 19,000-lb. Cases 2 and 3 explore stresses from non-Hertzian contact pressures found earlier with a worn wheel (cf Table 3-4); Case 4 to 7 involve a change of wheel or crown radius or normal load, and Cases 8 to 11 treat effects of tangential loads, presuming full slip with friction (as considered by Hamilton and Goodman but now with elliptical load patterns). The location of sites within the rail head for which stresses were determined are shown in Figure 3-22. Results from these calculations are shown graphically in figures that follow.



(Contours show $\sqrt{J_2}/\sigma_{\max}$ for $f=0.5$. Cf. Figure 3-19.)

FIGURE 3-21. COMPARISON CONTOURS OF SECOND STRESS INVARIANT FOR CYLINDRICAL CONTACT WITH SLIP FORM FRAC3D

TABLE 3-5. CASES ANALYZED FOR SUBSURFACE STRESS DISTRIBUTIONS

Case No.	Wheel size, inch	Rail Crown Radius, inch (or rail size)	Wheel Vertical Load, lb	Coefficient of Friction		Worn Wheel/Rail Contact Position		Remarks
				Lateral	Longitudinal	y_{rc} , inch	y_{wc} , inch	
1	33	10	19,000	-	-	-	-	Cf. Case 1 of Table 5
2	33	(133 CFI)	19,000	-	-	0.6	1.25	Cf. Case 4 of Table 8
3	33	(133 CFI)	19,000	-	-	0.8	1.70	Cf. Case 7 of Table 8
4	36	10	19,000	-	-	-	-	Cf. Case 6 of Table 5
5	40	10	19,000	-	-	-	-	Cf. Case 7 of Table 5
6	33	14	19,000	-	-	-	-	Cf. Case 8 of Table 5
7	33	10	50,000	-	-	-	-	Cf. Case 5 of Table 5
8	33	10	19,000	0.5	-	-	-	Full lateral slip
9	33	10	19,000	0.3	-	-	-	Full lateral slip
10	33	10	19,000	-	0.5	-	-	Full longitudinal slip
11	33	10	19,000	-	0.3	-	-	Full longitudinal slip

3-44

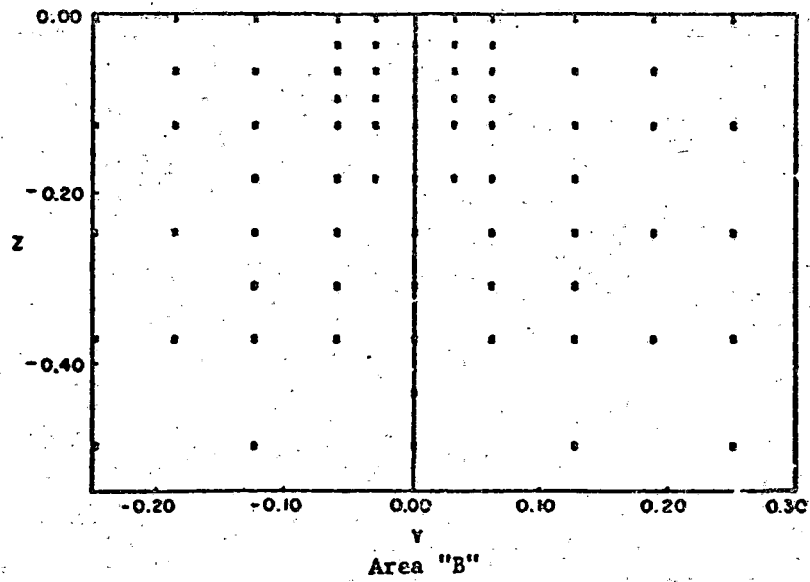
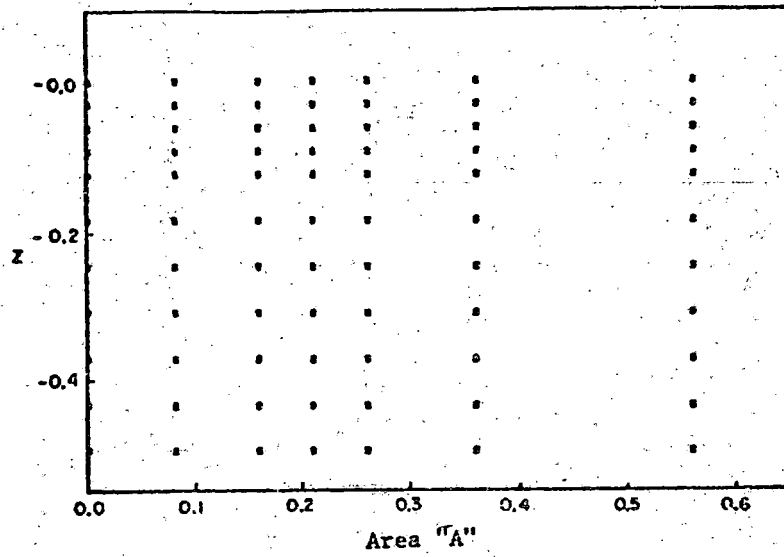
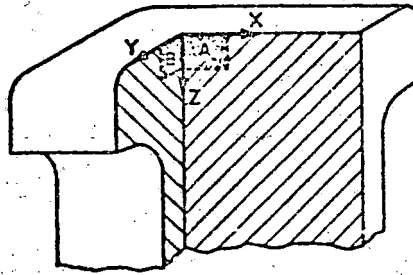


FIGURE 3-22. STRESS CALCULATION LOCATIONS WITHIN ELASTIC BRICK MODEL

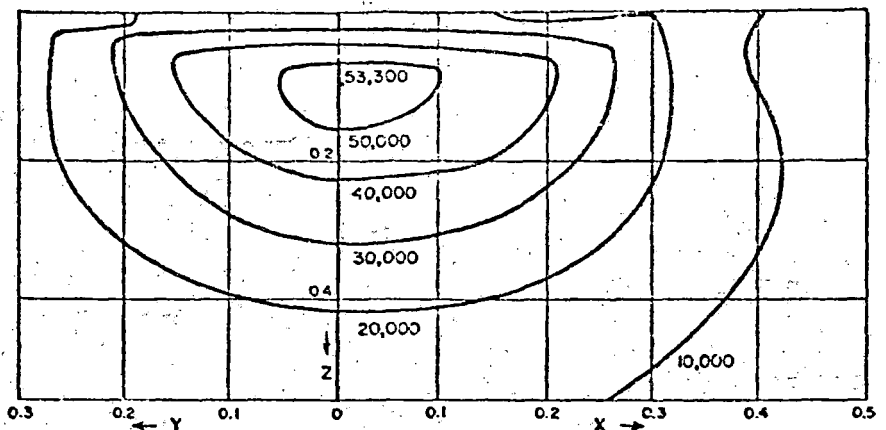
Figure 3-23 presents the results of the analysis for the base line case (Case 1) showing distributions of all six stress components on two planes normal to the running surface at the center of contact. It also shows the octahedral stress implied by those six components. The octahedral stress has importance as an indicator of whether plastic flow might arise from contact stresses, and the six individual stress components have importance as the quantities which can be added to other kinds of stress (e.g., flexural or residual stresses) in evaluating multi-source stress distributions. It may be noted that the stresses shown here compare favorably with those shown earlier in Figure 1-3, as they should. (Small discrepancies may arise from coarse representation of surface loads used as input to FRAC3D.) Because of the symmetry for that case, the lateral shear stress τ_{yz} vanishes where $y = 0$ (that is on area A), the longitudinal shear stress τ_{zx} vanishes where $x = 0$ (that is on area B), and the remaining shear stress τ_{xy} is zero on both these planes.

Figure 3-24 shows the effect of particular non-Hertzian contact pressure distributions on the subsurface octahedral and lateral shear stresses by combining results from Cases 2, 3, and 1. The non-Hertzian cases chosen correspond to Cases 4 and 7 of Table 3-4, so the contact pressures are shown by Cases 4 and 7 in Figure 3-18. (The latter of those cases also correspond to Load IV in Figure 3-17, but the profile fitting process made the load distribution there somewhat different.) It can be seen here that skewness of the contact pressure distributions in the y -direction leads to skewness of the subsurface stresses in that same direction. However, at depths greater than 0.2 inch, the effect of that skewness becomes quite small. Thus for studies of stresses around cracks well buried in the rail head, it is reasonable to neglect the non-Hertzian aspect of contact stresses, and to employ simply the stresses arising from Hertzian contact. For stresses nearer to the surface, which may induce plastic flow, the non-Hertzian effects can accentuate the stresses, as Figure 3-24 shows. It is possible of course that more exaggerated non-Hertzian stress might arise for other particular instances, but those shown here are thought to be representative.

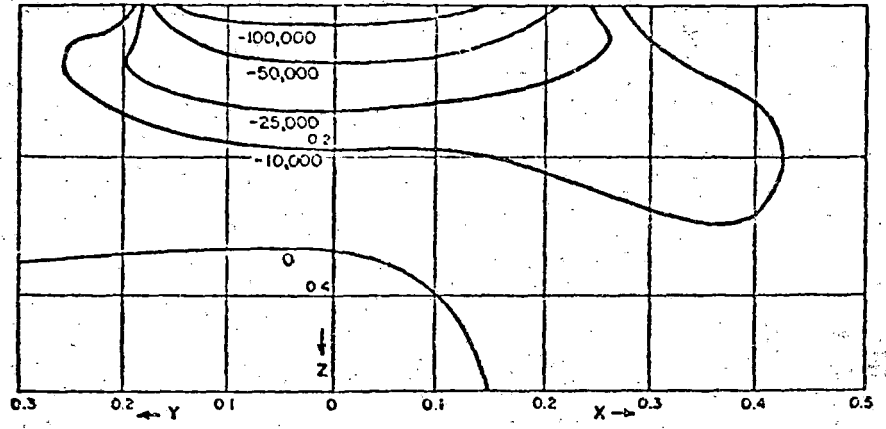
The effects on the subsurface octahedral shear stress from increasing the wheel radius are shown in Figure 3-25 by combining results from Cases 5, 4,

Stress ~ psi
 X, Y, Z ~ inch

(a) Octahedral
 Stress, τ_{oct}



(b) Longitudinal
 Stress, σ_x



(c) Transverse
 Stress, σ_y

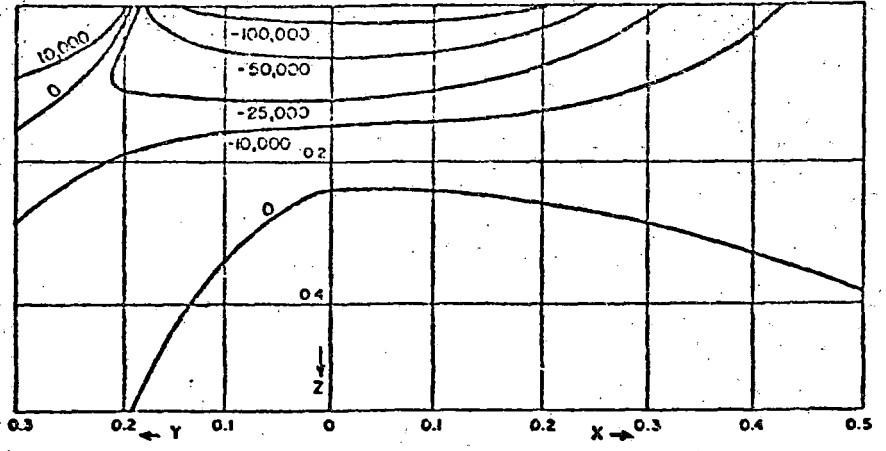
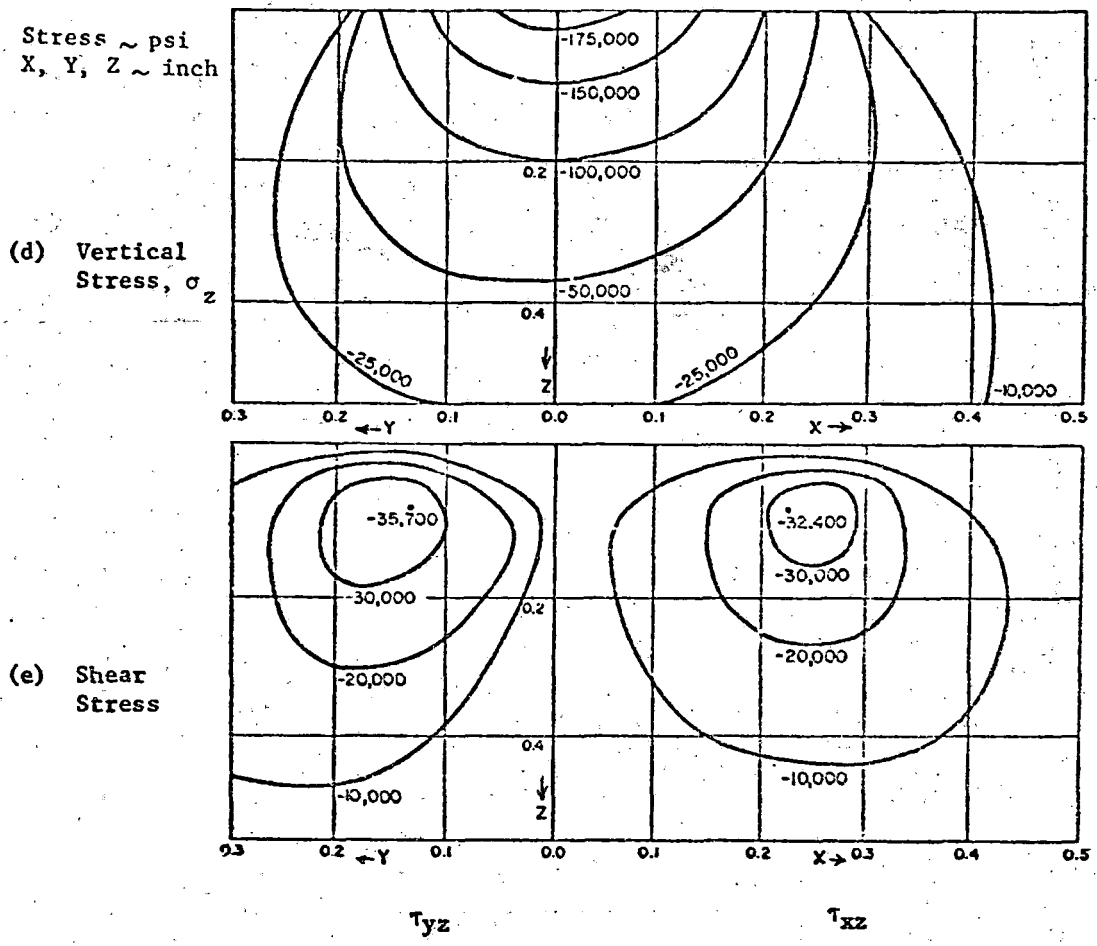


FIGURE 3-23. STRESS CONTOURS FOR (BASELINE) LOAD CASE 1 (19,000-LB LOAD, 33-INCH WHEEL, 10-INCH CROWN RADIUS)

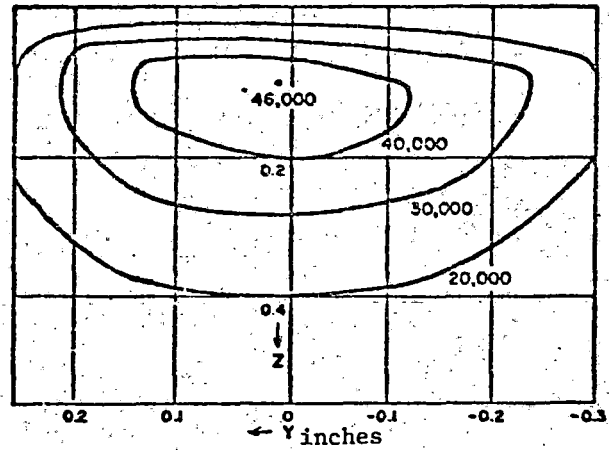


Note that $\tau_{xy} = 0$ on Areas A and B. (Cf. Figure 3-22.)

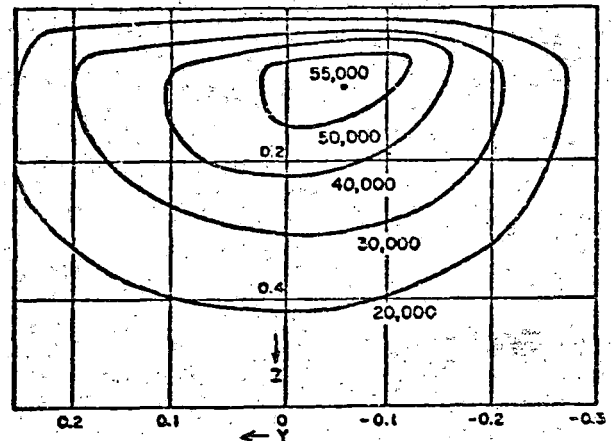
FIGURE 3-23. (CONTINUED)

Stress ~ psi
X, Y, Z ~ inch

(a) Octahedral Stress τ_{oct} for
Worn Contours (Case 2),
 $y_{rc} = 0.6$ inch, $y_{wc} = 1.25$
inches



(b) Octahedral Stress τ_{oct} for
Worn Contours (Case 3),
 $y_{rc} = 0.8$ inch, $y_{wc} = 1.70$
inches



(c) Octahedral Stress τ_{oct} for
Hertz Distribution (Case 1)

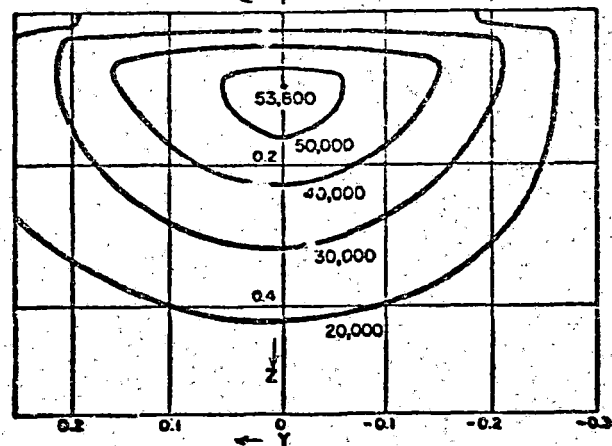
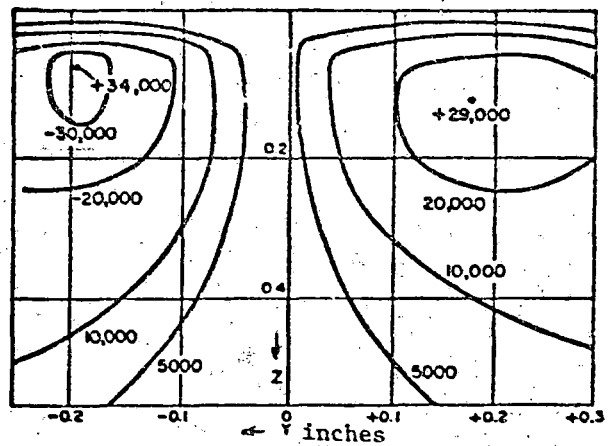


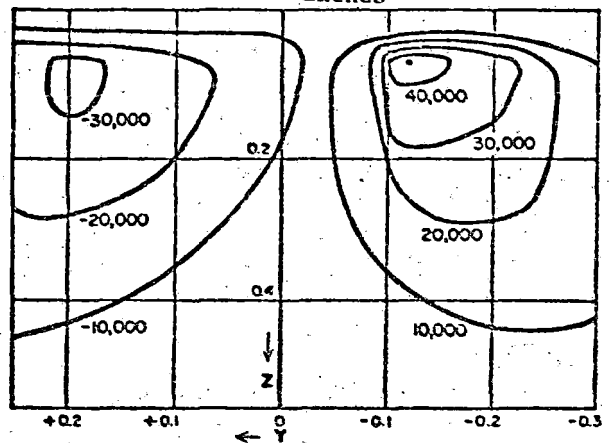
FIGURE 3-24. STRESS CONTOURS FOR NON-HERTZIAN AND HERTZIAN PRESSURE DISTRIBUTIONS

Stress ~ psi
 X, Y, Z ~ inch

(d) Transverse Shear Stress τ_{yz}
 for Worn Contours (Case 2),
 $y_{rc} = 0.6$ inch, $y_{rw} = 1.25$
 inches



(e) Transverse Shear Stress τ_{yz}
 for Worn Contours (Case 3),
 $y_{rc} = 0.8$ inch, $y_{rw} = 1.70$
 inches



(f) Transverse Shear Stress τ_{yz}
 for Hertz Distribution
 (Case 1)

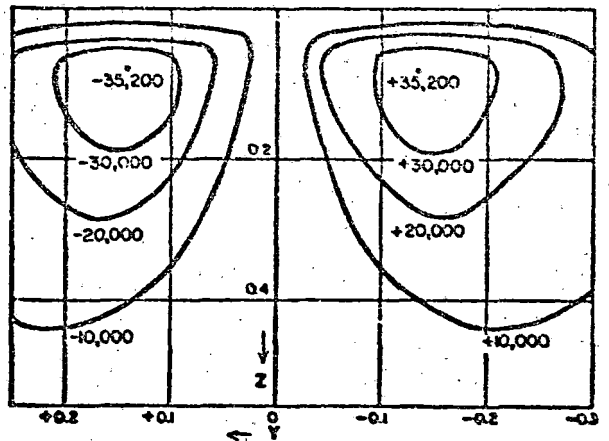
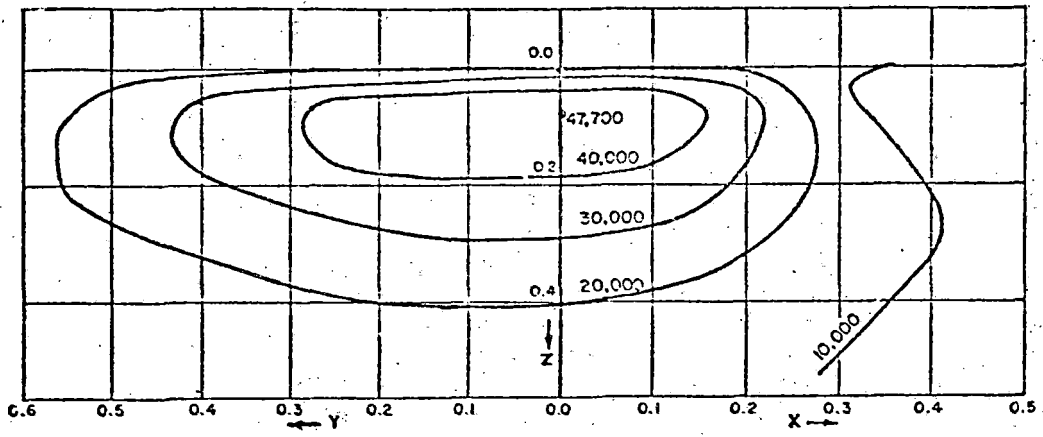
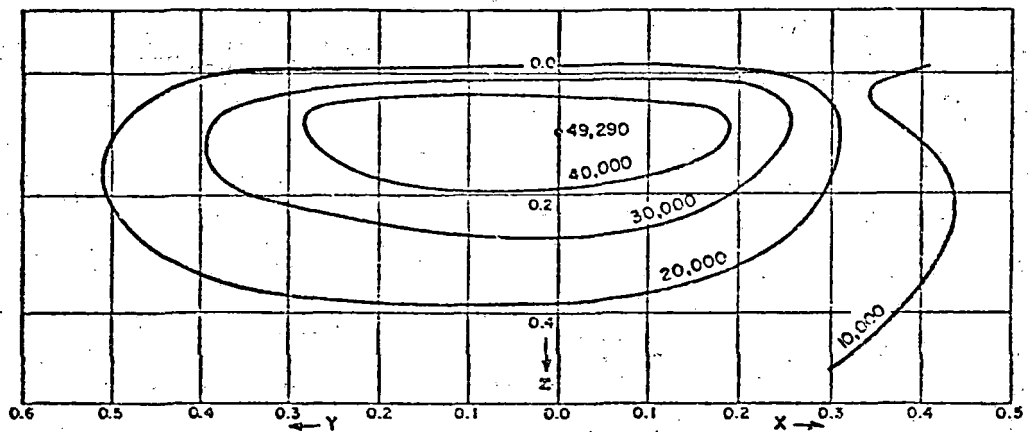


FIGURE 3-24. (CONTINUED)

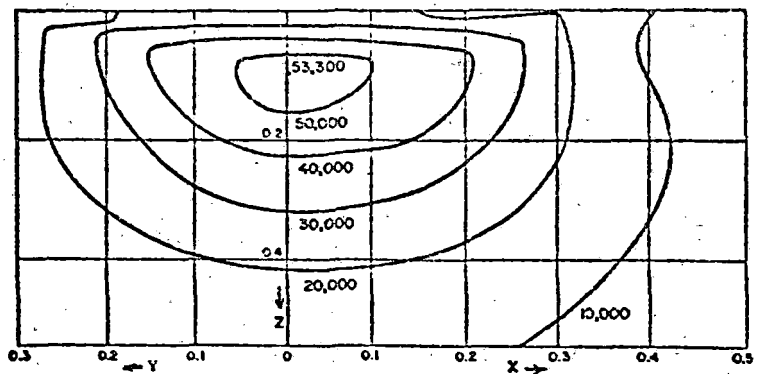


(a) 40-inch wheel (Case 5)



(b) 36-inch wheel (Case 6)

Stress ~ psi
 X, Y, Z ~ inch



(c) 33-inch wheel (Case 1)

FIGURE 3-25. EFFECT OF WHEEL RADIUS ON OCTAHEDRAL SHEAR STRESS IN RAIL WITH 10-INCH CROWN RADIUS AND 19,000-LB LOAD

and 1. As can be seen, changing the wheel radius from 33 to 40 inches lowers the maximum octahedral shear stress from 53,300 psi to 47,700 psi. The cases shown in this figure correspond to Cases 7, 6, and 1 of Table 3-1.

Figure 3-26 shows how changing either the rail crown radius or the vertical load affects the subsurface octahedral shear stress by combining results from Cases 6 and 1 or Cases 1 and 7 of Table 3-5. A 33-inch wheel is presumed in all three cases shown, but in part (a) the rail crown radius (14 inches) is presumed larger than for the baseline case, while in part (c) the load (50,000-lb) is presumed larger than for the baseline case. Part (b) again shows the baseline case. As the figure shows, and as was anticipated, increasing the crown radius to 14 inches decreases the maximum octahedral shear stress (from 53,300 psi to 51,000 psi), while increasing the load to 50,000-lb increases the maximum octahedral shearing stress (from 53,300 psi to 74,000 psi). The cases shown in this figure correspond to Cases 8, 1, and 5 of Table 3-1.

The effect of tangential tractions combined with normal loads are treated by Cases 8 to 11 in Table 3-5, with results being shown in Figure 3-27 and 3-28. In Figure 3-27, the effects of lateral surface shear stress (τ_{yz}) are shown by combining results from Cases 8, 9, and 1. The tangential load is taken to be f times the vertical load, similar to cases in which there is no locking between the surfaces, i.e., the condition of full slip. It is important that as f increases the location of the maximum octahedral shearing stress moves toward the running surface of the rail, so that for $f = 0.5$ the location of the maximum is on the surface. A similar shift occurs in the lateral shear stress τ_{zy} . Hence, with lateral traction being added to the circumstances of the baseline case, first yield from contact stresses should appear on the rail surface rather than below it as was the case for purely normal loading. This implies that the state of plastic deformation in the rail is likely to be quite different in those sections of track subjected to lateral traction, such as on curves when sideward slippage may occur, as compared to that in tangent track where the load is primarily normal. Of course lateral traction also increases τ_{oct} , τ_{yz} , and σ_y as shown in Figure 3-27. It is reasonable to expect that much more severe deformation would occur in these cases because of the nature of constraints on the plastic flow. Plastic deformation under

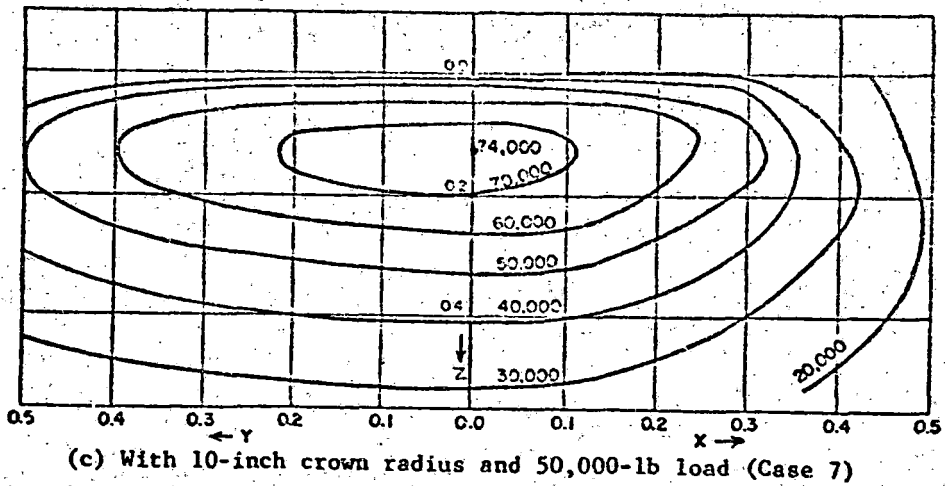
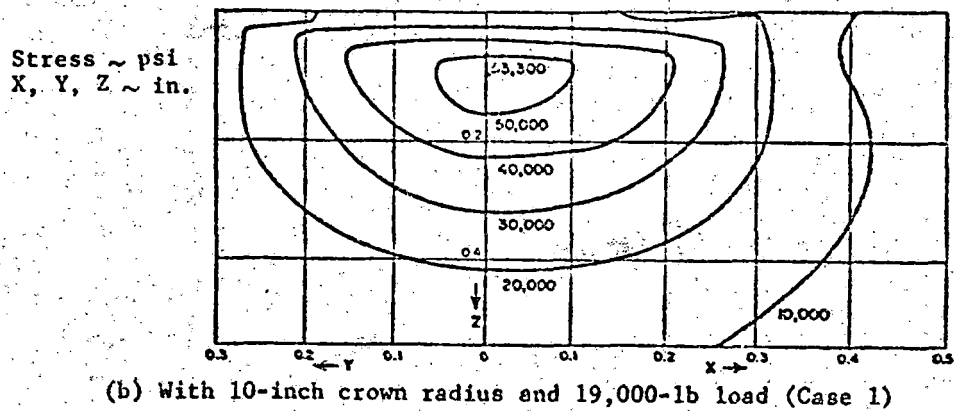
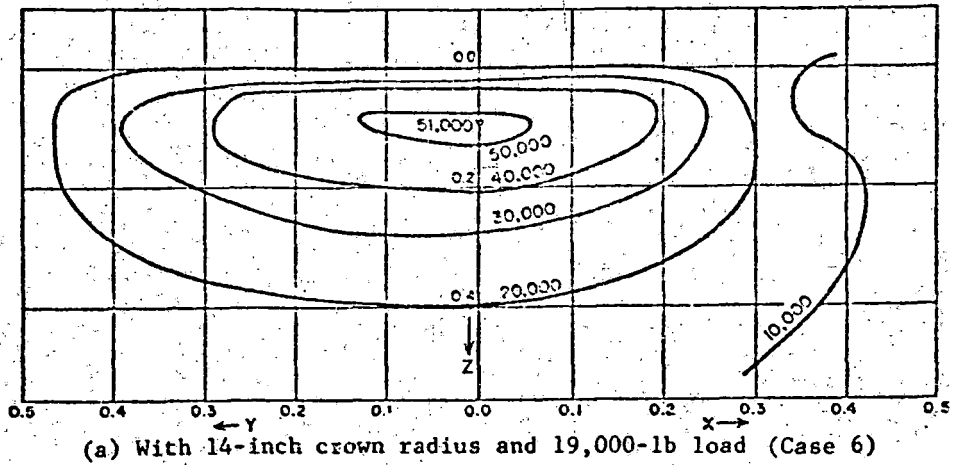
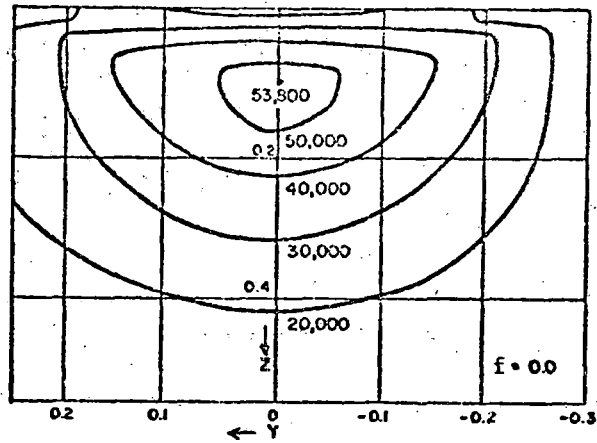
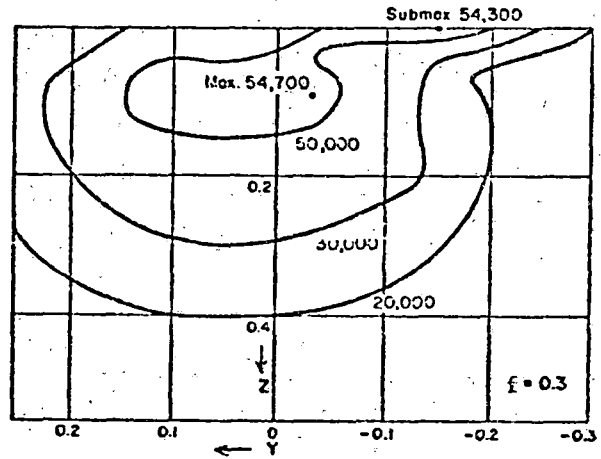
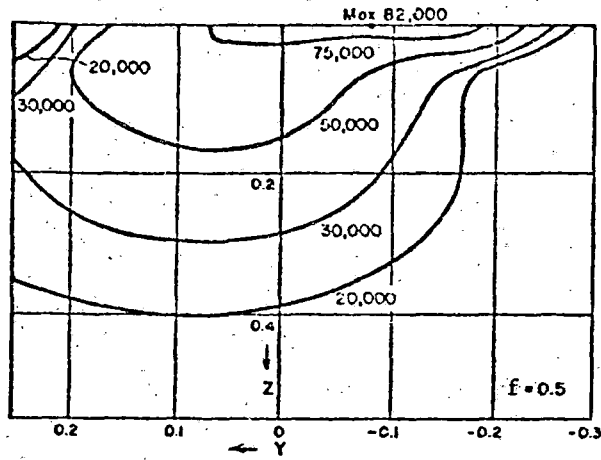


FIGURE 3-26. EFFECTS OF RAIL CROWN RADIUS AND OF VERTICAL LOAD ON OCTAHEDRAL SHEAR STRESS IN RAIL UNDER 33-INCH WHEEL.

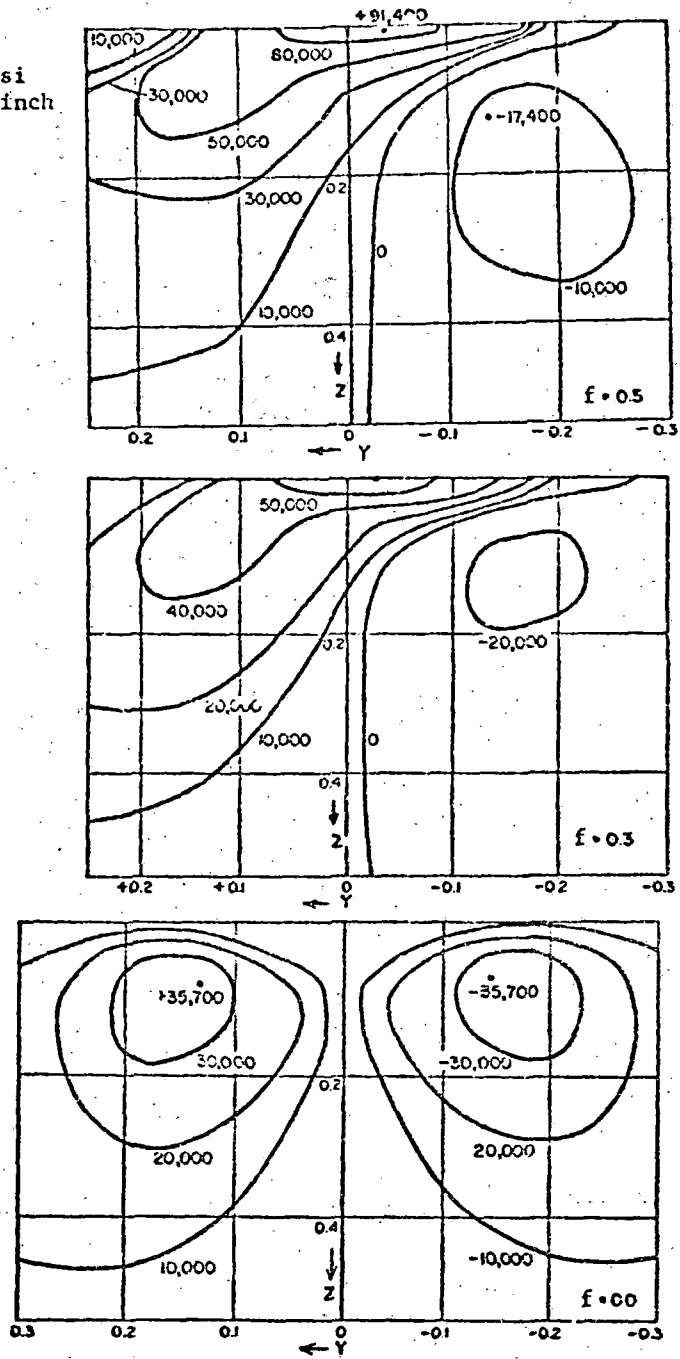
Stress ~ psi
 X, Y, Z ~ inch



(a) Octahedral Stress

FIGURE 3-27. STRESS CONTOURS FOR COMBINED VERTICAL AND LATERAL LOADING
 (33-INCH WHEEL, 10-INCH RAIL CROWN, 19,000-LB VERTICAL LOAD)

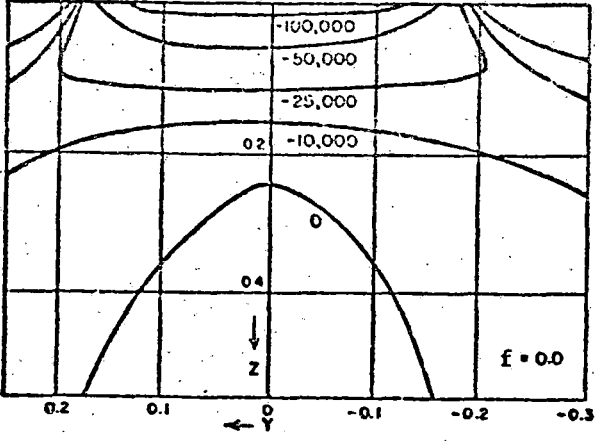
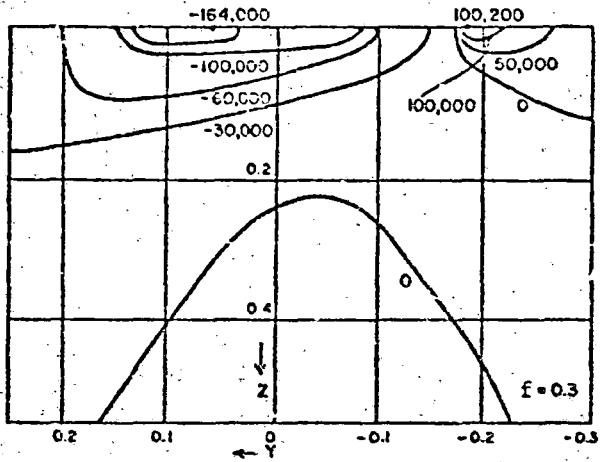
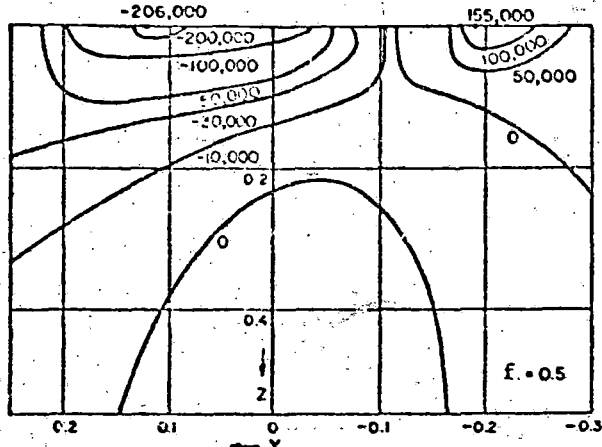
Stress ~ psi
 X, Y, Z ~ inch



(b) Transverse Shear Stress, τ_{yz}

FIGURE 3-27. (CONTINUED)

Stress ~ psi
 X, Y, Z ~ inch



(c) Transverse Stress, σ_y

FIGURE 3-27. (CONTINUED)

normal loading is generally represented as occurring within a subsurface "bulb" or cylindrical region along the length of the rail.

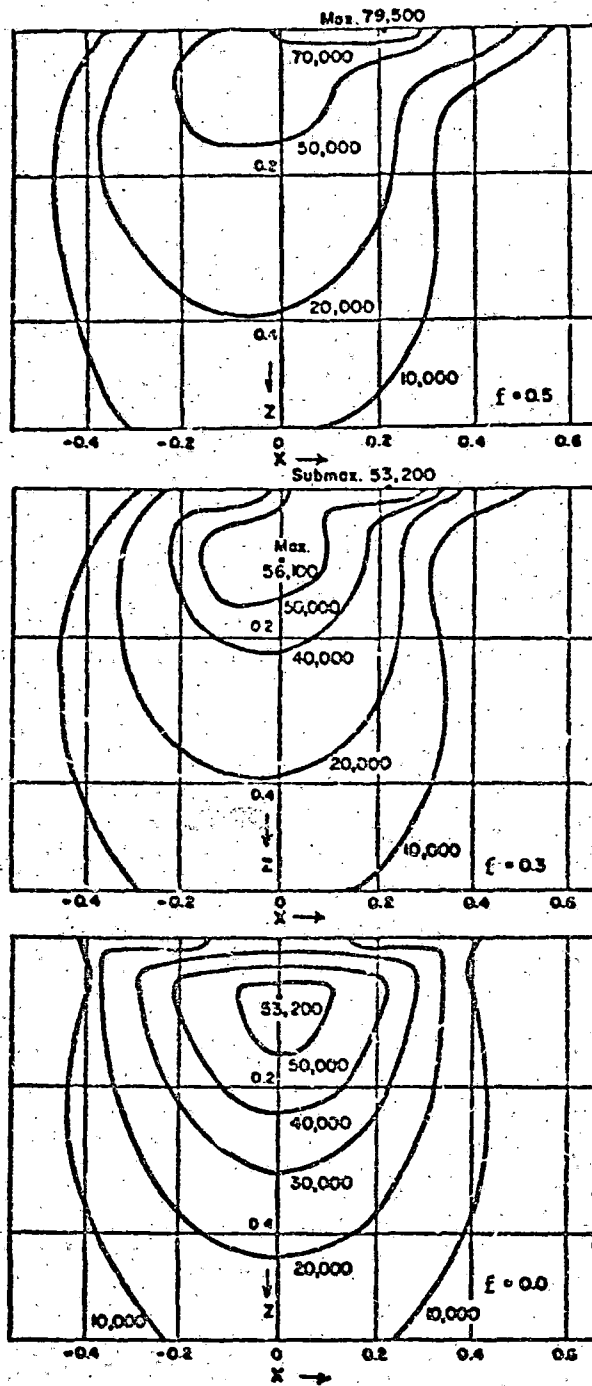
Similar effects are noted from longitudinal tractions, as shown in Figure 3-28 by combining results from Cases 10, 11, and 1 of Table 3-5. The resulting stresses are, however, somewhat smaller than for the lateral slip cases. Longitudinal tractions, of course, arise from starting or braking and from axle windup on curves.

A consequence of lateral traction that can be important is the formation of rail head edge cracks. Figure 3-29 shows a general stress pattern that has been observed where rail head edge cracks form. The figure also compares the pattern with transverse stresses σ_y shown for the case with $f = 0.5$ in Figure 3-27. It can be seen that under lateral traction a very high tensile stress region develops immediately adjacent to the contact area. Clearly such a stress field would have an opening effect on an edge crack of the type shown.

In characterizing "shelly" failures in Japan, Nakamura et al [3-28] describe surface cracks that were found to occur on both curved and tangent track. They suggested that the cracks are formed by slip between the wheel and rail. The findings here tend to support this hypothesis.

Finally, maximum subsurface values of τ_{oct} , τ_{yz} , and τ_{zx} for varying loads are shown in Figure 3-30 for cases involving a new 33-inch wheel in contact with a rail having a 10-inch crown or under the worn-wheel contacts described by Cases 4 and 7 of Table 3-4.

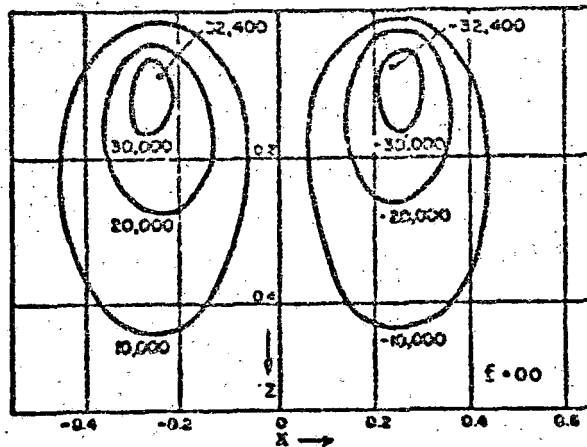
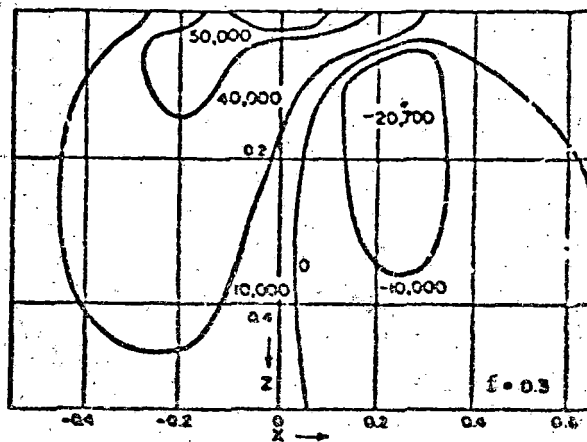
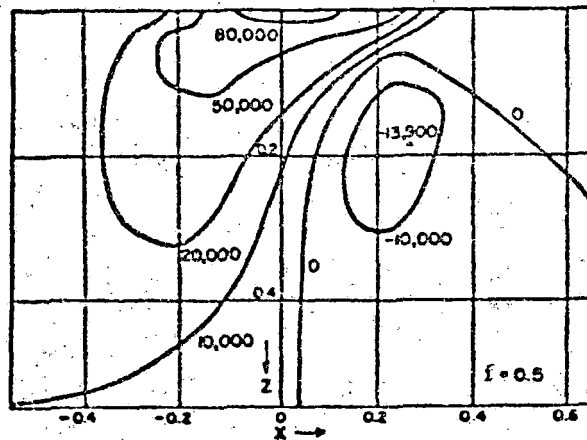
Stress ~ psi
 X, Y, Z ~ inch



(a) Octahedral Stress

FIGURE 3-28. STRESS CONTOURS FOR COMBINED VERTICAL AND LONGITUDINAL LOADING (33-INCH WHEEL, 10-INCH RAIL CROWN, 19,000-LB VERTICAL LOAD)

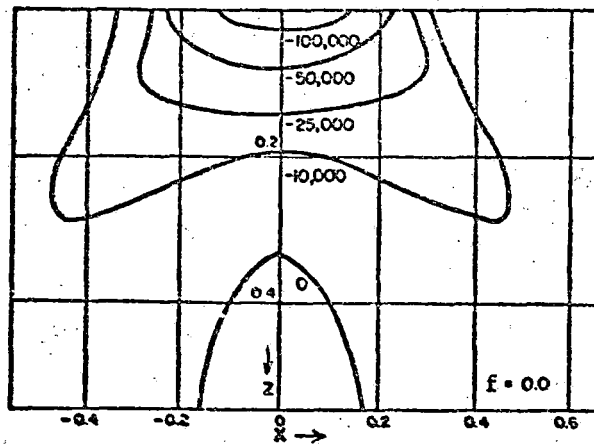
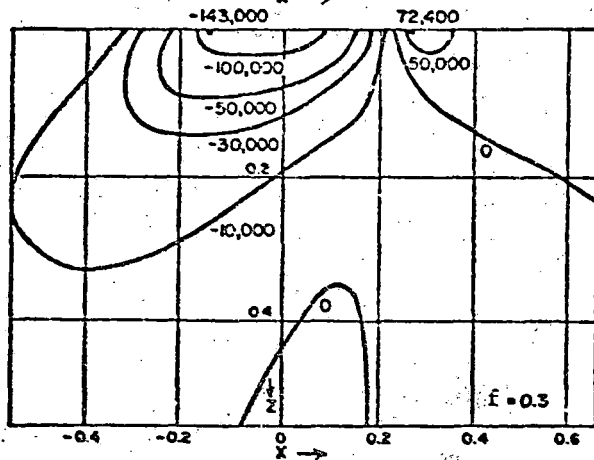
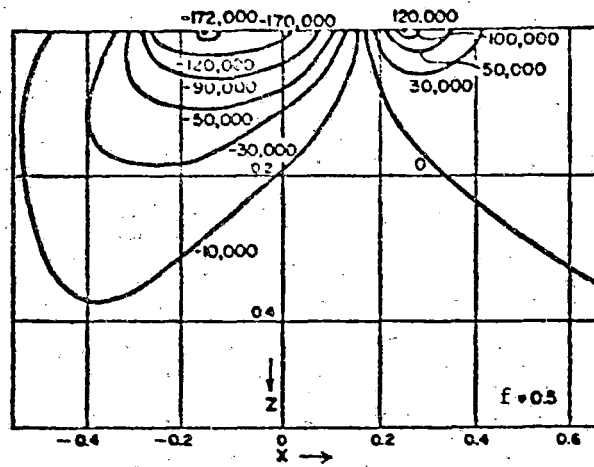
Stress ~ psi
 X, Y, Z ~ inch



(b) Longitudinal Shear Stress, τ_{zx}

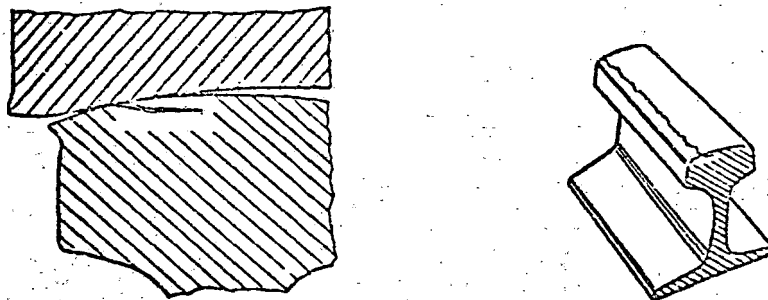
FIGURE 3-28. (CONTINUED)

Stress ~ psi
X, Y, Z ~ inch

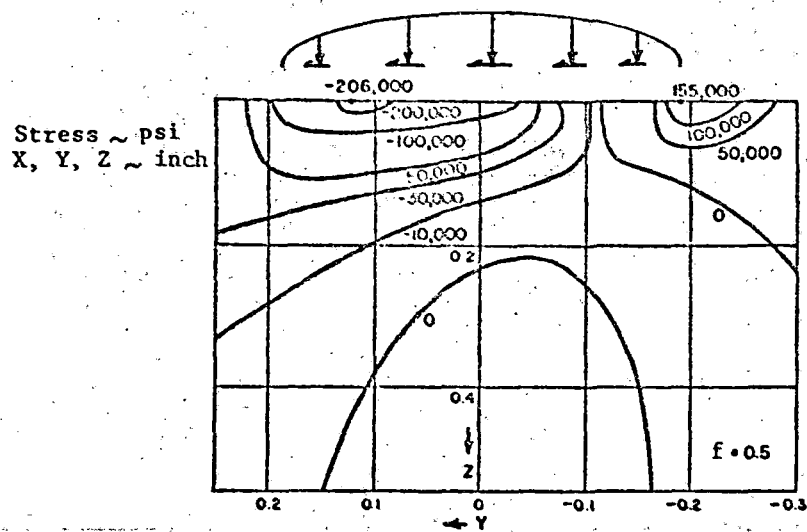


(c) Longitudinal Stress, σ_x

FIGURE 3-28. (CONTINUED)

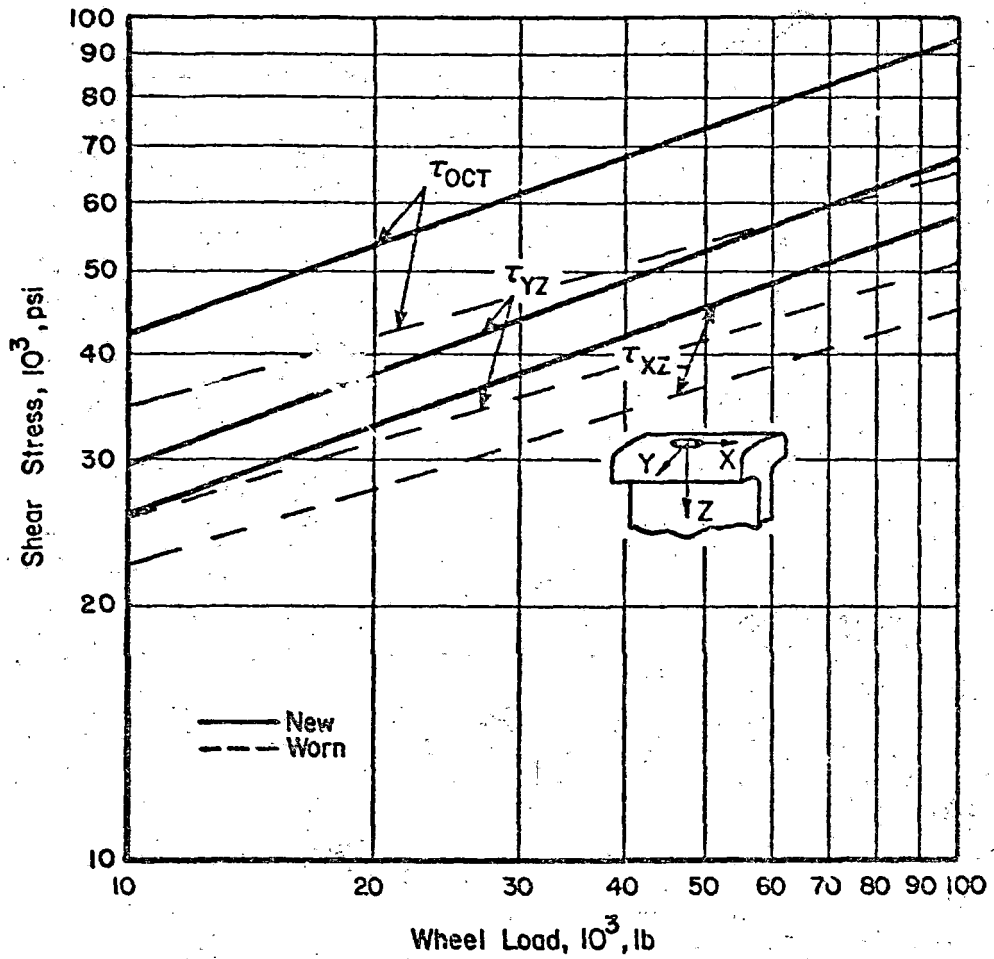


(a) Observed Edge Cracks in Rail Heads



(b) Transverse Stresses in the Rail Head (σ_y)

FIGURE 3-29. POSSIBLE RELATIONSHIP BETWEEN EDGE CRACKS IN RAILS AND TRANSVERSE STRESSES FROM LATERAL FRICTION LOAD



NEW 33-INCH DIAMETER WHEEL AND 132-LB RAIL, OR
WORN 33-INCH DIAMETER WHEEL AND 132-LB RAIL

FIGURE 3-30. EFFECTS OF WHEEL LOAD AND WEAR ON
SHEAR STRESS IN RAIL HEAD

4. SUBSURFACE STRESS DISTRIBUTION IN RAIL HEADS DUE TO PLASTIC DEFORMATION

New rails generally have residual stresses which are due to the manufacturing process. Since wheel loads in excess of approximately 19,000-lb result in plastic deformation of the rail head of new rails, the residual stress field begins to change immediately upon exposure to rail traffic. Gradually, a new residual stress field is developed having a zone of compressive stress directly beneath the tread surface. Below the compressive zone is a region of tensile stress. It is believed that the region of tensile stress is of profound importance in the development of several types of head cracking. Horizontal defects, for example, are known to initiate in that zone of residual tensile stress [4-1].

The development of residual stress due to rolling contact has been treated in the literature, though not widely. Of most significance to the study of residual stress are the papers of Johnson [4-2], Merwin and Johnson [4-3], Johnson and Jefferis [4-4], Martin and Hay [4-5], and the ORE C53 report [4-6].

4.1 PREVIOUS INVESTIGATIONS OF SUBSURFACE STRESSES DUE TO PLASTIC DEFORMATION

In order to have relatively simple circumstances for early analyses of residual stress, Johnson [4-2], and Merwin and Johnson [4-3] considered the two dimensional case of a rigid cylinder rolling on an elastic-plastic flat. (This case was understood also to apply closely to the rolling contact of two disks.) The plane deformation implicit for this case, plus presumed uniformity of stresses in the rolling direction (here the x-direction), implies that the only components of residual stress that can arise are

$$\sigma_x^r = f_1(z) \text{ and } \sigma_y^r = f_2(z) \quad , \quad (4-1)$$

where y measures lateral distance and z is depth below the tread. For this cylindrical contact case, the residual stress components σ_z , τ_{yz} , τ_{zx} and τ_{xy} do not appear.

Predictions of plastic flow, of course, depend on the yield criterion, for which Johnson considered three possible choices. Among these, one extreme is the Tresca criterion which predicts plastic flow if the maximum shear stress exceeds k , the yield stress of the material in simple shear. The other extreme was the maximum reduced stress criterion which predicts plastic flow if the maximum deviation of a principal normal stress from the mean of the principal normal stress exceeds $2k$. An intermediate criterion was that of von Mises, which predicts plastic flow if the second stress invariant J_2 exceeds k^2 , that is if

$$J_2 \equiv \frac{1}{6}[(\sigma_x - \sigma_y)^2 + (\sigma_y - \sigma_z)^2 + (\sigma_z - \sigma_x)^2] + \tau_{yz}^2 + \tau_{zx}^2 + \tau_{xy}^2 > k^2 \quad (4-2)$$

For the stress distributions arising with their form of cylindrical contact, Merwin and Johnson observed that, for increasing load, plastic flow would be initiated directly below the center line of contact at depths and contact pressures for the three criteria as follows:

<u>Yield criterion</u>	<u>Maximum contact pressure</u>	<u>Depth</u>
Maximum reduced stress	2.7 k	0.67 a
Von Mises	3.1 k	0.70 a
Tresca	3.3 k	0.78 a

Here a is the half width of contact in the rolling direction. It is of interest that for an elastic sphere contacting a plane, the prediction of maximum contact pressure for plastic flow initiation using the von Mises criterion is not greatly different, namely 3.0 k . Thus, there are differences in predictions of plastic flow according to the various criteria, but the predictions have much in common. The von Mises criterion is generally accepted as being applicable to steels, so it is the one which will be used most frequently here, but the use of the Tresca condition also will be examined.

If the contact load between two bodies is sufficient, plastic flow occurs in the interior of one or both of the contacting bodies producing residual

stresses which remain after the load has passed. If these residual stresses are properly related to the contact stresses, they reduce the tendency of the material to flow under the contact stresses during the next loading cycle, and eventually their countereffect may become large enough so that there is no further plastic yielding. Then shakedown is said to have occurred. In order to investigate circumstances in which shakedown should occur, Johnson and his colleagues employed Melan's theorem [4-7] which states first that if any residual stress can be found which, together with stress due to load, constitutes a system within the yield limit, then under repeated loading the system will shake down to some system of purely elastic deformation. Conversely (according to the theorem), if no such system of residual stress can be found, then the system will not shake down and continued plastic deformation will occur at each passage of the load. It should be noted that this theorem does not predict what the residual stresses will be, nor does its use ordinarily require knowledge of what they are; yet it offers much opportunity for deciding whether shakedown will or will not occur.

Applying the Tresca condition for yielding, Johnson [4-2] showed that along a line with fixed y and z , shakedown would occur if some σ_x^r could arise such that

$$\frac{1}{4} (\sigma_x^e + \sigma_x^r - \sigma_z^e)^2 + (\tau_{zx}^e)^2 < k^2, \quad (4-3)$$

where σ_x^e , σ_z^e and τ_{zx}^e are elastic components of contact stress that vary as functions of the variable x . It is clear that no value of σ_x^r could assure this relation if τ_{zx}^e exceeds k anywhere along the line. Therefore, considering the z and x where τ_{zx}^e is greatest (this being at $z = 0.500a$, $x = 0.867a$ for his case), Johnson suggested a σ_x^r to counterbalance $\sigma_x^e - \sigma_z^e$ there, and showed that an accompanying σ_y^r could be found so that the relation (4-3) would be met all along the line at that depth z . Thus, he showed that shakedown can occur (and by Melan's theorem will occur) if the maximum value of τ_{zx}^e does not exceed k . Since that value of τ_{zx}^e for Johnson's case is $0.250 p_0$, where p_0 is the maximum contact pressure, he thus showed that shakedown will occur if

$$p_0 < 4.0k. \quad (4-4)$$

His associated residual stresses for use with the Tresca criterion were $\sigma_x^r = -0.134 p_0$ and $\sigma_y^r = -0.040 p_0$. Alternatively, considering the von Mises criterion, Johnson found that shakedown would occur if $p_0 \leq 4.0 k$, but then he found it more advantageous to postulate the residual stresses $\sigma_x^r = -0.134 p_0$ and $\sigma_y^r = -0.213 p_0$. The variation of stresses along a line at depth $z = 0.50a$, as shown by Johnson, both with and without his postulated residuals for the von Mises criterion, are shown in Figure 4-1 [4-2].

Shakedown theory based on Melan's theorem does not of itself predict what residual stresses may actually arise, but Merwin and Johnson [4-3] undertook that task for their case of cylindrical contact. In order to do that, they assumed that the strain cycle during a cycle involving plastic flow remains identical with the strain cycle that fully elastic behavior would imply. Where stresses reached a level to produce plastic flow, they assumed the material to be perfectly plastic and applied the Prandtl-Reuss equations to calculate the increment of stress to apply to the next increment in the strain cycle. This procedure is inexact to the extent that the stresses do not satisfy the equilibrium equations during much of the calculation, but Merwin and Johnson undertook to restore equilibrium at the end of each cycle. They performed calculations for residual stresses presuming contact loads such that $p_0 = 4.0 k$ (the shakedown limit), or $p_0 = 4.8 k$, or $p_0 = 5.5 k$, with results as shown in Figure 4-2. They also showed experimental results for σ_x^r as a function of depth after one passage of the heaviest load which were in reasonably good agreement with the calculated curve. The computations for all these loads showed that, above the shakedown limit, a steady state condition was reached quickly in which additional shearing strain in the surface in the forward direction was incurred with each new cycle but without increase of residual stress. For higher loads, the steady state residual stresses became larger and penetrated more deeply into the body. Of course, the steady state stresses were dependent on the presumption of perfectly plastic flow, and they would have been postponed or eliminated by a presumption of a strain hardening material. It may also be noted that the residual stresses they computed were compressive rather than tensile, but this is conceivably dependent on the presumption of cylindrical contact so that sideward flow was denied.

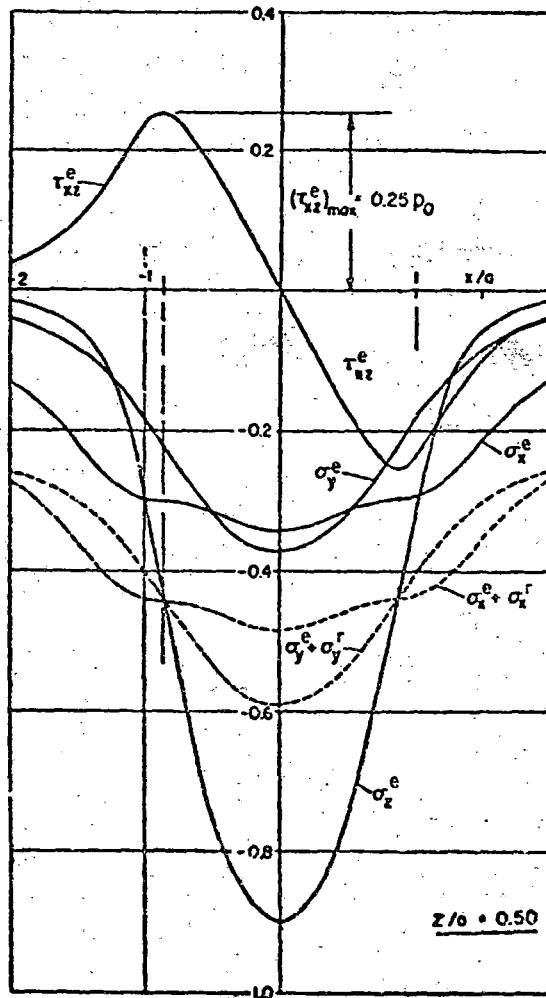


FIGURE 4-1. STRESS FIELD BENEATH A CYLINDER CONTACTING A PLANE, INCLUDING RESIDUAL STRESSES PROMOTING SHAKEDOWN [4-2]

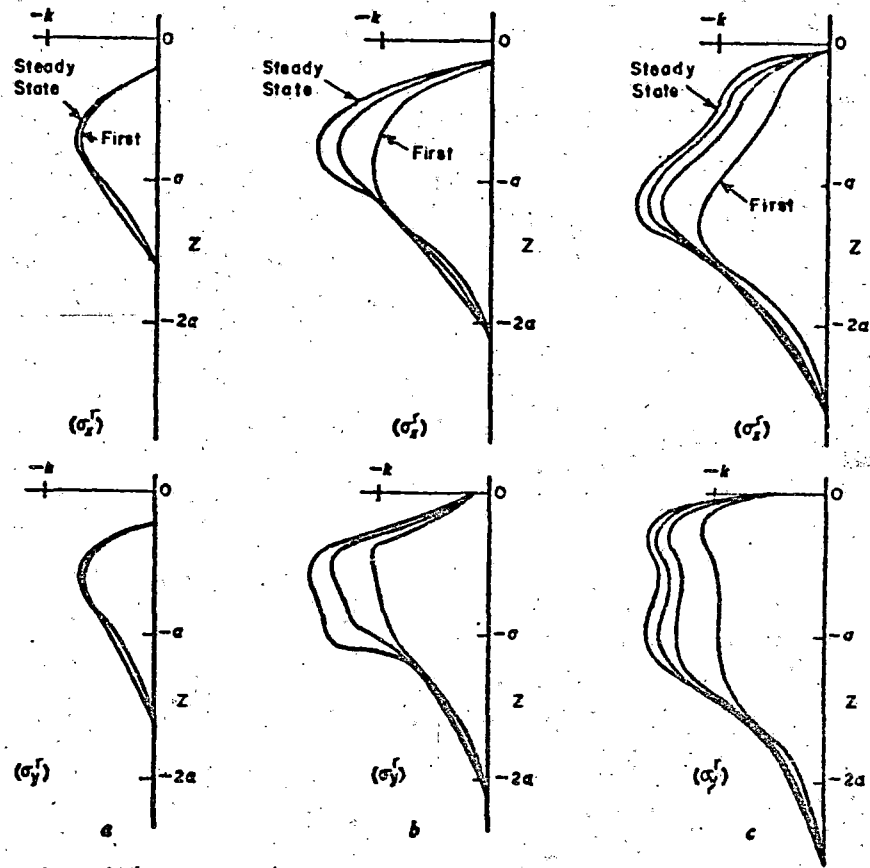


FIGURE 4-2. BUILDUP OF RESIDUAL STRESS (σ_x) AND (σ_y) WITH REPEATED PASSAGES OF THE LOAD DUE TO CYLINDRICAL CONTACT [4-3]

In a further paper, Johnson and Jefferis [4-4] considered how the inclusion of a tangential load T as well as a normal load P (such as from friction during contact) would alter the shakedown limit during cylindrical contact. The tangential load, of course, changes τ_{zx} , increasing it in one direction, decreasing it in the other. Under full slip, i.e., T and P vary proportionately, they found shakedown limits as shown in Table 4-1. Their underlying theory presumed either Tresca or von Mises yield criteria.

TABLE 4-1. EFFECT OF FULL-SLIP SURFACE TRACTIONS ON SHAKEDOWN LOAD

T/P	Shakedown Load, p_0/k
0.000	4.00
0.100	3.56
0.200	3.21
0.300	2.90
0.364	2.75

Johnson and Jefferis also considered shakedown for three-dimensional contact stresses, like for a ball bearing. Their discussion was largely qualitative, considering what factors would apply to the three-dimensional problem. They specifically emphasized the importance of the shear stress component τ_{zx}^e which is not countered by residual stress, and for a sphere rolling on a plane, they suggested an appropriate shakedown limit with $p_0 = 4.8 k$.

Martin and Hay [4-5] applied the stress calculation approach of Johnson to the problem of wheel/rail contact. In order to determine the three-dimensional residual stresses, they used an indirect finite element method to a model of a 132-lb RE rail head, computing the stress histories during one or more cycles in which plastic flow would occur. They divided load cycles into increments, assuming for each increment that the strains change according to

elasticity theory. Then they applied Prandtl-Reuss equations to determine plastic flow if the corresponding incremented stresses were large enough to cause yielding. They apparently tolerated lack of equilibrium during the plastic flow but restored equilibrium by the end of each cycle. The strain cycle they applied at a particular subsurface Node A, directly below the center of an eccentric contact, is shown in Figure 4-3, together with the buildup of stresses during passage of a normal load. They were particularly concerned with the process of rail shelling, so the residual stress σ_z^r was of most interest to them. The distributions of σ_z^r which they had accumulated after one and after six passages of the load are shown in figure 4-4. The single load had passed over Point 9, while the repeated loads had passed over Points 9, 8, 7, 9, 8, 7. These results show tensile stresses σ_z^r inside the rail head, and they show it broadening because of variation in point of load application, so they offer a beginning of an explanation of rail head shelling.

4.2 RECENT INVESTIGATIONS OF RESIDUAL STRESSES IN RAIL HEADS

4.2.1 An Approximate Theory for Three-Dimensional Shakedown

In order to gain further insight into the possibility of shakedown for three-dimensional stresses arising from the ellipsoidal loads characteristic of wheel/rail contact, a brief study was made of those stresses using Melan's theorem, as described in Appendix C. The treatment there is only approximate, in that it employs somewhat idealized approximations of stress components along the longitudinal direction in the rail head. It also presumes a relation between contact stresses and residual stresses unlike any presumed by Johnson, Merwin or Jefferis, but the novelty here is acceptable because postulated stresses of arbitrary forms are admissible for use with Melan's theorem. Thus, it is presumed that the four possible residual stresses, σ_x^r , σ_y^r , σ_z^r and τ_{yz}^r , are respectively proportional to the maxima of the corresponding elastic components along the same longitudinal line in the rail head. Using a von Mises yield criterion, it follows from these presumptions that shakedown will occur if and only if

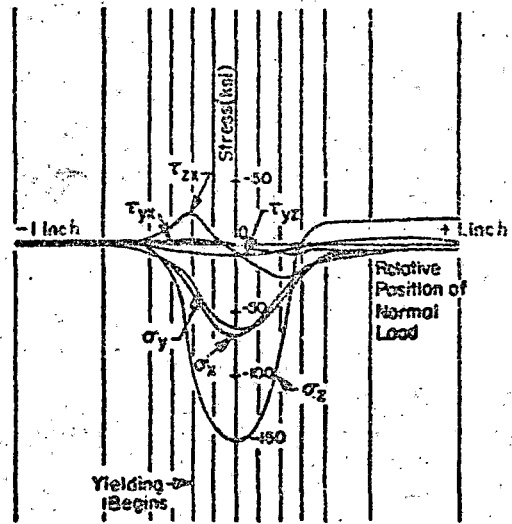
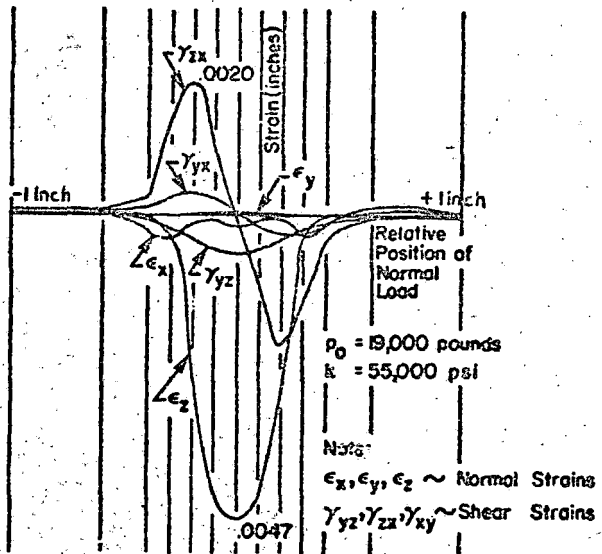
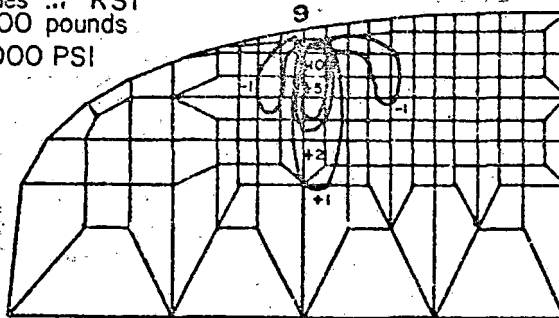


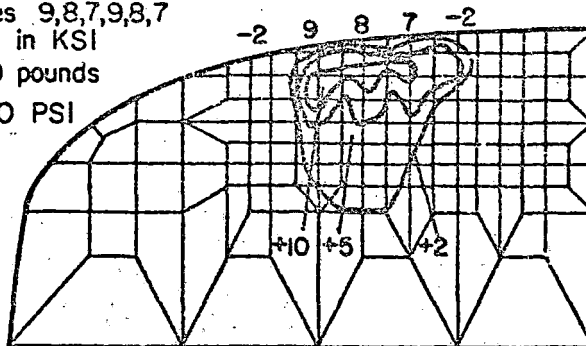
FIGURE 4-3. STRAIN AND STRESS CYCLES AT A SUBSURFACE AS USED IN COMPUTING RESIDUAL STRESSES [4-5]

Normal load passes over Node 9
 All values in KSI
 $p_0 = 19,000$ pounds
 $k = 55,000$ PSI



Vertical Stress σ_z , psi

For a normal load passing
 over Nodes 9,8,7,9,8,7
 All values in KSI
 $p_0 = 19,000$ pounds
 $k = 55,000$ PSI



Vertical Stress σ_z , ksi

FIGURE 4-4. CALCULATED VERTICAL RESIDUAL STRESS AFTER ONE AND AFTER SIX LOAD CYCLES [4-5]

$$[(\tau_{zx}^e)^2 + (\tau_{xy}^e)^2]_{\max} < k^2, \text{ and}$$

(4-5)

$$\frac{1}{6}[(\sigma_x^e - \sigma_y^e)^2 + (\sigma_y^e - \sigma_z^e)^2 + (\sigma_z^e - \sigma_x^e)^2 + 6(\tau_{yz}^e)^2]_{x=0} < 4k^2,$$

where $x = 0$ is a center plane of contact. The second of these conditions seems generally less demanding. Also, $\tau_{xy}^e = 0$ on the longitudinal center plane where $y = 0$, so that on that plane, where shakedown seems most difficult, the criterion for shakedown again becomes $|\tau_{zx_{\max}}^e| < k$, as Johnson proposed. It is interesting to note that the residual stresses chosen as optimum among the class of stresses postulated here are $-1/2$ times the maxima of the corresponding elastic components. Since the largest normal stresses of contact are compressive, this means that tensile stresses may reasonably be postulated for the residual of the normal stress components. This agrees with the expectation that tensile longitudinal and lateral residual stresses from three-dimensional contact stresses may arise, even though Johnson chose compressive stresses for the corresponding residuals in his shakedown theory for cylindrical contact.

4.2.2 Remarks on Calculation of Residual Stresses

An attempt was made to compute residual stresses that should be expected from the three-dimensional stresses due to wheel/rail contact. The undertaking was to eliminate the questionable presumption used by Johnson et al., and to some extent by Martin and Hay, that the strains are equal to those computed from elastic contact theory. The need for doing this was found by using a finite element program and calculating the longitudinal and vertical strains that would arise in two-dimensional cases (such as with cylindrical contact) presuming alternatively that the body is either a) elastic, b) elastic - perfectly plastic, or c) elastic - plastic - strain hardening. A stress-strain curve for rail steel is shown in Figure 4-5. It was found from a longitudinally oriented specimen from used rail investigated in the DOT-TSC-1076 program. This material can be modeled as being elastic-perfectly

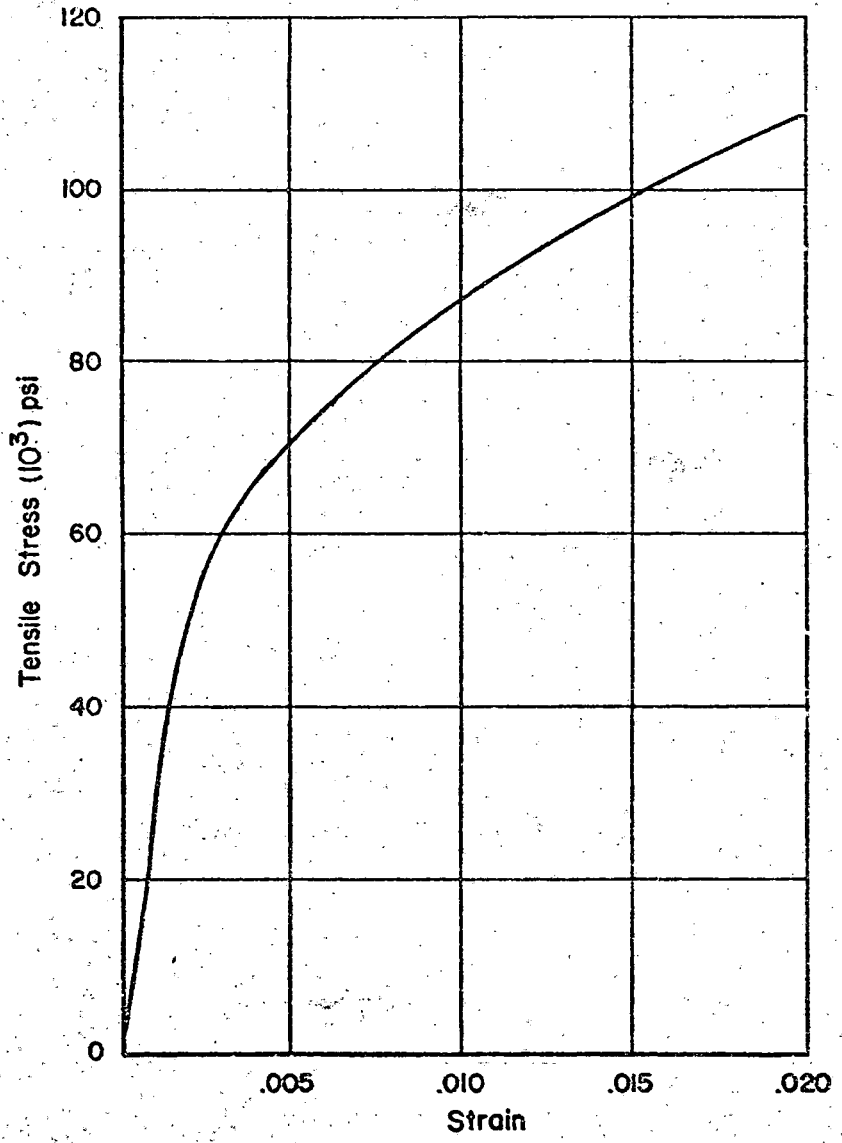


FIGURE 4-5. TENSILE STRESS-STRAIN CURVE FOR LONGITUDINAL RAIL-HEAD SPECIMEN

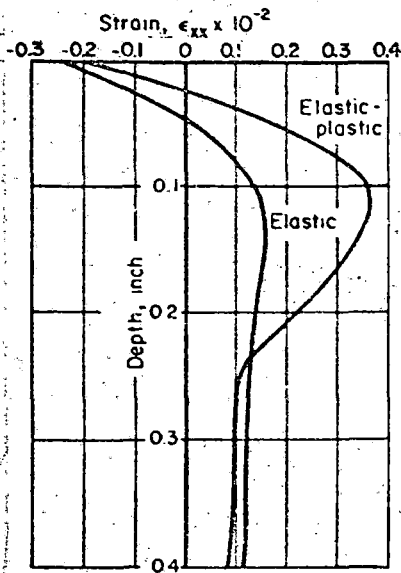
plastic with a tensile yield stress of 95,000 psi, or a yield stress in pure shear of 55,000 psi as Martin presumed in his calculations [4-5].

Taking the yield stress in simple shear for the elastic-perfectly plastic material to be $k = 55,000$ psi, three cases of Hertzian contact loading were considered, with the maximum contact pressure p_0 being 4.0 k, 4.8 k, or 5.5 k (that is 220,000 psi, 264,000 psi, or 302,000 psi). These cases correspond to those in Figure 4-2, with the first representing shakedown. The calculated stresses at varying depths below the center of contact from this two-dimensional analysis are shown in Figures 4-6 and 4-7. In all cases, there are significant differences between strains calculated for the elastic and elastic-plastic materials respectively. The difference is more severe when the actual stress-strain characteristics are used (that is when work hardening is presumed). Thus, the presumption of a strain state that is linearly scaled with respect to an elastic solution looks untrustworthy for calculation of either two- or three-dimensional residual stresses unless, perhaps, there is little plastic flow.

Computations of three-dimensional residual stresses were performed using methods similar to those of Martin and Hay, but alternatively using either an elastic strain cycle as they had or an elastic-plastic strain cycle. Unfortunately, the use of the elastic-plastic strain cycle gave residual stresses which fluctuated greatly near the tread surface, so that they were even less plausible than those obtained using the elastic strain, which themselves seemed somewhat problematic. The source of the trouble was not identified, but it seemed clear that calculations of residual stresses involve many difficulties. One difficulty that should be expected, for example, in calculations employing finite elements is that finite element calculations with contact loads applied at a few nodal points tend to distort the conditions near the load area where some of the most important plastic flow would occur. This kind of distortion could have affected calculations made by other investigators also.

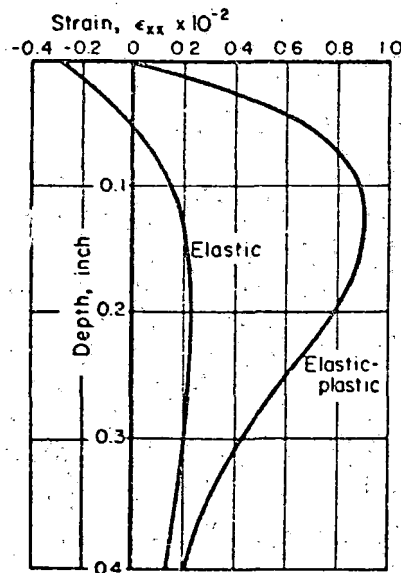
An outline of the method that was used is furnished in Appendix D, but its value is now uncertain.

The general conclusion drawn from this experience is that, for the present, it is preferable to determine residual stresses by measuring them. This



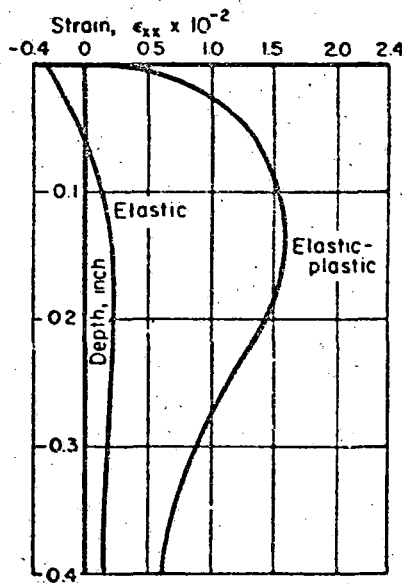
$p_0 = 220,000$ psi

Elastic Versus Elastic /Perfectly Plastic



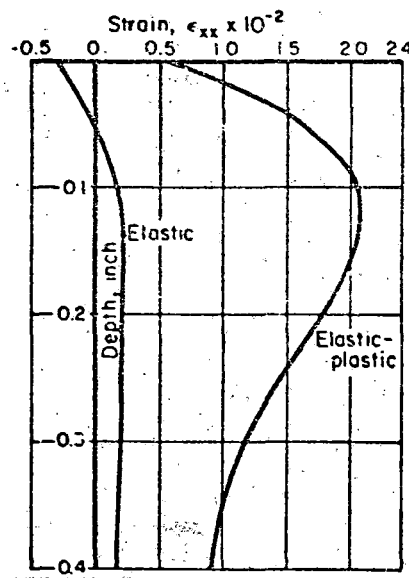
$p_0 = 264,000$ psi

Elastic Versus Elastic /Perfectly Plastic



$p_0 = 302,000$ psi

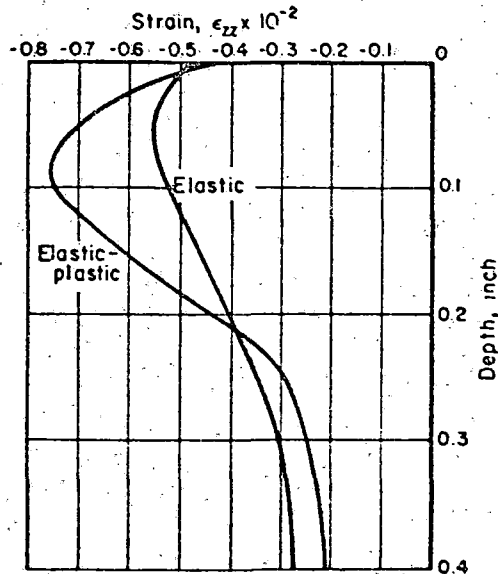
Elastic Versus Elastic /Perfectly Plastic



$p_0 = 300,000$ psi

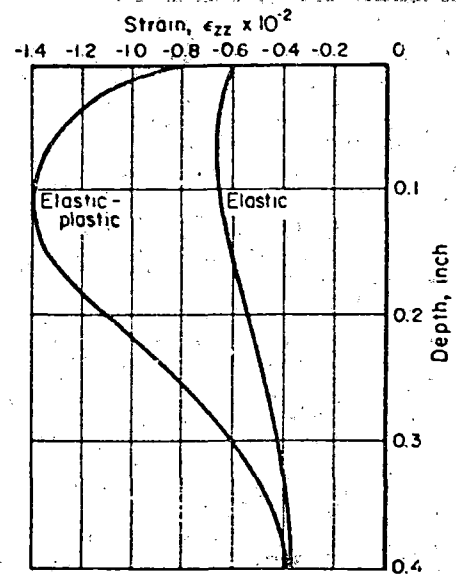
Elastic Versus Actual Stress-Strain

FIGURE 4-6. LONGITUDINAL STRAINS DUE TO CYLINDRICAL CONTACT IN ELASTIC AND ELASTIC/PLASTIC BODIES



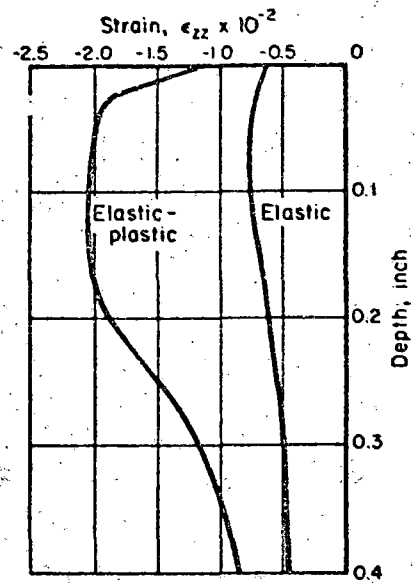
$p_0 = 220,000$ psi

Elastic Versus Elastic / Perfectly Plastic



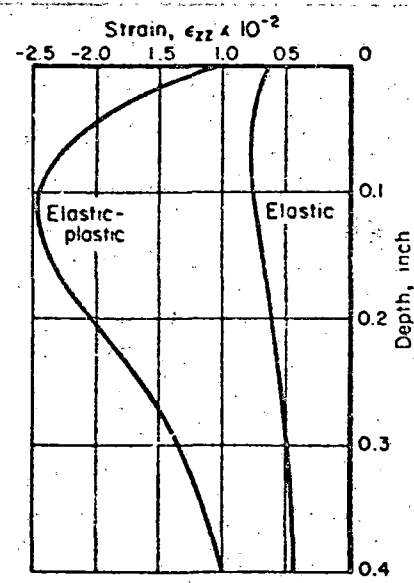
$p_0 = 264,000$ psi

Elastic Versus Elastic / Perfectly Plastic



$p_0 = 302,000$ psi

Elastic Versus Elastic / Perfectly Plastic



$p_0 = 302,000$ psi

Elastic Versus Actual Stress-Strain

FIGURE 4-7. VERTICAL STRAINS DUE TO CYLINDRICAL CONTACT, IN ELASTIC AND ELASTIC/PLASTIC BODIES

is especially true when one considers the great variety of loading situations imposed on a rail in service.

4.2.3 Laboratory Measurements of Residual Stresses

In order to get measurements of some residual stresses under controlled conditions, and also to have measurements which might be compared to residual stress calculations such as those of Martin and Hay [4-5], some laboratory experiments were performed as described in Appendix E. The head region of a 132-lb RE rail was simulated by trimming 175-lb crane rails. The latter specimens were mounted firmly to minimize rail bending stresses, and then were subjected to one or three passages of a 14,500-lb wheel load. Strain gages were then affixed and the specimens were sectioned in such ways that residual strains produced by the rolling could be deduced as a result of relaxation caused by the sectioning. Redundant cases indicated that the calculated stress, at least for the one-pass specimen, were measured to within errors having standard deviations of the order of 800 to 1,400 psi. The results obtained for residual stress σ_x^r , σ_y^r , σ_z^r (that is longitudinal, lateral, and vertical) at various depths along a vertical line through the center top of the rail are shown in Figures 4-8, 4-9 and 4-10. (Compare Tables E-5 and E-3.)

These residual stresses deduced from measured strains show the largest value to be that for σ_x^r at depth 0.070 in. The σ_y^r is also large at that depth. These large stresses are compressive, so they should contribute little to possible crack growth. Tensile stresses shown here are small and lie at a depth of about 0.50 in. It may be noticed, however, that all three components at that depth increase with the increasing number of passes. This suggests that with many passes of the load, substantial tensile stresses might develop at that general depth. Comparison of the stresses in Figure 4-10 with those calculated by Martin and Hay (see Figure 4-4) shows some similarity, but their stresses are generally higher. Some of this discrepancy might be attributable to the lower load amplitude in the laboratory test.

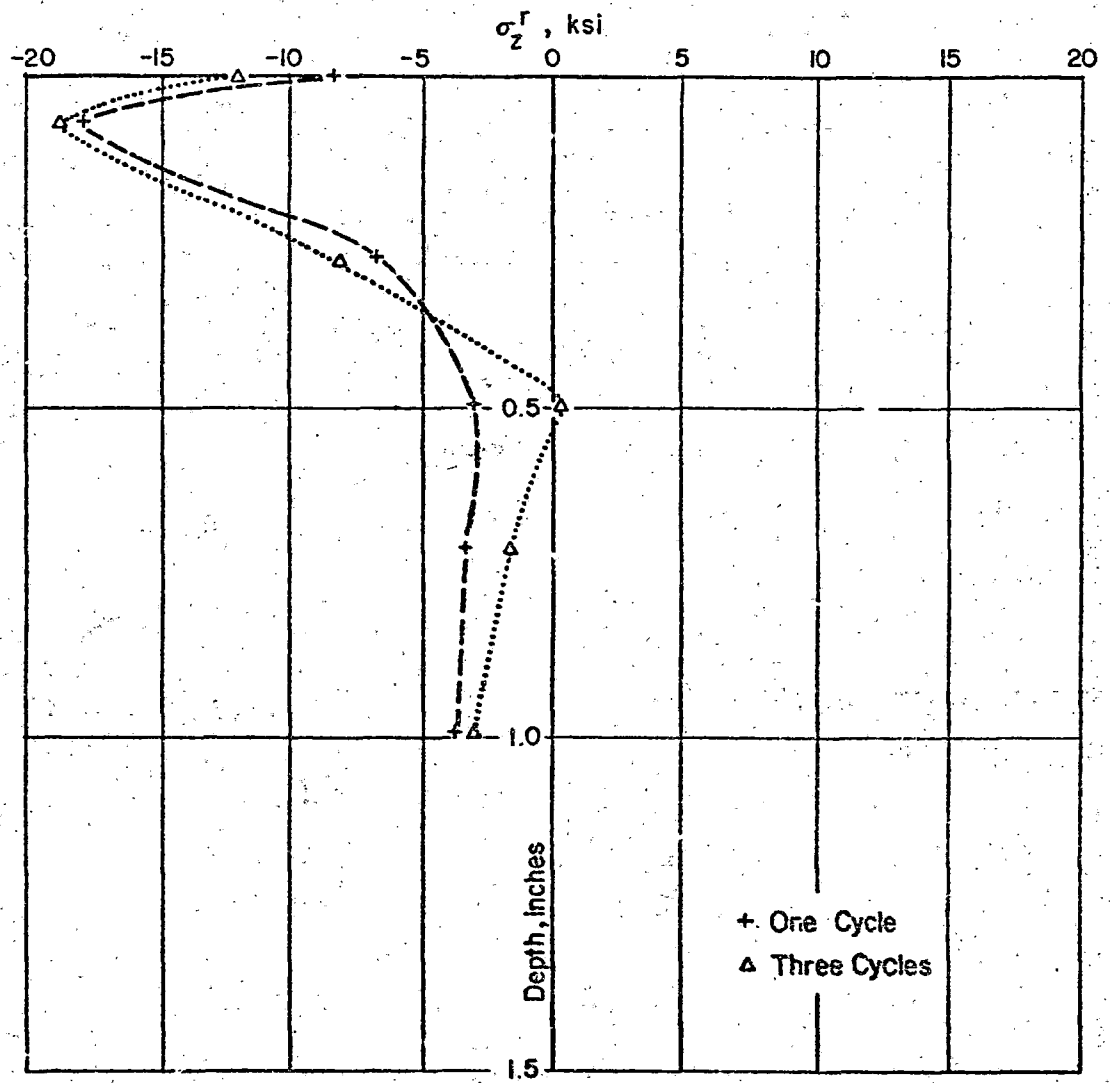


FIGURE 4-8. LONGITUDINAL RESIDUAL STRESSES MEASURED AFTER ONE AND THREE LOAD CYCLES RESPECTIVELY

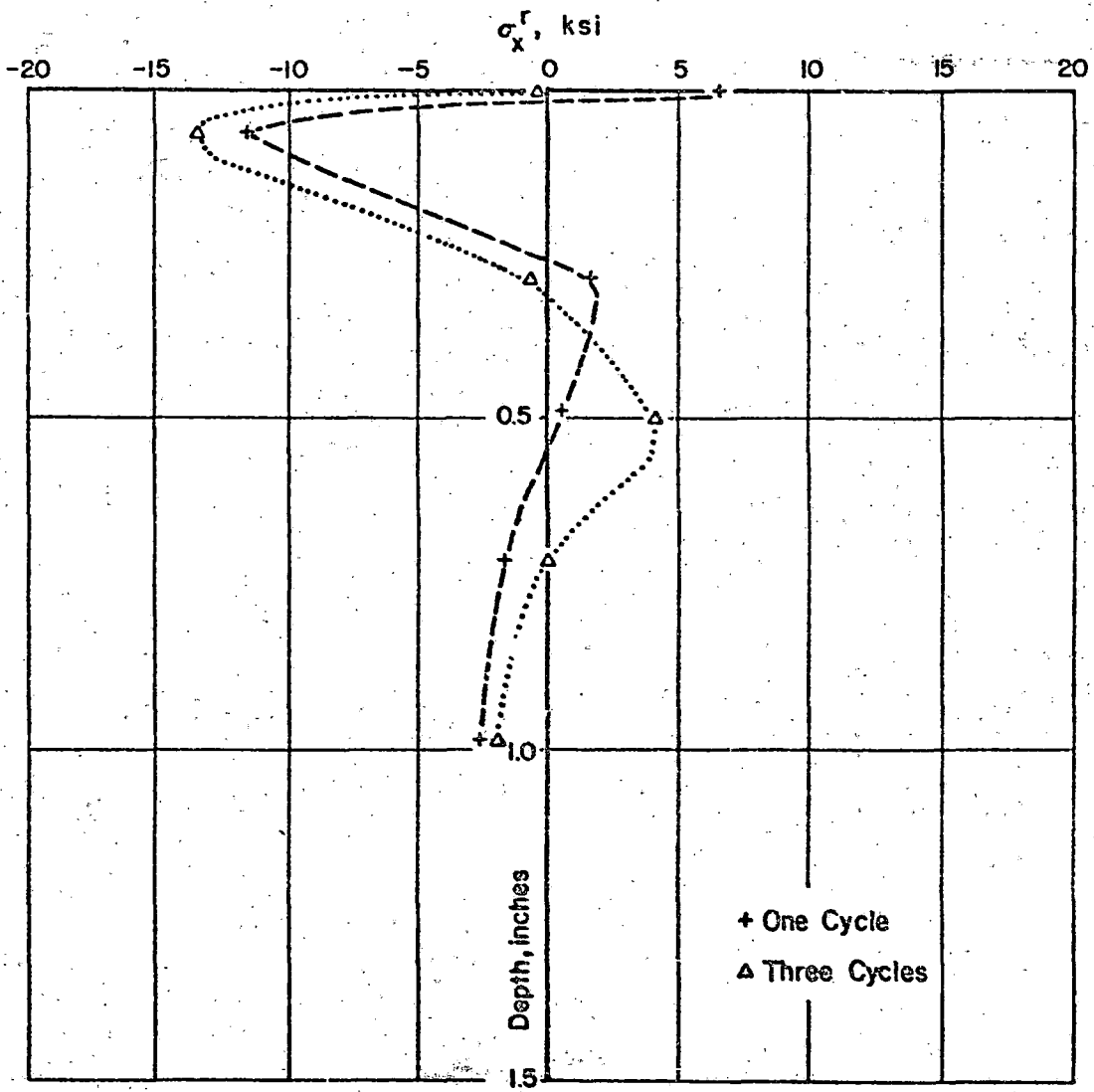


FIGURE 4-9. TRANSVERSE RESIDUAL STRESSES MEASURED AFTER ONE AND THREE LOAD CYCLES RESPECTIVELY

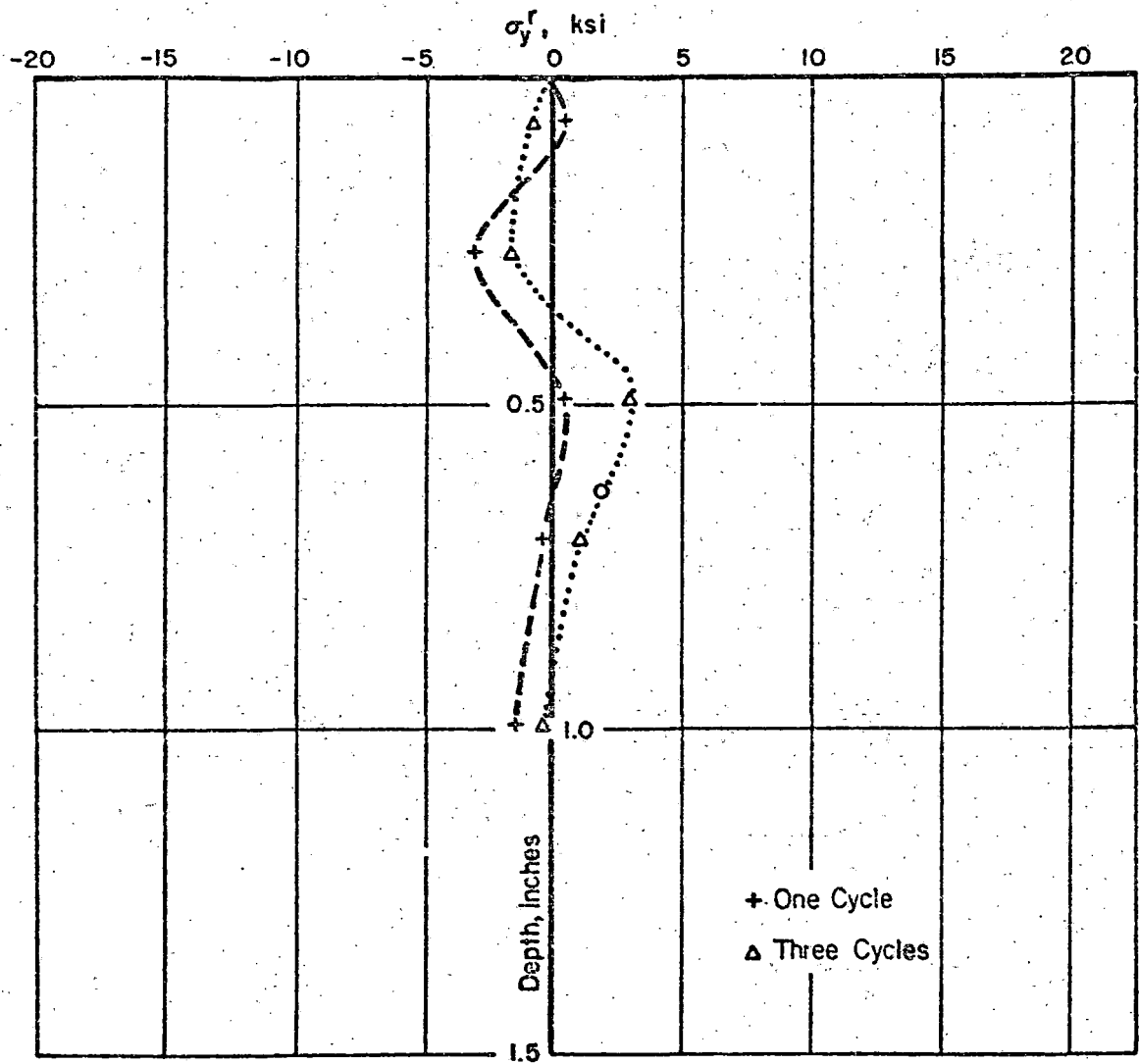


FIGURE 4-10. VERTICAL RESIDUAL STRESSES MEASURED AFTER ONE AND THREE LOAD CYCLES RESPECTIVELY

4.2.4 Residual Stresses of Rails in Service

Measurements of residual stresses in rails that have been in service for significant lengths of time are not abundant, but a few such data have been presented recently by Groom [1-19], some of which are shown in Figure 1-4. The rail involved in that figure was a 132-lb RE rail which had been used in tangent track subjected to about 300 million gross tons of general traffic with average speed 40 mph and maximum 55 mph. During the sectioning procedure, the rail head was instrumented with biaxial strain gages at 45 positions so that a fairly comprehensive view of the residual stresses could be inferred.

Figure 1-4 shows only one component of the residual stresses directly, namely σ_x^r , but the referenced report provides enough data so that other components can be deduced. Thus, for this rail head, it has been deduced that the four coordinate components of stress not expected to vanish vary as shown in Figure 4-11. These results relate, of course, to a single rail head, but they represent real conditions, and the uncertainties which affect them are only those involved in reasonably familiar experimental procedures, not those involved in use of the questionable assumptions affecting existing analytical results. Thus, these results probably are at least among the most realistic values now available for residual stresses in rail heads.

Several features of the residual stresses shown in Figure 4-11 deserve comment. Many of the normal stresses are compressive in nature which might influence further plastic flow. The largest value shown here -53,000 psi for σ_y^r , at a point where the greatest principal stress was -59,800 psi, and on the tread surface σ_y^r reaches about -41,000 psi, but these compressive values may not be the values of most interest. If tensile values are fairly large, they are more interesting since they promote crack growth.

The largest tensile stresses among the normal stresses is a value 37,500 psi for σ_y^r at a point where the greatest principal stress reaches 41,300 psi. Also, there is a fairly large interior region where σ_y^r exceeds 30,000 psi. This component of stress would contribute to crack growth in vertical planes in the longitudinal direction. The high tensile value of σ_x^r is

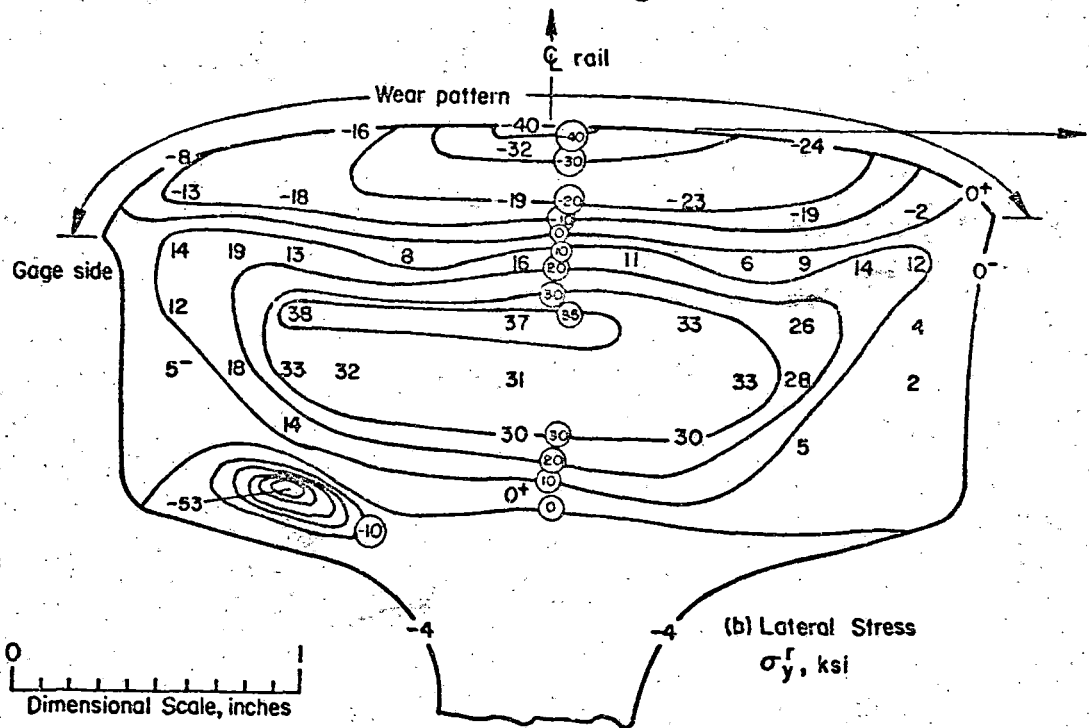
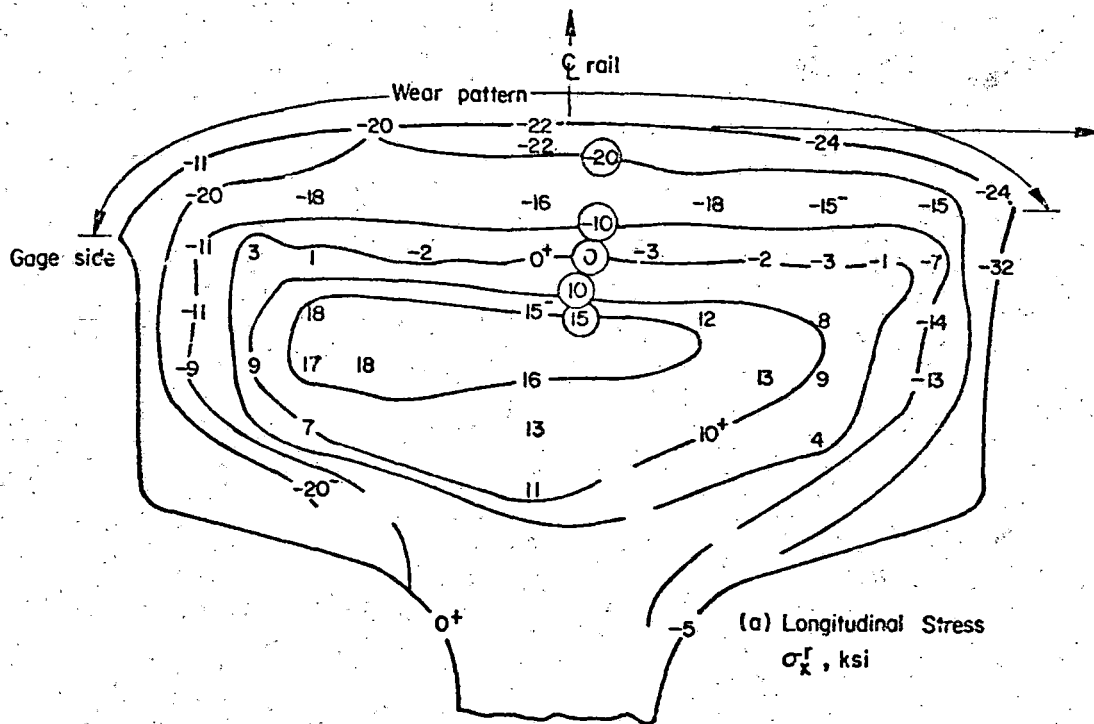


FIGURE 4-11. RESIDUAL STRESSES MEASURED IN RAIL FROM SERVICE

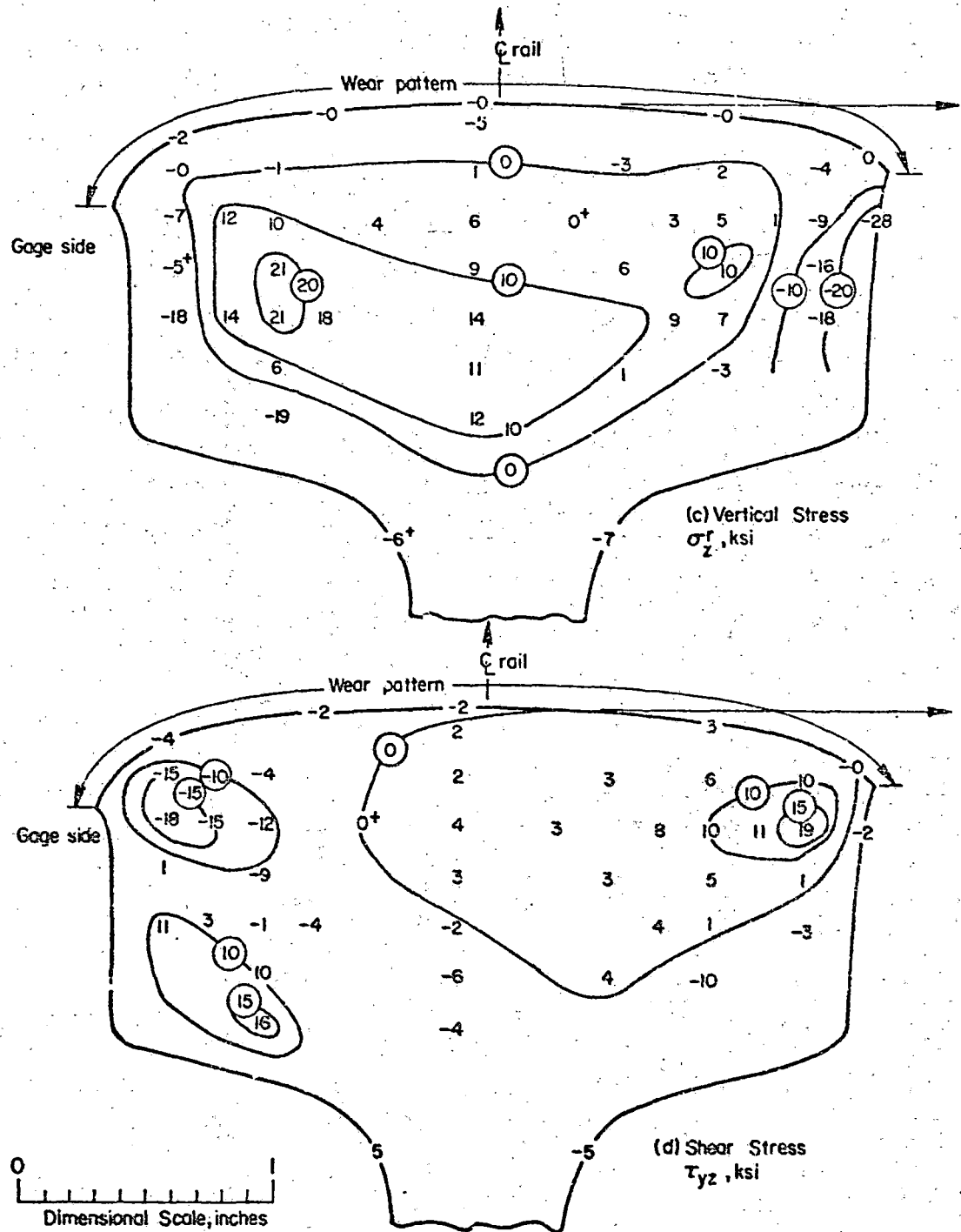


FIGURE 4-11. (CONTINUED)

18,400 psi, and there is a significant region where σ_x^r exceeds 15,000 psi. That stress component may contribute to crack growth in vertical planes in the transverse direction. There is a small, eccentric region where σ_z^r exceeds 20,000 psi, reaching a maximum of 21,200 psi at the same point where the greatest principal stress reaches 41,300 psi. This stress might promote crack growth in the horizontal plane, though the span for this action seems narrow. Thus, cracking in planes parallel to the coordinate direction finds its most encouragement here for vertical, longitudinal planes, but other orientations might also be susceptible for cracking.

The prospect for shelling of the rail, as considered by Martin and Hay [4-5] appears relatively less important here than it seemed to Martin and Hay. An explanation for this may be found in the lateral scattering of the centers of contact among wheels passing over the rail. As shown in Figure 4-4, they began to consider this effect but did not pursue it to the lengths which actual rail traffic would justify. The breadth of the lateral scattering is also implicit in the pattern shown in Figure 4-11 for τ_{yz}^r , since τ_{yz}^r for a single passing load should be nearly antisymmetric around a vertical longitudinal plane through the center of contact, but that antisymmetry is evidently blurred over a broad central zone. Pursuing the concept of this antisymmetry, the pattern for τ_{yz}^r also seems to imply that the average position for the center of contact was well toward the gage side of the rail.

These patterns of residual stresses do not reveal all the possibilities for distributions of residual stresses, nor all possible effects they might have on rail fracture, but they do provide a reasonable start toward understanding these matters.

5. STRESSES AROUND RAIL-HEAD CRACKS

The previous sections have been concerned with descriptions of stresses in rails resulting from various wheel-rail loading conditions. These descriptions help in developing an understanding of the mechanics of the rail, but, without a failure criterion, limit loads or design lives still cannot be calculated. Only qualitative design modifications can be inferred.

One approach to determining the design life of a rail is to assume that damage proceeds in two stages characterized by (1) the time to nucleate a crack and (2) the period necessary to propagate the crack to a critical size after which complete fracture and separation occurs. For estimation of the time necessary to initiate flaws, the main requirements beyond what has been developed in earlier sections are a failure criterion and a method for calculating the accumulation of material damage due to load environment.

In this section methods for describing stresses around railhead cracks of types depicted in Figure i-1 will be illustrated. These stress distributions control the propagation stage of rail damage. The flaws will be assumed as totally embedded elliptical cracks, which is probably typical for many flaws in early stages of their development. Coupling these stress descriptions with loading histories and recognized formulas for computing the number of cycles for each increment of crack length would be useful in predicting failure times, since a significant part of the design life may be spent in propagating a flaw to failure.

5.1 SOME FUNDAMENTALS OF FRACTURE MECHANICS

Fracture mechanics methodology was developed in order to predict the life expectancy of flawed structures subjected to cyclic loads. It provides a means by which prediction, on a statistical basis, can be made for growth of a flaw propagating from a small defect. For this purpose, the application of fracture mechanics to rail failure problems requires the following input information:

- 1) the spectrum of loads applied by the passing wheels and thermal actions,
- 2) the local stress fields resulting from the load environment,
- 3) the mechanical and fracture properties (yield strength, tensile strength, fracture toughness, etc.) of the rail steel in which the stress field occurs.

With this information, fracture mechanics can be used to address specific questions [5-1] such as:

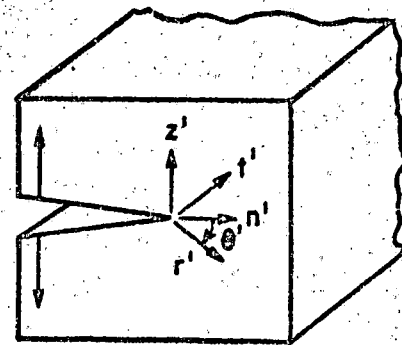
- 1) What is the residual strength as a function of crack size?
- 2) What size of crack can be tolerated at the expected service load, i.e., what is the critical crack size?
- 3) How long does it take for a crack to grow from a certain initial size to the critical crack size?
- 4) What size of pre-existing flaw can be permitted at the moment the structure starts its service life?
- 5) How often should the structure be inspected for cracks?

A detailed exposition of the principles of fracture mechanics can be found in Reference 5-1.

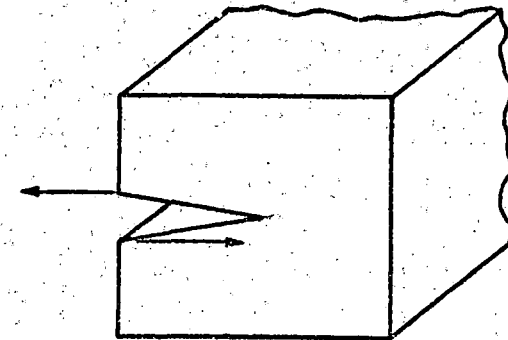
The growth of a crack in a body subjected to a general loading may be viewed in terms of the three modes [5-1] illustrated in Figure 5-1. Stresses acting perpendicular to the crack face are responsible for the opening, or Mode I, behavior. Shear loads may cause sliding, (Mode II) or tearing (Mode III action). Mode I action is usually the most important, but general crack growth is attributable to the combined actions of all three modes. It may be added that in the presence of a crack, the stress fields around it can usually be calculated by only applying on the crack face the negatives of the stresses calculated on the basis that the crack is absent. Thus the crack loads are effectively loads contributed by the presence of the crack.

With the presumption that the stresses on the crack face are known, stress analysis can be used to determine stress patterns in the vicinity of

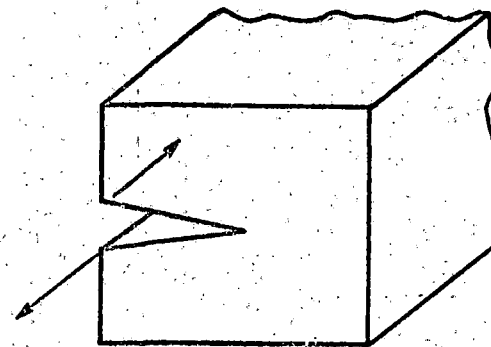
5-3



Crack Opening Mode (K_I)



Crack Shear Mode (K_{II})



Crack Tearing Mode (K_{III})

FIGURE 5-1. THREE MODES OF CRACK PROPAGATION

the crack. If the body is presumed to be linearly elastic, then the stress components become infinite at the crack front, varying in proportion to $1/\sqrt{r'}$ where r' is distance from the crack front. In view of this, using local coordinates n' , t' , z' as illustrated in Figure 5-1, the stress intensity factors mentioned in Chapter I, corresponding to the three modes depicted in Figure 5-1 are defined as follows:

$$\begin{aligned} K_I &= \lim_{n' \rightarrow 0} \sqrt{2\pi n'} [\sigma_{n'n'}]_{z'=0} , \\ K_{II} &= \lim_{n' \rightarrow 0} \sqrt{2\pi n'} [\tau_{z'n'}]_{z'=0} , \\ K_{III} &= \lim_{n' \rightarrow 0} \sqrt{2\pi n'} [\tau_{n't'}]_{z'=0} . \end{aligned} \quad (5-1)$$

These quantities are concise and may be shown to imply much useful information about stress fields near the crack front and about tendencies for crack growth, even though they are based on the somewhat generous assumption that the stresses everywhere are within the elastic range.

As an example of stresses near a crack front, consider a crack of length $2a$ in an infinite body under plane strain subjected to the action of a remote uniform tensile stress σ_0 normal to the crack plane. Taking r' to be distance from one of the crack tips and θ' to be angular offset from crack plane (as in Figure 5-1), it can be shown [5-1] that in the vicinity of the crack tip the stresses are:

$$\begin{aligned} \sigma_{n'n'} &= \sigma_0 \sqrt{\frac{a}{2r'}} \cos \frac{\theta'}{2} \left(1 - \sin \frac{\theta'}{2} \sin \frac{3\theta'}{2}\right) , \\ \sigma_{t't'} &= 2\nu\sigma_0 \sqrt{\frac{a}{2r'}} \cos \frac{\theta'}{2} , \\ \sigma_{z'z'} &= \sigma_0 \sqrt{\frac{a}{2r'}} \cos \frac{\theta'}{2} \left(1 + \sin \frac{\theta'}{2} \sin \frac{3\theta'}{2}\right) , \\ \tau_{z'n'} &= \sigma_0 \sqrt{\frac{a}{2r'}} \sin \frac{\theta'}{2} \cos \frac{\theta'}{2} \cos \frac{3\theta'}{2} , \\ \tau_{n't'} &= \tau_{t'z'} = 0 . \end{aligned} \quad (5-2)$$

These equations show only the first terms of respective series expansions, so they are valid only in a limited region around the crack front [5-1]. It may be seen that these equations have the generalized form

$$\sigma_{ij} = \frac{K_I}{\sqrt{2\pi r'}} f_{ij}(\theta') \quad (5-3)$$

where

$$K_I = \sigma_o \sqrt{\pi a} \quad (5-4)$$

Thus K_I here provides a description for stresses near the crack front. Similar equations may also be derived for stresses arising from shearing stresses applied far from the crack, using K_{II} or K_{III} instead of K_I . Alternate relations could be derived relating K_I , K_{II} and K_{III} to stresses near the crack front without presuming plane strain conditions.

The quantities K_I , K_{II} and K_{III} , are measures of the strength of the stress field at the crack tip. There exist values of these factors below which crack extension during cyclic loading will most likely not occur; these are called threshold values. There also exist critical values of these factors above which fracture will probably occur due to a single load application; these values, denoted by K_{Ic} , K_{IIc} and K_{IIIc} , are material parameters.

An alternative approach to describing effects of elastic stress fields in a crack region, is based on energy concepts. The idea, known as the Griffith criterion, states that crack extension will occur only if the strain energy in the body that would be released if crack extension occurred, is equal to energy or work done on the body during the crack extension. The equivalence of the Griffith criterion and the concept of stress intensity factors can be shown. The criterion is valid as long as the plastic zone around the crack front is small in comparison with the crack size. Several other criteria have been formulated to predict crack extension in high toughness materials also, where plastic deformations may be more extensive, but, in general, their applicability is more limited.

As was mentioned previously, for the stress intensity factors to be meaningful in predicting design life of a structure, it must be considered in relation to the material's mechanical and fracture properties. For non-cyclic

load application, the equality of the stress intensity factor and the fracture toughness of the material is often used as the failure criterion. For cyclic load application, the amplitude of the variation in the stress intensity factor corresponding to each load cycle will give rise to a specific cyclic crack growth rate. The relationship between the crack growth rate (often written as da/dn , n being the number of load cycles) and the stress intensity factor is determined by laboratory observations of crack extension in small specimens subjected to cyclic loadings. Very often the relationship between da/dn , K and the incremental ΔK depends on a variety of factors and is represented by an empirical or semiempirical equation. A large number of these relationships have been developed. Some of the more effective ones are described in Reference 5-2. Data of this type have been obtained for rail steels as a part of the DOT-TSC-1076 research program.

5.2 ANALYSES OF STRESSES AROUND CRACKS IN RAIL HEADS

5.2.1 Methods of Crack Stress Analysis

Analyses of stresses around cracks in rail heads can be performed in more than one way. In recognition of the specialized shape of a rail and of the various kinds of stress systems which may act on it, it may seem that finite element crack analyses might be most appropriate. Therefore, some effort was put into obtaining finite element solutions for stresses around railhead cracks. It was found, however, that such calculations were quite expensive because of lengthy assembly and computing times associated with finite element models having the necessary mesh refinements. Efforts were made to improve the accuracy of the stress intensity solution by using a crack closure method based on energy release rate [5-3], but in view of the need for a less expensive methodology consideration was given to simplified methods based on formulas for stress intensity factors around elliptical cracks. For cracks under normal loads, these formulas were developed by Shah and Kobayashi [5-4], while for shearing loads they were developed by Smith and Sorensen [5-5].

Shah and Kobayashi's analysis considered an elliptical crack embedded in an infinite medium that is subjected to a stress distribution normal to the crack face, describable by a third order polynomial in two variables. Thus, if x' and y' are the local coordinates in the plane of the elliptical crack and the origin is located at the center, the periphery of the crack, i.e., the crack front, is given by

$$\frac{x'^2}{a^2} + \frac{y'^2}{b^2} = 1 \quad (5-5)$$

Shah and Kobayashi assumed that the pressure on the crack face was of the form:

$$p(x', y') = A_{00} + A_{10}x' + A_{01}y' + A_{20}x'^2 + A_{11}x'y' + A_{02}y'^2 + A_{30}x'^3 + A_{21}x'^2y' + A_{12}x'y'^2 + A_{03}y'^3 \quad (5-6)$$

Their formulation can be viewed as being also applicable to situations where the crack is buried deeply enough so that the effects due to external surfaces of the body could be ignored. If the surfaces are nearer to any point along the crack front than the major axis of the crack, their analysis can be expected to give poor results unless the external surfaces are specifically considered.

Shah and Kobayashi's analysis employed the set of 10 constants, A_{ij} , in Equation (5-6) to describe the load and another set of 10 stress-function constants for describing the variations of the stress-intensity factor K_I along the crack front. They developed a system of ten simultaneous equations relating the two sets of constants. Appendix F contains analytical expressions corresponding to the formulation in Reference [5.4]. Appendix F, however, shows that by reorganizing their theory it is possible to solve for their stress-function constants algebraically, so that they can be evaluated as linear combinations of the load constants, with coefficients depending on the eccentricity of the ellipse.

In order to formulate the solution for K_I , one may consider the ellipse to be as shown in Figure 5-2, with the semi-axes a and b and the parametric angle ϕ . Also let

$$k' = b/a \quad \text{and} \quad k = (1 - k'^2)^{1/2}, \quad (5-7)$$

and let A_r be a reference stress, usually taken as A_{00} if that is not zero. Then in terms of reorganized stress-function constants γ_{ij} (see Appendix F), the stress intensity factor K_I is given by

$$\frac{K_I}{A_r \sqrt{\pi a}} = 4 \sqrt{k' (1 - k'^2 \cos^2 \phi)^{1/4}} \left[\gamma_{00} + \gamma_{10} \cos \phi + \gamma_{01} \sin \phi - 4\gamma_{20} \cos^2 \phi + \gamma_{11} \sin \phi \cos \phi - 4\gamma_{02} \sin^2 \phi - 4\gamma_{30} \cos^3 \phi - 4\gamma_{21} \cos^2 \phi \sin \phi - 4\gamma_{12} \cos \phi \sin^2 \phi - 4\gamma_{03} \sin^3 \phi \right]. \quad (5-8)$$

As in Appendix F, let the load constants A_{ij} be expressed in dimensionless form by defining

$$\kappa_{ij} = \frac{A_{ij} a^i b^j}{A_r}. \quad (5-9)$$

The relationship between the load constants κ_{ij} and the stress-function constants γ_{ij} is formulated in Appendix F for any value of k' , but it is appropriate here to show it for some particular cases. Thus for $k' = 1$, as it is when the ellipse becomes a circle, it can be shown that

$$\begin{aligned} \gamma_{00} &= \frac{1}{2\pi} [\kappa_{00} + \frac{1}{5}(\kappa_{20} + \kappa_{02})], \\ \gamma_{01} &= \frac{1}{3\pi} [\kappa_{10} + \frac{1}{7}(3\kappa_{30} + \kappa_{12})], \\ \gamma_{10} &= \frac{1}{3\pi} [\kappa_{01} + \frac{1}{7}(\kappa_{21} + 3\kappa_{03})], \\ \gamma_{20} &= \frac{1}{60\pi} (-3\kappa_{20} + \kappa_{02}), \\ \gamma_{11} &= \frac{4}{15\pi} \kappa_{11}, \\ \gamma_{02} &= \frac{1}{60\pi} (\kappa_{20} - 3\kappa_{02}), \end{aligned} \quad (5-10)$$

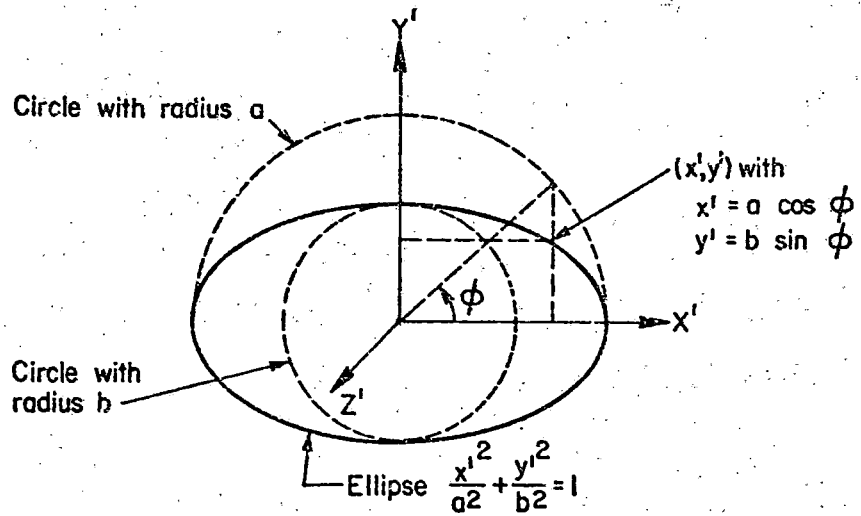


FIGURE 5-2. NOTATION FOR ELLIPTICAL CRACK

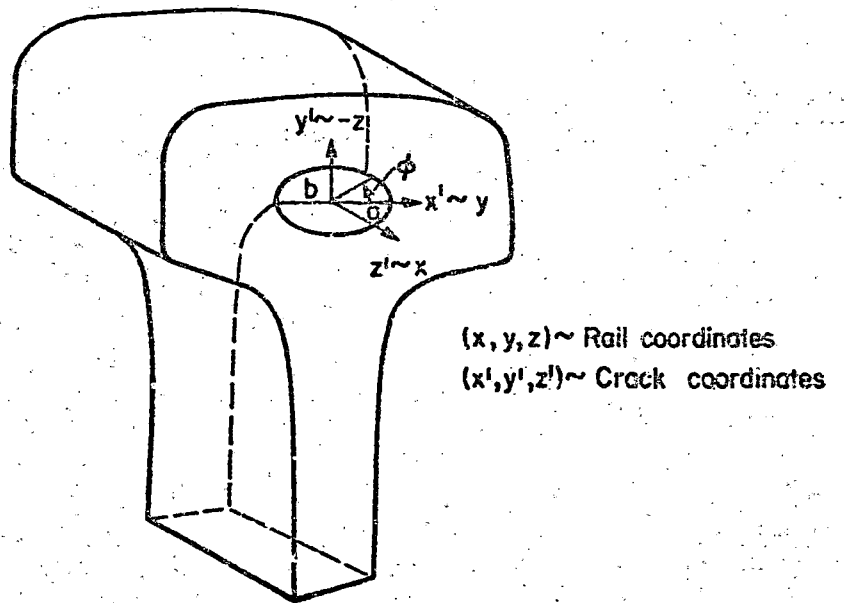


FIGURE 5-3. RELATION BETWEEN RAIL COORDINATES AND LOCAL COORDINATES FOR A TRANSVERSE FISSURE

$$Y_{30} = \frac{1}{105\pi}(-3\kappa_{30} + \kappa_{12}) ,$$

$$Y_{21} = \frac{1}{105\pi}(-5\kappa_{21} + 3\kappa_{03}) ,$$

$$Y_{12} = \frac{1}{105\pi}(3\kappa_{30} - 5\kappa_{12}) ,$$

$$Y_{03} = \frac{1}{105\pi}(\kappa_{21} - 3\kappa_{03}) .$$

Alternatively taking $k' = 0.5$ (that is $a = 2b$) the solution for the Y_{ij} becomes

$$Y_{00} = 0.20643141 [\kappa_{00} + \frac{1}{5}(\kappa_{20} + \kappa_{02})] ,$$

$$Y_{10} = 0.16380454 [\kappa_{10} + \frac{1}{7}(3\kappa_{30} + \kappa_{12})] ,$$

$$Y_{01} = 0.11865443 [\kappa_{01} + \frac{1}{7}(\kappa_{21} + 3\kappa_{02})] ,$$

$$Y_{20} = -0.02666517 \kappa_{20} + 0.007449899 \kappa_{02} ,$$

$$Y_{11} = 0.10867004 \kappa_{11} ,$$

$$Y_{02} = 0.00744990 \kappa_{20} - 0.01726190 \kappa_{02} ,$$

$$Y_{30} = -0.01593369 \kappa_{30} + 0.00454431 \kappa_{12} ,$$

$$Y_{21} = -0.02123300 \kappa_{21} + 0.01129074 \kappa_{03} ,$$

$$Y_{12} = 0.01363294 \kappa_{30} - 0.01829161 \kappa_{12} ,$$

$$Y_{03} = 0.00376358 \kappa_{21} - 0.00960409 \kappa_{03} .$$

(5-11)

These alternative cases are used in some illustrative calculations which are given below. Using Appendix F, comparable solutions can be derived readily for any value of k' .

In a somewhat parallel fashion Smith and Sorenson [5-4] analyzed stresses arising from tangential loads on an elliptical crack of the form shown in Figure 5-2. They presumed that the stresses on the crack faces are of the type

$$\begin{aligned} \tau_{z'x'} &= \sum_m \sum_n A_{mn} x'^m y'^n \quad \text{for } 0 \leq m+n \leq 3, \\ \tau_{y'z'} &= \sum_m \sum_n B_{mn} x'^m y'^n \quad \text{for } 0 \leq m+n \leq 3. \end{aligned} \quad (5-12)$$

These cubic polynomial representations of the load functions include 20 coefficients, that is ten A_{mn} and ten B_{mn} . In order to express the stress intensity factors K_{II} and K_{III} due to these loads, they introduced twenty stress function constants a_{mn} and b_{mn} which could be found from the coefficients A_{mn} , B_{mn} by solving 20 simultaneous linear equations having coefficients involving a , b , k , k' and elliptic integrals $K(k)$ and $E(k)$. Here too, as Appendix F shows, it is possible to reorganize their work in such a way that the 20 simultaneous equations can be solved algebraically. The process of reorganization also revealed some inconsistencies which arose in the long algebraic manipulations underlying their formulas. The reorganization, fortified by comparison with Bell's formulas for stresses around a circular crack [5-5], shows fairly convincingly what the stress-intensity formulas for the elliptical crack with shearing loads as above should be. Thus, using dimensionless load constants λ_{mn} and μ_{mn} in place of A_{mn} and B_{mn} , and using dimensionless stress function constants α_{mn} and β_{mn} in place of a_{mn} and b_{mn} , Appendix F shows α_{mn} and β_{mn} as linear combinations of λ_{mn} and μ_{mn} with coefficients depending only on the eccentricity of the ellipse and Poisson's ratio ν . Presuming $\nu = 0.30$, Appendix F displays these solutions for the α_{mn} and β_{mn} with purely numerical coefficients first for $k' = 1$ and later for $k' = 0.5$, in a form similar to that shown above for a normally loaded crack. In addition, the stress intensity factors K_{II} and K_{III} can be displayed as expressions

comparable to that shown for K_I , but having 20 terms instead of 10. Details are shown in Appendix F.

The analytic solutions derived for K_I , K_{II} and K_{III} arising from load functions expressed as cubic polynomials of x' and y' are quite convenient to use. The confinement of the degree of the polynomials to three or less still allows fair flexibility in the loads to be considered. It should perhaps be remarked that if $p(x',y')$ arises as a change of stress owing to the presence of the crack, then it should nowhere be negative, since normal stress can be transmitted across a crack if it is compressive whereas a tensile stress can not be so transmitted.

5.2.2 Illustrative Evaluations of Stress Intensity Factors

In order to apply the simplified formulae for stress intensity factors to railhead cracks it is necessary first to get cubic polynomial representations for the stress field that would act on the plane of the crack were the crack absent and to convert it into the three stress components acting normal and tangential to the crack face. The coordinate conversion of course depends on the orientation of the crack. If the crack is a transverse fissure, then the relation between the crack coordinates (x',y',z') and the rail coordinates (x, y, z) is that shown by Figure 5-3, in particular

$$x' = y, \quad y' = -z, \quad z' = x. \quad (5-13)$$

The precise expression to use for the load depends on both the position in the rail and the component (or components) of the stress interrupted by the presence of the crack. Thus there are many possible crack loads that could be analyzed on the basis of the railhead stress patterns described in the preceding chapters. The intent here is not to survey all possible patterns, but instead to provide some illustrations of stress intensity factors arising at a few locations, around hypothetical transverse fissures.

Consider first, cracks that are located in the transverse plane passing through the center of the wheel/rail contact. The rail stress component which

may produce significant stress intensity factors, K_I , around such cracks is the tensile stress σ_x . Reviewing the possibilities among stresses already analyzed (Chapters 2, 3, 4) one finds tensile stress σ_x predominantly due to the subsurface residual stress σ_x^r , with additional contributions due to flexural and contact stresses. It must be noted that in the vicinity of the load, the flexural and contact stresses in the rail head are for the most part negative, and hence their role on K_I will be subtractive. But the same is not true with respect to K_{II} and K_{III} . The sum of the longitudinal elastic flexure and contact stresses is denoted here as σ_x^e . Thus significant crack openings can arise on these cracks whenever $\sigma_x^r + \sigma_x^e$ is positive.

The range where σ_x^r itself is tensile is shown in Figure 4-10 in Chapter 4. It is eccentric toward the gage side, and is centered about 0.87 inch below the tread surface. The positions where measurements were made are somewhat few, considering that no compressive stresses are significant here. Nevertheless, the tensile values σ_x^r were fitted as required by Shah and Kobayashi, with emphasis on the higher values and on general location of the boundaries of the tensile zone. In terms of the coordinates shown in Figure 1-2, the following approximate expression was obtained. Dimensionally y and z are in inches and σ_x^r is pounds per square inch.

$$\sigma_x^r(0,y,z) = 18667 - 2333y - 8667y^2 - 2667y^3 - 112000(0.87-z)^2, \quad (5-14)$$

where the global coordinates y and z are related to the local coordinates x' , y' (centered on the crack face) by, $y = x'$ and $0.87-z = y'$.

The data for determining $\sigma_x^e(0,y,z)$ were taken from the calculations underlying Figure 2-5, with emphasis on the zone where σ_x^r is tensile enough to overcome the compressive values given by σ_x^e . This gave the expression

$$\sigma_x^e(0,y,z) = -6058 - 5181(0.87-z) - 4716(0.87-z)^2 - 5718(0.87-z)^3 \quad (5-15)$$

Combining this with the residual stress pattern shows the total longitudinal stress on the relevant part of the plane $x = 0$ to be

$$\sigma_x(0, y, z) = 12609 - 2333y - 5181(0.87-z) - 8667y^2 - 116716(0.87-z)^2 - 2667y^3 - 5718(0.87-z)^3 \quad (5-16)$$

Since the above is everywhere positive on the face of the crack hypothesized here and tensile rail stresses induce positive crack loads $p(x', y')$, the coefficients of this expression are those needed for the Shah and Kobayashi treatment. That is (in psi)

$$A_{00} = 12609, A_{01} = -2333, A_{0i} = -5181, A_{20} = -8667, A_{11} = 0,$$

$$A_{02} = -116716, A_{30} = -2667, A_{21} = A_{12} = 0, A_{03} = -5718$$

Further pursuit of the analysis depends on the shape of the crack.

Consider circular cracks, which are special cases of elliptical cracks, for which the general solution for the constants γ_{ij} in terms of load constants κ_{ij} has already been shown. Taking $A_r = A_{00} = 12609$, and assigning a value to the radius a (which equals b for the circular case), the values of the κ_{ij} follow readily from the values of the A_{ij} , and from them the constants γ_{ij} follow also. Thus it is found that for circular cracks on the plane $x = 0$, centered 0.87 inch below the top of the rail, the values of K_I (- psi inch) for two possible crack radii are:

$$K_I = 28269 [0.15752 - 0.00436 \sin\phi - 0.00727 \sin^2\phi - 0.00003 \sin^3\phi + \cos\phi (-0.00198 + 0.00002 \sin^2\theta)] \quad \text{for } a = 0.1 \text{ inch,}$$

or

$$K_I = 48964 [0.14441 - 0.013191 \sin\phi - 0.06546 \sin^2\phi - 0.00089 \sin^3\phi + \cos\phi (-0.00637 + 0.00042 \sin^2\theta)] \quad \text{for } a = 0.3 \text{ inch} \quad (5-17)$$

These solutions are shown in Figure 5-4. The smaller crack here is small enough so that there is little variation of the load across its face, therefore its stress intensity factor K_I is fairly uniform. The larger crack, because it has to relax the stress over a larger area, experiences generally higher values of K_I . Also, the variation of K_I is stronger because of the variation in the load on the crack face. The crack approaches the boundary of the tensile stress region most closely where $\phi = 90^\circ$ so it is reasonable that its K_I should be lowest there. It is farthest from that boundary where $\phi = 180^\circ$, so the high value of K_I there is also reasonable. Since crack growth generally proceeds more easily with high K_I , these results suggest why railhead cracks may tend to grow into an elliptical form.

Next consider an elliptical crack in the transverse plane through the center of contact. Let it to be centered 0.87 inch below the top of the tread surface. Taking its semiaxes to be $a = 0.6$ inch and $b = 0.3$ inch so that $k' = 0.5$, it conforms to the second set of solutions shown for the constants γ_{ij} in terms of the κ_{ij} . Here, presuming again the same overall load distribution and taking $A_T = A_{00}$ (although the latter choice is immaterial) it is found that

$$K_I = 48963 (1 - 0.75 \cos^2 \phi)^{1/4} [0.16025 - 0.01470 \sin \phi - 0.04858 \sin^2 \phi - 0.00100 \sin^3 \phi + \cos \phi (-0.02430 + 0.00540 \sin^2 \phi)], \text{ for } a = 0.6 \text{ inch, } b = 0.3 \text{ inch.}$$

Again taking $a = 0.2$ inch and $b = 0.1$ inch, it is found similarly that

$$K_I = 28269 (1 - 0.75 \cos^2 \phi)^{1/4} [0.20130 - 0.00488 \sin \phi - 0.00540 \sin^2 \phi - 0.00004 \sin^3 \phi + \cos \phi (-0.00629 + 0.00020 \sin^2 \phi)], \text{ for } a = 0.2 \text{ inch, } b = 0.1 \text{ inch. (5-18)}$$

These solutions are shown in Figure 5-5. Here again the curve for the smaller crack reflects little load variation, so the variations in the K_I curve result mainly from the ellipticity of the crack. The K_I curve for the larger crack reflects both the ellipticity of the crack and the variations of the crack load. It is interesting that the maximum K_I is slightly less than was found

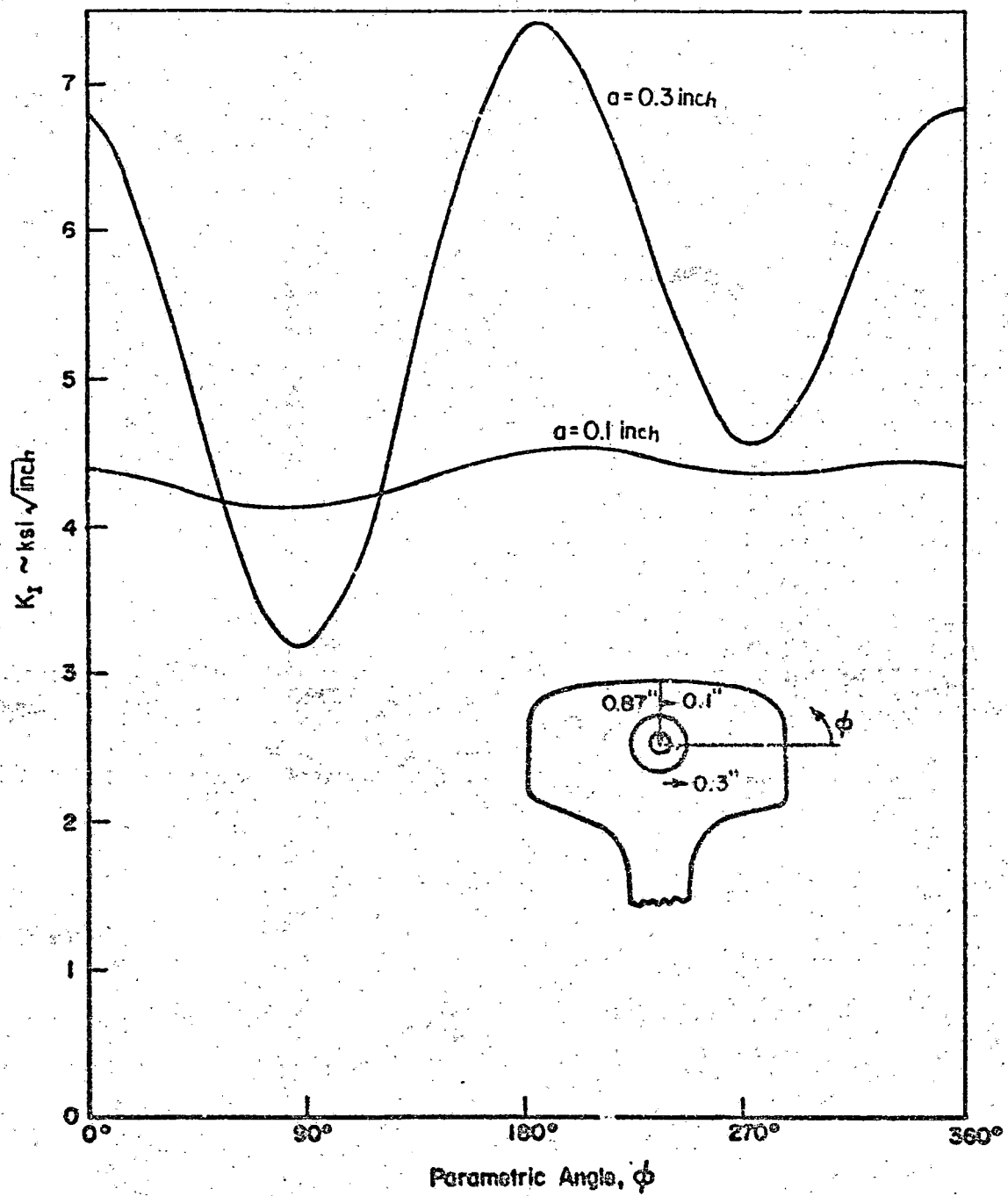


FIGURE 5-4. STRESS INTENSITY FACTOR K_I AROUND CIRCULAR TRANSVERSE CRACKS BELOW THE CENTER OF WHEEL/RAIL CONTACT

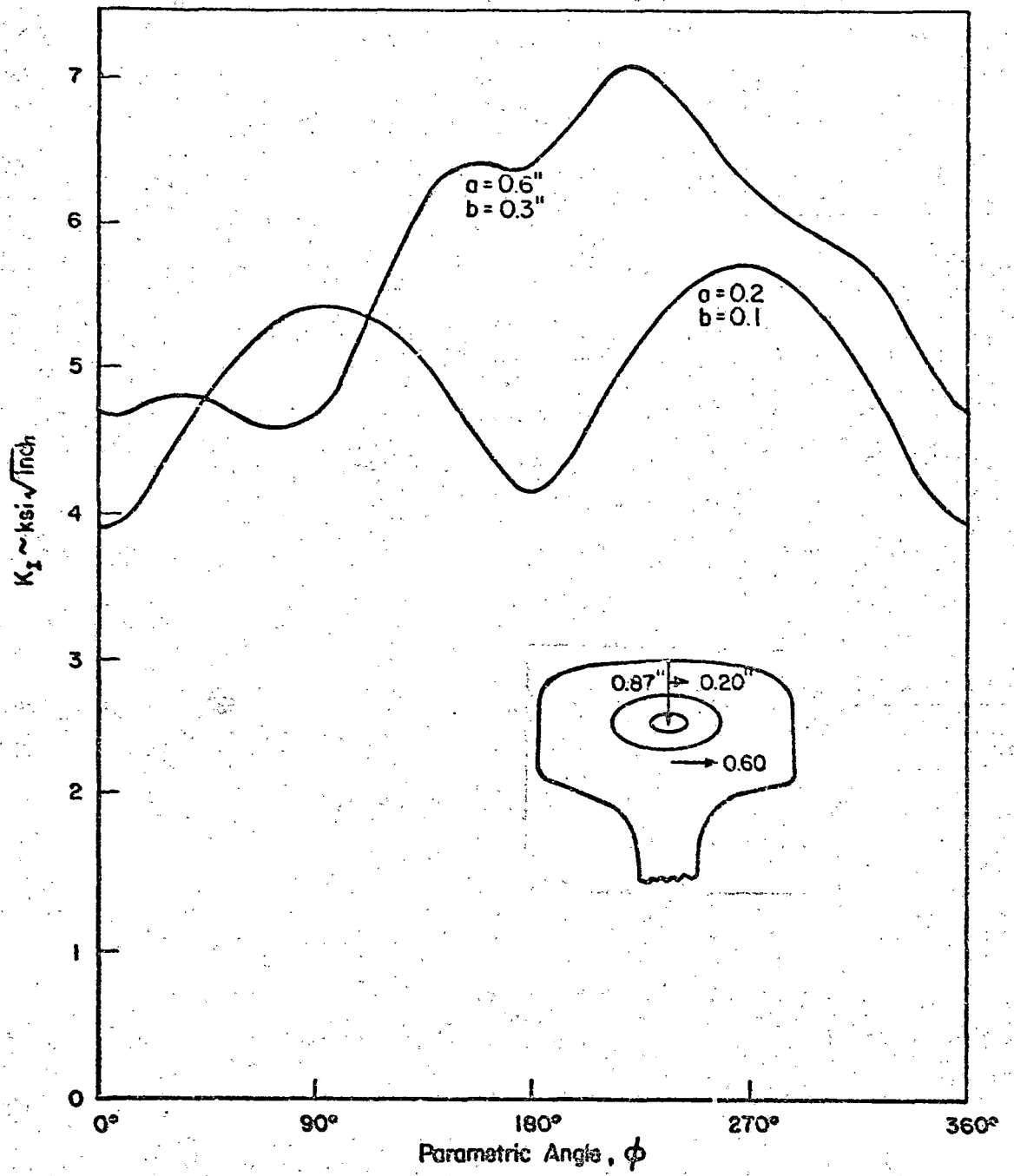


FIGURE 5-5. STRESS INTENSITY FACTOR K_I AROUND ELLIPTICAL TRANSVERSE CRACKS BELOW THE CENTER OF WHEEL/RAIL CONTACT

for the circular crack with radius 0.3 inch, and it occurs at a slightly different angular position. The minimum K_I for this larger ellipse also is not as low as the K_I calculated for the larger circle, perhaps reflecting the fact that the elliptical crack front is more gently curved than the circle is near $\phi = 90^\circ$. The intricate influences of overall crack load, the load variation, and the curvature of the crack front are not all intuitively obvious.

All the computed K 's to this point were found for $x = 0$. Of course for points farther from the contact patch the component σ_x^e would change, so that the stress intensity factors too would vary from those shown here. The range of that variation would have some influence on the rate of crack growth, at least according to some crack-growth theories. In addition, away from the plane $x = 0$ shearing stresses τ_{zx} and τ_{xy} can arise which also would affect a transverse fissure.

In order to show some of the variation in K_I with changing distance from the contact region, and also to show some effects due to shear stress components on a transverse crack, consider next the same large elliptical crack when the center of contact is one inch away from the crack plane, so that $x = -1.0$ inch. The residual stress pattern σ_x^r acting on the crack plane, were the crack absent, is independent of x , but the stress σ_x^e contributed by the flexural and contact stresses changes. Fitting it in the same manner as before to data for the $\sigma_x(-1, y, z)$, drawn from Appendix B, shows

$$\sigma_x^e(-1, y, z) = -7345 - 5500(0.87 - z) + 2400y^2 - 2510(0.87 - z)^2 + 4250y^2(0.87 - z) - 645(0.87 - z)^3 \quad (5-19)$$

Adding this to σ_x^r shows that the combined normal load distribution on the crack is

$$\sigma_x(-1, y, z) = 11322 - 2333y - 5500(0.87 - z) - 6267y^2 - 114510(0.87 - z)^2 - 2667y^3 + 4250y^2(0.87 - z) - 645(0.87 - z)^3 \quad (5-20)$$

The normal load on the crack here is the above function, but with $y + x'$ and $(0.87-z) + y'$ as before. From this load distribution, calculating K_I as before shows

$$K_I = 43966 (1-0.75 \cos^2 \phi)^{1/4} [0.16649 - 0.01317 \sin \phi - 0.06278 \sin^2 \phi - 0.00418 \sin^3 \phi + \cos \phi (-0.02707 + 0.00602 \sin^2 \phi)] \quad (5-21)$$

There are no residual stress components τ_{zx}^r or τ_{xy}^r , but on the plane where $x = -1$ shear stresses do arise due to flexural and contact actions. Using the same data for these components as appear in Appendix B, and fitting them in the same general way as for other components, it was found that

$$\begin{aligned} \tau_{zx}(-1, y, z) &= -2760 - 1690 (0.87-z) + 2600y^2 - 2680 (0.87-z)^2 \\ &\quad + 4000y^2 (0.87-z) + 1200 (0.87-z)^3, \quad \text{and} \\ \tau_{xy}(-1, y, z) &= 1800y + 2500y (0.87-z) - 2580y^3. \end{aligned} \quad (5-22)$$

The units for τ , y , z are as before. The shear loads contributed by the crack are the negatives of these with $y + x'$ and $(0.87-z) + y'$. The coefficients of these functions, with signs reversed, provide the load constants A_{mn} and B_{mn} respectively as used in the Smith and Sorenson theory discussed in Appendix F. Thus using the solution for the constants λ_{ij} and u_{ij} in terms of reorganized load constants α_{ij} and β_{ij} for the case where $k' = 0.5$, one obtains the coefficients for the solutions for K_{II} and K_{III} as shown in that appendix. These stress intensity factors are (again in $\text{psi} \sqrt{\text{inch}}$).

$$K_{II} = \frac{3883}{(1-0.75 \cos^2 \phi)^{1/4}} [0.06381 - 0.43399 \sin \phi - 0.04328 \sin^2 \phi - 0.20343 \sin^3 \phi - 0.08971 \sin^4 \phi] \quad (5-23)$$

$$K_{III} = \frac{2718 \cos \phi}{(1-0.75 \cos^2 \phi)^{1/4}} [-0.22909 - 0.13573 \sin \phi - 0.13800 \sin^2 \phi - 0.09997 \sin^3 \phi]. \quad (5-24)$$

These stress intensity factors, together with K_I are drawn in Figure 5-6. It can be seen that these factors K_{II} and K_{III} are smaller than K_I , but they are large enough to add significantly to possible effects from K_I . Thus, though K_I is slightly smaller at $x = -1$ inch from the wheel load than at $x = 0$, as comparison of Figures 5-5 and 5-6 shows, the overall effect of the stress intensity factors may not be less at $x = -1$ inches. Precise comparison of effects at $x = -1$ with those at $x = 0$ depends, of course, on how effects from K_I , K_{II} and K_{III} combine.

5.2.3 Observations on Calculations of Stress Intensity Factors

The calculations of stress intensity factors presented here treat only a few transverse fissures at only two positions with respect to the center of typical wheel/rail contact. Of course, as a wheel rolls past a possible fissure in the rail head, that fissure is exposed progressively to the stress distributions at all distances from the wheel rail contact. At the points considered in the illustrations, the longitudinal stress from rail flexure is compressive, but at more remote points it can be tensile. Adding tensile flexural stress to the tensile residual stress would increase the overall tensile stress and hence increase K_I . Two of the most significant values of stress intensity factor K_I arising at a fixed point in the rail are the highest and lowest that occur during the passage of the wheel (or of two or more wheels if their rail stress fields overlap). The importance of the lowest value is its effect on the range of the stress intensity factor.

It was observed earlier that among the components of residual stress the value of σ_y^r becomes most highly tensile, at least among the data considered. Of course there are flexural and contact stresses which are added to this during wheel passage. These components become significant for crack growth if longitudinal vertical fissures are considered. The magnitude of σ_y^r suggests that stress intensity factors arising on cracks of this kind are often larger than those found above. Of course, this kind of crack might become very long before reaching a surface of the rail, so study of it might properly have features different from those involved in studying transverse fracture.

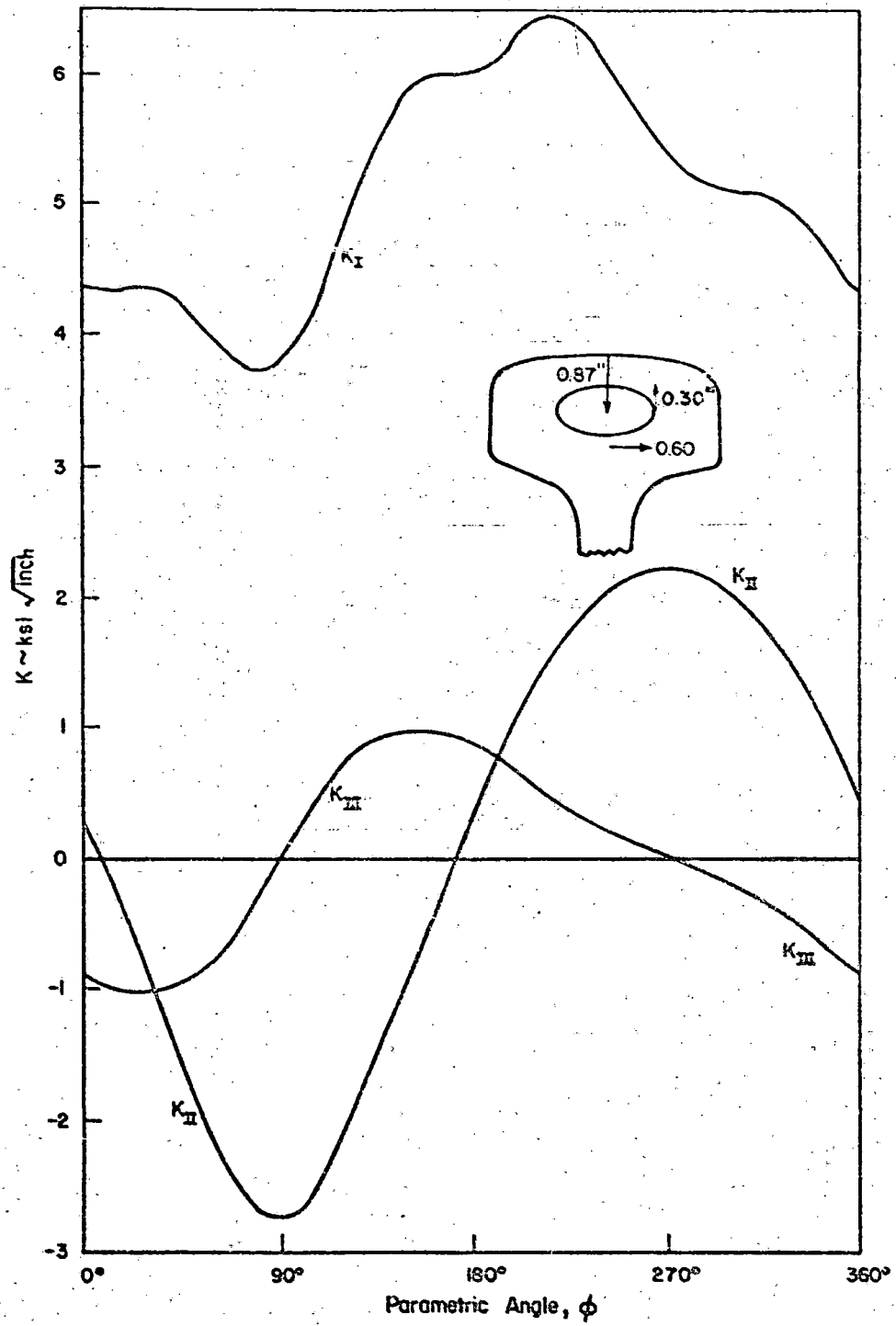


FIGURE 5-6. STRESS INTENSITY FACTORS K_I , K_{II} , K_{III} AROUND ELLIPTICAL TRANSVERSE CRACK IN PLANE 1 INCH FROM CENTER OF CONTACT

Longitudinal, horizontal cracks (horizontal split heads), associated with stress components σ_z also give rise to significant stress intensity factors, as some of the values of σ_z^r suggest.

Complete application of stress intensity factor calculations would carry them into calculations of crack growth. The methodology introduced here could be useful for that so long as the crack can be treated as essentially elliptical and not too close to a rail surface. Treatment of cracks approaching a surface would require considerable extension to the methodology presented here.

6. LABORATORY STUDY OF BOLTED-JOINT BEHAVIOR

The investigations of the central region of the rail focused upon evaluating the principal stress inducing mechanisms in rolling contact. These mechanisms are altered by the presence of the discontinuity represented by mechanical, bolted rail joints. This region of the rail exhibits unique behavior which generates unique failure modes in the rail end region.

As part of the study of rail joint area stresses, some laboratory tests were performed to provide data on joint behavior that would qualitatively indicate the effects of the various parameters. Additionally, it was envisioned that some of the experimental results could be used to compare against numerically computed values for stresses at typical joints. To this end, experiments were conducted to determine the internal joint forces and to ascertain the stresses at locations where rail end cracks commonly initiate.

In the study, a rail joint removed from service was instrumented and re-assembled in the laboratory. The joint was subjected to a variety of loading conditions in a specially constructed test fixture which had been designed to simulate actual track foundations.

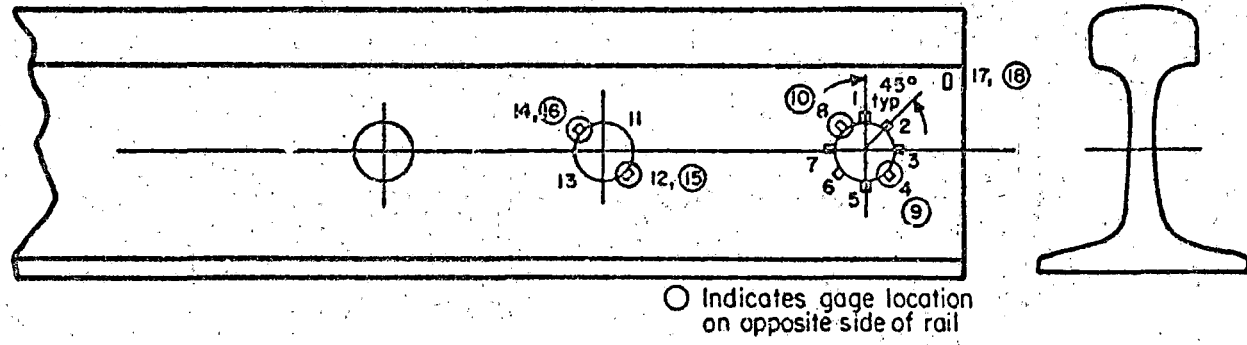
The following subsections present descriptions of the joint, the test system, instrumentation and loading procedure, and some results of the tests.

6.1 DESCRIPTION OF THE TEST SETUP AND PROCEDURES

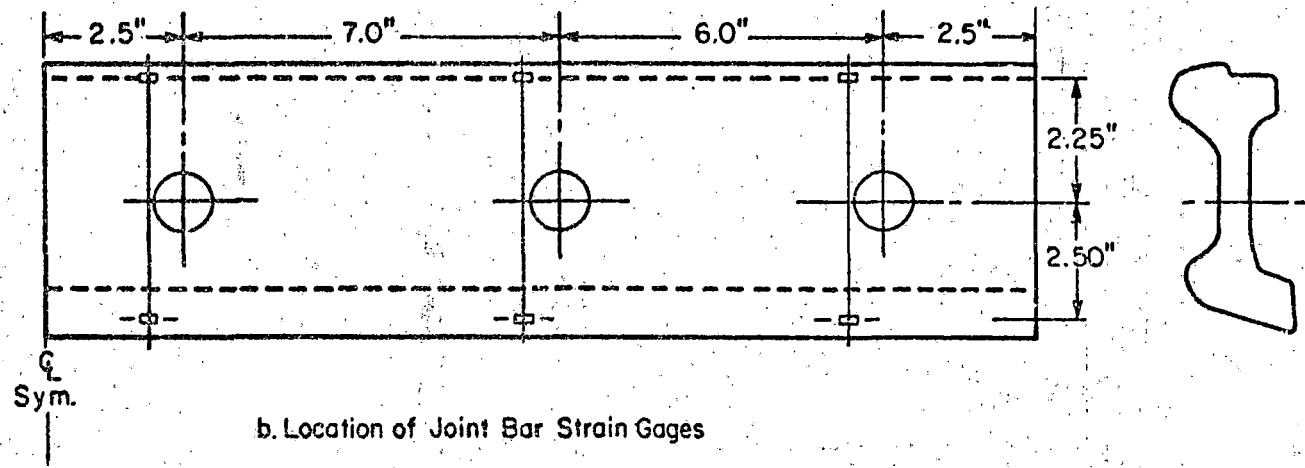
6.1.1 The Joint

Although many different types of joint bars are in use today, a symmetrical type was selected for modeling purposes because of its simplicity. The joint removed from service consisted of two 131-pound RE rails manufactured by Bethlehem Steel in 1945 at their Steelton Works and two short-toe joint bars of the same vintage. It was found that each bar had a moment of inertia of 14.86 inches⁴. The hole spacing of the joint is shown in Figure 6-1. As used in the test facility, each rail was cut down to 13 feet from its original 39-foot length.

6-2



a. Rail End Strain Gage Locations



b. Location of Joint Bar Strain Gages

FIGURE 6-1. JOINT GEOMETRY AND STRAIN GAGE LOCATIONS

The joint was supplied through the courtesy of the Southern Railroad. Approximately 400- to 580-million-gross tons of traffic had passed over it. Examination of the rail ends indicated extensive wear-in of the joint bars. Also, the rail head was quite worn.

6.1.2 Description of the Test Facility

The test facility constructed for this investigation is shown in Figure 6-2. It consisted of a structural steel frame 26 feet long, constructed of 12-inch-wide flange beams. Attached to this frame were structures for supporting hydraulic actuators and ties. The simulated test track consisted of the rail joint described earlier mounted on 14 aluminum I-beam "ties" acting as simply supported beams spaced 22 inches apart. The spacing of the tie supports could be varied to allow span changes for modifying the tie stiffness and, ultimately, the track modulus. Assuming that the system was supporting a 131-pound RE rail, the effective track modulus could be varied from 1 to 10 ksi. The lateral stiffness of the foundation was provided by the action of the ties in longitudinal tension. Since this value could not be changed, the lateral track modulus was constant at a value of 33 ksi.

Loads were applied to the test joint in the vertical and lateral directions by means of two hydraulic actuators acting through electrical resistance load cells. The vertical actuator was arranged so that up to a 0.75 inch load eccentricity (offset from centerline of the rail) could be obtained. The lateral actuator loaded the rail at a point 6.25 inches above its base. Both actuators were controlled by separate pressure sources which could be varied independently of each other.

6.1.3 Instrumentation

The first four aluminum ties on either side of the load actuators were instrumented with strain gages to monitor both vertical force by measuring bending stress in the tie and lateral force by measuring axial stress in the tie. The gage for measuring vertical tie force was positioned at the center of the lower flange of each of the instrumented ties. The lateral force gage

6-4

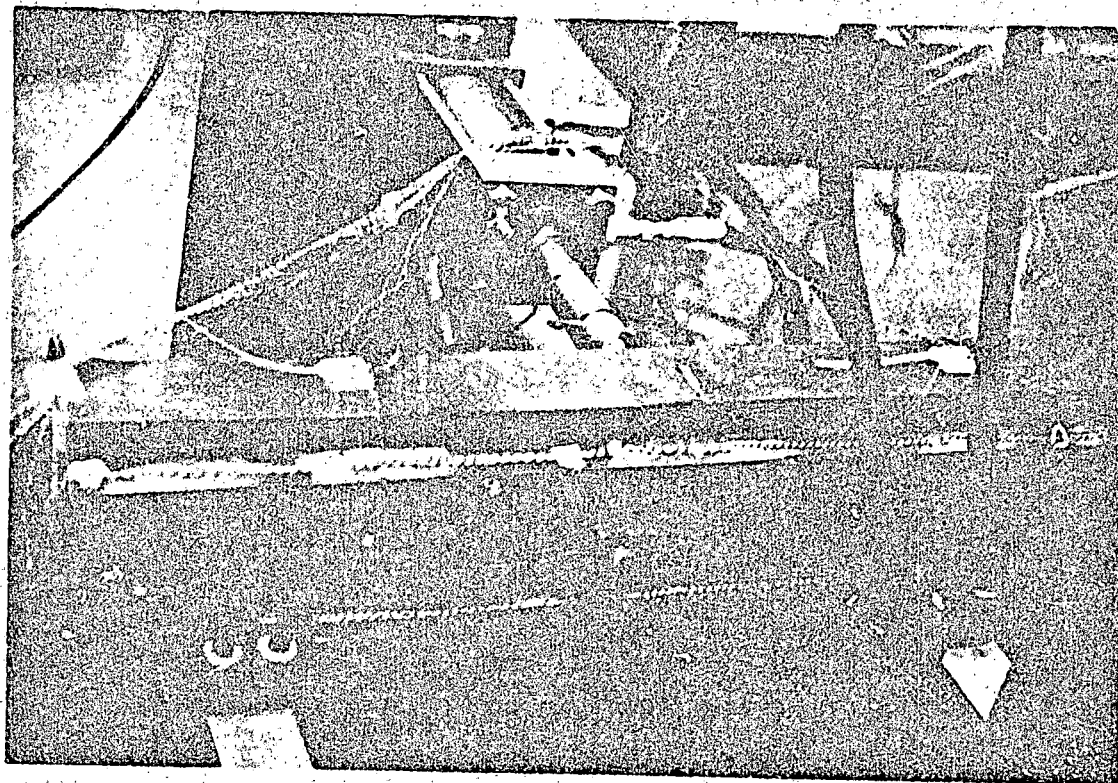


FIGURE 6-2. TEST SETUP FOR LABORATORY VALIDATION STUDIES

was positioned adjacent to a stress concentrating hole on the neutral axis of each tie. Figures 6-3 and 6-4 present calibration curves for both the vertical and lateral force transducers.

Instrumented track bolts were used to monitor bolt tensions in the joint. Each of the six bolts were provided with two strain gages mounted on milled flats on opposite sides of the shank. This arrangement was used to cancel bending effects. The bolts were calibrated in a universal testing machine in uniaxial tension and were found to have a constant factor of 0.0438 micro-strain/pound.

Deflection of the center of the rail joint was measured with a dial indicator relative to the floor of the laboratory.

Both joint bars and rail ends were instrumented for strain measurement. The location of those gages are shown in Figure 6-1. Gage positions on the joint bars were chosen for determining the magnitude and locations of the internal joint resultants, rather than for determination of maximum joint bar stresses. The rail gages were positioned to measure maximum stresses at points of particular interest where crack initiation has occurred in rail in service.

6.1.4 Calculation of Foundation Parameters

As was noted before, it was possible to vary the track modulus in the rail test fixture. Beam-on-elastic-foundation theory assumes the rail to be supported on a continuous foundation. Track modulus, U , is the key parameter in the continuous foundation model. The representation of the rail resting on discrete supports employs an equivalent spring of spring constant, K_T . The equivalent spring constant, K_T , is related to the continuous foundation parameter, U , by

$$K_T = \frac{E_T}{l_T} * U \quad (6-1)$$

where l_T is the spacing between ties. In discretizing the continuous foundation model, it was assumed that each tie supports the span between adjacent ties. The bending stiffness for a simply supported beam (the length of rail between adjacent ties) is

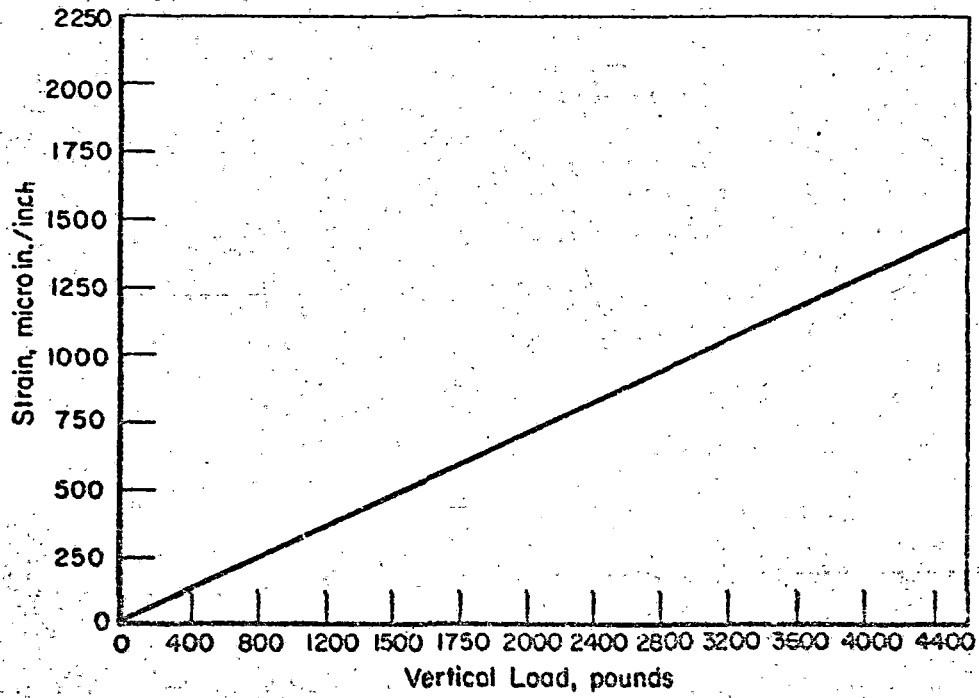


FIGURE 6-3. ALUMINUM TIE CALIBRATION CURVES--BENDING (STRAIN GAGE BRIDGE OUTPUT VERSUS VERTICAL LOAD)

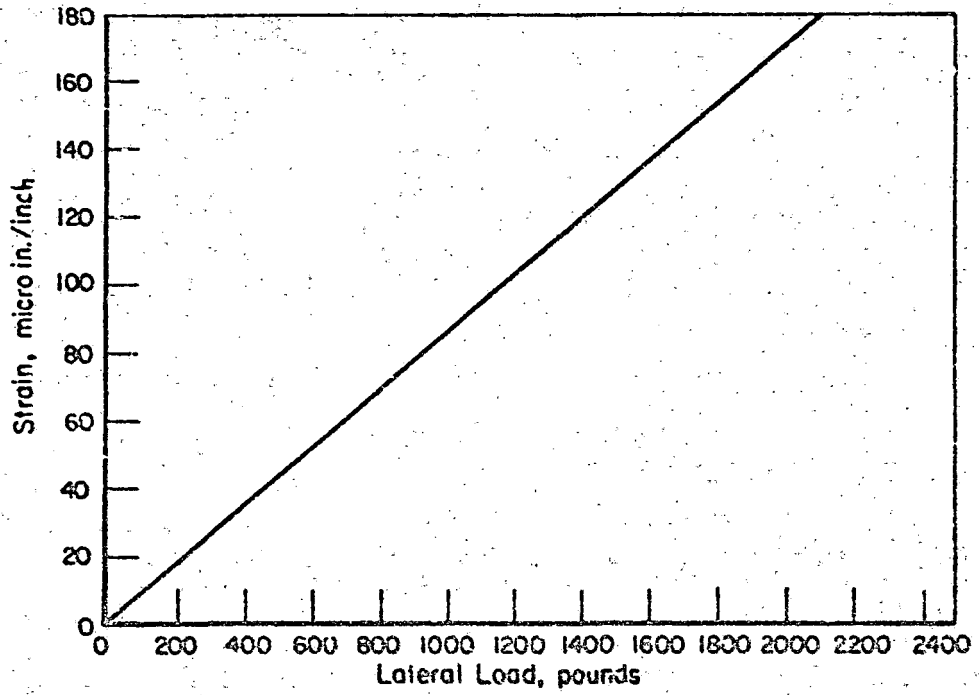


FIGURE 6-4. ALUMINUM TIE CALIBRATION CURVES--TENSION (STRAIN GAGE BRIDGE OUTPUT VERSUS LATERAL LOAD)

$$K_T = 48EI/l_T^3$$

(6-2)

Relations (6-1) and (6-2) were used to calculate the span between the adjacent 3-inch aluminum I-beam that supported the rail in the test fixture. Each 3-inch aluminum beam had a moment of inertia of 2.54 inches⁴ about the axis of bending in the vertical plane. Support spans corresponding to track foundation moduli of 1000 psi, 5000 psi, and 10,000 psi were used in the tests that were conducted.

6.2 RESULTS OF LABORATORY EVALUATIONS

6.2.1 Selection of Test Cases

Table 6-1 lists the specifications for tests conducted using the facilities just described and shows stresses calculated from strain measurements that were obtained. The tests were structured to investigate the effects of the important joint parameters: bolt tension, vertical and lateral load magnitudes, load position, foundation modulus, and combined loads. The effect of varying tensions in the bolts of a joint over the total range likely to be encountered in service was also studied. A variety of longitudinal and lateral load positions were used on either side of the rail end. The lateral load, when applied, was placed at the same longitudinal location as the vertical load. A foundation modulus value of 5000 psi was selected as the baseline level, with foundation moduli of 1000 and 10,000 psi used to show trends. Some results of the tests indicated in Table 6-1 are discussed in the following.

6.2.2 Effects of Bolt Tension Only

Previous investigations have shown that the magnitude of bolt tension can have a profound effect on the state of stress in the joint. High bolt tensions have been recommended to maintain the effectiveness of the joint to counteract wear and loosening of the bolts. The bolts wedge the joint bars

DRAFT 6-72

MATCH

TABLE 6-1. MEASURED BOLT HOLES STRESSES UNDER LOADS OF VARIOUS KINDS

Case	Specifications						Incremental Stresses Calculated from Strain Readings at Gages, ksi*																	
	Bolt Tens. kips	Vert Load kips	Ecc. inCh	Lat Load kips	Long Pos. inCh	Vert Mod ket	First Hole						Back				Second Hole				End of Web			
							Front			Back			Front		Back		17(F)	18(B)						
							1	2	3	4	5	6	7	8	9	10	11	12	13	14	15	16		
1	5	0	-	0	-	-	0.8	3.6	4.1	1.3	1.5	4.0	4.0	1.3	-2.0	-1.3	4.4	3.6	1.7	7.8	2.6	1.4	-0.7	1.0
2	15	0	-	0	-	-	0.8	9.1	12.1	3.2	3.1	10.1	10.6	3.2	-2.6	-0.9	8.9	6.2	2.8	13.9	7.3	6.2	-0.6	1.7
3	25	0	-	0	-	-	0.6	13.9	19.9	4.0	2.4	14.7	17.8	6.2	-1.3	0.2	13.7	8.8	5.3	19.2	10.1	7.1	-1.0	3.2
4	30	0	-	0	-	-	0.3	15.8	24.0	6.2	2.2	16.2	21.4	8.0	-0.9	1.1	16.1	10.4	6.6	21.8	11.3	10.5	-1.0	3.7
5	**	0	-	0	-	-	0.0	11.3	20.7	7.6	2.3	12.2	19.5	9.0	-1.9	2.2	13.2	11.8	3.8	24.6	13.4	11.9	3.4	-5.6
6	**	20	0	0	0.0	5	-3.6	-0.5	-5.3	-4.5	-1.6	0.0	-1.3	-5.4	-3.5	-5.1	2.2	-1.3	3.8	-2.9	-3.8	-3.1	-3.6	-9.6
7	**	35	0	0	0.0	5	-5.2	-2.5	-7.4	-4.6	-2.8	-2.0	-1.7	-6.1	-4.4	-6.7	2.9	-2.2	5.3	-4.6	-5.9	-5.0	-3.6	-16.2
8	**	20	0.25	0	0.0	5	3.0	1.0	-5.0	-5.1	-1.6	0.0	-0.7	-5.0	-3.4	-6.1	2.6	-1.3	4.1	-2.7	-3.7	-3.5	-1.6	-10.0
9	**	20	0.50	0	0.0	5	-2.1	2.3	-4.1	-5.1	-2.0	-0.2	-0.5	-3.7	-2.7	-6.6	2.7	-1.3	3.9	-2.4	-3.9	-3.7	0.5	-13.3
10	**	20	0.75	0	0.0	5	-1.6	2.7	-3.4	-4.7	-1.9	-0.3	-0.3	-2.8	-1.9	-6.4	2.8	-1.3	3.8	-2.3	-3.6	-3.7	3.3	-20.7
11	30	0	-	10	-1.5	5	-2.4	0.6	6.1	3.7	-0.7	2.4	6.0	1.8	1.0	3.6	-0.7	3.2	1.5	0.9	3.8	4.1	17.8	-14.0
12	30	20	0.50	10	-1.5	5	-2.0	-3.0	-1.1	1.2	-0.5	-0.9	0.3	-1.0	-0.5	0.5	1.2	0.9	3.0	-1.3	-3.3	-2.0	-4.7	-11.5
13	-30	35	0	0	-1.5	5	-2.1	-9.2	-3.2	4.6	-0.7	-6.1	-1.2	2.8	1.7	2.9	0.5	0.0	2.2	-1.4	-4.0	-2.8	-1.6	-20.6
14	30	35	0	0	-6.0	5	-1.9	0.8	-0.2	-1.1	0.4	3.6	1.3	-3.6	-4.1	-4.2	1.1	-0.5	2.1	-1.8	2.1	-2.2	7.5	-1.5
15	**	35	0	0	-8.0	5	-1.1	1.0	-0.9	-0.9	2.5	3.6	0.1	-2.8	-5.2	-3.9	1.3	-0.8	2.2	-2.0	-2.0	-2.0	5.4	-1.1
16	**	35	0	0	-10.0	5	-1.5	-0.7	-1.1	0.5	1.4	0.9	0.4	-1.6	-3.2	-2.5	1.6	-0.9	2.0	-1.9	-1.7	-2.2	3.6	-0.8
17	**	20	0	0	0.0	10	-3.6	-0.5	-5.5	-4.6	-1.6	0.0	-1.3	-5.5	-3.7	-5.2	2.1	-1.8	3.1	-2.9	-3.5	-3.1	-6.1	-7.3
18	**	20	0	0	0.0	1	-4.5	-2.9	-5.3	-2.6	-2.2	-2.5	-1.4	-3.7	-1.7	-3.5	1.1	-1.6	2.7	-3.1	-2.6	-2.5	-3.6	-6.9
19	**	20	0.50	0	0.0	10	-2.1	2.2	-4.4	-5.3	-2.0	-0.3	-0.8	-3.8	-2.7	-6.8	2.6	-1.5	3.4	-2.2	-3.6	-3.7	-1.4	-11.3
20	15	20	0	0	-1.5	5	-1.3	-2.1	-0.7	1.0	-0.2	-0.5	0.2	-0.8	-0.6	-0.4	0.9	-1.0	1.6	-1.9	-1.7	-1.6	-2.6	-14.3
21	5	20	0	0	-1.5	5	-0.7	-3.2	-1.5	1.4	-0.4	-2.5	-0.8	1.0	1.3	1.8	0.7	-0.1	0.8	-1.4	-1.1	-1.1	1.1	-11.5
22	30	20	0	10	-1.5	5	-2.8	-3.2	-0.7	1.7	0.1	-0.3	1.1	-1.1	-2.0	-0.2	0.9	2.0	3.2	-0.9	-4.7	-1.9	8.0	-22.1
23	20	20	0	0	0.0	5	-3.4	1.3	-6.8	-6.8	-1.6	0.6	-2.0	-7.0	-7.7	-6.1	1.5†	-1.6†	2.4†	-2.0†	-2.0	-1.8	-3.1	-4.4
24	20	20	0	0	1.75	5	0.4	-2.9	-8.7	-3.4	0.0	-1.9	-5.4	-5.3	-2.3	-4.6	1.5	-1.6	2.0	-2.1	-2.0	-1.8	-0.4	-0.5
25	20	20	0	0	2.75	5	1.6	-4.4	-6.6	-0.6	0.4	-3.2	-5.4	-2.0	0.2	-2.8	1.6	-2.3	2.1	-2.4	-2.2	-2.3	-0.6	-0.7
26	20	20	0	0	4.00	5	0.3	-6.2	-4.6	1.6	0.3	-5.0	-5.1	1.0	1.8	0.5	1.7	-2.8	2.3	-2.8	-2.7	-2.6	-0.6	-0.6

6-9

* Cases 1 to 5 show stresses from bolt tension only. Cases 6 to 26 show added stresses incurred by simulations of loads.
 ** Bolt tensions were about 29, 20, 29, 20, 29, 29 kips, but the resulting bolt hole stresses were nearly like those from uniform bolt tension 30 kips, as Cases 4 and 5 show. Head-web junction stresses for those cases differ.
 † These entries were computed using bolt tension contributions like those for Case 24.

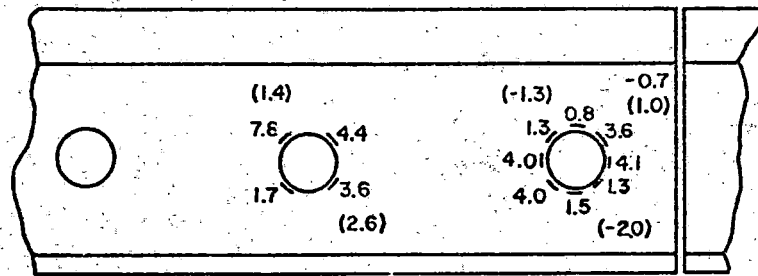
between the head and base of the rail, thus stretching the web. Thus, the effect of bolt tension on the circumferential stresses at the bolt holes and on the stress at the head-web junction is important. Measurements of these stresses due to bolt tension only are shown in Figure 6-5 for four uniform levels of bolt tension. The numbers shown in these and similar subsequent figures are stress magnitudes in ksi, tangent to the periphery of the bolt hole or tension at the head-web junction. Minus values denote compression. Parenthetic values were obtained from gages affixed to the back side of the web.

The part of Figure 6-5 for bolt tension equal to 30 kip shows rather high tensile stresses occurring at gage positions 3 and 7. Nonuniformities in the mating parts result in bending as well as tension in the web, and this accounts for differences between the front and back. The lack of compression at strain gage position 1 (see Figure 6-1) which might be expected by viewing the web as an infinite sheet with a hole under tension, may reflect longitudinal (and vertical) restraints due to the relatively stiff head and base of the rail. The distribution of stress around the front side of the hole nearest the rail end is shown also in Figure 6-6, together with the effect of bolt tension at several locations. The effect of bolt tension at these locations is seen to be quite linear.

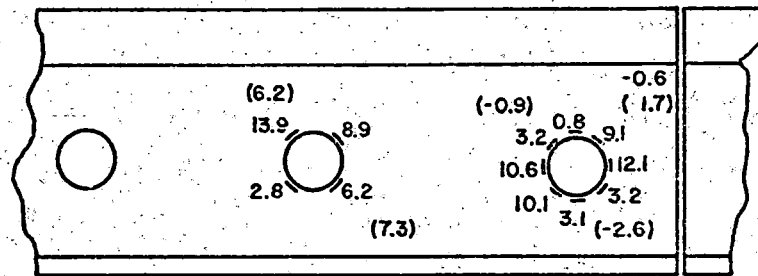
Cases 6 to 10 and 15 to 19 in Table 6-1 employed bolt tensions somewhat less than 30 kip, reflecting a state of natural loosening. Case 5, which represents observations made before the load of Case 6 was applied, shows the stresses measured under this mild loosening. Comparing stress measurements for Cases 4 and 5 shows that the stresses were little affected by this much loosening, though they could have been much changed by further loosening.

6.2.3 Effects of Vertical Loading on Centerline

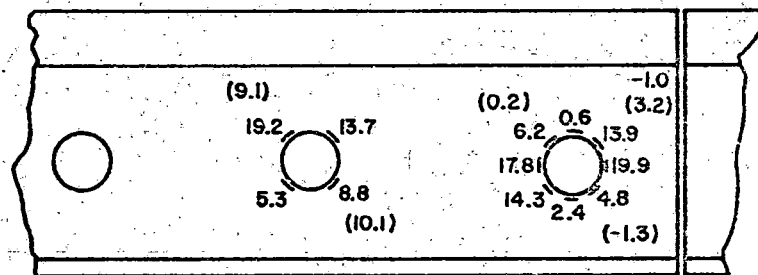
Cases 6 and 7 show the additional increments of stresses due to either of two levels of vertical loads applied centrally at the joint. Under train loads, these values are superimposed upon the initial stresses due to bolt tension only. All three of these sets of measurements are shown in Figure 6-7, and their variation is shown further in Figure 6-8. It can be seen that



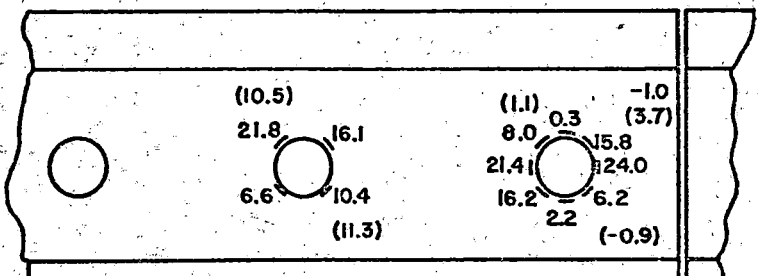
Bolt Tension 5 kip (Case 1)



Bolt Tension 15 kip (Case 2)

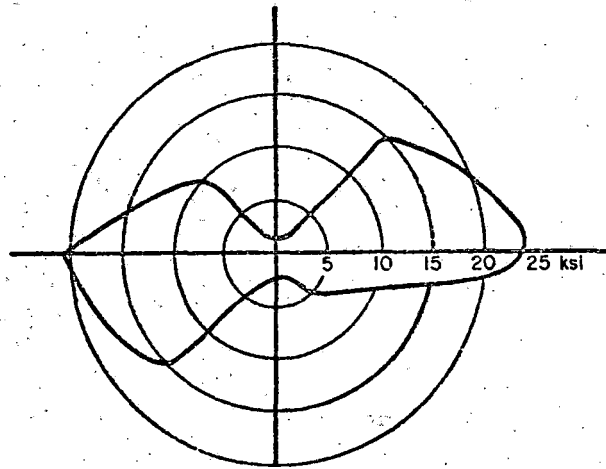


Bolt Tension 25 kip (Case 3)



Bolt Tension 30 kip (Case 4)

FIGURE 6-5. CONTRIBUTION TO BOLT HOLE STRESSES (IN KSI) BY VARIOUS BOLT TENSIONS



First Hole Distribution (30,000 lbs)

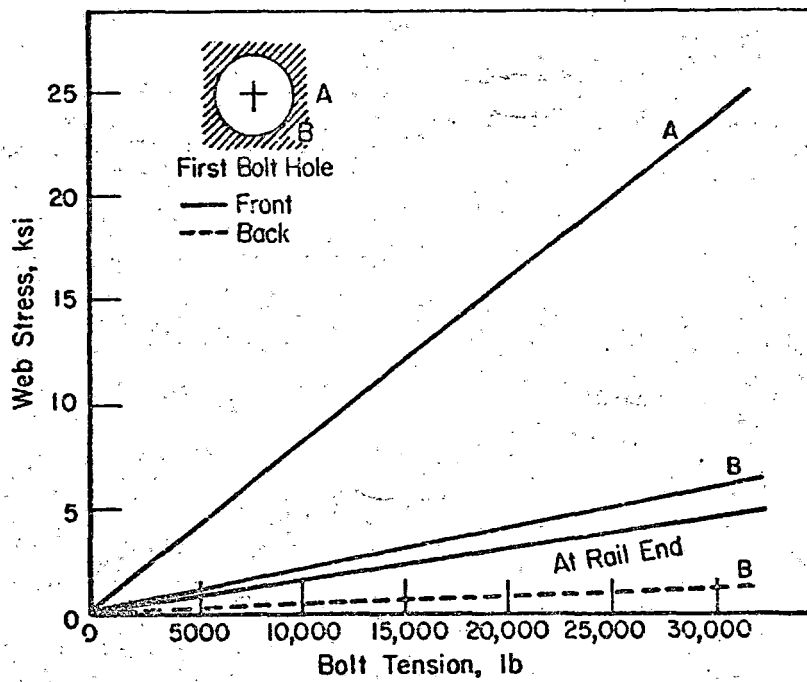
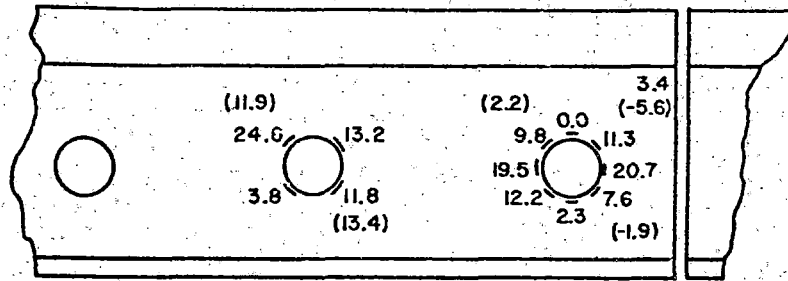
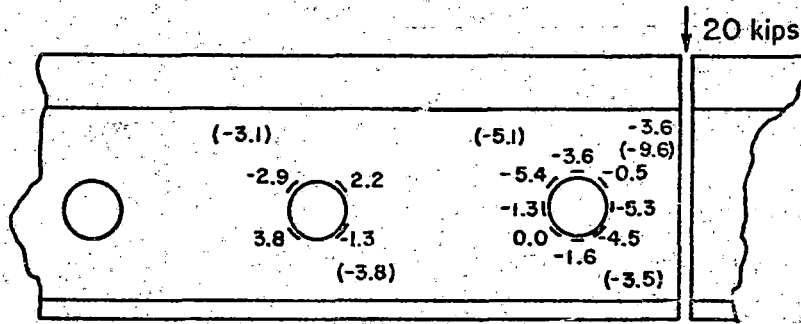


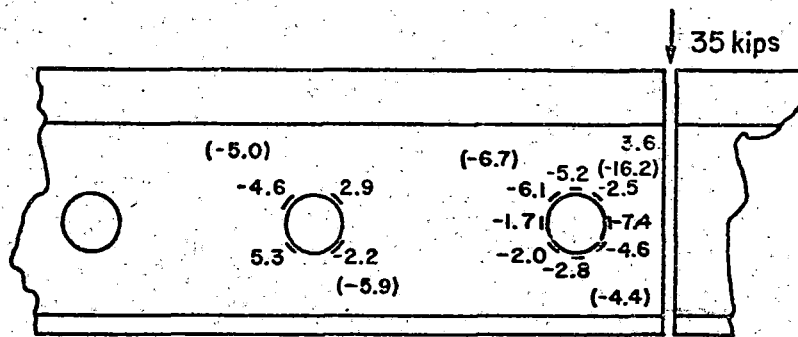
FIGURE 6-6. EFFECT OF BOLT TENSION ONLY ON WEB STRESSES



Bolt Hole Stresses from Bolt Tension Only (Case 5),
Bolt Tensions 28,19,28,24,28,28 kips



Increments of Bolt Hole Stresses due to 20,000 lb
Vertical Load Centered on Joint, Bolt Tensions
28,19,28,24,28,28 kips (Case 6)



Increments of Bolt Hole Stresses due to 35,000-lb
Vertical Load Centered on Joint, Bolt Tensions
28,19,28,24,28,28 kips (Case 7)

FIGURE 6-7. BOLT HOLE STRESSES DUE TO BOLT TENSION APPROXIMATELY
EQUAL TO 30 KIPS AND TWO VERTICAL LOADS CENTERED ON
THE JOINT

(Foundation Modulus = 5000 psi)

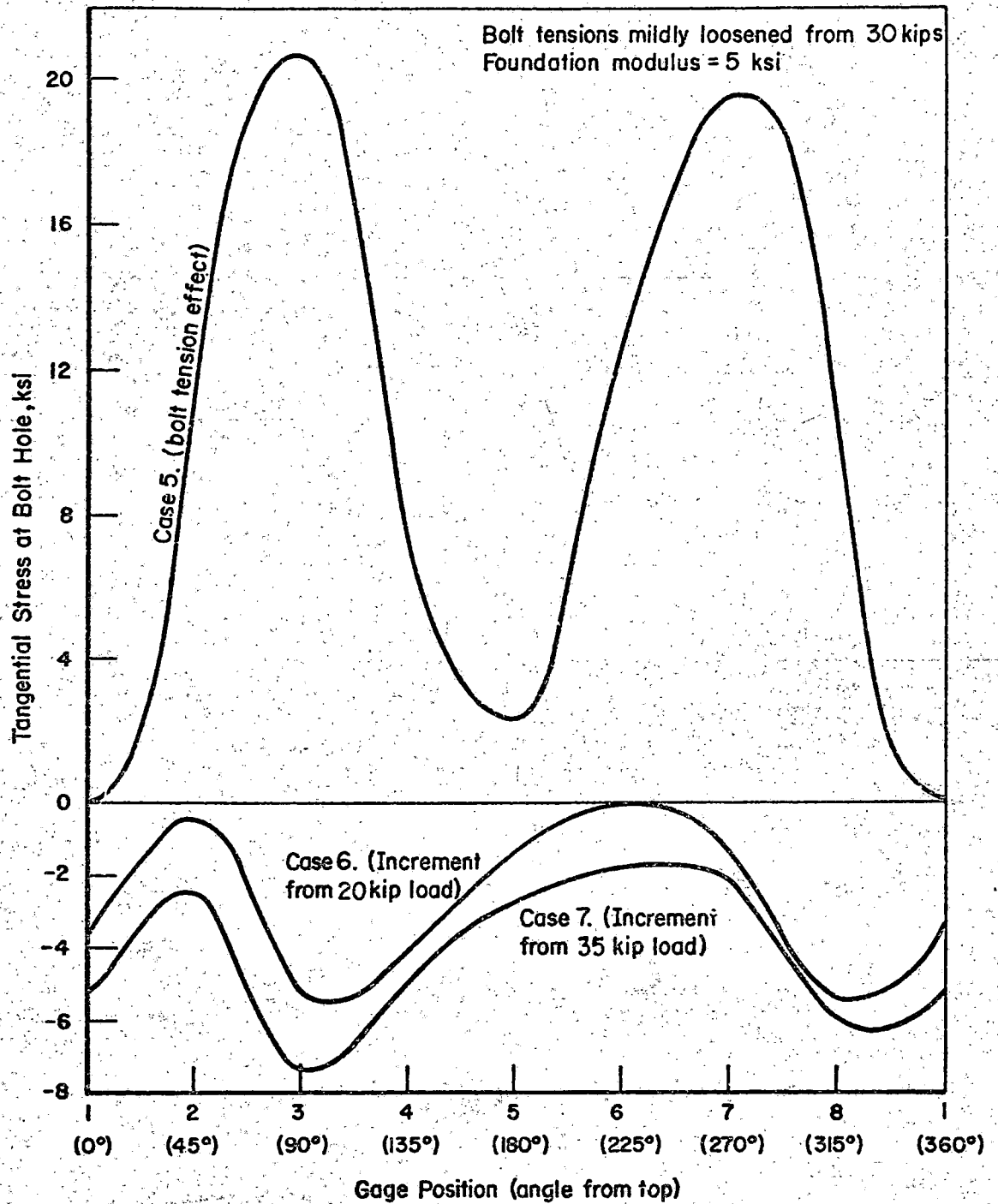


FIGURE 6-8. VARIATION OF TANGENTIAL STRESS ON FRONT SIDE OF FIRST BOLT HOLE DUE TO BOLT TENSION AND TWO VERTICAL LOADS

with this bolt tension the stresses are dominated by that tension but the vertical loading changes the stresses significantly.

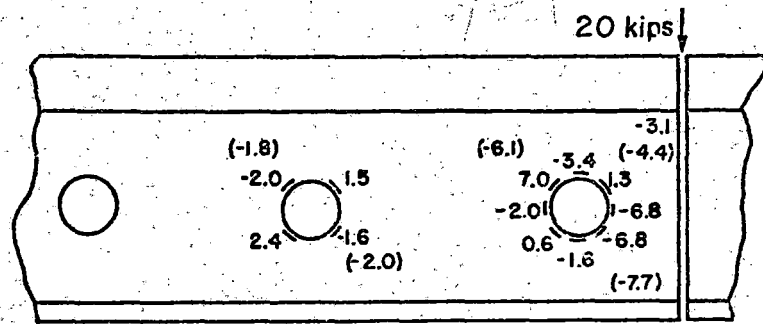
Movement of the point of wheel/rail contact along the rail alters the effect of the vertical load on bolt hole stresses. The changes in the stresses caused by varying longitudinal placements of a 20 ksi vertical load away from the joint are shown by several cases in Table 6-1. Cases involving four positions are illustrated in Figure 6-9, which shows measurements found when the load position was at the joint or 1.75 or 2.75 or 4.0 inches from the joint towards the rail with the gages. The longitudinal variations of the incremental stresses due to the load, as measured by six of the gages, are shown further in Figure 6-10. These measurements were made with a somewhat reduced bolt tension, namely 20 kips. It can be seen that the variation is very similar for diametrically opposite gages but is displaced with respect to the variations at other gages. The magnitude of this variation is also large enough to be significant.

6.2.4 Effect of Eccentric Vertical Loading

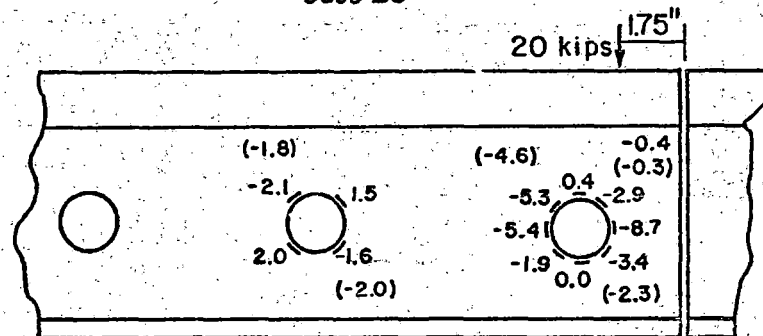
Cases 8, 9 and 10 of Table 6-1 delineate the effects of eccentric vertical load applied at the joint. Up to 0.75 inch eccentricity was used for this test. Figure 6-11 shows the incremental stresses incurred by a 20 kip vertical load on the rail with slightly loosened bolts, and Figure 6-12 shows the variation of these stresses around the bolt hole. These increments to the bolt holes stresses are fairly similar to those shown in Figure 6-8, but those from the eccentric load tend to be more tensile. The largest effects from eccentric loading, however, can be seen in the stresses at the head-web junction, as shown in Figure 6-11.

6.2.5 Effect of Lateral Load

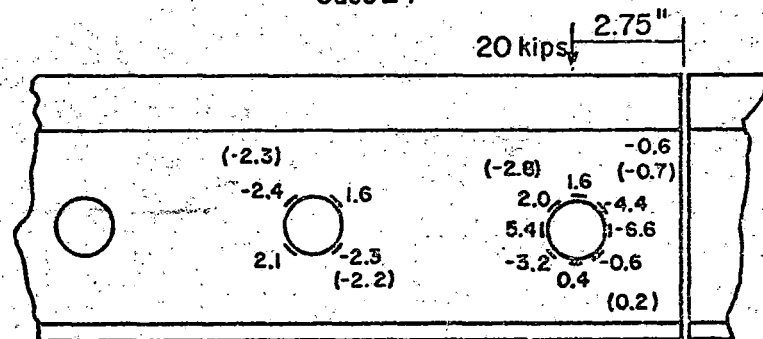
Cases 11, 12 and 22 show effects due to the application of a 10-kip lateral load to the rail head. It is observed that the lateral load results in tensile stress increments of relatively small magnitude. Of particular



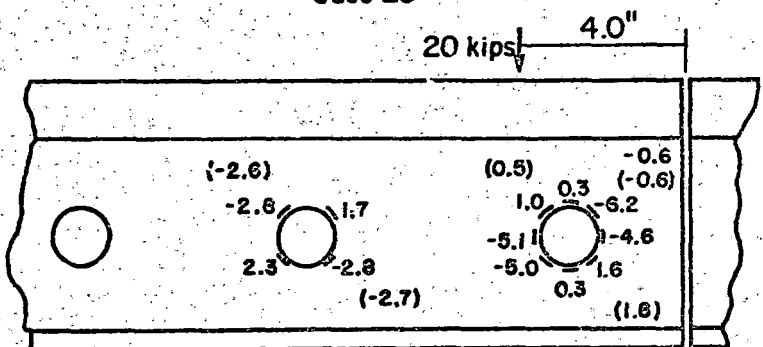
Case 23



Case 24



Case 25



Case 26

Bolt Tensions=20 kips, Foundation Modulus = 5000 psi

FIGURE 6-9. INFLUENCE OF LONGITUDINAL POSITION OF LOAD ON INCREMENTAL BOLT-HOLE STRESSES (IN KSI) DUE TO 20,000-LB VERTICAL LOAD

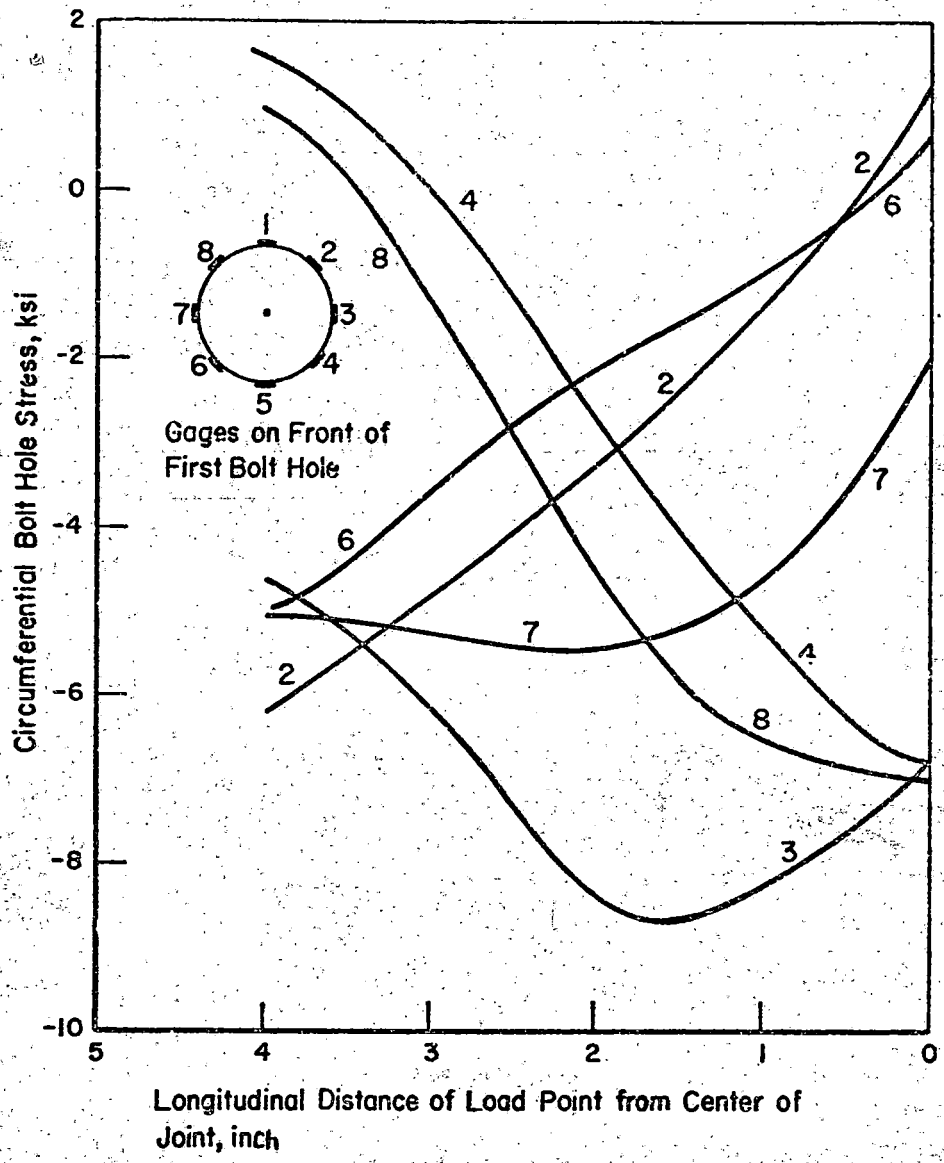
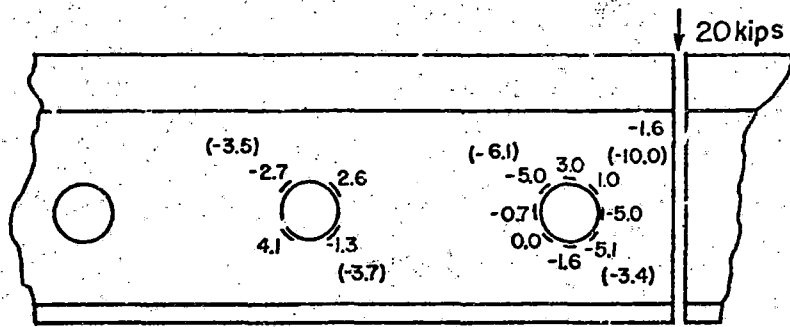
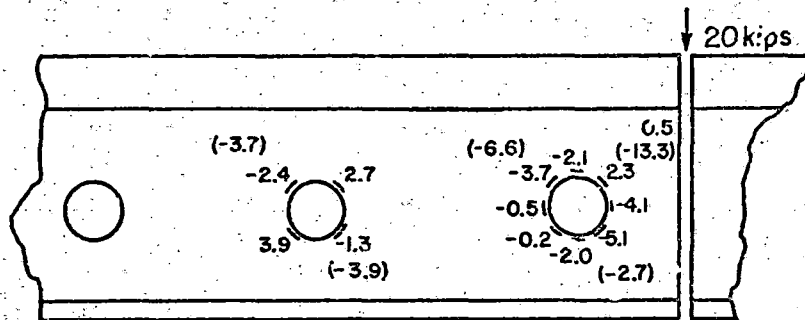


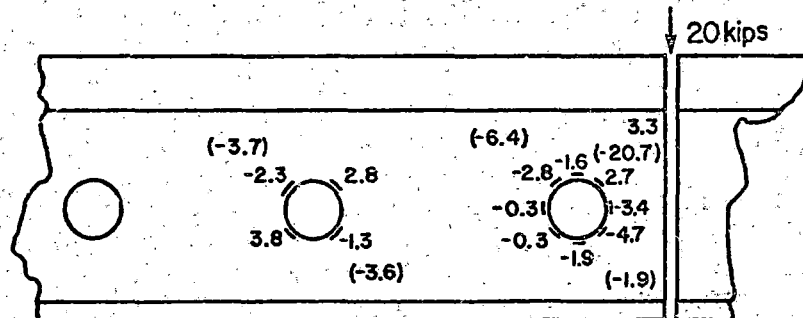
FIGURE 6-10. LONGITUDINAL VARIATIONS OF BOLT-HOLE-STRESS INCREMENTS DUE TO 20,000-LB VERTICAL LOAD (BOLT TENSION 20 KIPS)



Increments of Bolt Hole Stresses due to 0.25 inch Eccentric Vertical Load (Case 8)



Increments of Bolt Hole Stresses due to 0.50 inch Eccentric Vertical Load (Case 9)



Increments of Bolt Hole Stresses due to 0.75 inch Eccentric Vertical Load (Case 10)

FIGURE 6-11. EFFECT OF ECCENTRICITY ON BOLT-HOLE STRESSES DUE TO 20,000-LB VERTICAL LOAD (WITH BOLT TENSION APPROXIMATELY EQUAL TO 30 KIPS)

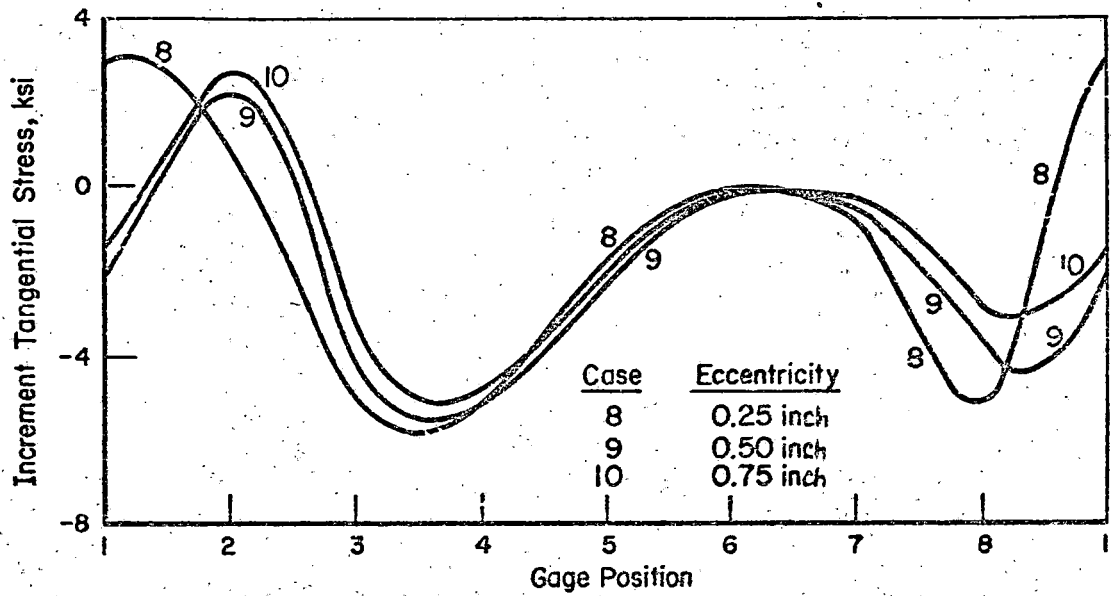
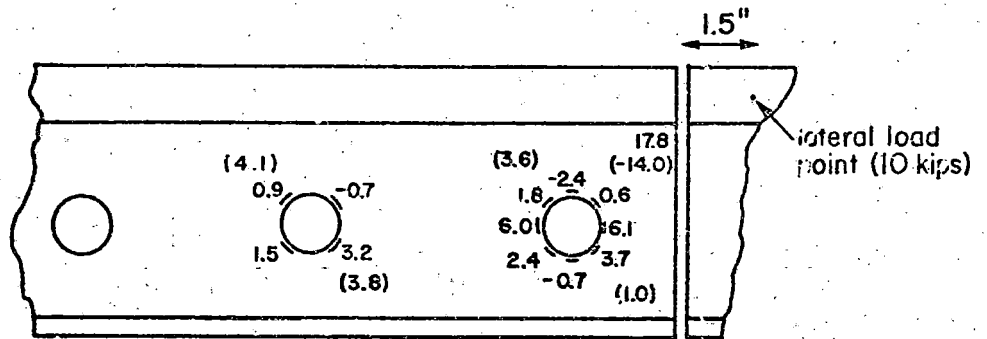


FIGURE 6-12. INCREMENTS OF TANGENTIAL STRESS ON FRONT SIDE OF FIRST BOLT HOLE DUE TO ECCENTRICITY OF 20,000-LB VERTICAL LOAD AT JOINT

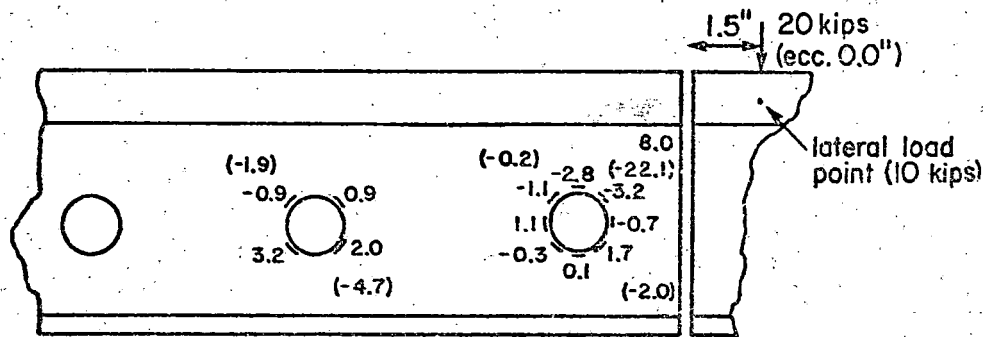
importance may be the very large tensile stress occurring in the fillet region at the rail head. Figure 6-13 presents results for the combined vertical and lateral loading, including Case 12 in which the vertical load also has an eccentricity 0.50 inch. These loading cases are detrimental to rail life.

6.2.6 Effect of Variation in Foundation Modulus

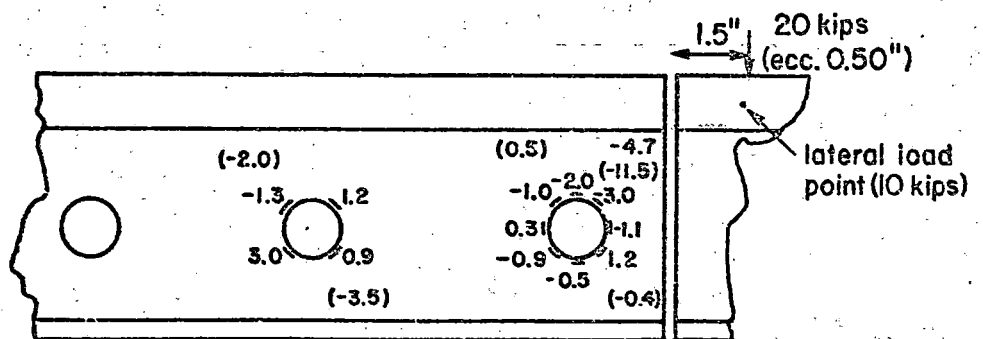
Figure 6-14 presents the effect of variation in foundation modulus on the first bolt hole stresses. The moduli considered were 1, 5, and 10 ksi respectively. It is observed that this change in support condition had a considerable effect on the stress at the upper 45-degree position and on that at the lower 45-degree position. Figure 6-15 also presents these results, and there it can be seen that the stresses change considerably as the modulus changes from 1000 psi to 5000 psi, but not as it changes from 5000 psi to 10,000 psi.



Increments of Bolt Hole Stresses due to 10,000 lb. Lateral Load (Case 11)

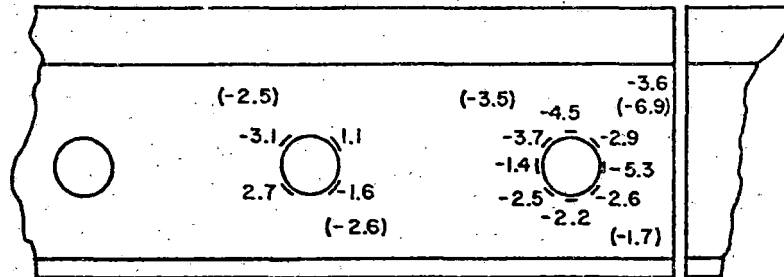


Increments of Bolt Hole Stresses due to 10 kip Lateral Load and 20 kip Vertical Load (Case 22)

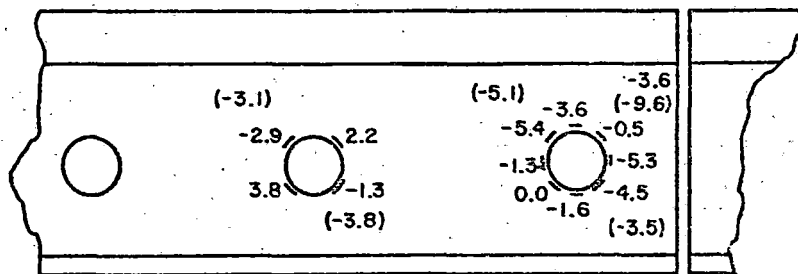


Increments of Bolt Hole Stresses due to 10 kip Lateral Load and 20 kip Eccentric Vertical Load (Case 12)

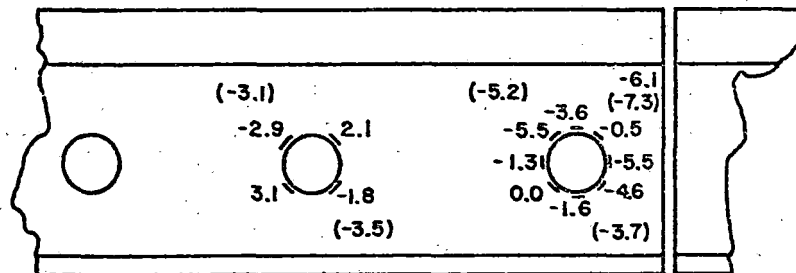
FIGURE 6-13. EFFECT OF LATERAL AND VERTICAL LOADS ON BOLT-HOLE STRESSES (WITH BOLT TENSION 30 KIPS)



Foundation Modulus 1000 psi (Case 18), Bolt Tensions 29,19,29,23, 28,28 kips



Foundation Modulus 5000 psi (Case 6), Bolt Tensions 28,19,28,23,28,28 kips



Foundation Modulus 10,000 psi (Case 17), Bolt Tensions 29,19,28,23,29,28 kips

FIGURE 6-14. INFLUENCE OF FOUNDATION MODULUS ON INCREMENTAL BOLT-HOLE STRESSES DUE TO 20,000-LB VERTICAL LOAD

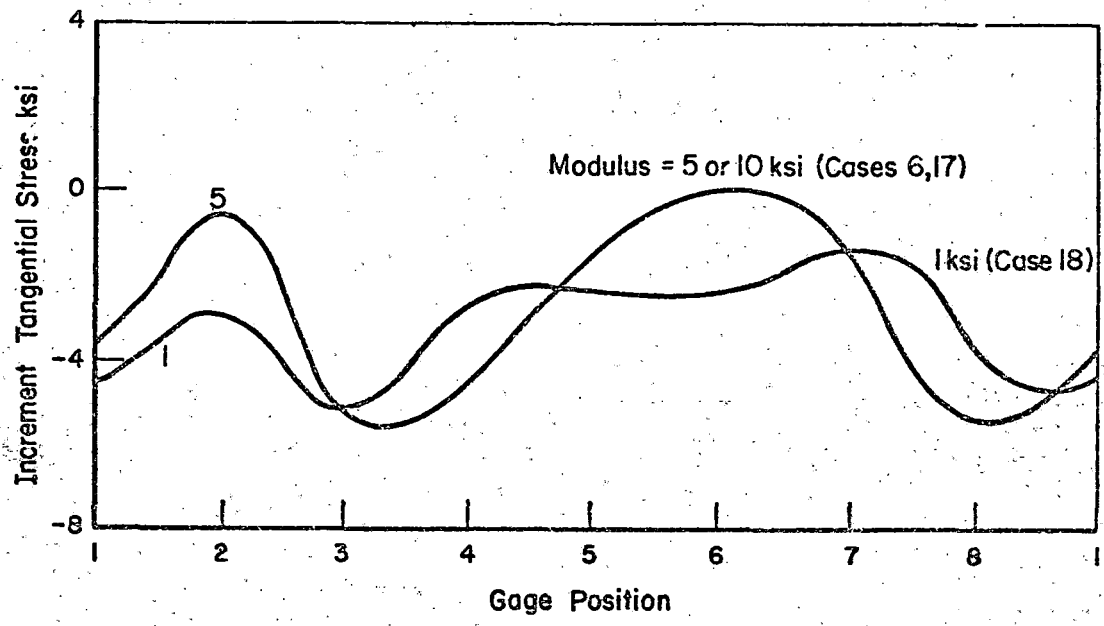


FIGURE 6-15. INFLUENCE OF FOUNDATION MODULUS ON INCREMENTAL TANGENTIAL STRESS ON FRONT SIDE OF FIRST BOLT HOLE DUE TO 20,000-LB VERTICAL LOAD AT JOINT

7. LOAD TRANSFER IN BOLTED JOINTS

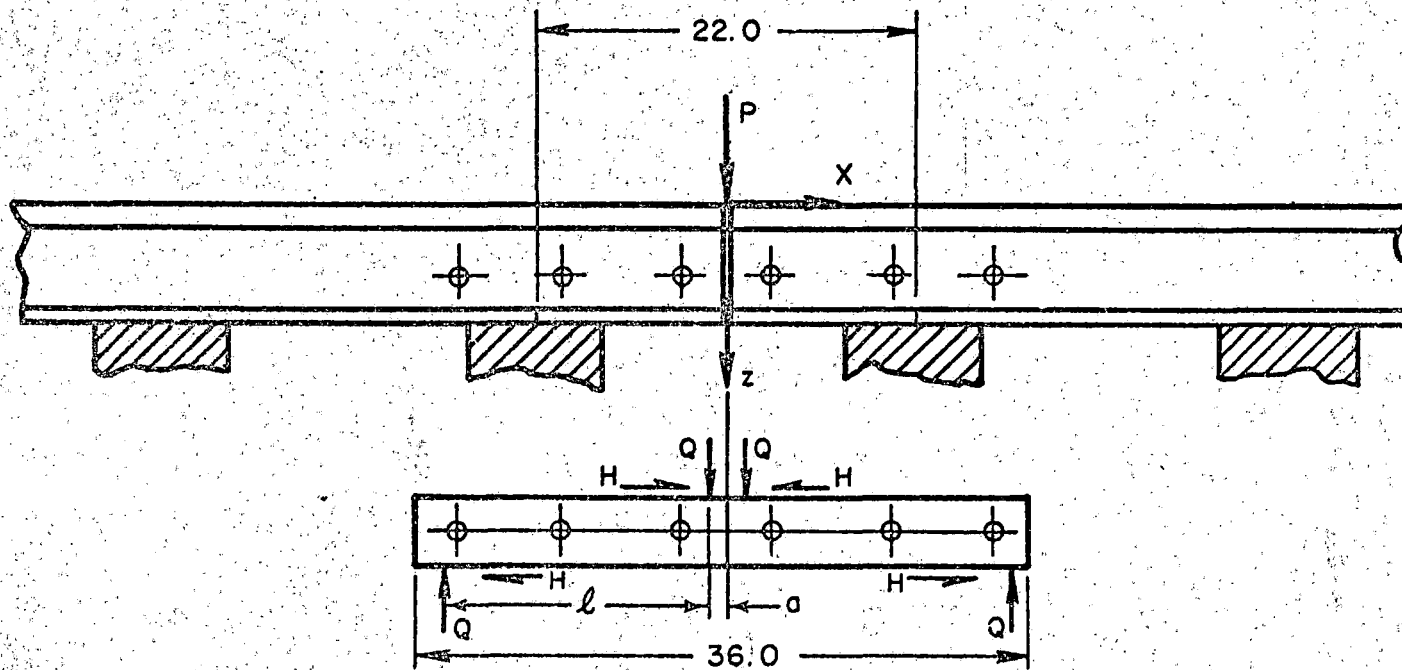
Joint bars bridge the discontinuous rail ends by providing for the transfer of bending moment. In presently recommended symmetric joint bar types, however, the moment of inertia of the two joint bars is significantly less than that of the continuous rail. As a result, the presence of the joint disrupts the uniform bending stiffness of the rail, and of necessity the uniform distribution of the tie bearing pressures that might otherwise exist. Because of this, rail deflections can be significantly greater at joints, and even under the best of circumstances, the bolted joint in its present form creates a weak spot in the track structure.

This chapter presents analytical methods for assessing load transfer and the results of their application to calculating the internal joint forces acting between bar and rail as a result of rail bending. The first subsection presents an approximate method for calculating joint resultants using beam-on-elastic-foundation models. The second subsection describes a two-dimensional finite-element load transfer model and the results obtained with it. The two analytical approaches are compared with experimental results and the techniques assessed in relation to the overall joint problem in the final subsection.

7.1 A SIMPLIFIED APPROACH TO LOAD TRANSFER: BEAM ON ELASTIC-FOUNDATION MODEL OF JOINTED-RAIL TRACK

Before beam-on-elastic-foundation analysis is applied to a rail containing a bolted joint, the mechanisms of joint bar action are discussed qualitatively. Figure 7-1 depicts the type of joint being considered together with its important dimensions. The action of the joint bar is to transmit moment by being placed in a state of four-point bending, as shown in Figure 7-1. The forces Q are the resultants of contact pressure distributions.

It was reported by Talbot [7-1] that the upper load bearing areas extended approximately 2 inches from the rail end and have their centroids about 1 inch from the rail end. For a 24-inch-joint bar, the lower bearing is thought to be 3 inches long and is approximately 7 inches away from the upper



7-2

FIGURE 7-1. RAIL JOINT DIMENSIONS AND JOINT BAR FREE-BODY DIAGRAM, INCHES

bearing area. For 36-inch-joint bars, the centroids of the lower bearing areas tend to be somewhat further away than for the 24-inch-joint bars.

Bending moments may also be reacted in rail joints by the action of frictional forces, H , as shown in Figure 7-1. The limiting value of these moments is, however, quite small when compared to moments that result from the normal bearing forces. The maximum contribution of frictional forces may amount to 13 percent of the applied moment.

It is immediately apparent that regardless of the wheel position, all of the moment must be carried by the joint bars at the center of the joint. Examination of the partition in bending moment between joint bar and rail arising from a passing, static wheel load indicates that maximum joint bar moment and, hence, maximum joint bar resultant, Q , occurs with the wheel directly over the center of the joint. Figure 7-2 [7-1] presents the distribution of bending moment when the wheel load is directly over the rail ends. For a load some distance away from the joint center, the relative proportion of moment is shown in Figure 7-3 [7-1]. Although from these examples, it is seen that the maximum static joint bar moment occurs when the load is directly over the joint, it will now be shown that the maximum total moment will occur when the maximum dynamic load condition occurs.

The presence of a rail joint invariably leads to a local perturbation in the support conditions, which in turn, leads to a dipping of the joint. This dip in the joint gives rise to a pair of dynamic, joint impact forces, referred to in rail literature, as P_1 , the rail end impact force and P_2 , the point of full load application on the running on rail. These forces can be many times larger than the static wheel load, depending on a number of factors. P_1 occurs first and is generally much larger in magnitude but of much shorter duration than P_2 . Also, the former occurs at a point near the end of the running on rail and is of sufficiently high frequency to be reacted primarily by the rail itself without resulting in appreciable bending or reaction in the ballast. Thus, P_1 is generally regarded as being primarily responsible for the extensive rail end batter that often occurs at dipped joints. P_2 , however, occurs 6 to 8 milliseconds later as the rail and wheel rebound from joint passage and reaching full suspension loads. P_2 is of sufficiently low frequency to be reacted by the ties and ballast in the usual fashion. Thus,

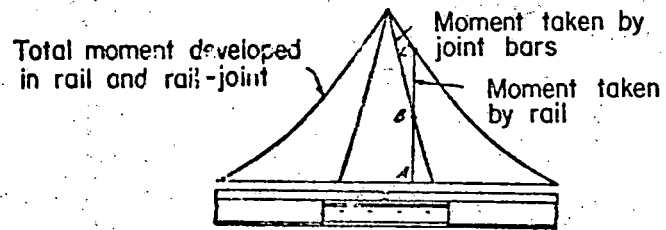


FIGURE 7-2. DIVISION OF MOMENT BETWEEN RAIL AND JOINT BARS [7-1]

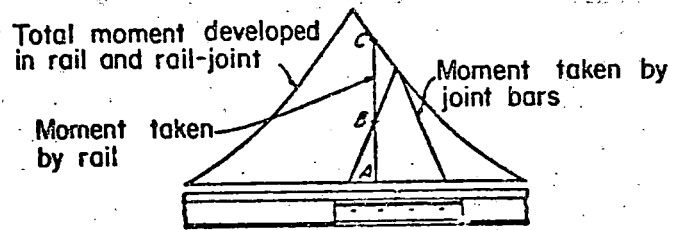


FIGURE 7-3. MOMENT IN RAIL AND JOINT BARS - WHEEL AWAY FROM RAIL END [7-1]

the maximum wheel load, and by implication, bending moment that will be of concern in the problem of rail end cracking will occur about 5 to 8 inches from the end of the running on rail. The joint reactions resulting from this dynamic load on the running on rail will have the same effect on the running off rail end in the joint.

The beam-on-elastic-foundation model is now applied to the case of rails connected with a bolted joint.

The modeling of the rail as a beam-on-elastic foundation represents the earliest attempt to describe the behavior of loaded rail. This approach was introduced by Winkler [7-2] in the latter part of the 19th Century. (Historical data and a more detailed description of the approach were presented by Johns and Davies [7-3].) For the infinite rail, as shown in Figure 2-1, the basic differential equation governing the vertical deflection W is,

$$EI \frac{d^4 W}{dx^4} + kW = 0 \quad (7-1)$$

and has the solution

$$W(x) = \frac{P\beta}{2k} e^{-\beta x} (\sin \beta x + \cos \beta x) \quad (7-2)$$

$$\beta = \sqrt[4]{\frac{k}{4EI}}$$

where P = the applied load

k = the foundation modulus of the track

EI = the stiffness of the rail.

Equation (7.2) yields, upon differentiation, the moment equation,

$$M(x) = \frac{P}{4\beta} e^{-\beta x} (\cos \beta x - \sin \beta x) \quad (7-3)$$

The results from Equations (7-1) and (7-3) are conveniently illustrated in Reference 7-3 in the nondimensional graphical form presented in Figure 2-3.

It is important to note that although the beam-on-elastic-foundation model assumes a continuous foundation, it is applicable to cross-tie track as long as the tie spacing l_t is less than that given by

$$l_t = \frac{\pi}{4} \sqrt[4]{\frac{4EI}{k}} \quad (7-4)$$

a result first presented by Hetenyi [7-4].

Numerous investigations, as described in [7-3] have shown this approach yields results that are in good agreement with experiment when the value of k is known accurately.

Talbot [7-1] described a beam-on-elastic-foundation solution based on the assumption that the resisting moment at the joint is less than that in the rest of the rail. A parameter, K , is then defined as the ratio of the resisting moment of the joint to the resisting moment the rail would have at that location if the joint were absent. A brief consideration shows that the inequality $0 \leq K \leq 1.0$ must hold. The limiting case $K = 0$ corresponds to the situation of two free, unconnected, rail ends (as shown in Figure 7-4) while $K = 1.0$ corresponds to the case of a continuous rail (Figure 7-5). It is observed that for the discontinuous rail end, the deflection can be approximately twice as large as that for the continuous rail.

The parameter, K , may be regarded as a load-transfer coefficient which expresses the relative efficiency of the joint. Its magnitude for a given track situation is related to the relative moments of inertia of the joint bars and the rail cross-section.

Assume that the maximum bending moment for the joint loading situation depicted in Figure 7-1 is given by

$$M(0) = P/(4\beta) \quad (7-5)$$

Assuming that the joint is less stiff than a perfectly efficient joint, and using the factor K as suggested by Talbot [7-1]

$$K = M_J/M(x)$$

yield,

$$M_J = KM(x) = \frac{KP}{4\beta} e^{-\beta x} (\cos \beta x - \sin \beta x) \quad (7-6)$$

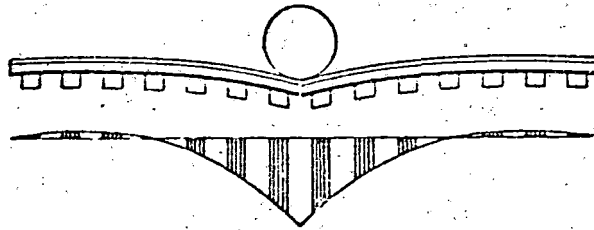


FIGURE 7-4. DEPRESSION OF RAIL AND UPWARD REACTION FORCES AT AND FROM THE TIES FOR A SINGLE WHEEL LOAD WHEN NO MOMENT IS RESISTED AT THE RAIL ENDS [7-1]

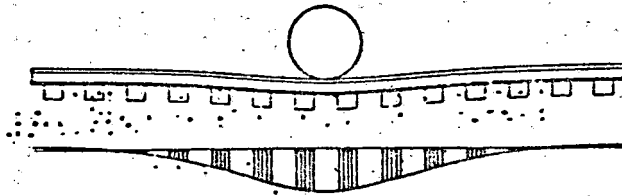


FIGURE 7-5. DEPRESSION OF RAIL AND UPWARD REACTION FORCES AT END FROM THE TIES FOR A SINGLE-WHEEL LOAD [7-1]

But for a joint bar in four-point bending

$$M_J = Ql \quad (7-7)$$

where Q and l have the same definition as in Figure 7-1. Substituting Equation (7-7) into Equation (7-6) and solving for Q yields the magnitude of the joint bar resultants

$$Q = \frac{KP}{4\beta l} e^{-\beta x} (\cos \beta x - \sin \beta x) \quad (7-8)$$

In this expression, K and l are, for the time being, undetermined quantities. It is emphasized that, as shown in Figure 7-1, Q always acts opposite to P and tends to bend the rail end up.

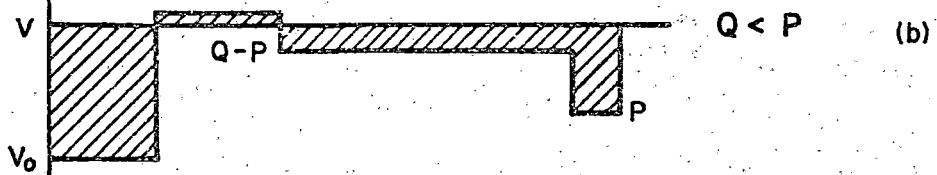
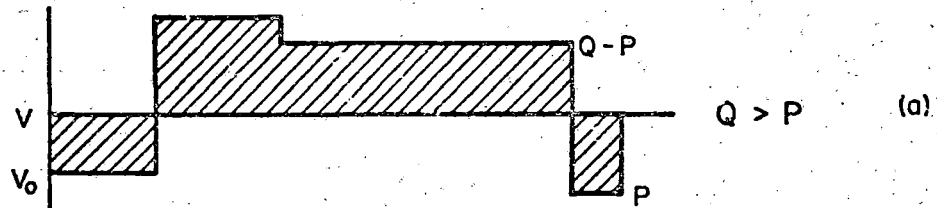
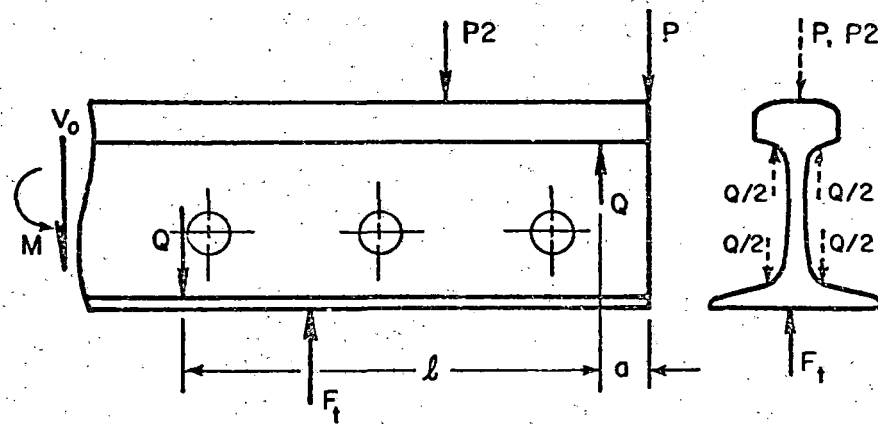
Equation (7-8) yields important information on the behavior of joints, in particular the condition for which end cracking is likely to occur at a specific location and direction. Of particular interest, when the wheel load is at the rail end, the situation

$$Q > P \quad (7-9)$$

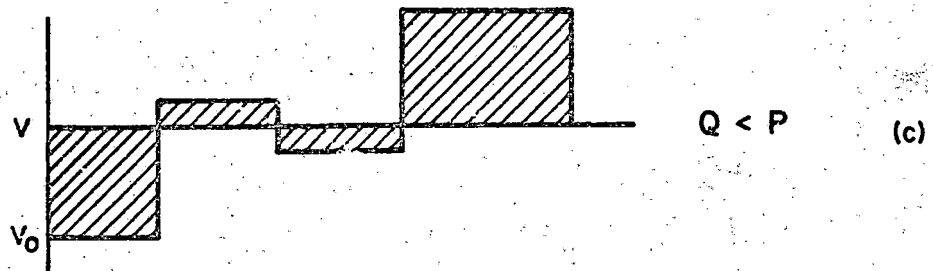
is created if

$$K/4\beta l > 1 \quad (7-10)$$

To illustrate this situation in relation to that when $Q < P$, consider the free body and shear diagrams shown in Figure 7-6. At the first bolt hole, the shear is positive or negative depending on whether or not $Q > P$. As will be shown later, positive shear results in the maximum tangential stress occurring 90 degrees away from the maximum shear due to negative shear. It is hypothesized that this phenomenon accounts for the location of failures observed in service. However, when the wheel load represents the P2 case, the wheel is past the first bolt hole, i.e., the shear at the location is entirely due to Q and, hence, is always positive (as is also shown in Figure 7-6).



(a) and (b) are possible shear diagrams for rail end load



(c) is shear diagram when P2 occurs

FIGURE 7-6. FREE-BODY AND SHEAR DIAGRAM FOR A RAIL END FOR VARIOUS WHEEL LOAD POSITIONS

Examination of Equation (7-8) shows Q to vary with the unknown parameter, K . As was mentioned previously, its value for a particular joint will depend on the relative moments of inertia of the rail ends and joint bars.

The undetermined quantities are now considered. For a given case, K may be calculated by rewriting its definition as

$$K = M_j/M = \frac{P/4\beta_j}{P/4\beta} = \frac{\beta}{\beta_j} \quad (7-11)$$

When the sum of the moment of inertias of the two joint bars is taken as I_j , and the foundation parameter K is held constant, Equation (7-11) yields:

$$K = (I_j/I_{\text{rail}})^{0.25} \quad (7-12)$$

The parameter given by this result represents the upper bound of possible joint efficiency. For the 132-pound RE rail and short-toe joint bars, it is found that

$$K = (29.7/88.2)^{0.25} = 0.762 \quad (7-13)$$

The other unknown parameter in Equation (7-8), l , is now considered. Recall that l is the distance between the joint bar resultants. Talbot [7-1] reports that little variation in l occurs under different loading conditions for a given joint. Examination of a typical symmetrical joint bar suggests that the possible range of variation cannot be too large.

It is important to note, however, that for a 24-inch-joint bar, l may be almost as small as half that for a 36-inch-joint bar. Thus, significantly larger internal reactions may be expected in the shorter joint bars. The magnitude of l in any given case will be a function of the bolt tension and the joint bar fit as affected by wear and initial tolerances. Unfortunately, the effects of both of these variables cannot be quantified directly by using the beam-on-elastic-foundation model. However, the effect of bolt tension on bolt hole stress has already been delineated experimentally, as was shown in Table 6-1. Variation in bolt tension has its most pronounced effect, on the

incremental stresses due to wheel loads, for values less than about 4,000 pounds/bolt. The reversal in maximum tensile stress locations for values less than 1,000 pounds/bolt, suggest that a transition to $Q < P$ behavior occurs. From Table 6-1, it is hypothesized that large bolt tensions are not required to develop sufficient wedging action to ensure full effectiveness of the joint. Further implications of the experimental work will be discussed when the approach summarized by Equation (7-8) and the numerical approach to be described are compared with the laboratory results.

The effects of parametric variation of l are now considered for a range of values of k . For the 132-pound RE rail with symmetric 36-inch joint bars, the relation between Q and P are shown for $K = 0.762$, in Figures 7-7 through 7-11. In each case, l is varied from 10.0 to 15.0 inches. Plotted on the graph is the line $Q = P$ which divides the regimes of positive and negative shear force in the first bolt hole region when the wheel load is at the rail end. Also plotted is a constant line representing the value of Q that causes joint bar yielding at the extreme fiber. Referring to Figure 7-1, the maximum bending stress is given by

$$\sigma = \frac{Qlc}{I_j} \quad (7-14)$$

For this particular case, $l = 13$ inches, $c = 2.5$ inches, and $I_j = 29.7$ inches⁴. Thus, assuming a tensile yield stress of 70.1 ksi [7-5] for the joint bars, the onset of yielding is given with sufficient accuracy by $Q = 64.1$ kips for $l = 13$ inches.

Examination of Figures 7-7 through 7-11 show the effect of foundation modulus. A decreasing foundation modulus, that occurs under a dipped joint, leads to increasing joint reaction, Q . This local pathological condition was cited as the important contributing factor in the Hither Green accident [7-6].

So far the discussion has been limited to the action of vertical wheel loads along the centerline of the rail. It is also possible for both eccentric vertical and lateral wheel loads to occur. The action of the lateral loads at joints may be modeled in exactly the same way as has been described for vertical load cases. This is not presented, however, since the magnitude

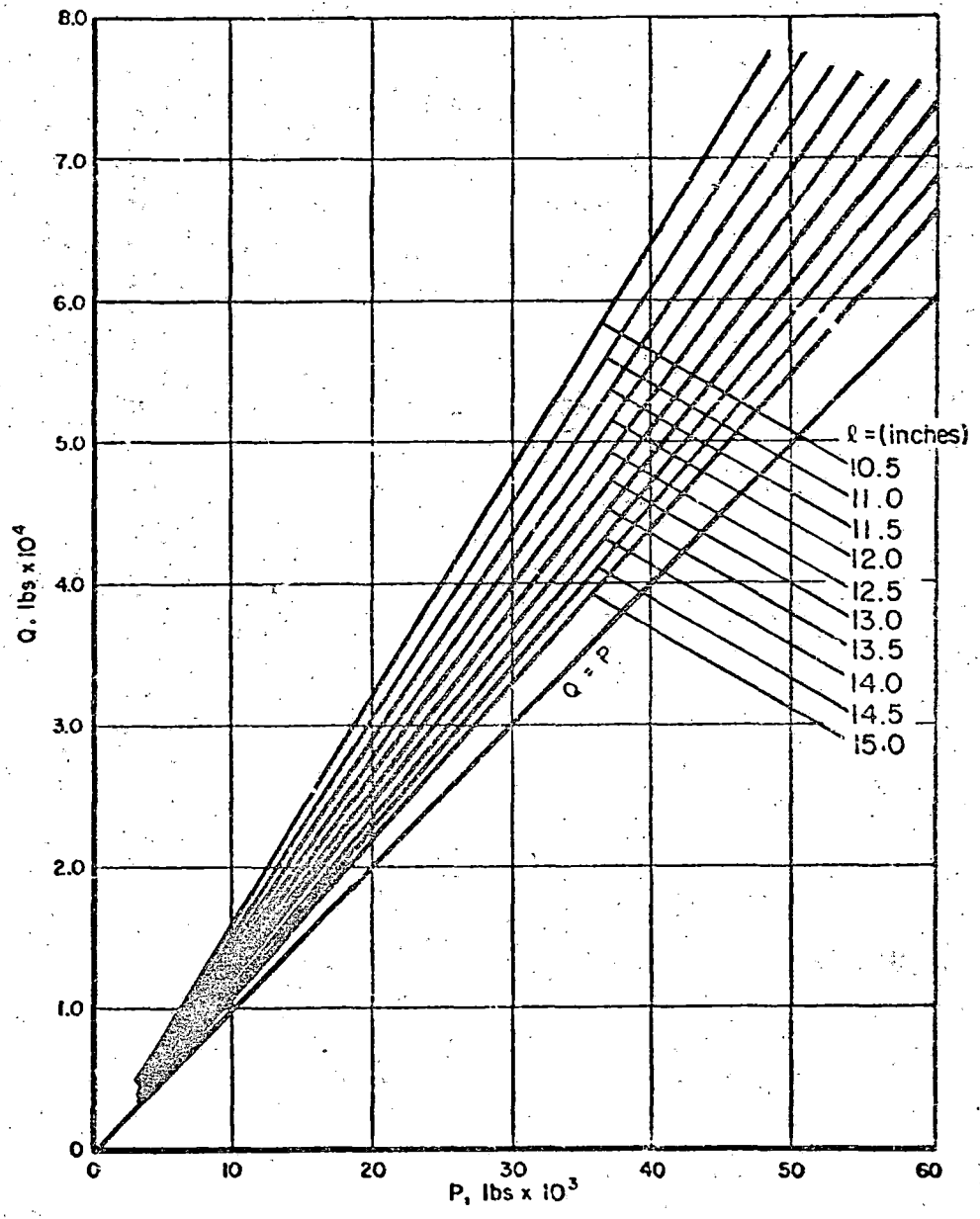


FIGURE 7-7. JOINT RESULTANT Q AS A FUNCTION WHEEL LOAD FOR FOUNDATION STIFFNESS $k = 200$ PSI

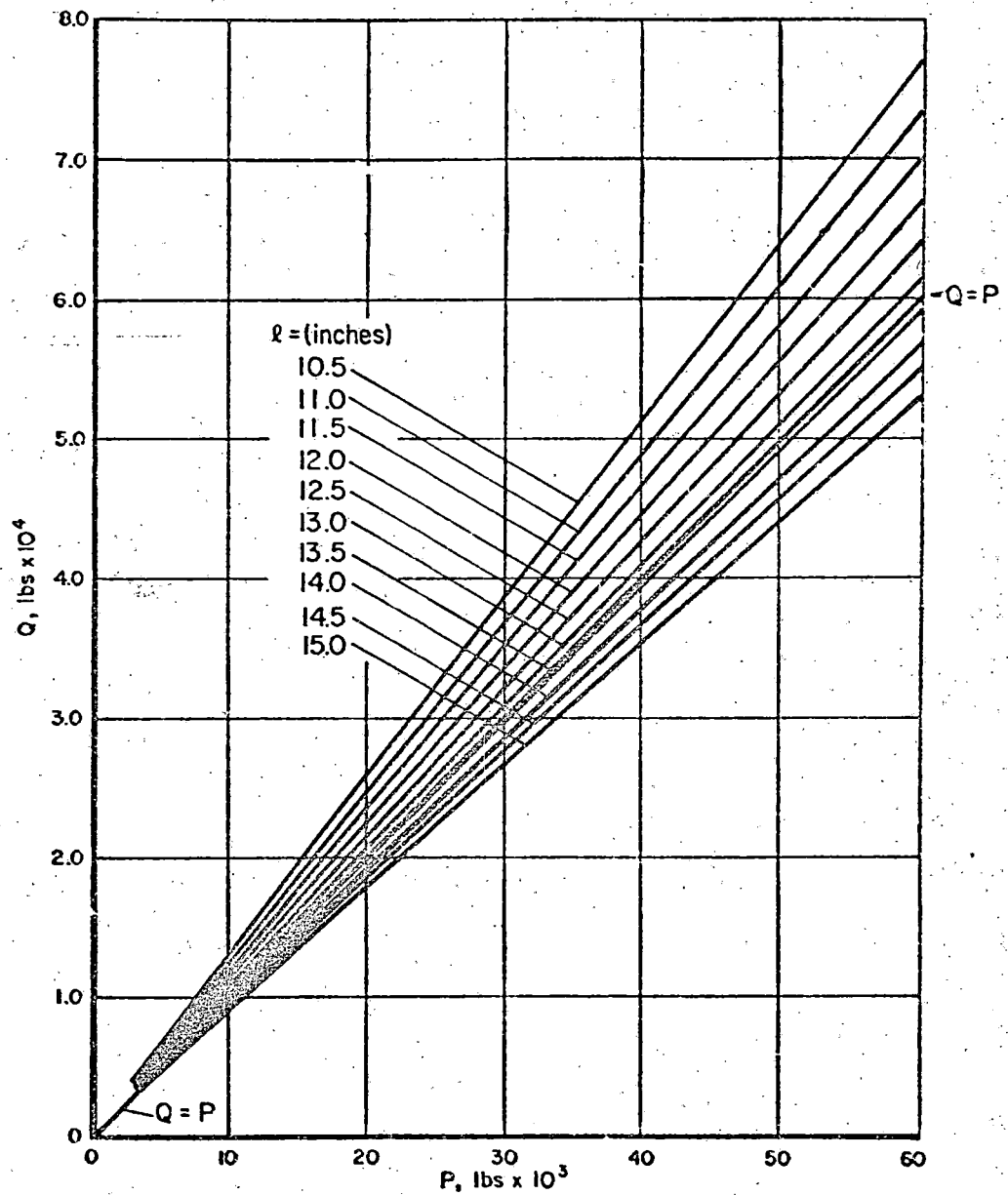


FIGURE 7-8. JOINT RESULTANT Q AS A FUNCTION WHEEL LOAD FOR FOUNDATION STIFFNESS $k = 500$ PSI

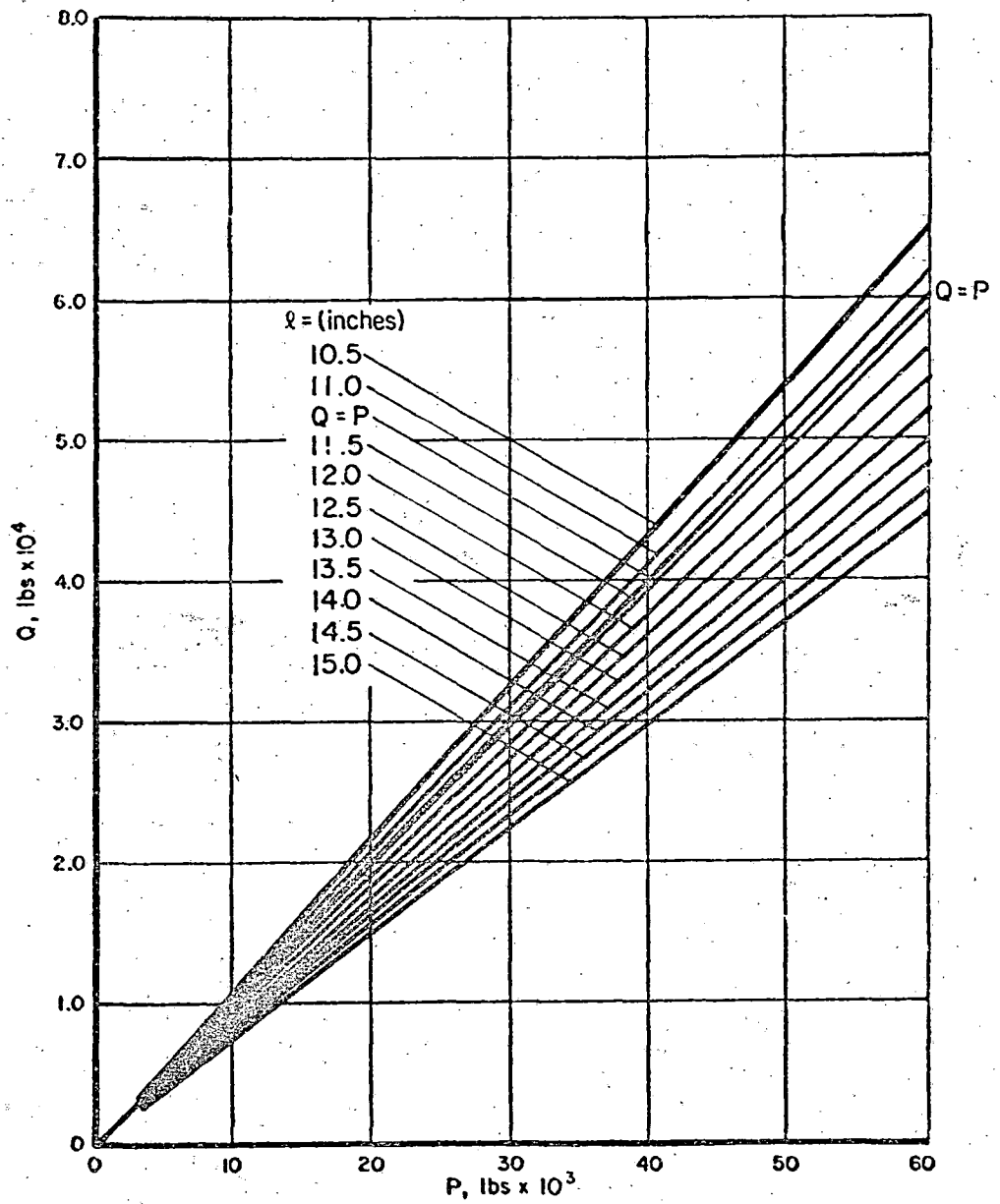


FIGURE 7-9. JOINT RESULTANT Q AS A FUNCTION WHEEL LOAD FOR FOUNDATION STIFFNESS $k = 1,000$ PSI

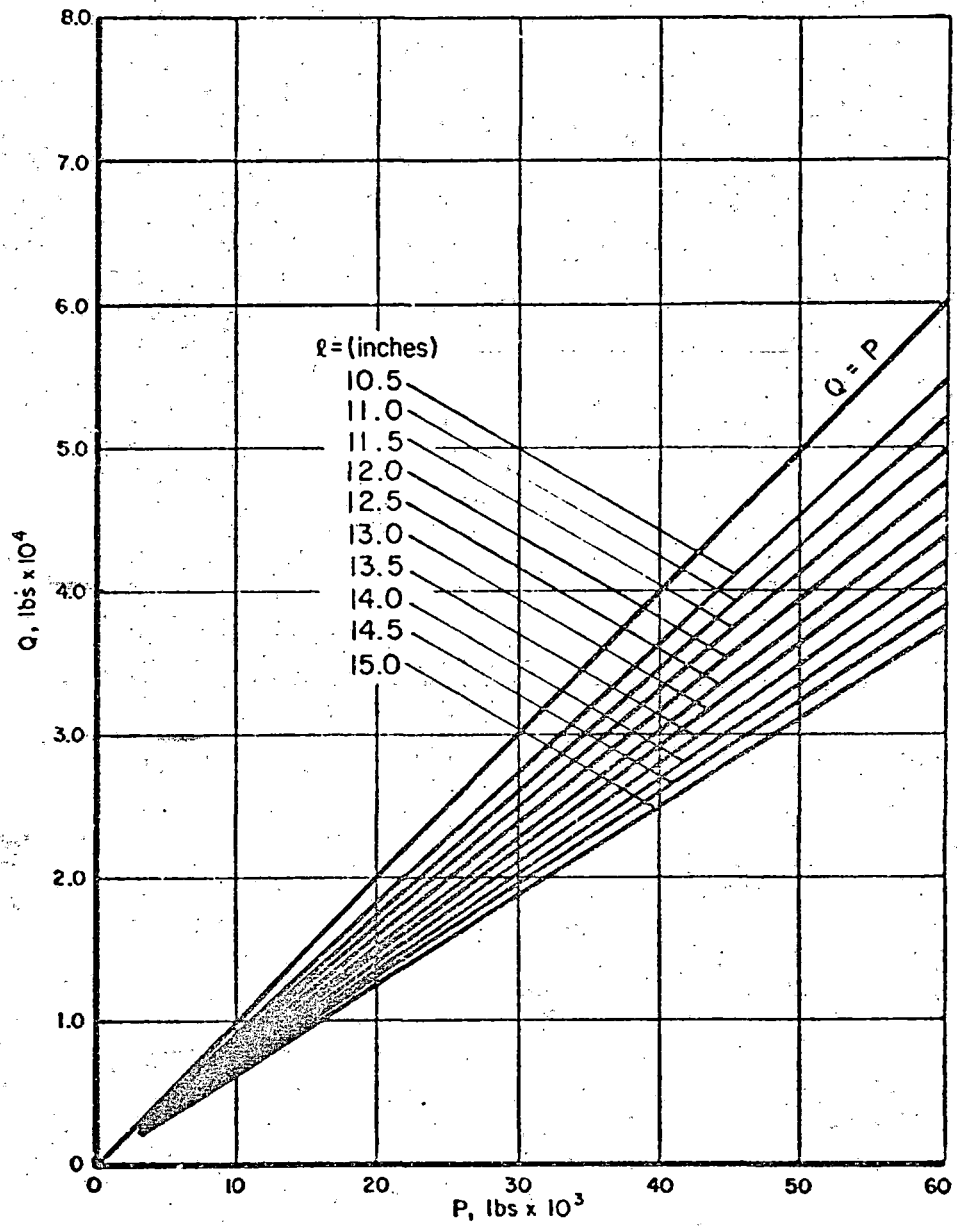


FIGURE 7-10. JOINT RESULTANT Q AS A FUNCTION WHEEL LOAD FOR FOUNDATION STIFFNESS $k = 2,000$ PSI

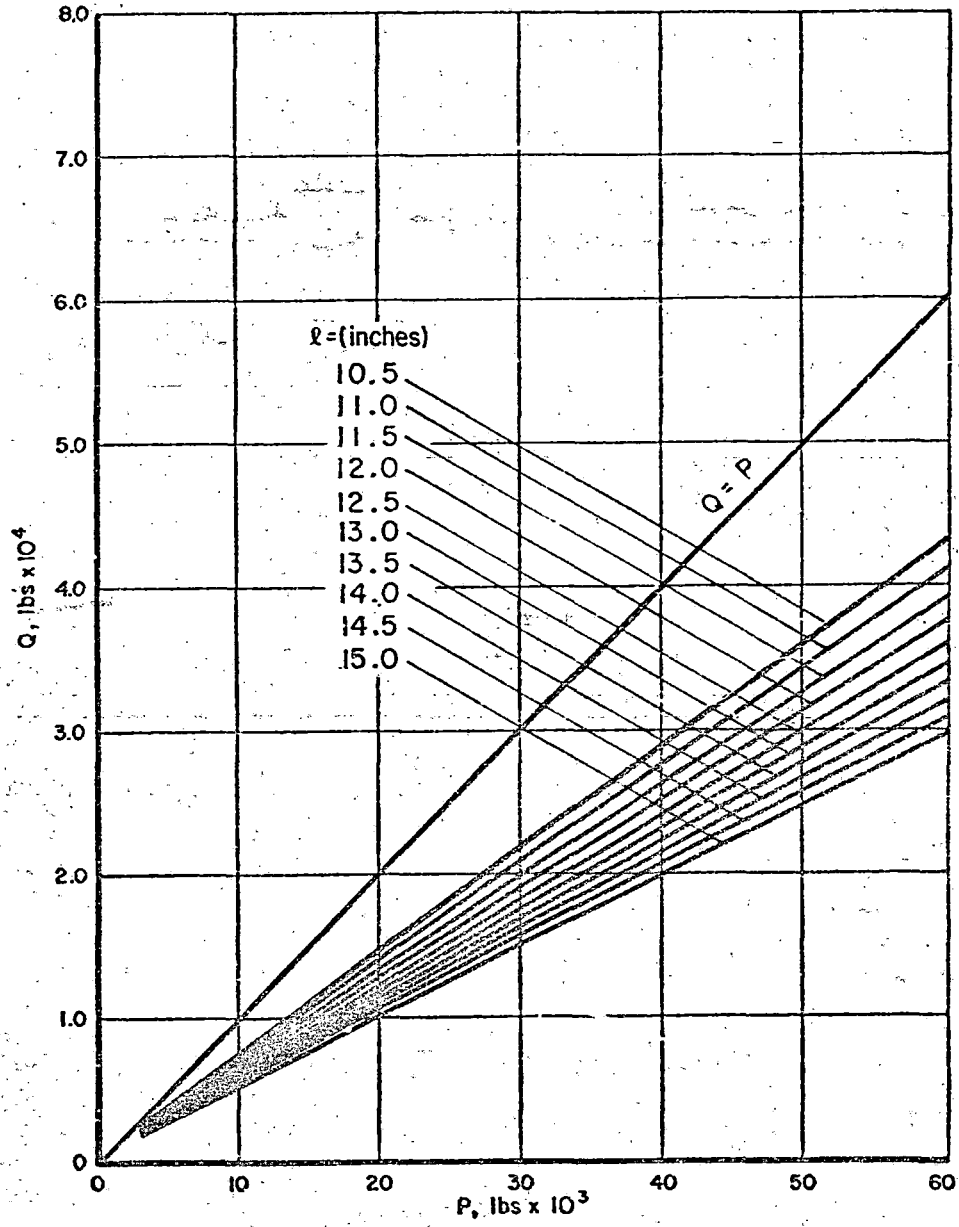


FIGURE 7-11. JOINT RESULTANT Q AS A FUNCTION WHEEL LOAD FOR $k = 5,000$ PSI

of lateral loads due to curving or creepage can only be small compared to the dynamic vertical load. Although these effects are not considered from a load transfer standpoint, combined loadings are analyzed in the stress analysis of rail ends considered in the next chapter.

This section has presented a simplified approach to the calculation of joint bar resultants. A very useful relationship, Equation (7-8), which is suitable for use in a crack-growth-prediction program was defined, which allows the calculation of internal resultants for a variety of situations. The following sections of this chapter discuss a more sophisticated approach to load transfer and compare the various results with experimental data.

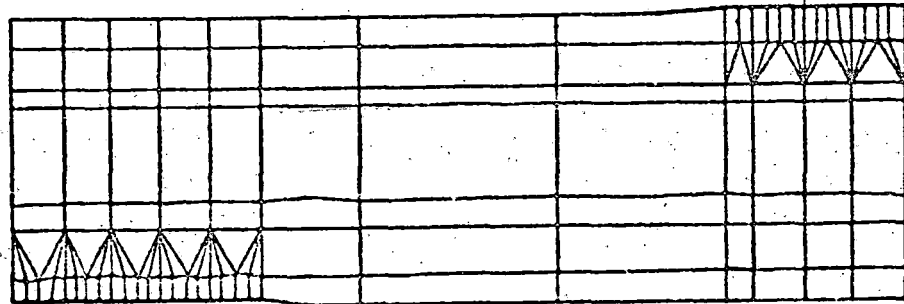
7.2 NUMERICAL LOAD TRANSFER MODELING

Although the simplified approach, presented in the previous section, has the advantage of being economical and easy to use, the presence of the more-or-less indeterminate parameter, f , poses a real disadvantage. Because of this, a numerical method that would predict both the magnitude and location of Q was pursued. It consisted of finite-element models of rail joints that could be used to solve iteratively for the internal forces. The formulation and application of these models is discussed in the following subsections.

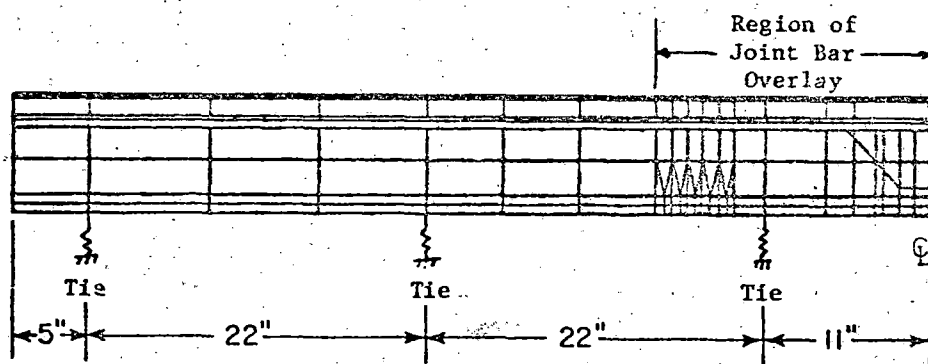
7.2.1 Finite-Element Models

Two finite-element models of joint load transfer were developed. The first of these, shown in Figure 7-12, was a symmetrical model designed to simulate the case of symmetrical wheel loading. The second, shown in Figure 7-13, was a rail-joint model permitting arbitrary location of the wheel load and the assumption of a bolt hole crack. Since the principles guiding the model-developments were the same, only the symmetric model will be described in detail.

The model consists of two pieces, a single joint bar of double thickness and the rail end. A standard 132-pound RE rail joint with headfree bars was simulated. The rail end was assumed to be 60.0 inches long and was supported by three ties spaced 22 inches apart. The model mesh was two-dimensional and



(a) Joint bar model (enlarged)



(b) Rail end model

FIGURE 7-12. TWO-DIMENSIONAL LOAD-TRANSFER SYMMETRICAL MODEL

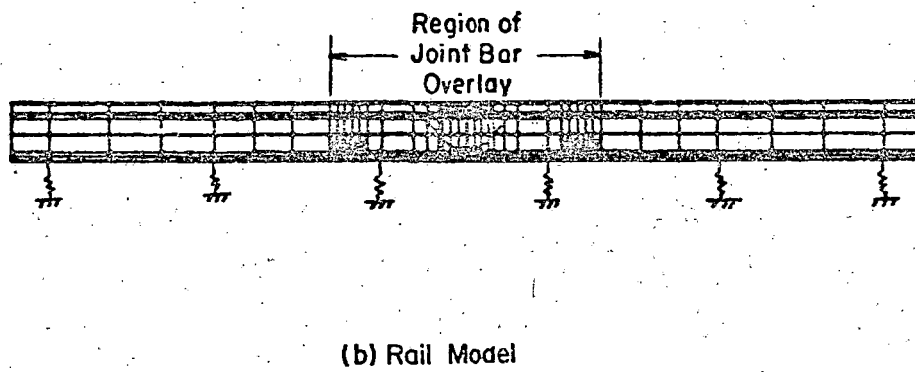
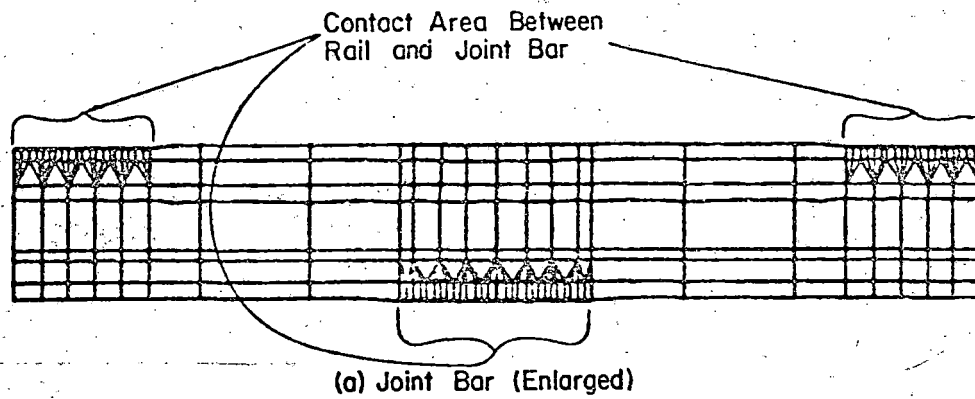


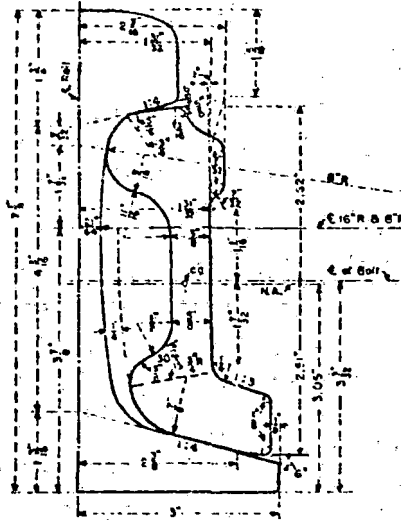
FIGURE 7-13. FULL RAIL-JOINT TWO-DIMENSIONAL LOAD-TRANSFER MODEL

thus capable of modeling the noneccentric vertical load cases only. The model size required for a three-dimensional model would be very large. The stiffness of the elements of the joint bar and rail ends were varied to simulate the sectional properties of the components. The simplified cross sections utilized are shown in Figures 7-14 and 7-15. The cross sections were approximated by rectangular sections. Eight node, isoparametric quadrilateral elements were used having the "thicknesses" shown in the figure.

Contact between rail and joint bar was assumed to occur over certain limited regions at the end and center of the bar as shown in Figure 7-12. These regions are 5.0 and 3.5 inches long for the outboard and inboard areas, respectively. The contact areas have significantly finer meshing than the rest of the model. Linear spring elements were used to connect the adjacent regions of contact between the joint and the rail end. Examination of the mating areas between the joint bar and rail indicated that essentially conformal, line contact could be expected to occur between them. The magnitude of the coupling stiffness reflected the influence of the joint fit and bolt tension. The implication of this stiffness variable and its relation to load transfer will be discussed in a later subsection.

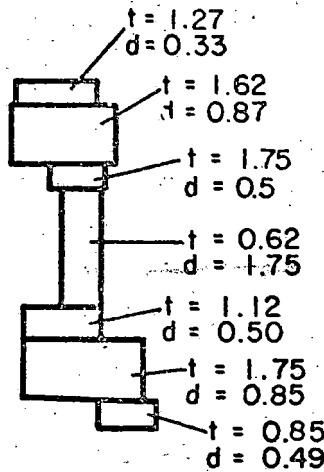
Boundary conditions were enforced to simulate actual track as closely as possible. Ties were represented by linear spring elements attached between the rail model and immovable points. The stiffness of these springs were sized by referring to foundation moduli defined in the beam-on-elastic-foundation sense. This was accomplished by discretizing the continuous foundation. For this purpose, it was assumed that the distributed resistance between ties was lumped at the adjoining ties. Thus, the appropriate spring rate was obtained by multiplying the modulus by the tie spacing, in this case, 22 inches. Boundary conditions at the end of the rail were formulated to simulate the bending stiffness of the infinitely long rail from which the model had been "cut". For this purpose, a beam-on-elastic-foundation model of a semi-infinite rail with an end moment was used. For this situation, Hetenyi [7-4] presents the following expression for the rotation of the beam end

$$\theta(0) = \frac{4M \beta^3}{k} \quad (7-15)$$



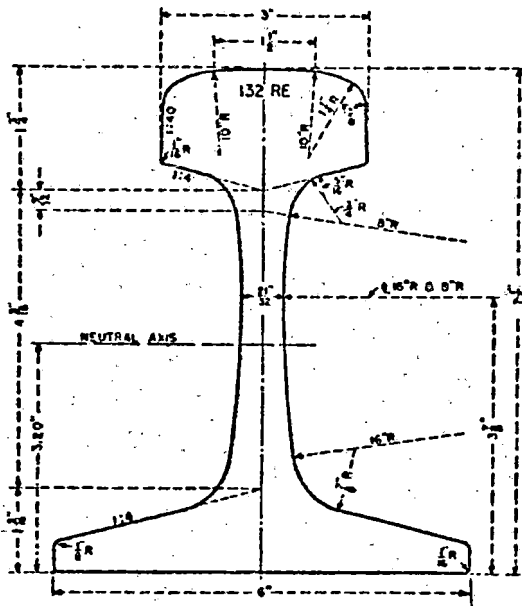
ASSEMBLY Physical Properties	SECTION	
	One Bar	Two Bars
Moment of Inertia in. ⁴	14.86	29.7
Section { Above n.a. in. ²	5.37	11.3
Modulus { Below n.a. in. ³	5.92	11.8
Area sq in	5.65	11.3
Net weight, 24-in length, lb	37.7	75.4
Net weight, 34-in length, lb	56.5	113.0

(a) Joint Bar and Properties

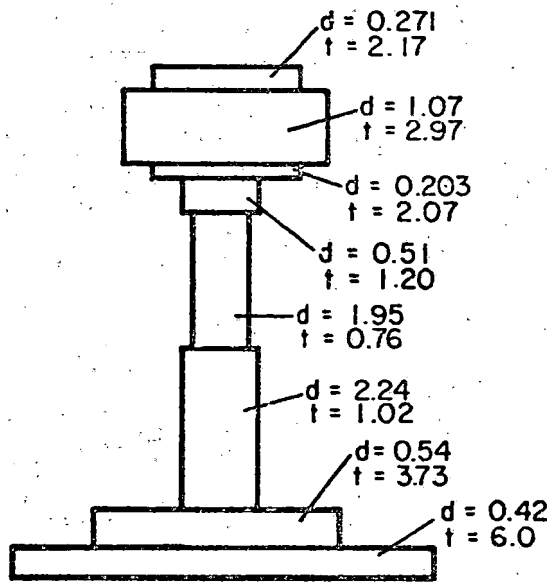


(b) Joint Bar: 2-Dimensional Model

FIGURE 7-14. SIMPLIFIED 132-LB RE JOINT BAR CROSS SECTION



(a) Actual Rail Cross-section



(b) Simplified 2-Dimensional Model

FIGURE 7-15. SIMPLIFIED 132-LB RE RAIL SIMULATED BY 2-D ELEMENTS OF VARYING THICKNESS

which may be rearranged to give

$$M = (k/4B^3)\theta \quad (7-16)$$

Since this has the same form as the moment-rotation relation

$$M = G\theta$$

The rotational stiffness may be identified as being

$$G = \frac{k}{4} \left(\frac{k}{4EI} \right)^{3/4}$$

In the finite-element model, this stiffness was represented by two linear springs which could resist rotation and whose stiffness values were chosen to be consistent with Equation (7-17). Assuming small rotations and letting the springs of stiffness K' be separated by a distance d , the relation

$$K' = \frac{k}{2d^2 \left(\frac{k}{4EI} \right)^{3/4}}$$

was obtained. For some typical values of foundation moduli, the necessary spring rates are presented in Table 7-1, for $d = 12$ inches.

TABLE 7-1. SPRING STIFFNESS FOR SIMULATING CONTINUOUS RAIL RESISTANCE TO BENDING

Foundation Modulus, psi	Spring Stiffness, K' (lb/in)
500	5.43×10^5
1000	6.46×10^5
5000	9.66×10^5

For the symmetrically loaded case, only the translational freedom in the vertical plane was imposed on the joint bar at its centerline.

Reasonableness of results using the finite element model was validated by comparing it with a strength of materials solution for a rail end undergoing cantilever bending. Figure 7-16 shows the agreement between the stresses obtained by the two alternate approaches.

7.2.2 Method of Solution

In order to calculate the force distribution between the rail and the joint bar, i.e., the forces acting in the contact springs, the model was solved iteratively. The general-finite code, ADINA [7-7] was used. The solution procedure was as follows:

- 1) Carry out finite element computations with all of the contact springs attached
- 2) Examine the results and identify regions where separation is indicated. Disconnect the corresponding springs since the foundation being simulated cannot resist tension with respect to the rail
- 3) Recompute, and perform step (2).

This procedure continues until the solution converges. The final set of forces is regarded as the solution for the contact resultants for the particular load case. The components at the upper and lower contact regions are then summed and the centroids calculated. Approximately four iterations were necessary for obtaining a convergent solution.

7.2.3 Numerical Results for Joint Reactions

The selection of spring stiffnesses for coupling the joint bars to the rail end was made in accordance with certain hypotheses about bolted joints. As stated earlier, it appears that bolt tension and conditions of fit are not critical beyond the point necessary for full joint action. Based on this it was assumed that as long as the finite-element components are connected by

7-25

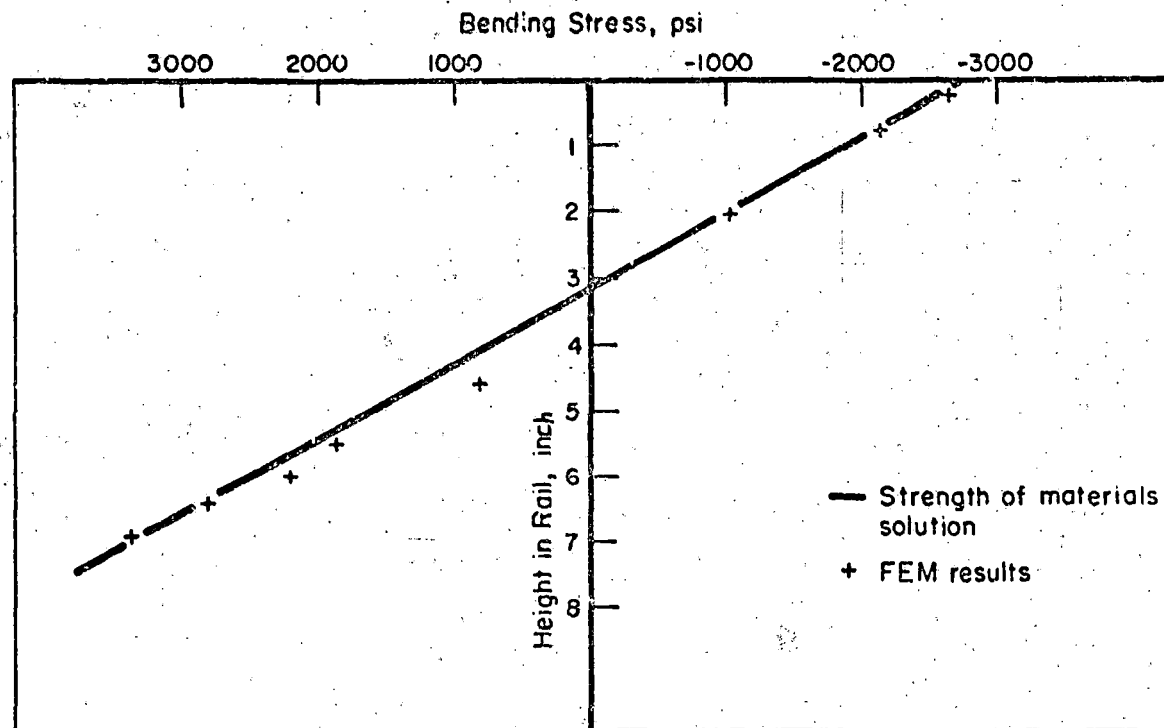


FIGURE 7-16. CANTILEVER BENDING STRESS COMPARISON FOR A PLAN 8.2 INCHES FROM LOADED END FOR THE FINITE ELEMENT RAIL END AND STRENGTH-OF-MATERIALS SOLUTIONS

springs having "reasonable" stiffnesses, their magnitudes are relatively arbitrary. It will be shown that such an assumption is reasonable. A very simple strength of materials calculation was used to estimate a reasonable spring stiffness, based on the spacing between springs. It was assumed that each spring affected a region spanning half the distance between each spring on either side of it. Thus a rectangular volume of .25 x .75 x 5.13 inches was used in conjunction with the familiar expression $\delta = Pl/AE$. From this a spring stiffness of 1.1×10^6 lb/in. was obtained. This value was used for all contact springs in the finite-element model. The effect of varying that stiffness was investigated by using a value for the spring stiffness that was two orders of magnitude larger.

The finite-element models were used to assess the effect of variation in foundation modulus on joint reactions. Table 7-2 presents the matrix of cases studied and a summary of the results. In the table, it is observed that the variation in spring stiffness did not significantly affect the magnitude of the joint reaction. As can be expected from the earlier studies, the force Q varies inversely with foundation modulus. The full rail model was used to simulate the situation where the load was longitudinally displaced with respect to the end of the rail (Case E). It was found that in this situation, the bending-up of the rail head resulted in moving the contact point between the rail and the joint beyond where it could be simulated by the existing finite element mesh. This case would result in large values for Q .

7.3 COMPARISON OF APPROACHES TO CALCULATING JOINT REACTIONS

In this subsection, the experimentally determined values for Q are presented and compared with the analytical results obtained previously.

7.3.1 Calculation of Joint Bar Resultants From Strain Gauge Data

As was described in the section on the instrumentation of the joint bars, strain gages were placed in such a way as to provide a description of bending

TABLE 7-2. MATRIX OF EVALUATIONS PERFORMED AND NUMERICAL RESULTS FOR FINITE-ELEMENT/LOAD-TRANSFER MODELS

Case No.	Load, Kips	Longitudinal Load Position, inch		Foundation Modulus, ksi	Joint Spring Rate, Lb /inch	Q ₁ , kips ^(a)	FINITE ELEMENT RESULTS		
		0.0	7.0				Q ₂ , kips ^(a)	a, inch	l, inch
A	20	X		5.0	10 ⁸	10.0	10.5	0.250	13.0
B	20	X		5.0	10 ⁶	10.7	10.4	0.600	13.4
C	20	X		1.0	10 ⁶	17.2	17.3	0.589	14.3
D	20	X		0.5	10 ⁶	22.5	19.2	0.670	14.5
E	20		X	5.0	10 ⁶	---b	---	---	---

- a. Q₁ was determined from the full rail joint model; Q₂ from the symmetrical finite element model.
- b. Rail end contact region was found to be beyond the region represented by the mesh; no further results were obtained.

stress, and hence, by calculation, bending moment along the length of both joint bars. From the resultant bending moment diagram, the magnitude and location of the joint resultants was calculated.

Since both joint bars were strain gaged on the top and bottom, four sets of essentially redundant information on joint bar bending stresses were available from each test. Data from the two sets of top and the two sets of bottom gages were averaged and, using the flexure formula, plotted as bending moment. Figures 7-17 and 7-18 present two typical sets of joint bar bending moments. These data were fitted using straight lines between data points. The magnitude of the resultants were given by the slopes of these fitted lines. Because the moment was known only at six longitudinal positions, it was not possible to precisely determine the location of the resultants by this method. Table 7-3 presents a summary of the resultants calculated by this method for several load cases. Examination of the table shows the effects of variation in bolt tension, foundation modulus, and load. The magnitude of Q is affected considerably by the latter two parameters but not by bolt tension. Data for bending moment were not available for bolt tensions less than 5 kips/bolt. The previously described experimental work suggests that the reaction would have decreased significantly for lower bolt tensions.

7.3.2 Comparison of Analytical and Experimental Results

Results from the three approaches for calculating Q , viz. Equation (7-8), the numerical analysis, and experiment are depicted in Figure 7-19. Figure 7-19 presents Q as function of foundation modulus for a constant wheel load of 20 kips. The agreement between the three sets of results is seen to be good. It is concluded that the methods developed adequately describe the mechanics of joint action under the influence of vertical bending. Having reached this stage, it was then possible to proceed to the calculation of stresses in the rail end.

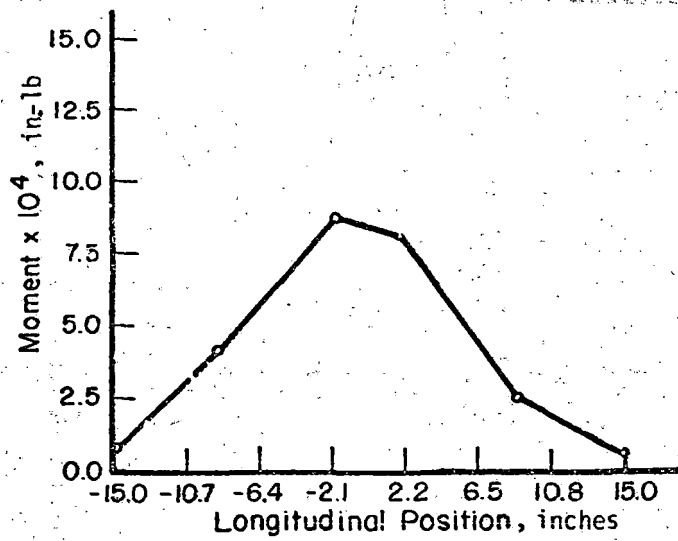


FIGURE 7-17. JOINT BAR BENDING MOMENTS FOR 20 KIP WHEEL LOAD

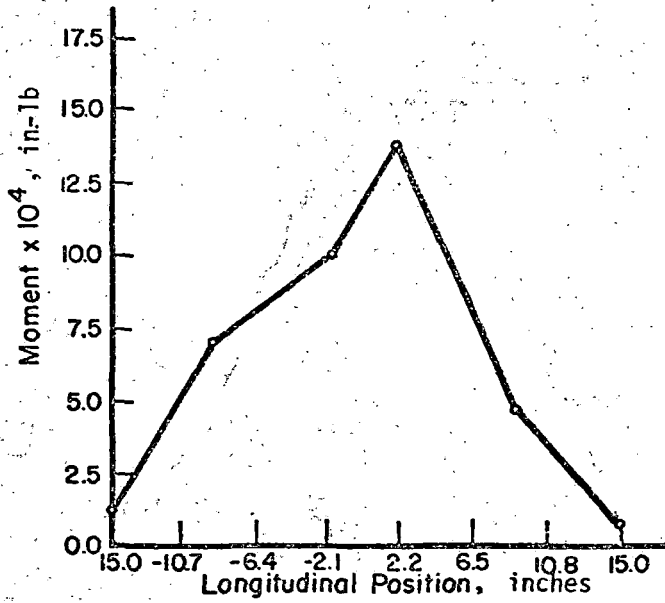


FIGURE 7-18. JOINT BAR BENDING MOMENTS FOR 35 KIP WHEEL LOAD

TABLE 7-3. EXPERIMENTALLY DETERMINED VALUES
FOR JOINT BAR RESULTANT

Load (KIPS)	Foundation Modulus (ksi)	Bolt Tension (KIPS/Bolt)	Q (Kips)
20	5	T2 ^a	11.6
35	5	T2	18.6
20 ^b	5	15	10.4
20	1	T2	16.9
20 ^b	5	5	10.9
20	10	T2	9.1

- a. The respective bolt tensions being 29, 20, 29, 20, 29, 29 KIPS
- b. Load located 1.5 inches from joint center (At $x = 1.5$ inches, using beam-on-elastic-foundation model, moment at joint center is 92% of maximum moment. Note that the variation in bolt tension does not significantly effect Q.

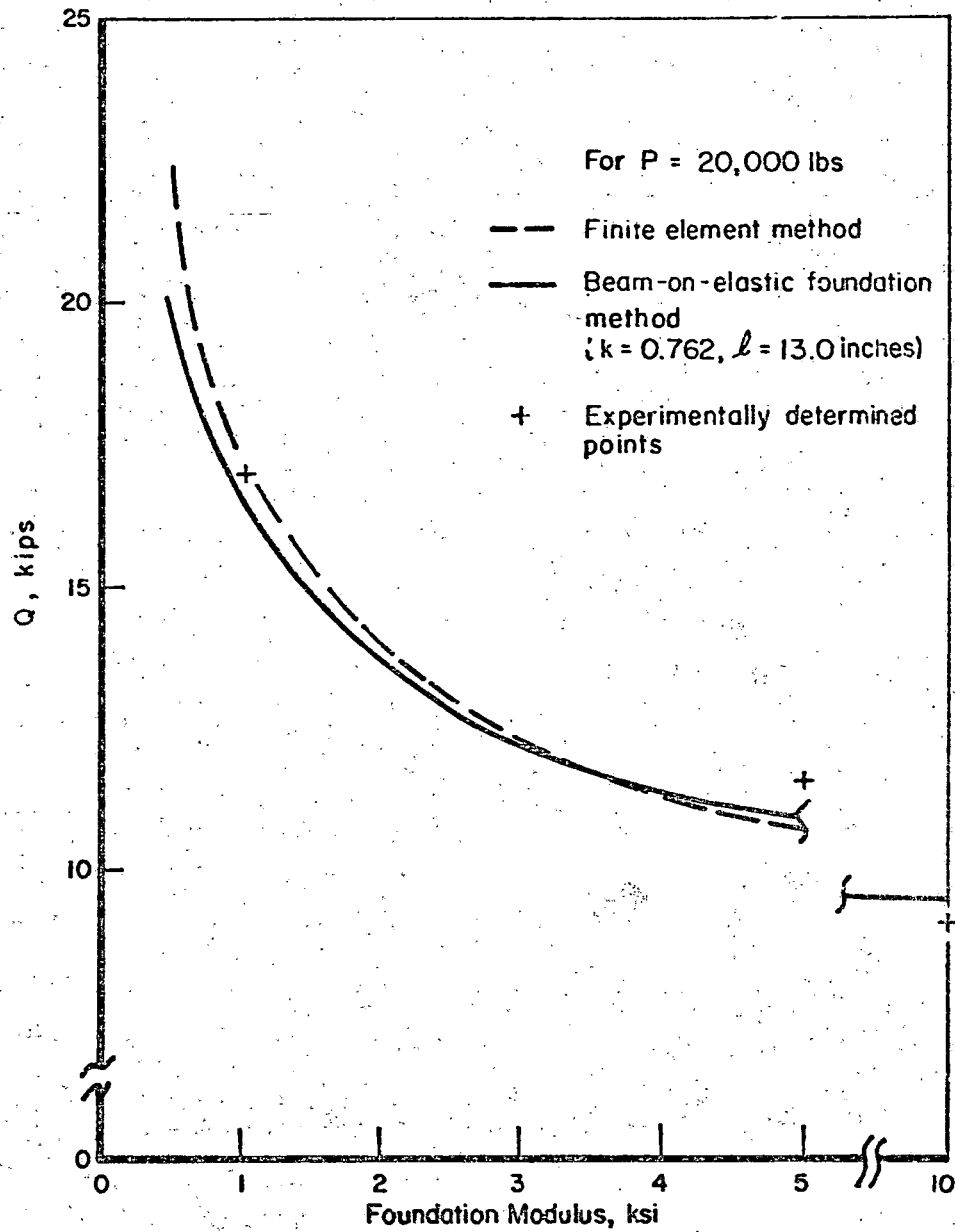


FIGURE 7-19. COMPARISON OF FINITE ELEMENT, BEAM-ON-ELASTIC FOUNDATION AND EXPERIMENTAL RESULTS FOR Q

8. STRESSES IN THE RAIL END

In the previous section, joint bar reactions were calculated allowing the force system of wheel load, tie loads and joint reaction loads imposed on the rail under various loading conditions to be completely defined. These can then be used to determine the state of stress in the rail end region for several loading situations. The results from the latter analysis are presented in this chapter. Stresses in the rail end are caused both by bolt tension and by the action of passing wheels. Those due to bolt tension remain a constant "pre-stress" as long as the bolt tension is unchanging. The largest stresses are caused by passing wheels which give rise to dynamic forces. In the present analysis, wheel loads were treated as quasistatic and having a constant amplitude. For calculation of rail end stresses, generally, a three-dimensional finite-element model was used. Stresses around the bolt hole were also estimated by means of an approximate closed form solution.

8.1 METHODS OF CALCULATING RAIL-END STRESSES

The complex geometry of the rail end, including as it does both bolt holes and radical changes in section, necessitates the use of numerical analysis for obtaining a general assessment of stresses. For this purpose, a three-dimensional finite-element model for use with the general purpose code ADINA was formulated.

The model consisted of 21-node brick-type elements simulating a 15-inch-long section of 132-pound RE rail end having only the first bolt hole modeled. The model is shown in three different views in Figure 8-1. Relatively fine meshing was provided around the bolt hole and in the upper fillet region at the rail end. The model was composed of 162 elements consisting of 698 nodes. Since there were 2034 active degrees of freedom, the computing time involved in stiffness decomposition was quite high. Subsequent analyses, in which the loading was varied but the boundary conditions remained the same, were performed with the decomposed stiffness matrix generated for earlier load cases. In formulating the boundary conditions for the finite-element model, no effort

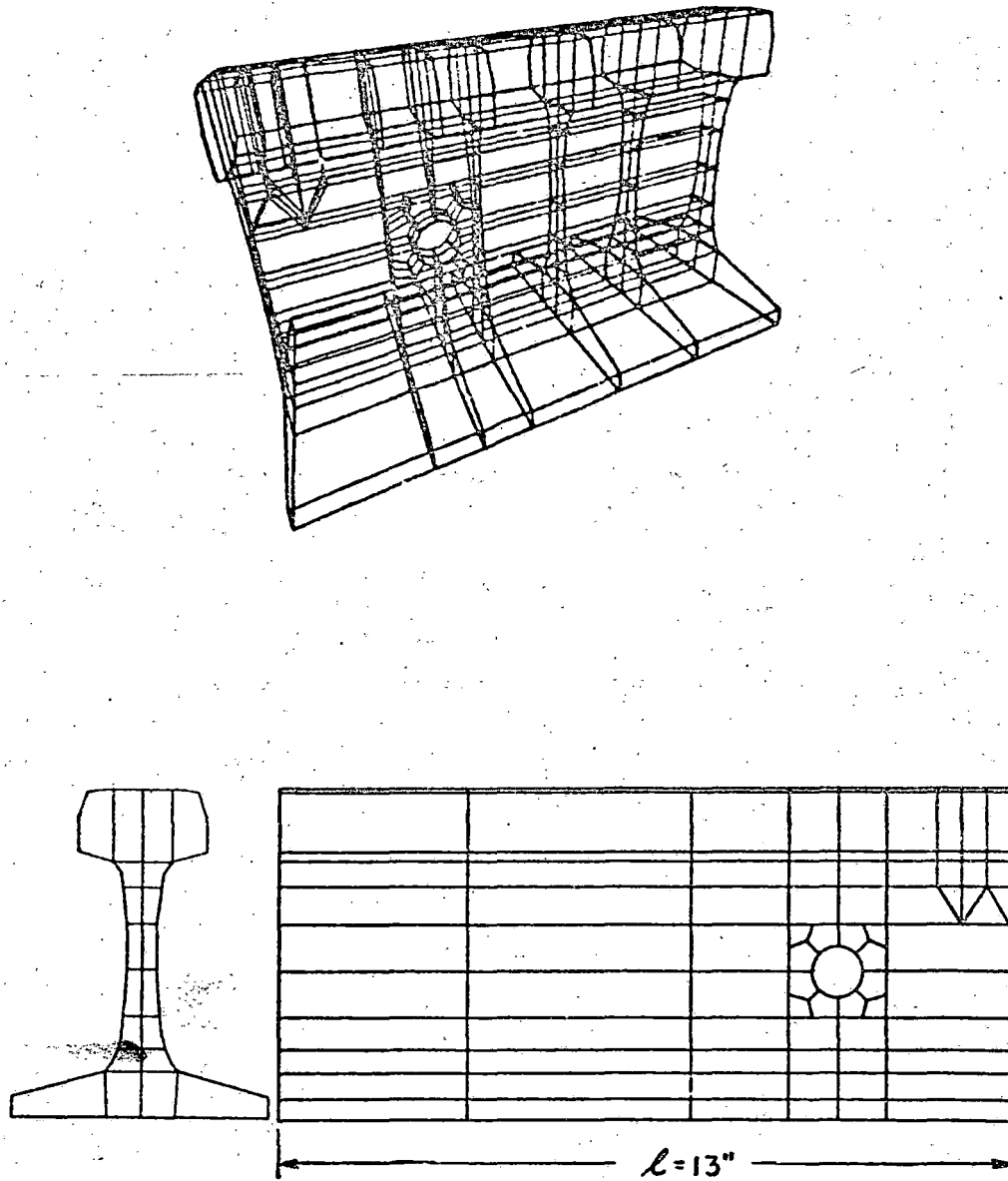


FIGURE 8-1. THREE VIEWS OF THE FINITE-ELEMENT/RAIL-END MODEL

was made to simulate the rigid body displacement of the rail end as the track deflects. Thus, the cut end of the rail was built-in, i.e., the deflections were held to zero ($u_x = u_y = u_z = 0$). The effects of the first tie (past the center of the joint) was simulated by a vertical force representing tie support as approximated by the beam-on-elastic-foundation approach. Wheel load and joint reactions were applied to the various positions in the x-y plane on the running surface and underside of the head, respectively.

It was mentioned in the introductory chapter that individual bolt tensions could be as large as 30,000 pounds. This large tension was recommended for providing reserve tension against bolt loosening due to wear, even though it was inferred by experiments supplementing those of Chapter 6 that tensions of 5,000 pounds were sufficient to develop the full strength of the joint. The results of the experimental study showed that the maximum tangential stress around the bolt holes occurred on the longitudinal centerline of the bolt hole, and that the value at positions where cracking has been shown to most commonly occur, was significantly less.

Although it would be possible to resolve the bolt tensions into wedging forces that could be applied to the three-dimensional finite-element model of the rail end, simulating the effects of the action of the joint bar being drawn into place by the bolts, this was not done because the static stresses were regarded as being insignificant at the locations of interest. This is particularly true for lower bolt tensions (5,000 pounds/bolt and less) which are likely to occur during the life of a rail joint.

Although the finite-element model will be shown to provide a complete picture of rail-end stresses, its use is somewhat cumbersome for designers. Thus, an attempt was made to adapt some form of closed form solution to the problems of rail end stress calculations. No method was found for providing a general stress picture or for calculating stresses at the critical head/web region, but an existing approach was modified for analyzing the tangential stresses around the bolt hole. Savin [8-1] presents the following expression for the tangential stress around a hole in a cantilever beam of rectangular cross section in bending:

$$\sigma_{\theta} = \frac{P}{I} \left\{ R (\ell' - a) [\sin\theta - \sin 3\theta] + [(2H^2 - R^2) \sin 2\theta + R^2 \sin 4\theta] \right\} \quad (8-1)$$

where the variables are defined in the insert in Figure 8-2. Examination of this expression shows that the first term represents the effect of bending, and the second term accounts for the effect of shear. The first term may be neglected when the hole is close to the end of the beam, because the bending moment is small. Since the moment of inertia, the I in the equation, was originally taken to be that for a rectangular cross section, some adjustments in the parameter must be made for the rail cross section. This is accomplished by calculating the depth of a rectangular cross section having the same moment of inertia as the rail. Assuming unit thickness, the equivalent depth is

$$H = (3I/2)^{1/3}$$

Thus Equation (8-1) may be rewritten to calculate the maximum tangential stress as

$$\sigma_{\max} = 2.62 PI^{-1/3}, \quad (8-2)$$

at the 45-degree positions, assuming R is much less than H . Figure 8-2 presents maximum bolt-hole stress as a function of wheel load for a 132-pound RE rail joint, where $l = 13.0$ inches, for a variety of foundation moduli, with the wheel 5.0 inches away from the rail end. Again it has been assumed that the radius of the bolt hole, R , is small compared to H . In this computation, Q , that refers to the joint resultant is given by the linear elastic foundation solution, Equation (7-8).

8.2 FINITE-ELEMENT RESULTS

This subsection describes a variety of potentially important wheel loading positions that were analyzed, using the finite-element model. For the purposes of validating the various approaches, the condition of $K = 0$, i.e., a loaded rail end without joint bars is first considered. A rail-end load of 10,000 pounds was applied to the finite-element model and to Equation (8-1).

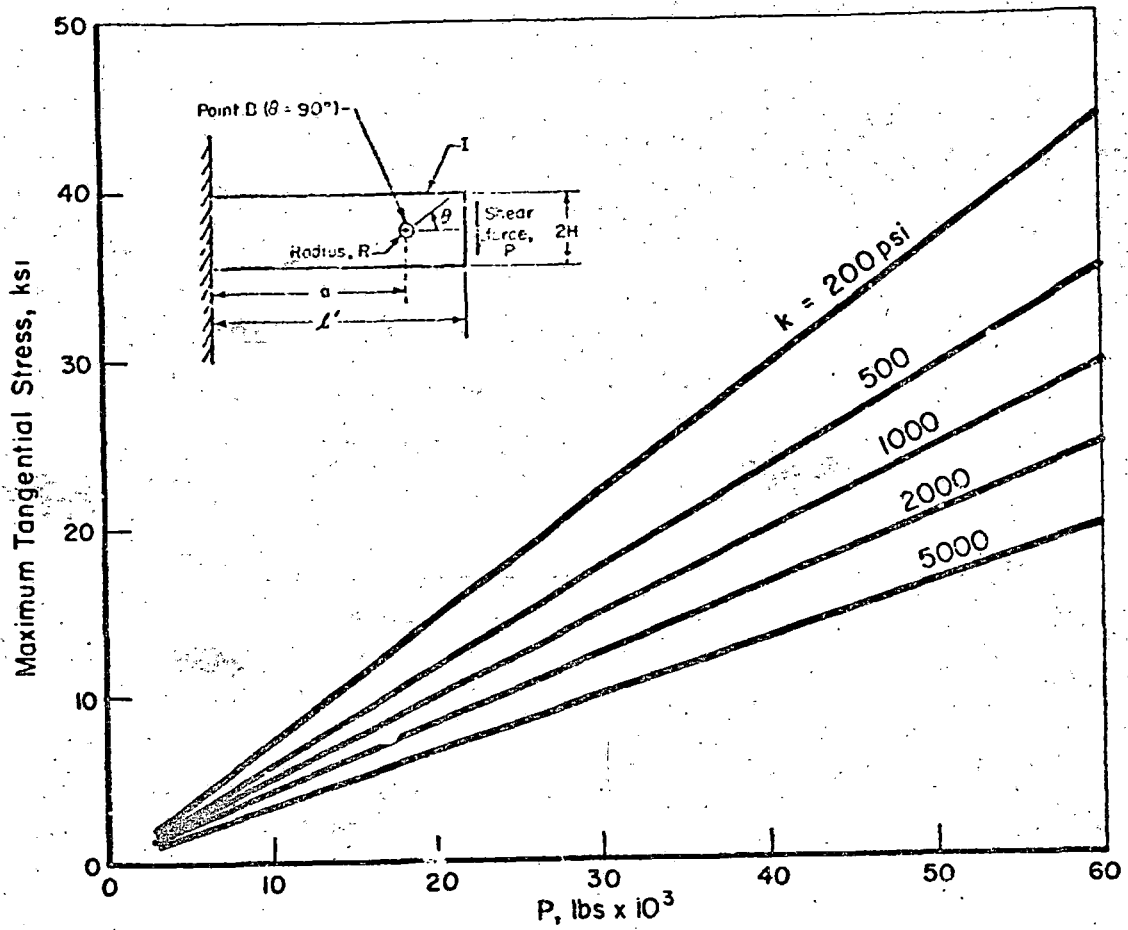


FIGURE 8-2. MAXIMUM TANGENTIAL STRESS AS A FUNCTION OF WHEEL LOAD FOR 132-LB RE JOINT AT VARIOUS FOUNDATION MODULI

The results are compared with strain gage data for the same case as in the polar plot of Figure 8-3. Good agreement was found between the finite-element model and the approximate equation. The experimental results were somewhat lower in magnitude.

The remainder of the cases examined present results when the wheel load (P2) was located 8.0 inches from the rail end. Stresses for a central vertical load of 30,000 pounds were first considered. Stresses in the rail web in the region of the bolt hole were due to the action of the 30,000-lb wheel load and a 17,000-pound Q located 0.50 inches from the rail end. The resulting stresses at a number of important locations throughout the rail end are shown in Figure 8-4. It is observed that the distribution around the bolt hole has the same shape as that for the rail end loading, but that because of the reversal in the sign of the vertical shear, as was discussed in the previous chapter, the position of the maximum tensile stress has rotated 90 degrees. The largest vertical stress occurring in the region of head/web fillet is located near the point of application of the joint bar resultant. Because the resultant was modeled as a concentrated load rather than a distribution, this result is not particularly significant. Figure 8-5 shows vertical and tangential stress for a rail with a 0.75-inch eccentric 30,000-pound load. In this modeling, it was assumed that torque resulting from the eccentricity would be reacted equally by the rail extending away from the load in both directions. This implied that the joint transmitted 100 percent of the torque. The figure shows that the stresses are no longer symmetric on either side of the rail centerline. The maximum tangential stresses are increased on one side of the bolt hole, but are decreased considerably on the other side. Similar observations apply to the head/web region vertical stresses.

Figure 8-6 presents vertical and tangential stresses for the case of a rail loaded on its upper surface by a 10,000-pound lateral load. The resulting torque is reacted by joint bar forces in the same way as for the eccentric vertical load. The lateral force was assumed to give rise to joint bar forces proportional to forces due to a vertical load on the same joint. (It should be noted, though, that it is impossible to conceive of a situation when a purely lateral load would appear on the rail.) As would be expected, the distribution of tangential stresses around the bolt hole are radically different

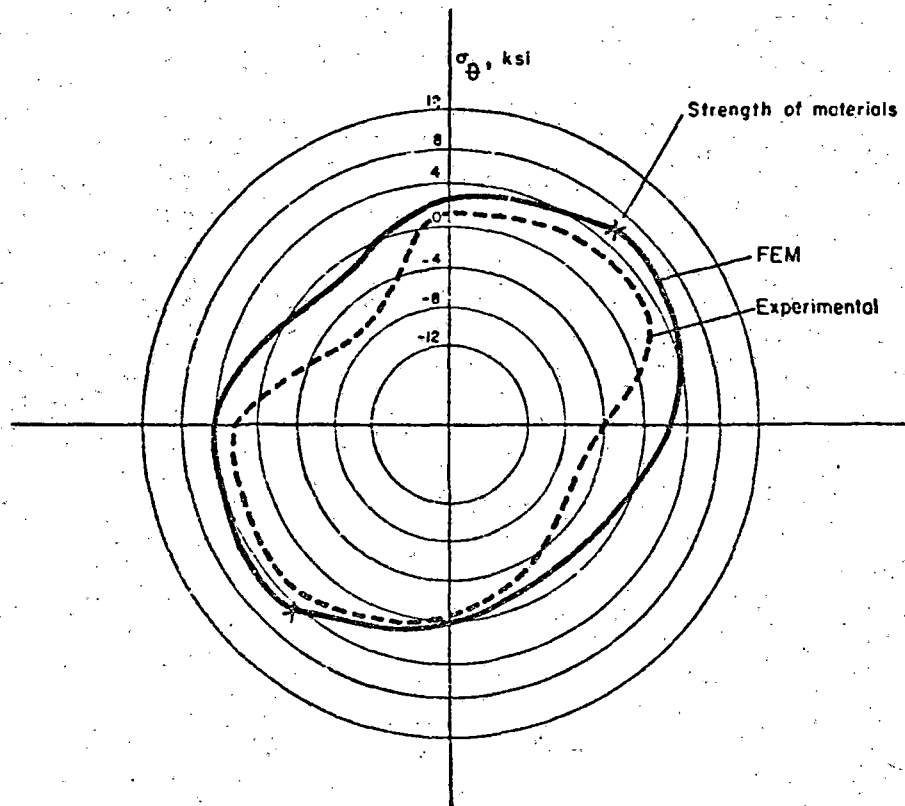


FIGURE 8-3. POLAR PLOT COMPARISON OF EXPERIMENTAL, FINITE ELEMENT AND APPROXIMATE ANALYTICAL RESULTS FOR BOLT-HOLE STRESSES (VERTICAL WHEEL LOAD OF 10 KIPS AT RAIL END)

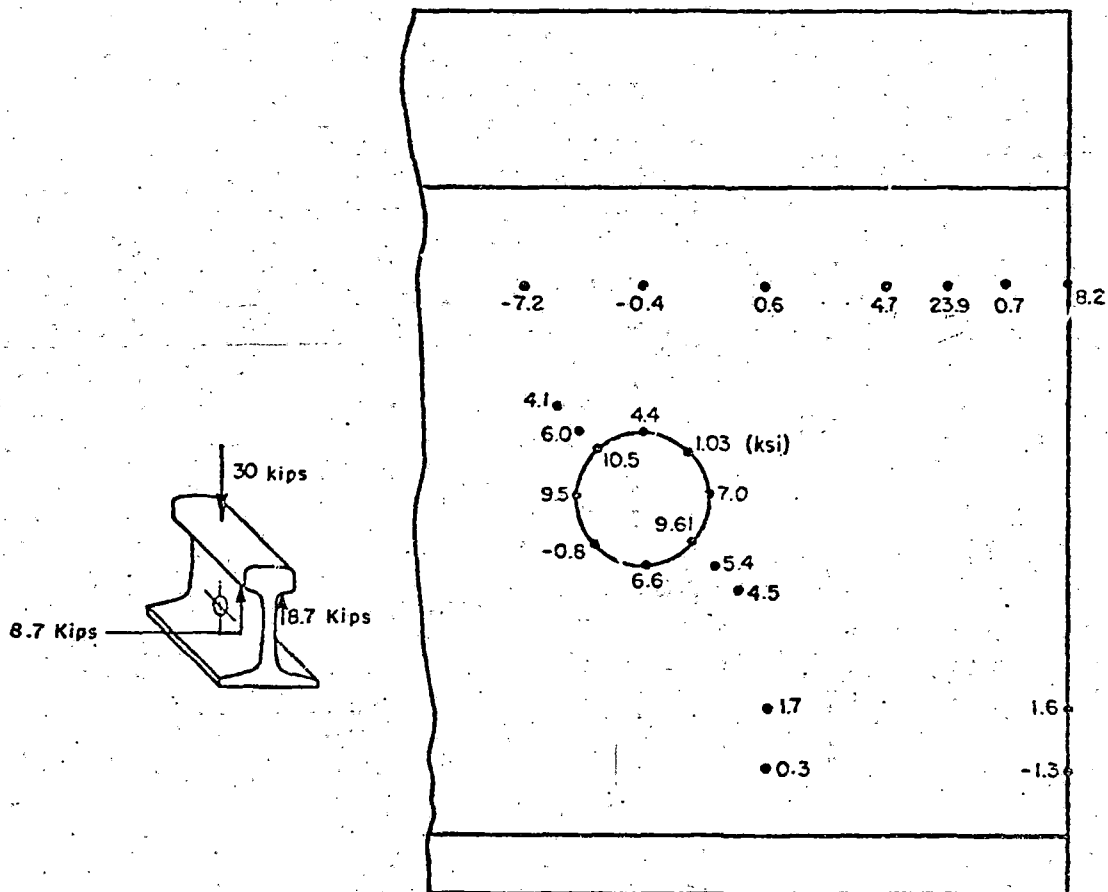
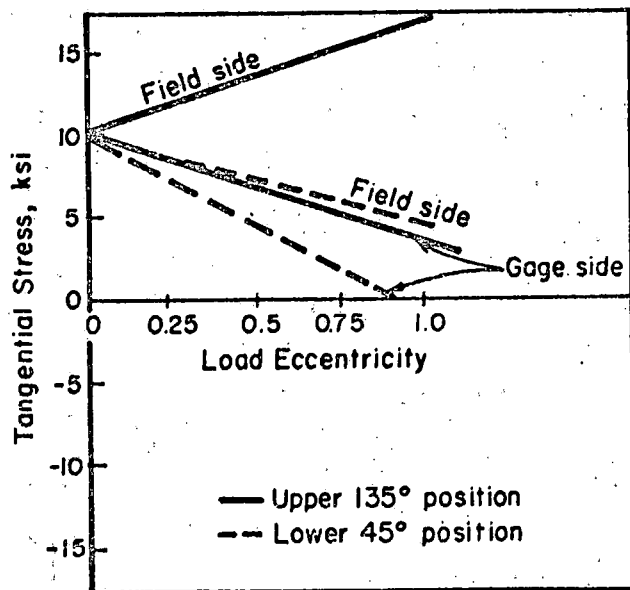
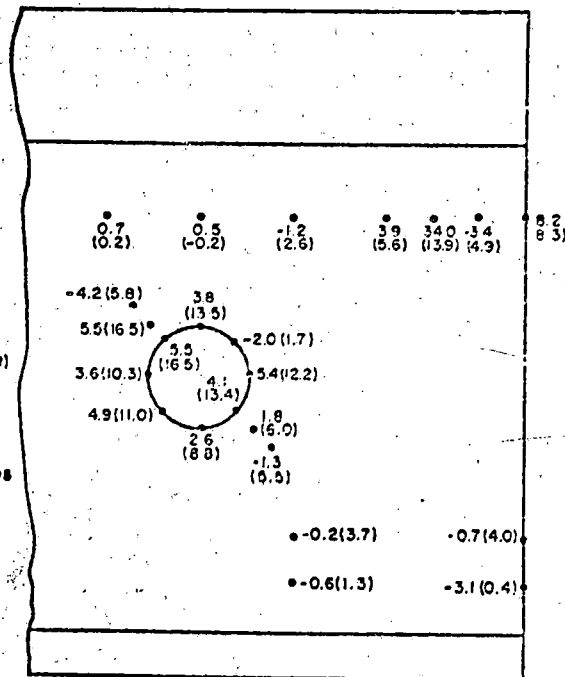
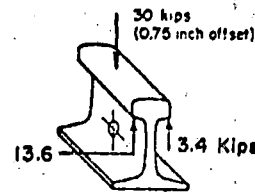


FIGURE 8-4. CENTRAL VERTICAL LOAD RESULTS--BOLT-HOLE STRESSES ARE TANGENTIAL, ALL OTHERS ARE VERTICAL STRESSES (WHEEL LOAD 8 INCHES FROM RAIL END FOR ALL CASES)

6-8



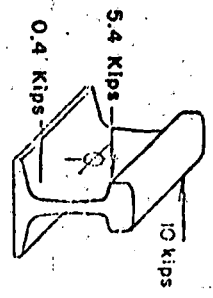
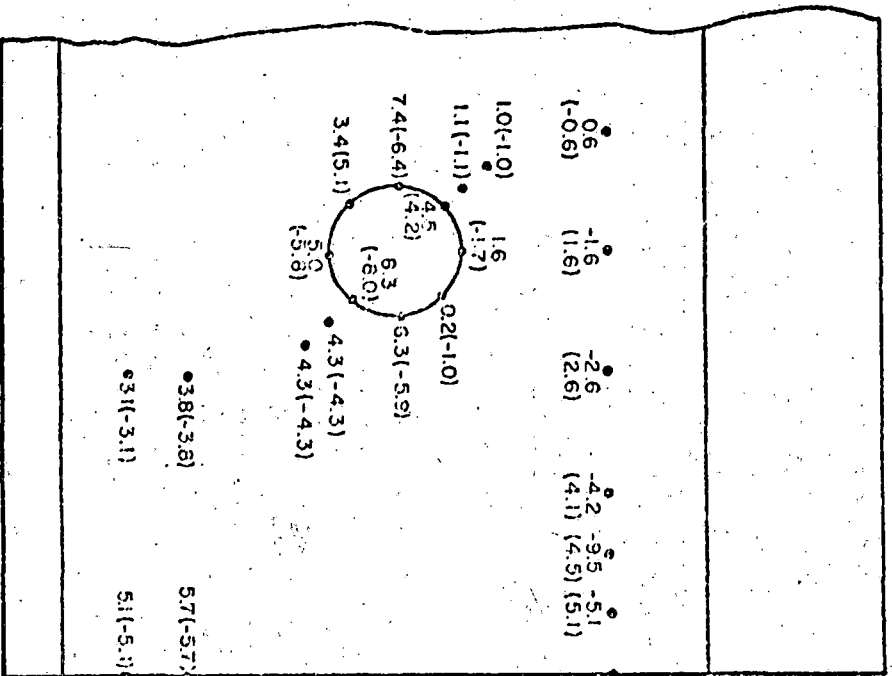
Dependency of Maximum Tangential Stress on Eccentricity



0.75 inch Eccentric Load Case

Refer to stresses on opposite side

FIGURE 8-5. ECCENTRIC VERTICAL LOAD RESULTS



() Refer to stresses on opposite side

FIGURE 8-6. LATERAL LOAD RESULTS

than from the vertical loading cases. Head-web stresses are substantially smaller than those previously encountered. Several of the computed bolt hole stresses compare favorably with the experimental values shown in Figure 6-13. The main departures, for stresses at the top and bottom of the hole, probably arise from web bending accentuated in the calculation by the extreme localization of the joint bar resultant.

It is useful to conclude this section by considering the combinations of loading which are likely to occur in service. The most severe case treated was where the lateral force and vertical load eccentricities produce torques. Lateral loads can arise due to friction and creep forces on the tread or through flanging action. In curving situations, the two torques due to flanging and creep forces tend to cancel each other, resulting in a net overturning moment due to the predominance of flange force upon creep saturation. However, in this condition, the vertical load is generally acting near the gage corner of the rail head. In such a case, the net overturning moment on the rail is generally directed to the field side.

Consideration of Figures 8-5 and 8-6 suggests that the combined action of lateral and an eccentric vertical load may be significant in promoting crack growth. Vertical stresses in the head web region and the stresses of the bolt hole circumference at 45° and 235° are increased by the combined action. This action combined with the action of the P2 force may influence the growth of cracks in this region.

9. STRESS-INTENSITY FACTORS FOR RAIL-END CRACKS

In the previous section, magnitudes and locations of maximum stress in the rail end were identified for various loading conditions. It has been indicated that this information can be used directly for the calculation of the time required to initiate fatigue-crack and can be used indirectly for predicting rates of fatigue crack propagation. For a fracture-mechanics analysis the direction of flaw growth must be known beforehand or assumed; knowledge of the positions and orientations of maximum principal stresses makes the selection possible. In this section, stress-intensity factors are calculated for cracked rail ends using several different techniques of varying generality. Computations of stress-intensity factor as a function of crack length, for bolt-hole cracks and head-web separations, are made for various loading conditions and the implications of these data for rail failure are discussed.

9.1 METHODS OF CALCULATING STRESS-INTENSITY FACTORS FOR CRACKED-RAIL ENDS

It was noted in the previous chapter that the stress state in the web was symmetrical about the rail centerline only for the case of central vertical loading. Thus, the state in the web under the most generalized loading conditions is three dimensional. Nonetheless, because of the formidable difficulties inherent in both the prediction and use of three-dimensional stress-intensity-factor data, it was decided to deal with the average stresses due to central loading, and to model plane stress conditions only. At the present time, this simplification is also warranted by the absence of field data on the distribution of lateral wheel positions at joints. The radically more expensive and complicated three-dimensional analysis would be more justified only if precise load data exist. Thus, all of the remaining discussion is devoted to either simple closed-form expressions for three-dimensional crack geometries, or to two-dimensional analyses.

Bolt-hole flaws may be analyzed by using several closed-form relations that have been derived for simple geometries and loadings, or through a more general numerical approach. The closed-form expressions are useful for rather short cracks when the stress field may be assumed to nearly correspond to the distribution around a hole in an infinite sheet. The first of these approaches is to assume that the initial defect has the form of a semielliptical surface flaw which propagates normally from the inner surface of the bolt hole as shown in Figure 9-1. Broek [9-1] presents the following solution for the maximum value of Mode I stress-intensity factor

$$K_I = \frac{1.12 \sigma}{\Psi} \sqrt{\pi a} \quad (9-1)$$

where Ψ is a correction factor given by

$$\Psi = \sqrt{\phi^2 - 0.212 \left(\frac{\sigma}{\sigma_{TYS}} \right)^2}, \quad (9-2)$$

σ_{TYS} being the ultimate tensile stress of the material, and

$$\phi = \frac{3\pi}{8} + \frac{\pi}{8} \frac{a^2}{c^2}. \quad (9-3)$$

This form of ϕ is an approximation of an elliptic integral of the second kind. σ in Equation (9-1) is assumed to be the local stress at the point of interest on the surface of the bolt hole. The value is determined from either the finite-element solution or the closed-form solution described in the previous chapter.

The second approach is based on the solution of Bowie [9-2]. For the flaw geometry, Figure 9-2, of a through-crack emanating from a hole in a panel in uniform tension, Bowie proposed the solution,

$$K_I = \sigma \sqrt{\pi a} f_B \left(\frac{a}{D} \right) \quad (9-4)$$

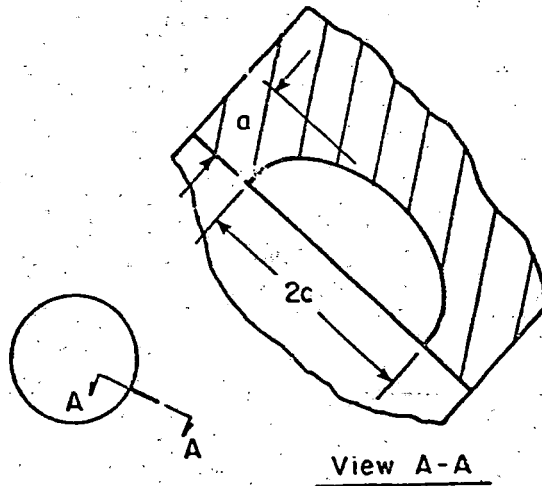


FIGURE 9-1. SEMI-ELLIPTICAL SURFACE FLAW GEOMETRY

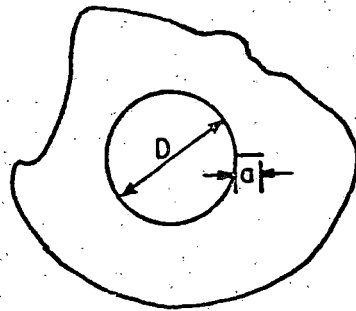


FIGURE 9-2. THROUGH-CRACK FROM HOLE

where f_g is a geometric function. If, however, it is assumed that σ is the local stress at the crack rather than the remote stress in the panel, it is correct to write

$$K_I = \sigma \sqrt{\pi a} \quad (9-5)$$

An approximate method may also be used for calculating K_I for head/web separation cracks. This approach is only applicable to those situations where the flaw is in its initial stages, initiating either as a surface flaw or as an initial circular crack. The surface flaw formulation has already been discussed. The solution for an embedded penny shaped crack was given by Sneddon [9-3] as

$$K_I = \frac{2}{\pi} \sigma \sqrt{\pi a} \quad (9-6)$$

where a is the crack radius and σ is the uniform far field stress acting normal to the crack plane. Since this expression was derived for an infinite medium, it is surmised that when Equation (9-6) is applied to a plate, the crack diameter should be no more than one-third of the plate thickness, as recommended by Shah and Kobayashi [9-4].

As has been pointed out, these closed-form solutions are appropriate only to situations where the cracks are rather short, and the local stress field can be assumed to be constant were the crack absent. On the other hand, a finite-element approach to stress intensity factor calculations provides the most general means for analyzing rail end cracks.

Following the technique applied to aerospace structures by Smith and Davies [9-5], use was made of two-dimensional finite-element models that could be "unzipped" along the crack line through the use of double-noding and very stiff coupling springs. The forces arising in these springs and the nodal point deflections of the "cracked" nodes were then used to calculate stress-intensity-factor values by the modified crack closure integral approach [9-6]. This approach was used for both bolt hole and head/web cracking.

Two cracked finite-element rail-end models, one for each flaw type, were developed and are shown in Figures 9-3 and 9-4. This was done to keep the model sizes reasonable. The first of these models, Figure 9-3, was designed to calculate bolt-hole crack stress-intensity factors for the flaw geometry that would result from positive shearing force existing in the rail at the bolt hole, i.e., the crack oriented at -45 and $+135$ degrees with respect to the positive horizontal axis. The second model simulates a head/web separation. In this model the crack line is located in the fillet region 5.3 inches from the base and is 7.8 inches long. In both cases, the dual-noded crack line is shown by heavy lines in the figures. Both models correspond to a 15-inch-long 132-pound RE section. The bolt-hole model had 143 elements and 264 nodes. The head/web model consisted of 224 elements and 303 nodes. The elements were two-dimensional, plane-stress types and were primarily quadrilaterals. In all respects other than the presence of the crack line and bolt hole, these models were very similar to the load transfer finite-element models described in Chapter 7. The idealized boundary conditions used in conjunction with the three-dimensional rail-end model were also used here, i.e., the rail end was treated as built-in. Linear spring elements that coupled some nodes along the crack line were uncoupled to simulate cracking by setting the stiffness to a small number. The nodal forces required to close the crack were computed for various crack tip positions and crack decrements. These nodal forces were in turn used to calculate the crack closure integral.

9.2 STRESS-INTENSITY-FACTOR RESULTS FOR BOLT-HOLE CRACKS

Stress-intensity factors were calculated for a number of bolt-hole cracks using both the closed form and finite-element approaches. All of the calculations were conducted for a particular joint situation and wheel load. These results can easily be extended to other cases by assuming a linear relation between wheel load and stress-intensity factor. For an elliptical surface flaw, it was assumed that the crack depth, a , was related to crack width, $2c$, by an aspect ratio, f , so that

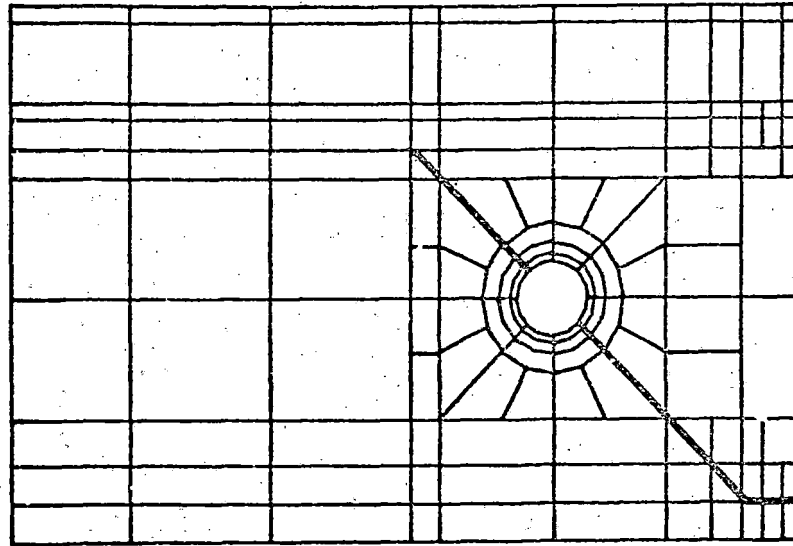


FIGURE 9-3. BOLT-HOLE CRACK FINITE ELEMENT MODEL

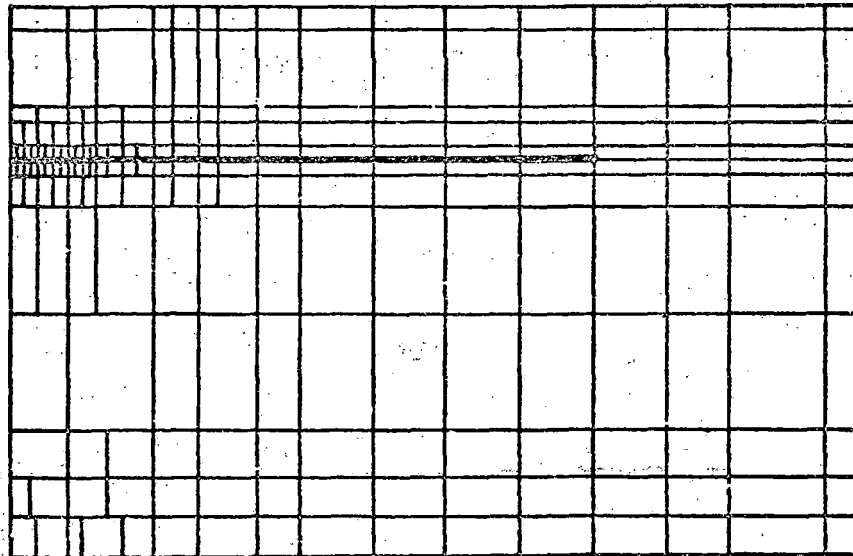


FIGURE 9-4. HEAD/WEB SEPARATION FINITE ELEMENT MODEL

In the present analysis, values of f were varied from 0.5 to 0.9. A maximum tangential stress of 24,200 psi was assumed with a 64,086 psi value for yield stress of the rail steel, which corresponds to a 39,000-pound value for Q . This result was obtained with the three-dimensional finite-element model discussed in the previous chapter. A Q of this magnitude was used for all of the stress-intensity-factor value calculations that are presented in this chapter. Figure 9-5 presents the stress intensity factors for various surface flaws obtained by using Equation 9-1. It is observed that the largest K_I values are obtained for the crack having the smallest value of f ; i.e., a shallow shaped flaw. Upon examination of Figure 7-26, the stress distribution at the bolt hole shows that the maximum stress decays quite rapidly with distance from the edge of the hole. Thus, the approximations for K_I would be expected to be in error for crack lengths greater than 0.10 inch. Calculations using the closed form expression, Equation 9-4, were also made using the formulation for a short through-crack presented earlier. The resulting stress-intensity-factor values are presented in Figure 9-6. In comparing these results with those of the surface flaw, it is observed that the through-crack curve falls somewhat above the $f = 0.5$ line. It is to be expected that the surface flaw would approach the through-crack value in the limit as the former becomes shallower.

Figures 9-7 through 9-9 present stress-intensity-factor results for bolt-hole cracks as calculated by the finite element/crack closure integral method. Several different crack configurations were considered. These were:

- 1) A single crack emanating from the bolt hole at a -45 degree orientation with respect to the positive horizontal axis.
- 2) A crack growing on opposite sides of the bolt hole along a critical plane.
- 3) A crack where the lower crack line has broken through to the rail end, but cracking is still proceeding on the upper line.

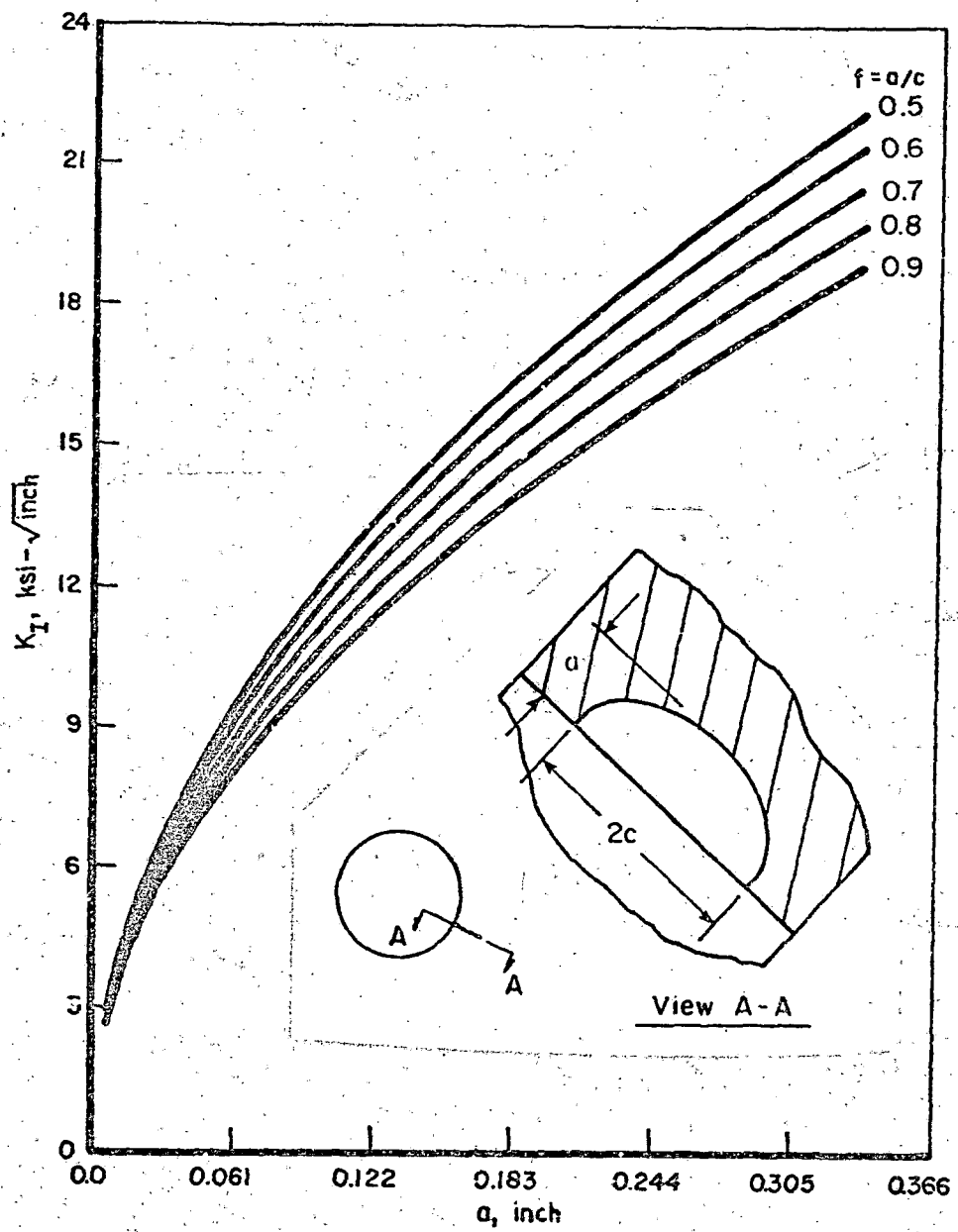


FIGURE 9-5. K_I FOR BOLT-HOLE CRACK COMPUTED ON THE BASIS THAT THE FLAW IS A SURFACE FLAW; JOINT BAR REACTION $Q = 39$ KIPS

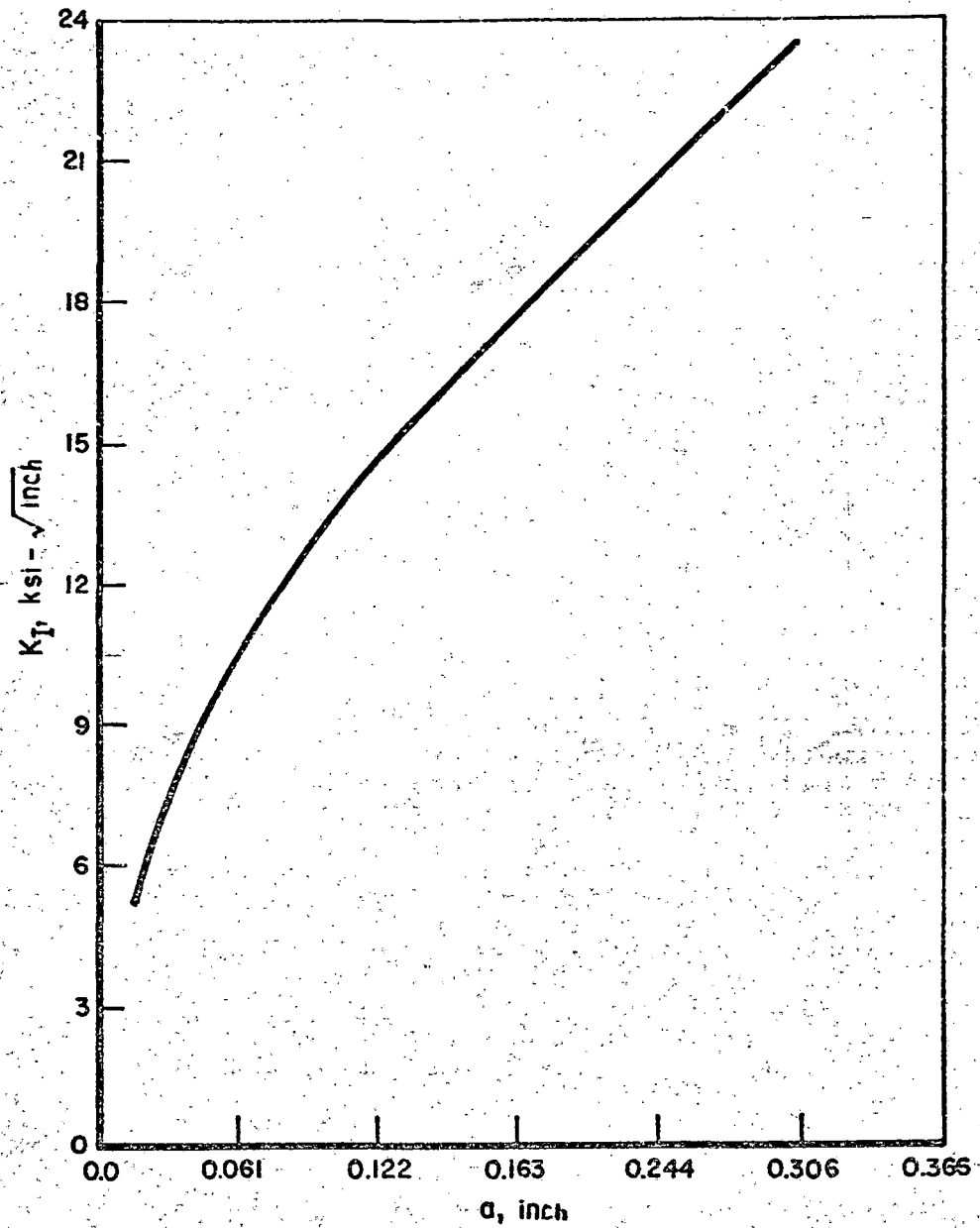


FIGURE 9-6. K_T FOR BOLT-HOLE CRACK WHICH IS ASSUMED TO BE A THROUGH THICKNESS FLAW; JOINT BAR REACTION
 $Q = 39$ KIPS

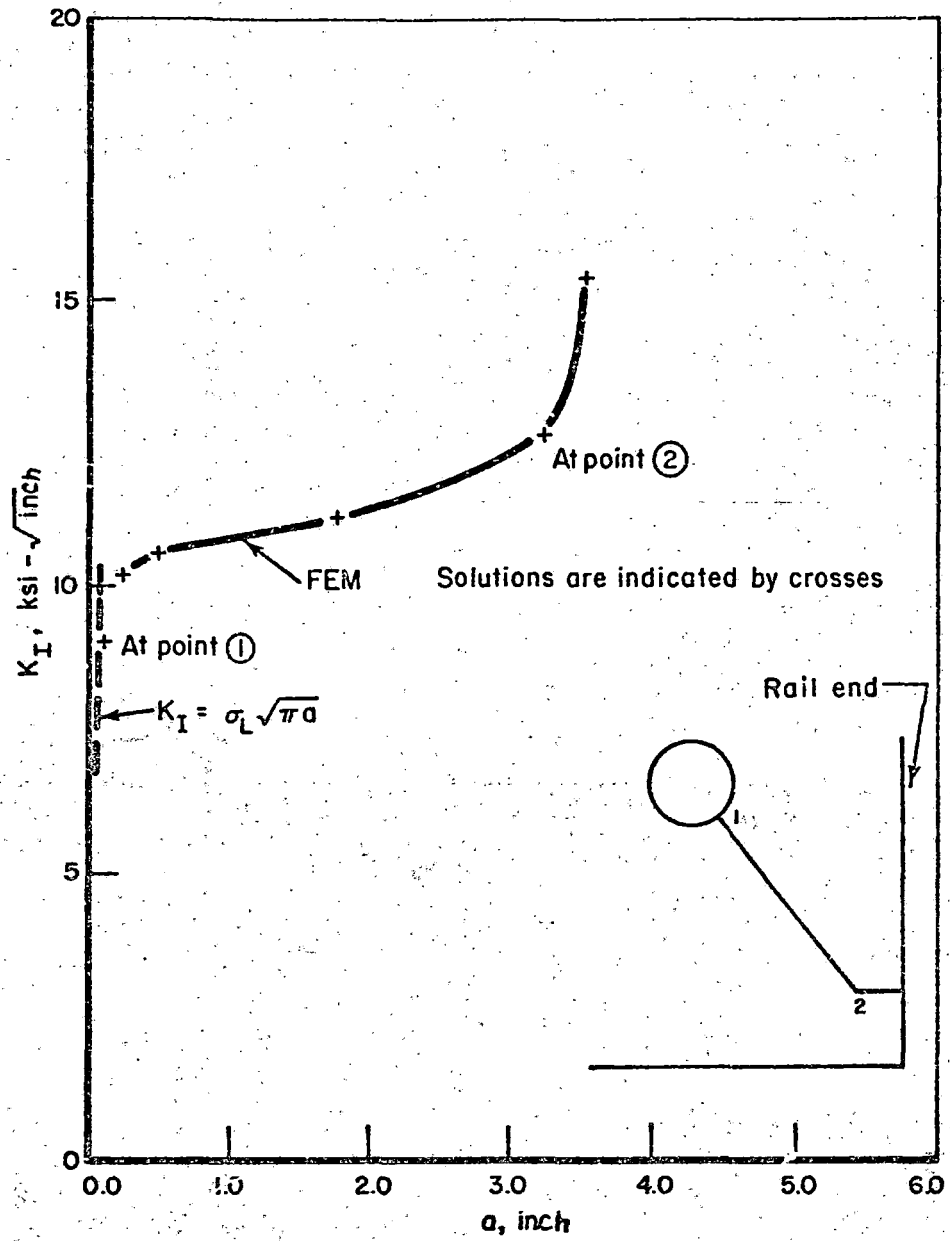


FIGURE 9-7. STRESS-INTENSITY FACTORS FOR A LOWER BOLT-HOLE CRACK

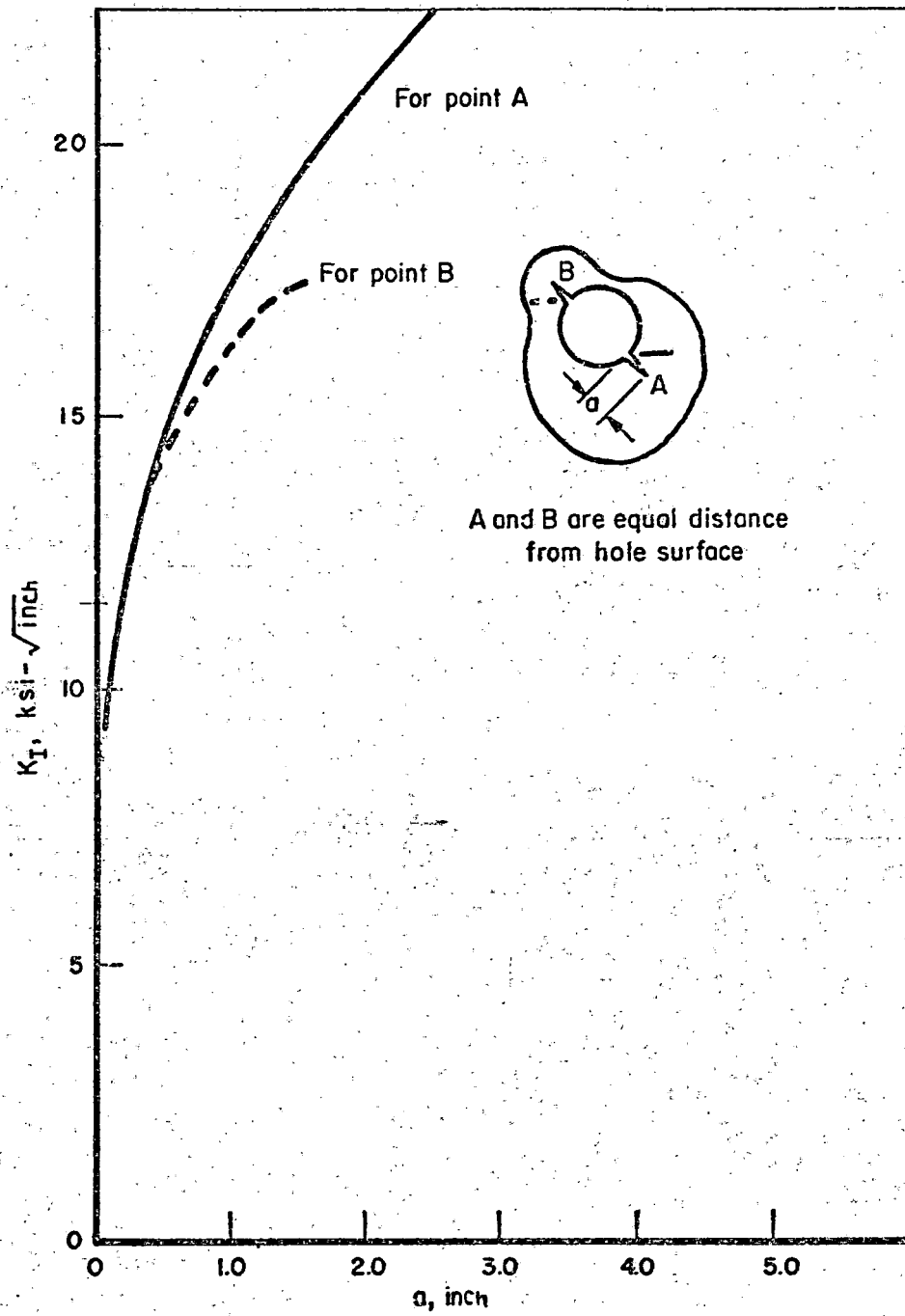


FIGURE 9-8. STRESS INTENSITY FACTOR FOR CRACKS EMANATING FROM DIAMETRICALLY OPPOSITE POINTS OF A BOLT HOLE; JOINT BAR REACTION $Q = 39$ KIPS

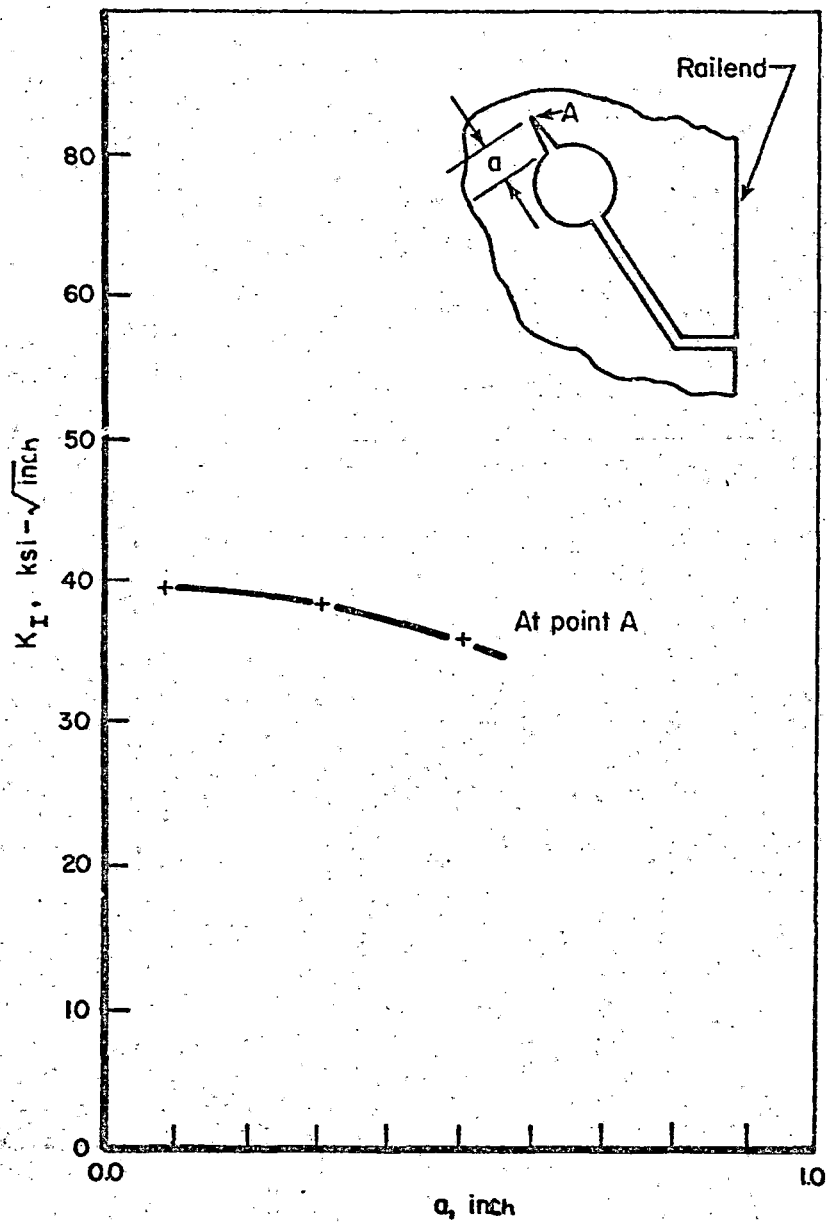


FIGURE 9-9. STRESS INTENSITY FACTOR FOR A BOLT HOLE CRACK EMANATING FROM DIAMETRICALLY OPPOSITE POINTS OF THE HOLE (LOWER EMANATION HAS TURNED AND BROKEN THROUGH TO RAIL END); JOINT BAR REACTION $Q = 39$ KIPS

The results presented in Figure 9-7 are first considered in relation to the closed form solutions already discussed. The through-crack calculation yields a K_I value of $13.2 \text{ ksi}\sqrt{\text{inch}}$ for a 0.10-inch crack length, while the K_I for the surface flaw has a maximum value of $11.7 \text{ ksi}\sqrt{\text{inch}}$ when $a = 0.1$ inch. The finite element calculation produces a result of $9.1 \text{ ksi}\sqrt{\text{inch}}$ for the same crack length. It is to be expected that the finite-element result would be less than either of the value obtained from closed form expressions because the latter do not take into account the reduction in stress away from the bolt hole when the crack is absent. Thus, it is concluded that the three approaches show reasonably good agreement for short crack lengths.

Further examination of Figure 9-7 shows that a maximum stress-intensity factor of $12.8 \text{ ksi}\sqrt{\text{inch}}$ is reached when the crack is assumed to turn and run longitudinally. With the crack 3.0 inches from the rail end, a maximum value of $15 \text{ ksi}\sqrt{\text{inch}}$ was calculated.

Figure 9-8 presents results for a double crack. It is observed that at the shorter crack lengths the stress-intensity-factor values are the same for both crack tips. Further, it is observed that at 0.10 inch crack length, the results are about the same as those recorded for a single-sided crack. At longer crack lengths, however, much larger stress-intensity-factor values are obtained for the double crack.

The situation where the lower crack has already broken out but the upper crack is still propagating toward the head is presented in Figure 9-9. It is observed that this cracking proceeds with a rather high, nearly constant stress-intensity factor, as the flaw approaches the fillet region.

Now that a number of possible crack geometry combinations have been considered, it is possible to imagine the sequence in which bolt-hole cracking occurs. Since in the early stages of crack growth the maximum values of stress-intensity factor are obtained for the double crack, it is quite likely that bolt-hole defects will propagate on both sides of the hole. It is observed, that as the crack grows longer the lower crack tip attains the higher K_I value. More rapid cracking will occur on the lower branch until the crack breaks out of the rail end near the lower flange fillet region. At some time during this process, the very high stress-intensity-factor values shown in Figure 9-9 will occur for the upper branch crack tip, and so the upper

crack branch will rapidly propagate toward the rail head. At some point in the upper head fillet, the crack will turn because of the increasing resistance to cracking engendered by the increasing fillet thickness. Before these stages are reached, it is possible that under actual wheel loading, K_I will reach critical values for both branches, resulting in unstable crack growth.

9.3 STRESS-INTENSITY-FACTOR VALUES FOR HEAD-WEB SEPARATION SITUATION

The head/web separation was modeled, in its initial states, as an embedded circular crack in a uniform stress field, described by Equation (9-6). Figure 9-10 presents results for this case, where a $\sigma = 25,000$ psi stress field was assumed normal to the crack plane.

The finite-element head/web separation model was then used to calculate stress-intensity-factor values for cracks where the flaw had already grown from the embedded defect to a through-crack. Two flaw geometries in this state were analyzed. The first of these, as shown in Figure 9-11, consisted of a crack growing away from the initiation site, with an uncracked ligament remaining between that site and the rail end. The second, Figure 9-12, presents results for the situation where the flaw on one side has broken through to the rail end. This second case is considered the most likely of the two. In this situation, which may be visualized in terms of the action of the joint bar resultant Q prying up the rail head, very large stress-intensity-factor values are quickly achieved. It must be expected from this result that very rapid crack growth is likely to occur for the head/web separation once the crack has broken through to the rail end.

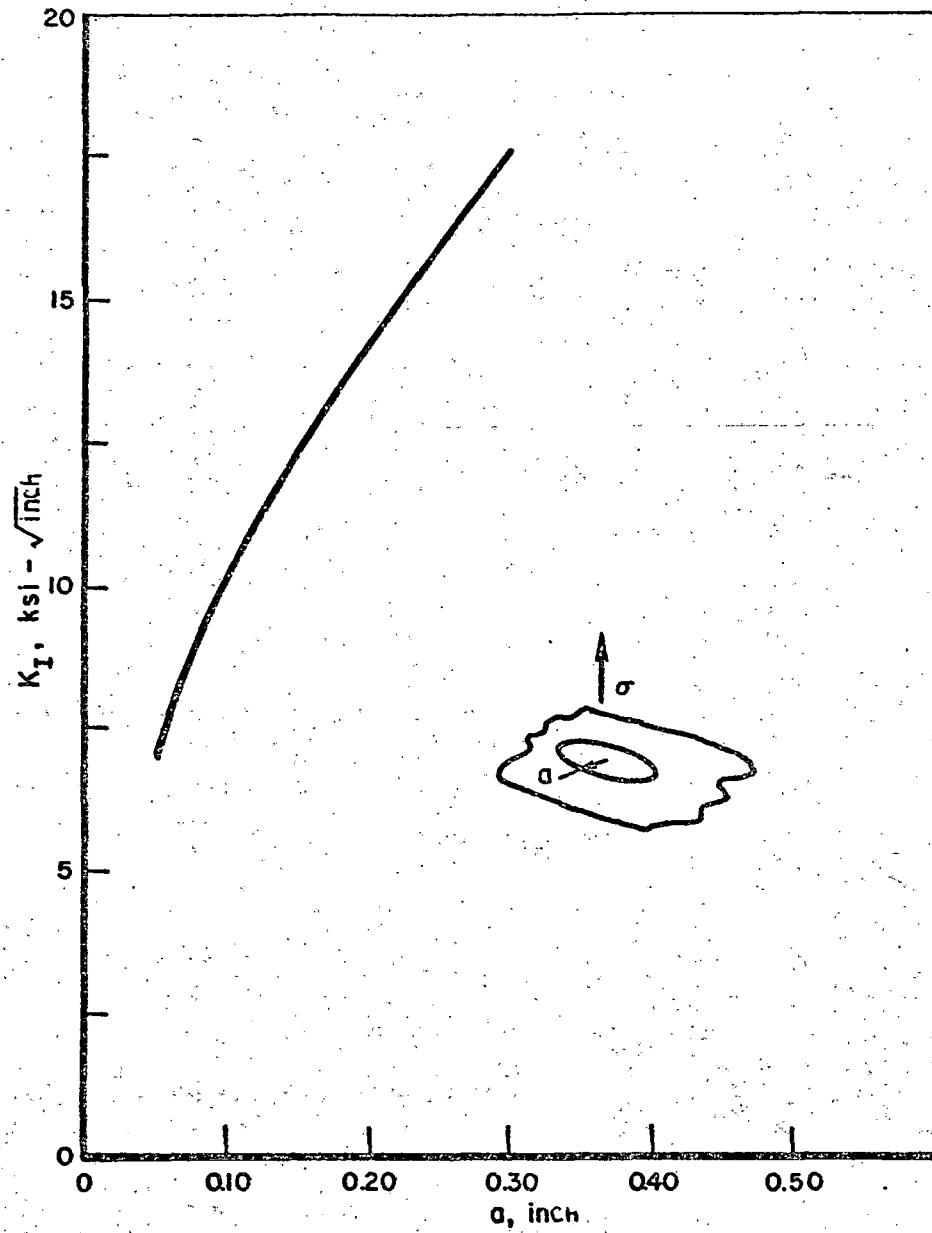


FIGURE 9-10. K_I FOR HEAD/WEB SEPARATION MODELED AS CIRCULAR EMBEDDED CRACK FOR $\sigma = 25,000$ PSI

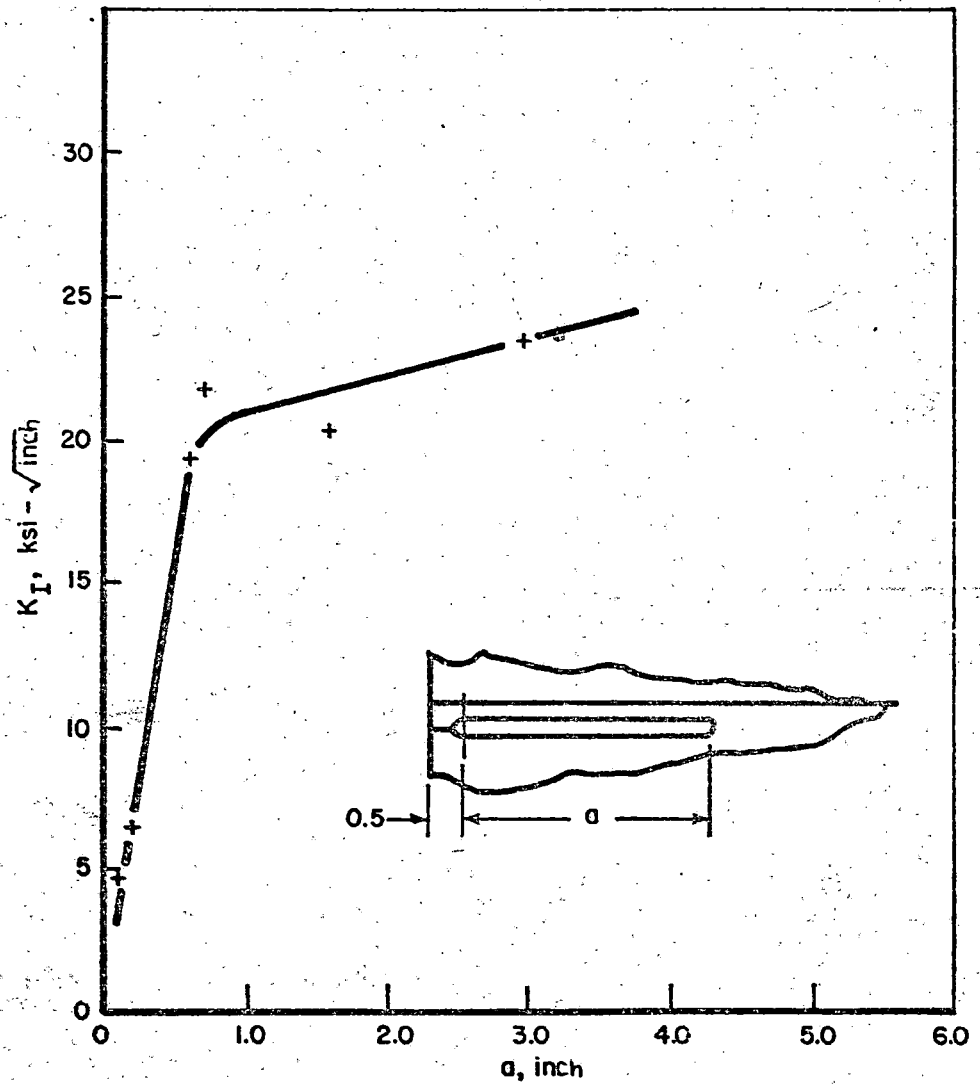


FIGURE 9-11. STRESS-INTENSITY FACTOR FOR HEAD/WEB SEPARATION GROWING BOTH DIRECTIONS; CRACK CONFIGURATION (A), WITH $\sigma = 25,000$ PSI

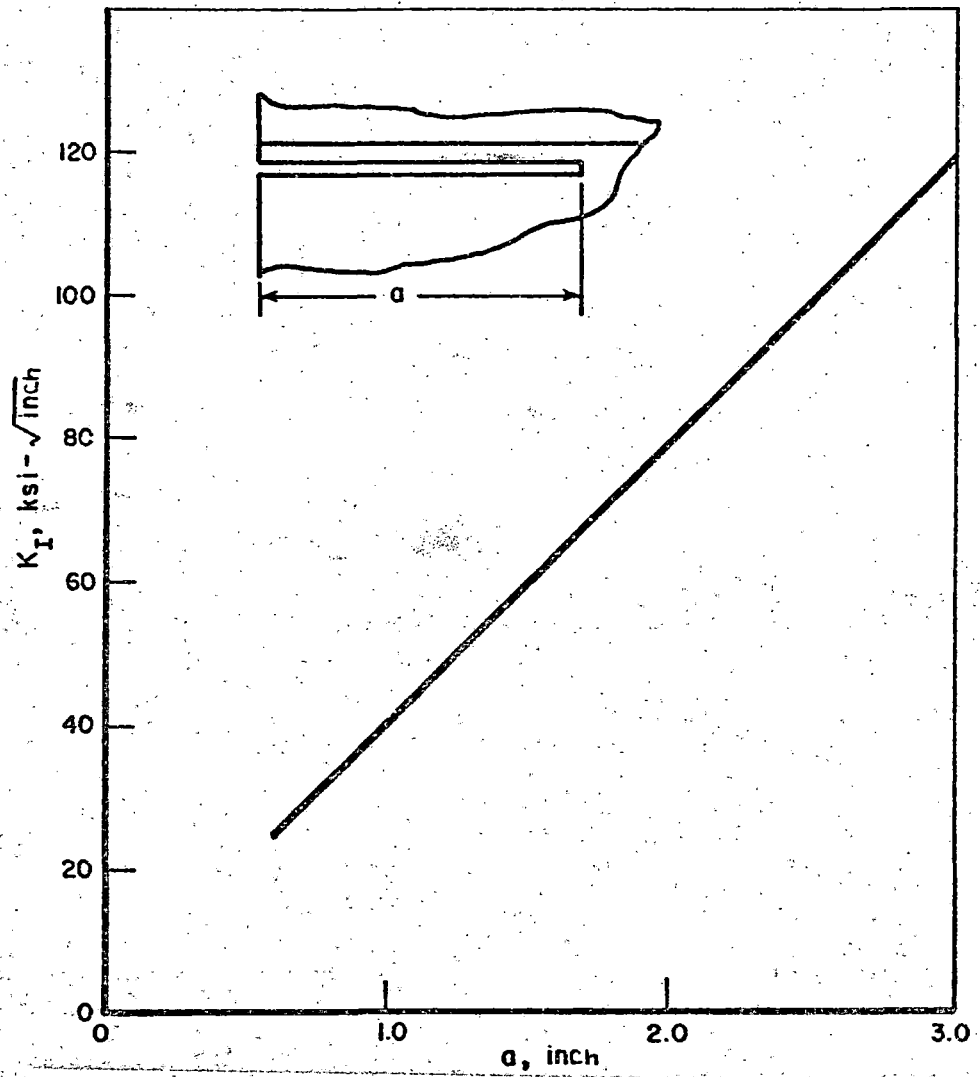


FIGURE 9-12. STRESS-INTENSITY FACTOR FOR AN OPEN HEAD/WEB SEPARATION WITH $\sigma = 25,000$ PSI

9-17/9-18

10. CONCLUSIONS AND SUGGESTIONS FOR FUTURE WORK

The major goal of the present investigation has been to assemble information about stresses that may contribute to deterioration or fracture of railroad rails. Such information is needed because of the imperative concern to improve rail track reliability in the United States. The stresses are shown to be of several kinds, interrelated in their causes and effects, yet distinct enough to warrant individual attention. The most sweeping distinction is whether the stresses occur in midrail or end sections, since their controlling factors differ, yet both sections are frequently subject to failure.

Midrail stresses have been studied for many years, as the many publications about them attest, yet their variety and interrelationships which may lead to rail failure still deserve much elucidation. Thus this report treats bending stress (perhaps the most familiar subject of the past), contact stresses, residual stresses, and crack stresses, and finds subtleties in each class and many interrelationships between the classes.

An example of a subtlety regarding rail bending is that it was found helpful to view the rail head near contact as a beam supported on the elastic foundation provided by the web, in addition to regarding the rail as a beam on the elastic foundation provided by the ties, ballast and subgrade. The finite element calculations of flexural stresses, depicted here in considerable detail, show this rail-head bending effect in the variations of at least two stress components. More broadly, those calculations show how six components of stress vary under idealized loading conditions, and they also show effects of varying foundation stiffness and of eccentric and lateral loading. Much more could be shown by such calculations, such as changes due to wearing of the rail. Subjects such as contact stresses, however, demand further refinements.

A subtlety of contact stresses is the extent to which they may be affected by fine details of the rail and wheel profiles. Means were introduced both for showing how details of the profiles affect the contact pressure distribution and what subsurface stresses arise from a given distribution. The local

stresses of contact are high enough to cause plastic flow, but fortunately these stresses decay rapidly away from the contact region. This report shows calculations of the subsurface stresses for a variety of load conditions, including some with tangential forces in the surface, and some for realistic non-standard wheel/rail profiles. Fortunately, for many purposes the presumption of ideal profiles suffices.

There is much evidence that rail heads in service undergo plastic deformations, which induce significant residual stresses in the interior of the rail, but description of those stresses is still sparse. Efforts to predict those stresses analytically have involved assumptions with questionable validity, and like laboratory experiments they are limited to initial phases of an essentially long process. Therefore, in this report, though both analysis and experimentation were attempted, reliance has been placed on a few measurements of residual stresses in rails from service. The specialized nature of these results are recognized, so, much work remains to be done regarding these stresses. Yet they appear to have a key role in crack growth and fracture, since they become tensile in a substantial region. The much larger contact stresses, in contrast, are mainly compressive, so their role in fracture seems more related to growth of residual stresses.

Crack propagating stresses can arise internally in rails if there is a crack in a region where the enveloping normal stress is tensile or tangential stresses are significant. The strongest possibility identified here for tensile stress comes from the residual stresses in rail heads, but flexural and contact stresses interpose cyclic alterations on them, so those stresses also influence possible crack growth. Therefore, the stress intensity factor calculations given here are based on realistic overall stress fields. These factors vary substantially along the edges of the cracks, which were presumed to be elliptical in the present work. Hence, attention is given as to how variations of stress distribution and the size of the crack influence those factors. The calculations of stress intensity factors were made using formulas that were available for buried elliptical cracks subjected to non-uniform normal and tangential loads, after first compacting the formulas. The methodology used here could be applied to many more hypothetical cracks and crack loads, and can furnish a basis for crack growth studies. Consideration of cracks near rail surfaces would require modifications in the methodology,

which, in turn, would complicate the procedure unless generous engineering approximations were used. Much further work could be done in these areas.

The study of stresses in rail ends was conducted in different ways, since that region involves such special considerations as how joint bars and bolt tensions affect the bending moment transmitted from one rail to the next, and how bolt holes affect stress concentrations in the web. Somewhat countering these complications is the observation that considerable study of rail bending can be conducted viewing the rail in planar form, so that two-dimensional finite element analysis produces useful approximate results. Thus finite element methods were used to expand beam theory study of joint bar reactions with the rail, including the effect of foundation modulus.

In order to study the distribution of stresses that might contribute to fracturing of a rail at a bolt hole or at the head web connection, a finite element model of the rail end was prepared with detailed elements around a bolt hole. It was used to compute circumferential stress around the periphery of the hole. Laboratory measurements were made to verify the stress variations around the hole. Then stress intensity factors were calculated for postulated flaws at positions in the bolt hole where cracking is known to occur, using simplified engineering formulas.

Viewing the program broadly, it may be seen that finite element methods provided opportunity for several new forms of stress evaluation. Finite element methods were most successful in the study of flexural stresses in the rail, for which much suggestive graphic information was obtained. Validation studies employing a photoelastic model and strain gages suggested that the results were generally accurate and adequate for many engineering purposes. Construction of a comprehensive data base that would highlight the effect of various parameters on rail stresses is recommended. The method of computing subsurface stresses beginning with elemental surface loads was also quite successful and serves as a useful complement to the finite element approach in determining stresses near the wheel/rail contact.

Residual stress calculation remains the most problematic area in the study of midrail stresses. The mathematical model developed seemed capable of predicting trends in residual stress formation, but it seemed very demanding of accuracy and would be hard to pursue to an extent that would predict

effects of realistic, extended service. Because of this it is suggested that the best approach for further work would probably be an experimental one in which measurements would be made at various stages of rail life. This could be done using service load conditions, preferably with some control so that gross tonnage would be known accurately. At the time of writing of this report, a program (DOT-TSC-1426, 1695) on experimental lines for determining residual stress distributions was well underway. In the future, after further increases in computing speed have been effected, it may be appropriate to return to analysis of residual stress growth.

The simplified method applied for computing stress intensity factors around railhead cracks, namely that derived from theories of Shah and Kobayashi or of Smith and Sorensen, offers a good link between stress evaluations and projections of crack growth. Together with stress distributions already computed and distributions which should be obtained through the studies recommended above, this method could be used to supply input for substantial study of crack growth. That study should account how stress intensity factors change under a passing load and what load spectrum a crack might be called to endure. Such studies should be made unless more general methods for computing stress intensity factors become available, such as might treat non-elliptical cracks growing faster where their stress intensity factors are higher. There is much room for fundamental developments in this area.

The study of rail end stresses is a good subject for further experimental work, both for determining how variations in structure and loading affect stress distributions, and for finding how crack growth proceeds. Formation of residual stresses and the role of fretting in the cracking process at rail ends are subjects that have hardly been addressed thus far in a quantitative manner. Further work in these areas also is recommended.

REFERENCES FOR SECTION 1

- 1-1. Federal Railroad Administration, "Bulletin No. 141, Summary and Analysis of Accidents on Railroads in the United States", Office of Safety, (December 1972).
- 1-2. NTSB-RSS-74-1, "Broken Rails: A Major Cause of Train Accidents", National Transportation Safety Board, (January 1974).
- 1-3. Railway Track & Structures, (January 1974), p 18-20.
- 1-4. Kecskes, O. S., Rail International, (September 1972), p 493-502.
- 1-5. Summary of Rail Failures, prepared by Sperry Rail Service, (1974).
- 1-6. "Track Safety Standard", Federal Railroad Administration, Office of Safety, (December 22, 1972).
- 1-7. Rail Defect Manual, Sperry Rail Service, (1964).
- 1-8. Smith, F. W., Emery, A. F., and Kobayashi, A. S., "Stress Intensity Factors for Semi-Circular Cracks, Part 2--Semi-Infinite Solid", Trans. ASME J. Appl. Mech., Vol. 34, (1967), p 953-959.
- 1-9. Smith, F. W. and Alavi, M. J., "Stress Intensity Factors for a Penny Shaped Crack in a Half Space", Eng. Frac. Mech., Vol. 3, (1971), p. 241-254.
- 1-10. Bell, J. C., "Stress Analysis for Structures with Surface Cracks", NASA CR159400, Report to NASA-Lewis Research Center, from Battelle Columbus Laboratories under Contract No. NAS3-21020, (1978).
- 1-11. Wise, S., Lindsay, D., and Duncan, I.G.T., "The Strength of Rails with Particular Respect to Rail Joints", Proc. Inst. Mech. Engrs., Vol. 174, No. 9, (1960), p 371-407.
- 1-12. Timoshenko, S., "Method of Analysis of Static and Dynamical Stresses in Rail", Proceedings of the Second International Congress for Applied Mechanics, Zurich, (1927). See also Collected Papers of Stephen P. Timoshenko, McGraw-Hill, New York, (1953).
- 1-13. "Stress Measurements on 131-lb RE Rail in Tangent and in a 6-degree Curve Under Regular Traffic--Norfolk & Western Railway--1945", AREA Proceedings, Vol. 48, (1947), p 768-784.
- 1-14. Thomas, H. R. and Hoersch, V. S., "Stresses Due to the Pressure of One Elastic Solid Upon Another", Univ. Illinois Eng. Expt. Sta. Bull., Vol. 212, (1930), p 54.

- 1-15. Radzimovsky, E. I., "Stress Distribution and Strength Condition of Two Rolling Cylinders Pressed Together", Univ. Illinois Eng. Expt. Sta. Bull., 408 (1953).
- 1-16. Fessler, H. and Ollerton, E., "Contract Stresses in Toroids Under Radial Loads", Brit. J. Appl. Phys., Vol. 8, (1957), p 387-393.
- 1-17. Leis, B. N., "Cyclic Inelastic Deformation and Fatigue Resistance Characteristics of a Rail Steel", Rail Steels--Developments, Processing, and Use, ASTM STP644, D. H. Stone and G. G. Knupp, Eds., American Society for Testing and Materials, (1978), p 449-468.
- 1-18. Groom, J. J., "Residual Stress Determination", Final Report on Task 2 for Contract DOT-TSC-1426, from Battelle Columbus Laboratories to Department of Transportation, Transportation Systems Center, (1979).
- 1-19. Anon., "The Effect of Stress Raisers Around a Bolt Hole on the Fatigue Life of a Rail", American Railway Engineering Association (AREA) Proceedings, Vol. 56, No. 521, (1952), p 960-975.
- 1-20. Talbot, A. N., et al, "Stresses in Railroad Track", American Railway engineering Association (AREA) Proceedings, Vol. 31, (1930), p 66-333.
- 1-21. Babb, A. S., "Experimental Stress Analysis of Rails", Proc. Instn. Mech. Engrs., Vol. 180, Part 1, No. 41, (1965), p 949-979.
- 1-22. Code, C. J., et al, "Effect of Bolt Spacing on Rail Web Stresses Within the Rail Joint", American Railway Engineering Association (AREA) Proceedings, Vol. 49, (1948), p 464-485.
- 1-23. Koyama, K. and Sasaki, N., "Stresses at Rail Joints as Influenced by Bolt Holes", Rwy, Tech. Res. Inst., Vol. 1, No. 3, (1960), p 45-49.
- 1-24. Anon., "Stresses Around the Bolt Hole of a Rail With the Joint in Tension", American Railway Engineering Association (AREA) Proceedings, Vol. 54, (1953), p 1254-1261.
- 1-25. Anon., "Measurements of Stresses in 132-RE Rail on Tangent Track - Santa Fe Railway, American Railway Engineering Association (AREA) Proceedings, Vol. 51, (1950), p 626-640.
- 1-26. Anon., "Measurements of Stresses in 115-RE Rail on Tangent Track - North Western Railway", American Railway Engineering Association (AREA) Proceedings, Vol. 52, (1951), p 690-704.
- 1-27. Code, C. J., "Relative Hazard Involved in Web Cracks of Varying Length Detected by Audigage", Penn Central Transportation Company, Test Report No. 784, (November 1962).
- 1-28. Wise, S., "Work Hardening Bolt Holes in Rail Ends", Rail International, (1960), p 863-865.

- 1-29. Anon., "Broaching Holes in Rails", Rwy. Gaz., Vol. 124, (1968), p 892.
- 1-30. Nield, B. J. and Goodman, W. H., "Dynamic Loading at Rail Joints", Rwy. Gaz., (August 15, 1969), p 616-619.
- 1-31. Jenkins, H. H., Stephenson, J. E., Clayton, G. A., Morland, G. W., and Lyons, D., "The Effect of Track and Vehicle Parameters on Wheel/Rail Vertical Dynamic Form", Railway Engineering Journal, (January 1974), p 2-26.
- 1-32. Bjork, J., "Dynamic Loading at Rail Joints - Effect of Resilient Wheels", Rwy. Gaz., (June 5, 1970), p 430-434.
- 1-33. Anon., "Test of Rail Joint Impact Effects on the C & N.W.," American Railway Engineering Association (AREA) Proceedings, Vol. 57, (1956), p 865.
- 1-34. Ahlbeck, D. R., et al, "Evaluation of Analytical and Experimental Methodologies for the Characterization of W/R Loads", DOT Report, (1976).
- 1-35. Sneddon, I. N., "The Distribution of Stress in the Neighbourhood of a Crack in an Elastic Solid", Proc. Roy. Soc., London, Ser. A, Vol. 187, (1946), p 229-260.
- 1-36. Bell, J. C., "Stresses from Arbitrary Loads on a Circular Crack", Int. J. Fracture, Vol. 15, (1979), p 85-104.
- 1-37. Bell, J. C., "Stresses from Variously Loaded Circular Cracks", J. Struct. Div. Am. Soc. Civ. Engrs., Vol 103, (1977), p 355-376.
- 1-38. Besuner, P. M., "Fracture Mechanics Analysis of Rails with Shell-Initiated Transverse Defects", Report to American Association of Railroads, from Failure Analysis Associates under Contract FAA-75-1-19(B), (November 1975).
- 1-39. Shah, R. I. and Kobayashi, A. S., "Stress Intensity Factor for an Elliptical Crack Under Arbitrary Normal Loading", Eng. Frac. Mech., Vol. 3, (1971), p 71-96.
- 1-40. Smith, F. W. and Sorenson, D. R., "Mixed Mode Stress Intensity Factors for Semielliptical Surface Cracks", Colorado State University Final Report for NASA, Grant NGL-06-002-063, (June 15, 1974).
- 1-41. Shah, R. C. and Kobayashi, A. S., "Stress Intensity Factors for an Elliptical Crack Approaching the Surface of a Semi-Infinite Solid", Int. J. Fracture, Vol. 9, (1973), p 133-146.

- 1-42. Brock, D. and Rice, R. C., "Fatigue Crack Growth Properties", Battelle Columbus Laboratories Final Report to U.S. Dept. of Transportation, DOT-TSC-1076, (1977).
- 1-43. Lankford, J. and Kusenberger, F. N., "Initiation of Fatigue Cracks in 4340 Steel, Metallurgical Trans., Vol. 4, (February 1973), p 553-559.
- 1-44. Bowles, C. Q. and Schijve, J., "The Role of Inclusions in Fatigue Crack Initiation in an Aluminum Alloy", Int. J. Fracture, Vol. 9, No. 2, (June 1973), p 171-179.
- 1-45. Harkgard, G., "A Theoretical Study of the Influence of Inclusions upon the Initiation and Growth of Fatigue Cracks in Steel", Jernkant, Ann. Vol. 155, (1971), p 239-294.
- 1-46. Paris, P. C., Gomer, M. P., and Anderson, W. E., "A Rational Analytic Theory of Fatigue", The Trend in Engineering, University of Washington, Seattle, Vol. 13, No. 1, (1961).
- 1-47. Paris, P. C. and Erdogan, F., "A Critical Analysis of Crack Propagation Laws", Trans. ASME, J. Basic Eng., Vol. 85D, (1963), p 528-534.
- 1-48. Forman, R. G., Kearney, V.E., and Egle, R. M., "Numerical Analysis of Crack Propagation in a Cyclic-Loaded Structure", Trans. ASME, J. Basic Eng., Vol. 89D, (1967), p 459-464.
- 1-49. Colliprest, J. E., Jr., and Ehret, R. M., "A Generalized Relationship Representing the Sigmoidal Distribution of Fatigue Crack Growth Rates", Rockwell International Report, (1979).
- 1-50. Davies, K. B., and Johns, T. G., "Preliminary Description of Stresses in Railroad Rail at Bolted Joints", Battelle Columbus Laboratories Interim Report to U.S. Department of Transportation, (March 15, 1978). (Available through N.T.I.S.)

REFERENCES FOR SECTION 2

- 2-1. Winkler, E., "Die Lehre von der Elastizität und Festigkeit", Verlag H. Dominikus, Prag, 1867.
- 2-2. Schwedler, J. W., "On Iron Permanent Way", Proceedings, Institution of Civil Engineers, London, 1882, p 95-118.
- 2-3. Zimmerman, H., "Die Berechnung des Eisenbahnoberbaues", Verlag W. Ernst & Sohn, Berlin, 1888.
- 2-4. Timoshenko, S. P., "Method of Analysis of Static and Dynamical Stresses in Rail", Proceedings of the Second International Congress of Applied Mechanics, Zurich, 1927. See also Collected Papers of S. P. Timoshenko, McGraw-Hill, New York, 1953.
- 2-5. Hetenyi, M., Beams on Elastic Foundations, University of Michigan Press, 1946.
- 2-6. Johns, T. G., and Davies, K. B., "A Preliminary Description of Stresses in Railroad Rail", Interim Report No. FRA-ORD-76-294 to Department of Transportation, November 1976.
- 2-7. Prause, R. H., et al., "Assessment of Design Tools and Criteria for Urban Rail Track Structures. Vol. I. At-Grade Tie-Ballast Track", Department of Transportation Report No. UMTA-MA-06-0025-74-3, Reprint July 1974, p 18.
- 2-8. Talbot, A. N., "Progress Report on the Special Committee on Stresses in Track", AREA Proceedings, Vol. 18, 21, 24, 26, 31, 35, 42, Chicago, Illinois. (Vol. 42 was dated 1941.)
- 2-9. Timoshenko, S. P., and Langer, B. F., "Stresses in Railroad Track", ASME Transactions, Vol. 54, 1932, p 277-290.
- 2-10. Eisenmann, J., "Stress Distribution in the Permanent Way Due to Heavy Axle Loads and High Speeds", AREA, Bulletin 622, September-October, 1964, p 24-59.
- 2-11. Kerr, A. D., "The Stress and Stability Analyses of Railroad Tracks", Journal of Applied Mechanics, December 1974, p 841-848.
- 2-12. Clarke, C. W., "Track Loading Fundamentals, Parts 1-7", Railway Gazette, Vol. 106, 1957.
- 2-13. McConnell, D. P., and Perlman, A. B., "An Investigation of the Structural Limitations of Railroad Track", Interim Report to Department of Transportation under Contract DOT-TSC-1575, June 1979.

- 2-14. Leaf, W., "Research on Rail Section", Western Metals, September 1947, p 20-24.
- 2-15. Code, C. J., "A Method of Calculating the Maximum Stress in the Web of Rail Due to an Eccentric Vertical Load", Proc. 46th Convention AREA, Vol. 48, 1947, p 987-991.
- 2-16. Martin, G. C., and Hay, W. W., "The Influence of Wheel-Rail Contact Forces on the Formation of Rail Shells", ASME 72-WA/RT-8, 1972.

REFERENCES FOR SECTION 3

- 3-1. Hertz, H., "Über die Berührung fester elastischer Körper", 1881, reprinted in "Gesammelte Werke von Heinrich Hertz", Vol. 1, (1895), p 155-173.
- 3-2. Belyayev, N. M., "Application of Hertz' Theory to the Calculation of Local Stresses at the Contact Point of Wheels and Rails", (in Russian), *Vesnik Inzhenerov i Tekh.*, Vol. 2 (1917), *Memoirs on the Theory Structures*, Petrograd, (1924).
- 3-3. Dinnik, A. N., "Hertz' Formula and Its Experimental Verification", (in Russian), *Zhurnal russk. fiz.-Khm, ob-va, fiz., otd.*, Vol. 38, Part 1, No. 4, (1906), p 242-249.
- 3-4. Way, S., "Pitting Due to Rolling Contact," *J. Appl. Mech.*, 2, (1935), pp 49-58, p 110-114.
- 3-5. Karas, F., "Werkstoffanstrengung beim Druck Achsenparalleler Waizen nach den gebräuchlichen Festigkeitshypothesen", *Forsch. Ingenieur*, Vol. 11, (1940), p 334-339.
- 3-6. Radzimovsky, E. I., "Stress Distribution and Strength Condition of Two Rolling Cylinders Pressed Together", *Univ. Illinois Eng. Expt. Sta. Bull.* 408, (1953), p 40.
- 3-7. Palmgren, A. and Sundberg, K., "Once Again on the Subject of Ball Bearing Load Capacity", (in Swedish), *Tek. Tidskr. (Mekanik)*, Vol. 49, (1919), p 57-67.
- 3-8. Thomas, H. R. and Hoersch, V. A., "Stresses Due to the Pressure of One Elastic Solid Upon Another", *Univ. Illinois Eng. Expt. Sta. Bull.* 212, (1930), 54 p.
- 3-9. Weibull, W., "Stresses in the Contact of Elastic Bodies", (in Swedish), *Tek. Tidskr. (Mekanik)*, Vol. 49, (1919), p 160-163.
- 3-10. Lundberg, G. and Odqvist, F.K.G., "Studies on Stress Distributions in the Vicinity of the Contact Region Between Bodies, With Applications", (in Swedish, English Summary), *Ing. Vetenskaps Akad. Handl.* 116, (1932), p 64.
- 3-11. Fessler, H. and Ollerton, E., "Contact Stresses in Toroids Under Radial Loads", *Brit. J. Appl. Phys.*, (1957), p 387-393.
- 3-12. Seely, F. B. and Smith, J. O., *Advanced Mechanics of Materials*, John Wiley and Sons, 2nd Ed., (1967).
- 3-13. Johns, T. G. and Davies, K. B., "A Preliminary Description of Stresses in Railroad Rail", Report No. FRA-ORD-76-294, U.S. Department of Transportation, (November 1976).

- 3-14. Carter, F. W., "On the Action of a Locomotive Driving Wheel", Proc. Roy. Soc., London, A112, (October 1926), p 151-157.
- 3-15. Mindlin, R. D., "Compliance of Elastic Bodies in Contact", J. Appl. Mech., Vol. 16, (1949), p 259-268.
- 3-16. Poritsky, H., "Stresses and Deflections of Cylindrical Bodies on Contact with Application to Contact of Gears and of Locomotive Wheels," J. Appl. Mech., Vol. 72, (1950), p 191-201.
- 3-17. Johnson, K. L., "Surface Interaction Between Elastically Loaded Bodies Under Tangential Forces," Proc. Roy. Soc. A, Vol. 230, (1955), p 531-549.
- 3-18. Johnson, K. L., "Energy Dissipation at Spherical Surfaces in Contact Transmitting Oscillating Forces," J. Mech. Engr. Sci., Vol. 3, No. 4, (1961), p 362-369.
- 3-19. Johnson, K. L., "Tangential Traction and Micro-slip in Rolling Contact," included in Rolling Contact Phenomena, T. Bidwell, editor, Elsevier, ASME, (1962), pp 6-28.
- 3-20. Johnson, K. L., "A Shakedown Limit in Rolling Contact," Proceedings Fourth U.S. National Congress Applied Mechanics, ASME, Berkeley, California, (1962), p 971-975.
- 3-21. Johnson, K. L. and Jefferis, J. A., "Plastic Flow and Residual Stresses in Rolling and Sliding Contact," Proc. Symp. Fatigue in Rolling Contact, Inst. Mech. Engrs., (London) Vol. 177, (1963), p 95.
- 3-22. Conry, T. F. and Seireg, A., "A Mathematical Programming Method for Design of Elastic Bodies in Contact", J. Appl. Mech., 70 WA/APM-52, (1970).
- 3-23. Johns, T. G. and Leissa, A. W., "The Normal Contact of Arbitrarily Shaped Multilayered Elastic Bodies", Symposium on the Contact of Deformable Bodies, IUTAM, Univ. of Twente, Enschede, (August 1974).
- 3-24. Cooperrider, N. K., et. al., "Analytical-Experimental Investigation of Wheel-Rail Constraint Relationships", Dept. of Transportation Contract DOT-US-40018, Interim Report.
- 3-25. Smith, J. O., Lui, C. K., "Stresses Due to Tangential and Normal Loads on an Elastic Solid with Application to Some Contact Stress Problem," Trans. ASME, J. Appl. Mech., Vol. 75. No. 6, (June 1953), p 157-166.
- 3-26. Hamilton, G. M. and Goodman, L. E., "The Stress Field Created by a Circular Sliding Contact," Trans. ASME, J. Appl. Mech., (June 1966), p 371-376.

- 3-27. Bell, J. C., "Continuous Analysis of Stresses From Arbitrary Surface Loads on a Half-Space," Int. J. Solids Structures, Vol. 16, (1980), p 1069-1091.
- 3-28. Nakamura, R., et. al., "The Rail Shelly Crack in Japan," Quarterly Report RTRI, Vol. 6, No. 3, (1965), p 34-44.

REFERENCES FOR SECTION 4

- 4-1. Hyler, W. S., and Grover, H. J., "The Study of Simulated Rails Under Repeated Rolling Loads", Final Report to AAR and AISI, Battelle Memorial Institute, (August 31, 1953).
- 4-2. Johnson, K. L., "A Shakedown Limit in Rolling Contact", Proceedings Fourth U.S. National Congress Applied Mechanics, ASME, Berkeley, California, (1962), p 971-975.
- 4-3. Merwin, J. E., and Johnson, K. L., "An Analysis of Plastic Deformation in Rolling Contact", Proceedings of the Institution of Mechanical Engineers, Vol. 177, No. 25, (1963), p 676-685.
- 4-4. Johnson, K. L., and Jefferis, J. A., "Plastic Flow and Residual Stresses in Rolling and Sliding Contact", Proc. Symp. Fatigue in Rolling Contact, Inst. Mech. Engrs., London, Paper 5, (1963), p 50-61.
- 4-5. Martin, G. C., and Hay, W. W., "The Influence of Wheel Rail Contact Forces on the Formation of Rail Shells", ASME 72-WA/RT-8, (1972).
- 4-6. Office for Research and Experiments of the International Union of Railways, "Study of Fatigue Phenomena of the Rail in the Contact Zone with the Wheel," Rail International, Vol. 3, No. 13, (September 1973), p 741-794.
- 4-7. Symonds, P. S., "Shakedown in Continuous Media", Trans. ASME, J. Appl. Mech., Vol. 73, (1951), p 85.

REFERENCES FOR SECTION 5

- 5-1. Broek, D., Elementary Engineering Fracture Mechanics, Noordhoff, Leyden, (1974).
- 5-2. Davies, K. B. and Feddersen, C. E., "Inverse Hyperbolic Tangent Model of Fatigue Crack Growth", Journal of Aircraft, Vol. 12, No. 12, (December 1975), p 943-947.
- 5-3. Hellen, T. K., and Blackburn, W. S., "The Calculation of Stress Intensity Factors in Two and Three Dimensions Using Finite Elements", in Computational Fracture Mechanics, ed. Rybicki, E. F. and Benzley, S. E., ASME Publ, (1975), p 103-120.
- 5-4. Shah, R. I. and Kobayashi, A. S., "Stress Intensity Factor for an Elliptical Crack Under Arbitrary Normal Loading", Eng. Frac. Mech., Vol. 3, (1971), p 71-96.
- 5-5. Smith, F. W., and Sorenson, D. R., "Mixed Mode Stress Intensity Factors for Semielliptical Surface Cracks", Colorado State University Final Report for NASA, Grant NGL-06-002-063, (June 15, 1974).
- 5-6. Bell, J. C., "Stresses from Arbitrary Loads on a Circular Crack", Int. J. Fracture, Vol. 15, (1979), p 85-104.

REFERENCES FOR SECTION 7

- 7-1. Talbot, A. N., et al, "Stresses in Railroad Track", Proc. American Railway Engineering Association, AREA, Vol. 31, 1930, p 66-333.
- 7-2. Winkler, E., Die Lehre von der Elastizitat und Festigkeit, Verlag H. Dominikus, Prague, 1867.
- 7-3. Johns, T. G., and Davies, K. B., "Preliminary Description of Stresses in Railroad Rail at Bolted Joints", U.S. Dept. of Transportation Interim Report (document available through the National Technical Information Service, Springfield, Virginia), March 1978.
- 7-4. Hetenyi, M., Beams on Elastic Foundation, University of Michigan Press, Ann Arbor, 1961.
- 7-5. Leis, B. N., and Laflen, J. H., "Cyclic Inelastic Deformation and Fatigue Resistance of a Rail Steels", in Proceedings of the ASTM Symposium on Rail Steels, ASTM STP 644, 1978, p 449-468.
- 7-6. Anon., "Derailment Near Hither Green", Railway Gazette, Vol. 124, 1968, p 753.
- 7-7. Bathe, K. J., "ADINA, A Finite Element Program for Automatic Dynamic Nonlinear Analysis", MIT Report 82448-1, 1975.

REFERENCES FOR SECTION 8

- 8-1. Savin, G. N., Stress Concentration Around Holes, Translated by W. Johnson, Pergamon Press, (1961), p 94.

REFERENCES FOR SECTION 9

- 9-1. Broek, D., Elementary Engineering Fracture Mechanics, Sijthoff and Noordhoff, Netherlands, (1978).
- 9-2. Bowie, O. L., "Analysis of an Infinite Plate Containing Radial Cracks Originating at the Boundary of an Internal Circular Hole", J. Math. and Phys., Vol. 25, (1956), p 60-71.
- 9-3. Sneddon, I., "The Distribution of Stresses in the Neighborhood of a Crack in an Elastic Solid", Proc. Royal Soc., Vol. 187, (1946), p 229-260.
- 9-4. Shah, R. C. and Kobayashi, A. S., "Stress Intensity Factor for an Elliptical Crack Under Arbitrary Normal Loading", Eng. Frac. Mech., Vol. 3, (1971), p 71-96.
- 9-5. Smith, S. H. and Davies, K. B., "Damage Tolerance Analysis of C-141 Wing Plank Riser-Runout Structures", BCL Report No. G-6246, (June 1976).
- 9-6. Hellen, T. K. and Blackburn, W. S., "The Calculation of Stress Intensity Factors in Two and Three Dimensions Using Finite Element", Computational Fracture Mechanics, E. F. Rybicki and S. E. Benzley, eds., American Society of Mechanical Engineers, (1975).

APPENDIX A

VALIDATION OF FINITE ELEMENT FULL-RAIL MODELS

In order to validate the results obtained from finite element models of rails, extensive photoelastic tests were conducted. The numerical results were also compared with strain gage and deflection results obtained from the literature and other BCL programs. This validation effort is described in the two following subsections.

Photoelastic Validation Tests

For the purpose of validating the finite element models, a full scale photoelastic model of a 132-lb RE rail was fabricated and analyzed using the three-dimensional stress freezing technique.

Model Preparation

There are a number of materials suitable for three-dimensional photoelastic models but most of these popular resins cure in such a way that they must be machined to final shape from a rough casting. For a model of a 132-lb rail, machining to final shape was considered impractical, so it was decided early in this program to cast the photoelastic models to final shape. Very few photoelasticians in the United States employ such a procedure, but there are several British researchers, most notably Fessler [A-1], who do. Since Fessler and others had already found a resin suitable for this application, the same one was used here. It contains

100 parts per weight Araldite 6060,

30 parts per weight Phthalic Anhydride.

A description of the casting procedure follows.

In order to cast a model, a mold is required. In this instance, a piece of new 132-lb rail was used for the mold core. The mold was made using a two-phase silicone rubber/plaster-of-paris construction procedure. The first phase was the application of a layer of GE RTV 630 silicone rubber to the rail

core. To insure a smooth casting surface, the rail was first sanded and cleaned with a strong metal conditioner. The pits were then filled with epoxy and the entire rail was coated with vaseline petroleum jelly to provide a release for the RTV 630. Because the RTV 630 was fairly thin (easily pourable), it was applied in a number of separate pourings. Temporary dams were required to confine each pour which was generally about 1/8th-inch deep. The RTV was mated to four aluminum angles; two each running along the top and bottom of the rail as shown in Figure A-1. The angles were provided to insure accurate alignment when the mold was subsequently split open and refitted in use.

To provide a semirigid backing for the silicone liner, a plaster-of-paris casing was poured around the rail and silicone, using a sheet metal exterior mold. To assure good bonding between the casing and the liner, the silicone liner was covered with surgical gauze. The gauze was cemented to the silicone liner using Dow Corning bath tub sealer. Thus, the plaster of paris flowing in and around the gauze provided interlocking attachment. The completed mold is shown in Figure A-2. The final step was removal of the rail. The mold was then ready for use.

Since the completed mold was open on both ends, filling the mold in the vertical position required that the lower end be sealed. This was done by fastening a piece of silicone rubber sheet to the bottom of the mold with Dow Corning tube sealer. The dead weight of the mold on the silicone sheet also provided additional sealing.

The procedure outlined below was used to make the two castings that were poured.

- 1) The required weight of resin was calculated using the specific gravity of the resin and curing agent (1.22) and the volume of the mold.
- 2) The resin, which was solid at room temperature, was heated to about 130 C to 140 C. (The resin melts somewhere below 100 C.)
- 3) The required weight of Phthalic Anhydride (a white crystalline powder) was stirred into the resin. The combined resin and curing agent, hereafter called the resin, was then continuously stirred at 120 C to 125 C until the Phthalic anhydride was totally dissolved

A-3

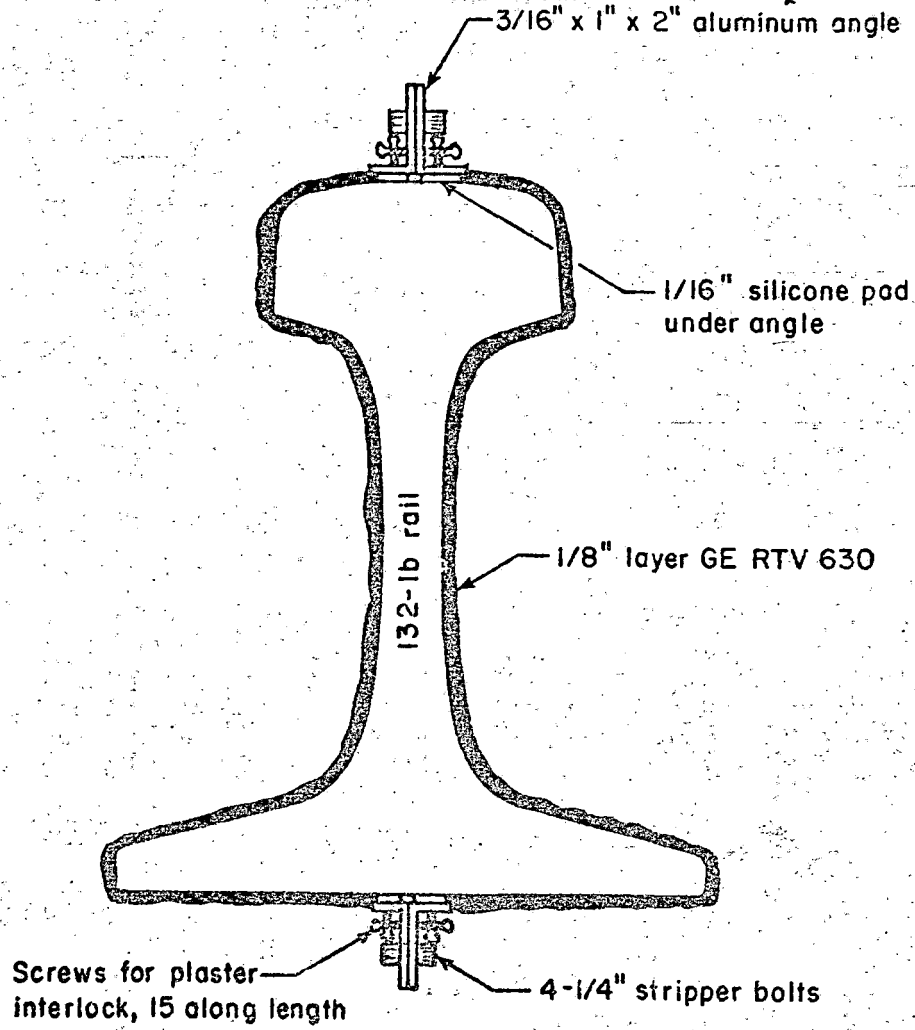


FIGURE A-1. 132-LB RAIL CORE WITH RTV AND ALUMINUM FLANGES INSTALLED

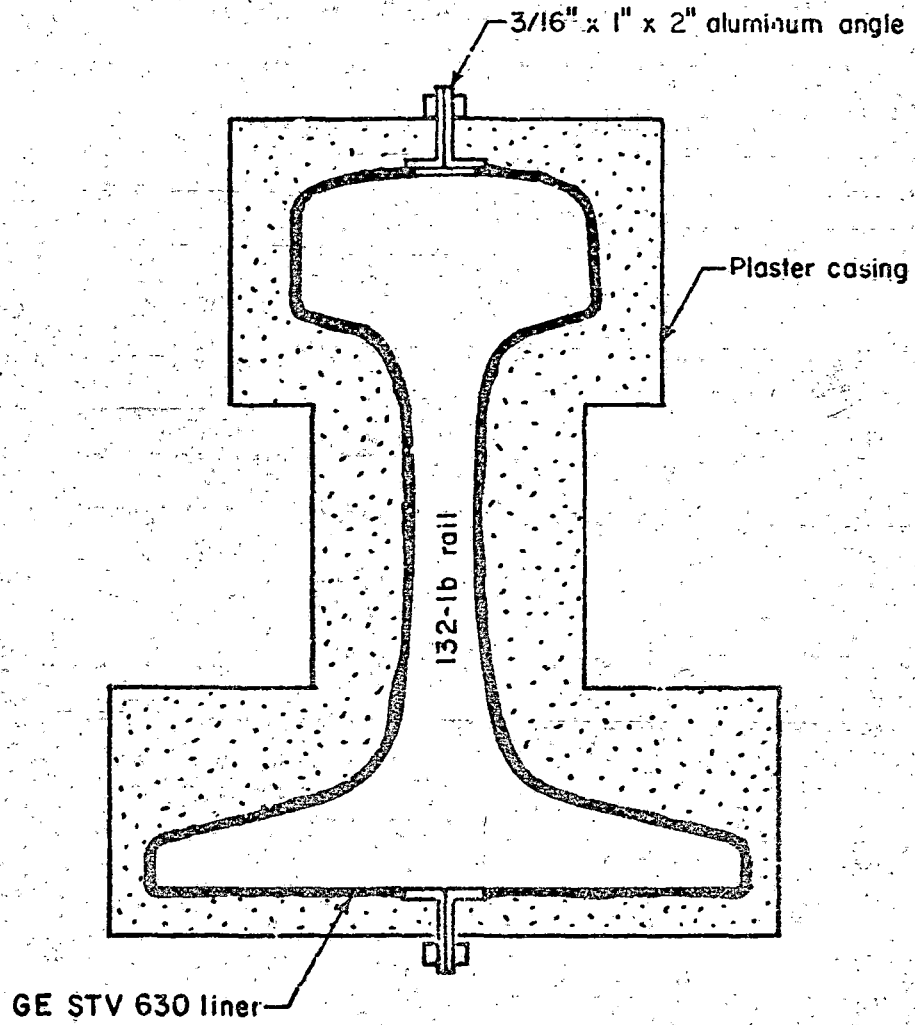


FIGURE A-2. COMPLETED MOLD WITH 132-LB RAIL CORE STILL IN PLACE

and invisible. In mixing large batches, a double boiler of mineral oil was used to heat the resin.

- 4) Prior to casting, the mold was sprayed liberally with Kraxo 1711 release agent and then preheated to 125 C.
- 5) The 125 C mixed resin was then poured into the 125 C preheated mold. An effort was made to pour the resin down the side of the mold, but this was difficult.
- 6) After the model was poured, the oven temperature was reduced to 110 C and the model was given several days to cure.
- 7) The oven was allowed to cool down over a 12-hour period, and the model was subsequently removed from the mold while still hot to touch. The model was immediately postcured to 125 C to remove residual fringe patterns. Finally, the model was cooled to room temperature over a 36-hour period.

While the same procedure was used with both castings, the second casting contained residual fringes that could not be removed by the post-curing to 160 C. The residual fringes were longitudinal and confined principally to the rail head.

No trouble was encountered in removing the castings from the mold. Although the mold lining would have been good for many pourings, the plaster casing was no longer sound. After the two pourings, the mold casing contained many cracks and no longer provided the required rigidity for the silicone liner. Had steel angles been used and had the exterior mold been left in position, the mold would have been more durable. If another mold were to be made, a reinforced epoxy casing would be considered. The plaster casing was removed in anticipation of reusing the liner.

Loading of the Model

A loading fixture was required that could withstand the 130 C environment of the stress freezing cycle. Gravity loads are generally preferable for this type of work because of their stability, but because a load of 400 pounds was to be used, another technique of load application was needed.

Some observations on the reasons for conducting the test are appropriate. It was planned initially that the three-dimensional photoelastic model would simulate actual track and loading conditions. However, if this were done, and if results from the photoelastic model differed significantly from results from the finite-element model, a difficult question would be posed: do the results differ because of

- a) errors in the photoelastic analysis,
- b) errors in the FEM (finite-element method) analysis, or
- c) errors in the matching of the boundary conditions?

Because the purpose of the photoelastic analysis was to provide a validation of the finite element models, it seemed prudent to remove as many sources of discrepancy as possible. Thus, it was concluded that the simpler the boundary conditions were, the better would be the chances of proper validation. The simple support was thus selected as the boundary condition for the bottom of the rail since it represents the least complex situation. A point load was thought to be unreasonable due to the large local deformation that would result in the contact area. In order to reduce these deformations, an elliptical loading patch was employed with major and minor axes of 0.54 inch and 0.38 inch, respectively. These dimensions are typical of contact for a steel rail and wheel. Even with the elliptical load patch, the difference in the model's Poisson's ratio and finite deformations that occur invalidate laws of similitude in the contact area.

The loading fixture that was finally designed and built is shown in Figure A-3. It employs a high temperature, 2-1/2-inch bore, Bimba pneumatic cylinder for load application and is fully adjustable to provide different spans and eccentricities of loading. The fixture was made so that it would slide into the oven as a shelf. A nitrogen cylinder and a low pressure regulator were selected as a pressure source for the cylinder. Pressure was monitored continuously during stress freezing so that the stability of loading could be measured. In order to provide the most accurate relationship between the applied pressure and the cylinder force, the system was calibrated with a load cell.

Reproduced from
best available copy.

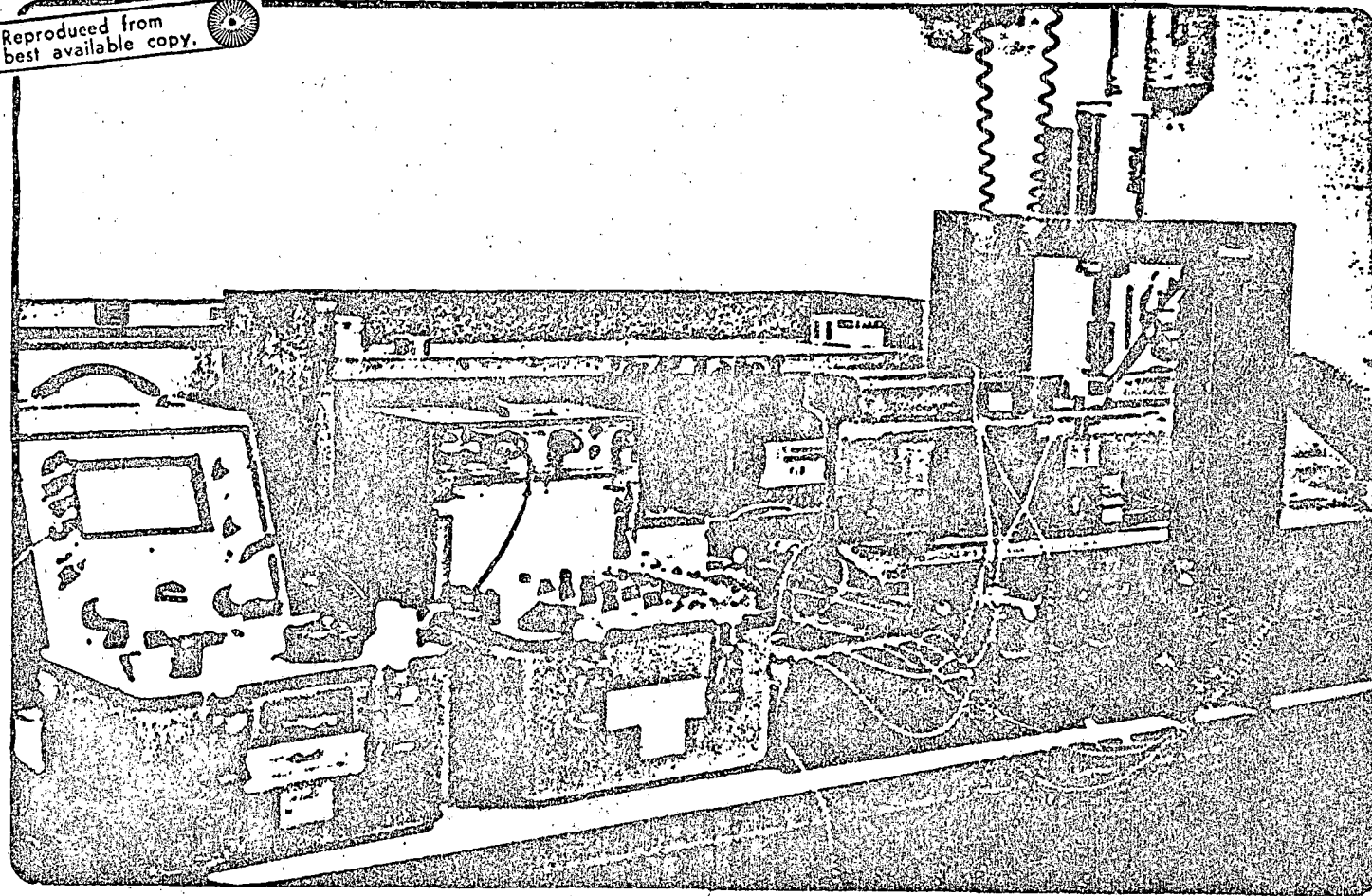


FIGURE A-3. PHOTOGRAPH OF THE INSTRUMENTED MODEL INSTALLED IN THE LOADING FIXTURE

Strain-Gage Results

Any experimental endeavor involves possibilities of error or even complete failure. Since three-dimensional photoelastic work contains many risks, it was desirable to use independent checks. Thus, a number of strain gages were applied to the photoelastic model. The strain gages were also to provide data for an asymmetric load case, for which the photoelastic model was rendered unusable by residual fringes.

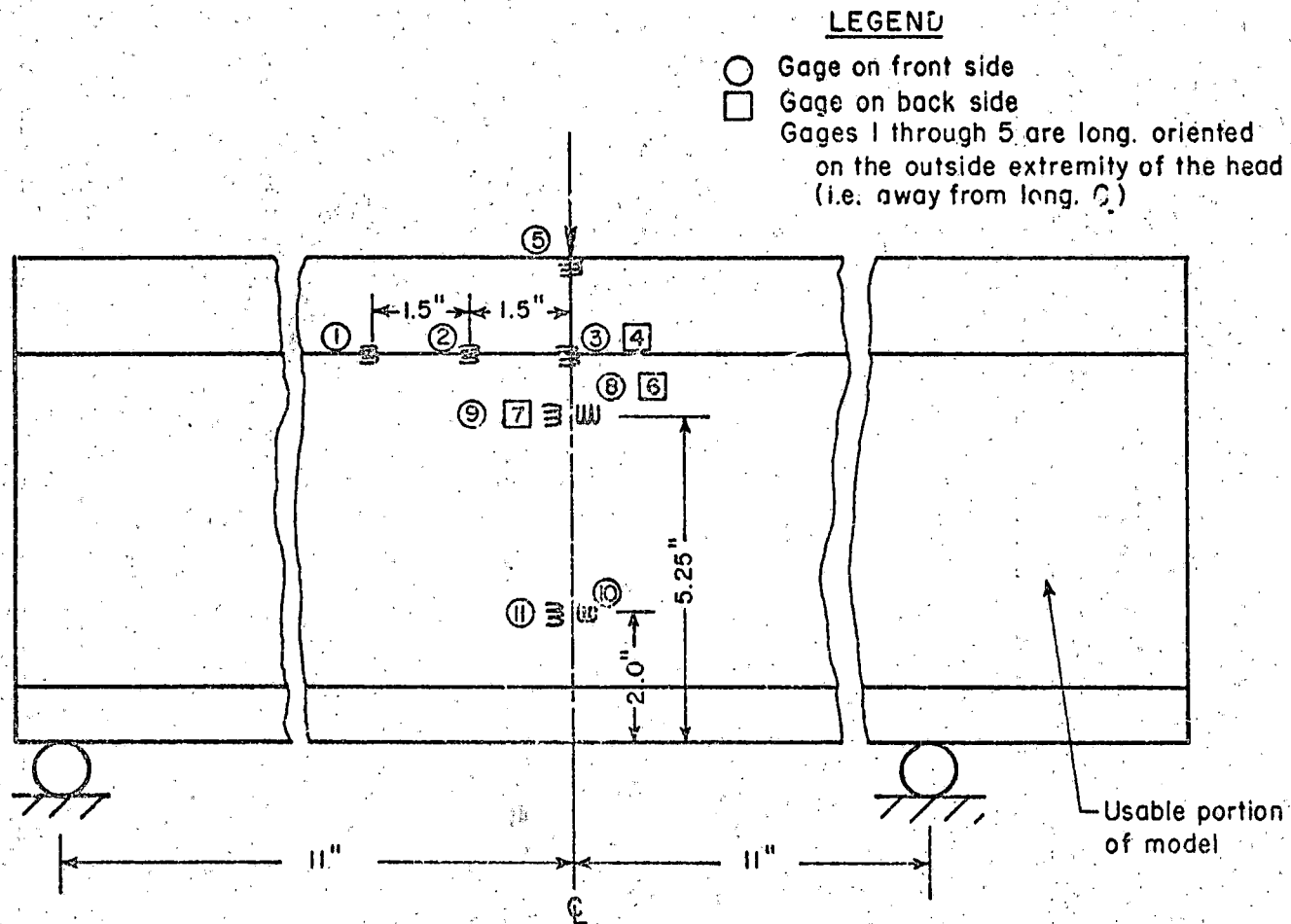
Eleven 120 ohm foil strain gages with a gage length of 0.062 inch were applied to the photoelastic model at the locations shown in Figure A-4. (Other analyses had indicated that these points would be interesting). Two load cases were applied, a centered load of 464 pounds and a 0.75-inch off-set load of 275 pounds. Table A-1 gives averaged results for a number of load applications. For the sake of comparison, actual rail stresses measured by Battelle are shown also, as are some results reported by the AAR [A-2] for cases where their information was sufficient to calculate stresses. One of these strains is also used in the next section in the discussion of the photoelastic results.

In order to evaluate stresses from the strains, the room temperature modulus was required. To do this, a calibration bar was instrumented with two additional strain gages. The instrumented bar was then tested under bending and uniaxial tension. The results of the calibration indicated a room temperature modulus of 493,000 psi.

Stress Freezing and Slicing of the Model

The test fixture was placed in the oven and the photoelastic model was installed in it. The strain gages were used again to obtain a load position that would provide minimal eccentricity of loading as shown in Figure A-5. The support rollers of the load fixture were adjusted for a span of 22 inches. The model was then heated to 125 C over a 12-hour period and the temperature was allowed to stabilize for several hours.

Up until this time, the model was unloaded. Care was taken in the stress freezing load. An optimal stress freezing load should produce readable (that



A-9

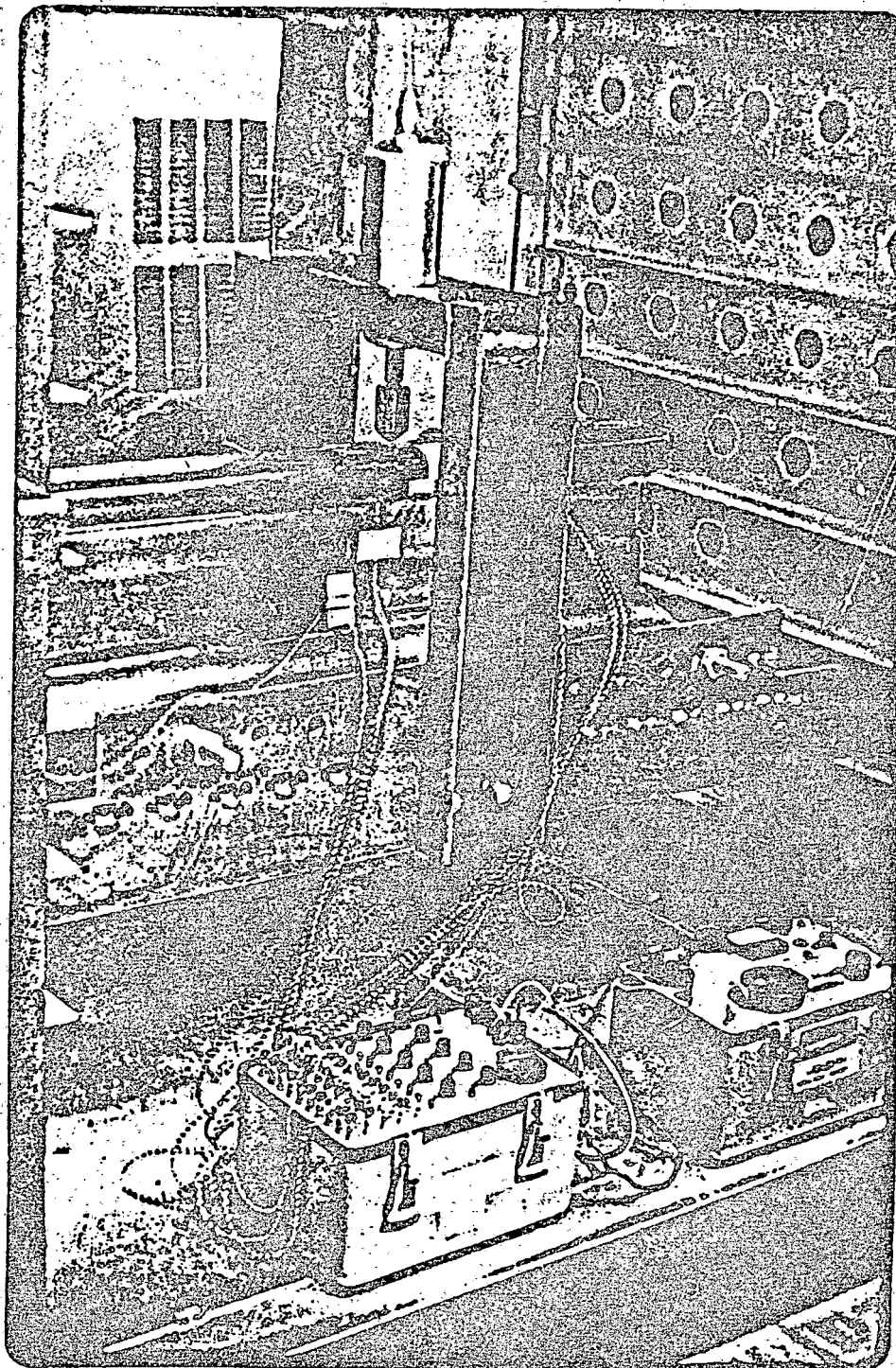
FIGURE A-4. STRAIN GAGE LOCATIONS

TABLE A-1. REDUCED STRAIN DATA

Gage Location	in./in.	464-lb Symmetric Load			275 lb Asymmetric Load Offset .75 inch			
		, psi from data*	, psi BCL**	, psi AAR	in./in.	, psi from data	, psi BCL	, psi AAR
1	-87	-43	-64	---	-87	-43*	---	---
2	-48	-24	-30	--	-73	-36*	---	---
3	+132	+65	+59	--	+222	+109	---	---
4	+69	+34	+59	--	-37	-18*	---	---
5	-252	-124	-112	--	-199	-98*	---	---
6	-267	-132	-120	-139	+40	+28	---	+24
7	+79	0	2	--	+51	+34	---	---
8	-295	-143	-120	-139	-420	-220	---	-199
9	+102	7	2	--	+44	-44	---	---
10	-85	-35	-26	-87	-61	-30	---	0
11	+78	+28	+19	---	20	1	---	---

*Gages 1 to 5 were placed near edge, so the stress fields there were presumed uniaxial. Gages 6 and 7 were considered to be a hair measuring the strains, for a biaxial stress field, presuming $\nu = 0.3$. So also were gages 8, 9 and 10, 11.

**These are stresses measured on Florida East Coast Railroad tracks, scaled to conditions like those in the photoelastic tests.



WATC

E.D. TYPING

FIGURE A-5. PHOTOGRAPH OF THE LOADING FIXTURE AND MODEL IN THE OVEN

is not excessively high or low) fringe values in the bulk of the photoelastic model, particularly in the areas of suspected stress concentration. Furthermore, it is desirable to keep deflection small enough that small deflection theory is valid. All photoelastic modeling materials frequently used in stress freezing are allegedly linear elastic and perfectly brittle. Thus, material nonlinearity is not ordinarily considered. After all factors were considered, a target load of 354 pounds (75 psi at the nitrogen cylinder) was selected.

The load was gradually applied to the model by adjustment of the regulator on the nitrogen cylinder. At a load of 141 pounds (31 psi at the nitrogen cylinder) the model was visually checked in the oven. The check revealed the specimen to be deformed quite visibly, so any plans of further loading were dropped. After load application, the model was allowed to soak for an additional 12 hours and then cooled over a 36-hour period.

After cooling down, the model was removed from the load fixture. Visual observation of the deformed photoelastic model revealed that the head of the rail had bent excessively, although the bottom flange revealed no sudden change in curvature and was deflected as would be expected. This event is shown rather well in Figure A-6. Previous analytical studies had indicated the rail head responds like a beam or an elastic foundation (the web). However, the degree to which this occurred in the model was not anticipated. A partial explanation of this event could be offered by the low epoxy modulus at temperature. The modulus of the rail at temperature was estimated on the basis of the measured deflection assuming that the deflection was given by

$$W = \frac{PL^3}{48EI} + \frac{P\sqrt[4]{k}}{2k} \quad \text{with } k = \frac{tE}{d} \quad (\text{A-1})$$

which represents the sum of the deflections due to simple beam bending and head bending (on the web). The modulus is given by

$$E = \frac{P}{2W} \left[\frac{L^3}{24I} + d \frac{(t/4Id)^{1/4}}{t} \right] \quad (\text{A-2})$$

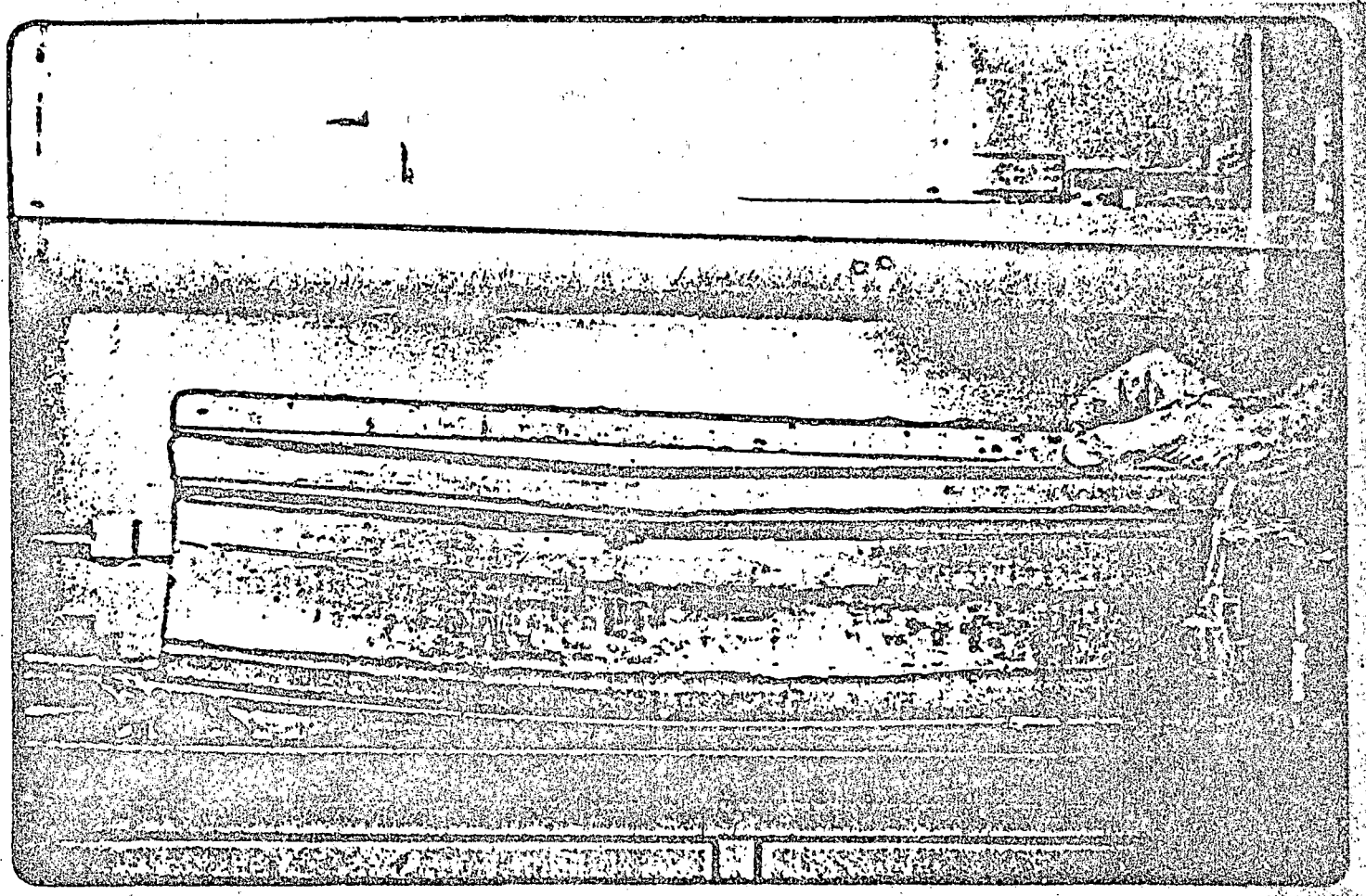


FIGURE A-6. PHOTOGRAPH OF THE STRESS FROZEN RAIL

NOTE: The unused portion of the rail on the right was not used because of casting flaws.

From this expression it was found that $E = 1521$ psi. Using this value to calculate for the deflection of the head alone, it was found that 72 percent of the total deflection was due to this cause. This compares with the 20 percent that might be expected for a steel rail. This discrepancy suggests that difficulty of constructing a full scale, full rail photoelastic model for the purpose of examining flexural situations.

Before the model was sliced, it was observed and photographed extensively in the transverse direction. Figure A-7 is a photograph of the isochromatic fringe pattern obtained in the central portion of the rail. It can be seen from the figure that the model appears to be loaded in the center of the span.

In two-dimensional photoelasticity, the isochromatic fringe order provides the difference in principal stress magnitude throughout the model. At free boundaries, this fringe order reduces to the tangential stress (that is the principal stress parallel to the rail profile) at the surface directly, because the second principal stress is zero. In three-dimensional photoelasticity, slices are cut from the model and viewed as two-dimensional slices. The fringe order is not modified by the slicing procedures. Planes of symmetry are planes that have no surface shear and are therefore principal planes; therefore, slices from a three-dimensional photoelastic model that coincide with planes of symmetry provide the same information as the two dimensional slice, i.e., the difference in principal stresses. The third principal stress, whether zero or nonzero, does not enter the observation. A different case is present when an arbitrarily located plane is considered. In arbitrary planes, the isochromatics give twice the maximum in plane shearing stress. On boundaries, the component of tangential stress that is seen is that determined by the orientation of the slice.

Because principal planes provide more than usual information, they are employed in any slicing strategy. Hence, Planes 1, 2, and 10 were natural selections for slices as shown in Figure A-8. Additionally, Slices 3 through 9 were selected to provide information on the distribution of the vertical σ_z stress.

The procedure for removing the slices was complicated by the fact that the model had undergone significant deformation. The first step was to locate the slices accurately on the model. This was done on a surface plate with the

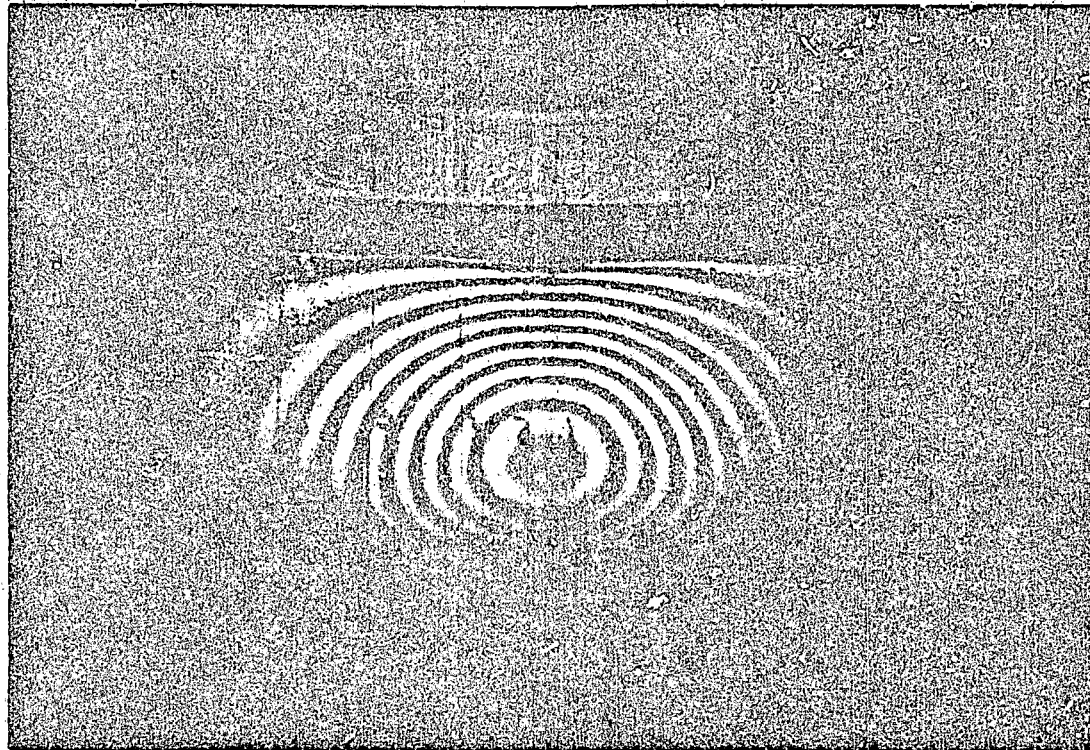
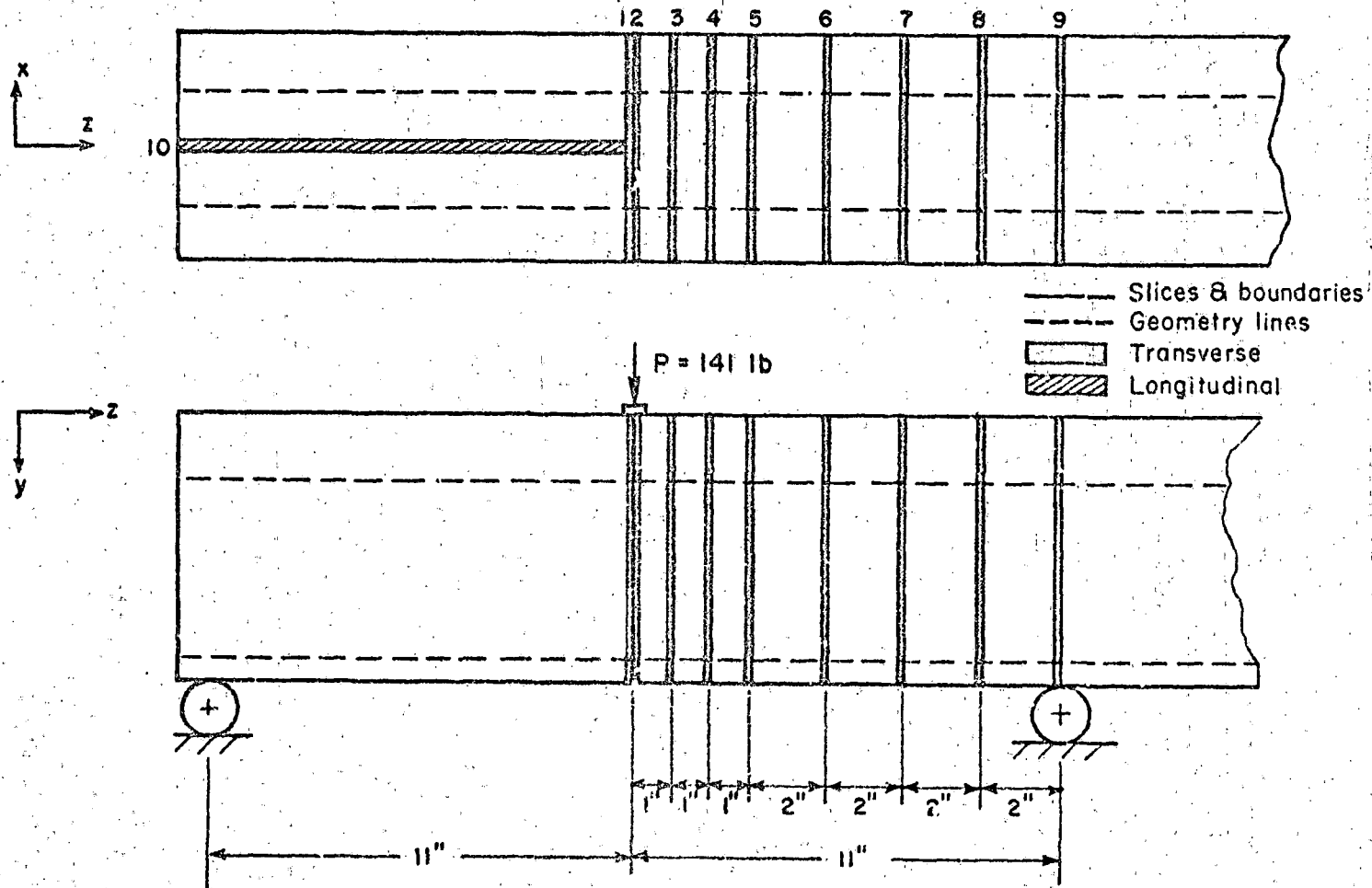


FIGURE A-7. ISOCHROMATIC FRINGE PATTERN IN THE CENTRAL PORTION OF THE RAIL PRIOR TO SLICING



A-16

FIGURE A-8. DIAGRAM OF SLICING STRATEGY

help of several jigs. After the slices were located, they were cut on a band-saw. It was determined that a six teeth/inch blade operating at 100 ft/min with forced air cooling could cut the slices with no noticeable heating. This combination is much different from what others have reported using, but the rail model was unusually massive. The slices were not quite flat after removal and no attempt was made to make them planar. For better optical clarity, the slices were hand sanded with several grades of wet-or-dry paper and mineral oil. After sanding, thickness measurements were made on all the slices.

In order to allow assignment of quantitative significance to the isochromatic fringe orders, a calibration factor must first be known. To determine this factor, a separate calibration bar was poured and cured. The calibration bar was then stress frozen under uniaxial stress. The resulting fringe pattern gave a calibration constant of 1.414 psi-inch/fringe.

Comparison of Photoelastic and Finite Element Analyses

The results of the photoelastic analysis were encouraging. Of primary consideration here are Slices 2 and 3. The isochromatic fringe patterns for these slices are shown in Figures A-9 and A-10. Of particular interest is the comparison of the tangential surface stress on Slices 2 and 3. Figures A-11 and A-12 graphically show this stress determined from photoelasticity. They also show corresponding stresses found by a strain gage and by finite element calculations using isoparametric brick-type elements with the shapes shown in Figure A-13 and having up to 21 nodes in an element.

The most distinguishing difference between stresses found by the different techniques comes from the reversal of sign of finite element stress above the upper fillet. The photoelastic results clearly did not show this reversal. It is thought to be a peculiarity of the finite element results attributable to use of excessively large elements. Nevertheless, the agreement among the various results is generally good, so that the finite element method is generally indicated, though with warning to use more and smaller elements. This modification was incorporated in a revised finite element model. There is also qualitative agreement between the shapes of the isochromatic lines in Figure A-9 and the contours for normal stress σ_y and σ_z in Figure B-2 and B-3, though those pertain to cases with boundary conditions different enough to discourage quantitative comparison.

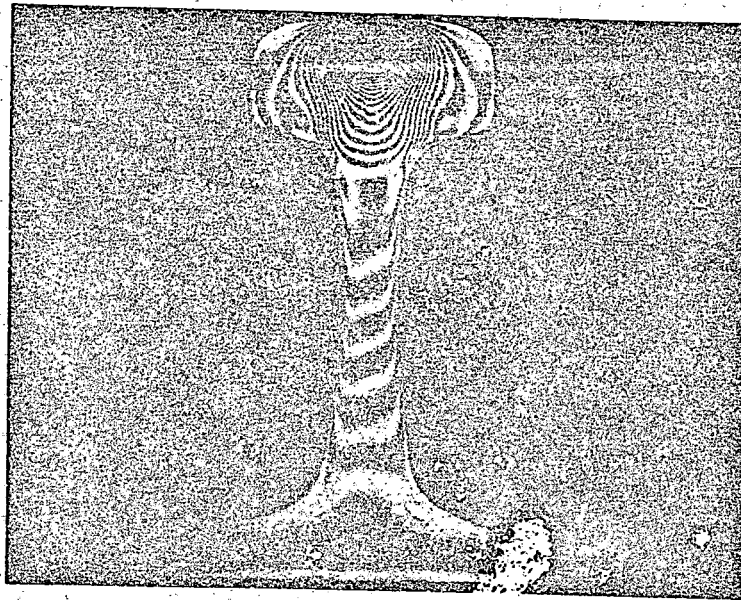
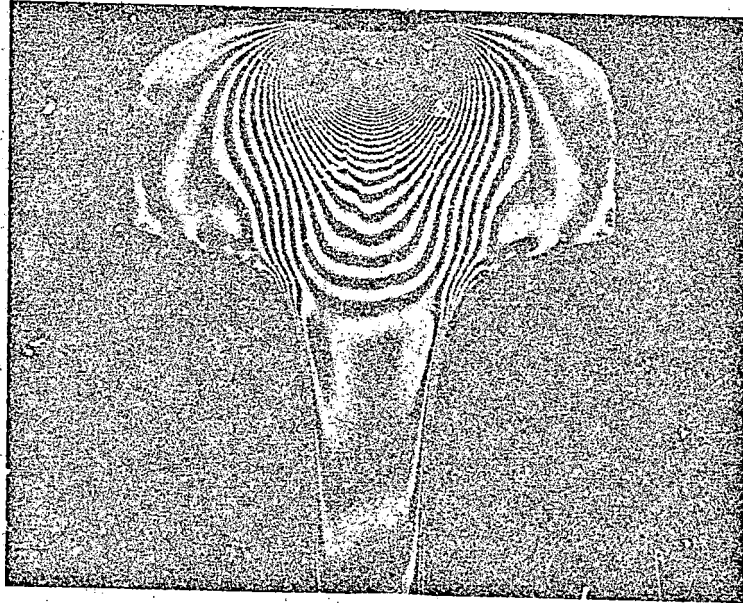


FIGURE A-9. ISOCHROMATIC FRINGE PATTERNS IN SLICE 2

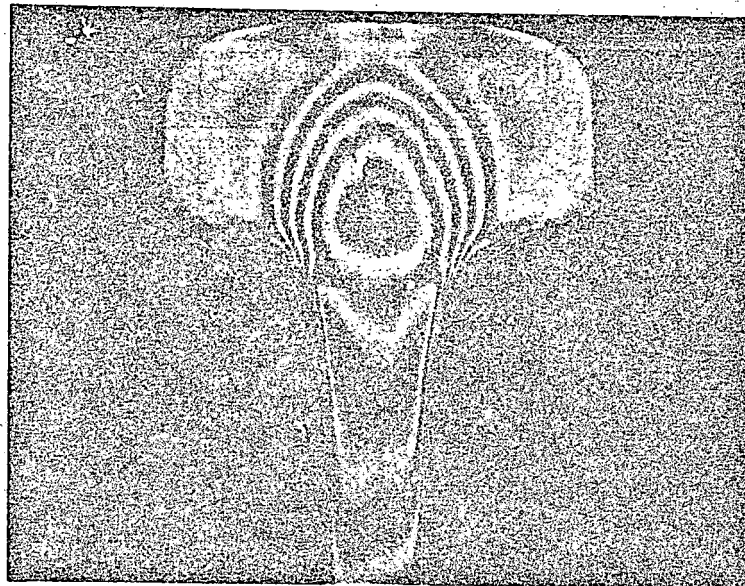
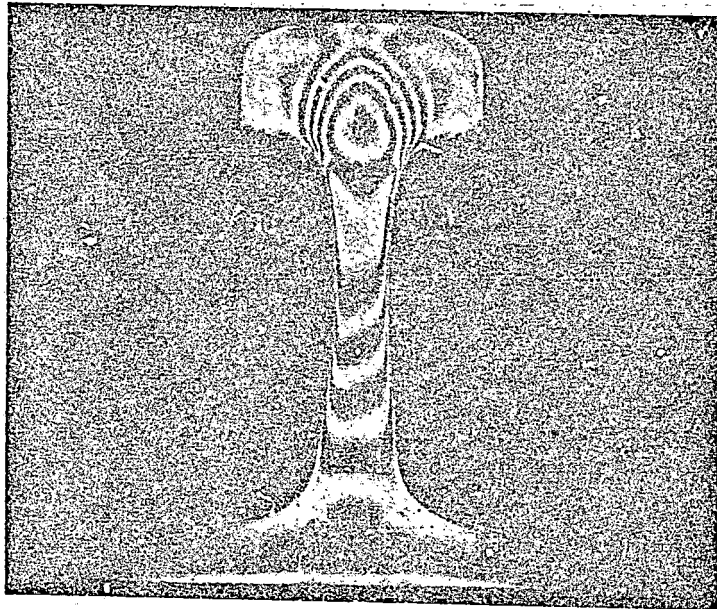
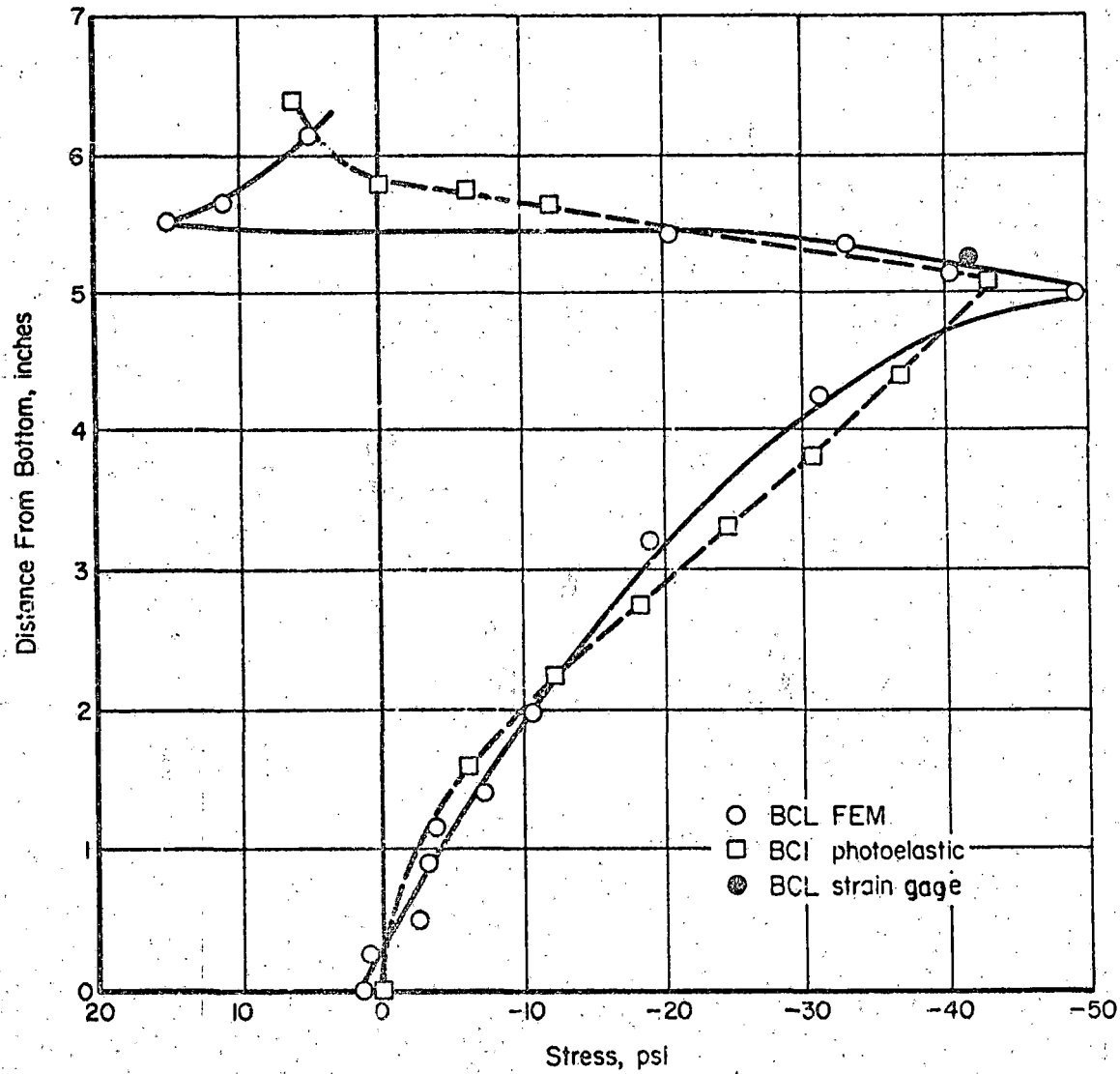


FIGURE A-10. ISOCHROMATIC FRINGE PATTERNS IN SLICE 3



A-20

FIGURE A-11. COMPARISON OF TANGENTIAL SURFACE STRESS ON PLANE 2

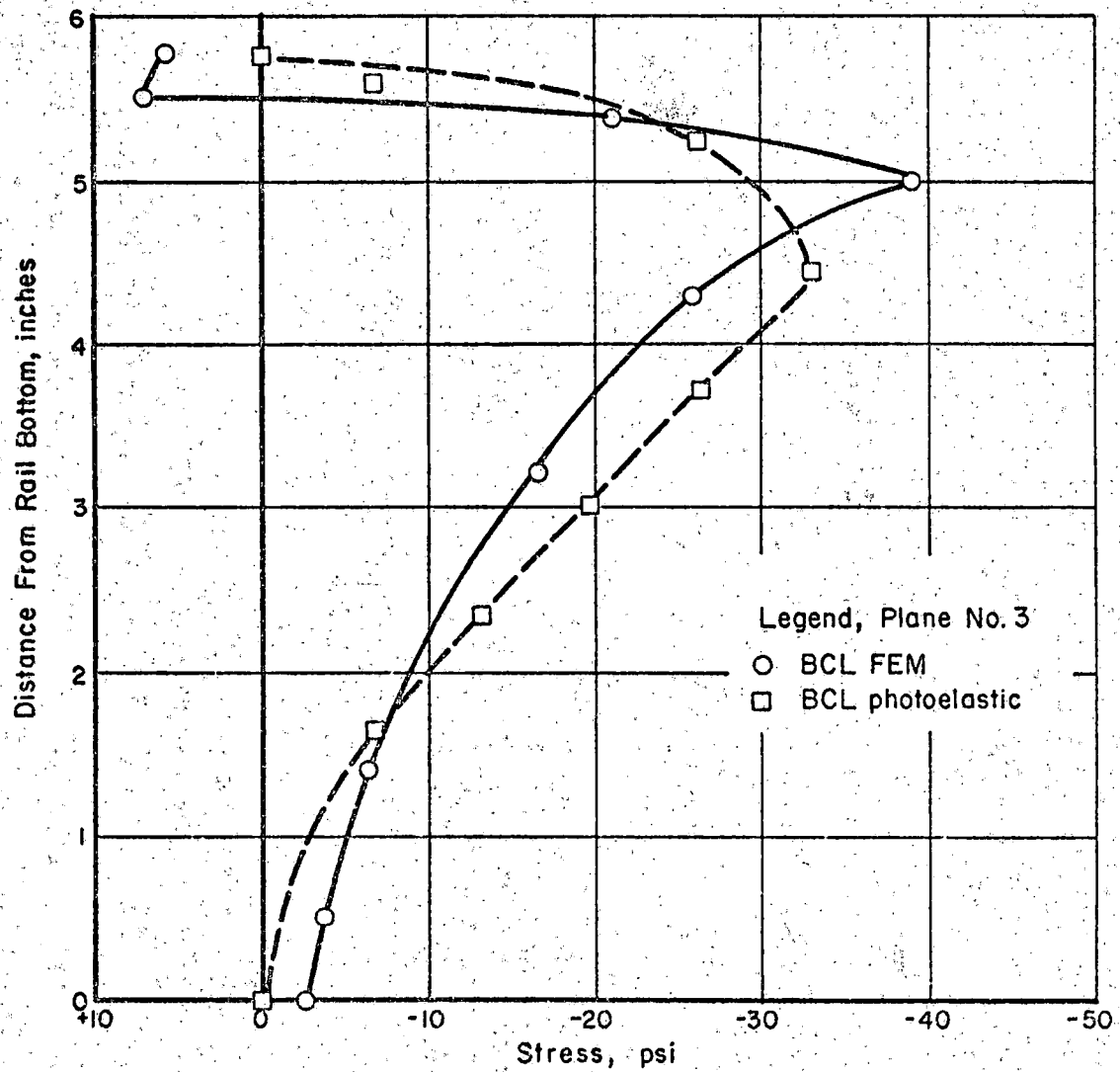


FIGURE A-12. COMPARISON OF TANGENTIAL SURFACE STRESS ON PLANE 3.

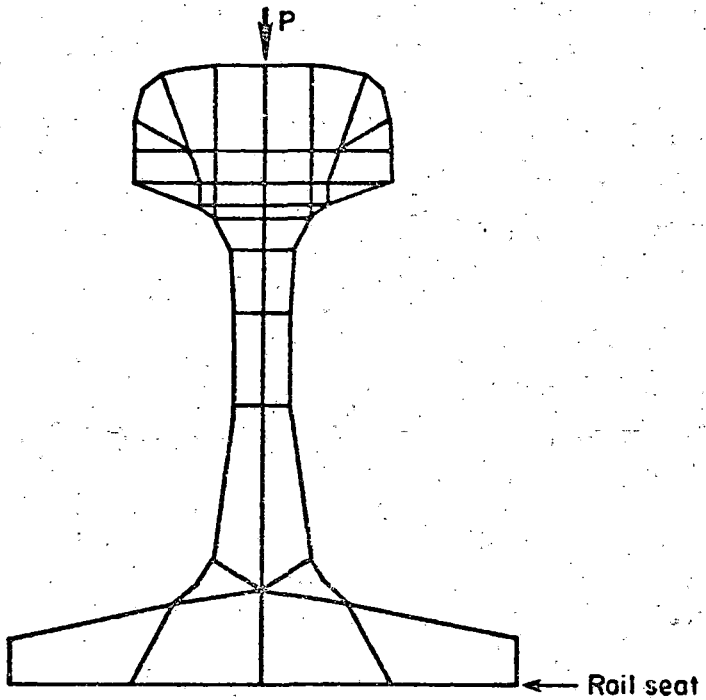
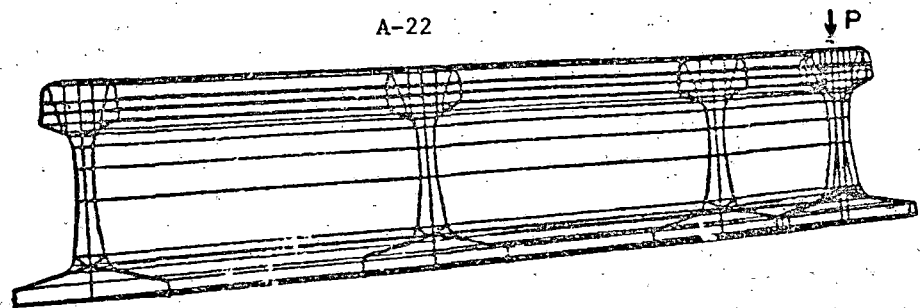


FIGURE A-13. FULL RAIL MODEL (USING 20-NODED ELEMENTS)

Of particular interest in Figures A-9 and A-10 is the rather severe "skin effect" in the web area of the model. The reason for this effect is not entirely clear, however, it is thought that it was introduced in the casting or curing process. It is particularly perplexing that the web area is so much more seriously affected than the other portions of the model.

Validation on the Basis of Strain Measurements
and Deflection Calculations

Strain gage results from three different sources were used to validate finite element calculations. These sources were AAR published data [A-1], BCL track measurements from the Florida East Coast Railroad [A-3] (FEC) and BCL strain gage measurements on the photoelastic model (discussed earlier). Rail deflection results from finite element calculations were compared with strength of materials calculations for a simply-supported beam.

Figure A-14 presents a comparison of the tangential stress distribution on a plane section under a central load. Finite element results for foundation moduli of 589 psi and 10,000 psi are compared with AAR [A-2] experimental results for a foundation modulus of 1600 psi. While reasonably good agreement is found in the fillet region, considerable variation occurs in the middle web. It is probable that this is due to the coarseness of the mesh in the finite-element model in that area.

A result obtained with a pair of gages on the BCL photoelastic model (Gages 6 and 7 in Table A-1) is compared with the full rail finite element results in Figure A-11, after scaling to the load carried in the photoelastic test. Good agreement is observed for the tangential stress.

Figure A-15 compares the deflection of the full rail finite element model with that from strength of materials beam theory calculations based on spring constants representing the FEC foundation. As can be seen, excellent agreement exists between the finite element and simple beam theory results.

On the basis of these comparisons, it was concluded that the finite element models formulated allowed the calculations of flexural stresses with sufficient accuracy in most parts of the rail. Ideally, however, full-rail models should have somewhat finer meshing than that shown in Figure A-13.

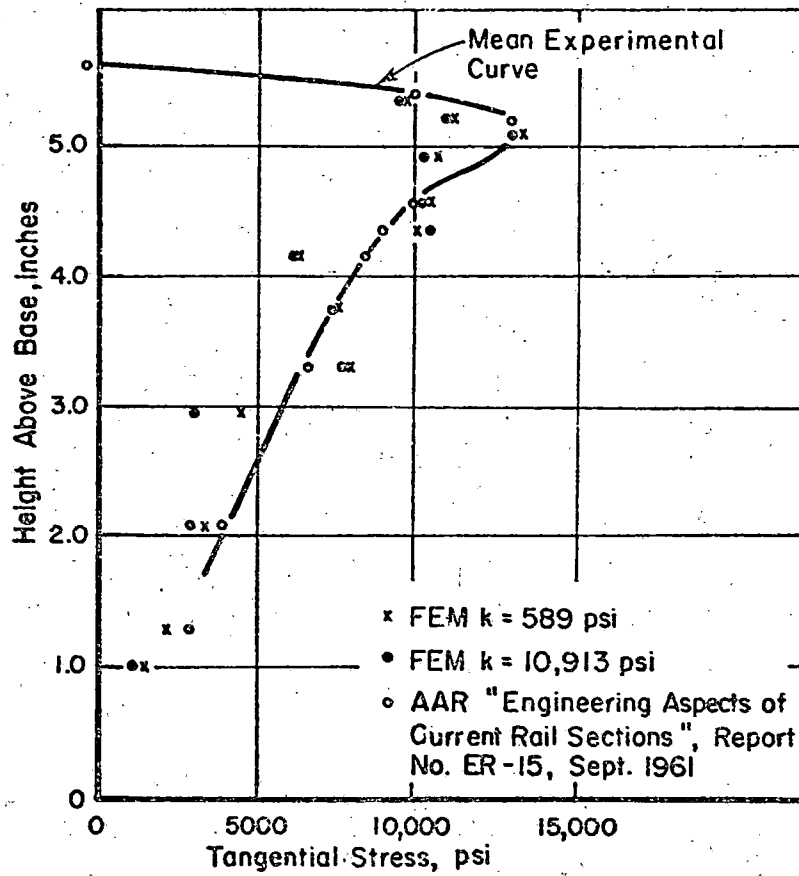


FIGURE A-14. COMPARISON OF TANGENTIAL STRESS FOUND BY STRAIN GAGES AND FROM FINITE ELEMENT MODEL

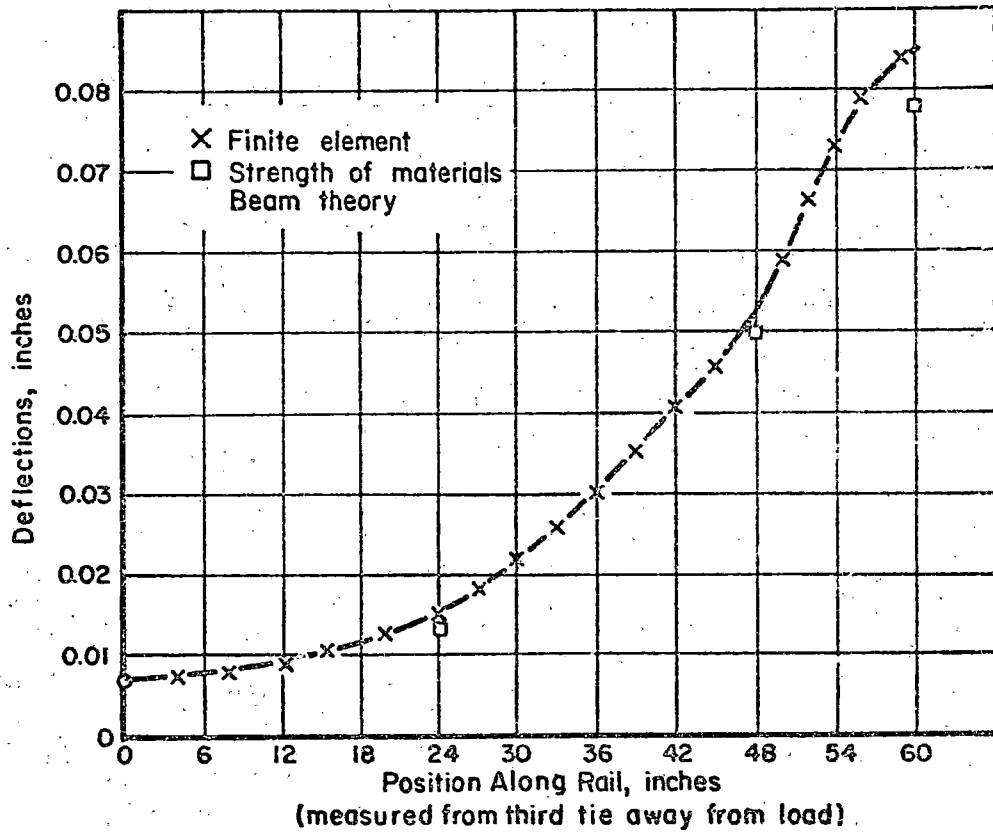
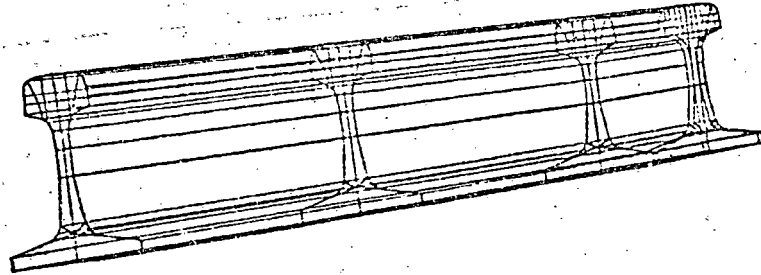


FIGURE A-15. COMPARISON OF RAIL DEFLECTIONS FROM THE FINITE ELEMENT MODEL AND FROM SIMPLE BEAM THEORY

REFERENCES

- A-1. Precision Casting of Epoxy-Resin Photoelastic Models, Fessler, H. and Perla, M., Journal of Strain Analysis, Vol. 8, No. 1, (1975).
- A-2. AAR, "Engineering Aspects of Current Rail Sections", Report No. ER-15, (September 1961).
- A-3. Prause, R. H., et al, "An Analytical and Experimental Evaluation of Concrete Crosstie and Fastener Loads" Report FRA/ORD-77/71, prepared for DOT/FRA by BCL, (December 1977).

APPENDIX B
FLEXURAL STRESSES

Contours Show
 σ_x in psi

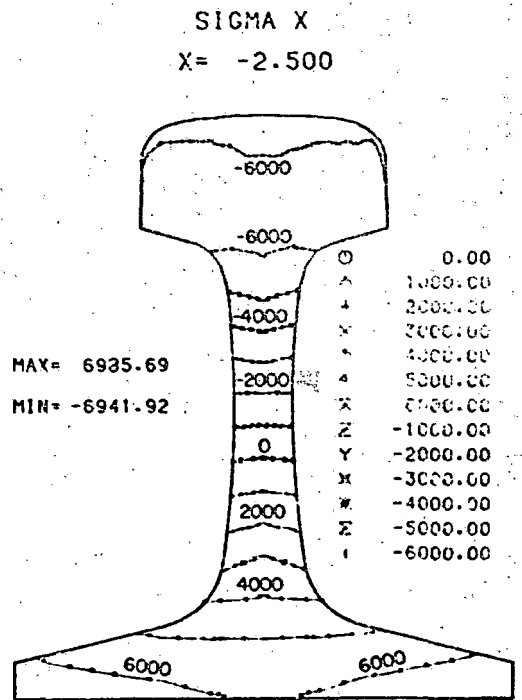
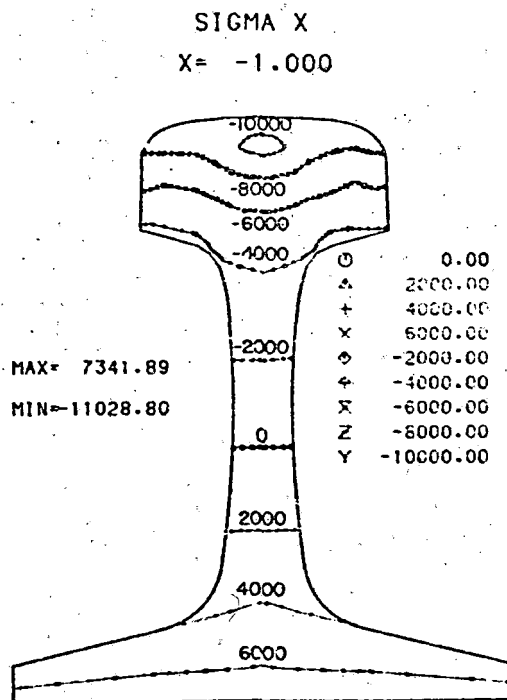
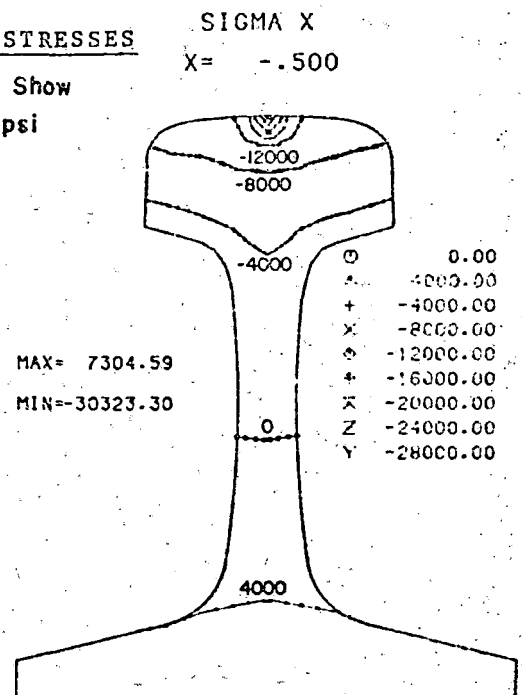
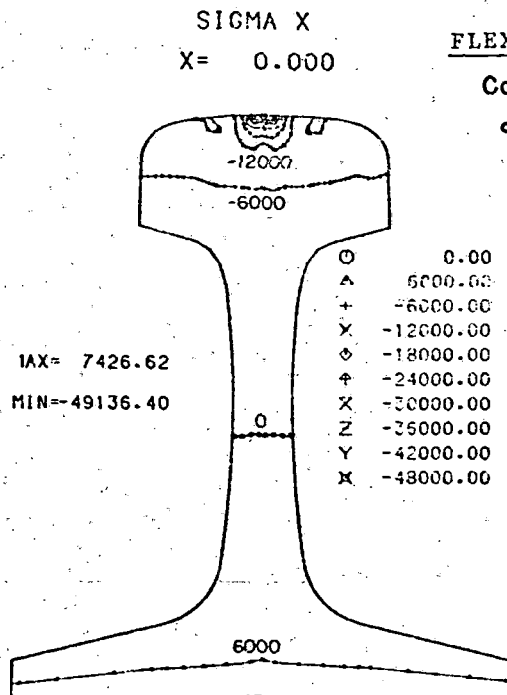
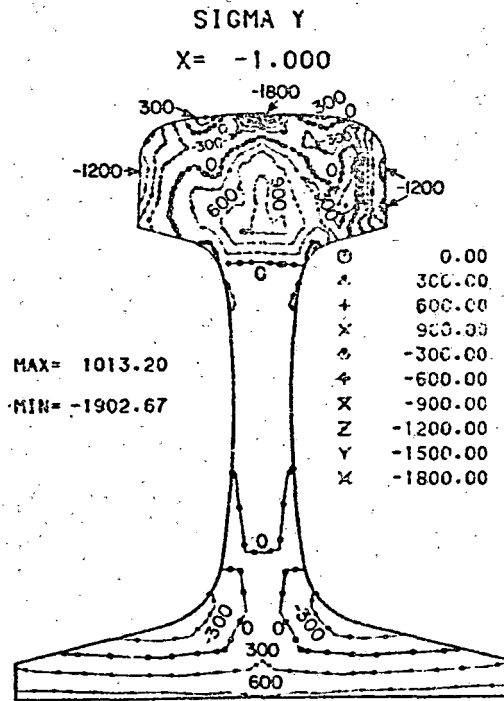
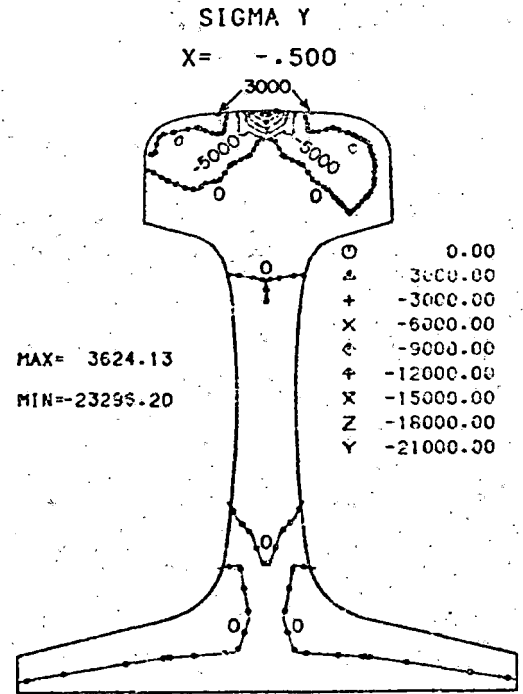
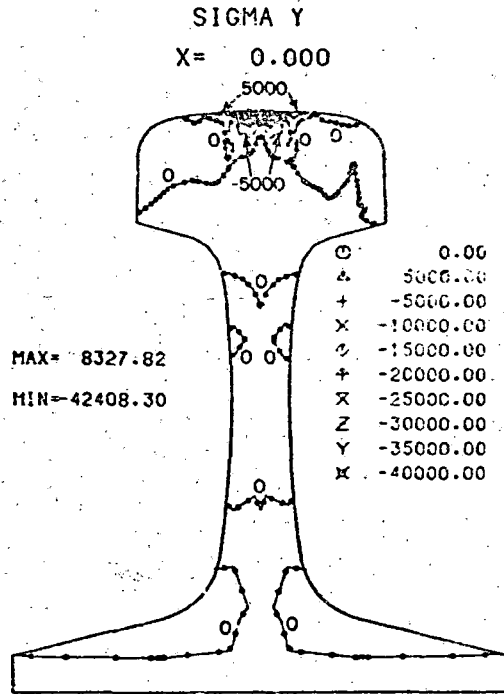


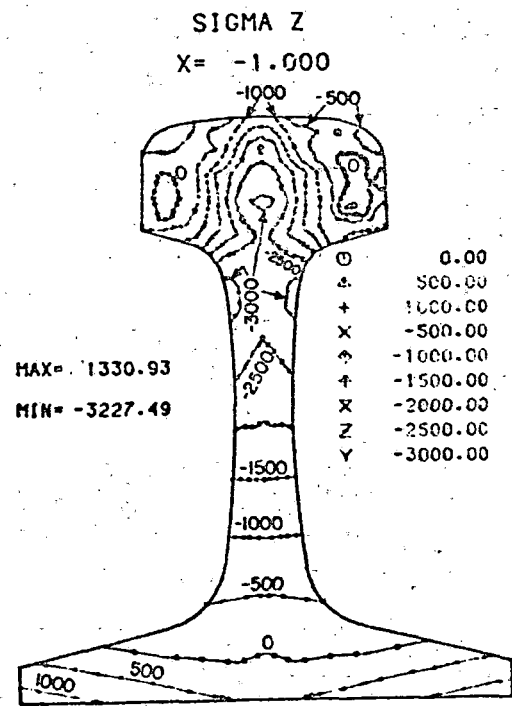
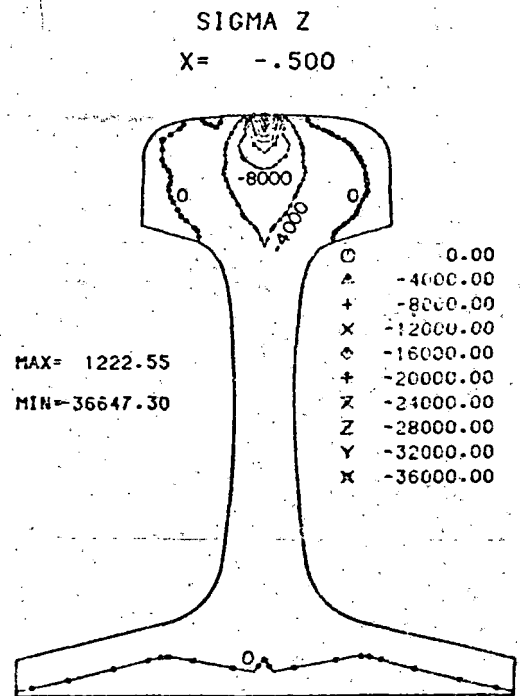
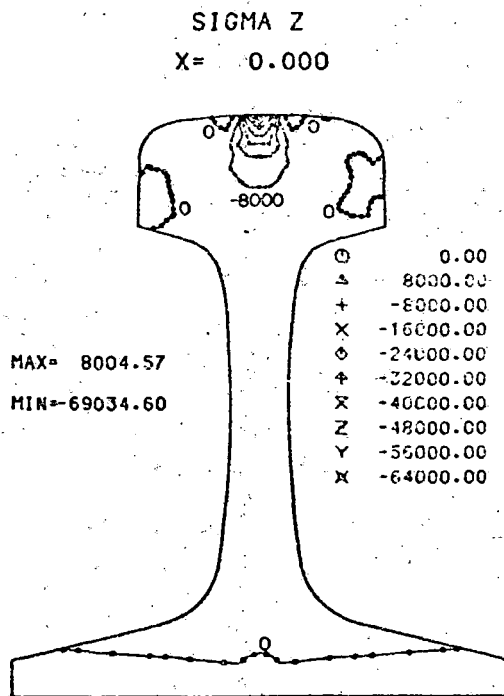
FIGURE B-1. LONGITUDINAL STRESS IN 132-LB RE RAIL UNDER 19,000-LB CENTERED VERTICAL LOAD (Cf. TABLE 2-2, CASE 1)

B-2



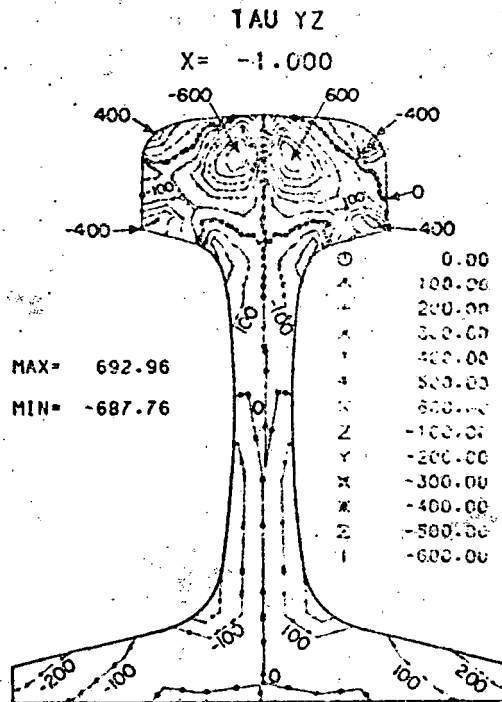
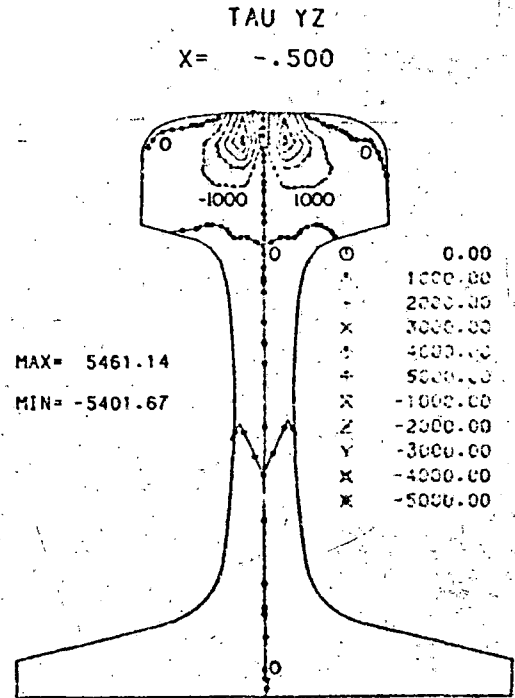
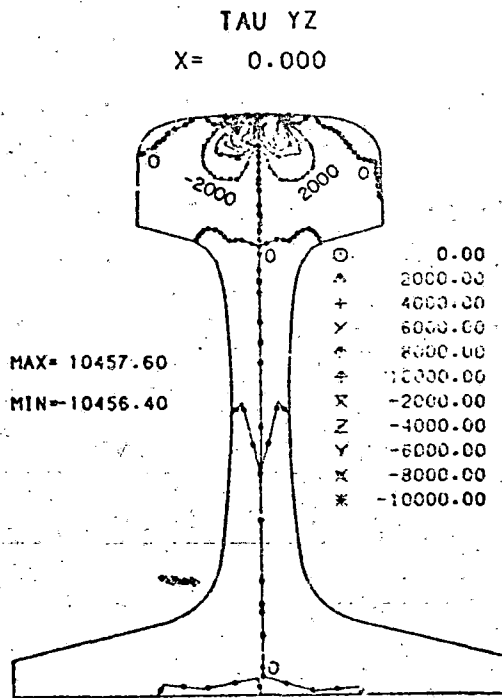
Contours Show σ_y in psi

FIGURE B-2. LATERAL STRESS IN 132-LB RE RAIL UNDER 19,000-LB CENTERED VERTICAL LOAD (Cf. TABLE 2-2, CASE 1)



Contours Show σ_z in psi

FIGURE B-3. VERTICAL STRESS IN 132-LB RE RAIL UNDER 19,000-LB CENTERED VERTICAL LOAD (Cf. TABLE 2-2, CASE 1)



Contours Show τ_{yz} in psi

FIGURE B-4. SHEAR STRESS τ_{yz} IN 132-LB RE RAIL UNDER 19,000-LB CENTERED VERTICAL LOAD (Cf. TABLE 2-2, CASE 1)

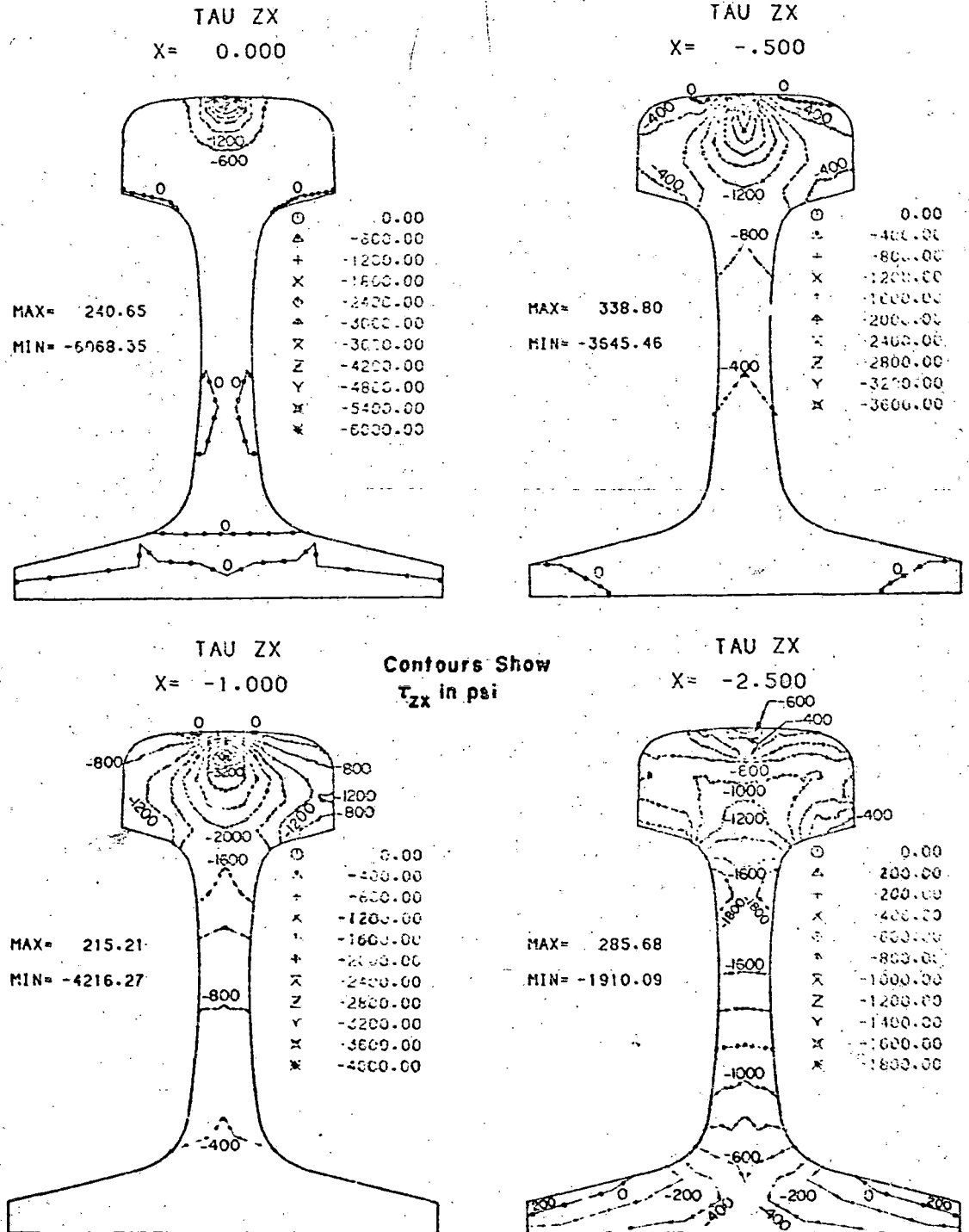


FIGURE B-5. SHEAR STRESS τ_{zx} IN 132-LB RE RAIL UNDER 19,000-LB CENTERED VERTICAL LOAD (Cf. TABLE 2-2, CASE 1)

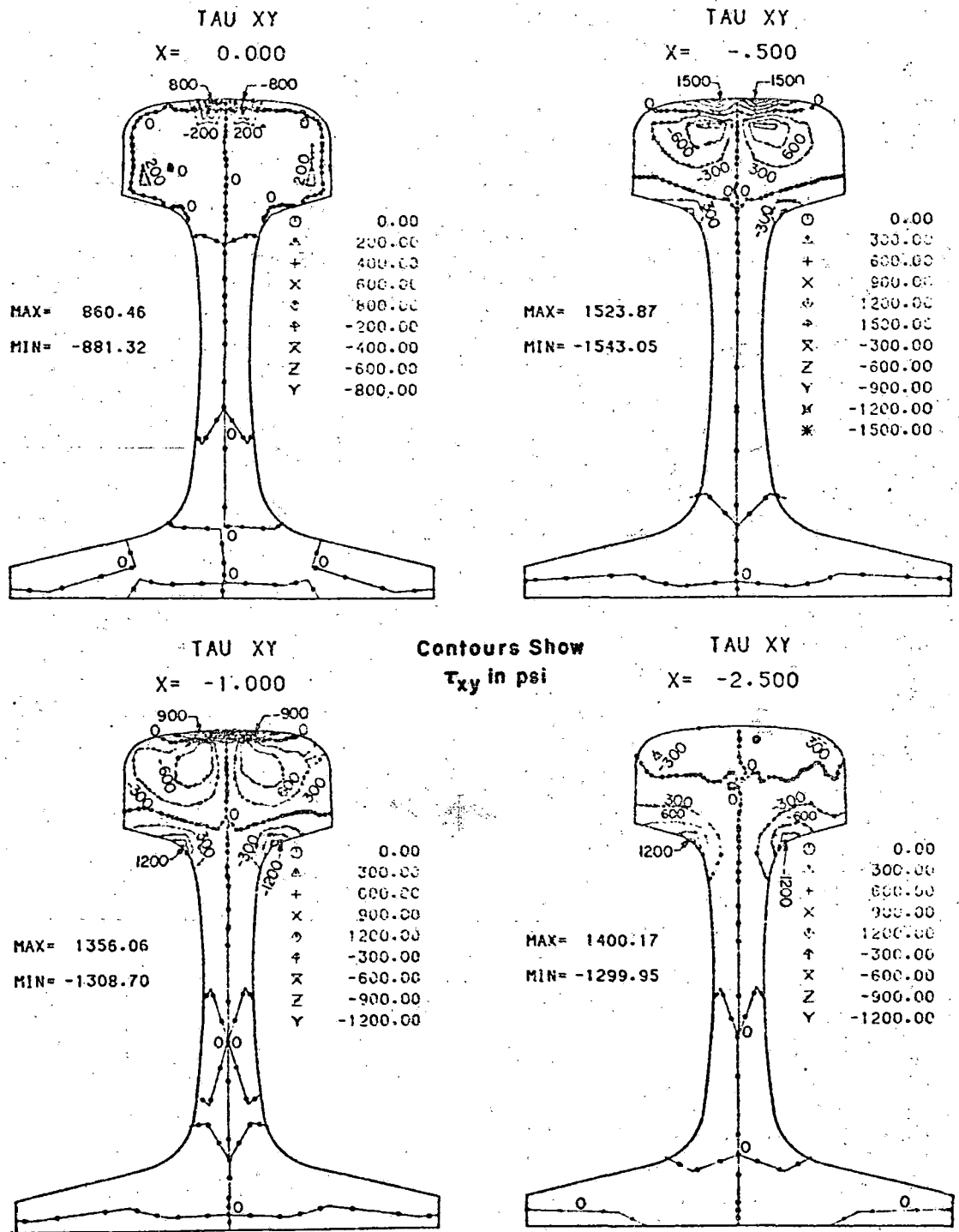


FIGURE B-6. SHEAR STRESS τ_{xy} IN 132-LB RE RAIL UNDER 19,000-LB CENTERED VERTICAL LOAD (cf. TABLE 2-2, CASE 1)

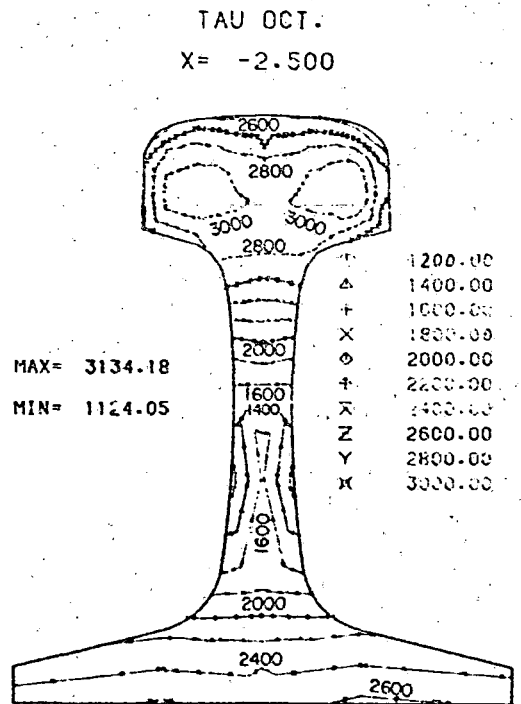
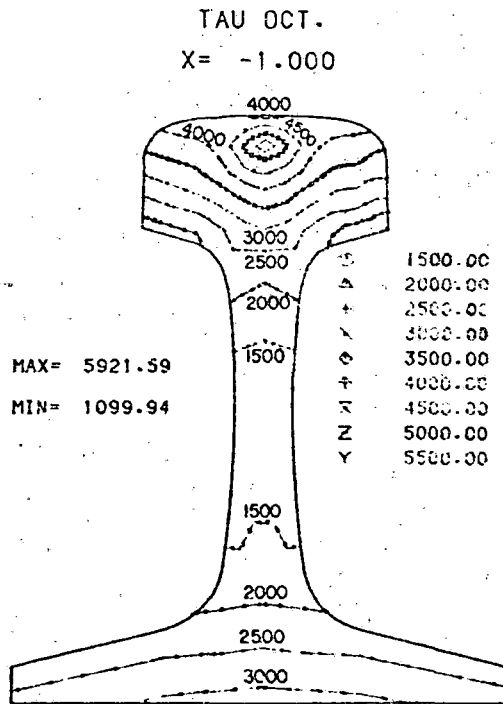
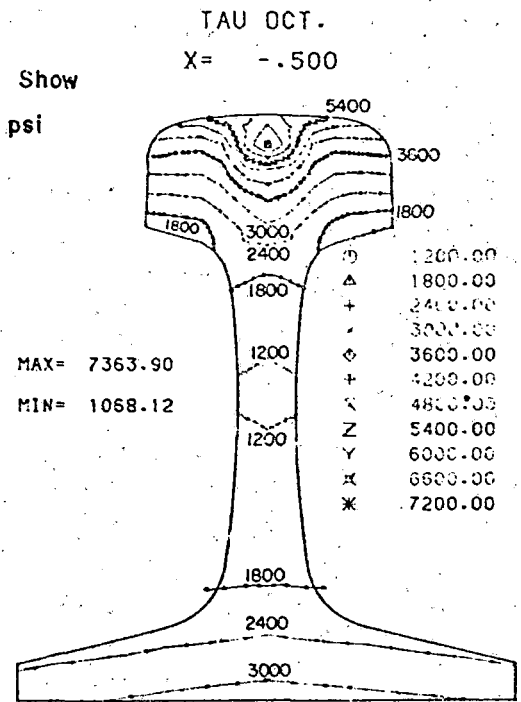
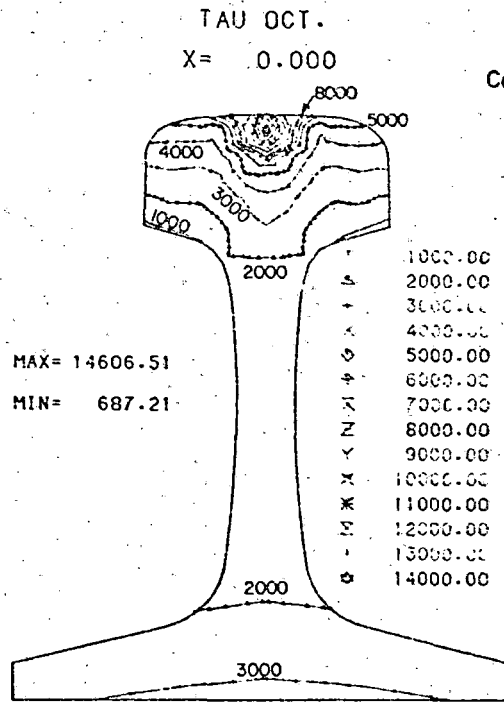


FIGURE B-7. OCTAHEDRAL SHEAR STRESS IN 132-LB RE RAIL UNDER 19,000-LB CENTERED VERTICAL LOAD (Cf. TABLE 2-2, CASE 1)

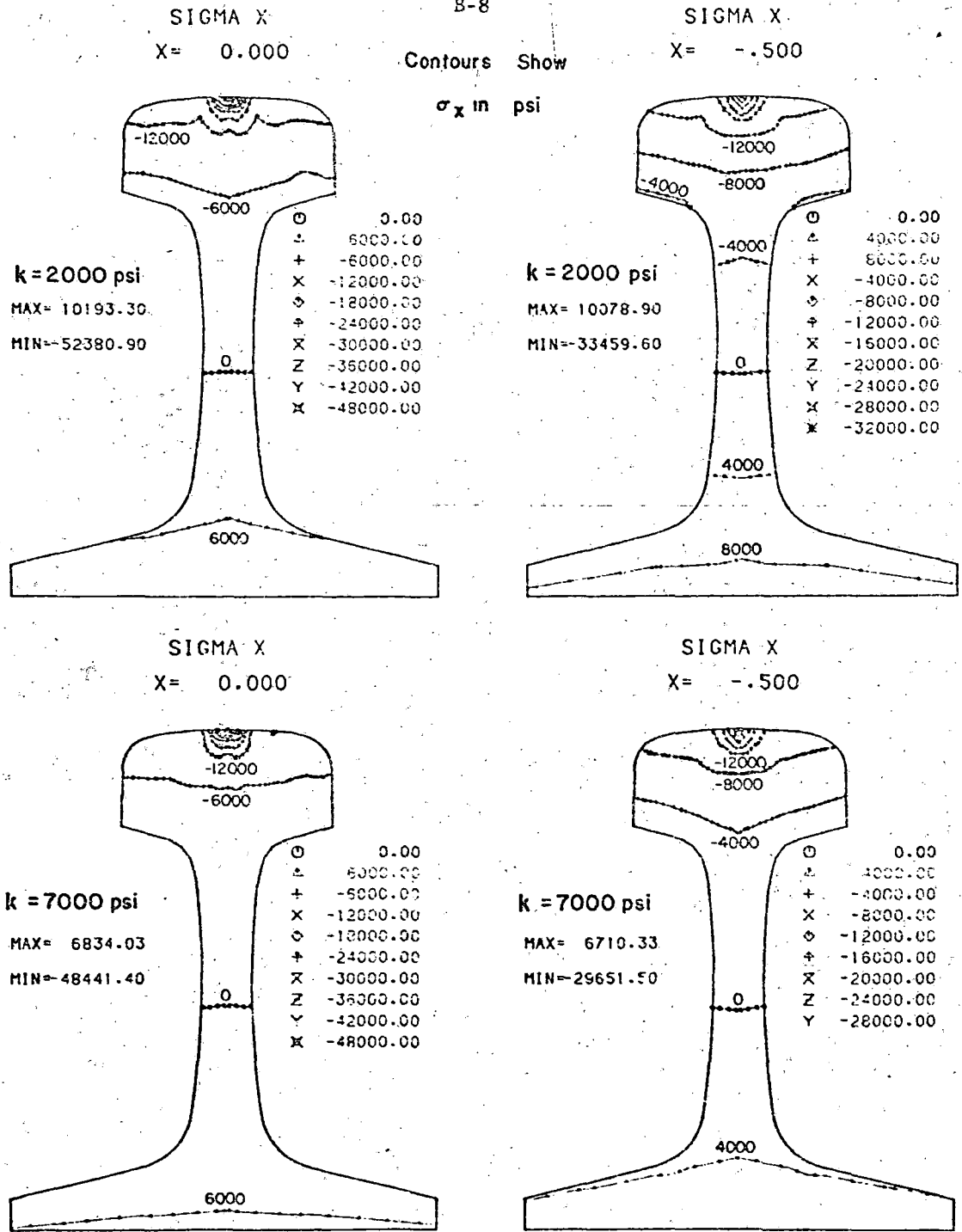


FIGURE B-8. EFFECT OF FOUNDATION STIFFNESS ON LONGITUDINAL STRESS IN 132-LB RE RAIL UNDER 19,000-LB CENTERED VERTICAL LOAD (Cf. TABLE 2-2, CASES 2 AND 3)

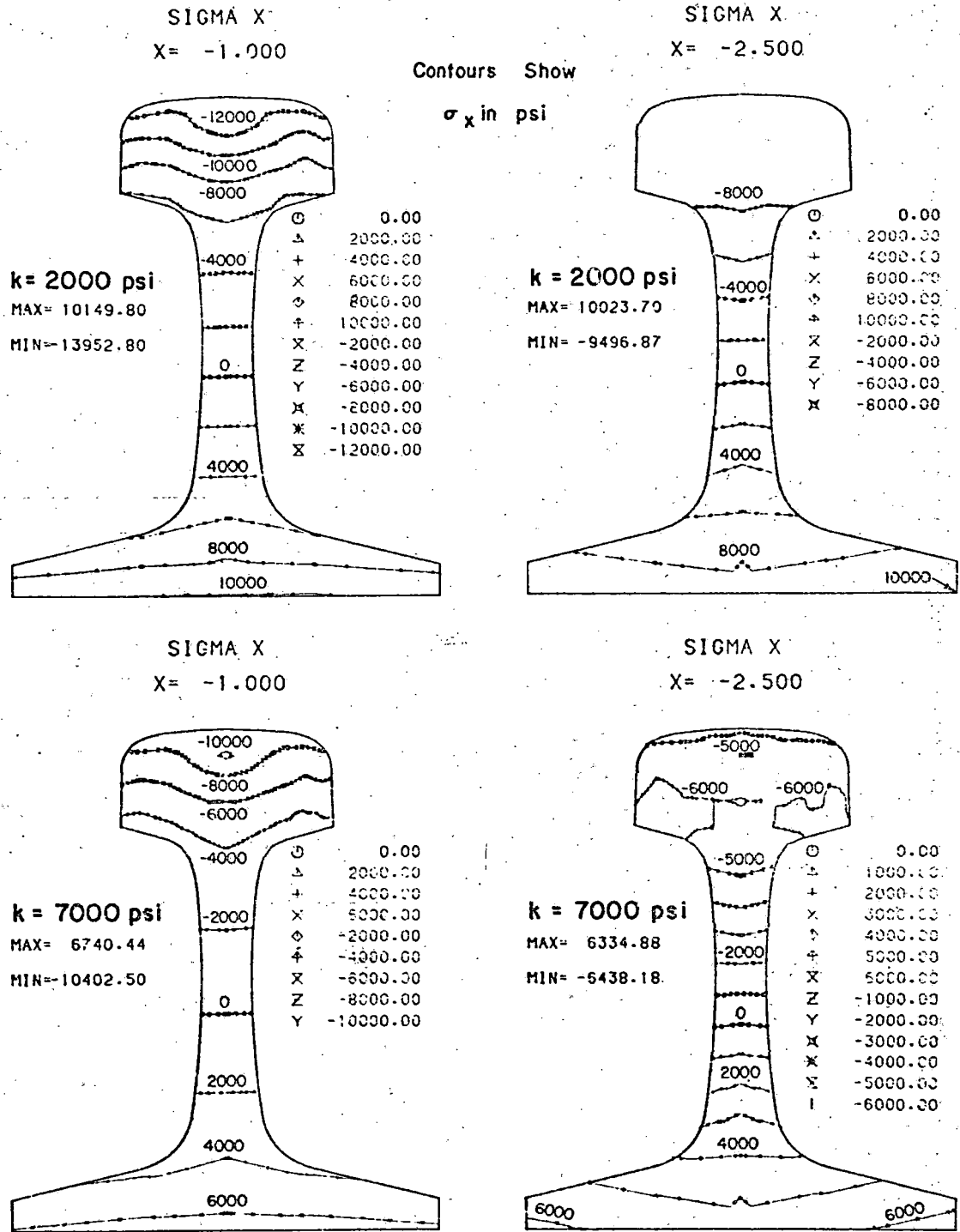


FIGURE B-8. (CONTINUED)

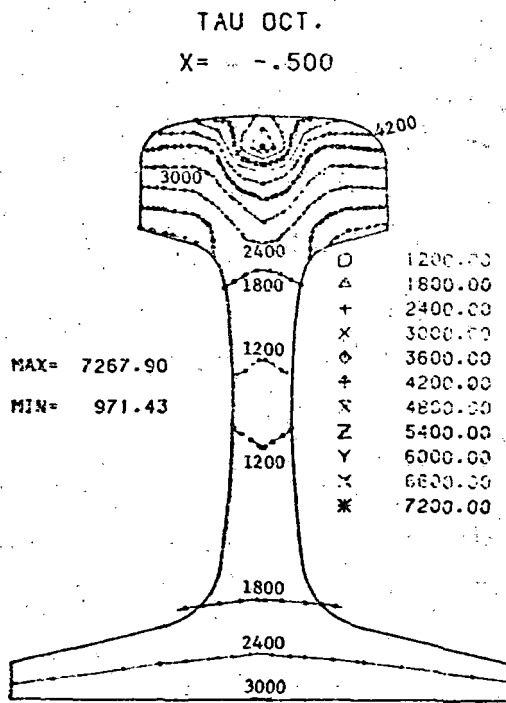
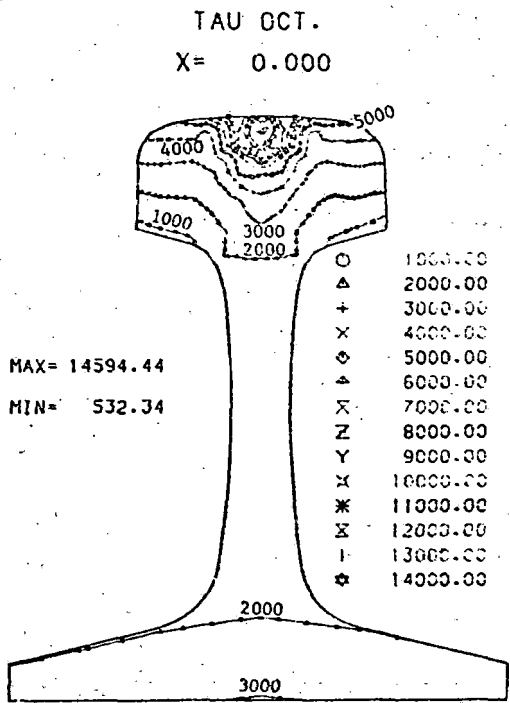
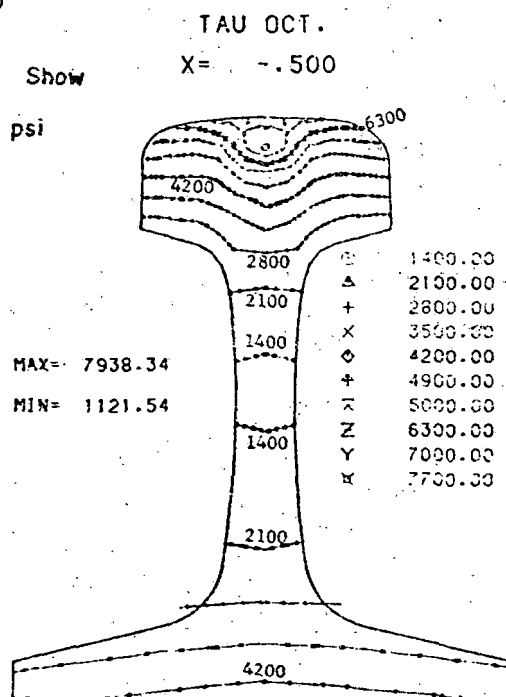
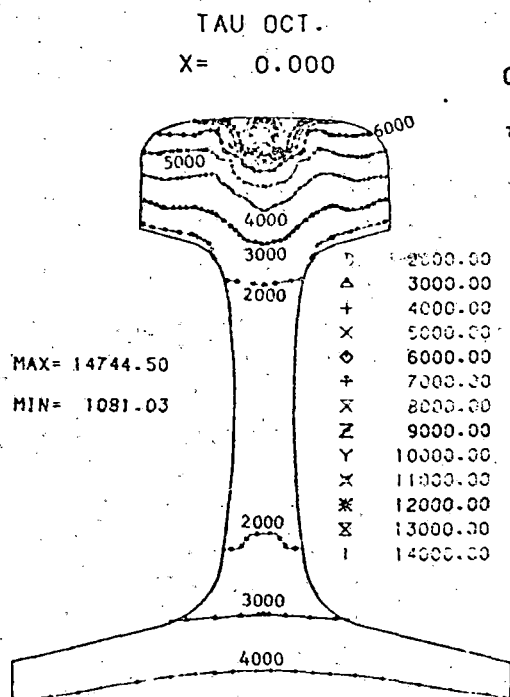


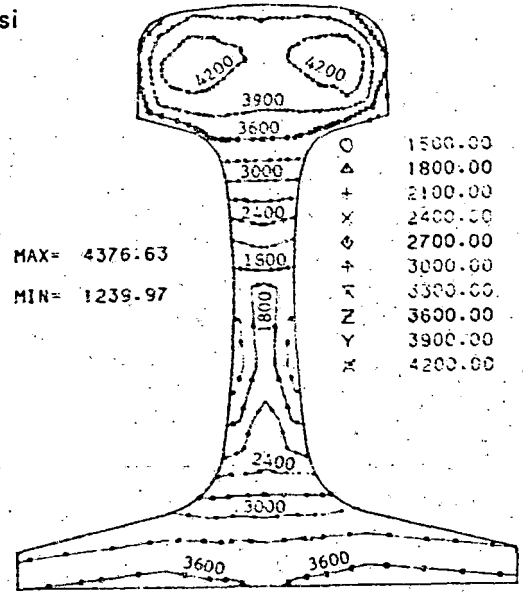
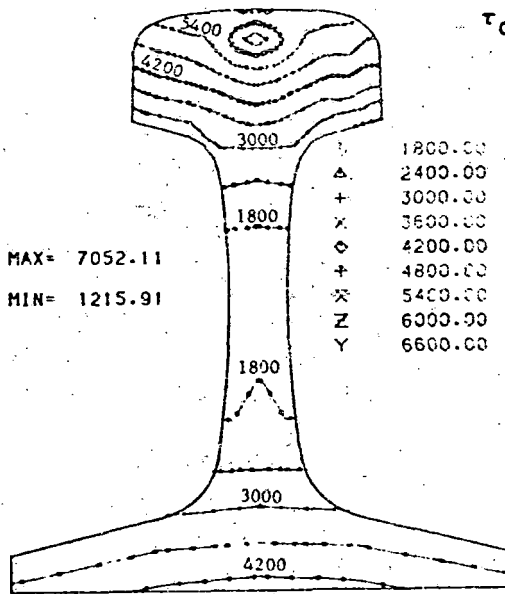
FIGURE B-9. EFFECT OF FOUNDATION STIFFNESS ON OCTAHEDRAL SHEAR STRESS IN 132-LB RE RAIL UNDER 19,000-LB CENTERED VERTICAL LOAD (CF. TABLE 2-2, CASES 2 AND 3)

TAU OCT.
X= -1.000

Contours Show

TAU OCT.
X= -2.500

τ_{oct} in psi



TAU OCT.
X= -1.000

TAU OCT.
X= -2.500

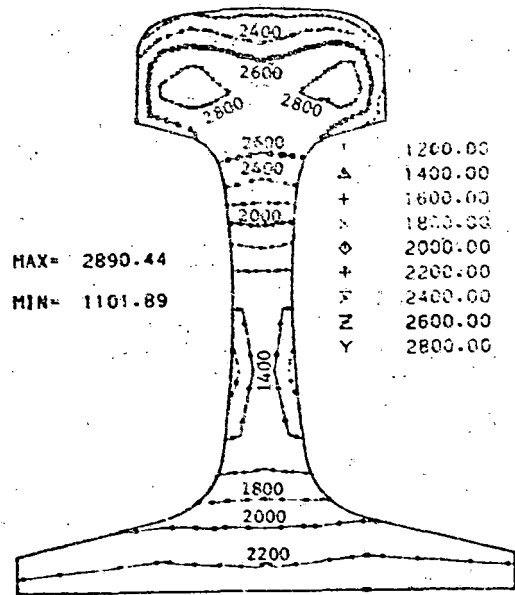
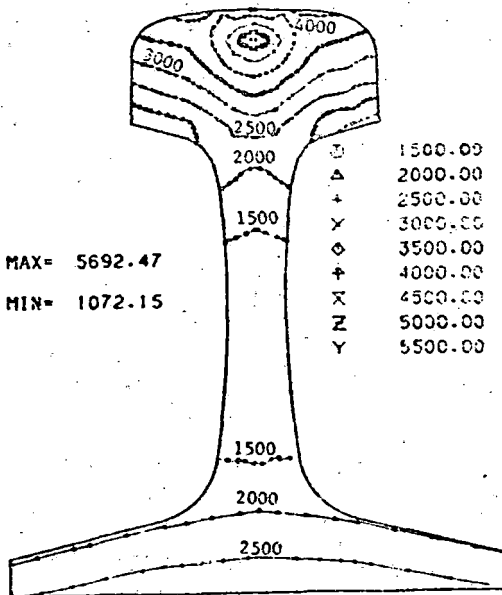


FIGURE B-9. (CONTINUED)

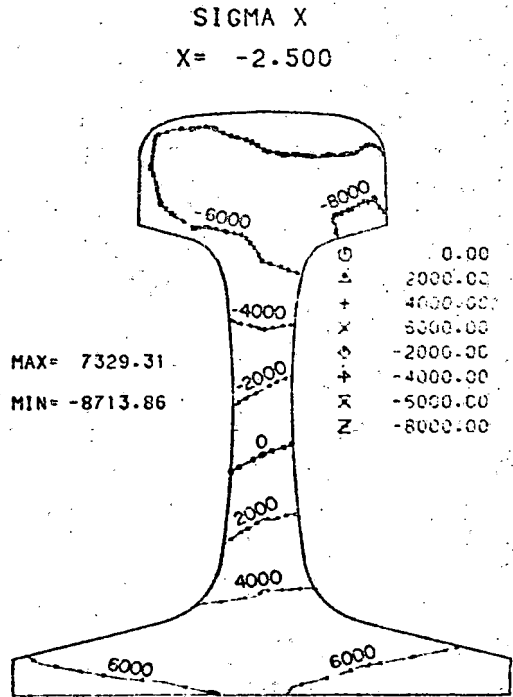
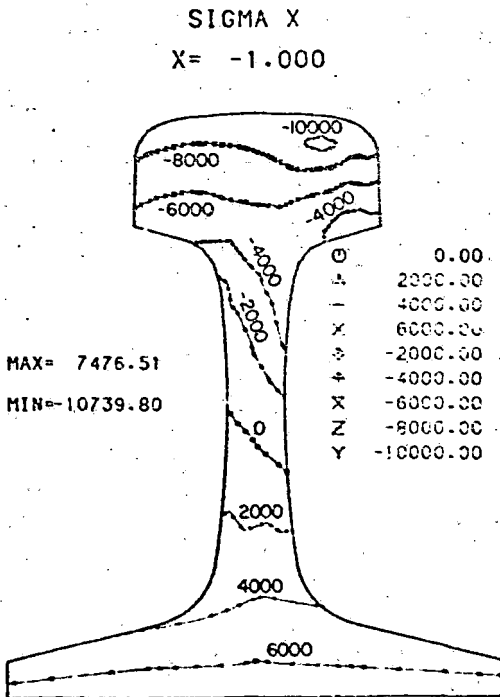
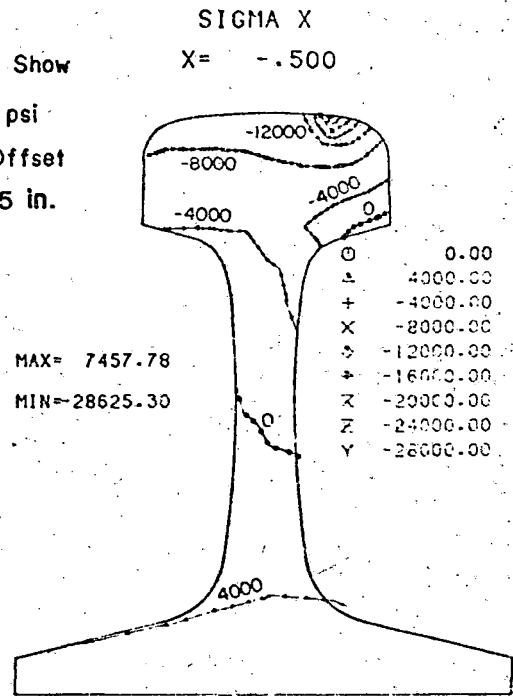
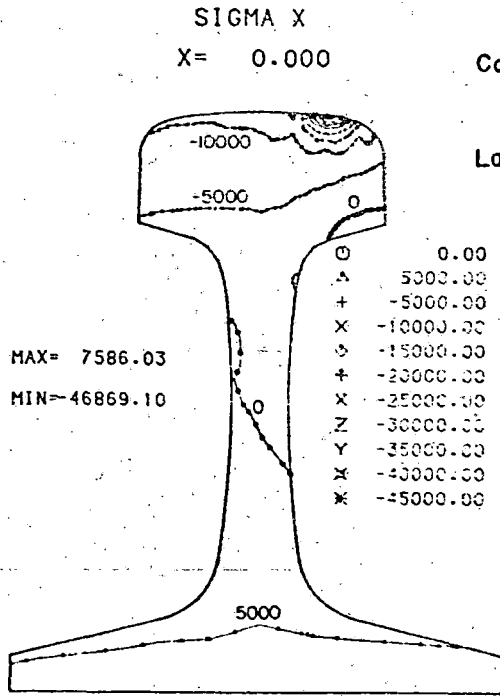


FIGURE B-10. LONGITUDINAL STRESS IN 132-LB RE RAIL UNDER 19,000-LB ECCENTRIC VERTICAL LOAD (Cf. TABLE 2-2, CASE 4)

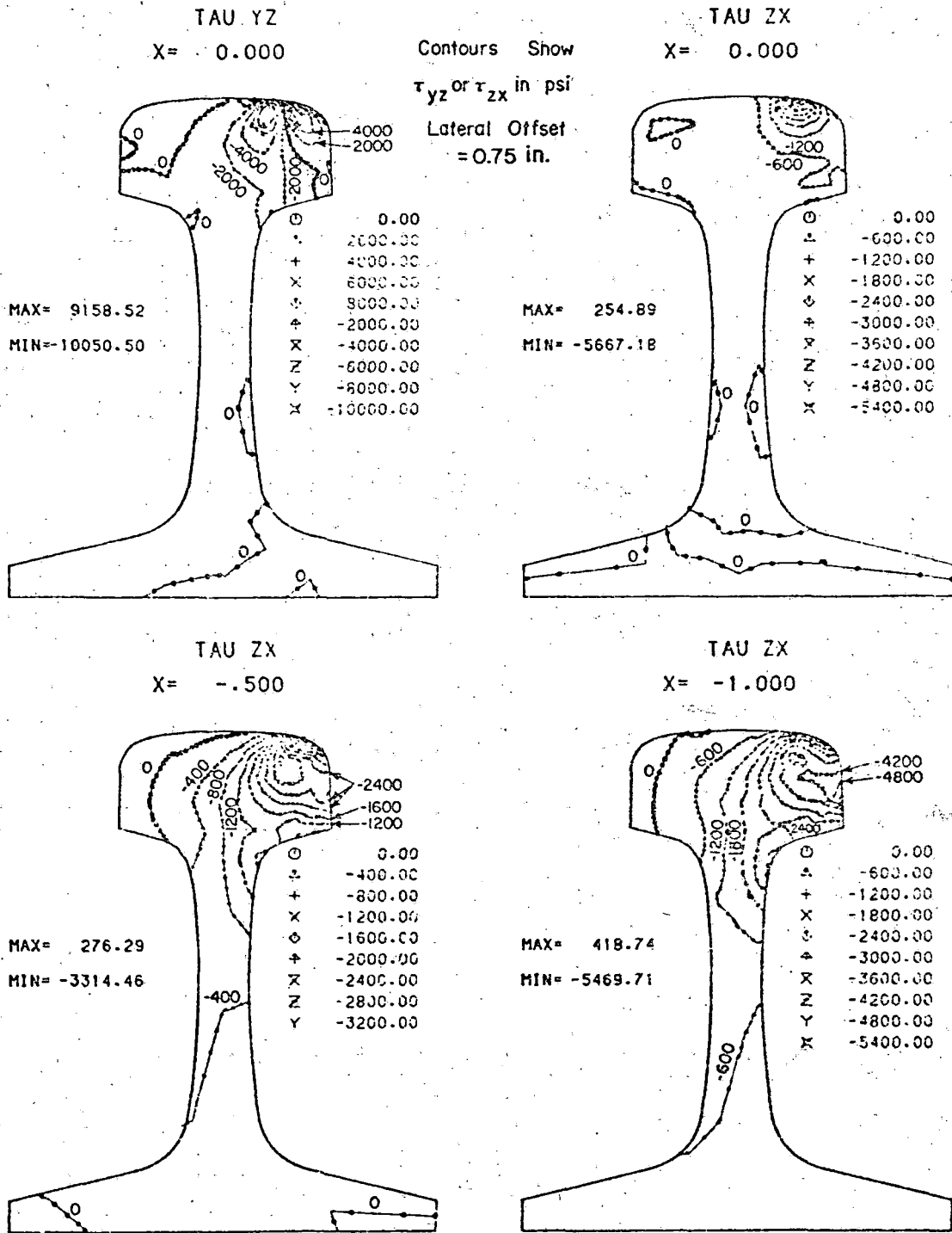


FIGURE B-11. SHEAR STRESS COMPONENTS IN 132-LB RE RAIL UNDER 19,000-LB ECCENTRIC VERTICAL LOAD (Cf. TABLE 2-2, CASE 4)

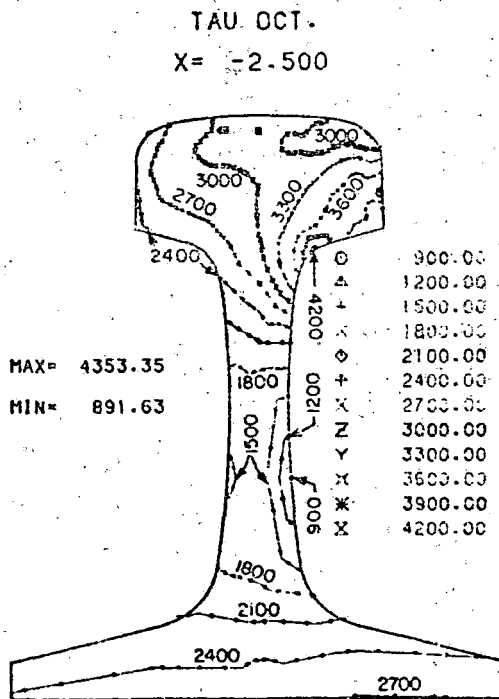
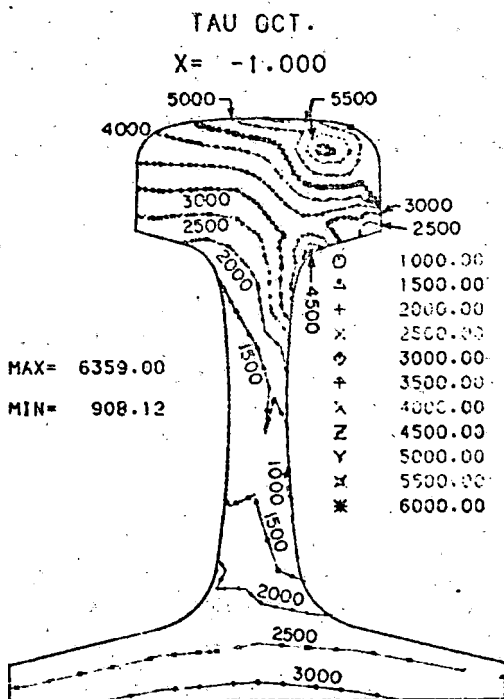
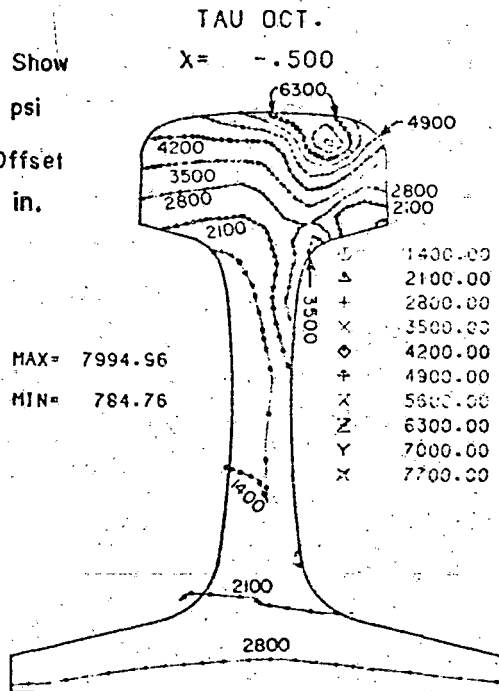
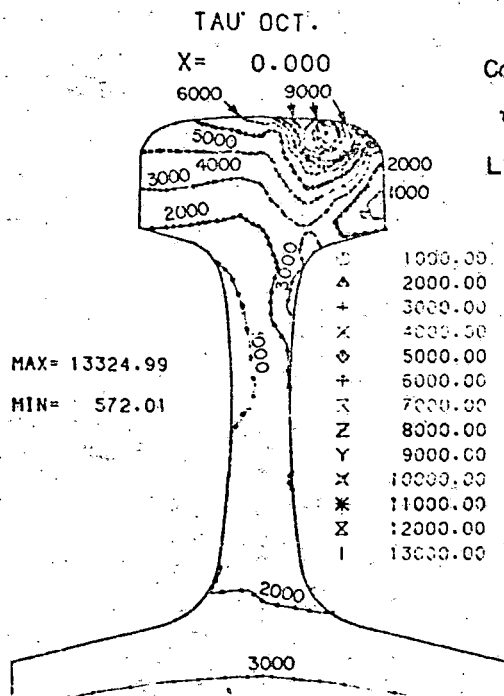


FIGURE B-12. OCTAHEDRAL SHEAR STRESS IN 132-LB RE RAIL UNDER 19,000-LB ECCENTRIC VERTICAL LOAD (Cf. TABLE 2-2, CASE 4)

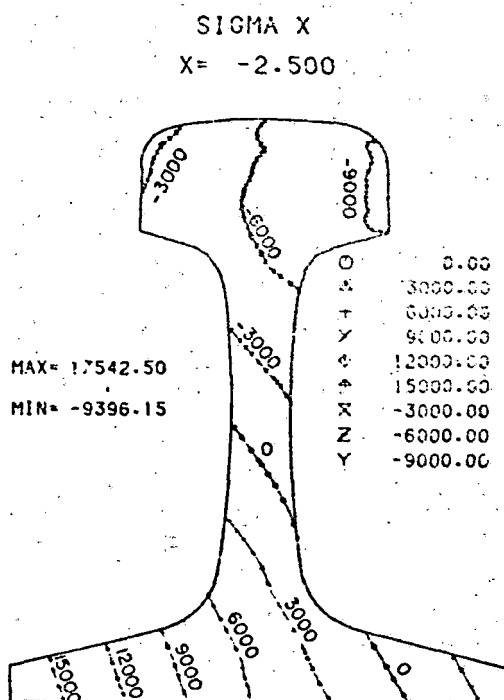
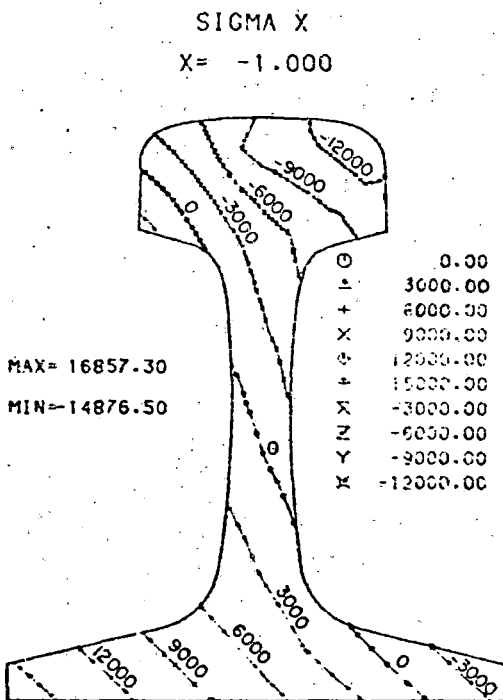
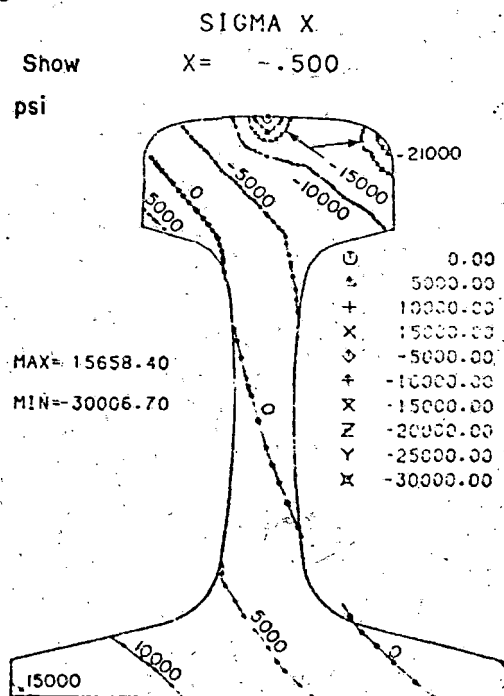
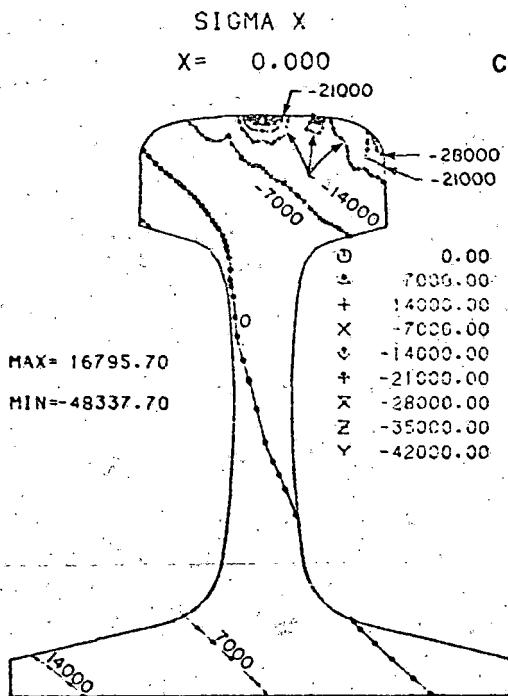


FIGURE B-13. LONGITUDINAL STRESS IN 132-LB RE RAIL UNDER 19,000-LB VERTICAL AND 10,000-LB LATERAL LOAD (Cf. TABLE 2-2, CASE 5)

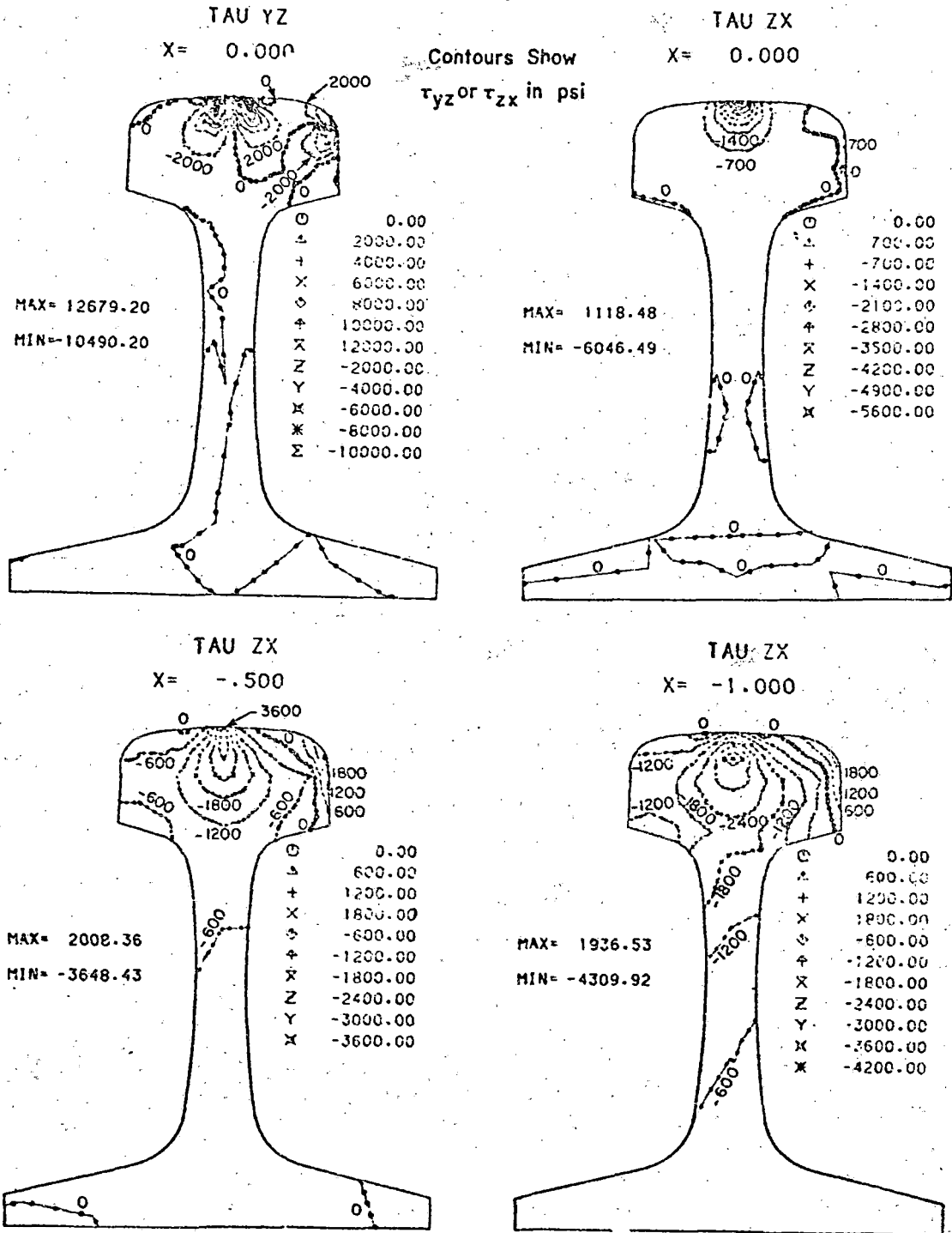


FIGURE B-14. SHEAR STRESS COMPONENTS IN 132-LB RE RAIL UNDER 19,000-LB VERTICAL AND 10,000-LB LATERAL LOAD (Cf. TABLE 2-2, CASE 5)

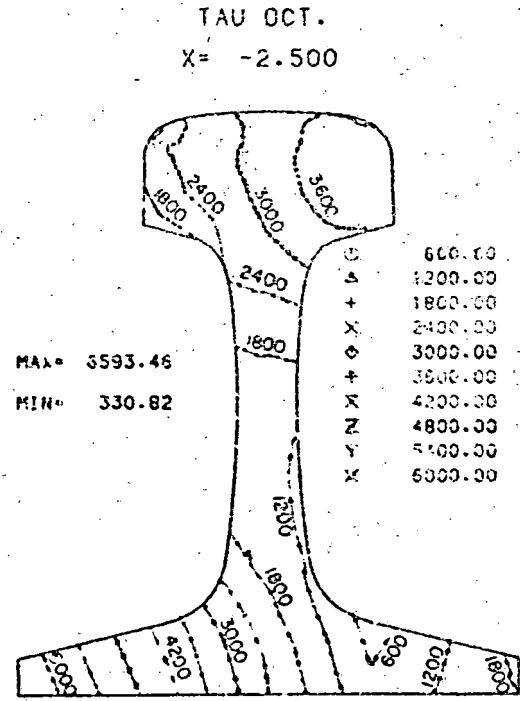
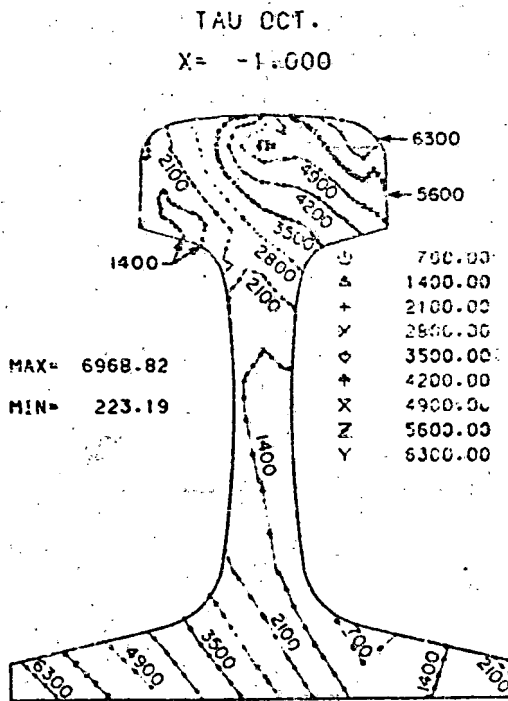
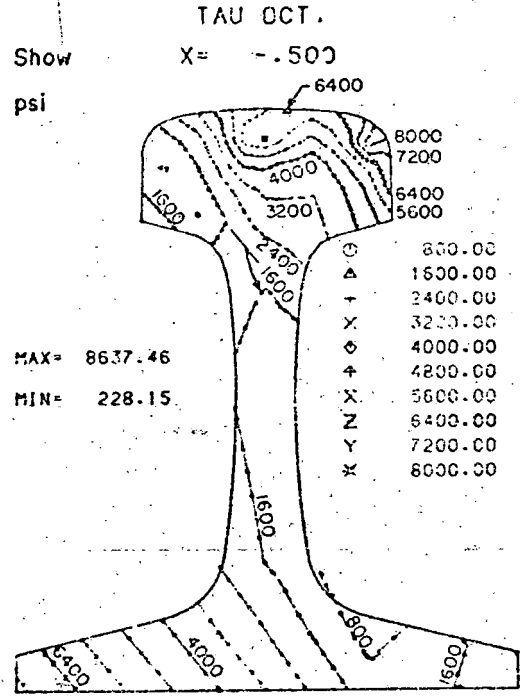
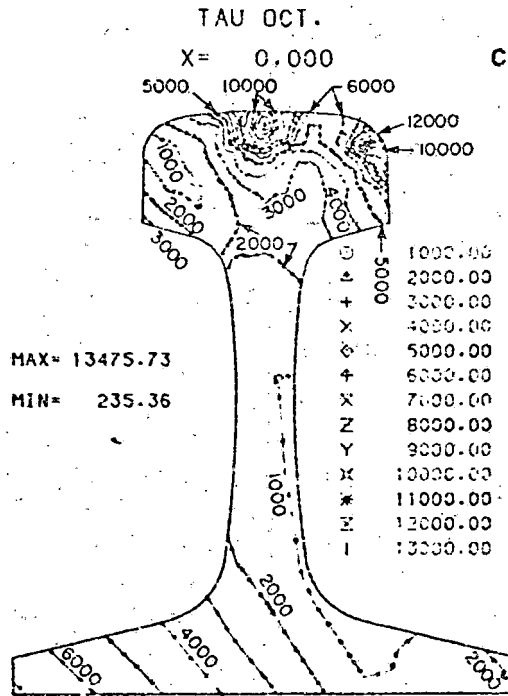


FIGURE B-15. OCTAHEDRAL SHEAR STRESS IN 132-LB RE RAIL UNDER 19,000-LB VERTICAL AND 10,000-LB LATERAL LOAD (Cf. TABLE 2-2, CASE 5)

APPENDIX C

SHAKEDOWN OF STRESSES FROM ROLLING CONTACT

Possibilities for Cylindrical Contact

The presence of residual stresses may counteract contact stresses sufficiently to prevent plastic flow, even though the latter alone might produce such flow. To illustrate such conditions, consider the cylindrical contact case as treated by Merwin and Johnson [C-1], but revise their coordinate system to agree with Figure 1-3, so that x varies in the direction of rolling, y varies laterally, and z vertically, with the origin at the center of contact. By assuming plane deformation, they observed that the only residual stresses possible relate to the components σ_x and σ_z . They presumed also that yielding would occur only where the principal shear stress τ in the xz plane exceeds some value k , that is where

$$\tau \equiv \frac{1}{2} \sqrt{(\sigma_x^e - \sigma_z^e)^2 + 4\tau_{zx}^2} > k \quad (C-1)$$

If the components of stress are only those from elastic contact theory, here denoted as σ_x^e , σ_z^e , and τ_{zx}^e , then τ is maximum where $x = 0$ and $z = 0.786$ times the half-width of contact. Its value there is $0.300p_0$ where p_0 is the maximum contact pressure. Thus if $p_0 > k/0.300 = 3.33k$, plastic flow will occur unless there is some counteracting stress such as residual stress.

Now suppose that at $x = 0$ (so that $\tau_{zx}^e = 0$) there is a region where the elastic stresses alone would make τ exceed k . There

$$\tau^e \equiv \frac{1}{2} \sqrt{(\sigma_x^e - \sigma_z^e)^2} = \frac{1}{2} (\sigma_x^e - \sigma_z^e) \text{ if } \sigma_x^e > \sigma_z^e \quad (C-2)$$

Merwin and Johnson assumed in effect, that $\sigma_x^e > \sigma_z^e$, and where $\tau^e > k$ they postulated the pattern of residual stress to be

$$\sigma_x^r = 2(k - \tau^e) \quad (C-3)$$

When this σ_x^r is included in σ_x , the principal shear stress at $x = 0$ under load becomes

$$\tau = \frac{1}{2} \sqrt{[\sigma_x^e + 2(k - \tau^e) - \sigma_z^e]^2} = k \quad (C-4)$$

which does not exceed k , though this σ_x^r , acting independently of any other stress, would make τ exceed k if $(\sigma_x^e - \sigma_z^e)$ were greater than $4k$ somewhere on the plane $x = 0$. Then they appealed to Melan's theorem [C-2] which states that if any residual stress can be found which, together with the stress due to load, constitutes a system within the yield limit, then under repeated loading the system will shake down to some system of purely elastic deformation. Conversely, according to Melan's theorem, if no such residual stress can be found the system will not shake down and continued plastic deformation will occur at each passage of the load.

The residual stress postulated by Merwin and Johnson was designed to counteract stresses on the plane $x = 0$, but different residual stresses could have been postulated to lessen τ elsewhere, and if it had been desired they could have nullified the contribution to τ from the normal stresses σ_x and σ_z at some crucial position. However, no residual τ_{zx} is possible and no residual σ_x^r and σ_z^r could counteract the contribution to τ made by τ_{zx}^e , so the maximum τ arising under elastic cylindrical contact cannot be less than the maximum value of τ_{zx}^e . Thus if the maximum of τ_{zx}^e exceeds k , shakedown cannot be achieved, and plastic flow will occur with each passage of the load. There are evidently other limitations which also should be considered for shakedown, as is suggested by the difficulty of preserving Merwin and Johnson's postulated σ_x^r during unloading if under load $(\sigma_x^e - \sigma_z^e) > 4k$ somewhere on the plane $x = 0$.

The theory of shakedown from Merwin and Johnson, contains hints for the development for more general elliptical Hertzian contact. It is apparent that simplifying assumptions are needed if that theory is to be kept even moderately simple.

Shakedown Under Elliptical Hertzian Contact

For three-dimensional stresses, it is frequently assumed that plastic flow occurs if $J_2 > k^2$, where k is a constant (equal to the tensile yield stress divided by $\sqrt{3}$) and J_2 is the second stress invariant

$$J_2 = \frac{1}{6}[(\sigma_x - \sigma_y)^2 + (\sigma_y - \sigma_z)^2 + (\sigma_z - \sigma_x)^2] + \tau_{yz}^2 + \tau_{zx}^2 + \tau_{xy}^2 \quad (C-5)$$

Under rolling contact in the x-direction (using the notation of Figure 1-3), residual stresses may develop with four stress components, namely

σ_x , σ_y , σ_z and τ_{yz} , but not τ_{zx} nor τ_{xy} since the residual deformations do not vary in the x-direction. Suppose that, under a given load of Hertzian form, elastic behavior would produce components σ_x^e , σ_y^e , σ_z^e , τ_{yz}^e , τ_{zx}^e and τ_{xy}^e if the unloaded body were stress free, but that actually there are also residual stress components σ_x^r , σ_y^r , σ_z^r , and τ_{yz}^r . These residual stress components may vary in the y and z directions, but not in the x-direction. Then the stress invariant to be compared with k^2 is

$$J_2 = \frac{1}{6}[(\sigma_x^e + \sigma_x^r - \sigma_y^e - \sigma_y^r)^2 + (\sigma_y^e + \sigma_y^r - \sigma_z^e - \sigma_z^r)^2 + (\sigma_z^e + \sigma_z^r - \sigma_x^e - \sigma_x^r)^2] + (\tau_{yz}^e + \tau_{yz}^r)^2 + (\tau_{zx}^e)^2 + (\tau_{xy}^e)^2 \quad (C-6)$$

In order to study variations of J_2 in the x-direction, one may employ the following idealized but nevertheless representative approximations for the elastic stress components:

$$\begin{aligned} \sigma_x^e &= \frac{c_1 x_1^2}{x^2 + x_1^2}, & \sigma_y^e &= \frac{c_2 x_1^2}{x^2 + x_1^2}, & \sigma_z^e &= \frac{c_3 x_1^2}{x^2 + x_1^2}, \\ \tau_{yz}^e &= \frac{c_4 x_1^2}{x^2 + x_1^2}, & \tau_{zx}^e &= \frac{2c_5 x_1 x}{x^2 + x_1^2}, & \tau_{xy}^e &= \frac{2c_6 x_1 x}{x^2 + x_1^2}, \end{aligned} \quad (C-7)$$

where x_1 and the c 's do not vary with x . These approximations conform to the fact that for Hertz contact the first four of these stresses are symmetric around $x = 0$ while the last two are antisymmetric. By suitable choices for x_1 and the c 's, which represent respective maximum values, these expressions agree with as many stress components as are shown in Figure 1-3. To these components one adds the respective residual stresses. Then, putting $\xi = x/x_1$, one finds

$$J_2(\xi) = \frac{A}{(\xi^2+1)^2} + \frac{B}{(\xi^2+1)} + C, \quad \text{where}$$

$$A = \frac{1}{6} [(c_1 - c_2)^2 + (c_2 - c_3)^2 + (c_3 - c_1)^2 + 6c_4^2] - 4(c_5^2 + c_6^2),$$

$$B = \frac{1}{3} [(c_1 - c_2)(\sigma_x^r - \sigma_y^r) + (c_2 - c_3)(\sigma_y^r - \sigma_z^r) + (c_3 - c_1)(\sigma_z^r - \sigma_x^r) + 6c_4 \tau_{yz}^r] + 4(c_5^2 + c_6^2),$$

$$C = \frac{1}{6} [(\sigma_x^r - \sigma_y^r)^2 + (\sigma_y^r - \sigma_z^r)^2 + (\sigma_z^r - \sigma_x^r)^2 + 6(\tau_{yz}^r)^2] \quad (C-8)$$

Also

$$\frac{\partial J_2}{\partial \xi} = -\frac{4A\xi}{(\xi^2+1)^3} - \frac{2B\xi}{(\xi^2+1)^2} = -\frac{2\xi[2A+B(\xi^2+1)]}{(\xi^2+1)^3}, \quad (C-9)$$

which vanishes if $\xi = 0$, if $\xi \rightarrow \pm \infty$, or if $\xi^2 = \xi_m^2 \equiv -1 - \frac{2A}{B}$ provided that value is non-negative. Thus the extreme values of $J_2(\xi)$ are

$$J_2(0) = A+B+C, J_2(\pm\xi_m) = C - \frac{B^2}{4A} \text{ if } \xi_m \text{ is real, and } J_2(\pm\infty) = C \dots \quad (C-10)$$

Also

$$\frac{\partial^2 J_2}{\partial \xi^2} = -4A \frac{1-5\xi^2}{(\xi^2+1)^4} - 2B \frac{1-3\xi^2}{(\xi^2+1)^3}, \text{ so} \quad (C-11)$$

$$\left[\frac{\partial^2 J_2}{\partial \xi^2} \right]_{\xi=0} = -2(2A+B) = 2B\xi_m^2, \text{ and } \left[\frac{\partial^2 J_2}{\partial \xi^2} \right]_{\xi=\pm\xi_m} = -\frac{B^3}{2A^3}(2A+B) = \frac{B^4 \xi_m^2}{2A^3} \dots \quad (C-12)$$

Until the signs of A and B are determined, it is premature to say whether the various extreme values of J_2 are minima or maxima.

To progress further in studying the behavior of $J_2(\xi)$ one may postulate a set of residual stresses. Since it is analytically advantageous and physically not implausible, it will be postulated here that the residual stresses are proportional to the maxima of their related elastic contact stresses. In particular, let

$$\sigma_x^r = -\lambda c_1, \sigma_y^r = -\lambda c_2, \sigma_z^r = -\lambda c_3, \tau_{yz}^r = -\lambda c_4 \dots \quad (C-13)$$

Also let

$$C_e = \frac{1}{6}[(c_1 - c_2)^2 + (c_2 - c_3)^2 + (c_3 - c_1)^2 + 6c_4^2], \quad C_t = c_5^2 + c_6^2 \dots \quad (C-14)$$

Then

$$A = C_e - 4C_t, \quad B = -2\lambda C_e + 4C_t, \text{ and } C = \lambda^2 C_e \dots \quad (C-15)$$

and it follows that

$$J_2(\xi) = C_e \left[\frac{1}{\xi^2+1} - \lambda \right]^2 + \frac{4C_t \xi^2}{(\xi^2+1)^2} \dots \quad (C-16)$$

Then the extrema of $J_2(\xi)$ are

$$J_2(0) = (1-\lambda)^2 C_e, \quad J_2(\pm\infty) = \lambda^2 C_e, \quad \text{and}$$

$$J_2(\pm\xi_m) = C_t \left[1 - \frac{(1-2\lambda)^2 C_e}{C_e - 4C_t} \right] \quad \text{if } \xi_m \text{ is real.} \quad (\text{C-17})$$

To decide whether ξ_m is real so that the conditional extrema exist, note that

$$\xi_m^2 = -\frac{2A+B}{B} = \frac{(1-\lambda)C_e - 2C_t}{\lambda C_e - 2C_t}, \quad (\text{C-18})$$

and that this quantity is non-negative if $[\lambda C_e - 2C_t][(1-\lambda)C_e - 2C_t] > 0$. This implies that the reality of ξ_m depends on the value of λ and on whether $C_e > 4C_t$ or $C_e < 4C_t$. In particular it can be shown that:

$$\text{if } C_e > 4C_t, \text{ then } \xi_m \text{ is real if also } \frac{2C_t}{C_e} < \lambda < \frac{C_e - 2C_t}{C_e},$$

$$\text{if } C_e < 4C_t, \text{ then } \xi_m \text{ is real if also } \frac{C_e - 2C_t}{C_e} < \lambda < \frac{2C_t}{C_e}. \quad (\text{C-19})$$

Note that $C_e > 4C_t$ implies $A > 0$, while $C_e < 4C_t$ implies $A < 0$. If $C_e = 4C_t$, the only choice for λ is $1/2$, and then it follows that $J_2(\xi) \equiv C_e/4$. If $C_e \neq 4C_t$ the possibilities are more varied.

If $C_e > 4C_t$, that is $A > 0$, and λ is chosen to make ξ_m real, then $\frac{\partial^2 J_2}{\partial \xi^2}$ is positive at $\xi = \pm\xi_m$, so the values $J_2(\pm\xi_m)$ are minima, and the $J_2(0)$ and $J_2(\pm\infty)$ are maxima. To minimize the greater maximum, one should choose $\lambda = 1/2$, so that $J_2(0) = J_2(\pm\infty) = C_e/4 > C_t$. If λ were not chosen to make ξ_m real, then either $J_2(\infty)$ or $J_2(\pm\xi_m)$ would be a maximum, with value larger than $C_e/4$, and thus would be less advantageous.

If $C_e < 4C_t$, that is $A < 0$, then both $J_2(\pm\xi_m)$ and the larger of $J_2(0)$ or $J_2(\pm\infty)$ are minimized by taking $\lambda = 1/2$, so again that is the value that should

be taken for λ . In that case $J_2(\pm\xi_m) = C_t$, while $J_2(0) = J_2(\pm\infty) = C_e/4 < C_t$, so the value of C_t is critical in determining whether plastic flow will cease, that is whether shakedown occurs.

Thus for the stresses under elliptical Hertzian contact, it has been shown on the basis of plausible approximations for the variation of the stress components in the rolling direction, that if the residual stresses are (not implausibly) proportional by the factor $-\lambda$ to the maxima of the respective components of elastic contact stress, then the maximum value of $J_2(\xi)$ can be limited best by taking $\lambda = 1/2$. Then also there are five extrema of $J_2(\xi)$, and they are (since also $\xi_m^2 = 1$):

$$J_2(0) = J_2(\pm\infty) = C_e/4, \text{ and } J_2(\pm 1) = C_t. \quad (\text{C-20})$$

Here it is the larger of the values $C_e/4$ and C_t which should be compared with k^2 in deciding whether shakedown of contact stresses will occur. Of course C_e is simply the peak value of $J_2(\xi)$ along the line under consideration without including any residual stresses, and C_t is the maximum contribution made to J_2 by the components τ_{zx} and τ_{xy} which are not counteracted by residual stresses.

To decide whether $C_e/4$ or C_t is typically larger, consider the case illustrated in Figure 1-3. There, because the line considered is on the plane $y = 0$, the components τ_{yz}^e and τ_{xy}^e vanish, and the maxima of the other stress components show

$$C_1 = -42 \text{ ksi}, C_2 = -35 \text{ ksi}, C_3 = -149 \text{ ksi}, C_4 = 34 \text{ ksi}. \quad (\text{C-21})$$

From these values it follows

$$C_e/4 = 1030 \text{ ksi}^2, \text{ and } C_t = 1156 \text{ ksi}^2, \quad (\text{C-22})$$

so it is the magnitude of C_t which is critical for whether there will be plastic flow. If the yield stress for the material is taken to be 95 ksi, as for

a strain hardening steel, $k = 95/\sqrt{3}$ ksi = 55 ksi, then $k^2 = 3025$ ksi². Since this is greater than the C_t for the stresses of Figure 1-3, it follows from Melan's theorem that shakedown of the stresses would occur for that case, though the size of C_e ($= 4120$ ksi² $>$ 3025 ksi²) shows that plastic flow would occur readily in the absence of residual stress. If C_t were large enough to surpass k^2 , then plastic deformation would occur on every pass of the load unless the body could develop more effective residual stresses of some class not included here (that is not uniformly proportional to the maxima of contact stress components).

C-9/C-10

REFERENCES

- C-1. Merwin, J. E. and Johnson, K. L., "An Analyses of Plastic Deformation in Rolling Contact", Proceedings of the Institution of Mechanical Engineers, Vol. 177, No. 25, (1963), p 676-685.
- C-2. Symonds, P. S., "Shakedown in Continuous Media", J. Appl. Mech., Trans. ASME, Vol. 73, (1951), p 85.

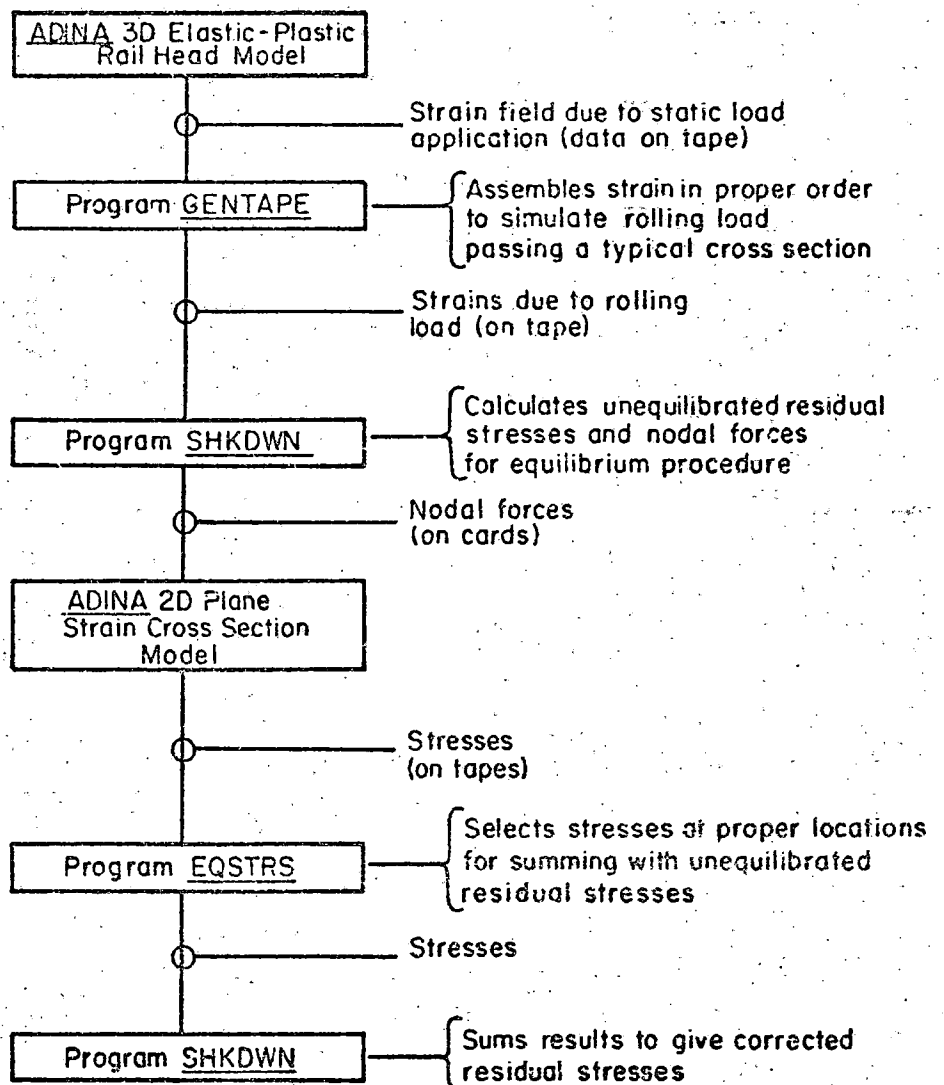
APPENDIX D

DESCRIPTION OF A MODEL FOR DETERMINING RESIDUAL STRESSES IN RAILS

A numerical method for the calculation of residual stresses due to wheel/rail contact was developed. This analysis extends the work of Merwin and Johnson [D-1] and Martin and Hay [D-2] in that it is three dimensional, utilizes a direct finite element approach, and can account for the effects of work hardening.

Outline of Plan

The flow diagram presented in Figure D-1 summarizes the calculation procedure. The first step in the computation of the residual stresses resulting from wheel passage is to determine the subsurface strains using the specified load and contact distributions with the three dimensional finite element model and the computer program ADINA. These strains are then input to program GENTAPE which assembles the strain cycles at the mesh (nodal) points of the model to simulate the passage of a rolling load. These strains are then operated upon by program SHKDWN. This code really forms the most important component of the procedure since it is here that the elasto-plastic calculations are made. Resulting from the operation of this program are a set of unequilibrium residual stresses as they exist in the rail head. These nodal forces are then input to a plane-strain two dimensional finite element model having the same mesh as those assumed originally. Resulting from this calculation is a set of stresses representing the unequilibrium portion of the residual stresses calculated earlier. These are then assembled from the integration point stresses by program EQSTRS in the proper order for summation with the original residual stresses. This is accomplished by program SHKDWN at which point the residual stresses due to the pass of the load are printed out. At this point the calculation procedure can either be terminated or the analysis of another cycle of loading can be made. If the latter course is chosen, it proceeds in a manner identical to that just described.



For next rolling cycle -

Residual stresses are summed with elastic results for work-hardened rail in Program GENTAPE. This result is then input to SHKDOWN and the process outlined above is repeated.

FIGURE D-1. FLOWCHART OF RESIDUAL STRESS CALCULATION PROCEDURE

Description of Procedures

Elastic subsurface stresses in rails have been analyzed previously by Martin and Hay [D-1] using an indirect finite element method. Their approach was adopted because of limitations on the computing machinery available at that time. Subsequent progress in code development obviated the need for that type of analysis in the present work. An elasto-plastic finite element model of the rail head was developed to provide strain-cycle information for the residual stress model. This consists of a quarter section model of the rail head in which two vertical planes of symmetry are assumed. Thus, the model consists of a rectangular solid measuring 1.2- by 1.2- by 1.3 inches. It has a constant cross section mesh repeated at varying intervals along the length of the model. It includes 630 isoparametric-brick elements consisting of 1340 nodes. Loading was applied to this model in the form of a 19,000-lb Hertzian contact distribution having semi-major and minor axes of dimensions 0.27 and 0.189 inches. To avoid the additional complication of flexural stresses, the model was presumed to be supported by a rigid foundation.

The elements directly under the load were constituted of a nonlinear material so that elasto-plastic analysis could be performed. Prior to this, however, the model was run elastically, both for the purposes of comparison with other solutions and validation and for use in the residual stress work. Comparisons were made with closed form solutions, with the elastic brick (FRAC3D) results and with finite element results of Martin and Hay [D-2]. Good agreement between the solutions was found.

For the purposes of the elasto-plastic finite element analysis, a bi-linear, strain hardening, stress-strain curve was assumed. This curve was based on laboratory uniaxial tension tests using material machined from an actual rail head. Table D-1 summarizes the mechanical property results of these tests.

TABLE D-1. TENSILE TEST DATA ON RAIL STEEL

SPEC. NO.	TEST TEMP. ° F	DIAM., INCH	AREA, INCH ²	YIELD STRESS (.2%) ksi	ULT. TENSILE STRESS (ksi)	% ELONGATION	ELASTIC MODULUS (ksi)
027	RT	0.2516	.04972	69.4	136.4	10.0	29,000
029	RT	0.2492	.04877	61.7	125.5	12.0	29,400

The elasto-plastic finite element analysis was conducted incrementally without equilibrium iteration. Five loading steps were required to achieve 100% of the 19,000-lb total applied load; these increments were 68%, 72%, 78%, 88%, and finally 100% of the load.

For the purposes of the residual stress analysis, it was necessary to construct a strain cycle simulating the passage of a rolling load for a single cross-sectional plane. This was done from the simple static contact cases analyzed by the finite element method. It was assumed that the strain seen at any point in the rail head would be the same as that seen by any other point lying on the same horizontal (longitudinal) at some time. Thus, the variation in strain along a given longitudinal line due to a static load was taken to be the same as the strain at a point as a loaded wheel passed by. A computer program was written to assemble a magnetic tape describing the strain cycles for the nodal points of the cross-section. The results of this compilation are shown for the elastic case in Figure D-2 and for the elasto-plastic case in Figure D-3. Here x is measured longitudinally, y laterally, and z vertically. The elastic strain in the z -direction is compared with that determined by Martin and Hay [D-2] by the indirect finite-element solution. Good agreement is found for the components. These particular strain cycles were computed for a point lying at a depth 0.75 inches below the rail surface. Similar cycles, differing only in the magnitude of the components, exist for the other points in the plane. As can be seen and as would be expected, the elasto-plastic strains are of significantly greater magnitude.

Program SHKDN

Program SHKDN calculates unequibrated residual stresses on the basis of the following assumptions:

- 1) The elastic strain cycle derivable from a static contact situation is a sufficiently close approximation to the true elasto-plastic strain cycle of the rolling contact situation.

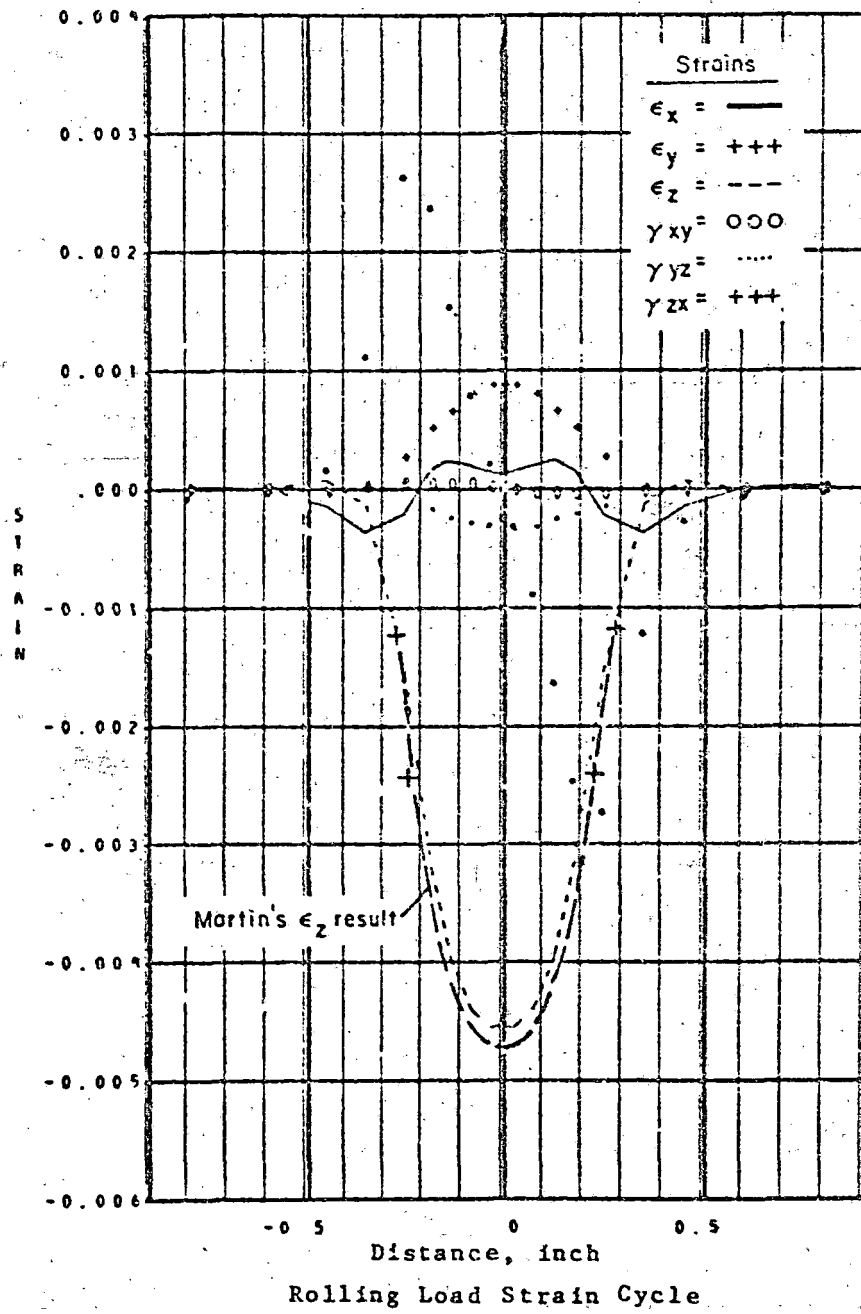


FIGURE D-2. ELASTIC STRAINS ALONG RAIL AXIS ON LONGITUDINAL PLANE OF SYMMETRY AND DEPTH = 0.075 INCH, DUE TO 19,000-LB LOAD

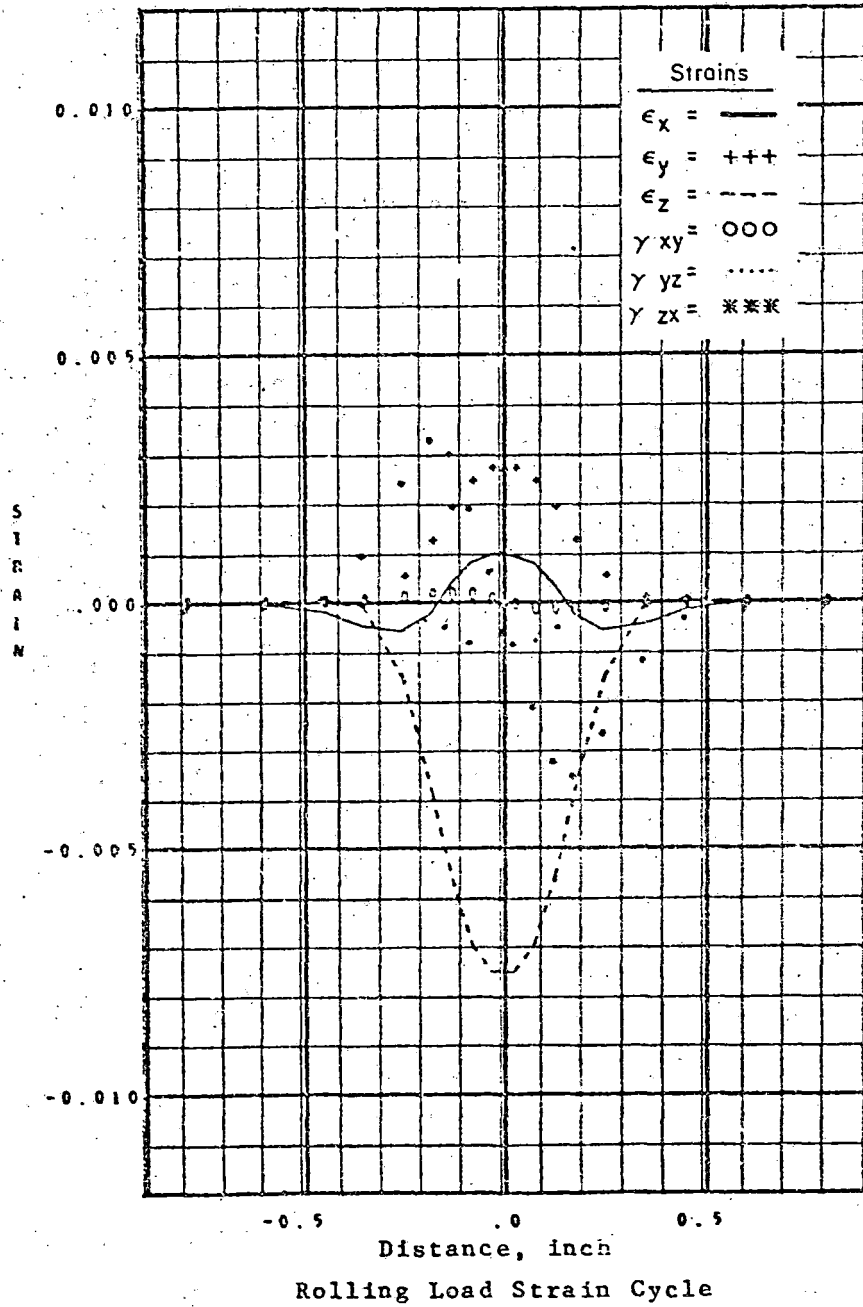


FIGURE D-3. ELASTIC-PLASTIC STRAINS ALONG RAIL AXIS ON LONGITUDINAL PLANE OF SYMMETRY AND DEPTH = 0.075 INCH, DUE TO 19,000-LB LOAD

- 2) The material is isotropic, elastic-plastic obeying an isotropic strain hardening law. Its yielding is described by the Von Mises criterion and the Prändtl-Reuss equations.
- 3) Every plane of the rail remains identical to every other plane in the rail both in terms of residual stress and material properties. Thus σ_{xz} and σ_{yx} are everywhere zero when no load is present.
- 4) A vertical plane of symmetry is assumed to exist on the longitudinal centerline of the rail. Thus, only half the rail head is included in the analysis.

Analysis proceeds in the program in the following manner:

- 1) Various problem parameters are read in, including the coefficients of the linear equation describing the stress-strain curve, the yield stress, Poisson's ratio, the problem size, and so forth.
- 2) Strain cycle information is read from a tape on a mesh point-by-mesh point basis. For each increment of strain, the stresses at all of the points in the cross-section are evaluated before moving on to the next increment. After the strain tensor at a point is read in, the strain components are transformed into deviatoric stress components by the relation,

$$S_{ij} = \sigma_{ij} - S_m \quad (i=j=1,2,3) \quad (D-1)$$

where

$$S_m = \sigma_{ii}/3 \quad (i=1,2,3) \quad (D-2)$$

At the same time, the strain deviation gradient is calculated using a three point divided difference approximation to the derivative.

Thus,

$$\left. \frac{d\epsilon_{ij}}{dx} \right|_n = \frac{\epsilon_{ij}|_n - \epsilon_{ij}|_{n-1}}{x_n - x_{n-1}} + (x_n - x_{n-1}) \left(\frac{\frac{\epsilon_{n+1} - \epsilon_n}{x_{n+1} - x_n} - \frac{\epsilon_n - \epsilon_{n-1}}{x_n - x_{n-1}}}{x_{n+1} - x_{n-1}} \right) \quad (D-3)$$

is the gradient at the point in the mesh. Finally, the equivalent strain for the current strain level is calculated using the familiar expression

$$\epsilon_{ef} = \frac{2}{3} [(\epsilon_{11} - \epsilon_{22})^2 + (\epsilon_{22} - \epsilon_{33})^2 + (\epsilon_{33} - \epsilon_{11})^2 + \frac{3}{2} (\epsilon_{12}^2 + \epsilon_{23}^2 + \epsilon_{13}^2)]^{1/2} \quad (D-4)$$

- 3) Using the results from the uniaxial stress strain curve, the von Mises yield criterion,

$$\epsilon_{ef} < \epsilon_z \quad (D-5)$$

where ϵ_z is the strain at yield (for the first approach to yielding) is applied. If yield has not occurred at that mesh point, the stress is merely assumed to be that given by Equation (D-1). The program then proceeds to the next mesh point and repeats the sequence of computations. If, however, it is found that yielding has occurred, then the increment of stress due to current value of strain is calculated using the Prandtl-Reuss equations. These are generally written in terms of deviatoric stress and strain as

$$\dot{S}_x = 2G[\dot{\epsilon}_x - \frac{\dot{W}}{2k^2} S_x]$$

$$\dot{S}_y = 2G[\dot{\epsilon}_y - \frac{\dot{W}}{2k^2} S_y]$$

$$\dot{S}_z = 2G[\dot{\epsilon}_z - \frac{\dot{W}}{2k^2} S_z]$$

$$\dot{\tau}_{xy} = G[\dot{\gamma}_{xy} - \frac{\dot{W}}{k^2} \tau_{xy}]$$

$$\dot{\tau}_{yz} = G \left[\dot{\gamma}_{yz} - \frac{\dot{W}}{k^2} \tau_{yz} \right]$$

$$\dot{\tau}_{xz} = G \left[\dot{\gamma}_{xz} - \frac{\dot{W}}{k^2} \tau_{xz} \right] \quad (D-6)$$

where G is the elastic shear modulus, k is the yield stress in simple shear, dots indicate time rates of change, and

$$\dot{W} = S_x \dot{\epsilon}_x + S_y \dot{\epsilon}_y + S_z \dot{\epsilon}_z + \tau_{yz} \dot{\gamma}_{yz} + \tau_{zx} \dot{\gamma}_{zx} + \tau_{xy} \dot{\gamma}_{xy} \quad (D-7)$$

Specifically, the time rate of change indicated above is replaced by the gradient in the rolling direction so that,

$$\frac{\Delta S_x}{\Delta x} = 2G \left(\frac{\Delta \epsilon_x}{\Delta x} - \frac{\Delta W \Delta x}{2k^2}^{-1} S_x \right), \quad \frac{\Delta \tau_{xz}}{\Delta x} = G \left(\frac{\Delta \gamma_{xz}}{\Delta x} - \frac{\Delta W \Delta x}{k^2}^{-1} \tau_{xz} \right),$$

$$\frac{\Delta S_y}{\Delta x} = 2G \left(\frac{\Delta \epsilon_y}{\Delta x} - \frac{\Delta W \Delta x}{2k^2}^{-1} S_y \right), \quad \frac{\Delta \tau_{xy}}{\Delta x} = G \left(\frac{\Delta \gamma_{xy}}{\Delta x} - \frac{\Delta W \Delta x}{k^2}^{-1} \tau_{xy} \right),$$

(D-8)

$$\frac{\Delta S_z}{\Delta x} = 2G \left(\frac{\Delta \epsilon_z}{\Delta x} - \frac{\Delta W \Delta x}{2k^2}^{-1} S_z \right), \quad \frac{\Delta \tau_{yz}}{\Delta x} = G \left(\frac{\Delta \gamma_{yz}}{\Delta x} - \frac{\Delta W \Delta x}{k^2}^{-1} \tau_{yz} \right),$$

where $\frac{\Delta W}{\Delta x}$ is the rate of plastic work is given by

$$\begin{aligned} \frac{\Delta W}{\Delta x} = & S_x \frac{\Delta \epsilon_x}{\Delta x} + S_y \frac{\Delta \epsilon_y}{\Delta x} + S_z \frac{\Delta \epsilon_z}{\Delta x} \\ & + \tau_{xy} \frac{\Delta \gamma_{xy}}{\Delta x} + \tau_{yz} \frac{\Delta \gamma_{yz}}{\Delta x} + \tau_{xz} \frac{\Delta \gamma_{xz}}{\Delta x} \end{aligned} \quad (D-9)$$

- 4) When the strain cycle has been completed, a system of locally compatible residual stresses remain. However, since stresses at the various levels have been computed independently of each other, overall equilibrium is not satisfied. To remedy this, the resultant planar nodal forces are calculated that would give rise to the system of stresses just calculated if considered with respect to an assumed finite element mesh. This is accomplished by integrating the equation of equilibrium over the indicated elements. Thus, the forces at the center of the element are given by

$$F_y = \iint \left(-\frac{\partial \sigma_{yy}}{\partial y} + \frac{\partial \tau_{yz}}{\partial z} \right) dydz ,$$

$$F_z = \iint \left(-\frac{\partial \sigma_{zz}}{\partial z} + \frac{\partial \tau_{yz}}{\partial y} \right) dydz . \quad (D-10)$$

These resultant forces are apportioned equally to the four corner nodes of the assumed finite element mesh. Actually what occurs in the program is somewhat more involved than what has just been described, but these mechanical details, involved as they are with the finite element methods, will not be elaborated upon here. Nodal forces representing the residual stress system are finally output on punched cards.

Equations (D-8) were the forms of the Prandtl-Reuss relations actually used in the program. The strain rates used for a particular point in the strain cycle were those given by Equation (D-3). The increments of stress computed with Equation (D-8) are then added to the stresses computed at the previous increment of strain. This process continues during the strain cycle until unloading of a point occurs. After this, stress is again calculated elastically and further unloading proceeds elastically.

Two-Dimensional Finite-Element Railhead
Cross Section Model

This planar symmetrical model, which is exactly the same as the cross section of the three-dimensional railhead model, has 53 linear elements. The boundary conditions are appropriately arranged to simulate railhead support as described with the earlier model. The analyses are performed using the nodal forces produced from the unequilibrated residual stresses by program SHKDN. The resulting stresses are output on tape.

Program EQSTR

This code, which is structurally almost identical to GENTAPE, arranges the stress output from the two-dimensional finite element model in a sequence that corresponds to that of the mesh points in Program SHKDN. Once again, this program is of little interest from a mechanics standpoint, so it will not be discussed further.

The stress computation procedure is then completed by subtracting the stresses computed by the finite element model (representing the unequilibrated portion of the computed stresses) from the original residual stress. Thus, at each mesh point

$$s_{ij} | k = s_{ij}^{ur} | k - s_{ij}^{fe} | k \quad (D-11)$$

where $s_{ij}^{fe} | k$ is the finite element component at the kth mesh point. The resulting stress deviations are then output as the final residual stress state for that load pass. This operation is also accomplished with Program SHKDN. A similar procedure is followed for the next pass of the load.

D-13/D-14

REFERENCES

- D-1. Merwin, J. E. and Johnson, K. L., "An Analysis of Plastic Deformation in Rolling Contact", Proceedings of the Institution of Mechanical Engineers, Vol. 177, (1963), p 676-685.
- D-2. Martin, G. C. and Hay, W. W., "The Influence of Wheel-Rail Contact Form on the Formation of Rail Shells", TRANS-ASME 72-WA/RT-8, (1972).

APPENDIX E

MEASUREMENTS OF REPRESENTATIVE RESIDUAL STRESSES
DUE TO ROLLING CONTACT ON RAILS

Destructive experimental measurements of the residual stresses developed during rolling contact on stress relieved rails were made in order to characterize the way residual stresses grow. For this purpose, special rail specimens were prepared and subjected to rolling loads under controlled conditions. The three-dimensional residual stress field was then determined, using the Battelle Slicing Technique.

Description of Test Specimen

Simulated-rail specimens were machined from 175-lb crane rail sections, Figure E-1. These specimens had a 10-inch crown radius and were 40 inches long. A spectrographic analysis of the steel chemistry is presented in Table E-1, showing fractional percents for alloying elements.

TABLE E-1. SPECTROGRAPHIC ANALYSIS OF CRANE RAIL STEEL

C	Mn	P	S	Si	Cu	Sn	Ni	Cr	Mo	Al	V	Zr	Ti	B	Co	W	
.71	.80	.015	.039	.13	.18	.015	.072	1.00	.016	.013	.006	.004	.004	.002	.005	.006	.005

The specimen geometry, trimmed down from a heavier rail, was chosen in order to isolate the contact stress phenomena as much as possible from bending effects of the rail. Thus, the section was made as stiff as was reasonably possible using an available rail section. Special care was taken in fabricating the specimen so as to assure uniformity of the crown radius and flatness

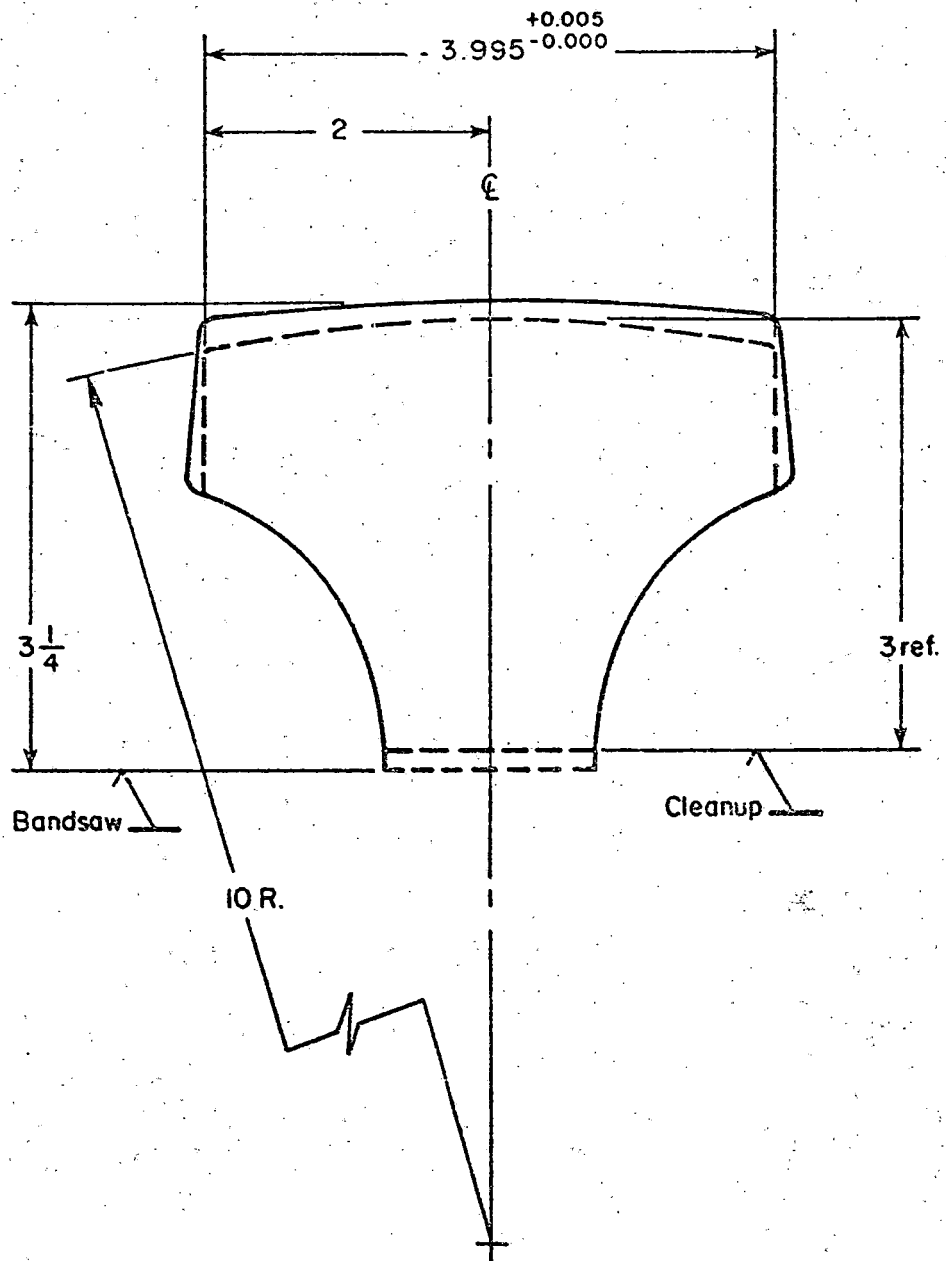


FIGURE E-1. CROSS SECTION THROUGH TEST SPECIMEN

of the web bottom. For the rolling operation, the rails were mounted on a firm base. In order to approach the ideal situation assumed in mathematical modelling, the specimens were subjected to an extensive stress relieving process that reduced them to a stress-free state prior to testing. This procedure is outlined in Table E-2.

The stress relieving processes resulted in a lower tensile yield stress than was expected in a rolled rail. The stress-strain characteristics for the material are presented in Figure E-2.

TABLE E-2. SUMMARY OF THE STRESS RELIEVING PROCEDURE

Time/Date	Temperature, F	Remarks
3:30 p.m./12-17	78	Start Heat-Up
9:05 p.m./12-20	1150	Reached 1150
6:45 p.m./12-22	1250	Reached 1250
8:40 a.m./12-23	1263 ^(a)	Turn Off - Cool Down
9:32 a.m./12-27	382	Removed From Oven
4:37 p.m./12-28	250	Removed Insulation
8:21 a.m./12-29	78	Stress Relief Complete

(a) Time at relieving temperature was 14 hours.

Description of Loading Apparatus

The rolling load tests were conducted by Battelle staff at the AAR Research Center in Chicago, Illinois. The tests were conducted on a cantilever wheel/rail loading fixture which had a stroke of 34 inches and was capable of applying loads in excess of 100,000 lbs. In this fixture, the rail,

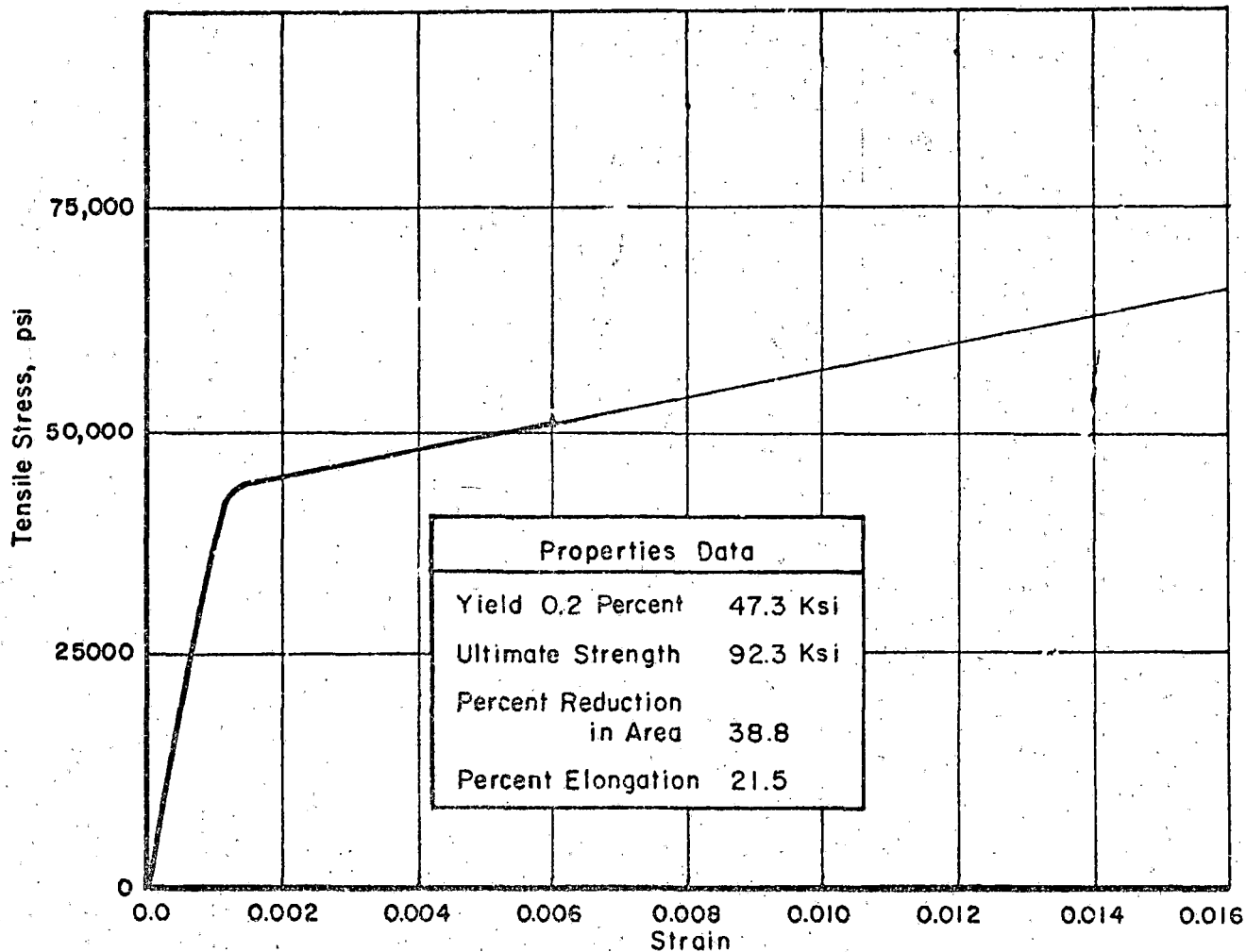


FIGURE E-2. STRESS-STRAIN CHARACTERISTICS FOR RAIL TEST SPECIMEN

driven by a slider crank, moves under the rolling 36-inch wheel, which had been turned and refaced for these experiments. To further eliminate the possibility of bending of the specimen, a head-holding fixture was constructed to provide additional support.

Test Cases

A total of four specimens were subject to rolling. Two of these were rolled with a load of 10,000 lbs and two were rolled at 14,500 lbs. In these cases, the rolling load was passed over a first specimen once and a second specimen three times. All of the rolling passes were in the same direction and were made as near as possible to the centerline of the rail head. It was noted that the applied load fluctuated approximately 2000 pounds during each traverse. This was probably the result of wear in the machine slider support rollers.

Battelle's Slicing Technique

The Battelle Slicing Technique for determining the three dimensional residual stress field in a rail consists of substantial modifications and unique combinations of techniques developed by Yasojima and Machii [E-1] and by Kalakoutski [E-2] and by Meier [E-3]. The technique of Yasojima and Machii is modified in that a much thinner slice (~0.25 inch) than normal is taken. The thin slice is then subsliced (diced). The Meier technique was applied essentially unaltered to determine the longitudinal strain ϵ_x . The first y-z slice results in the longitudinal stress σ_x being relieved at each point in the slice. The strains (ϵ_y and ϵ_z in the y-z plane) are modified by a simple multiple of σ_x at each point (namely strains due to Poisson's effect), $\sigma_x \nu/E$, added at each point. By dicing the y-z slice the modified strains (ϵ'_y and ϵ'_z) can be determined. Knowing ϵ_x , ϵ'_y and ϵ'_z permits the original strain state to be determined readily. Finally from the original strain components, ϵ_x , ϵ_y , and ϵ_z , the residual stress field, σ_x , σ_y and σ_z is determined point by point.

Mathematical Formulation

Using the coordinate system as shown in Figure E-3, the assumptions for the residual stress field are as follows:

1. The residual stresses include σ_x , σ_y , σ_z , and τ_{yz} but not τ_{xz} or τ_{xy} .
2. The stresses or strains that originally exist in the rail are not increased during slicing to an extent that causes plastic flow. Also, upon unloading, the σ - ϵ curve is the line $\epsilon = \sigma/E$.
3. The material is everywhere homogeneous, linear elastic, and isotropic.

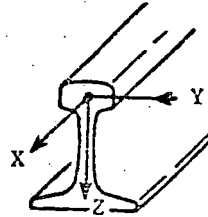


FIGURE E-3. RAIL COORDINATE SYSTEM

On the basis of the third assumption, the principal residual stresses in the rail are as follows:

$$\sigma_x = \frac{E}{(1+\nu)(1-2\nu)} [(1-\nu)\epsilon_x + \nu(\epsilon_y + \epsilon_z)] ,$$

$$\sigma_y = \frac{E}{(1+\nu)(1-2\nu)} [(1-\nu)\epsilon_y + \nu(\epsilon_x + \epsilon_z)] ,$$

$$\sigma_z = \frac{E}{(1+\nu)(1-2\nu)} [(1-\nu)\epsilon_z + \nu(\epsilon_x + \epsilon_y)] , \quad (E-1)$$

where σ_x , σ_y , and σ_z are the residual stresses and ϵ_x , ϵ_y , and ϵ_z are the residual strains. (For simplicity, the isotropic constitutive equations are presented; but the method is equally well suited for orthotropic materials.) Conversely, the actual strains in the rail expressed in terms of the stresses are given by

$$\begin{aligned}\epsilon_x &= \frac{1}{E} [\sigma_x - \nu(\sigma_y + \sigma_z)] , \\ \epsilon_y &= \frac{1}{E} [\sigma_y - \nu(\sigma_x + \sigma_z)] , \\ \epsilon_z &= \frac{1}{E} [\sigma_z - \nu(\sigma_x + \sigma_y)] .\end{aligned}\quad (E-2)$$

Now on the rail in question, let us apply a stress σ_x on the rail cross section, i.e., on the y-z plane, everywhere equal in magnitude but opposite to the original stress field. In doing this, ϵ_y and ϵ_z of Equation (E-2) are incremented in the manner described above.

Because of the absence of residual stress components τ_{xz} and τ_{xy} , the stress σ_x must be a self-equilibrating stress and does not upset the equilibrium of stresses in the y-z plane. Therefore, the change in σ_x incurred during slicing would only increment the strains ϵ_y and ϵ_z by a Poisson effect and would not alter the stresses σ_y and σ_z . Therefore, if the y-z section is subsliced, the strains ϵ'_y and ϵ'_z in the slice after the section is made are given by the original strains, ϵ_y and ϵ_z , plus the increment $\nu\sigma_x/E$, that is

$$\epsilon'_y = \epsilon_y + \nu\sigma_x/E \quad \text{and} \quad \epsilon'_z = \epsilon_z + \nu\sigma_x/E .\quad (E-3)$$

Substituting $\nu\sigma_x/E$ from Equation (E-1) yields:

$$\begin{aligned}\epsilon'_y &= \epsilon_y + \frac{\nu}{(1+\nu)(1-2\nu)} [(1-\nu)\epsilon_x + \nu(\epsilon_y + \epsilon_z)] , \\ \epsilon'_z &= \epsilon_z + \frac{\nu}{(1+\nu)(1-2\nu)} [(1-\nu)\epsilon_x + \nu(\epsilon_y + \epsilon_z)] .\end{aligned}\quad (E-4)$$

From the Meier technique, the original ϵ_x is determined directly. Substituting its value in Equation (E-4) permits evaluation of ϵ'_y and ϵ'_z , since ϵ'_y and ϵ'_z are determined experimentally from the diced y-z slice.

For positions on the top surface, the residual stress component σ_z is zero. Thus, for points on that surface

$$\epsilon_z = -\frac{\nu}{1-\nu}(\epsilon_x + \epsilon_y) \quad (E-5)$$

Thus measurements of residual strains ϵ_x and ϵ_y on that surface suffice to imply values of all three components of residual strain.

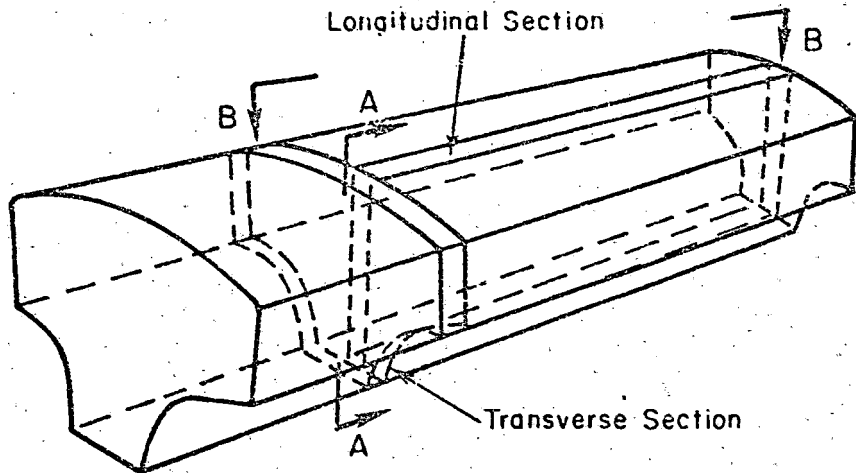
The strains arising from the sectioning process, that is the measured and calculated strains ϵ_x , ϵ_y , ϵ_z should be interpreted as the negatives of the original residual strains, hence the stresses implied by the measured strains should be interpreted as the negatives of the original residual stresses.

Experimental Procedure

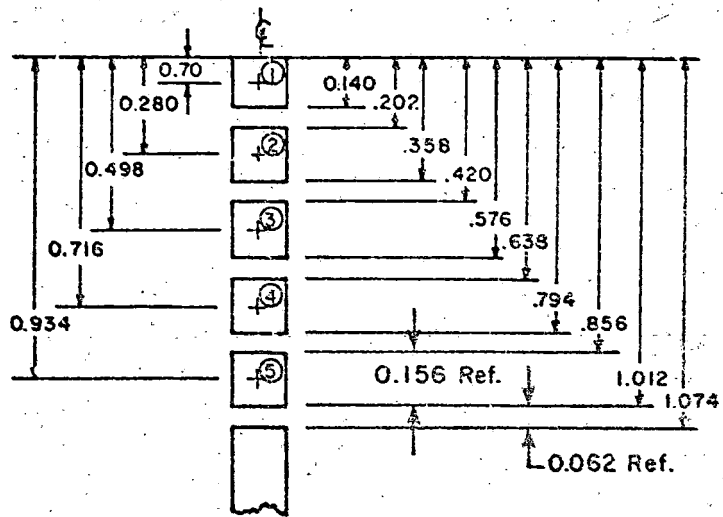
After the rolling load operations at Chicago, mentioned earlier, the specimens were returned to the Columbus Laboratories where the Battelle sectioning technique was applied to the specimens subjected to the 14,500-lb. load. This procedure was carried out in the following steps:

- 1) Biaxial strain gages were applied along the centerline of the rail on the running surface at the location shown in Figure E-4 (c).
- 2) The 0.25-inch thick, transverse Yasojima-Machi slice was cut from the simulated rail specimens with a bandsaw. Readings on the strain gages were recorded.
- 3) Biaxial strain gages were applied to the face of this slice along the vertical centerline [Figure E-4 (b)] after hand sanding the face with emery cloth.
- 4) The strain gage-bearing blocks shown in Figure E-4 (b) were then cut out on the bandsaw and the resulting strain fluctuations recorded.
- 5) Scribe marks were applied to the specimen where the Meier section was to be cut out.

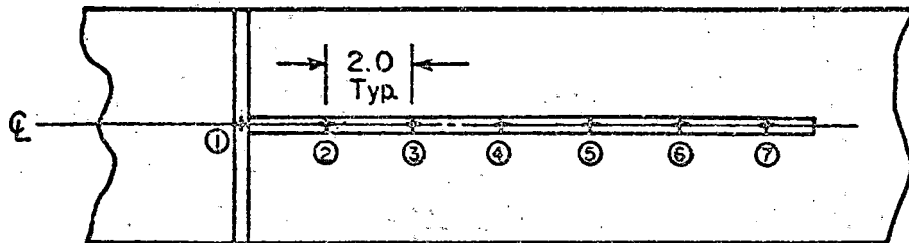
E-9



a. Sectioning of specimen



b. Location of longitudinal rods in longitudinal section (seen in direction A-A). Gages on transverse slice at same depths.



c. Location of surface strain gages on longitudinal rod No. 1 (seen in direction B-B)

FIGURE E-4. SECTIONING OF RAIL SPECIMENS

- 6) The Meier slab was then cut from the rail specimen once again using the bandsaw. The change in length between the scribe marks was measured. Strain variations were monitored during the cutting out procedure.
- 7) The five longitudinal rods, Figure E-4 (b), were cut from the slab after the ends of the latter had been ground and polished.
- 8) The final length of the rods were measured in the BCL metrological facilities. Strains on the top of the rail were monitored during this step.
- 9) Finally, strain gage bearing cubes were cut from the uppermost rod and the change in strain recorded.

In this way, triaxial strain readings were obtained at five locations at varying depth in the rail and biaxial surface strains were found at seven places on the surface of the rail.

Statistical Study of Experimental Variability in Stress Measurements

To assess the variability inherent in the strain gage sectioning procedure, a series of measurements of stresses along the surface centerline of the rail were made. It was assumed that since the load was relatively constant over the length from which the gages were to be removed, the stresses would also be constant.

As described earlier, a total of seven biaxial gages were applied and the corresponding areas then sectioned from the upper surface of each specimen. One of the gages was located on the transverse slice while the other six were along the surface longitudinal rod.

Table E-3 presents the results of this series of measurements for the two specimens. The first two columns list the measured strains. The stress components shown in the next two columns were computed using the procedure described earlier. The first set of values listed for each specimen correspond to the gage readings from the transverse slice. Mean stresses and

standard deviations were calculated using the data from the remaining six measurements. The single load pass specimen, Number 1, shows far less variation in stress than does the three-pass specimen. It is suspected that some irregularity in the three pass rolling produced non-uniform stress along the top surface of Specimen 2. Thus the large scatter in stresses calculated for that specimen may not be due to variance in the measuring process. Moreover, such a scatter need not be expected at points deeper in the rail. Therefore, the standard deviations shown for Specimen 1 are probably representative of accuracies attainable by this procedure.

Experimental Results

The "raw" strain readings obtained during the dissection procedure are presented in Table E-4. This table includes both the results obtained from the dicing of the transverse slice and the removal of the rods for both specimens.

Table E-5 presents the subsurface strains and stresses evaluated from the data in Table E-4 by the analytical methods described earlier. The surface strain, as measured by the centerline strain gages and resultant stresses calculated by presuming $\sigma_z = 0$ at the top surface, are shown in Table E-3.

TABLE E-3. SURFACE RESIDUAL STRESSES WITH STATISTICAL EVALUATIONS

Strains Produced by Slicing		Residual Stresses, psi	
ϵ_x^r	ϵ_y^r	σ_x^r	σ_y^r
Specimen 1 (1 loading pass)			
0.000230	-0.000189	-5713 ^(a)	3956 ^(a)
0.000388	-0.000335	-9478	7207
0.000345	-0.000305	-8357	6643
0.000372	-0.000315	-9148	6705
0.000343	-0.000322	-8123	7223
0.000344	-0.000275	-8621	5664
0.000294	-0.000224	-7477	4477
Mean Stresses (last six gages)		-8534	6320
Standard Deviation		657	707
Specimen 2 (3 loading passes)			
0.000369	-0.000199	-10197 ^(a)	2911 ^(a)
0.000423	-0.000142	-12541	498
0.000385	-0.000047	-12227	-2258
0.000156	-0.000240	-2769	6369
0.000490	-0.000244	-13741	3198
0.000449	-0.000008	-14723	-4177
0.000550	-0.000079	-17351	-2835
Mean Stresses (last six gages)		-12225	-132
Standard Deviation		4552	3695

(a) Gages located on transverse slice.

TABLE E-4. SUBSURFACE STRAIN AND DISPLACEMENT MEASUREMENTS

Location Number	<u>Yasojima-Machi Strains</u>			<u>Meier Deformations^(a)</u>		
	ϵ_z	ϵ_y	δl inch	l_o inch	l_f inch	Depth inch
	<u>Specimen No. 1</u>					
1	-0.000138	0.000394	-0.000040	12.0636	12.0696	0.070
2	0.000121	-0.000081	-0.000028	12.0636	12.0662	0.280
3	-0.000006	-0.000007	-0.000018	12.0636	12.0648	0.498
4	-0.000002	0.000046	-0.000009	12.0637	12.0648	0.716
5	0.000027	0.000066	0.000000	12.0637	12.0648	0.934
	<u>Specimen No. 2</u>					
1	-0.000121	0.000459	-0.0002360	12.0627	12.0688	0.070
2	0.000045	0.000014	-0.0001653	12.0628	12.0660	0.280
3	-0.000060	-0.000113	-0.0001102	12.0639	12.0638	0.498
4	-0.000051	0.000016	-0.0000551	12.0629	12.0638	0.716
5	-0.000018	0.000066	0.0000000	12.0630	12.0640	0.934

(a) δl = length change due to removal of slab from rail,
 l_o = initial length before slicing out rods,
 l_f = final length of rods,
 so that total deformation is $\Delta L = \delta l + (l_f - l_o)$.

TABLE E-5. SUBSURFACE RESIDUAL STRAINS AND STRESSES

Position No.	Strains Produced by Slicing			Residual Stresses (psi)		
	ϵ_z	ϵ_y	ϵ_x	σ_z^r	σ_y^r	σ_x^r
	<u>Specimen No. 1</u>					
1	-0.000319	0.000212	0.000494	652	-11624	-18112
2	0.000052	-0.000149	0.000211	-3187	1473	-6860
3	-0.000031	-0.000032	0.000091	267	290	-2571
4	-0.000033	0.000014	0.000086	-389	-1496	-3153
5	-0.000011	0.000027	0.000087	-1542	-2442	-3806
	<u>Specimen No. 2</u>					
1	-0.000310	0.000269	0.000486	-550	-13935	-18929
2	-0.000038	-0.000069	0.000251	-1621	-906	-8305
3	-0.000057	-0.000110	0.000065	3095	4318	260
4	-0.000066	0.000000	0.000065	1523	-23	-1526
5	-0.000048	0.000035	0.000081	-59	-1997	-3054

REFERENCES

- E-1. Yasojima, Y. and Machii, K., "Residual Stresses in the Rail", Permanent Way, No. 26, Vol., 8, No. 1, Japan, 1965.
- E-2. Kalakoutsky, H., "The Study of Internal Stresses in Cast Iron and Steel", London, 1888, also St. Petersburg, 1889.
- E-3. Meier, H., "Eigenspannungen in Eisenbahnschienen" (Residual Stresses in Railroad Rails), Vereines deutscher Ingenieur Zeitschrift, Vol. 81, No. 12 p 362-363. March 20, 1937.

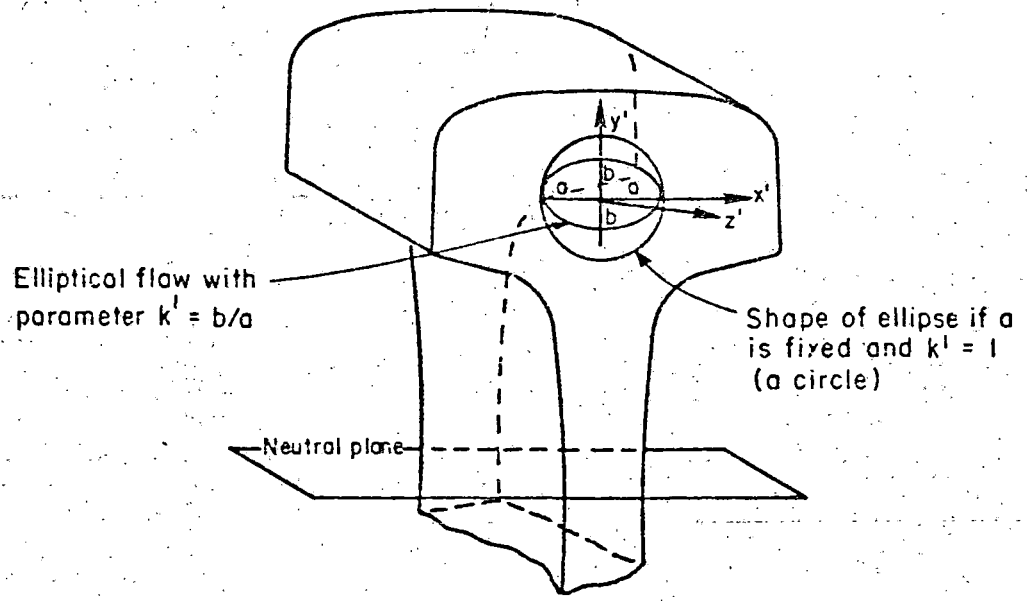
APPENDIX F

STRESS INTENSITY FACTORS FOR LOADED ELLIPTICAL CRACKS

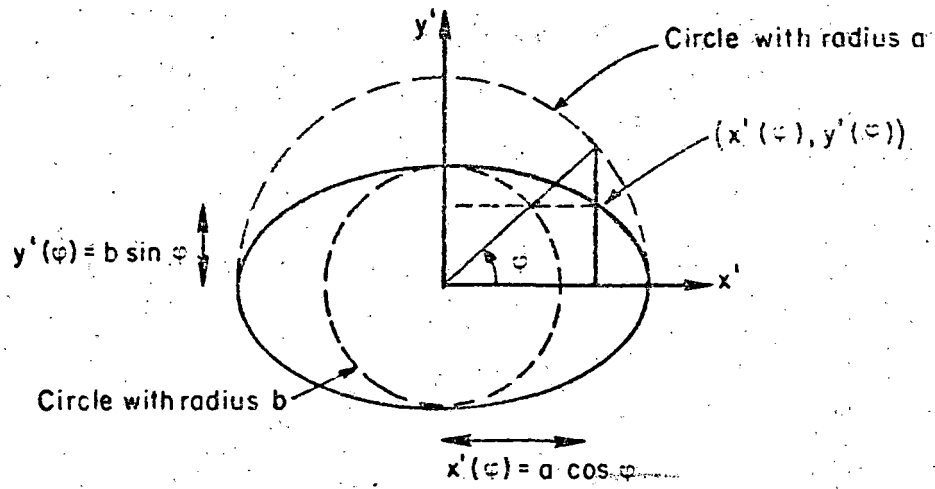
In order to quantify the large stresses which arise around the edge of a crack, it is customary to describe them in terms of stress intensity factors K_I , K_{II} , and K_{III} . According to linear elastic fracture analysis, key stresses near the edge of a loaded crack increase in proportion to $1/\sqrt{r}$, where r is distance from that edge. Thus the stress intensity factors K_I , K_{II} , and K_{III} are factors by which $1/\sqrt{2\pi r}$ should be multiplied to represent σ_z , τ_{zn} and τ_{zt} for small r , where σ_z is the stress component normal to the crack plane and τ_{zn} and τ_{zt} are shear stresses acting on the crack plane in directions normal and tangential to the crack edge. If the stresses which would arise in a certain region with no crack present can be approximated by third order polynomial, then the stress intensity factors around elliptical cracks there can be derived from theories by Shah and Kobayashi [F-1] for K_I , or by Smith and Sorenson [F-2] for K_{II} and K_{III} . Local coordinates (x', y', z') used for such analyses are shown in Figure F-1, which also illustrates the parameter angle ϕ and the flaw semi-axes a and b . These theories apply readily only if the flaw is not too near a surface of the body containing the crack. Since well embedded cracks are themselves important, attention will be limited to them. Other analyses which have treated stresses around surface cracks include those by Smith, Emery and Kobayashi [F-3], Thresher and Smith [F-4], Raju and Newman [F-5], and Bell [F-6].

The theories of Shah and Kobayashi [F-1] or Smith and Sorenson [F-2] are somewhat complicated analytically, but it has been found possible to simplify their results considerably beyond the forms provided by their authors, as will be shown here. Since effects from normal loads are simplest, those will be considered first.

F-2



a. Location of an Elliptical Flow



b. Variation of (x', y') on Ellipse with Parameter φ

FIGURE F-1. NOTATION USED FOR ELLIPTICAL FLAW IN RAIL

Stress Intensity Factors from Normal Loads

General Formulas

Shah and Kobayashi considered an elliptical crack embedded in an infinite body subjected to a normal load $p(x',y')$ ($\sim \sigma_z$) on the crack face of the form

$$p(x',y') = A_{00} + A_{10}x' + A_{01}y' + A_{20}x'^2 + A_{11}x'y' + A_{02}y'^2 + A_{30}x'^3 + A_{21}x'^2y' + A_{12}x'y'^2 + A_{03}y'^3 \quad (F-1)$$

Their analysis, however, did not express the stress intensity factor K_I directly in terms of the coefficients A_{ij} of the load. Instead, it provided a system of equations relating those constants to another set of constants c_{ij} used in expressing the stress potential function, and then expressed the stress intensity factor in terms of the constants c_{ij} . Their equations relating the A_{ij} to the c_{ij} have analytic coefficients $K_{m,n}$ which are moderately complex quantities depending on a and b , the semi-axes of the ellipse, on k' ($= b/a$) and k ($= \sqrt{1 - k'^2}$), and on the complete elliptic integrals $K(k)$ and $E(k)$. By reorganizing their expressions for the $K_{m,n}$ it has been found possible to solve for their c_{ij} explicitly in terms of their A_{ij} , thus greatly simplifying the use of their theory for calculating the stress intensity factor K_I . A byproduct of this simplification is that it also shows how their theory can lead to a treatment for circular cracks, for which the vanishing of k makes their original formulas indeterminate.

In order to reorganize Shah and Kobayashi's theory, we may begin by choosing a reference stress A_r , which usually will be taken to be A_{00} if that is not zero, but may be chosen to be any convenient fixed stress. Also let G be the shear modulus. Then define dimensionless load constants κ_{ij} as follows:

$$\kappa_{ij} = A_{ij} a^i b^j / A_r \quad (F-2)$$

Define new dimensionless constants γ_{ij} related to their constants c_{ij} as follows:

$$\gamma_{ij} = \frac{2Gc_{ij}}{A_r a^{i+1} b^{j+2}} \quad (F-3)$$

In order to reexpress their coefficient functions $K_{m,n}$ introduce the functions

$$\begin{aligned} f_1(k) &= 4E(k), \\ f_2(k) &= \frac{8}{k^2} [k'^2 K(k) - (1-2k^2)E(k)], \\ f_3(k) &= \frac{8}{k^4} [(2-k^2)k'^2 K(k) - 2(1-k^2+k^4)E(k)], \\ f_4(k) &= \frac{8}{k^6} [(-8+15k^2-3k^4)k'^2 K(k) + (8-19k^2+9k^4-6k^6)E(k)], \end{aligned} \quad (\text{F-4})$$

where $K(k)$ and $E(k)$ are complete elliptic integrals of the first and second kinds, respectively. Note that these functions have indeterminacies for both $k=0$ (the circle) and $k=1$ (the line ellipse), but those indeterminacies are resolvable. In fact

$$\begin{aligned} f_1(0) &= 2\pi, \quad f_2(0) = 6\pi, \quad f_3(0) = -\frac{15\pi}{2}, \quad f_4(0) = -\frac{105\pi}{4}, \\ f_1(1) &= 4, \quad f_2(1) = 8, \quad f_3(1) = -16, \quad f_4(1) = -64. \end{aligned} \quad (\text{F-5})$$

Then all of Shah and Kobayashi's coefficient functions $K_{m,n}$ relating their constants A_{ij} to their constants c_{ij} can be expressed as linear combinations of the functions $f_i(k)$ multiplied by powers of a and b . Because of the many implied relationships among the $K_{m,n}$ it is not necessary to use all those functions in reexpressing the solution of their equations, but it is helpful to observe these relationships, denoting revised versions of $K_{m,n}$ as $K'_{m,n}$:

$$\begin{aligned} K'_{1,1} &\equiv ab^2 K_{1,1} = f_1, \\ K'_{2,2} &\equiv a^3 b^2 K_{2,2} = \frac{1}{2} f_2, \\ K'_{3,3} &\equiv ab^4 K_{3,3} = 3f_1 - \frac{1}{2} f_2, \\ K'_{5,5} &\equiv a^3 b^4 K_{5,5} = -\frac{1}{2} f_3; \\ K'_{4,4} &\equiv a^5 b^2 K_{4,4} = -5f_2 - f_3, \end{aligned} \quad (\text{F-6})$$

$$K_{4,6} \equiv a^3 b^4 K_{4,6} = f_3,$$

$$K_{6,4} \equiv a^3 b^4 K_{6,4} = f_3,$$

$$K_{6,6} \equiv ab^6 K_{6,6} = -30f_1 + 5f_2 - f_3;$$

$$K_{7,7} \equiv a^7 b^2 K_{7,7} = -\frac{35}{3}f_2 - \frac{14}{3}f_3 + \frac{1}{3}f_4,$$

(F-6, cont.)

$$K_{7,9} \equiv a^5 b^4 K_{7,9} = \frac{7}{3}f_3 - \frac{1}{3}f_4,$$

$$K_{9,7} \equiv a^5 b^4 K_{9,7} = 7f_3 - f_4,$$

$$K_{9,9} \equiv a^3 b^4 K_{9,9} = f_4;$$

$$K_{8,8} \equiv a^5 b^4 K_{8,8} = 7f_3 - f_4,$$

$$K_{8,10} \equiv a^3 b^6 K_{8,10} = f_4,$$

$$K_{10,8} \equiv a^3 b^6 K_{10,8} = \frac{1}{3}f_4,$$

$$K_{10,10} \equiv ab^8 K_{10,10} = -70f_1 + \frac{35}{3}f_2 - \frac{7}{3}f_3 - \frac{1}{3}f_4.$$

The new functions $K_{m,n}$ are dimensionless forms depending only on the axis ratio $k' = b/a$ or on $k = (1 - k'^2)^{1/2}$. Comparable dimensionless forms can be made from all of Shah and Kobayashi's coefficients $K_{m,n}$, but the others are not needed in stating final solutions.

By using the revised load constants κ_{ij} and unknown constants γ_{ij} , together with the new coefficient functions $K_{m,n}$ depending only on the four functions $f_i(k)$, Shah and Kobayashi's system of ten simultaneous equations becomes readily solvable in algebraic terms. Putting

$$D_2 = K_{4,4} K_{6,6} - K_{6,4} K_{4,6},$$

$$D_3 = K_{8,8} K_{10,10} - K_{10,8} K_{8,10},$$

$$D_4 = K_{7,7} K_{9,9} - K_{9,7} K_{7,9},$$

(F-7)

the solution becomes

$$\begin{aligned}
 \gamma_{00} &= \frac{1}{K_{1,1}} \kappa_{00} & + \frac{1}{5K_{1,1}} \kappa_{20} & + \frac{1}{5K_{1,1}} \kappa_{02} \\
 \gamma_{10} &= \frac{1}{K_{2,2}} \kappa_{10} & & + \frac{3}{7K_{2,2}} \kappa_{30} & + \frac{1}{7K_{2,2}} \kappa_{12} \\
 \gamma_{01} &= \frac{1}{K_{3,3}} \kappa_{01} & & + \frac{1}{7K_{3,3}} \kappa_{21} & + \frac{3}{7K_{3,3}} \kappa_{03} \\
 \gamma_{20} &= \frac{K_{6,6}}{D_2} \kappa_{20} & - \frac{K_{4,6}}{D_2} \kappa_{02} & & \\
 \gamma_{11} &= \frac{1}{K_{5,5}} \kappa_{11} & & & \\
 \gamma_{02} &= -\frac{K_{6,4}}{D_2} \kappa_{20} & + \frac{K_{4,4}}{D_2} \kappa_{02} & & \\
 \gamma_{30} &= \frac{K_{9,9}}{D_4} \kappa_{30} & - \frac{K_{7,9}}{D_4} \kappa_{12} & & \\
 \gamma_{21} &= \frac{K_{10,10}}{D_3} \kappa_{21} & - \frac{K_{8,10}}{D_3} \kappa_{03} & & \\
 \gamma_{12} &= -\frac{K_{9,7}}{D_4} \kappa_{30} & + \frac{K_{7,7}}{D_4} \kappa_{12} & & \\
 \gamma_{03} &= -\frac{K_{10,8}}{D_3} \kappa_{21} & + \frac{K_{8,8}}{D_3} \kappa_{03} & &
 \end{aligned} \tag{F-8}$$

In terms of the now available constants γ_{ij} and the parametric angle φ for points on the ellipse, Shah and Kobayashi's stress intensity factor K_I is given by

$$\frac{K_I}{A_r \sqrt{\pi a}} = 4\sqrt{k'} (1 - k^2 \cos^2 \varphi)^{\frac{1}{2}} \left[\gamma_{00} + \gamma_{10} \cos \varphi + \gamma_{01} \sin \varphi - 4\gamma_{20} \cos^2 \varphi + \gamma_{11} \sin \varphi \cos \varphi - 4\gamma_{02} \sin^2 \varphi \right. \\
 \left. - 4\gamma_{30} \cos^3 \varphi - 4\gamma_{21} \cos^2 \varphi \sin \varphi - 4\gamma_{12} \cos \varphi \sin^2 \varphi - 4\gamma_{03} \sin^3 \varphi \right] \tag{F-9}$$

The formulas given here provide direct means for finding the stress intensity factor K_I from given load constants A_{ij} . The first step can be to use the axis ratio k' to find k and hence the four functions $f_i(k)$. From these there follow the sixteen given functions $K_{m,n}$, and from them the coefficients applied to the revised load constants α_{ij} in the above solution for the γ_{ij} . Using the dimensions of the ellipse, the constants α_{ij} can be calculated from the given A_{ij} , and applying these produces the solution for the γ_{ij} and hence the equation for K_I .

Cracks Under Tension and Bending

To provide some simple illustrative results from this theory, suppose the the only non-vanishing load constants A_{ij} are A_{00} and A_{01} , as would be true when simple bending stress is superposed on uniform tension in a body such as a rail. Then the non-vanishing γ_{ij} are

$$\gamma_{00} = \frac{\alpha_{00}}{K_{1,1}} = \frac{\alpha_{00}}{f_1} = \frac{A_{00}/A_r}{4E(k)}, \text{ and} \tag{F-10}$$

$$\gamma_{01} = \frac{\alpha_{01}}{K_{3,3}} = \frac{\alpha_{01}}{3f_1 - \frac{1}{2}f_2} = \frac{A_{01}b/A_r}{12E(k) - \frac{4}{b}[k'^2K(k) - (1-2k^2)E(k)]} = \frac{k^2A_{01}/A_r}{4[(1+k^2)E(k) - k'^2K(k)]}$$

Then the stress intensity factor becomes

$$K_I = A_{00}\sqrt{\pi a} (1-k^2 \cos^2 \varphi)^{\frac{1}{2}} \left[C_k + \frac{A_{01}b}{A_{00}} C'_k(k) \sin \varphi \right], \text{ where} \tag{F-11}$$

$$C_k = \frac{\sqrt{k'}}{E(k)}, \quad C'_k = \frac{k^2\sqrt{k'}}{(1+k^2)E(k) - k'^2K(k)}$$

Specifying the eccentricity of the elliptical crack makes it possible to evaluate the coefficients C_k and C'_k , as is illustrated by the following short table:

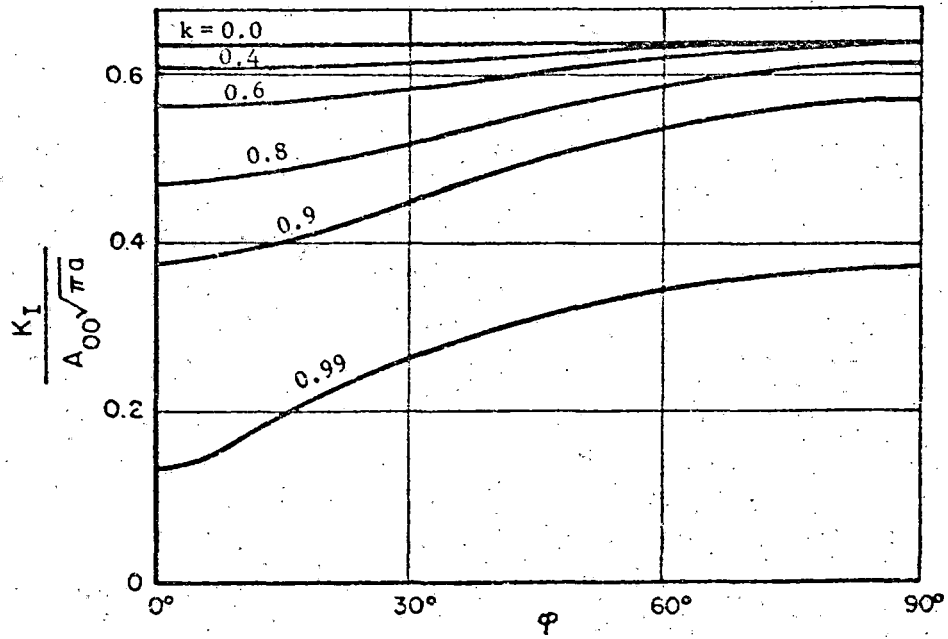
k	0	0.2	0.4	0.6	0.8	0.9	0.99	1
k'	1.00000	0.97980	0.91652	0.80000	0.60000	0.43589	0.14107	0
K(k)	1.57080	1.58690	1.64003	1.75077	1.99534	2.28063	3.35711	∞
E(k)	1.57080	1.55494	1.50591	1.41307	1.27634	1.17170	1.02849	1
C_k	0.63662	0.63658	0.63573	0.63074	0.60689	0.56347	0.37559	0
C'_k	0.42441	0.42250	0.41485	0.39647	0.36057	0.31691	0.18689	0

To illustrate the effect of the constant part of the normal load (that is with only $A_{00} \neq 0$), values in the above tabulation can be used to express $K_I/(A_{00}\sqrt{\pi a})$ as a function of φ for each value of k in the table. These functions vary as shown in the first part of Figure F-2. To illustrate the effect of the variable part of the normal load associated with bending (that is with only $A_{01} \neq 0$), similar results were found for $K_I/(A_{01}b\sqrt{\pi a})$, and they are shown in the second part of Figure F-2. Of course, for a crack in the head of a rail under pure bending both these kinds of load would be present in proportions varying with distance of the flaw from the neutral plane of the rail. Thus, for example, consider possible transverse flaws with horizontal major axes of length $2a$ situated at distance $10a$ above the neutral plane of the rail in bending. Then $A_{01}b/A_{00} = 0.1k'$, and, for flaws with eccentricities included in the above tabulation, the stress intensity factor varies as shown in Figure F-3. For these flaws, the high values of the stress intensity factor occurs at the top of the ellipse (at $\varphi = \frac{\pi}{2}$), where the crack is farthest from the neutral axis, and the value is largest for the circular crack (with $k = 0$).

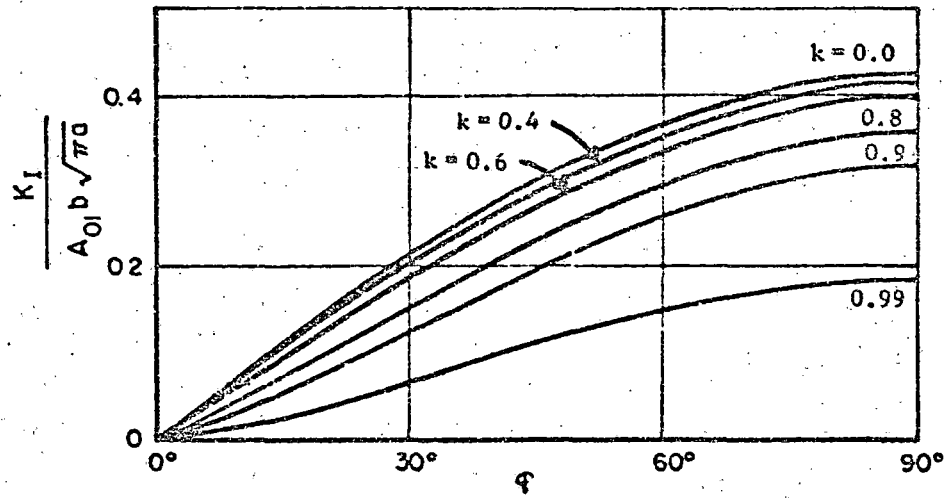
To quantify the stress intensity factor K_I from this theory, one must specify a , A_{00} and A_{01} . Thus, pursuing the examples of Figure F-3, consider an ellipse with $a = 0.3$ inch situated with center 3 inches above the neutral bending plane of the rail, so that $A_{01}b/A_{00} = 0.1k'$. To get a representative A_{00} , consider the bending moment in the rail above a particular tie beyond which ties at distances 24 and 48 inches support loads -333.96 lb and -267.57 lb respectively, so that the moment desired is 20858 in.-lb. (These numbers were computed from test data recorded on the Florida East Coast Railroad.) Taking the moment of inertia of the rail to be 88.2 inches⁴, the tensile stress at a position 3 inches above the neutral plane is, according to beam theory,

$$\sigma_x = \frac{20858 \times 3}{88.2} = 709.45 \text{ lb/in.}^2$$

Taking this as the value of A_{00} , one finds $A_{00}\sqrt{\pi a} = 688.74 \text{ lb/in.}^{3/2}$. Multiplying this value by values shown in Figure F-3 for a chosen k yields the stress intensity factor at positions around the edge of the elliptical crack having that value of k .

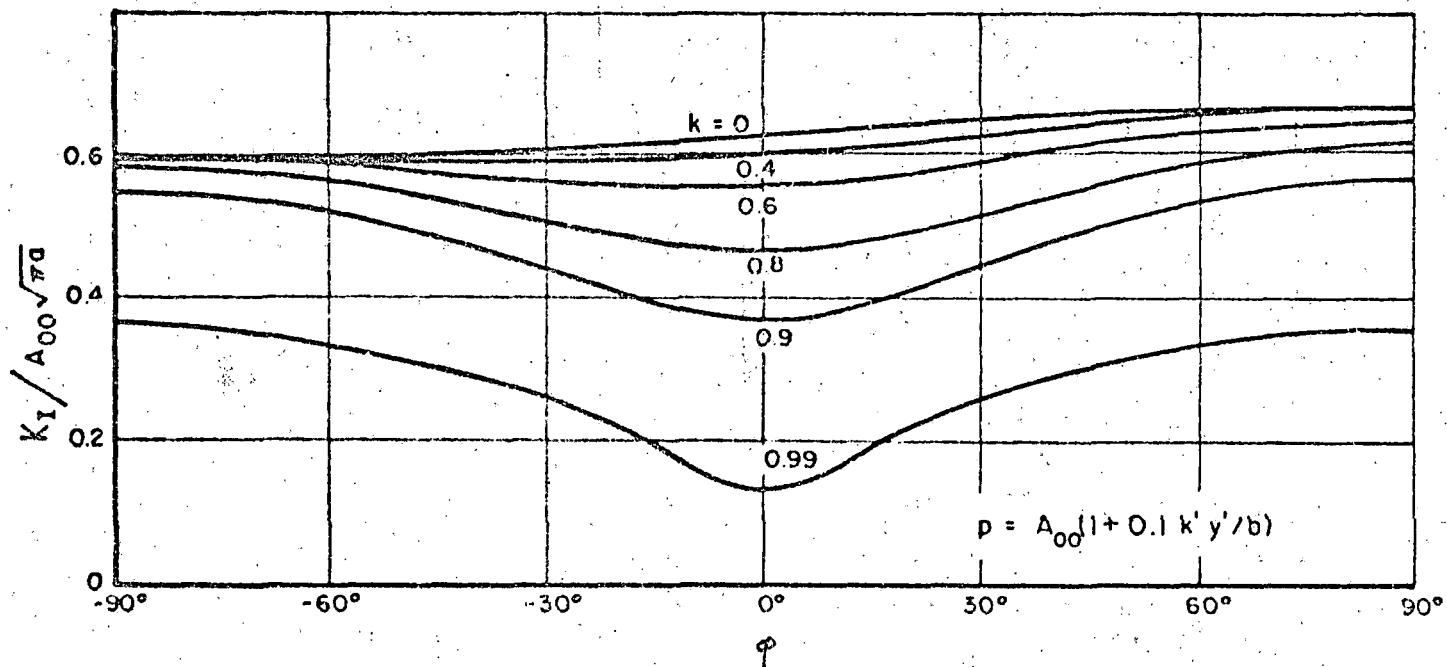


a. Effect of Uniform Part of Normal Load



b. Effect of Linear Part of Normal Load

FIGURE F-2. STRESS INTENSITY FACTORS FROM NORMAL LOADS OF BASIC TYPES ACTING ON AN ELLIPTICAL CRACK



F-10

FIGURE F-3. STRESS INTENSITY FACTORS ALONG REPRESENTATIVE ELLIPTICAL CRACKS FROM A NORMAL LOAD INCLUDING A BENDING LOAD

Stress Intensity Factors from Shearing LoadsReorganization of Smith and Sorenson Formulas

Smith and Sorenson also considered an embedded elliptical crack

$$\frac{x'^2}{a^2} + \frac{y'^2}{b^2} = 1, \quad z' = 0, \quad (\text{F-12})$$

as in Figure 1, and they presumed its face subjected to the shear loads

$$\begin{aligned} \tau_{z'x'} &= \sum_{m=0}^3 \sum_{n=0}^3 A_{mn} x'^m y'^n, \\ \tau_{y'z'} &= \sum_{m=0}^3 \sum_{n=0}^3 B_{mn} x'^m y'^n, \end{aligned} \quad (\text{F-13})$$

except that the ranges of summation include only $0 \leq m+n \leq 3$. The load constants A_{mn} and B_{mn} here number 20. Paralleling the theory of Shah and Kobayashi, Smith and Sorenson introduced a stress function involving 20 arbitrary constants a_{mn} and b_{mn} for $0 \leq m+n \leq 3$, and proceeded laboriously to construct a system of 20 simultaneous linear equations, showing each load constant A_{mn} or B_{mn} as a linear function of the stress-function constants a_{mn} and b_{mn} . They denoted the coefficients of these equations as $K_{i,j}$ with i and j ranging from 1 to 20, and they presented them in tabular form as combinations of auxiliary functions denoted as M_1, M_2, \dots, M_{29} . The M 's were shown as algebraic functions of $a, b, k' (=b/a), k (= \sqrt{1-k'^2}), K(k)$ and $E(k)$. Their plan for treatment of a specific ellipse under a given pattern of loads was to evaluate all the M 's, then all the $K_{i,j}$, then to find the constants a_{mn} and b_{mn} from the given load constants by solving the 20 simultaneous equations, and finally to evaluate stress intensity factors K_{II} and K_{III} by using these a_{mn} and b_{mn} in formulas they provided for K_{II} and K_{III} . Such calculations are long and tedious, and they offer many opportunities for making mistakes. Therefore, an effort has been made here to organize and simplify this theory. Insofar as Smith and Sorenson's mathematical entities appear, their notation has been preserved. Moreover, a correction for one misprint in their paper has been included since they confirmed the correction in direct conversation. (It makes their polynomial β_{27} multiplying

$E(k)$ in N_{27} be $8k^4k'^2 + 3k^2k'^2 + 2k^2 - 8$.)

To begin simplifying Smith and Sorenson's formulas, let

$$\lambda_{mn} = \frac{A_{mn} a^m b^n m! n!}{A_{ref} (m+n)!} (1 + \delta_0^{m+n}), \quad \mu_{mn} = \frac{B_{mn} a^m b^n m! n!}{A_{ref} (m+n)!} (1 + \delta_0^{m+n}),$$

$$\alpha_{mn} = \frac{2G a_{mn} \cdot 2^{m+n} (m+n+1)!}{A_{ref} a^{m+1} b^{n+2}}, \quad \beta_{mn} = \frac{2G b_{mn} \cdot 2^{m+n} (m+n+1)!}{A_{ref} a^{m+1} b^{n+2}},$$
(F-14)

where G is the shear modulus, A_{ref} is a reference stress to be chosen later, and

$$\delta_0^{m+n} = \begin{cases} 1 & \text{if } m+n = 0 \\ 0 & \text{if } m+n \neq 0 \end{cases}.$$
(F-15)

Also let

$$K_{i,j} = \frac{1}{2G} K_{i,j} a^{m_i + n_i + 1} b^{n_i + n_j + 2} \frac{m_i! n_i! (1 + \delta_0^{m_i + n_i})}{(m_i + n_i)!} / [2^{m_j} + n_j (m_j + n_j + 1)!],$$

where the constants m_i, n_i, m_j and n_j are determined by the order of the indices used in their 20 x 20 system of equations, so that

$$m_i = m \text{ for the } i^{\text{th}} \text{ row,} \quad n_i = n \text{ for the } i^{\text{th}} \text{ row}$$

$$m_j = m \text{ for the } j^{\text{th}} \text{ column,} \quad n_j = n \text{ for the } j^{\text{th}} \text{ column}$$

In particular, inspection of their report shows they used:

$$m_i \text{ (or } m_j) = \left. \begin{array}{ll} 0 & \text{if } i \text{ (or } j) = 1, 3, 6, 10, 11, 13, 16, 20 \\ 1 & \text{if } i \text{ (or } j) = 2, 5, 7, \quad 12, 15, 17 \\ 2 & \text{if } i \text{ (or } j) = 4, 8, \quad 14, 18 \\ 3 & \text{if } i \text{ (or } j) = 9, \quad 19 \end{array} \right\}, \text{ and}$$
(F-16)

$$n_i \text{ (or } n_j) = \left. \begin{array}{ll} 0 & \text{if } i \text{ (or } j) = 1, 2, 4, 9, 11, 12, 14, 19 \\ 1 & \text{if } i \text{ (or } j) = 3, 5, 8, \quad 13, 15, 18 \\ 2 & \text{if } i \text{ (or } j) = 6, 7, \quad 16, 17 \\ 3 & \text{if } i \text{ (or } j) = 10, \quad 20 \end{array} \right\}.$$

Then their equation (2.16) is equivalent to

$$[K_{i,j}] \begin{Bmatrix} \alpha_{m_j n_j} \\ \beta_{m_j n_j} \end{Bmatrix} = \begin{Bmatrix} \lambda_{m_i n_i} \\ \mu_{m_i n_i} \end{Bmatrix} \quad (F-17)$$

This reformulation has the immediate advantage that all terms of the matrix and the vectors are dimensionless. Further advantages will appear later in the coefficients that are to be used.

Smith and Sorenson tabulated their 82 non-zero functions $K_{i,j}$ by listing numerical constants A, B, C, p, q for each pair of indices i, j so that

$$K_{i,j} = A [B(1-\nu)M_p + C\nu M_q] \cdot 2G, \quad (F-18)$$

with ν being Poisson's ratio. In the replacement of $K_{i,j}$ by the revised function $K_{i,j}$, the doubled shear modulus $2G$ is cancelled out, and their constant A is largely cancelled by the new factor $m_i! n_i! (1 + \delta_0^{m_i+n_i}) / [(m_i + n_i)! 2^{m_j+n_j} (m_j + n_j + 1)!]$. The dimensional factors $a^{m_i+m_j+1}$ and $b^{n_i+n_j+1}$ are included in $K_{i,j}$ so that they can be divided out of the functions M_p and M_q in order to get dimensionless functions M_p and M_q . Considering how the various M_p 's contribute to the $K_{i,j}$, these dimensional factors are uniquely determined for 18 of their 29 functions M_p , and 5 of their M_p 's can be ignored since they contribute nothing to the stress intensity formulas, but for 6 of their M_p 's (those with $p = 4, 8, 9, 18, 19, 20$) three forms of dimensionless factor might be used. In defining the functions M_p , the factor $a^{m_i+m_j+1} b^{n_i+n_j+2}$ to be chosen here is the unique factor associated with M_p (if there is a unique one) or else the associated factor having the lowest power of b. Concurrently, each M_p will be multiplied by a numerical constant which experience has shown to be convenient, intending to cancel this constant out by dividing it into AB and AC. This leads to the introduction of the functions M_p shown in the following list.

$$\begin{aligned}
M_1 &= -4ab^2 M_1 = \frac{8}{k^2} [-k'^2 K(k) + (1-k^2) E(k)] \\
M_2 &= -4ab^2 M_2 = \frac{8}{k^2} [k'^2 K(k) - E(k)] \\
M_3 &= 4ab^2 M_3 = 8 [0 \cdot k'^2 K(k) - E(k)] \\
M_4 &= 2a^3 b^2 M_4 = \frac{4}{k} [-2k'^2 K(k) + (2-k^2) E(k)] \\
M_5 &= -2a^3 b^2 M_5 = \frac{4}{k^2} [k'^2 K(k) - (1-2k^2) E(k)] \\
M_6 &= -2ab^4 M_6 = \frac{4}{k^2} [-k'^2 K(k) + (1+k^2) E(k)] \\
M_7 &= a^3 b^4 M_7 = \frac{2}{k} [(2-k^2) k'^2 K(k) - 2(1-k^2+k^4) E(k)] \\
M_8 &= -3a^5 b^2 M_8 = \frac{2}{k^6} [(8+k^2) k'^2 K(k) - (8-3k^2-2k^4) E(k)] \\
M_9 &= -3a^3 b^4 M_9 = \frac{2}{k^6} [-(8-9k^2) k'^2 K(k) + (8-13k^2+3k^4) E(k)] \\
M_{10} &= 3a^5 b^2 M_{10} = \frac{2}{k^4} [-2(1+2k^2) k'^2 K(k) + (2+3k^2-8k^4) E(k)] \\
M_{11} &= 3ab^6 M_{11} = \frac{2}{k^4} [-2(1-3k^2) k'^2 K(k) + (2-7k^2-3k^4) E(k)] \\
M_{14} &= 6a^3 b^2 M_{14} = \frac{4}{k^2} [(2+k^2) k'^2 K(k) - 2(1-k^4) E(k)] \\
M_{15} &= 6ab^4 M_{15} = \frac{4}{k^4} [(2-3k^2) k'^2 K(k) - 2(1-2k^2) E(k)] \\
M_{16} &= -15a^5 b^2 M_{16} = \frac{2}{k^6} [-(8+3k^2+4k^4) k'^2 K(k) + (8-k^2+k^4-8k^6) E(k)] \\
M_{17} &= -15ab^6 M_{17} = \frac{2}{k^6} [(8-19k^2+15k^4) k'^2 K(k) - (8-23k^2+23k^4) E(k)] \\
M_{18} &= 5a^7 b^2 M_{18} = \frac{2}{3k^8} [-(48+8k^2+4k^4) k'^2 K(k) + (48-16k^2-9k^4-8k^6) E(k)] \\
M_{19} &= 3a^5 b^4 M_{19} = \frac{2}{k^8} [(16-16k^2-k^4) k'^2 K(k) + (-16+24k^2-4k^4-2k^6) E(k)] \\
M_{20} &= 5a^3 b^6 M_{20} = \frac{2}{3k^8} [-(48-104k^2+60k^4) k'^2 K(k) + (48-128k^2+103k^4-15k^6) E(k)]
\end{aligned}$$

(F-19)

$$\begin{aligned}
M_{21} &= -5a^7 b^2 M_{21} = \frac{2}{3k^6} [(8+13k^2+24k^4)k'^2 K(k) - (8-9k^2+16k^4-48k^6) E(k)] \\
M_{22} &= -5ab^8 M_{22} = \frac{2}{3k^6} [-(8-29k^2+45k^4)k'^2 K(k) + (8-33k^2+58k^4+15k^6) E(k)] \\
M_{25} &= 35ab^8 M_{25} = \frac{2}{3k^8} [(48-160k^2+193k^4-105k^6)k'^2 K(k) + 8(-6+23k^2-33k^4+22k^6)E(k)] \\
M_{27} &= -a^5 b^4 M_{27} = \frac{2}{3k^6} [(-8+k^2+4k^4)k'^2 K(k) + (8-5k^2-5k^4+8k^6) E(k)] \\
M_{28} &= -a^3 b^6 M_{28} = \frac{2}{3k^6} [(8-15k^2+3k^4)k'^2 K(k) - (8-19k^2+9k^4-6k^6) E(k)] \\
M_{29} &= 35a^7 b^2 M_{29} = \frac{2}{3k^8} [(48+16k^2+17k^4+24k^6)k'^2 K(k) + 8(-6+k^2-k^6+6k^8) E(k)]
\end{aligned}$$

(F-19, cont.)

The functions M_1, M_2, \dots, M_{29} are quite interdependent. One way of showing this is to express them in terms of the following five functions (with limits noted as $k \rightarrow 0$):

$$\begin{aligned}
F_1(k) &= E(k) & ; \frac{2}{\pi} F_1(0) &= 1 \\
F_2(k) &= \frac{1}{k^2} [k'^2 K(k) - E(k)] & ; \frac{2}{\pi} F_2(0) &= -\frac{1}{2} \\
F_3(k) &= \frac{1}{k^4} [2k'^2 K(k) - (2-k^2) E(k)] & ; \frac{2}{\pi} F_3(0) &= -\frac{3}{8} \\
F_4(k) &= \frac{1}{k^6} [(8+k^2)k'^2 K(k) + (-8+3k^2+2k^4) E(k)] & ; \frac{2}{\pi} F_4(0) &= -\frac{15}{16} \\
F_5(k) &= \frac{1}{k^8} [(16-16k^2-k^4)k'^2 K(k) + (-16+24k^2-4k^4-2k^6) E(k)] & ; \frac{2}{\pi} F_5(0) &= \frac{105}{128}
\end{aligned}$$

(F-20)

Using these functions we find

$$\begin{aligned}
M_1 &= -8F_1 - 8F_2 \\
M_2 &= 8F_2 \\
M_3 &= -8F_1 \\
M_4 &= -4F_3 \\
M_5 &= 8F_1 + 4F_2 \\
M_6 &= 4F_1 - 4F_2
\end{aligned}$$

(F-21)

$$M_7 = -4F_1 - 2F_2 + 2F_3$$

$$M_8 = 2F_4$$

$$M_9 = 10F_3 - 2F_4$$

$$M_{10} = -16F_1 - 8F_2 - 2F_3$$

$$M_{11} = -6F_1 + 12F_2 - 2F_3$$

$$M_{14} = 8F_1 + 4F_2 + 4F_3$$

$$M_{15} = -12F_2 + 4F_3$$

$$M_{16} = -16F_1 - 8F_2 - 2F_3 - 2F_4$$

$$M_{17} = 30F_2 - 20F_3 + 2F_4$$

(F-21, cont.)

$$M_{18} = (14F_4 - 6F_5)/3$$

$$M_{19} = 2F_5$$

$$M_{20} = (-70F_3 + 14F_4 - 6F_5)/3$$

$$M_{21} = (96F_1 + 48F_2 + 12F_3 + 2F_4)/3$$

$$M_{22} = (30F_1 - 90F_2 + 30F_3 - 2F_4)/3$$

$$M_{25} = (-210F_2 + 210F_3 - 28F_4 + 6F_5)/3$$

$$M_{27} = (16F_1 + 8F_2 + 2F_3 - 2F_4)/3$$

$$M_{28} = (12F_1 + 6F_2 - 16F_3 + 2F_4)/3$$

$$M_{29} = (96F_1 + 48F_2 + 12F_3 + 16F_4 + 6F_5)/3$$

Using Smith and Sorenson's table of coefficients for the functions $K_{i,j}$ and converting it to a corresponding table for the revised functions $K_{i,j}$, while replacing the functions M_p by the revised functions M_p , it can be shown that

$$K_{i,j} = B'(1-\nu)M_p + C'\nu k^{(2-|B|+\ell)}M_q, \quad (\text{F-22})$$

where p , q and the new B' and C' are given in Table F-1, and the value of ℓ is

$$\ell = \begin{cases} +1 & \text{if } (p,q)=(6,4), (7,8), (11,9), (22,20), (27,18) \text{ or } (28,19) \\ -1 & \text{for all other pairs } (p,q) \end{cases}$$

In comparison to Smith and Sorenson's corresponding table, Table F-1 has no tabulation of constants A , since they have been absorbed into the other constants in the revision process. Moreover, the variation of signs of the constants B' here is nearly eliminated and the constants C' here are nearly all unity. The near unanimity of these patterns for B' and C' after the revision raises the issue of whether there are further errors in Smith and Sorenson's tabulation of their functions, beyond the one already noted in their M_{27} , though their conversation confirming that error also confirmed they knew of no further errors. This subject will be pursued further by considering forms their formulas take for a circular crack.

Before resolving the possibility of errors in Table F-1, it is proper to note that revised formulation greatly simplifies the calculation of the auxiliary functions here called the M_p , since the further auxiliary functions α_p , β_p , and γ_p used by Smith and Sorenson have been eliminated, and the M_p 's here are now simple combinations of five relatively simple functions $F_i(k)$, $i = 1,2,3,4,5$. The new functions $F_i(k)$ and M_p depend only on the ratio $k' = b/a$ (or $k = \sqrt{1-k'^2}$), so they may be computed if only b/a is assigned. If ν also is assigned, then the functions $K_{i,j}$ may be computed also, and limits for all these functions may be found conveniently as $k' \rightarrow 1$ as for a circular crack. (By contrast, Smith and Sorenson's formulas were crowded with varying powers of a and b separately, and consideration of the limiting case as $k' \rightarrow 1$ there was badly obscured in intricate, indeterminate expressions.)

TABLE F-1. COEFFICIENTS FOR REVISED FUNCTIONS $K_{i,j}$ (Before Correction *)

i,j	B'	C'	p	q
1,1	1	1	3	1
1,4	1	1	5	14
1,6	1	1	6	4
1,15	0	1	-	4
2,2	1	1/3	5	14
2,7	1	1	7	8
2,9	1	1	10	16
2,13	0	1	-	4
2,18	0	1	-	8
2,20	0	1	-	9
3,3	1	1	6	4
3,8	1	1	7	8
3,10	1	1	11	9
3,12	0	1	-	4
3,17	0	1	-	9
3,19	0	1	-	8
4,4	1	1	10	16
4,6	1	1	7	8
4,15	0	1	-	8
5,5	1	1	7	8
5,14	0	1	-	8
5,16	0	1	-	9
6,4	1	1	7	8
6,6	1	-1	11	9
6,15	0	1	-	9
7,7	1	1	28	19
7,9	1	1	27	18
7,18	0	1	-	19
7,20	0	1	-	20
8,8	1	1	27	18
8,10	1	1	28	19
8,17	0	1	-	19
8,19	0	1	-	18
9,7	1	1	27	18
9,9	1	1	21	29
9,18	0	1	-	18
9,20	0	1	-	19
10,8	1	1	28	19
10,10	1	1	22	20
10,17	0	1	-	20
10,19	0	1	-	19

i,j	B'	C'	p	q
11,5	0	1	-	4
11,11	1	1	3	2
11,14	1	1	5	4
11,16	1	1	6	4
12,3	0	1	-	4
12,8	0	1	-	8
12,10	0	1	-	9
12,12	1	1	5	4
12,17	1	1	7	9
12,19	1	1	10	8
13,2	0	1	-	4
13,7	0	1	-	9
13,9	0	1	-	8
13,13	1	1/3	6	15
13,18	1	1	7	9
13,20	1	1	11	17
14,5	0	1	-	8
14,14	1	1	10	8
14,16	1	1	7	9
15,4	0	1	-	8
15,6	0	1	-	9
15,15	1	1	7	9
16,5	0	1	-	9
16,14	1	1	7	9
16,16	-1	-1	11	17
17,8	0	1	-	19
17,10	0	1	-	20
17,17	1	1	28	20
17,19	-1	1	27	19
18,7	0	1	-	19
18,9	0	1	-	18
18,18	1	1	27	19
18,20	1	1	28	20
19,8	0	1	-	18
19,10	0	1	-	19
19,17	1	1	27	19
19,19	1	1	21	18
20,7	0	1	-	20
20,9	0	1	-	19
20,18	1	1	28	20
20,20	1	1	22	25

*Entries for these pairs (i,j) need correction: (17,19), (6,6), (16,16), (2,2), (13,13), (11,16). Plausible corrections are presented in the following discussion.

In order to treat cracks with specific load patterns, one must assign the load constants A_{mn} and B_{mn} which now (together with a, b and a reference stress A_{ref}) define the dimensionless load constants λ_{mn} and μ_{mn} in preparation for finding the dimensionless stress function constants α_{mn} and β_{mn} . If $A_{00} \neq 0$, it is normally a good choice for A_{ref} , but other choices may be made as circumstances require. Before embarking toward solution for α_{mn} and β_{mn} , however, it is well to organize the equations to be solved.

A map of the non-vanishing functions $K_{i,j}$ shows that Smith and Sorenson's 20 x 20 systems of equations can be treated by solving the following subsystems. Note that the unknowns in each of these four subsystems are mutually exclusive:

$$\left. \begin{aligned} K_{7,7} \alpha_{12} + K_{7,9} \alpha_{30} + K_{7,18} \beta_{21} + K_{7,20} \beta_{03} &= \lambda_{12} \\ K_{9,7} \alpha_{12} + K_{9,9} \alpha_{30} + K_{9,18} \beta_{21} + K_{9,20} \beta_{03} &= \lambda_{30} \\ K_{18,7} \alpha_{12} + K_{18,9} \alpha_{30} + K_{18,18} \beta_{21} + K_{18,20} \beta_{03} &= \mu_{21} \\ K_{20,7} \alpha_{12} + K_{20,9} \alpha_{30} + K_{20,18} \beta_{21} + K_{20,20} \beta_{03} &= \mu_{03} \end{aligned} \right\} \text{(IV A)}$$

$$\left. \begin{aligned} K_{8,8} \alpha_{21} + K_{8,10} \alpha_{03} + K_{8,17} \beta_{12} + K_{8,19} \beta_{30} &= \lambda_{21} \\ K_{10,8} \alpha_{21} + K_{10,10} \alpha_{03} + K_{10,17} \beta_{12} + K_{10,19} \beta_{30} &= \lambda_{03} \\ K_{17,8} \alpha_{21} + K_{17,10} \alpha_{03} + K_{17,17} \beta_{12} + K_{17,19} \beta_{30} &= \mu_{12} \\ K_{19,8} \alpha_{21} + K_{19,10} \alpha_{03} + K_{19,17} \beta_{12} + K_{19,19} \beta_{30} &= \mu_{30} \end{aligned} \right\} \text{(IV B)}$$

$$\left. \begin{aligned} K_{4,4} \alpha_{20} + K_{4,6} \alpha_{02} + K_{4,15} \beta_{11} &= \lambda_{20} \\ K_{6,4} \alpha_{20} + K_{6,6} \alpha_{02} + K_{6,15} \beta_{11} &= \lambda_{02} \\ K_{15,4} \alpha_{20} + K_{15,6} \alpha_{02} + K_{15,15} \beta_{11} &= \mu_{11} \end{aligned} \right\} \text{(III A)}$$

$$\left. \begin{aligned} K_{5,5} \alpha_{11} + K_{5,14} \beta_{20} + K_{5,16} \beta_{02} &= \lambda_{11} \\ K_{14,5} \alpha_{11} + K_{14,14} \beta_{20} + K_{14,16} \beta_{02} &= \mu_{20} \\ K_{16,5} \alpha_{11} + K_{16,14} \beta_{20} + K_{16,16} \beta_{02} &= \mu_{02} \end{aligned} \right\} \text{(III B)}$$

The above subsystems can be solved separately. Then the following subsystems may be solved for the remaining stress function constants.

$$\left. \begin{aligned} K_{2,2} \alpha_{10} + K_{2,13} \beta_{01} &= \lambda_{10} - K_{2,7} \alpha_{12} - K_{2,9} \alpha_{30} - K_{2,18} \beta_{21} - K_{2,20} \beta_{03} \\ K_{13,2} \alpha_{10} + K_{13,13} \beta_{01} &= \mu_{01} - K_{13,7} \alpha_{12} - K_{13,9} \alpha_{30} - K_{13,18} \beta_{21} - K_{13,20} \beta_{03} \end{aligned} \right\} \text{(II A)}$$

$$\left. \begin{aligned} K_{3,3} \alpha_{01} + K_{3,12} \beta_{10} &= \lambda_{01} - K_{3,8} \alpha_{21} - K_{3,10} \alpha_{03} - K_{3,17} \beta_{12} - K_{3,19} \beta_{30} \\ K_{12,3} \alpha_{01} + K_{12,12} \beta_{10} &= \mu_{10} - K_{12,8} \alpha_{21} - K_{12,10} \alpha_{03} - K_{12,17} \beta_{12} - K_{12,19} \beta_{30} \end{aligned} \right\} \text{(II B)}$$

$$K_{1,1} \alpha_{00} = \lambda_{00} - K_{1,4} \alpha_{20} - K_{1,6} \alpha_{02} - K_{1,15} \beta_{11} \quad \text{(I A)}$$

$$K_{11,11} \beta_{00} = \mu_{00} - K_{11,5} \alpha_{11} - K_{11,14} \beta_{20} - K_{11,16} \beta_{02} \quad \text{(I B)}$$

When the functions $K_{i,j}$ have been evaluated numerically, the preceding equations can be solved by ordinary numerical procedures. However, with the algebraic forms for the $K_{i,j}$ there is also a possibility for algebraic solution. The two subsystems of fourth order promise to complicate this process, but there is a possibility that some simplifications might be obtained by replacing the 82 non-zero functions $K_{i,j}$ by the shorter list of 29 functions M_p or by the much shorter list of five functions F_i . Experience with the parallel problem using normal loads instead of tangential loads suggests that several simplifying relationships would arise, though it is possible that the burden of the algebra would simply escalate. Consideration of the case of a circular crack, to be discussed below, should illuminate the prospects for algebraic solution for the stress-function constants α_{mn} and β_{mn} .

It remains to show how the stress intensity factors K_{II} and K_{III} can be found. Smith and Sorenson provide tables showing how K_{II} and K_{III} can be found in terms of individual stress function constants a_{mn} and b_{mn} . If their lists of formulas are combined in order to add all the contributions to K_{II} and K_{III} , and if the resulting formulas are reexpressed in terms of the load constants α_{mn} and β_{mn} found directly by solving the preceding sets of equations, it is found that

$$\frac{K_{II}}{A_{ref} \sqrt{\pi a}} = \frac{4\sqrt{k'}}{(1-k^2 \cos^2 \varphi)^{\frac{1}{4}}} \left[k' \cos \varphi (\alpha_{00} - \alpha_{10} \cos \varphi - \alpha_{01} \sin \varphi + \alpha_{20} \cos^2 \varphi + \alpha_{11} \sin \varphi \cos \varphi + \alpha_{02} \sin^2 \varphi - \alpha_{12} \sin^2 \varphi \cos \varphi - \alpha_{21} \sin \varphi \cos^2 \varphi - \alpha_{30} \cos^3 \varphi - \alpha_{03} \sin^3 \varphi) + \sin \varphi (\beta_{00} - \beta_{10} \cos \varphi - \beta_{01} \sin \varphi + \beta_{20} \cos^2 \varphi + \beta_{11} \sin \varphi \cos \varphi + \beta_{02} \sin^2 \varphi - \beta_{12} \sin^2 \varphi \cos \varphi - \beta_{21} \sin \varphi \cos^2 \varphi - \beta_{30} \cos^3 \varphi - \beta_{03} \sin^3 \varphi) \right], \quad (F-23)$$

$$\frac{K_{III}}{A_{ref} \sqrt{\pi a}} = \frac{4\sqrt{k'}(1-\nu)}{(1-k^2 \cos^2 \varphi)^{\frac{1}{4}}} \left[-\sin \varphi (\alpha_{00} - \alpha_{10} \cos \varphi - \alpha_{01} \sin \varphi + \alpha_{20} \cos^2 \varphi + \alpha_{11} \sin \varphi \cos \varphi + \alpha_{02} \sin^2 \varphi - \alpha_{12} \sin^2 \varphi \cos \varphi - \alpha_{21} \sin \varphi \cos^2 \varphi - \alpha_{30} \cos^3 \varphi - \alpha_{03} \sin^3 \varphi) + k' \cos \varphi (\beta_{00} - \beta_{10} \cos \varphi - \beta_{01} \sin \varphi + \beta_{20} \cos^2 \varphi + \beta_{11} \sin \varphi \cos \varphi + \beta_{02} \sin^2 \varphi - \beta_{12} \sin^2 \varphi \cos \varphi - \beta_{21} \sin \varphi \cos^2 \varphi - \beta_{30} \cos^3 \varphi - \beta_{03} \sin^3 \varphi) \right].$$

It may be noted that the same parenthesized quantities occur in K_{II} as in K_{III} , and indeed the two parenthesized quantities in K_{II} are alike except that the constants β_{mn} replace the constants α_{mn} .

The simplicity and symmetry of the stress-intensity factor solutions lend credibility to their accuracy and also show in part why the load constants and stress function constants were redefined as they are here. The search for simplicity and symmetry in the functions $K_{i,j}$ was less reassuring, however, and suggests further study such as the treatment of the circular crack discussed in the following. One may also notice the tantalizing question of whether some organization of this work might reveal enough pattern in the overall solution (including values of p and q , extension of the table of functions $F_i(k)$, and coefficients for them in determining the M_p) to project the form of an extended solution using higher order polynomials for loads.

Critique Provided by Circular Crack

The circular crack is an elliptical crack for which $k' = 1$ (and $k = 0$), so the preceding theory can be applied to it by letting $k \rightarrow 0$. The formulas for the circular crack also should have many predictable symmetries among them, so it should be possible to check many of them for mutual consistency. In particular, the influence on a load constant A_{mn} from a stress-function constant $a_{m'n'}$ (or $b_{m'n'}$) should be the same as the influence on a load constant B_{nm} from a stress function constant $b_{n'm'}$ (or $a_{n'm'}$), because these exchanges amount simply to interchanging the names for the x and y axes, and, with the axes of the ellipse equal, that should be immaterial. The circular crack is also a case for which independent analytic solutions for stress intensity factors exist for arbitrary tangential loads [F-7, F-8], and these offer further opportunities for checking the solutions for the elliptical crack, at least in its special form as a circle. Therefore, this special case of the elliptical crack will be analysed in considerable detail.

The values given above for the functions $F_i(0)$ for $i = 1, 2, 3, 4, 5$ make it possible to evaluate first the functions M_p and thence the 82 influence functions $K_{i,j}$ which show the dependence of the load constants on the stress-function constants. Therefore, those functions have been evaluated and grouped, as shown below, according to the systems of equations in which they occur. Labels have been added identifying pairs of functions which should be identical. The pairing is within the same system for Systems IVA, IVB, IIA and IIB, while for the other systems it is from System IIIA to System IIIB or from System IA to System IB. Thus $K_{7,7}$ in System IVA should equal $K_{18,18}$ in that same system, while $K_{4,6}$ in System IIIA should equal $K_{16,14}$ in System IIIB. Doubtful cases (such as those with irregular B' or C' in Table F-1) are marked by asterisks. The 82 functions $K_{i,j}$ for the circle are thus as follows.

For System IV A

$$K_{7,7} = [8(1-\nu) + 3\nu] 35\pi/128 \quad (1)$$

$$K_{7,9} = [8(1-\nu) + 5\nu] 35\pi/128 \quad (2)$$

$$K_{7,18} = [\quad 3\nu] 35\pi/128 \quad (3)$$

$$K_{7,20} = [\quad 5\nu] 35\pi/128 \quad (4)$$

$$K_{9,7} = [8(1-\nu) + 5\nu] 35\pi/128 \quad (5)$$

$$K_{9,9} = [40(1-\nu) + 35\nu] 35\pi/128 \quad (6)$$

$$K_{9,18} = [\quad 5\nu] 35\pi/128 \quad (7)$$

$$K_{9,20} = [\quad 3\nu] 35\pi/128 \quad (8)$$

$$K_{18,7} = [\quad 3\nu] 35\pi/128 \quad (3)$$

$$K_{18,9} = [\quad 5\nu] 35\pi/128 \quad (4)$$

$$K_{18,18} = [8(1-\nu) + 3\nu] 35\pi/128 \quad (1)$$

$$K_{18,20} = [8(1-\nu) + 5\nu] 35\pi/128 \quad (2)$$

$$K_{20,7} = [\quad 5\nu] 35\pi/128 \quad (7)$$

$$K_{20,9} = [\quad 3\nu] 35\pi/128 \quad (8)$$

$$K_{20,18} = [8(1-\nu) + 5\nu] 35\pi/128 \quad (5)$$

$$K_{20,20} = [40(1-\nu) + 35\nu] 35\pi/128 \quad (6)$$

For System III A

$$K_{4,4} = - [6(1-\nu) + 5\nu] 15\pi/16 \quad (1)$$

$$K_{4,6} = - [2(1-\nu) + \nu] 15\pi/16 \quad (2)$$

$$K_{4,15} = - [\quad \nu] 15\pi/16 \quad (3)$$

$$K_{6,4} = - [2(1-\nu) + \nu] 15\pi/16 \quad (4)$$

$$*K_{6,6} = - [6(1-\nu) - \nu] 15\pi/16 \quad (5)$$

$$K_{6,15} = - [\quad \nu] 15\pi/16 \quad (6)$$

$$K_{15,4} = - [\quad \nu] 15\pi/16 \quad (7)$$

$$K_{15,6} = - [\quad \nu] 15\pi/16 \quad (8)$$

$$K_{15,15} = - [2(1-\nu) + \nu] 15\pi/16 \quad (9)$$

For System IV B

$$K_{8,8} = [8(1-\nu) + 5\nu] 35\pi/128 \quad [1]$$

$$K_{8,10} = [8(1-\nu) + 3\nu] 35\pi/128 \quad [2]$$

$$K_{8,17} = [\quad 3\nu] 35\pi/128 \quad [3]$$

$$K_{8,19} = [\quad 5\nu] 35\pi/128 \quad [4]$$

$$K_{10,8} = [8(1-\nu) + 3\nu] 35\pi/128 \quad [5]$$

$$K_{10,10} = [40(1-\nu) + 5\nu] 35\pi/128 \quad [6]$$

$$K_{10,17} = [\quad 5\nu] 35\pi/128 \quad [7]$$

$$K_{10,19} = [\quad 3\nu] 35\pi/128 \quad [8]$$

$$K_{17,8} = [\quad 3\nu] 35\pi/128 \quad [3]$$

$$K_{17,10} = [\quad 5\nu] 35\pi/128 \quad [4]$$

$$K_{17,17} = [8(1-\nu) + 5\nu] 35\pi/128 \quad [1]$$

$$*K_{17,19} = [-8(1-\nu) + 3\nu] 35\pi/128 \quad [2]$$

$$K_{19,8} = [\quad 5\nu] 35\pi/128 \quad [7]$$

$$K_{19,10} = [\quad 3\nu] 35\pi/128 \quad [8]$$

$$K_{19,17} = [8(1-\nu) + 3\nu] 35\pi/128 \quad [5]$$

$$K_{19,19} = [40(1-\nu) + 5\nu] 35\pi/128 \quad [6]$$

For System III B

$$K_{5,5} = - [2(1-\nu) + \nu] 15\pi/16 \quad (9)$$

$$K_{5,14} = - [\quad \nu] 15\pi/16 \quad (8)$$

$$K_{5,16} = - [\quad \nu] 15\pi/16 \quad (7)$$

$$K_{14,5} = - [\quad \nu] 15\pi/16 \quad (6)$$

$$K_{14,14} = - [6(1-\nu) + \nu] 15\pi/16 \quad (5)$$

$$K_{14,16} = - [2(1-\nu) + \nu] 15\pi/16 \quad (4)$$

$$K_{16,5} = - [\quad \nu] 15\pi/16 \quad (3)$$

$$K_{16,14} = - [2(1-\nu) + \nu] 15\pi/16 \quad (2)$$

$$*K_{16,16} = + [6(1-\nu) + 5\nu] 15\pi/16 \quad (1)$$

(F-24)

For System II A			For System II B		
*K _{2,2}	=	[16(1-ν)+4ν] 3π/16 (1)	K _{3,3}	=	[16(1-ν)+4ν] 3π/16 [1]
K _{2,7}	= -	[10(1-ν)+5ν] 3π/16 (2)	K _{3,8}	= -	[10(1-ν)+5ν] 3π/16 [2]
K _{2,9}	= -	[30(1-ν)+25ν] 3π/16 (3)	K _{3,10}	= -	[30(1-ν)+5ν] 3π/16 [3]
K _{2,13}	=	[4ν] 3π/16 (4)	K _{3,12}	=	[4ν] 3π/16 [4]
K _{2,18}	= -	[5ν] 3π/16 (5)	K _{3,17}	= -	[5ν] 3π/16 [5]
K _{2,20}	= -	[5ν] 3π/16 (6)	K _{3,19}	= -	[5ν] 3π/16 [6]
K _{13,2}	=	[4ν] 3π/16 (4)	K _{12,3}	=	[4ν] 3π/16 [4]
K _{13,7}	= -	[5ν] 3π/16 (5)	K _{12,8}	= -	[5ν] 3π/16 [5]
K _{13,9}	= -	[5ν] 3π/16 (6)	K _{12,10}	= -	[5ν] 3π/16 [6]
*K _{13,13}	=	[16(1-ν)+4ν] 3π/16 (1)	K _{12,12}	=	[16(1-ν)+4ν] 3π/16 [1]
K _{13,18}	= -	[10(1-ν)+5ν] 3π/16 (2)	K _{12,17}	= -	[10(1-ν)+5ν] 3π/16 [2]
K _{13,20}	= -	[30(1-ν)+25ν] 3π/16 (3)	K _{12,19}	= -	[30(1-ν)+5ν] 3π/16 [3]
For System I A			For System I B		
K _{1,1}	= -	[2(1-ν) + ν] 2π (1)	K _{11,5}	=	[ν] 3π/4 (4)
K _{1,4}	=	[4(1-ν) + 3ν] 3π/4 (2)	K _{11,11}	= -	[2(1-ν) + ν] 2π (1)
K _{1,6}	=	[4(1-ν) + ν] 3π/4 (3)	K _{11,14}	=	[4(1-ν) + ν] 3π/4 (3)
K _{1,15}	=	[ν] 3π/4 (4)	*K _{11,16}	=	[4(1-ν) + ν] 3π/16 (2)

(F-24
cont.)

Examination of this list of values of the $K_{i,j}$ for a circle shows that most of the pairs which should be equal because of the symmetry here considered are indeed equal, but a few fail this test. Thus, in System IV B, $K_{17,19}$ is inconsistent with $K_{8,10}$. This discrepancy can be eliminated easily by changing the already suspicious sign of B' for $K_{17,19}$, while changing the sign of $K_{8,10}$ would involve much more extensive changes for Table F-1. Thus it is reasonable to believe that the sign of B' for $K_{17,19}$ should indeed be changed, even though Smith and Sorenson did not know of this need.

The symmetries required between System III A and System III B hold except for that between $K_{6,6}$ and $K_{14,14}$ and that between $K_{16,16}$ and $K_{4,4}$. Since $K_{6,6}$ was already a suspicious case, and the simple change of the sign of B for $K_{6,6}$ in Smith and Sorenson's table would smooth B' and provide the symmetry, it seems reasonable to make that change. Again the simple change of the sign for A in $K_{16,16}$ would not only smooth the values of B' and C' for the revised $K_{16,16}$, it would also provide the symmetry to $K_{4,4}$, so that correction too seems reasonable. These changes too were new to the original authors.

The symmetries that should exist within System II A are satisfied, as are those that should exist in System II B, but in System II A the values of C' for $K_{2,2}$ and $K_{13,13}$ are suspicious. To get a further check of these functions, formulas for the stress intensity factors K_{II} and K_{III} were derived from the Bell theory for the circular crack, presuming a crack load which could be described in Smith and Sorenson's notation by $\tau_{zx} = Sx/a$ while $\tau_{yz} = 0$. The Bell theory predicted

$$\frac{K_{II}}{S\sqrt{\pi a}} = -\frac{2}{3\pi} - \frac{4 \cos 2\phi}{3\pi(2-\nu)}, \quad \frac{K_{III}}{S\sqrt{\pi a}} = \frac{4(1-\nu) \sin 2\phi}{3\pi(2-\nu)} \quad (F-25)$$

In order for Smith and Sorenson's stress intensity formulas to produce this result from the given load, their constants must include

$$\alpha_{01} = \frac{4-\nu}{6\pi(2-\nu)} \quad \text{and} \quad \beta_{01} = -\frac{\nu}{6\pi(2-\nu)}, \quad (F-26)$$

but with the symmetries $K_{2,2} = K_{13,3}$ and $K_{2,13} = K_{13,2}$, System II A can produce that solution only if

$$K_{2,2} = K_{13,13} = [16(1-\nu)+12\nu]3\pi/16 \quad \text{and} \quad K_{2,13} = K_{13,2} = 4\nu \cdot 3\pi/16. \quad (F-27)$$

The discrepancy between these values and those found from Smith and Sorenson's formulas for the $K_{i,j}$ can be eliminated by multiplying their C for $K_{2,2}$ and $K_{13,13}$ by 3, and this also smooths the C' for $K_{2,2}$ and $K_{13,13}$ in Table F-1. This further correction is also recommended here.

The symmetries required between Systems IA and IB hold except for that between $K_{1,4}$ and $K_{11,16}$. To determine which of these functions is more

probably correct, a load may be presumed which involves using one of them. To involve $K_{1,4}$, consider a circular crack with the load

$$\tau_{zx} = S(x^2 + y^2)/a^2, \quad \tau_{yz} = 0. \quad (\text{F-28})$$

Then the only non-vanishing load constants are

$$A_{20} = S/a^2 \quad \text{and} \quad A_{02} = S/a^2,$$

so using S for A_{ref} the only non-vanishing λ_{mn} and μ_{mn} are

$$\lambda_{20} = 1 \quad \text{and} \quad \lambda_{02} = 1.$$

Then, by solving System III A (using the corrected $K_{6,6} = -[6(1-\nu)+\nu]15\pi/16$),

$$\alpha_{20} = -\frac{2}{15\pi}, \quad \alpha_{02} = -\frac{2}{15\pi(1-\nu)}, \quad \text{and} \quad \beta_{11} = \frac{2\nu}{15\pi(1-\nu)}.$$

(These values would have been more complicated without the correction to $K_{6,6}$.)

Then from System I B, temporarily using $K_{1,4} = [4(1-\nu)+\kappa\nu]3\pi/4$ with an unspecified constant κ , one finds

$$\alpha_{00} = -\frac{8+(\kappa-3)\nu}{20\pi(2-\nu)}.$$

These constants imply that the stress intensity factors K_{II} and K_{III} are

$$\frac{K_{\text{II}}}{\sqrt{\pi a}} = -\frac{8(5-\nu)+3\nu(\kappa-3)}{15\pi(2-\nu)} \cos \varphi, \quad \frac{K_{\text{III}}}{\sqrt{\pi a}} = \frac{8(5-4\nu)+3\nu(1-\nu)(\kappa-3)}{15\pi(2-\nu)} \sin \varphi. \quad (\text{F-29})$$

By using Bell's theory to get stress intensity factors from this same load, one finds expressions exactly like these become by putting $\kappa = 3$. Thus the value for $K_{1,4}$ derived from Smith and Sorenson's formulas has been vindicated by this test, but the value of $K_{11,16}$ has been disproved.

Identification of a correction for $K_{11,16}$ is not a simple matter. Multiplication of its C' by 3 to give the required $K_{11,16}$ for $k = 0$ would produce a unique irregularity in the table for C' , and infusion of a factor 3 in M_4 would produce havoc in the table for C' . A rederivation of a general expression for $K_{11,16}$ by the methods used by Smith and Sorenson would be very laborious, as indeed their original effort was. Nevertheless, some resolution of the mistake in $K_{11,16}$ is needed unless one agrees to avoid considering loads which would involve use of Systems III B and I B.

Some hope for resolution of this impasse can be sought in the possibility that for $K_{11,16}$ the given value of q is in error, so that perhaps some M_p other than M_4 should be used in its place. Among the 24 functions M_p used here, two assume values as $k \rightarrow 0$ which would yield the right limiting value for $K_{11,16}$ as $k \rightarrow 0$. These two are M_{14} and M_{15} , but again it is not clear which of these would be better or whether some unlisted M_p is needed.

A choice of a replacement for M_4 in $K_{11,16}$ should be made in a larger context than cases with $k = 0$, since the function should serve for all values of k , and differing M_p 's need not vary proportionately as k varies. Therefore, it is helpful to observe in Table F-1 that there is much repetition among the $K_{i,j}$. Thus, for example, $K_{2,7} = K_{3,8} = K_{4,6} = K_{5,5} = K_{6,4}$, since all have $p = 7$, $q = 8$, and $B' = C' = 1$. One may also gratefully observe that the five $K_{i,j}$ symmetric to these for the circular case are $K_{13,18}$, $K_{12,17}$, $K_{16,14}$, $K_{15,15}$ and $K_{14,16}$ which are equal to each other since all have $p = 7$, $q = 9$ and $B' = C' = 1$. Employing the corrections for the $K_{i,j}$ already proposed, this pattern of equalities among $K_{i,j}$'s which correspond in the symmetry to other $K_{i,j}$'s equivalent to each other in Table 1 is a widespread pattern in that table. Indeed it is universal if $q = 15$ for $K_{11,16}$, since then $K_{11,16} \equiv K_{13,13}$ as is commended for these two $K_{i,j}$'s because of their respective symmetries to $K_{1,4}$ and $K_{2,2}$ which are identical to each other.

From the above observations, it is therefore recommended that the following changes should be made in the the Smith and Sorenson formulas:

1. In β_{27} for M_{27} , change the sign of $-2k^2$ to + (as Sorenson agreed).
2. Reverse the sign of A for $K_{16,16}$.
3. Reverse the sign of B for $K_{17,19}$.
4. Reverse the sign of C for $K_{6,6}$.
5. Multiply C for $K_{2,2}$ by 3.
6. Multiply C for $K_{13,13}$ by 3.
7. In $K_{11,16}$, replace M_4 by M_{15} , that is put $q = 15$.

To justify these changes fully for the general elliptical crack, one should rederive the formulas for the $K_{i,j}$ (and hence the $K_{i,j}$), probably by redoing Smith and Sorenson's work. That, however, would be a major effort, too large for the present circumstances.

Using these changes to correct the $K_{i,j}$ for the circular crack, one obtains equations which can be solved algebraically for all the α_{mn} and β_{mn} in terms of the dimensionless load constants λ_{mn} and μ_{mn} . The solutions are

$$\begin{aligned}
 \alpha_{00} &= -\frac{1}{2\pi(2-\nu)} \left[\lambda_{00} + \frac{2}{5}(\lambda_{20} + \lambda_{02}) \right], \\
 \alpha_{10} &= \frac{1}{6\pi(2-\nu)} \left\{ (4-\nu) \left[\lambda_{10} + \frac{3}{7}(\lambda_{12} + \lambda_{30}) \right] - \nu \left[\mu_{01} + \frac{3}{7}(\mu_{21} + \mu_{03}) \right] \right\}, \\
 \alpha_{01} &= \frac{1}{6\pi(1-\nu)(2-\nu)} \left\{ (4-3\nu) \left[\lambda_{01} + \frac{3}{7}(\lambda_{21} + \lambda_{03}) \right] - \nu \left[\mu_{10} + \frac{3}{7}(\mu_{12} + \mu_{03}) \right] \right\}, \\
 \alpha_{20} &= \frac{2}{15\pi(2-\nu)} \left[-(3-\nu)\lambda_{20} + \lambda_{02} + \nu\mu_{11} \right], \\
 \alpha_{11} &= \frac{2}{15\pi(1-\nu)(2-\nu)} \left[-(8-8\nu+\nu^2)\lambda_{11} + \nu\mu_{20} + \nu(1-\nu)\mu_{02} \right], \\
 \alpha_{02} &= \frac{2}{15\pi(1-\nu)(2-\nu)} \left[(1-\nu)\lambda_{20} - (3-2\nu)\lambda_{02} + \nu\mu_{11} \right], \\
 \alpha_{30} &= \frac{1}{35\pi(2-\nu)} \left[-(8-\nu)\lambda_{12} + (8-3\nu)\lambda_{30} - 3\nu\mu_{21} + \nu\mu_{03} \right], \\
 \alpha_{21} &= \frac{1}{35\pi(1-\nu)(2-\nu)} \left[(40-45\nu+8\nu^2)\lambda_{21} - (8-7\nu)\lambda_{03} - \nu(7-8\nu)\mu_{12} - 3\nu\mu_{30} \right], \\
 \alpha_{12} &= \frac{1}{35\pi(1-\nu)(2-\nu)} \left[(40-35\nu+3\nu^2)\lambda_{12} - (1-\nu)(8-\nu)\lambda_{30} - \nu(7+\nu)\mu_{21} - 3\nu(1-\nu)\mu_{03} \right], \\
 \alpha_{03} &= \frac{1}{35\pi(1-\nu)(2-\nu)} \left[-(8-7\nu)\lambda_{21} + (8-5\nu)\lambda_{03} - 3\nu\mu_{12} + \nu\mu_{30} \right]; \\
 \beta_{00} &= -\frac{1}{2\pi(2-\nu)} \left[\mu_{00} + \frac{2}{5}(\mu_{20} + \mu_{02}) \right], \\
 \beta_{10} &= \frac{1}{6\pi(1-\nu)(2-\nu)} \left\{ -\nu \left[\lambda_{01} + \frac{3}{7}(\lambda_{21} + \lambda_{03}) \right] + (4-3\nu) \left[\mu_{10} + \frac{3}{7}(\mu_{12} + \mu_{30}) \right] \right\}, \\
 \beta_{01} &= \frac{1}{6\pi(2-\nu)} \left\{ -\nu \left[\lambda_{10} + \frac{3}{7}(\lambda_{12} + \lambda_{30}) \right] + (4-\nu) \left[\mu_{01} + \frac{3}{7}(\mu_{21} + \mu_{03}) \right] \right\}, \\
 \beta_{20} &= \frac{2}{15\pi(1-\nu)(2-\nu)} \left[\nu\lambda_{11} - (3-2\nu)\mu_{20} + (1-\nu)\mu_{02} \right], \\
 \beta_{11} &= \frac{2}{15\pi(1-\nu)(2-\nu)} \left[\nu(1-\nu)\lambda_{20} + \nu\lambda_{02} - (8-8\nu+\nu^2)\mu_{11} \right], \\
 \beta_{02} &= \frac{2}{15\pi(2-\nu)} \left[\nu\lambda_{11} + \mu_{20} - (3-\nu)\mu_{02} \right], \\
 \beta_{30} &= \frac{1}{35\pi(1-\nu)(2-\nu)} \left[-3\nu\lambda_{21} + \nu\lambda_{03} - (8-7\nu)\mu_{12} + (8-5\nu)\mu_{30} \right], \\
 \beta_{21} &= \frac{1}{35\pi(1-\nu)(2-\nu)} \left[-\nu(7+\nu)\lambda_{12} - 3\nu(1-\nu)\lambda_{30} + (40-35\nu+3\nu^2)\mu_{21} - (1-\nu)(8-\nu)\mu_{03} \right], \\
 \beta_{12} &= \frac{1}{35\pi(1-\nu)(2-\nu)} \left[-\nu(7-8\nu)\lambda_{21} - 3\nu\lambda_{03} + (40-45\nu+8\nu^2)\mu_{12} - (8-7\nu)\mu_{30} \right], \\
 \beta_{03} &= \frac{1}{35\pi(2-\nu)} \left[-3\nu\lambda_{12} + \nu\lambda_{30} - (8-\nu)\mu_{21} + (8-3\nu)\mu_{03} \right].
 \end{aligned} \tag{F-30}$$

These algebraic solutions for the stress function constants α_{mn} and β_{mn} for the circular crack are based on $K_{i,j}$ including the corrections already suggested so that

$$\begin{aligned} K_{17,19} &= [8(1-\nu) + 3\nu] 35\pi/128, \\ K_{6,6} &= - [6(1-\nu) + \nu] 15\pi/16, \quad K_{16,16} = - [6(1-\nu) + 5\nu] 15\pi/16, \\ K_{2,2} &= K_{13,13} = [16(1-\nu) + 12\nu] 3\pi/16, \\ K_{11,16} &= [4(1-\nu) + 3\nu] 3\pi/4. \end{aligned} \tag{F-31}$$

Further changes in the $K_{i,j}$ would alter at least some of these solutions, but it can be seen that these solutions exhibit the kind of symmetry that was demanded during the examination of the coefficients $K_{i,j}$. Therefore, a need for further corrections seems unlikely. Viewing them, one may speculate too on how complex the algebraic solutions would be for cases with non-zero k . For that more general case, the complexity of the solutions should be several times greater, since it would involve at least the five functions $F_i(k)$. One might pursue this analysis for the circular crack further by making a parametric study of how stress intensity factors vary with particular load constants, but before doing that one should consider that the alternate Bell theory treats a much wider variety of loads. (The limitation of the Bell theory is that it refers simply to a circular crack, not to elliptical cracks generally, but the loads there may have arbitrarily high order.)

The importance of the results given here for the circular crack is that they show so conclusively that there are non-trivial errors in the formulas Smith and Sorenson reported, and that they provide plausible corrections for them. They also reveal previously hidden order in the formulas which makes comparison with other analysis possible. Consideration of the corrections in the larger context of general elliptical cracks, however, still remains appropriate.

Evaluation of Effects from Shear Loads on Elliptical Cracks

General Solution for Stress Function Constants The reorganized formulas shown above as Systems IVA to IB provide an improved opportunity to solve for the stress function constants α_{mn} and β_{mn} needed in determining the coefficients for the stress intensity factors K_{II} and K_{III} . In showing this, note first that the determinants for the two fourth order systems are

$$\Delta_{4A} \equiv \begin{vmatrix} K_{7,7} & K_{7,9} & K_{7,18} & K_{7,20} \\ K_{9,7} & K_{9,9} & K_{9,18} & K_{9,20} \\ K_{18,7} & K_{18,9} & K_{18,18} & K_{18,20} \\ K_{20,7} & K_{20,9} & K_{20,18} & K_{20,20} \end{vmatrix}, \text{ and } \Delta_{4B} \equiv \begin{vmatrix} K_{8,8} & K_{8,10} & K_{8,17} & K_{8,19} \\ K_{10,8} & K_{10,10} & K_{10,17} & K_{10,19} \\ K_{17,8} & K_{17,10} & K_{17,17} & K_{17,19} \\ K_{19,8} & K_{19,10} & K_{19,17} & K_{19,19} \end{vmatrix}, \quad (F-32)$$

and denote cofactors of the elements $K_{i,j}$ of these determinants respectively as $C_{i,j}^{4A}$ or $C_{i,j}^{4B}$, so that for example

$$C_{9,7}^{4A} \equiv \begin{vmatrix} K_{7,9} & K_{7,18} & K_{7,20} \\ K_{18,9} & K_{18,18} & K_{18,20} \\ K_{20,9} & K_{20,18} & K_{20,20} \end{vmatrix}, \text{ and } C_{17,10}^{4B} \equiv \begin{vmatrix} K_{8,8} & K_{8,17} & K_{8,19} \\ K_{10,8} & K_{10,17} & K_{10,19} \\ K_{19,8} & K_{19,17} & K_{19,19} \end{vmatrix}. \quad (F-33)$$

Then the solutions for the α_{mn} and β_{mn} appearing in Systems IVA and IVB are:

$$\begin{aligned} \alpha_{12} &= [C_{7,7}^{4A} \lambda_{12} - C_{9,7}^{4A} \lambda_{30} + C_{18,7}^{4A} \mu_{21} - C_{20,7}^{4A} \mu_{03}] / \Delta_{4A}, \\ \alpha_{30} &= [-C_{7,9}^{4A} \lambda_{12} + C_{9,9}^{4A} \lambda_{30} - C_{18,9}^{4A} \mu_{21} + C_{20,9}^{4A} \mu_{03}] / \Delta_{4A}, \\ \beta_{21} &= [C_{7,18}^{4A} \lambda_{12} - C_{9,18}^{4A} \lambda_{30} + C_{18,18}^{4A} \mu_{21} - C_{20,18}^{4A} \mu_{03}] / \Delta_{4A}, \\ \beta_{03} &= [-C_{7,20}^{4A} \lambda_{12} + C_{9,20}^{4A} \lambda_{30} - C_{18,20}^{4A} \mu_{21} + C_{20,20}^{4A} \mu_{03}] / \Delta_{4A}, \end{aligned}$$

and

$$\begin{aligned} \alpha_{21} &= [C_{8,8}^{4B} \lambda_{21} - C_{10,8}^{4B} \lambda_{03} + C_{17,8}^{4B} \mu_{12} - C_{19,8}^{4B} \mu_{30}] / \Delta_{4B}, \\ \alpha_{03} &= [-C_{8,10}^{4B} \lambda_{21} + C_{10,10}^{4B} \lambda_{03} + C_{17,10}^{4B} \mu_{12} + C_{19,10}^{4B} \mu_{30}] / \Delta_{4B}, \\ \beta_{12} &= [C_{8,17}^{4B} \lambda_{21} - C_{10,17}^{4B} \lambda_{03} + C_{17,17}^{4B} \mu_{12} - C_{19,17}^{4B} \mu_{30}] / \Delta_{4B}, \\ \beta_{30} &= [-C_{8,19}^{4B} \lambda_{21} + C_{10,19}^{4B} \lambda_{03} - C_{17,19}^{4B} \mu_{12} + C_{19,19}^{4B} \mu_{30}] / \Delta_{4B}. \end{aligned} \quad (F-34)$$

Similarly, for Systems III A and III B, note that their determinants are

$$\Delta_{3A} \equiv \begin{vmatrix} K_{4,4} & K_{4,6} & K_{4,15} \\ K_{6,4} & K_{6,6} & K_{6,15} \\ K_{15,4} & K_{15,6} & K_{15,15} \end{vmatrix}, \text{ and } \Delta_{3B} \equiv \begin{vmatrix} K_{5,5} & K_{5,14} & K_{5,16} \\ K_{14,5} & K_{14,14} & K_{14,16} \\ K_{16,5} & K_{16,14} & K_{16,16} \end{vmatrix}, \quad (\text{F-35})$$

and let the cofactors of the elements $K_{i,j}$ in these determinants be denoted as $C_{i,j}^{3A}$ and $C_{i,j}^{3B}$ respectively. Then the solutions for the α_{mn} and β_{mn} appearing in the Systems III A and III B are:

$$\begin{aligned} \alpha_{20} &= \left[C_{4,4}^{3A} \lambda_{20} - C_{6,4}^{3A} \lambda_{02} + C_{15,4}^{3A} \mu_{11} \right] / \Delta_{3A}, \\ \alpha_{02} &= \left[-C_{4,6}^{3A} \lambda_{20} + C_{6,6}^{3A} \lambda_{02} - C_{15,6}^{3A} \mu_{11} \right] / \Delta_{3A}, \\ \beta_{11} &= \left[C_{4,15}^{3A} \lambda_{20} - C_{6,15}^{3A} \lambda_{02} + C_{15,15}^{3A} \mu_{11} \right] / \Delta_{3A}, \end{aligned}$$

and

(F-36)

$$\begin{aligned} \alpha_{11} &= \left[C_{5,5}^{3B} \lambda_{11} - C_{14,5}^{3B} \mu_{20} + C_{16,5}^{3B} \mu_{02} \right] / \Delta_{3B}, \\ \beta_{20} &= \left[-C_{5,14}^{3B} \lambda_{11} + C_{14,14}^{3B} \mu_{20} - C_{16,14}^{3B} \mu_{02} \right] / \Delta_{3B}, \\ \beta_{02} &= \left[C_{5,16}^{3B} \lambda_{11} - C_{14,16}^{3B} \mu_{20} + C_{16,16}^{3B} \mu_{02} \right] / \Delta_{3B}. \end{aligned}$$

The general algebraic solutions for Systems II A and II B are complicated by the appearance in the right hand members of constants obtained by solving Systems IVA and IVB. Nevertheless, it is possible to formulate general solutions conveniently using the following second order determinants:

$$D_j^{A1} = \begin{vmatrix} K_{2,j} & K_{2,13} \\ K_{13,j} & K_{13,3} \end{vmatrix} \text{ and } D_j^{A2} = \begin{vmatrix} K_{2,2} & K_{2,j} \\ K_{13,2} & K_{13,j} \end{vmatrix} \text{ for } j=7, 9, 18, 20,$$

(F-37)

and

$$D_j^{B1} = \begin{vmatrix} K_{3,j} & K_{3,12} \\ K_{12,j} & K_{12,12} \end{vmatrix} \text{ and } D_j^{B2} = \begin{vmatrix} K_{3,3} & K_{3,j} \\ K_{12,3} & K_{12,j} \end{vmatrix} \text{ for } j=8, 10, 17, 19.$$

Then the solutions for the constants α_{mn} and β_{mn} appearing in Systems II A and II B can be expressed as follows:

$$\alpha_{10} = (K_{13,13}^{\lambda} 10 - K_{2,13}^{\mu} 01) / \Delta_{2A}$$

$$- \frac{1}{\Delta_{2A} \Delta_{4A}} \left[\lambda_{12} \left(D_7^{A1} C_{7,7}^{4A} - D_9^{A1} C_{7,9}^{4A} + D_{18}^{A1} C_{7,18}^{4A} - D_{20}^{A1} C_{7,20}^{4A} \right) \right. \\ \left. + \lambda_{30} \left(-D_7^{A1} C_{9,7}^{4A} + D_9^{A1} C_{9,9}^{4A} - D_{18}^{A1} C_{9,18}^{4A} + D_{20}^{A1} C_{9,20}^{4A} \right) \right. \\ \left. + \mu_{21} \left(D_7^{A1} C_{18,7}^{4A} - D_9^{A1} C_{18,9}^{4A} + D_{18}^{A1} C_{18,18}^{4A} - D_{20}^{A1} C_{18,20}^{4A} \right) \right. \\ \left. + \mu_{03} \left(-D_7^{A1} C_{20,7}^{4A} + D_9^{A1} C_{20,9}^{4A} - D_{18}^{A1} C_{20,18}^{4A} + D_{20}^{A1} C_{20,20}^{4A} \right) \right],$$

$$\beta_{01} = (-K_{13,2}^{\lambda} 10 + K_{2,2}^{\mu} 01) / \Delta_{2A}$$

$$- \frac{1}{\Delta_{2A} \Delta_{4A}} \left[\lambda_{12} \left(D_7^{A2} C_{7,7}^{4A} - D_9^{A2} C_{7,9}^{4A} + D_{18}^{A2} C_{7,18}^{4A} - D_{20}^{A2} C_{7,20}^{4A} \right) \right. \\ \left. + \lambda_{30} \left(-D_7^{A2} C_{9,7}^{4A} + D_9^{A2} C_{9,9}^{4A} - D_{18}^{A2} C_{9,18}^{4A} + D_{20}^{A2} C_{9,20}^{4A} \right) \right. \\ \left. + \mu_{21} \left(D_7^{A2} C_{18,7}^{4A} - D_9^{A2} C_{18,9}^{4A} + D_{18}^{A2} C_{18,18}^{4A} - D_{20}^{A2} C_{18,20}^{4A} \right) \right. \\ \left. + \mu_{03} \left(-D_7^{A2} C_{20,7}^{4A} + D_9^{A2} C_{20,9}^{4A} - D_{18}^{A2} C_{20,18}^{4A} + D_{20}^{A2} C_{20,20}^{4A} \right) \right],$$

$$\alpha_{01} = (K_{12,12}^{\lambda} 01 - K_{3,12}^{\mu} 10) / \Delta_{2B} \quad (F-38)$$

$$- \frac{1}{\Delta_{2B} \Delta_{4B}} \left[\lambda_{21} \left(D_8^{B1} C_{8,8}^{4B} - D_{10}^{B1} C_{8,10}^{4B} + D_{17}^{B1} C_{8,17}^{4B} - D_{19}^{B1} C_{8,19}^{4B} \right) \right. \\ \left. + \lambda_{03} \left(-D_8^{B1} C_{10,8}^{4B} + D_{10}^{B1} C_{10,10}^{4B} - D_{17}^{B1} C_{10,17}^{4B} + D_{19}^{B1} C_{10,19}^{4B} \right) \right. \\ \left. + \mu_{12} \left(D_8^{B1} C_{17,8}^{4B} - D_{10}^{B1} C_{17,10}^{4B} + D_{17}^{B1} C_{17,17}^{4B} - D_{19}^{B1} C_{17,19}^{4B} \right) \right. \\ \left. + \mu_{30} \left(-D_8^{B1} C_{19,8}^{4B} + D_{10}^{B1} C_{19,10}^{4B} - D_{17}^{B1} C_{19,17}^{4B} + D_{19}^{B1} C_{19,19}^{4B} \right) \right],$$

$$\beta_{10} = (-K_{12,3}^{\lambda} 10 + K_{3,3}^{\mu} 10) / \Delta_{2B}$$

$$- \frac{1}{\Delta_{2B} \Delta_{4B}} \left[\lambda_{21} \left(D_8^{B2} C_{8,8}^{4B} - D_{10}^{B2} C_{8,10}^{4B} + D_{17}^{B2} C_{8,17}^{4B} - D_{19}^{B2} C_{8,19}^{4B} \right) \right. \\ \left. + \lambda_{03} \left(-D_8^{B2} C_{10,8}^{4B} + D_{10}^{B2} C_{10,10}^{4B} - D_{17}^{B2} C_{10,17}^{4B} + D_{19}^{B2} C_{10,19}^{4B} \right) \right. \\ \left. + \mu_{12} \left(D_8^{B2} C_{17,8}^{4B} - D_{10}^{B2} C_{17,10}^{4B} + D_{17}^{B2} C_{17,17}^{4B} - D_{19}^{B2} C_{17,19}^{4B} \right) \right. \\ \left. + \mu_{30} \left(-D_8^{B2} C_{19,8}^{4B} + D_{10}^{B2} C_{19,10}^{4B} - D_{17}^{B2} C_{19,17}^{4B} + D_{19}^{B2} C_{19,19}^{4B} \right) \right].$$

Finally, the solutions for α_{00} and β_{00} from Systems IA and IB are:

$$\alpha_{00} = \frac{1}{K_{1,1}} \left[\lambda_{00} - \lambda_{20} (K_{1,4} C_{4,4}^{3A} - K_{1,6} C_{4,6}^{3A} + K_{1,15} C_{4,15}^{3A}) / \Delta_{3A} \right. \\ \left. + \lambda_{02} (K_{1,4} C_{6,4}^{3A} - K_{1,6} C_{6,6}^{3A} + K_{1,15} C_{6,15}^{3A}) / \Delta_{3A} \right. \\ \left. - \mu_{11} (K_{1,4} C_{15,4}^{3A} - K_{1,6} C_{15,6}^{3A} + K_{1,15} C_{15,15}^{3A}) / \Delta_{3A} \right], \quad (F-39)$$

$$\beta_{00} = \frac{1}{K_{11,11}} \left[\mu_{00} - \lambda_{11} (K_{11,5} C_{5,5}^{3B} - K_{11,14} C_{5,14}^{3B} + K_{11,16} C_{5,16}^{3B}) / \Delta_{3B} \right. \\ \left. + \mu_{20} (K_{11,5} C_{14,5}^{3B} - K_{11,14} C_{14,14}^{3B} + K_{11,16} C_{14,16}^{3B}) / \Delta_{3B} \right. \\ \left. - \mu_{02} (K_{11,5} C_{16,5}^{3B} - K_{11,14} C_{16,14}^{3B} + K_{11,16} C_{16,16}^{3B}) / \Delta_{3B} \right].$$

These solutions for the 20 stress function constants α_{mn} and β_{mn} show directly their dependence on the 20 dimensionless load constants λ_{mn} using coefficients which depend only on the eccentricity ratio k and on ν . Of course, those coefficients are highly dependent on the functions $K_{i,j}$, and since the $K_{i,j}$ have been the subject of corrections, it is well to restate what their values are taken to be. Two effects of the corrections are that C' (of Table F-1) becomes universally equal to unity; and $B' = 1$ unless there is no function M_p , in which case $B' = 0$. By adopting an extra function $M_0 \equiv 0$, the column specifying B' can be dropped. Thus the proposed corrections imply that

$$K_{1,j} = (1-\nu)M_p + \nu k^r M_q, \quad \text{with } r = \delta_0^p + \ell', \quad (F-40)$$

where

$$\delta_0^p = \begin{cases} 1 & \text{if } p = 0 \\ 0 & \text{if } p \neq 0 \end{cases}, \quad \text{and}$$

$$\ell' = \begin{cases} 2 & \text{if } (p,q) = (6,4), (7,8), (11,9), (22,20), (27,18) \text{ or } (28,19) \\ 0 & \text{for all other pairs } (p,q) \end{cases},$$

with the values of p and q (and the consequent r) as shown in Table F-2.

TABLE F-2. COEFFICIENTS FOR REVISED FUNCTIONS $K_{i,j}$ (After Correction)

i,j	p	q	r	i,j	p	q	r
1,1	3	1	0	11,5	0	4	1
1,4	5	14	0	11,11	3	2	0
1,6	6	4	2	11,14	5	4	0
1,15	0	4	1	11,16	6	15	0
2,2	5	14	0	12,3	0	4	1
2,7	7	8	2	12,8	0	8	1
2,9	10	16	0	12,10	0	9	1
2,13	0	4	1	12,12	5	4	0
2,18	0	8	1	12,17	7	9	0
2,20	0	9	1	12,19	10	8	0
3,3	6	4	2	13,2	0	4	1
3,8	7	8	2	13,7	0	9	1
3,10	11	9	2	13,9	0	8	1
3,12	0	4	1	13,13	6	15	0
3,17	0	9	1	13,18	7	9	0
3,19	0	8	1	13,20	11	17	0
4,4	10	16	0	14,5	0	8	1
4,6	7	8	2	14,14	10	8	0
4,15	0	8	1	14,16	7	9	0
5,5	7	8	2	15,4	0	8	1
5,14	0	8	1	15,6	0	9	1
5,16	0	9	1	15,15	7	9	0
6,4	7	8	2	16,5	0	9	1
6,6	11	9	2	16,14	7	9	0
6,15	0	9	1	16,16	11	17	0
7,7	28	19	2	17,8	0	19	1
7,9	27	18	2	17,10	0	20	1
7,18	0	19	1	17,17	28	20	0
7,20	0	20	1	17,19	27	19	0
8,8	27	18	2	18,7	0	19	1
8,10	28	19	2	18,9	0	18	1
8,17	0	19	1	18,18	27	19	0
8,19	0	18	1	18,20	28	20	0
9,7	27	18	2	19,8	0	18	1
9,9	21	29	0	19,10	0	19	1
9,18	0	18	1	19,17	27	19	0
9,20	0	19	1	19,19	21	18	0
10,8	28	19	2	20,7	0	20	1
10,10	22	20	2	20,9	0	19	1
10,17	0	20	1	20,18	28	20	0
10,19	0	19	0	20,20	22	25	0

An implication of the above definitions and corrections is that

$$D_{17}^{B1} + D_{19}^{B1} \equiv \left| \begin{array}{c} (K_{3,17} + K_{3,19}) K_{3,12} \\ (K_{12,17} + K_{12,19}) K_{12,12} \end{array} \right| \equiv 0, \text{ and } D_8^{B2} + D_{10}^{B2} \equiv \left| \begin{array}{c} K_{3,3} (K_{3,3} + K_{3,10}) \\ K_{12,3} (K_{12,3} + K_{12,10}) \end{array} \right| \equiv 0, \quad (F-41)$$

as pursuit of the algebra shows. These relations pertaining to Systems IV B and II B have corresponding relations pertaining to Systems IV B and II B, namely

$$D_{18}^{A1} + D_{20}^{A1} \equiv \left| \begin{array}{c} (K_{2,18} + K_{2,20}) K_{2,13} \\ (K_{13,18} + K_{13,20}) K_{13,13} \end{array} \right| \equiv 0, \text{ and } D_7^{A2} + D_9^{A2} \equiv \left| \begin{array}{c} K_{2,2} (K_{2,7} + K_{2,9}) \\ K_{13,2} (K_{13,7} + K_{13,9}) \end{array} \right| \equiv 0, \quad (F-42)$$

as pursuit of algebra again shows, using the demonstrable relation that

$$2k^2 F_4 = 4F_1 + 2F_2 + 8F_3.$$

This symmetry among four vanishing sums of D's commends the correction applied to $K_{2,2}$ and $K_{13,13}$, which is the tripling of Smith and Sorenson's C. It does this for all values of k, not simply for the circle which has $k = 0$.

Illustrative Calculations for an Elliptical Crack To illustrate

calculations for a non circular crack, consider one with $k' = b/a = 0.5$. For it $k = \sqrt{3}/2$, so that $K(k) = 2.156515648$, $E(k) = 1.211056028$, and then

$$F_1(k) = 1.211056028, \quad F_2(k) = -0.8959028213, \quad F_3(k) = -0.7743328196,$$

$$F_4(k) = -2.094829391, \quad F_5(k) = 1.670836478.$$

Then the M 's become

$M_1 = -2.521225654$	$M_9 = -3.553669414$	$M_{19} = 3.341672956$
$M_2 = -7.167222570$	$M_{10} = -10.66100824$	$M_{20} = 4.950222343$
$M_3 = -9.688448224$	$M_{11} = -16.46850438$	$M_{21} = 19.92546355$
$M_4 = 3.097331278$	$M_{14} = 3.007505660$	$M_{22} = 32.64086965$
$M_5 = 6.104836939$	$M_{15} = 7.653502577$	$M_{25} = 31.40331406$
$M_6 = 8.427835397$	$M_{16} = -15.58008703$	$M_{27} = 4.950222340$
$M_7 = -4.601084109$	$M_{17} = 6.434197535$	$M_{28} = 5.785640580$
$M_8 = -4.189658782$	$M_{18} = 3.341672956$	$M_{29} = 13.49126601.$

In Table F-2, many pairings of M_p and M_q are repeated for two or more $K_{i,j}$, and with all such repetitions the value for r is also repeated. Thus among the 82 non-zero $K_{i,j}$, there are only 26 different values. The value derived for each combination (p,q) and the functions $K_{i,j}$ it represents are shown in the following list, presuming that $\nu = 0.3$.

(p,q)	$(1-\nu)M_p + \nu k^T M_q$	$K_{i,j}$ represented
(3,1)	-7.538281453	$= K_{1,1}$
(3,2)	-8.932080528	$= K_{11,11}$
(0,4)	0.4645996917	$= K_{1,15} = K_{2,13} = K_{3,12} = K_{11,5} = K_{12,3} = K_{13,2}$
(5,4)	5.202585241	$= K_{11,14} = K_{12,12}$
(6,4)	6.131784624	$= K_{1,6} = K_{3,3}$
(0,8)	-0.6284488173	$= K_{2,18} = K_{3,19} = K_{4,15} = K_{5,14} = K_{12,8} = K_{13,9} = K_{14,5} = K_{15,4}$
(7,8)	-3.534983285	$= K_{2,7} = K_{3,8} = K_{4,6} = K_{5,5} = K_{6,4}$
(10,8)	-8.719603403	$= K_{12,19} = K_{14,14}$
(0,9)	-0.5330504121	$= K_{2,20} = K_{3,17} = K_{5,16} = K_{6,15} = K_{12,10} = K_{13,7} = K_{15,6} = K_{16,5}$
(7,9)	-4.286859701	$= K_{12,17} = K_{13,18} = K_{14,16} = K_{15,15} = K_{16,14}$
(11,9)	-11.79447827	$= K_{3,10} = K_{6,6}$
(5,14)	5.175637555	$= K_{1,4} = K_{2,2}$
(6,15)	8.195535551	$= K_{11,16} = K_{13,13}$
(10,16)	-9.404110605	$= K_{2,9} = K_{4,4}$
(11,17)	-16.20197918	$= K_{13,20} = K_{16,16}$
(0,18)	0.9651296303	$= K_{8,19} = K_{9,18} = K_{18,9} = K_{19,8}$
(21,18)	15.87808375	$= K_{19,19}$
(27,18)	3.947720453	$= K_{7,9} = K_{8,8} = K_{9,7}$
(0,19)	0.5012509434	$= K_{7,18} = K_{8,17} = K_{9,20} = K_{10,19} = K_{17,8} = K_{18,7} = K_{19,10} = K_{20,9}$
(27,19)	4.467657525	$= K_{17,19} = K_{18,18} = K_{19,17}$
(28,19)	4.300573878	$= K_{7,7} = K_{8,10} = K_{10,8}$
(0,20)	0.7425333515	$= K_{7,20} = K_{10,17} = K_{17,10} = K_{20,7}$
(22,20)	23.21987543	$= K_{10,10}$
(28,20)	5.535015109	$= K_{17,17} = K_{18,20} = K_{20,18}$
(22,25)	32.26960297	$= K_{20,20}$
(21,29)	17.99520429	$= K_{9,9}$

(F-44)

These $K_{i,j}$ depend solely on k' and ν , not on loads, but they determine how α_{mn} and β_{mn} depend on any crack loads λ_{mn} and μ_{mn} . Thus from System IVA:

$$\alpha_{12} = 0.29302716\lambda_{12} - 0.06337514\lambda_{30} - 0.01530385\mu_{21} - 0.00313324\mu_{03},$$

$$\alpha_{30} = -0.06337514\lambda_{12} + 0.06998841\lambda_{30} - 0.01075395\mu_{21} + 0.00221570\mu_{03},$$

$$\beta_{21} = -0.01530385\lambda_{12} - 0.01075395\lambda_{30} + 0.28854426\mu_{21} - 0.04897311\mu_{03},$$

$$\beta_{03} = -0.00313324\lambda_{12} + 0.00221570\lambda_{30} - 0.04897311\mu_{21} + 0.03942666\mu_{03}.$$

From System IV B:

$$\alpha_{21} = 0.32258780\lambda_{21} - 0.05913049\lambda_{03} - 0.00900632\mu_{12} - 0.01520729\mu_{30},$$

$$\alpha_{03} = -0.05913049\lambda_{21} + 0.05409221\lambda_{03} - 0.00443076\mu_{12} + 0.00313325\mu_{30},$$

$$\beta_{12} = -0.00900632\lambda_{21} - 0.00443076\lambda_{03} + 0.23486398\mu_{12} - 0.06539698\mu_{30},$$

$$\beta_{30} = -0.01520729\lambda_{21} + 0.00313325\lambda_{03} - 0.06539698\mu_{12} + 0.08220625\mu_{30}.$$

From System III A:

$$\alpha_{20} = -0.12058230\lambda_{20} + 0.03554115\lambda_{02} + 0.01325786\mu_{11},$$

$$\alpha_{02} = 0.03554115\lambda_{20} - 0.09574022\lambda_{02} + 0.00669454\mu_{11},$$

(F-45)

$$\beta_{11} = 0.01325786\lambda_{20} + 0.00669454\lambda_{02} - 0.23604701\mu_{11}.$$

From System III B:

$$\alpha_{11} = -0.28685133\lambda_{11} + 0.01843213\mu_{20} + 0.00456057\mu_{02},$$

$$\beta_{20} = 0.01843213\lambda_{11} - 0.13301748\mu_{20} + 0.03458849\mu_{02},$$

$$\beta_{02} = 0.00456057\lambda_{11} + 0.03458849\mu_{20} - 0.07102262\mu_{02}.$$

Using results from Systems IVA and IV B, Systems II A and II B imply:

$$\alpha_{10} = 0.19420117\lambda_{10} + 0.08322907(\lambda_{12} + \lambda_{30}) - 0.01100914\mu_{01} - 0.00471820(\mu_{21} + \mu_{03}),$$

$$\beta_{01} = -0.01100914\lambda_{10} - 0.00471820(\lambda_{12} + \lambda_{30}) + 0.12264175\mu_{01} + 0.05256075(\mu_{21} + \mu_{03}),$$

$$\alpha_{01} = 0.16419566\lambda_{01} + 0.07036957(\lambda_{21} + \lambda_{03}) - 0.01466295\mu_{10} - 0.00628412(\mu_{12} + \mu_{30}),$$

$$\beta_{10} = -0.01466295\lambda_{01} - 0.00628412(\lambda_{21} + \lambda_{03}) + 0.19352156\mu_{10} + 0.08293781(\mu_{12} + \mu_{30}).$$

Using results from Systems III A and III B, Systems IA and IB imply:

$$\alpha_{00} = -0.13265623\lambda_{00} - 0.05306249(\lambda_{20} + \lambda_{02}) + 0.00000000\mu_{11},$$

$$\beta_{00} = 0.00000000\lambda_{11} - 0.11195600\mu_{00} - 0.04478240(\mu_{20} + \mu_{02}).$$

The many symmetries among the coefficients for these solutions for the stress function constants correspond to symmetries among coefficients in the systems of equations from which they were found, with those symmetries in turn coming from the many equalities among the $K_{1,j}$. The equality among pairs of coefficients in the solutions for α_{10} , β_{01} , α_{01} , β_{10} , α_{00} and β_{00} doubtlessly reflect some intrinsic order in the whole analysis, though that order is not now apparent in the formulas and does not appear in the arithmetic until almost the end of a long calculation. One other suggestive observation was that in solving Systems IA and IB the extended right-hand members of those equations were found to be

$$\lambda_{00} - K_{1,4}\alpha_{20} - K_{1,6}\alpha_{02} - K_{1,15}\beta_{11} = \lambda_{00} + 0.40000000(\lambda_{20} + \lambda_{02}) + 0.00000000\mu_{11},$$

and

$$\mu_{00} - K_{11,5}\alpha_{11} - K_{11,14}\beta_{20} - K_{11,16}\beta_{02} = \mu_{00} + 0.40000000(\mu_{20} + \mu_{02}) + 0.00000000\lambda_{11}. \quad (F-46)$$

These results too surely reflect inherent order in the overall analysis. Since all the corrections applied to Smith and Sorenson's formulas were used in obtaining these results, those corrections seem well vindicated.

With the solutions provided here for elliptical cracks with $k' = b/a = 0.5$ in a body with $\nu = 0.3$, it is now a simple matter to find the constants α_{mn} and β_{mn} for any given crack loads τ_{yx} and τ_{zx} represented in polynomial form including terms for which $0 \leq m+n \leq 3$. These constants in turn directly provide equations showing how stress intensity factors K_{II} and K_{III} vary along the crack front. Some information about how variation of the ratio k' ($= b/a$) would affect the solutions can be had by comparing results presuming $k' = 0.5$ with results for a circular crack ($k' = 1$) since solutions for a circular were presented above.

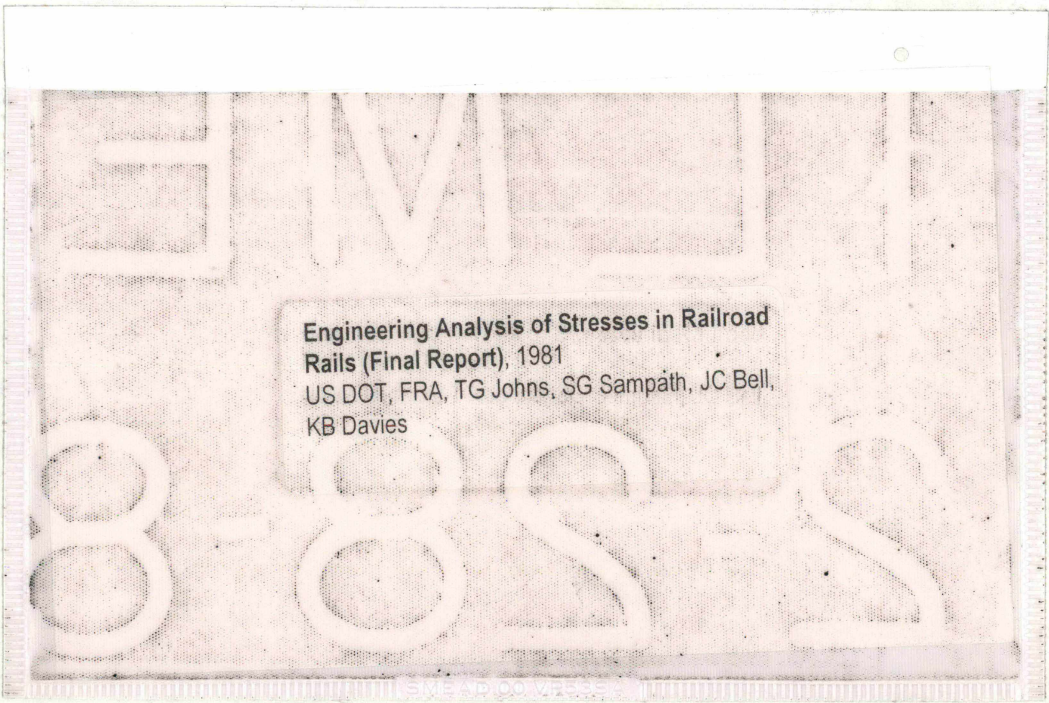
The solutions given here for α_{mn} and β_{mn} for the case with $k' = 0.5$ were used in the calculations for K_{II} and K_{III} reported in Chapter 5.

REFERENCES

- F-1. Shah, R. J., and Kobayashi, A. S., "Stress Intensity Factor for an Elliptical Crack Under Arbitrary Normal Loading", Eng. Frac. Mech., Vol. 3, (1971), p 71-96.
- F-2. Smith, F. W., and Sorenson, D. R., "Mixed Mode Stress Intensity Factors for Semielliptical Surface Cracks", Colorado State University Final Report for NASA, Grant NGL-06-002-063, (June 15, 1974).
- F-3. Smith, F. W., Emery, A. F., and Kobayashi, A. S., "Stress Intensity Factors for Semi-Circular Cracks, Part 2 - Semi-Infinite Solid", Trans. ASME, J. Appl. Mech., Vol. 34, (1967), p 953-959.
- F-4. Thresher, R. W., and Smith, F. W., "Stress Intensity Factors for a Surface Crack in a Finite Solid", Trans. ASME, J. Appl. Mech., Vol. 39, (1972), p 195-200.
- F-5. Raju, I. S., and Newman, J. C., Jr., "Improved Stress Intensity Factors for Semielliptical Surface Cracks in Finite Thickness Plates", NASA-TMX-72825, Langley Research Center, (May, 1977).
- F-6. Bell, J. C., "Stress Analysis for Structures with Surface Cracks", NASA CR-159400, Report to NASA-Lewis Research Center, from Battelle Columbus Laboratories under Contract No. NAS3-21020, (1978).
- F-7. Bell, J. C., "Stresses from Arbitrary Loads on a Circular Crack", Int. J. Fracture, Vol. 15, (1979), p 85-104.
- F-8. Bell, J. C., "Stresses from Various Loaded Circular Cracks", J. Struct. Div. Am. Soc. Civ. Engrs., Vol. 103, (1977), p 355-376.

APPENDIX G
REPORT OF NEW TECHNOLOGY

The work performed under this contract was an exploratory investigation into the stress patterns prevalent in existing railroad track. There were no new technologies developed as part of this effort.



**Engineering Analysis of Stresses in Railroad
Rails (Final Report), 1981**
US DOT, FRA, TG Johns, SG Sampath, JC Bell,
KB Davies

SMEAD 00 V2335

END

DATE

FILMED

12-28-81

NITIS

PROPERTY OF FRA
RESEARCH & DEVELOPMENT
LIBRARY